THIRD CONFERENCE ON

SONIC BOOM RESEARCH

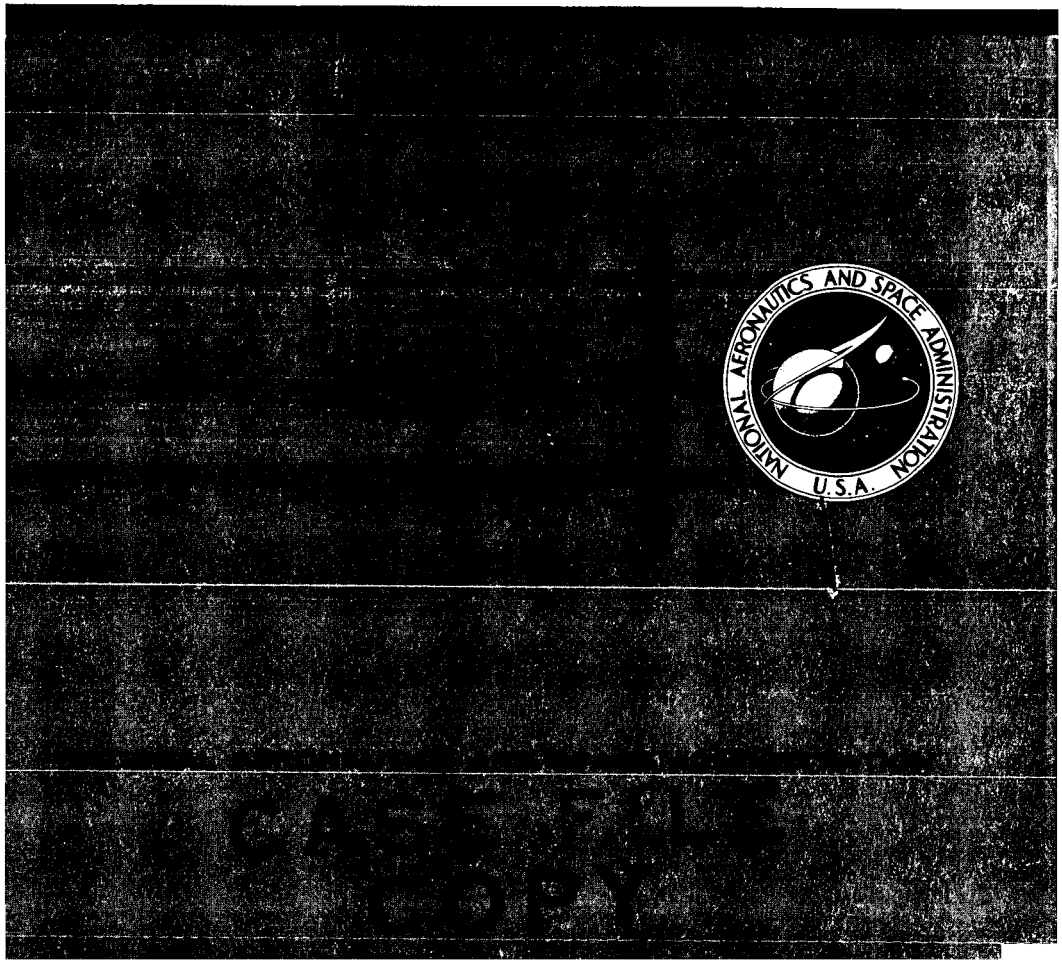

NASA SP-255

THIRD CONFERENCE ON SONIC BOOM RESEARCH

A conference held at NASA Headquarters, Washington, D.C., October 29-30, 1970

Edited by

IRA R. SCHWARTZ

Scientific and Technical Information Office 1971
NATIONAL AERONAUTICS AND SPACE ADMINISTRATION
Washington, D.C.

For sale by the Superintendent of Documents,
U.S. Government Printing Office, Washington, D.C. 20402
Price $2.00
Library of Congress Catalog Card Number 71–610001

Preface

The proceedings of the Third Conference on Sonic Boom Research, held at NASA Headquarters, Washington, D.C., on October 29 and 30, 1970, are reported in this NASA Special Publication. This conference was organized in the NASA Headquarters Office of Advanced Research and Technology and was attended by 150 scientists and engineers. It was, in essence, a follow-on meeting to the second sonic boom conference held on May 9 and 10, 1968, at NASA Headquarters, the proceedings of which are reported in NASA SP–180.

The objectives of this conference, as was the case in the second conference, were to evaluate the current status of the NASA-sponsored university and industry programs on sonic boom research, to review the current research programs at the NASA centers, to determine those areas of sonic boom research that are critical and need to be emphasized from the standpoint of commercial supersonic and hypersonic transport operation, and to determine which, if any, of the various avenues of research appear to be the most promising with regard to the prediction of sonic boom generation and propagation and the reduction of sonic boom overpressure. The human response problem was not covered in this conference. The structural response problem was covered to a very limited extent.

The first-day sessions of the conference were devoted to the presentation of the invited papers covering the status of research on the prediction of sonic boom generation and propagation. Dr. Antonio Ferri of New York University and Mr. I. Edward Garrick of NASA Langley Research Center served as chairmen of these sessions. The morning session of the second day was devoted to the presentation of the invited papers covering the status of research on aircraft configurations and methods for the minimization of sonic boom. Dr. Morton Friedman of Columbia University served as chairman of this session. The afternoon session of the second day was highlighted by panel discussions that summarized the progress and overall status of sonic boom research, determined those areas of research that demand more emphasis, and recommended directions for future research. Mr. Harvard Lomax of NASA Ames Research Center served as chairman of the panel and open discussion session.

A significant aspect of the conference was that most of the 29 papers presented reported new and important results. Reported progress ranged

from fairly complete work on the turbulent distortion of sonic boom of hypersonic transports, space shuttles, and orbiters, and also from improved theories for predicting the sonic boom more accurately in critical cases for current transport to criticisms and suggested improvements in wind-tunnel techniques. In the area of boom minimization, the NASA program has utilized the combined talents of Messrs. E. McLean, H. L. Runyan, and H. R. Henderson at NASA Langley Research Center; Dr. W. D. Hayes at Princeton University; Drs. R. Seebass and A. R. George at Cornell University; and Dr. A. Ferri at New York University to determine optimum equivalent bodies of revolution that minimize the overpressure, shock pressure rise, and impulse for given aircraft weight, length, Mach number, and altitude at operation. Simultaneously, research efforts of NASA and those of Dr. A. Ferri at New York University have provided indications of how real aircraft can be designed to provide values approaching these optimums. At the end of the meeting, the panel recommended continued and even expanded efforts in most areas of sonic boom research. Also, from these recommendations, it is apparent what the very minimum research program must be during this time of economic constraints.

Planning of the future sonic boom research program must take into account the fact that under the restrictions of the proposed Civil Aircraft Sonic Boom rule (14 CFR Part 91), the operation of commercial transport in any way that would cause sonic boom to reach the surface of the United States would be prohibited. Within the constraints of this limitation, there are three principal unknowns that must be determined: (1) the magnitude of the superboom that occurs during the initial climb and acceleration to cruise, (2) the feasibility of ferrying aircraft at slightly supersonic speeds over land areas as allowed by the proposed rule, and (3) the statistical spread of overpressures across the sonic boom corridor. In addition, and even more important, is the issue of what can be accomplished in minimizing the impact of the sonic boom. This issue, incidentally, is not within the context of the proposed rule but is related to the development of later-generation SST aircraft with acceptable sonic boom characteristics for normal flight operation over land.

Solutions to the first two issues are relevant to the impact of the sonic boom on commercial offshore installations, maritime transportation, and offshore recreational environment for pleasure boating. The solution to the third issue is relevant to the economic aspects of the aircraft operation. For example, when an aircraft is in straight and level flight at a given altitude and at a speed supersonic relative to the air at that altitude but subsonic to the air at the ground, there is no sonic boom at the ground. Because supersonic transports will have to be operated over land and one of their attractions is greatly increased speed over water routes, there is considerable interest in the possibility of overland opera-

tion at low supersonic speeds with increased utilization offsetting increased operating costs (840 mph versus 600 mph for current subsonic jets).

The determination of whether such aircraft flight operation will be feasible depends to a large extent on the likelihood of a superboom [1] occurring at the ground and the magnitude of the overpressure at the ground when it happens.

Development of the capabilities required to provide solutions to the first two issues listed above will require the scientists to formulate techniques that will predict pressure levels at a caustic [2] and also determine how these pressure levels are affected by topographical surfaces.

At this meeting, substantial progress was reported on the development of techniques for the prediction of pressure levels near a caustic. Dr. W. D. Hayes of Princeton University has shown that the caustic phenomenon is described by a simple variant of the transonic flow equation. Dr. R. Seebass of Cornell University was able to give a formal analytical solution to this equation for a simple incoming signal with a finite rise time. Also, Drs. Seebass and Murman of Cornell University have successfully extended the latter's technique for transonic flows to the calculation of solutions to the caustic problem. Drs. Gardner and Hayes of Princeton University are developing a shock-fitting numerical scheme that will provide refined answers. These results are in their preliminary stage; planned future research that was endorsed by the conference panel will be directed at understanding and extending these results and procedures to obtain reliable estimates of the magnitude of superbooms under various environmental conditions.

The NASA Langley Research Center has recently obtained sonic boom measurements from flight experiments to define the sonic boom pressure field at the shock wave extremity or caustic. These results are reported in these proceedings. Caustic signatures resulting in overpressure enhancement were observed at the shock wave extremities. The highest measured levels are on the order of three times the N-wave overpressures related to operations at higher supersonic Mach numbers.

Another theoretical problem area, which had been previously identified for practical considerations and importance and the research progress of which was discussed at this conference, is the effect of turbulence. Drs. George and Plotkin of Cornell University carried out calculations on the relationship between shock thickness and its turbulent field. They showed that there is an effective dissipation of energy due to

[1] Whenever an envelope of sound rays intersects the ground, magnified overpressures called superbooms occur.

[2] A caustic is formed whenever successively emitted sound rays have an envelope; this envelope is a caustic surface. Linear accelerations, turns, and pushovers cause the rays to have an envelope.

scattering, substantiating earlier research. George and Plotkin also provided a detailed picture of possible N-wave distortions including shock thickening.

It was concluded at the meeting that while theory has advanced to the point where the effects of turbulence are understood in a qualitative way, there is still much to be done to make quantitative predictions of turbulence effects a routine matter. For example, one of the serious questions that has arisen is the magnitude of turbulent distortion near the edges of the boom corridor. It has been suggested that the overpressure there could exceed its nominal value by a factor of 2; 1 time in 500. It will have to be determined whether or not such variations occur and the extent to which they occur by utilizing the theories of turbulent distortion and by careful flight-test experiments conducted under known meteorological conditions.

During the past two years, significant progress has been made in developing a sophisticated analysis of nonlinear effects on sonic boom as reported in Dr. Landahl's paper. This method of analysis provides an excellent means for assessing the accuracy of first-order theory, which is commonly used to approximate the flow field within a distance of a few body lengths. The second-order solution developed by Dr. Landahl, however, allows one to get within a distance from the body of one body length, which could be very important in accurately defining the Whitham F-function at Mach numbers of 3 and higher. Thus, although the usual method of predicting the far field and the related shocks by employing the Whitham F-function would normally be adequate for the very slender configurations at moderate Mach numbers, the F-function will be different from that derived by the nonlinear theory by terms that are of second order in equivalent body thickness ratio. To obtain accurate sonic boom calculations for complex configurations at high Mach numbers, there is a need for a better description of the near field than that provided by linearized theory.

Because most wind-tunnel experiments provide near-field data that are then extrapolated into the far field through the F-function approach, it is especially important from the theoretical point of view to define the near field accurately. The influence of configuration asymmetries on the shocks and on the signatures is not accounted for properly by the usual experimental techniques employed. Hence, the theoretical nonlinear analysis can be used to calculate corrections for near-field effects of wind-tunnel experiments that are directed at determining the Whitham F-function from measurements of the flow field near the body.

Another use for the nonlinear method is for the development of wind-tunnel correction formulas that must account for nonuniformities in the flow such as flow angularity, disturbances from model support, and local flow separations due to the low Reynolds number of the tests. Drs. Ferri

and Landahl discussed in their papers the fact that nonuniformities present in all wind tunnels can introduce errors that are important for the sonic boom measurements when the intensity level of the boom to be measured is small. Dr. Ferri emphasized the fact that if experimental techniques are to be utilized, the importance of such errors should be recognized and evaluated carefully in such tests. Dr. Landahl further emphasized the point that, analytically, it is simple to correct for linear effects, but for high Mach numbers, the nonlinear effects of flow nonuniformity become important and can be calculated approximately from his second-order theory.

Significant progress has been made in the area of sonic boom reduction during the last several years. Although it is not yet certain that major reductions in sonic boom overpressure can be achieved by practical modifications of aerodynamic configurations such as changes in sweep, dihedral, planform, redistribution of lift, etc., recent theoretical and experimental research does indicate that substantial reductions in overpressure can be obtained by modifying some of these aerodynamic parameters. The conclusions have been reached and accepted by several research groups.

During the meeting, Dr. A. Ferri presented some results of his investigations of the lower limits of sonic boom signatures that can be obtained with practical airplanes. Drs. W. D. Hayes and Weiskopf presented the optimum aircraft shape if the bangs of the boom (shock waves) are to be avoided. This result generalized early research by Drs. Seebass and George to include the beneficial effects of the aircraft's failure.

It was concluded at the meeting that progress has been so substantial that it is no longer possible to rule out a domestic version of the supersonic transport. Instead, the more effort that is put into the sonic boom minimization problem, the more such a transport appears feasible. It is imperative that work on sonic boom minimization continue.

The panel agreed that since the weight of the airplane is an important parameter, some effort should be placed on an investigation of possible changes: reduction of fuel consumption, type of engine fuel used, and structural weight. When this information becomes available, it will be possible then to determine the direction that should be taken and the potential possibilities that are available to the next generation of supersonic airplanes.

Some discussion at the meeting was directed to the feasibility of the hypersonic aircraft and its associated sonic boom level. However, to be practical, the hypersonic aircraft must have a long range. If it is to use that range effectively, it must have acceptable sonic boom characteristics. Thus, greater emphasis is needed on sonic boom associated with hypersonic transports.

Finally, an assessment of the overall status of sonic boom research covered during this meeting has indicated that significant progress has been made in our understanding and analysis of the following problem areas related to the prediction of the generation and propagation of sonic boom through real, stratified atmospheres. Also, substantial progress has been made in determining the optimum configurations that provide minimum sonic boom signatures. These lower bound signatures have been analytically related to real aircraft with significant reductions in overpressure. Experimental verification of these results are currently underway. Furthermore, there is a great deal that should be explored to improve the aerodynamic efficiency of the airplane. One way to reduce the sonic boom is to increase the overall efficiency of the aircraft. Improvements in the aerodynamic parameters of lift-to-drag ratio, structural efficiency, specific fuel consumption, and engine-thrust-to-weight ratio reduce the aircraft's sonic boom. In the process of reducing sonic boom by aircraft modifications, the aerodynamic parameters must not be penalized to any large extent. Thus, progress in this field, in which there have been intense feelings that little could be accomplished, is not only moving rapidly but in an encouraging fashion.

This research must be continued or even expanded if practical supersonic transports with minimum and acceptable sonic boom characteristics are to be built.

IRA R. SCHWARTZ
Aerodynamics and Vehicle Systems Division
Office of Advanced Research and Technology

Contents

Session III — CONFIGURATIONS FOR MINIMIZATION OF SONIC BOOM

M. FRIEDMAN, *Chairman*

SESSION IV—PANEL AND OPEN CONFERENCE DISCUSSIONS

E. H. LOMAX, *Chairman*

PANEL DISCUSSION

GENERAL REMARKS

I

PREDICTION OF SONIC BOOM GENERATION AND PROPAGATION—THEORY AND EXPERIMENT

Chairman: A. FERRI

Nonlinear Effects on Sonic Boom Intensity

M. LANDAHL, I. RYHMING, AND P. LOFGREN
Aeronautical Research Institute of Sweden

In an earlier paper (ref. 1) it was shown that first-order acoustic theory is capable of describing the supersonic flow at large distances from a three-dimensional body with a relative error of order ϵ^4, where ϵ is the thickness ratio of the equivalent body of revolution. Thus, for slender configurations the first-order theory will be quite accurate and higher order effects will be confined primarily to the near field where they will contribute to the Whitham F-function with terms that are of order ϵ^2 relative to linearized theory. Second-order slender-body theory was used to demonstrate that these terms may become quite important, particularly at high Mach numbers.

Van Dyke (ref. 2) has demonstrated that second-order theory gives a good approximation to surface pressure for axisymmetric flow. However, his solution is not uniformly valid for large distances, so it is not directly applicable to the sonic boom problem. Lighthill (ref. 3) indicated that second-order theory could be made uniformly valid by reinterpreting the distance downstream from the free-stream Mach cone as that of the distance downstream from the limit cone; i.e., effectively by readjusting the linearized characteristics as in the Whitham theory. It is the purpose of the present paper to show that the uniformly valid second-order solution can in fact be expressed in a very simple functional form, provided both families of characteristics are readjusted in the manner proposed by Lin (ref. 4) and further extended by Oswatitsch (ref. 5). It is also shown that the second-order, three-dimensional, far-field solution expressed in cylindrical coordinates can be cast in a similar form but will involve a readjustment of the angular coordinate as well. From this, conclusions are drawn as to how simple, approximate solutions can be constructed that are uniformly valid in the whole flow field.

LIN-OSWATITSCH VARIABLES

Lin (ref. 4) showed that first-order, small-perturbation acoustic theory for two-dimensional flow could be made uniformly valid if both dependent and independent variables were perturbed so as to represent the two

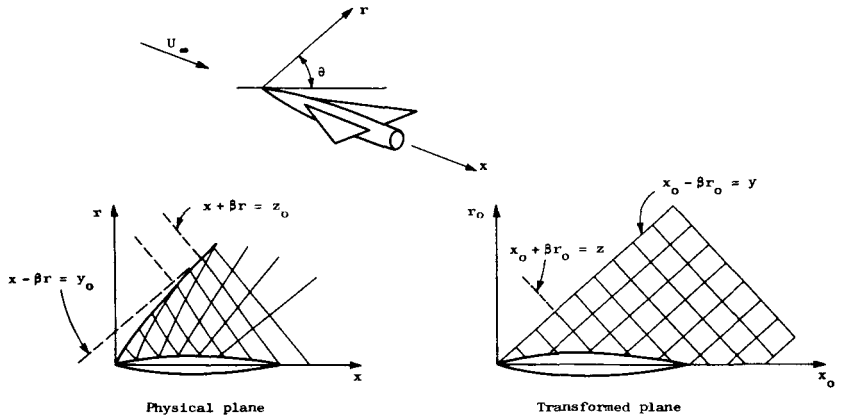

FIGURE 1. – Lin-Oswatitsch variables.

families of characteristics correctly to the order considered. Oswatitsch (ref. 5) has developed this idea further and also applied it to a number of three-dimensional problems.

We shall first consider the axisymmetric case. In Oswatitsch's method, new independent coordinates x_0 and r_0 (fig. 1) are introduced such that both families of characteristics become the straight lines

$$y = x_0 - \beta r_0 = \text{constant} \tag{1}$$

$$z = x_0 + \beta r_o = \text{constant} \tag{2}$$

The appropriate transformation can be found through integration of the Mach line slope expressions expanded to first order in perturbation velocities:

$y =$ constant:

$$\frac{dr}{dx} = \frac{1}{\beta} - \frac{K - M^2}{\beta} u + \frac{M^2}{\beta^2} v \tag{3}$$

$z =$ constant:

$$\frac{dr}{dx} = -\frac{1}{\beta} + \frac{K - M^2}{\beta} u + \frac{M^2}{\beta^2} v \tag{4}$$

where $K = (\gamma + 1)M^4/2\beta^2$, $\beta = \sqrt{M^2 - 1}$, and u and v are the dimensionless perturbation velocity components in the x and r directions, respectively. Hence, for $y =$ constant,

$$r = \frac{x}{\beta} - \frac{(K - M^2)}{\beta} \int u \, dx + \frac{M^2}{\beta^2} \int v \, dx + \text{constant} \tag{5}$$

the integrations to be carried out along $y=$ constant. Similarly for $z=$ constant,

$$r=-\frac{x}{\beta}+\frac{(K-M^2)}{\beta}\int_{z=\text{const.}} u\,dx+\frac{M^2}{\beta^2}\int_{z=\text{const.}} v\,dx+\text{constant} \tag{6}$$

To lowest order, $x=x_0$ and $r=r_0$. Hence, one can set $dx=dz/2$ in equation (5) and $dx=dy/2$ in equation (6). Furthermore, to lowest order one can for u and v use the linearized first-order solution. Expressed in terms of $y=x-\beta r$ and $z=x+\beta r$, the linearized equation for the perturbation velocity potential reads

$$2(z-y)\varphi_{yz}+\varphi_y-\varphi_z=0 \tag{7}$$

which can also be written in the following alternate forms:

$$\varphi_y=\frac{\partial}{\partial z}\left[2(z-y)\varphi_y-\varphi\right] \tag{8}$$

$$\varphi_z=-\frac{\partial}{\partial y}\left[2(z-y)\varphi_z+\varphi\right] \tag{9}$$

Hence

$$\int_{y=\text{const.}} u\,dx=\frac{1}{2}\int(\varphi_y+\varphi_z)\,dz=(z-y)\varphi_y+\text{constant} \tag{10}$$

and

$$\int_{z=\text{const.}} u\,dx=\frac{1}{2}\int(\varphi_y+\varphi_z)\,dy=(y-z)\varphi_z+\text{constant} \tag{11}$$

In a similar manner the integrals of v can be calculated. Replacing y and z by their expressions (1) and (2), we find that for the downstream characteristics,

$$x-\beta r=y+\frac{1}{2}K(z-y)\left(u-\frac{v}{\beta}\right)-M^2\varphi \tag{12}$$

whereas for the upstream ones,

$$x+\beta r=z-\frac{1}{2}K(z-y)\left(u+\frac{v}{\beta}\right)-M^2\varphi \tag{13}$$

Here we have chosen the integration constants y and z so that the zeroth-order expressions are recovered when there are no disturbances.

From equations (1) and (2), we then find the following transformation formulas:

$$x = x_0 - Kr_0 v - M^2 \varphi \tag{14}$$

$$r = r_0(1 - Ku) \tag{15}$$

For a three-dimensional flow, x_0 and r_0 coordinates defined by equations (1) to (4) in the same manner will form curved nonaxisymmetric surfaces with the angle θ as a parameter. It will then in general not be possible to carry out the integrations in closed form, because instead of equation (7) one would now have

$$2(z-y)\varphi_{yz} + \varphi_y - \varphi_z = \frac{2}{z-y}\varphi_{\theta\theta} \tag{16}$$

We shall use this to find approximations valid for large radial distances; i.e., for large $(z-y)$, for which we would expect that the terms with derivatives with respect to y dominate. Thus equation (16) may be rewritten as follows:

$$\frac{\partial}{\partial z}\left[\sqrt{z-y}\,\varphi_y\right] = \frac{1}{2\sqrt{z-y}}\left[\varphi_z + \frac{2}{z-y}\varphi_{\theta\theta}\right]$$

which can be solved by iteration, neglecting the right-hand side in the first approximation. This gives the following series solution in inverse powers of $(z-y)$:

$$\varphi_y = -\frac{F}{(z-y)^{1/2}} - \frac{F_1}{4(z-y)^{3/2}} + \frac{F_{1\theta\theta}}{(z-y)^{3/2}} + \cdots \tag{17}$$

where F is the Whitham F-function defined in the usual manner as

$$F(y, \theta) = \frac{1}{2\pi}\int_0^y \frac{f_t(t, \theta)\, dt}{\sqrt{y-t}} \tag{18}$$

with f being the equivalent source strength and

$$F_1(y, \theta) = \int_0^y F(y_1, \theta)\, dy_1 \tag{19}$$

Because

$$2\varphi_y = u - \frac{v}{\beta} \tag{20}$$

and

$$2\varphi_z = u + \frac{v}{\beta} = \frac{F_1}{(z-y)^{3/2}} + \cdots \tag{21}$$

we then have the following approximations for the first-order velocity components and perturbation potential at large distances:

$$u=-\frac{F}{(z-y)^{1/2}}+\frac{F_1}{4(z-y)^{3/2}}+\frac{F_{1\theta\theta}}{(z-y)^{3/2}}+\cdots \tag{22}$$

$$v=-\beta u+\frac{\beta F_1}{(z-y)^{3/2}}+\cdots \tag{23}$$

$$\varphi=-\frac{F_1}{(z-y)^{1/2}}+\cdots \tag{24}$$

These can now be introduced into the Mach line slope relations. From equation (24) it follows that

$$\frac{1}{z-y}\varphi_{\theta\theta}\simeq -2\frac{\partial}{\partial z}l(\varphi_{\theta\theta}) \tag{25}$$

for large distances, which can be used directly with equation (16) to yield the following approximation for the surfaces $y=$ constant:

$$x-\beta r=y+\frac{K}{2}(z-y)\left(u-\frac{v}{\beta}\right)-M^2\varphi+2K\varphi_{\theta\theta} \tag{26}$$

For the second set, $z=$ constant, there will be no change to lowest order. In terms of the variables x_0 and r_0, we thus find the following approximate expressions (cf. eqs. (17) and (18)):

$$x=x_0-Kr_0v-M^2\varphi+Kr_0\frac{\partial w}{\partial\theta} \tag{27}$$

$$r=r_0\left(1-Ku-\frac{K}{\beta}\frac{\partial w}{\partial\theta}\right) \tag{28}$$

where we have used the first-order expression for the third velocity component

$$w=\frac{1}{r_0}\varphi_\theta \tag{29}$$

As the contribution from the term $\partial w/\partial\theta$ would be small for both small and large distances, it is likely that equations (27) and (28) give good approximations to the Mach conoids everywhere. For large distances, r_0 will not deviate substantially from r, and it is then convenient to express the equation for the downstream characteristic surfaces in terms of x, r, and y. Making use of equations (20) to (24), we find after some calculations,

$$x-\beta r=y-kr^{1/2}F+\left(M^2-\frac{K}{4}\right)\frac{F_1}{\sqrt{2\beta r}}-K\frac{F_{1\theta\theta}}{\sqrt{2\beta r}} \tag{30}$$

where

$$k=\sqrt{2\beta}\ K=(\gamma+1)M^4/\beta^{3/2}\sqrt{2} \tag{31}$$

The first two terms on the right-hand side of equation (30) are recognized as those appearing in the Whitham theory. The additional terms arise from near-field effects in the first-order solution.

In Oswatitsch's method, the third variable, in this case θ, is also perturbed in a manner that involves the bicharacteristics of the flow. Here, we shall instead select the perturbation of θ so as to produce the simplest functional form for the second-order solution.

UNIFORMLY VALID SECOND-ORDER SOLUTION FOR AXISYMMETRIC FLOW

We shall determine a uniformly valid solution to second order for the axisymmetric case by making the appropriate transformations in Van Dyke's (ref. 2) second-order solution. His solution reads

$$\varphi_2=(1+M^2u)\varphi+Kruv-\tfrac{1}{4}M^2rv^3+\chi \tag{32}$$

Here χ is a homogeneous solution to the linearized equation, which will be omitted in the following analysis as it can always be absorbed in the first-order potential φ. The triple-product term is important only in the immediate neighborhood of the axis and will have an influence on the far field only insofar as it will modify the boundary values on the body surface. We shall therefore leave it out in what follows, as it can always be added later whenever needed.

By expansion in terms of x_0-x and r_0-r, it is easily seen by aid of equations (14) and (15) that an equivalent expression for φ_2 in terms of the transformed variables x_0 and r_0 is given by

$$\varphi_2=\varphi(x_0, r_0)-Kr_0vu \tag{33}$$

From this one may calculate the velocity components to second order remembering that

$$u=\frac{\partial\varphi}{\partial x_0}\qquad v=\frac{\partial\varphi}{\partial r_0} \tag{34}$$

and

$$\frac{\partial}{\partial x}\simeq(1+Kr_0v_{x_0}+M^2u)\frac{\partial}{\partial x_0}+Kr_0u_{x_0}\frac{\partial}{\partial r_0} \tag{35}$$

$$\frac{\partial}{\partial r}\simeq(Kr_0v_{r_0}+Kv+M^2v)\frac{\partial}{\partial x_0}+(1-Kr_0u_{r_0}+Ku)\frac{\partial}{\partial r_0} \tag{36}$$

to first order, for moderate r_0. The results are

$$u_2 = (1 + M^2 u)\, u(x_0, r_0) + \cdots \tag{37}$$

$$v_2 = (1 + M^2 u)\, \frac{r_0}{r}\, v(x_0, r_0) + \cdots \tag{38}$$

It is suggestive that the remaining coefficient may to the same order of magnitude be approximated by

$$1 + M^2 u \simeq \rho_\infty / \rho \tag{39}$$

The results, equations (33), (37), and (38), given in implicit forms by aid of equations (14) and (15), are uniformly valid to second order everywhere as they are equivalent to Van Dyke's solution for moderate values of r_0 and approach the first-order solutions for large distances, which was shown to be correct to order ϵ^4. The triple-product term can be added separately if so desired. It does not seem to be possible to include it through incorporation of additional terms in equations (14) and (15).

The above formulas are presently being used to calculate the Whitham F-function to second order for a parabolic spindle of thickness ratio $\epsilon = 0.0589$ at $M = 3$. As the slender-body theory was found to be quite inaccurate for this case, a new calculation procedure has been developed that is based on an improved quasi-cylindrical solution.

NONAXISYMMETRIC FLOW

As it is not possible to find a simple analytical solution for the near field of a general three-dimensional body, we shall instead make use of the previously developed second-order far-field solution. In the present notation, this solution [1] was given by

$$u_2 = -\frac{F(s, \theta)}{\sqrt{2\beta r}} + \frac{1}{\sqrt{2\beta r}\,(1 - k r^{1/2} F_s)} \left\{ [M^2(\gamma + \tfrac{5}{2}) - K] K F^2 F_s \ln(\beta r) \right.$$
$$+ \left[(F^2 + F_s F_1) \left(M^2 - \frac{K}{2} \right) - 2K(F_\theta^2 - F_s F_{1\theta\theta}) \right] \frac{1}{\sqrt{2\beta r}}$$
$$\left. + \left(\frac{F_1}{4} + F_{1\theta\theta} \right) \frac{1}{2\beta r} \right\} + \cdots \tag{40}$$

where

$$x - \beta r = s - k r^{1/2} F(s, \theta) \tag{41}$$

and

$$F_1(s, \theta) = \int_0^s F(s_1, \theta)\, ds_1 \tag{42}$$

[1] The terms involving derivatives with respect to θ were given incorrectly in ref. 1.

This solution was obtained by assuming βr to be large and of order ϵ^{-4}. The first and second approximations differ by terms of order ϵ^8, which would be unimportant in any practical situation. However, we are here interested in moderately large βr, for which the expansion still is a good one, but the second-order term will have some terms that give contributions of order ϵ^4. The term involving the logarithm will be at most of order ϵ^6 and will consequently be ignored; however, it can be completely absorbed in the first-order term if the characteristic variable is modified to a higher order.

A comparison of equation (41) with equation (30) shows that $s=y$ to lowest order. One can simplify equation (40) considerably by expressing it instead in terms of y. Expansion of equation (41) about $s=y$ gives

$$s=y+\frac{\left(M^2-\frac{K}{4}\right)F_1-KF_{1\theta\theta}}{(1-kr^{1/2}F_y)\sqrt{2\beta r}} \tag{43}$$

which, upon insertion into equation (40), gives

$$u_2=-\frac{F(y,\theta)}{\sqrt{2\beta r}}+\frac{1}{2\beta r}\left[\left(M^2-\frac{K}{2}\right)F^2+2KF_\theta^2\right]+\frac{1}{(2\beta r)^{3/2}}\left(\frac{F_1}{4}+F_{1\theta\theta}\right)+\cdots \tag{44}$$

where, again, we have ignored terms that give contributions of order ϵ^6 or higher. This can be further simplified by introducing r_0 as given by the first two terms of equation (29) and noting that the last terms arise from the asymptotic representation of the linear solution (cf. eq. (22)). A solution equivalent to equation (44) for large βr is therefore

$$u_2=(1+M^2u)u(x_0,r_0,\theta)+\frac{KF_\theta^2}{\beta r} \tag{45}$$

The last term can be absorbed in the linear solution by perturbing θ as well, setting

$$u_2=(1+M^2u)u(x_0,r_0,\theta_0)\simeq\frac{\rho_\infty}{\rho}u(x_0,r_0,\theta_0) \tag{46}$$

where

$$\theta=\theta_0+\Delta\theta \tag{47}$$

and

$$\Delta\theta=\frac{2KF_\theta}{\sqrt{2\beta r}}\simeq-2K\frac{\partial u}{\partial\theta_0} \tag{48}$$

It can be shown by an asymptotic analysis that the value of $\Delta\theta$ given by equation (48) is half of the angular displacement of the bicharacteristic (acoustic ray) along the Mach conoid through that point. With the aid of equations (27) and (28), we thus have a parametric representation of the second-order solution in terms of the first-order one that is of the same form as the axisymmetric solution (eq. (38)), except that now also the angular variable is perturbed. For the perturbation velocity potential one finds through integration over x_0 holding r_0 and θ_0 fixed, that

$$\varphi_2=\varphi(x_0, r_0, \theta_0)-Kr_0uv-2Ku_{\theta_0}\varphi_{\theta_0}+K\int_0^{x_0}\left[\left(u-\frac{v}{\beta}\right)u_{\theta_0\theta_0}+2u_{\theta_0}^2\right]dx_0' \tag{49}$$

By differentiation with respect to r, one finds after some calculations, that

$$v_2=\frac{\rho_\infty}{\rho}\frac{r_0}{r}v(x_0, r_0, \theta_0)+\cdots \tag{50}$$

It is thus seen that the second-order asymptotic solution for a nonaxisymmetric flow can be put in the same form as the axisymmetric uniformly valid one. The only difference is that the transformed variables become somewhat modified to account for nonaxisymmetric effects.

The third velocity component w is given only to first-order accuracy (eq. (29)) in this approximation because the nonlinear terms involving w and its derivatives become of higher order at large distances.

The transformation formulas developed account correctly for second-order effects only at large distances from the body, but their simple structure gives some hope that they might also apply to a good approximation near the body, thus considerably extending the usefulness of linearized theory. However, certain difficulties become readily apparent in practical applications. Thus, for example, one would obtain different results depending on how the body is located in the coordinate system. We shall therefore explore an alternative way to utilize the results obtained.

PERTURBATION OF A NONUNIFORM FLOW FIELD

In linearized aerodynamic theory, a common method to construct flow fields is to superimpose elementary solutions like those for a source or doublet so as to produce a velocity field satisfying a given set of boundary conditions. Thus, for example, by superimposing linear source distributions along each chord of a thin wing (fig. 2), one can produce the complete flow field for the nonlifting case. For the lifting case, one needs doublets as well, which can be obtained by differentiating the source solution with respect to z.

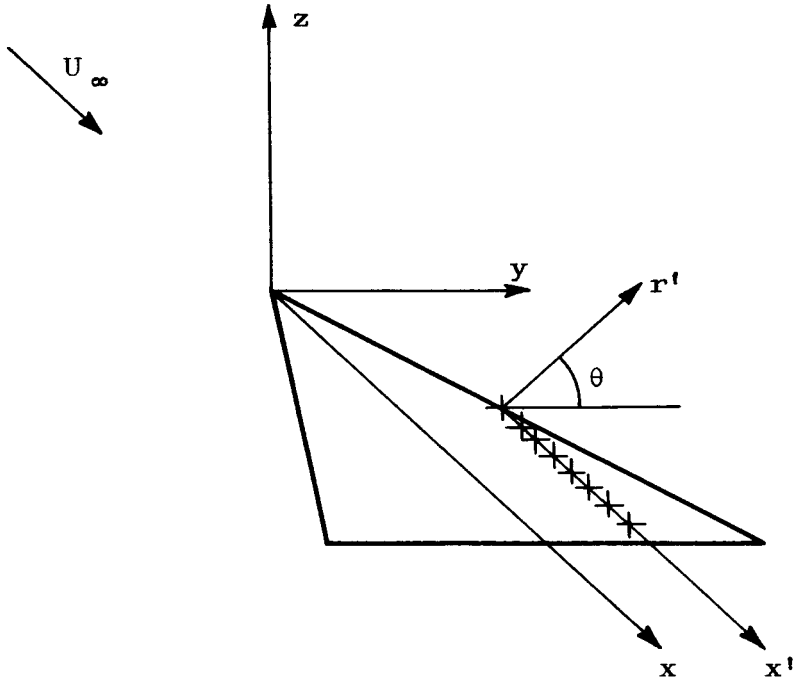

FIGURE 2. – Construction of nonlinear flow field through superposition.

It is possible in principle to use this general technique in a nonlinear flow problem also. The difference is that each additional infinitesimal source or line source distribution is located in a nonuniform flow field created by the other sources. To build up a nonlinear flow field, one would thus need the solution for a source or other flow element situated in a nonuniform flow. Previous applications of this idea, which is inherent in the method of parametric differentiation, have indicated that accurate results for surface pressures are obtained even if one ignores the effects of flow nonuniformity on the elementary solution, provided only that one bases the solution on the local flow properties at the singularity. This local approximation has been used successfully for the transonic flow around an airfoil (ref. 6) (for which it becomes identical with the method of local linearization by Spreiter and Alksne) and the high-Mach-number supersonic flow around bodies of revolution (ref. 7).

From a second-order solution, it is possible to calculate the first-order effects of flow uniformities on a sourcelike or other type of perturbation that is used to construct the flow. Let us for simplicity consider the situation depicted in figure 2; i.e., the perturbation caused by a line of sources along a given spanwise position. If the flow were uniform, the perturbation would be axisymmetric around the axis x'. It will therefore be con-

venient to work with a cylindrical coordinate system centered around x'. For simplicity we will omit the primes in the following explanation. We shall denote perturbed quantities by the symbol δ; thus $\delta\varphi$ is the first-order potential due to the perturbation and is independent of θ. The effects of flow nonuniformity will appear first in the next approximation $\delta\varphi_2$, which is to be obtained from a perturbation of the second-order solution, equation (49). When the velocity field is perturbed, the characteristic surfaces will also change by quantities proportional to the perturbation. If attention is fixed on a particular point (x, r, θ) in the field, it follows from equations (27) and (28) that the characteristic coordinates x_0 and r_0 will change by amounts δx_0 and δr_0 given by the equations

$$\delta x_0 \frac{\partial x}{\partial x_0} + \delta r_0 \frac{\partial x}{\partial r_0} = K r_0 \delta v + M^2 \delta\varphi \tag{51}$$

$$\delta x_0 \frac{\partial r}{\partial x_0} + \delta r_0 \frac{\partial r}{\partial r_0} = K r_0 \delta u \tag{52}$$

(For an axisymmetric perturbation, it turns out that to first order, $\delta\theta_0 = 0$.) From equation (49), one finds that

$$\delta\varphi_2 = \delta\varphi - K r_0 (u\delta v + v\delta u) + K \int_0^{x_0} \left(\delta u - \frac{\delta v}{\beta}\right) u_{\theta_0\theta_0}\, dx_0' + \delta x_0 \frac{\partial\varphi}{\partial x_0} + \delta r_0 \frac{\partial\varphi}{\partial r_0} \tag{53}$$

Upon solving δx_0 and δr_0 from equations (51) and (52) and simplifying, neglecting higher order terms, one obtains

$$\delta\varphi_2 = \delta\varphi(1 + M^2 u) + K \int_0^{x_0} \left(\delta u - \frac{\delta v}{\beta}\right) u_{\theta\theta}\, dx_0' \tag{54}$$

The factor $(1 + M^2 u)$ may be replaced by ρ_∞/ρ as before. The integral term represents the effects of nonaxisymmetry on the perturbation. This term will be small both near the axis and far from the axis and can probably be omitted altogether without serious loss of accuracy. This would leave the simple approximation

$$\delta\varphi_2 \simeq \frac{\rho_\infty}{\rho}\, \delta\varphi(x_0, r_0) \tag{55}$$

In the application of this approximate solution, the main computational work would be associated with the recalculation of the characteristic coordinates at each step. These would have to be found from numerical integration.

By differentiation with respect to $z = r \sin \theta$, one can in principle obtain a corresponding solution for a doublet. For a more general nonaxisymmetric perturbation, it becomes more convenient to work instead directly with the perturbed velocity components. The perturbations are then found, to lowest order, to propagate along the bicharacteristics of the basic nonuniform flow in accordance with geometrical acoustics.

CONCLUSIONS

By application of a coordinate perturbation to the second-order solution for axisymmetric flow in the manner of Lin (ref. 4) and Oswatitsch (ref. 5) so as to make both sets of characteristics appear as straight lines to first order, it was found possible to cast the results for the velocity components in very simple forms. An extension of Whitham's principle to second order has thereby been found, which is only slightly more complicated than the first-order one in that the first-order u-component is multiplied with the ratio of the free-stream density to local density. The same simple functional form was also found to apply at large distances for nonaxisymmetric flow when expressed in cylindrical coordinates except that then a perturbation of the third, angular, variable is needed as well. This would suggest that an approximate but very simple way to estimate the major nonlinear effects on the F-function would be to determine it for a modified body deformed in the same manner as the Mach conoids.

The second-order solution was used to determine the effect of a small sourcelike perturbation on a nonaxisymmetric flow. A simple approximation was proposed that is likely to show small errors everywhere. This could be employed in a calculation scheme to build up a nonlinear flow field through step-by-step small perturbations.

There are several other applications of the present results that readily suggest themselves, both to the sonic boom problem and to other supersonic flow-field problems. One often overlooked area of application of aerodynamic theory is that of the correction of wind-tunnel testing results. The solution for the small perturbation of a nonuniform flow field could be employed to devise simple formulas to correct for wind-tunnel flow imperfections, which are likely to have large effects at high Mach number. Another such application is to the correction of wind-tunnel measurements of the F-functions for near-field and nonlinear effects. This is considered in a separate paper in this volume.[2]

REFERENCES

1. LANDAHL, M. T.; RYHMING, I. L.; AND HILDING, L.: Nonlinear Effects on Sonic Boom Intensity. Second Conference on Sonic Boom Research, NASA SP–180, 1968, pp. 117–124.

[2] See p. 285.

2. VAN DYKE, M.: A Study of Second-Order Supersonic Flow Theory. NACA Rept. 1981, 1952.
3. LIGHTHILL, M. J.: Higher Approximations in Aerodynamic Theory. General Theory of High Speed Aerodynamics, W. R. Sears, ed., Princeton Univ. Press, 1954.
4. LIN, C. C.: On a Perturbation Theory Based on the Method of Characteristics. J. Math. Phys., Cambridge, Mass., vol. 33, no. 2, 1954.
5. OSWATITSCH, K.: Non-linear Problems in Wave Propagation. Rept. SSS–67–74, Space Science Seminar, George C. Marshall Space Flight Center, 1967.
6. RUBBERT, P.; AND LANDAHL, M. T.: Solution of Nonlinear Flow Problems Through Parametric Differentiation. Phys. Fluids, vol. 10, no. 4, 1967, p. 831.
7. KACPRZYNSKI, J. J.; AND LANDAHL, M. T.: Recent Developments in the Supersonic Flow Over Axisymmetric Bodies With Continuous or Discontinuous Slope. AIAA Paper no. 67–5, 1967.

Numerical Solutions for the Complete Shock Wave Structure Behind Supersonic-Edge Delta Wings

HARVARD LOMAX AND PAUL KUTLER
NASA Ames Research Center

At the second conference on sonic boom research, the senior author presented a paper (ref. 1) that suggested the possibility of studying certain aspects of the sonic boom problem by means of numerical finite-difference methods carried out on a digital computer that is coupled with a cathode-ray display tube. The idea was that the coalescing shock field surrounding not-so-slender wing-body combinations could be computed effectively if the calculations, as they were being carried out, were monitored by real-time reaction to visual displays. Since that time, this concept has been developed and its effectiveness at present can be assessed by the results presented in the following discussion.

SHOCK-CAPTURING TECHNIQUE

Two distinct techniques are used in practice to compute flows with surrounding and embedded shocks. One is referred to as a sharp-shock technique, and the other as a shock-capturing technique. Sharp-shock techniques isolate all shock waves by some complicated numerical and/or logical procedure and apply the Rankine-Hugoniot [1] shock relations across them to identify their strength and position. Shock-capturing techniques, on the other hand, advance the initial data through a fixed mesh, applying boundary conditions only at the body and in the free stream. Shock and expansion waves form and decay automatically without special treatments of any kind.

The acceptance of shock-capturing numerical methods is far from universal. The principal objections are their inability to resolve the shock location with absolute precision and their tendency to give spurious fluctuations for the magnitudes of the dependent variables in the vicinity of the shock. Our purpose here is to show that second-order shock-capturing methods currently available are reliable enough for many practical purposes, in particular, to study the shock structure about

[1] Or the appropriate weak solution in the sense developed by Lax in ref. 2.

lifting wings flying at supersonic speeds. This confidence is established by using such methods to compute a variety of known flow fields obtained from experiment or from calculations made using sharp-shock procedures; e.g., the method of characteristics. Some of these comparisons are presented below.

The success of a shock-capturing technique in correctly predicting complicated flow fields depends on the choice of the finite-difference scheme. The particular scheme used for all of our calculations is the variant of the second-order Lax-Wendroff method developed by MacCormack (ref. 3). It was applied to the conservation-law form of the Eulerian equations written for a generalized orthogonal coordinate system. The basic formulation of the gas-dynamic equations is

$$\mathbf{E}_\zeta + \mathbf{F}_\eta + \mathbf{G}_\xi + \mathbf{H} = 0$$

where

$$\mathbf{E} = \alpha \begin{vmatrix} \rho u \\ p + \rho u^2 \\ \rho uv \\ \rho uw \end{vmatrix}$$

$$\mathbf{F} = \beta \begin{vmatrix} \rho v \\ \rho uv \\ p + \rho v^2 \\ \rho vw \end{vmatrix}$$

$$\mathbf{G} = \gamma \begin{vmatrix} \rho w \\ \rho uw \\ \rho vw \\ p + \rho w^2 \end{vmatrix}$$

and

$$\mathbf{H} = f[p, \rho, u, v, w, \alpha, \beta, \gamma]$$

The MacCormack difference scheme is

$$\tilde{\mathbf{E}}_{j,k}^{n+1} = \mathbf{E}_{j,k}^{n} - \frac{\Delta\zeta}{\Delta\eta}\left(\mathbf{F}_{j+1,k}^{n} - \mathbf{F}_{j,k}^{n}\right) - \frac{\Delta\zeta}{\Delta\xi}\left(\mathbf{G}_{j,k+1}^{n} - \mathbf{G}_{j,k}^{n}\right) - \mathbf{H}_{j,k}^{n}\,\Delta\zeta$$

$$\mathbf{E}_{j,k}^{n+1} = \frac{1}{2}\left[\mathbf{E}_{j,k}^{n} + \tilde{\mathbf{E}}_{j,k}^{n+1} - \frac{\Delta\zeta}{\Delta\eta}\left(\tilde{\mathbf{F}}_{j,k}^{n+1} - \tilde{\mathbf{F}}_{j-1,k}^{n+1}\right)\right.$$

$$\left. - \frac{\Delta\zeta}{\Delta\xi}\left(\tilde{\mathbf{G}}_{j,k}^{n+1} - \tilde{\mathbf{G}}_{j,k-1}^{n+1}\right) - \tilde{\mathbf{H}}_{j,k}^{n+1}\,\Delta\zeta\right]$$

In every case a coordinate system was chosen such that the wing and/or body were parallel to at least one of the coordinate axes (conformal coordinate system). When this method is applied to the linear wave equation, one can show (see, e.g., ref. 4) that it has no "artificial viscosity," that it has dispersion proportional to the third space derivative of a velocity and that it has dissipation proportional to the fourth space derivative of a velocity. One can also show that it satisfies the "shift condition" (a concept developed in ref. 4), which is hypothesized to be a necessary condition for any optimum shock-capturing method.

RESULTS AND DISCUSSION

A variety of wings, bodies, and their combination have been used for flow-field simulations. Some are shown in figure 1. The conical bodies include wedges, cones, planar delta wings, and delta wings with dihedral mounted on conical bodies, all of which were at an angle of attack. (The latter two studies are restricted, at present, to supersonic leading edges.) The method of solution for the flow field about these particular bodies was simplified by the fact that the flow was conical for each. This permitted the use of a distance asymptotic procedure for solving the three-dimensional, hyperbolic, steady-flow equations. Nonconical flow-field calculations were obtained for two-dimensional airfoils and axisymmetric bodies and finally for the completely three-dimensional flow behind a lifting delta wing with supersonic leading edges.

The ability of a shock-capturing technique to predict the location and intensity of attached secondary shocks is demonstrated by the results shown in figures 2 and 3. Figure 2 shows the pressure distribution along vertical lines at various stations behind a circular arc airfoil in Mach 2 flow. Figure 3 shows similar pressure distributions behind a pointed ogive in Mach 5 flow. Both cases are compared with solutions computed

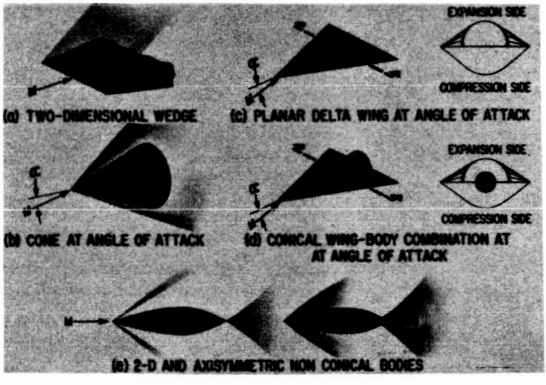

FIGURE 1. – Body configurations studied for flow-field simulations.

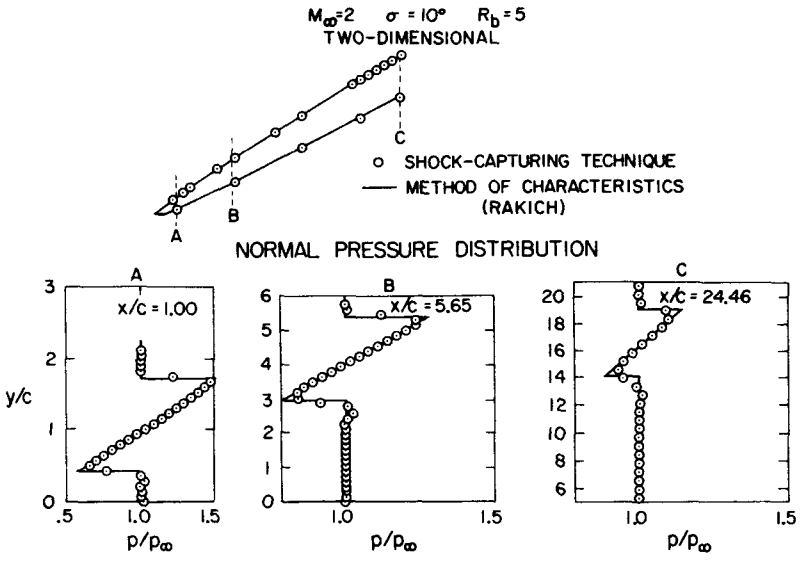

FIGURE 2. — Pressure distribution along vertical lines behind a circular arc airfoil.

by the method of characteristics. For both the two-dimensional and axisymmetric flow fields, the locations of the shock waves are predicted quite accurately by the shock-capturing technique. However, the peak overpressure of the waves is somewhat dissipated.

Consider next the flow about a cone. When the angle of attack of a cone in a supersonic flow field is increased so that supersonic crossflow velocities result, there exists the possibility of embedded shock waves forming on the lee side of the cone. This problem, although being multi-

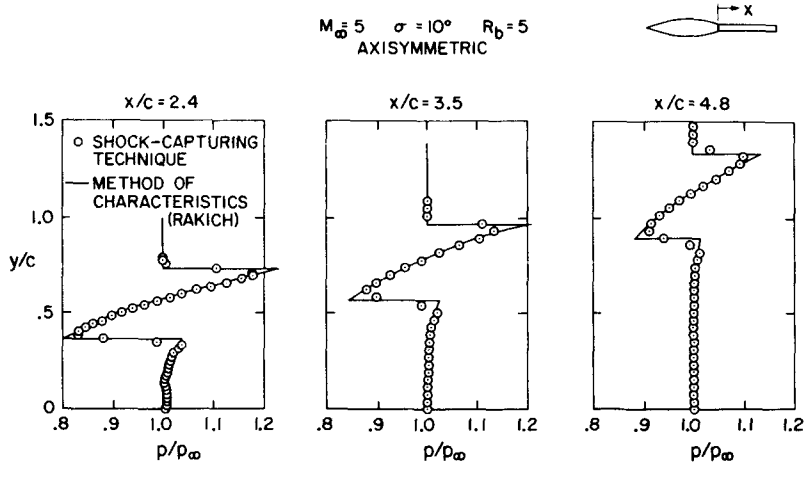

FIGURE 3. — Pressure distribution along vertical lines behind a pointed ogive.

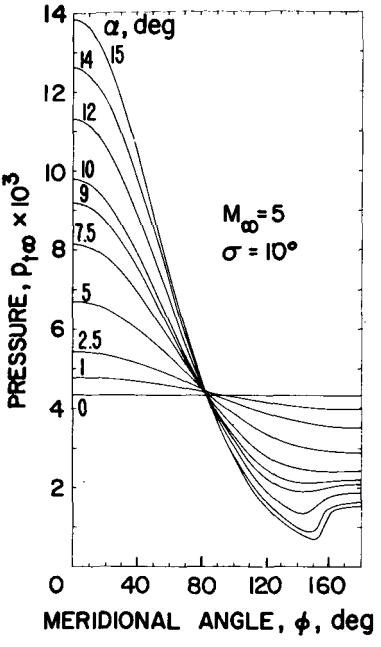

FIGURE 4.—Meridional pressure distribution for a 20° cone.

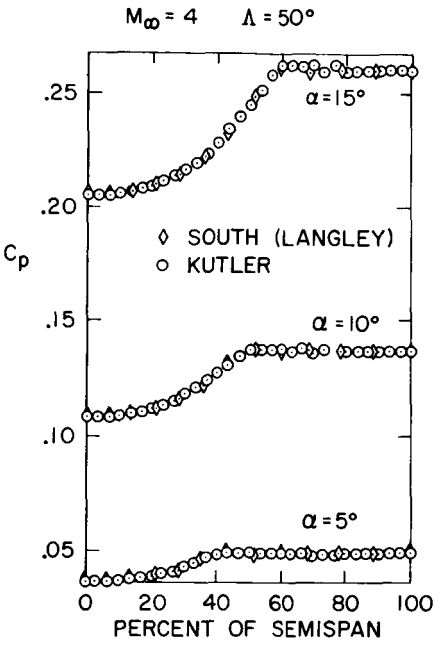

FIGURE 5.—Spanwise pressure distribution on compression side of planar delta wing.

shocked, poses no real problem for a shock-capturing technique. Figure 4 shows the meridional pressure distributions for various angles of attack of a 20° cone in Mach 5 flow. From this figure it can be seen that as the angle of attack is increased, a recompression region begins to form near the 150° meridional plane for an angle of attack of 9°. As the angle of attack is increased further, this recompression region intensifies and forms a shock wave near the 155° meridional plane for an angle of attack of 14°. Because shock-capturing techniques tend to spread shocks over two or three mesh intervals, they do not appear as sharp discontinuities. For the smaller angle-of-attack cases, the results were compared with those of Babenko, Moretti, Holt, and Jones (refs. 5, 6, 7, and 8, respectively) and all were in excellent agreement.

To determine the flow behind a planar supersonic-edge delta wing, it is first necessary to generate converged solutions for the conical flow field on both the compression and expansion sides. These can then be used as initial data for the wake flow calculations. This was done, and the results were compared with the best available theories. Figure 5 displays the variation of the pressure coefficient along the semispan for a 50° swept wing in Mach 4 flow at 5°, 10°, and 15° angles of attack. The results are compared with those of South (ref. 9). South, in turn, made comparisons with Voskresenskii (ref. 10) and found good agreement, and with

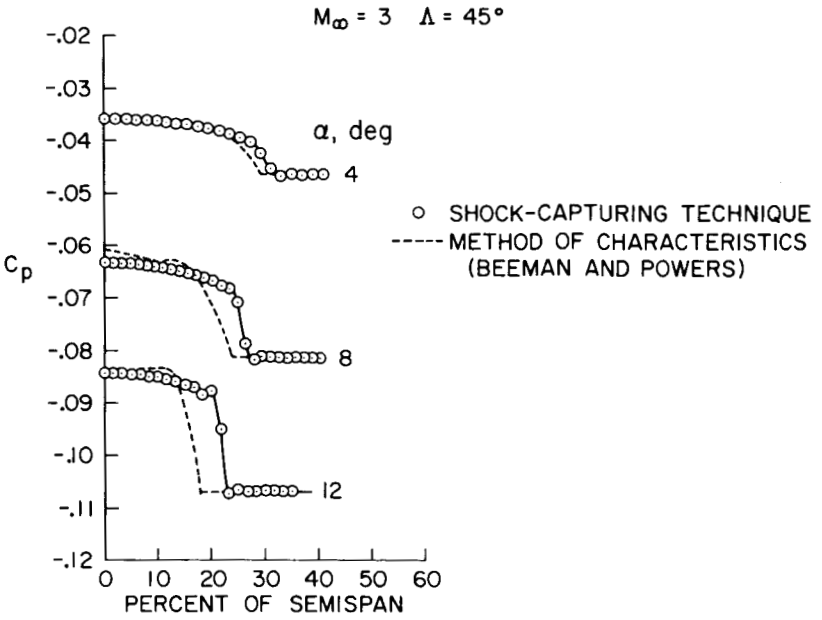

FIGURE 6. – Spanwise pressure distribution on expansion side of planar delta wing.

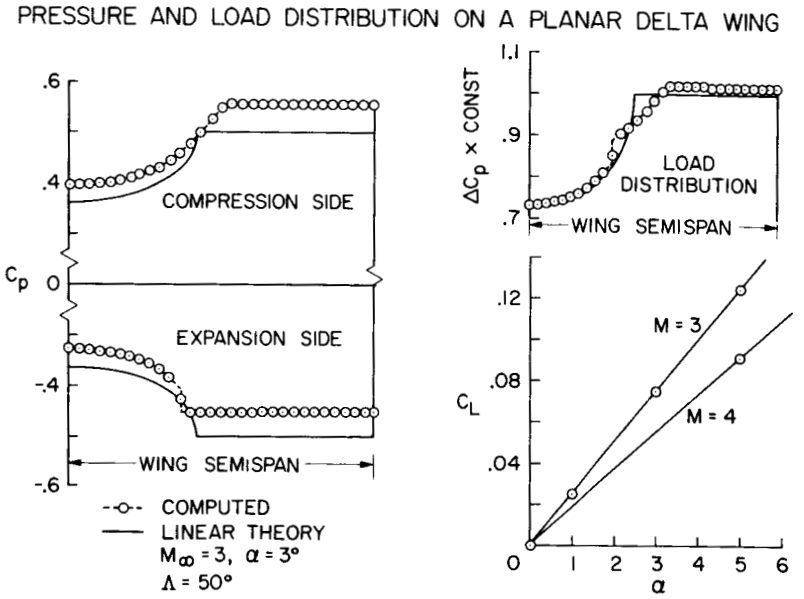

FIGURE 7. – Pressure and load distribution on a planar delta wing.

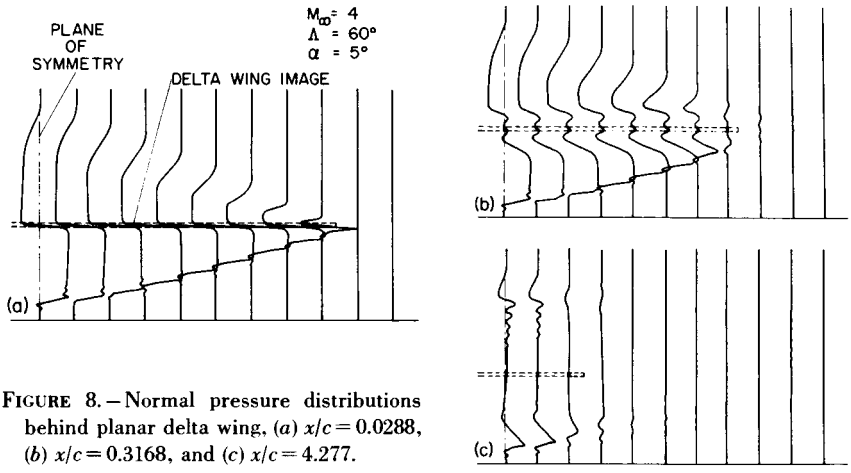

FIGURE 8.—Normal pressure distributions behind planar delta wing, (*a*) $x/c = 0.0288$, (*b*) $x/c = 0.3168$, and (*c*) $x/c = 4.277$.

Babaev (ref. 11) and found poor agreement. The present results substantiate South's good comparison with Voskresenskii.

The surface pressure coefficient on the expansion side of a 45° swept delta wing in Mach 3 flow for 4°, 8°, and 12° angles of attack is shown in figure 6. The results are compared with a method of characteristics technique devised by Beeman and Powers (ref. 12). The latter chose to neglect the weak crossflow shock, assuming instead an isentropic compression. The result of their assumption is evidenced by the disagreement in the location of the embedded shock. However, the pressure distributions on either side of the shock are in good agreement.

The results obtained for the compression and expansion side-flow fields of a 50° swept delta wing at 3° angle of attack in Mach 3 flow are compared with linear theory in figure 7. It is interesting to note that although there is considerable disagreement between the two theories for the individual surface pressure distributions and a slight disagreement in in the load distribution, there is almost no variation in the plot of C_L versus α for the two theories.

The two solutions for the upper and lower flow fields of the delta wing can be combined at the trailing edge to form the initial data plane from which calculations can be continued downstream. The results of such a computation are shown in figure 8, which is a reproduction of a sequence of photographs taken from the cathode-ray display tube as the flow field developed behind the wing. In figure 8(*b*), the formation of the trailing edge shock is clearly evident in the expansion region above the delta-wing image, as is the trailing edge expansion fan below the delta-wing image. The governing equations were solved in conical coordinates, thus giving the appearance of a shrinking wing in a fixed flow field as the integration proceeds downstream. All results shown in the figure were

obtained from an integration of the full Eulerian equations over a 69 by 32 mesh. About 20 min of central processing unit time on an IBM 360/67 were required to carry the solution from the trailing edge to 17 chord lengths [2] behind it. The calculations were monitored from a cathode-ray tube, and instabilities were suppressed when they appeared. This increased the real-time computation to about 30 min. The shock and rarefaction interaction were clearly evident in the moving pictures of the wake.

The case studied applied to a planar delta wing. The flow is conical so that the chord load distribution is triangular. Notice that the pressure distribution along the centerline below the wing is also nearly triangular after 4.3 chord lengths have been traversed. Future calculations will show these signatures along horizontal lines beneath the wing, but it is hypothesized at this time that the horizontal pressure distribution 4 chord lengths below the body will also be very nearly triangular. Nonlinear effects have, of course, been included, as well as complete interaction with both wingtips. One can speculate, therefore, that from the results shown in figure 8(*c*), the proper F-function could be determined and used to extrapolate the signature indefinitely. Studies along these lines are being carried out. Camber and thickness effects on simulated flows of the type just described are also projects of the immediate future.

REFERENCES

1. LOMAX, H.: Preliminary Investigation of Flow Field Analysis on Digital Computers With Graphic Display. Second Conference on Sonic Boom Research, NASA SP–180, 1968, pp. 67–71.
2. LAX, P. D.: Weak Solutions of Nonlinear Hyperbolic Equations and Their Numerical Computation. Commun. Pure Appl. Math., vol. 7, 1954, pp. 159–193.
3. MACCORMACK, R. W.: The Effect of Viscosity in Hypervelocity Impact Cratering. AIAA Paper no. 69–354, 1969, pp. 1–7.
4. KUTLER, P.; AND LOMAX, H.: The Computation of Supersonic Flow Fields About Wing-Body Combinations by "Shock-Capturing" Finite Difference Techniques. Paper presented at the Second Int. Conf. on Numerical Methods in Fluid Dynamics, Sept. 1970. To be published in Lect. Notes Phys.
5. BABENKO, K. I.; VOSKRESENSKII, G. P.; LYUBIMOV, A. N.; AND RUSANOV, V. V.: Three-Dimensional Flow of Ideal Gas Past Smooth Bodies. NASA TT F–380, 1966.
6. MORETTI, G.: Inviscid Flow Field Past a Pointed Cone at an Angle of Attack. TR no. 577, General Applied Science Laboratories, 1965.
7. HOLT, M.; AND NDEFO, D. E.: A Numerical Method for Calculating Steady Unsymmetrical Supersonic Flow Past Cones. J. Comput. Phys., vol. 5, 1970, pp. 463–486.
8. JONES, D. J.: Numerical Solutions of the Flow Field for Conical Bodies in a Supersonic Stream. Aeronautical Rept. LR–507, National Research Council of Canada, 1968.

[2] Only 4.3 chord lengths are shown here. The motion pictures presented at the conference carried the solution to 17 chord lengths at a Mach number $M_\infty=3$, an angle of attack $\alpha=3°$, and a sweep angle $\Lambda=50°$.

9. SOUTH, J. C.; AND KLUNKER, E. B.: Methods for Calculating Nonlinear Conical Flows. Analytic Methods in Aircraft Aerodynamics, NASA SP–228, 1969, pp. 131–158.
10. VOSKRESENSKII, G. P.: Numerical Solution of the Problem of a Supersonic Gas Flow Past an Arbitrary Surface of a Delta Wing in the Compression Region. Izv. Akad. Nauk SSSR, Mekh. Zhidk. Gaza, no. 4, 1968, pp. 134–142.
11. BABAEV, D. A.: Numerical Solution of the Problem of Supersonic Flow Past the Lower Surface of a Delta Wing. AIAA J., vol. 1, 1963, pp. 2224–2231.
12. BEEMAN, E. R.; AND POWERS, S. A.: A Method for Determining the Complete Flow Field Around Conical Wings at Supersonic/Hypersonic Speeds. AIAA Paper no. 69–646, 1969.

Theoretical Problems Related to Sonic Boom

W. D. HAYES, J. H. GARDNER, D. A. CAUGHEY, AND F. B. WEISKOPF, JR.
Princeton University

This paper is a brief report of research in progress at Princeton University on problems of wave propagation and sonic boom. Some of the problems studied are directly relevant to the sonic boom aspects of design and operation of supersonic aircraft. Others are concerned with general wave theory and concern phenomena more or less common to all propagating waves.

COMPUTATION OF TRANSONIC FLOWS WITH SHOCK WAVES

This investigation, carried out by Gardner using Princeton University's IBM 360/91 computer, had its inception in the nonlinear caustic problem. The passage of a sonic boom through a caustic is governed by equations that are essentially the same as the classical ones of transonic flow. A shock wave in a caustic region is expected to be a lambda shock.

The numerical method used was decided upon after trials with other methods. Within the flow field, a Lax-Wendroff algorithm is used. This algorithm is stable in transonic flows, although the stability is marginal and care must be taken in setting initial conditions. Appropriate boundary conditions to be imposed on the boundaries of the calculation domain are chosen. The new feature in the method lies in the treatment of shock waves. The usual method of treatment through spreading the shock over several mesh points was not used.

A shock is represented separately by a function describing its shape. Hugoniot conditions for the shock can be satisfied, in general, only if the shock is moving with a given calculable velocity. In the numerical method, this shock velocity is used to relocate the shock in the next iteration.

The lambda shock of the nonlinear caustic problem involves three shock waves that intersect at a triple point. The triple point and the point at which the shock disappears into the elliptic region are nonanalytic points for the flow. The computational task of keeping track of three shocks and their intersections imposed a complication on the numerical scheme that it seemed best to avoid until the other aspects of the numerical method were tested. Accordingly, this particular problem was put

aside after earlier calculations indicated that there would be some difficulty.

The problem taken up was that of a symmetric airfoil in transonic flow, with the flow subsonic at infinity. In this problem there is a single shock. The outer point at which the shock disappears into the elliptic region is easily handled. The foot of the shock on the airfoil is a non-analytic point in the flow field that requires separate treatment.

The calculational difficulty that has not as yet been overcome is instability or drifting of the shock. It is hoped that this difficulty can be solved in the near future.

SINGULAR RAYS

A singular ray is a ray in geometric acoustics (or optics) at which the solution is singular, so that the solution of geometric acoustics fails in its neighborhood. The problem becomes locally a diffraction problem and requires a full solution of the wave equation. Of particular interest in sonic boom problems are those rays for which the corresponding cutting plane passes through a straight leading (or trailing) edge. The particular aspect of singular ray problems of interest is the influence of nonlinear terms on their solution.

Two canonical problems may be distinguished. One is the singular ray as a singular direction for the F-function for a finite body. The other is the singular ray in a conical flow from a semi-infinite body. The linear solutions in both cases are well known. In the first case, we have come to the conclusion that the shock wave present absorbs the singular ray in such a way that the lateral gradients in the remaining wave system are asymptotically negligible. The standard Landau-Whitham treatment of wave distortion and shock development should apply without modification in the asymptotic field, with the lateral variable (usually the azimuth angle) entering only as a parameter. Thus there is no truly singular ray in the asymptotic nonlinear theory. Singular rays remain of interest in the near field before the Landau-Whitham asymptotic theory becomes valid.

In the conical case the singular ray is not trivial. The canonical equation governing this case had been found earlier by Kuo (ref. 1). Our result in this case is that the equations cannot be linearized by the distortion of the Landau-Whitham theory. This means that the plausible method of applying the standard distortion and shock fitting to the linear solution is incorrect. The problem can probably only be solved numerically, with the shock position appearing as an essential part of the solution.

BANGLESS BOOM OPTIMUMS

One conceivable way of solving the sonic boom problem for supersonic transport aircraft is to design them so that the signature at the ground

includes no shock wave. With the maximum shock strength labeled the "bang" and the impulse under the major lobe labeled the "boom," such a signature is a "bangless boom." The phenomenon of "freezing" of the signature shape in a stratified atmosphere makes this possibility more likely than would be concluded from formulas based upon a uniform atmosphere. This approach immediately suggests an optimization problem: For an aircraft of specified effective length at a high altitude, determine the maximum gross weight that causes no (or rather an incipient) shock wave on the ground. Other related optimization problems may be posed, but here we consider only the one. It is the basic problem of potential practical interest.

For no shock to appear in the final signature, the maximum slope of the F-function must be less than the inverse of the corresponding age variable. This maximum slope is designated A. Thus an inequality constraint is imposed upon the derivative of the F-function. The problem is to find the maximum of the total effective lift or gross weight

$$W = \int_0^L l(x_1)\, dx_1 \tag{1}$$

with the effective length given. For simplicity, the ray immediately beneath the aircraft is considered; results for other rays are no different essentially. The axial lift distribution l is related to the F-function through

$$l(x) = \frac{2\rho U^2}{\beta} \int_0^x \frac{F(x_1)\, dx_1}{(x-x_1)^{1/2}} \tag{2}$$

where $\beta = (M^2 - 1)^{1/2}$.

The solution is readily obtained on a heuristic basis. As in many optimization problems with inequality constraints, we expect the solution to satisfy the corresponding equality over most of the domain. Thus, over most of $0 < x < L$, $F' = A$. At switching points, we expect F to have a negative discontinuity. We can deduce that $F(0) \leqq 0$, that $l(L) = 0$, and that $l'(L) \geqq 0$. In the particular problem considered, the inequalities on $F(0)$ and $l'(L)$ are equalities. We conclude that $F(x)$ is given by

$$F = Ax \qquad 0 \leqq x < \tfrac{2}{3}L \tag{3a}$$

$$F = A(x - 2L/3^{1/2}) \qquad \tfrac{2}{3}L < x \leqq L \tag{3b}$$

The corresponding lift distribution function $l(x)$ is obtainable directly from equation (2).

One interesting task, carried out by Weiskopf, has been the justification of this result by the calculus of variations. Established methods for

problems with inequality constraints do not apply because of the intervention of the Abel transform, equation (2), in the problem. A nontrivial extension of the basic theory was needed. As one example of a detail, the condition $l(L)=0$ had to be used both as a boundary condition on l and, through equation (2), as an isoperimetric constraint on F.

We express the maximum effective gross weight of the aircraft under simplifying assumptions. The aircraft is in uniform level flight at a high altitude, and the ray immediately beneath the aircraft is considered. The appropriate age is that corresponding to an altitude difference of $\pi/2$ times the scale height $a^2/\gamma g$ at the aircraft altitude. The maximum gross weight is then

$$W_{\max}=\frac{128}{135\pi^{1/2}}\frac{(\gamma\beta g)^{1/2}\rho a L^{5/2}}{\frac{1}{2}(\gamma+1)M^2} \tag{4}$$

Note that this value depends on thermodynamic properties only at the aircraft altitude and is strongly dependent upon the effective length.

The maximum pressure in the signature may be expressed approximately, without the ground reflection factor, as

$$\left[\frac{\rho a}{\rho_0 a_0}\right]^{1/2}\Delta p_{\max}=\frac{45}{2^{1/2}\cdot 32}\frac{\beta^{1/2}W}{h^{1/2}L^{3/2}} \tag{5}$$

Here $\rho_0 a_0$ is the acoustic impedance at the ground. The quantity h is the aircraft altitude or, more strictly, ray tube width at the ground per unit azimuth angle at the aircraft.

For rays not immediately beneath the aircraft, if the effective axial lift distribution is unchanged by the change in the azimuth angle, equation (4) still holds. This result indicates that attention must be paid during aircraft design to the F-function over a range of azimuth angles. It would be clearly possible to have a bangless boom immediately beneath the aircraft with a strong bang appearing off to the side.

This result, equation (4), is to be contrasted with the classical Jones optimum (ref. 2) for the far field. To make the two cases more parallel, we pose Jones' problem as that of finding the maximum gross weight for a given shock strength Δp_{shock}. This result is

$$W_{\max}=2^{1/2}\cdot 4\,\frac{\frac{1}{2}(\gamma+1)hM^2L^{1/2}\,(\Delta p_{\text{shock}})^2}{\beta(\gamma\beta g)^{1/2}\rho_0 a_0} \tag{6}$$

under the same approximations for equations (4) and (5). The maximum effective gross weight here varies inversely as the acoustic impedance at the ground and is essentially independent of thermodynamic properties at the aircraft altitude. It has but a very weak dependence upon L.

Two principal implications of the basic equation (4) on a bangless boom aircraft design may be pointed out. The aircraft must not fly too high; the results for 30 000 ft appear reasonable and attainable, while those for 60 000 ft are out of reasonable range. The aircraft effective length must, by careful design, be made as large as possible. If the aircraft is to fly at high Mach number, there must be a vertical distribution of aerodynamic components, with some components located low and forward and others high and aft.

GENERAL WAVE THEORY

There is underway a development of general wave theory initiated and partly carried out by Whitham. This general theory, constructed for nonlinear dispersive waves, gives as a relatively simple special case the Blokhintsev invariance used in the theory of sonic boom with winds. Techniques developed for the computation of ray tube area in sonic boom problems can be generalized to analogous computations for linear dispersive waves.

Two papers by the senior author have appeared (ref. 3). One of these, on kinematic wave theory, presents the generalization of the ray tube area algorithms to dispersive waves. The other, on conservation of wave action, shows that a locally conserved action density exists in modal problems and that in linear acoustic problems this is twice the intrinsic kinetic energy density divided by the intrinsic frequency. The word "intrinsic" here means "as measured by an observer moving with the fluid."

In a paper in preparation it will be shown that the group velocity defined as a gradient of frequency in a wave number space has a clear-cut physical interpretation in terms of action flux in strongly nonlinear wave propagation. Problems of the type treated by Lighthill (ref. 4) are under study.

REFERENCES

1. KUO, Y. H.: A Similarity Rule for the Interaction Between a Conical Field and a Plane Shock. J. Aeronaut. Sci., vol. 22, 1955, pp. 504–505.
2. JONES, L. B.: Lower Bounds for Sonic Bangs in the Far Field. Aeronaut. Quart. J., vol. 18, 1967, pp. 1–21.
3. HAYES, W. D.: Proc. Roy. Soc. Lond. A, vol. 320, 1970, pp. 187–208, 209–226.
4. LIGHTHILL, M. J.: Contributions to the Theory of Waves in Non-Linear Dispersive Systems. J. Inst. Math. Its Appl., vol. 1, 1965, pp. 269–306.

The Effects of Atmospheric Inhomogeneities on Sonic Boom

A. R. GEORGE
Cornell University

The propagation of sonic booms in an idealized atmosphere containing only large-scale vertically stratified variations in properties is quite well understood. (For example, see refs. 1 and 2.) However, in addition to large-scale stratifications, the real atmosphere also contains less intense smaller scale inhomogeneities. These range from large-scale weather phenomena such as fronts and storm systems through internal waves to turbulent velocity, density, and temperature fluctuations. The turbulent fluctuations occur over a spectrum of scales down to a fraction of an inch. These inhomogeneities affect the propagation of waves in a number of ways.

Figure 1 shows an assortment of sonic boom signatures from each of two flights of a B–58 aircraft (ref. 3). The flights were made on two different days at slightly different flight Mach numbers, altitudes, etc. However, the most important difference between the two flights was that the wind velocity was low for one flight and strong and gusty for the other. Both sets of measurements show deviations from a simple N-wave shape, the differences being much more pronounced for measurements made under the more strongly turbulent gusty conditions. This correlation between turbulence level in the lower atmosphere and a variation from N-wave shape is well established (refs. 4 to 7). Inspection of data such as that in figure 1 allows the identification of several types of differences between the measured signatures and those predicted without accounting for atmospheric inhomogeneities. First, there are apparently random fluctuations about approximately the predicted wave shape. These are greatest directly behind the front and rear shocks and usually have little effect on the signatures far behind the shocks. The perturbations vary from signature to signature but are essentially identical in shape for the front and rear shocks of any given signatures. This indicates that the atmospheric inhomogeneities affecting the signatures are essentially uncorrelated between measuring stations but are essentially frozen over time scales of the order of time difference between the two shocks of a given signature. This is in accordance with knowledge of atmospheric turbulence. A second type of difference is that the shocks themselves

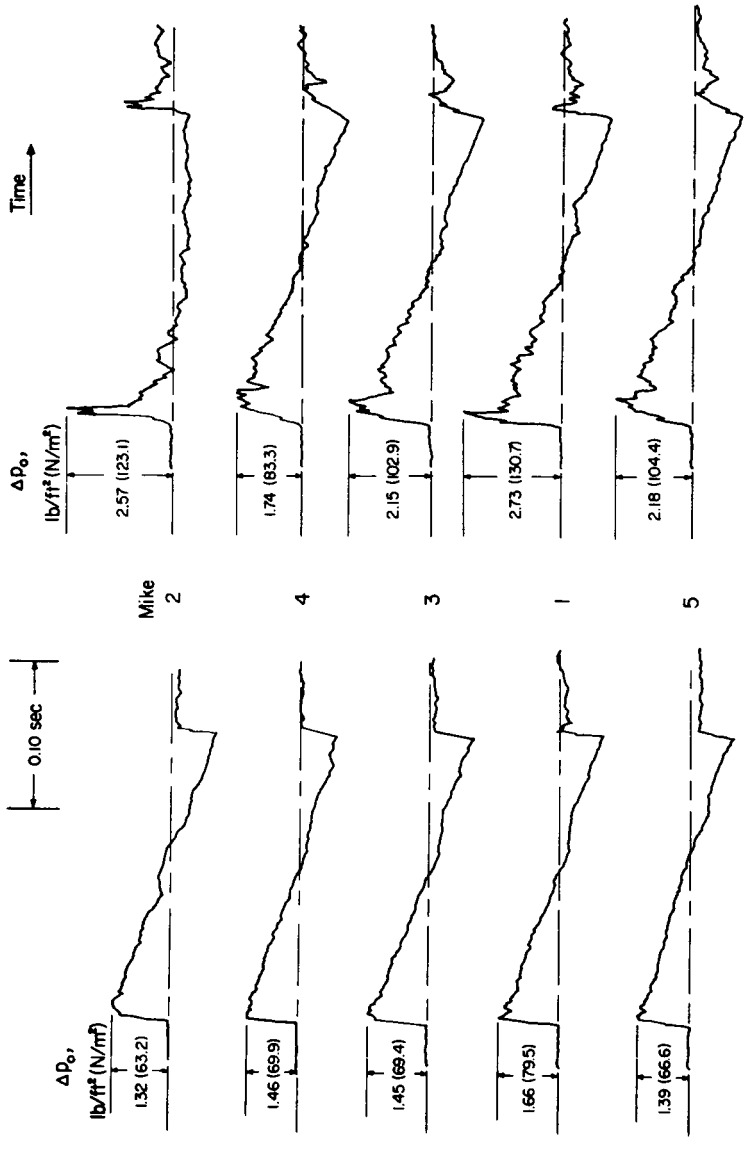

FIGURE 1.—Representative signatures for two different flights.

are several orders of magnitude thicker than the Navier-Stokes viscous shock structure would predict. Typically, the viscous shock thickness for shocks of this strength is 10^{-3} ft, whereas measured thicknesses range from approximately one to many feet. Third, there are apparently some variations in the overall strength of the waves from point to point for the same flight.

The random perturbations together with the overall strength changes contribute to variations in Δp, which is defined as the maximum overpressure of the wave. Experimental statistical studies have been made of $\Delta p/\Delta p_c$, where Δp_c is that calculated without turbulent effects (refs. 7 and 8). These studies have shown that log $(\Delta p/\Delta p_c)$ exhibits an approximately gaussian (normal) distribution. A typical plot of the probability of exceeding a given $\Delta p/\Delta p_c$ is shown in figure 2 (ref. 8). A straight line on these ordinates corresponds to a normal distribution of log $(\Delta p/\Delta p_c)$.

The area under the positive part of the signature is called the impulse and is one of the factors influencing the effect of a boom on structures. If the random fluctuations are distributed about a mean wave shape, the impulse variation is a measure of the variations in overall wave strength. Statistical studies of impulse variations (refs. 8 and 9) often show less variability than Δp, implying that some of the Δp fluctuations are due to random perturbations rather than overall level changes. Typical impulse probability data are shown in figure 3 (ref. 8).

The thickened shock structure is more difficult to document precisely because most experiments have measured the time to peak amplitude, which can sometimes grossly overestimate the rise time of the shock. (For example, see the uppermost left-hand signature in fig. 1, where Δp occurs well behind the shock.) Typical data are shown in figure 4 (ref. 8). It is apparent that the shock rise time is greater than 1 msec, but little more information on shock thickness can be obtained from this definition of rise time.

Unfortunately not enough signatures have been published to enable one to make definitive empirical correlations between the effects themselves and with atmospheric variables. Large quantities of signatures have been recorded, but usually only a few "illustrative" samples are shown in any given report. Depending on what is being illustrated, different types of signatures tend to be shown in different publications. Descriptive labels such as "normal," "peaked," "normal-peaked," etc., are sometimes reported for large numbers of signatures, but these labels are too subjective to be very informative.

GEOMETRIC ACOUSTICS

The first and simplest attempts at explaining some of the turbulent effects were based upon geometric acoustics. Random propagation speed

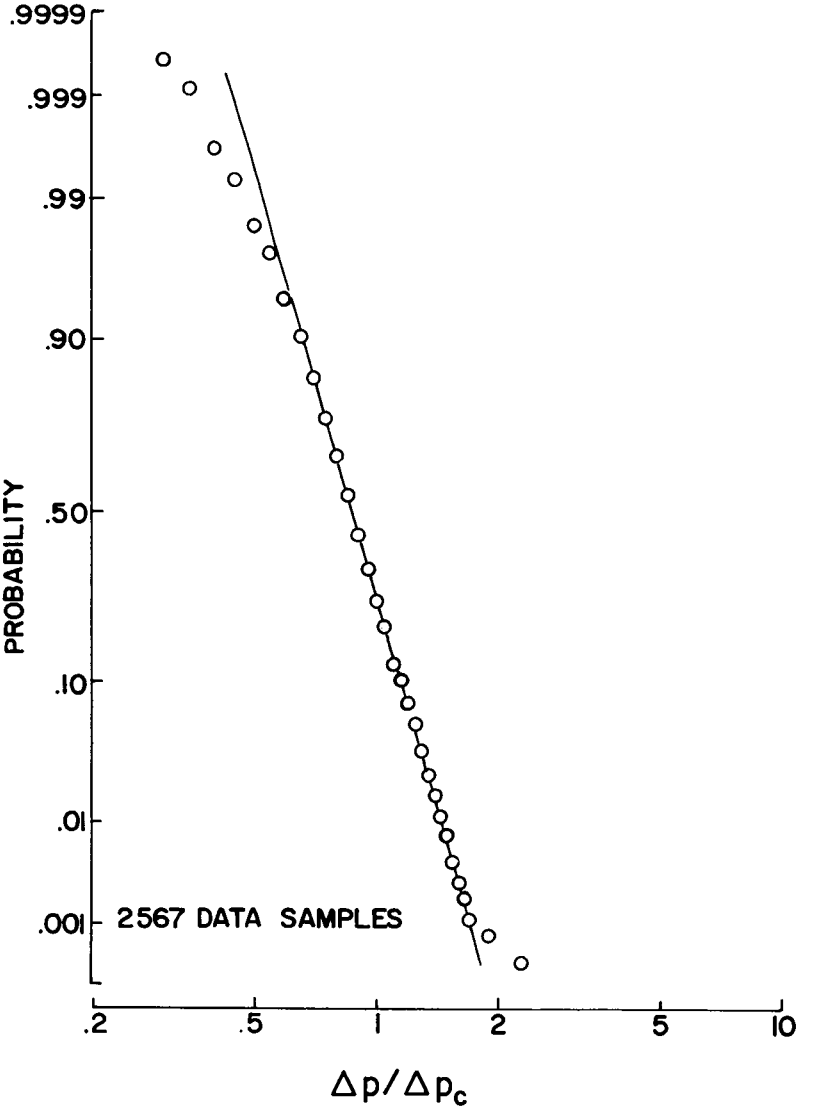

FIGURE 2.—Probability of equaling or exceeding Δp.

variations due to atmospheric temperature or velocity fluctuations can be envisioned as focusing or defocusing ray tubes passing through the inhomogeneities. Such a mechanism can only uniformly increase or decrease the strength of the N-waves as shown in figure 5. While this mechanism may partially explain impulse variations, it cannot explain changes in wave shape or shock thickness.

We will now examine the conditions for validity of the geometric

acoustics approach. First, the basic assumption of geometric acoustics requires $\lambda/L_0 \ll 1$, where λ is the wavelength and L_0 the length scale of the variations in the medium. The second limitation on the application of geometric acoustics is that diffraction phenomena be negligible (ref. 10, sec. 7.7; ref. 11, sec. 59). By Huygens' principle, we can consider any wavefront as made up of sources that emit hemispherical wavefronts forward, which make up the signal for future times. In the geometric

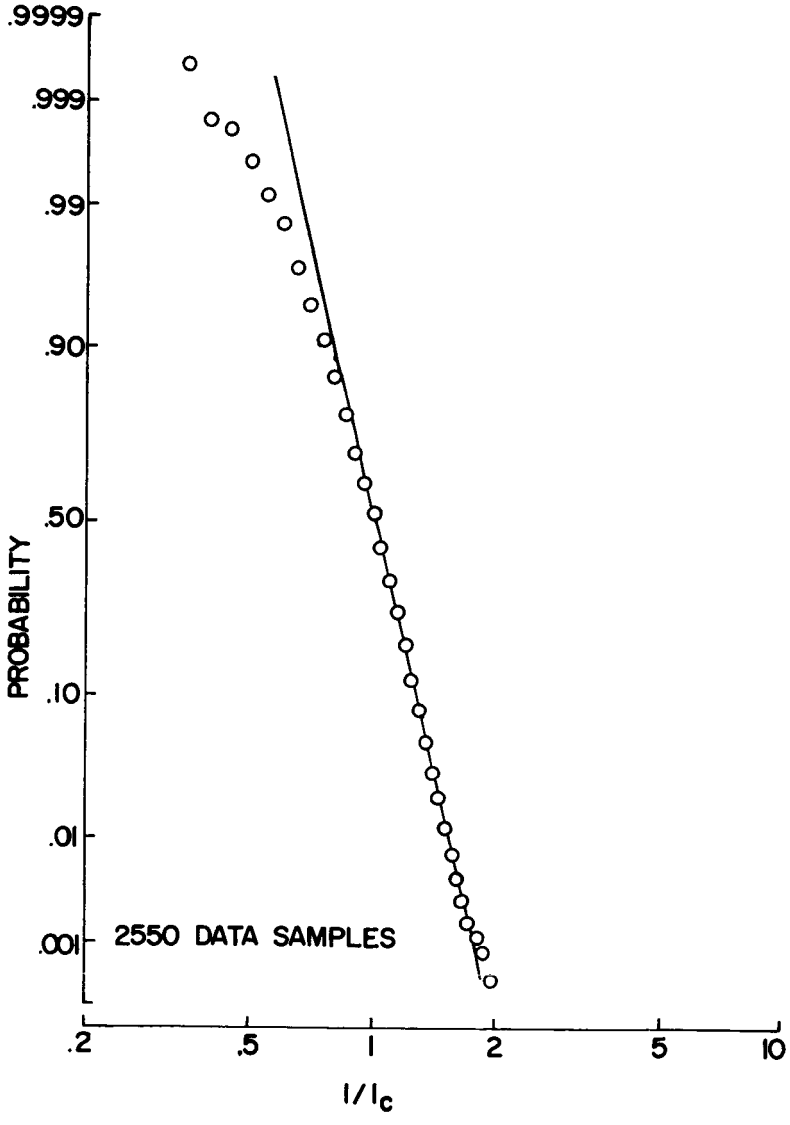

FIGURE 3.—Probability of equaling or exceeding impulse I.

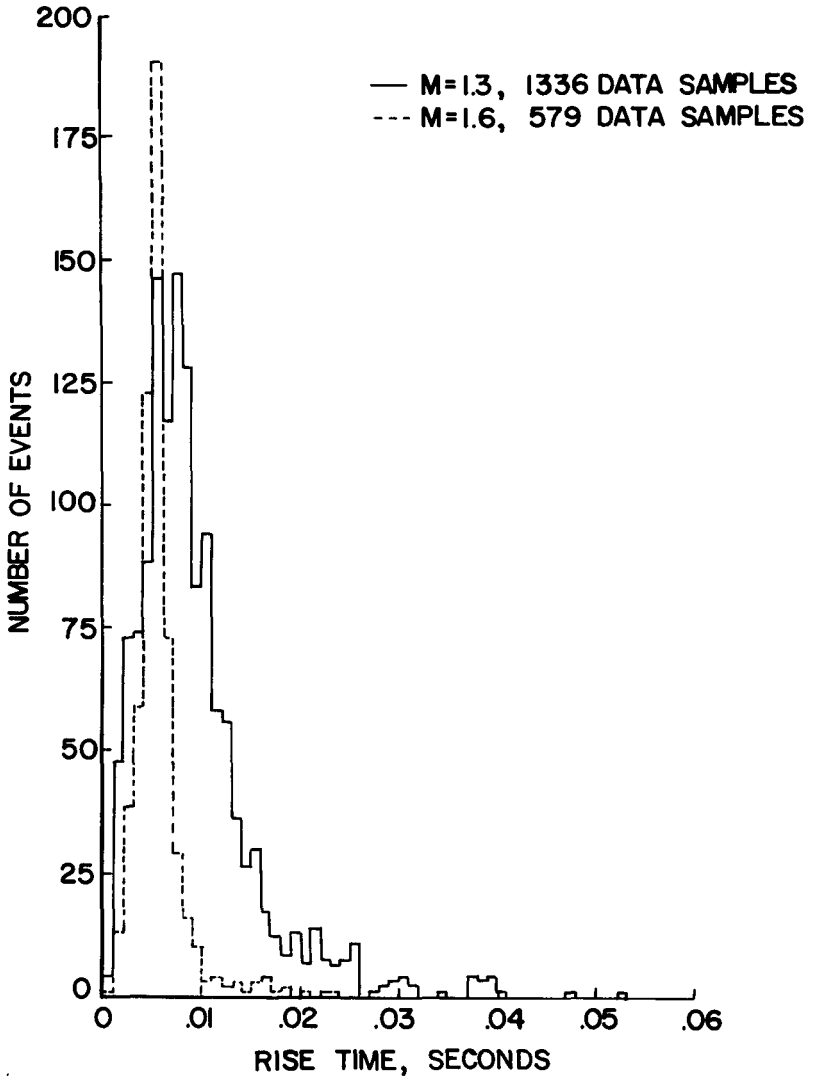

FIGURE 4.—Rise time to maximum pressure.

acoustics approximation, all of the wavelets from a given portion of a wavefront destructively interfere except in the ray tube associated with that portion of the front. Figure 6 shows wavelets from the two ends of a portion of a front of size L_0. For the interference to be destructive immediately outside of the ray tube of size L_0, we require that, after a propagation distance $D = a_\infty t$, the phase differences between the wavelets at the edge of the ray tube be large compared with a wavelength. From figure 7 this can be seen to require $D/\cos\theta - D \gg \lambda$ or for

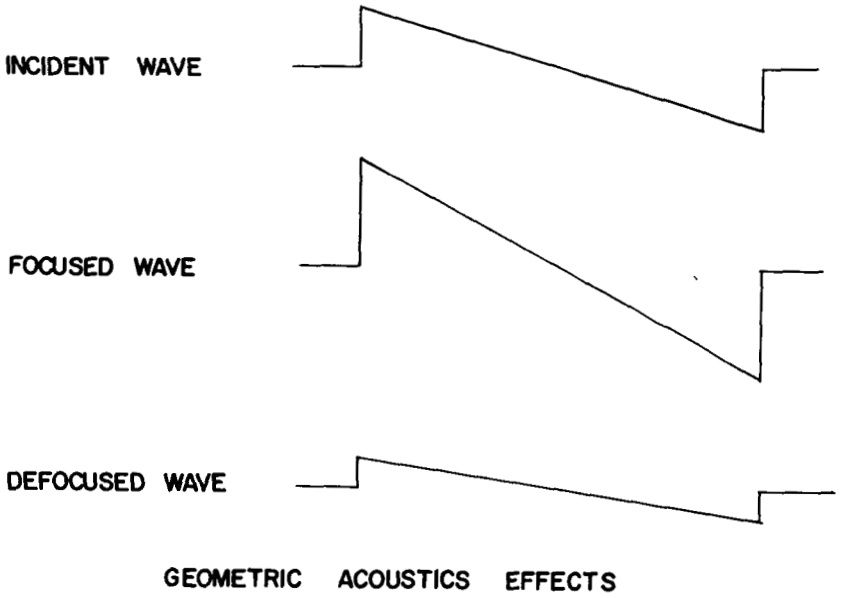

FIGURE 5. – Variations of N-wave level.

small θ, $\lambda D/L_0^2 \ll 1$; $\lambda D/L_0^2$ is sometimes called the diffraction parameter. Because geometric acoustics already requires $\lambda/L_0 \ll 1$, the additional requirement is that the propagation distance not be too large compared to L_0, the scale of variations in the medium. If $\lambda D/L_0^2$ is not small, diffraction effects are important and the concepts of ray tubes and wavefronts lose their usefulness.

Sonic boom signatures are typically several hundred feet long, thus containing Fourier components up to that wavelength. Then geometric

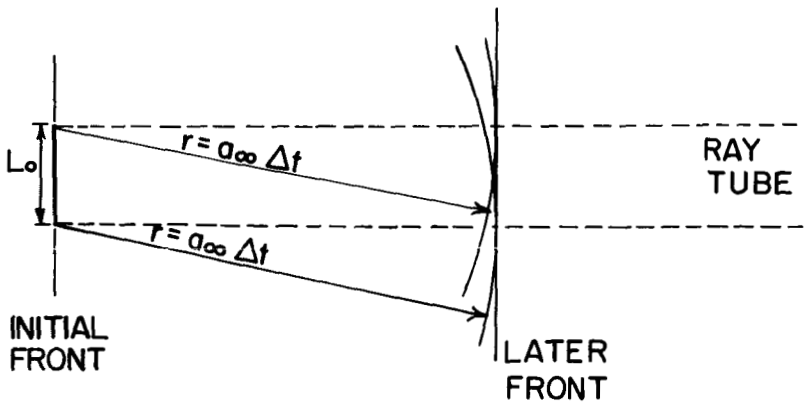

FIGURE 6. – Wavefronts from ends of initial wavefront segment.

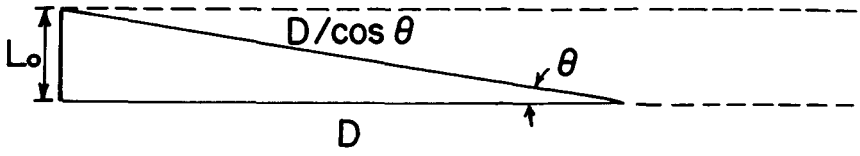

FIGURE 7.—Path lengths.

acoustics will only be valid for such large values of λ only when considering inhomogeneities with L_0 on the order of 10^3 ft or greater. This can be the case for moderate- to large-scale phenomena, such as inversion waves and thermals, but will not be true for the smaller eddies associated with turbulence in the atmospheric boundary layer.

Johnson (ref. 12) has applied geometric acoustics to find the overall level changes in sonic boom wave shapes due to inversion waves in the atmosphere. He carried out ray tracing calculations for a three-layer atmospheric inversion model with a sinusoidal height profile. The results show that these effects can be large enough to explain observed impulse variations. The initial stages of a program to experimentally verify the model was reported in annex D of reference 13 but apparently was not completed.

Pan (ref. 14) has also carried out a similar analysis for simple models of a cloud layer and a cold front. However, ne presents examples showing ground overpressure as a function of position for a fixed time. Measured signatures correspond to time variations at a fixed position (fixed ray). As his signature shapes correspond to varying rays, they are not relevant to explaining the observed signature shape changes.

DIFFRACTION AND SCATTERING

To account for the effects of the full spectrum of atmospheric inhomogeneities, diffraction must be accounted for. The most promising approach seems to be based upon small-perturbation scattering theory. As early as 1964, Kane and Palmer suggested that scattering theory might be applied to explain some of the characteristics of the perturbations in wave shapes and Δp (ref. 15). Pierce in 1968 demonstrated how diffraction can affect sonic boom wave shapes (ref. 16). He noted that diffraction can smear out some of the focusing effects predicted by geometric acoustics. As diffraction is more important for longer wavelengths, geometric focusing and defocusing affect primarily the shorter, higher frequency N-wave components (i.e., the parts of the signature near the shocks). Pierce presented an analysis, based on a Green's function solution, for a hypothetical model of an N-wave with an initial two-dimensional parabolic distortion in its otherwise plane wavefront. His results, shown in figure 8, demonstrate how focusing and defocusing can be

restricted to the parts of the wave near the fronts. Although his analysis is not suited for generalization to realistic models of atmospheric sonic boom propagation, it is noteworthy in that it demonstrates the transition between geometric acoustics

$$\frac{\lambda D}{L_0^2} \ll 1$$

and the scattering theories

$$\frac{\lambda D}{L_0^2} = \text{arbitrary}$$

that will be discussed next.

The analyses that have been most successful in explaining the random signal perturbations and shock thickening are based on the fact that the perturbations in velocity, sound speed, and density associated with

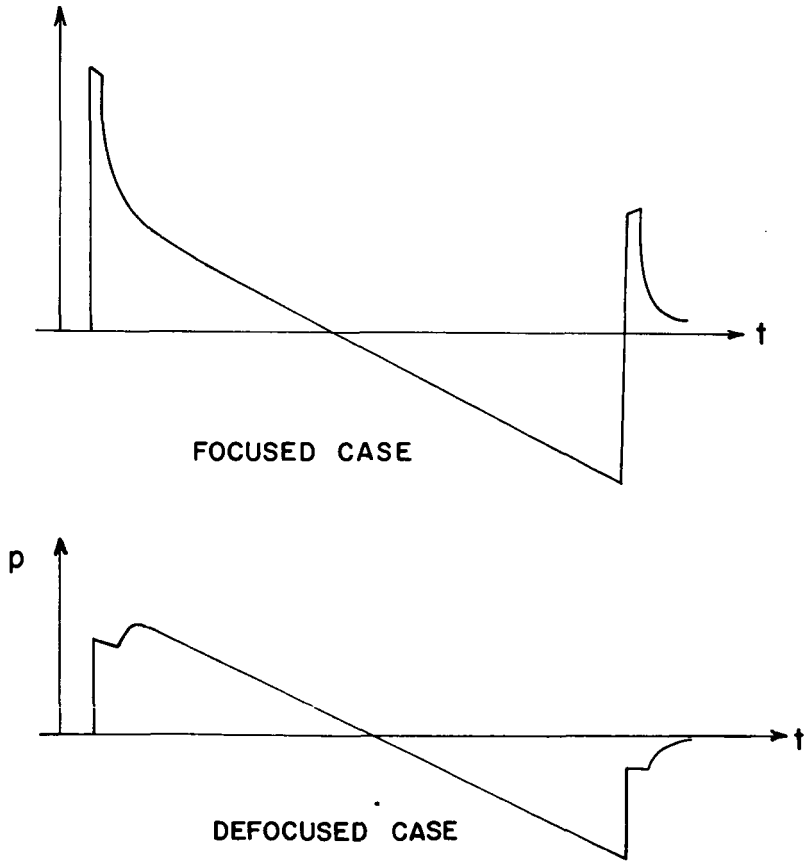

FIGURE 8.—Example of diffraction effects from reference 16.

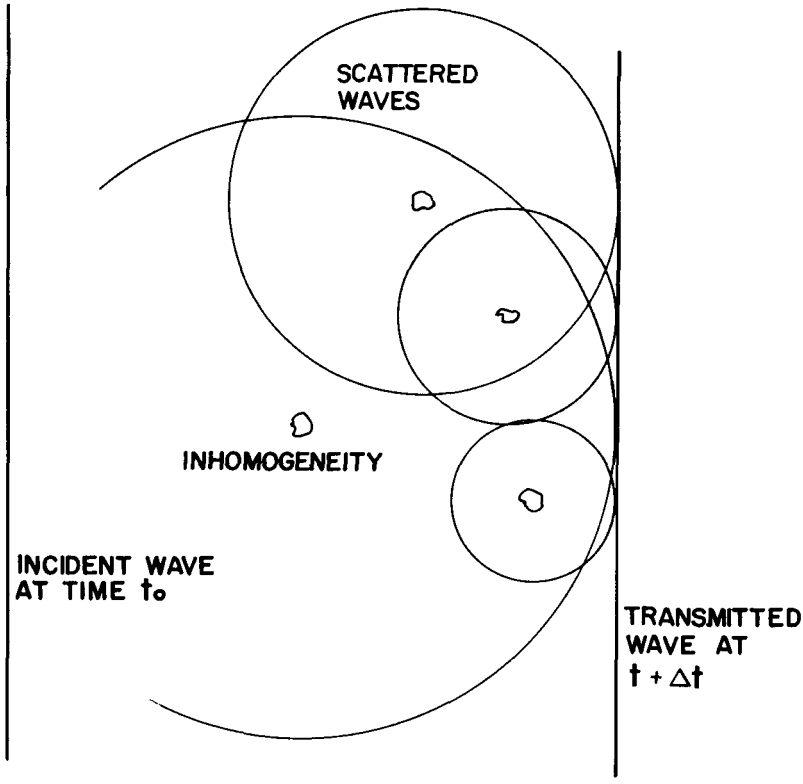

FIGURE 9.—Physical picture of scattering.

atmospheric turbulence are small. Thus waves propagate almost as if in a homogeneous medium, and the corrections to this lowest order behavior can be obtained by a perturbation scheme. The physical picture is sketched in figure 9. To lowest order, the incident wave propagates as a plane wave. As it passes over any particular inhomogeneity, the plane wave alone does not quite satisfy the exact equations of motion characterizing the inhomogeneous medium. A small correction is needed at each inhomogeneity, which thus acts as a source emitting a scattered wave. These scattered waves appear as perturbations at and behind the original wave and are the random fluctuations observed behind the shocks. As the scattered waves carry some energy out of the incident waves' direction, the original wave is modified by the energy lost. Because energy is second-order in wave strength, the energy loss associated with first-order scattered waves will have a second-order effect on wave structure.

In developing scattering theory, each of the dependent variables may be written as $( ) = ( )_\infty + ( )_T + ( )_W$, where $( )_\infty$ denotes the un-

disturbed spatial average, $(\ )_T$ the small fluctuations due to turbulence, and $(\ )_W$ the perturbations due to the wave. The turbulent fluctuations are taken as constant during the wave passage. The mass and momentum equations and entropy conservation can be combined to give for a perfect gas (refs. 17 and 18):

$$\frac{1}{a_\infty^2}\frac{\partial^2 p_W}{\partial t^2}-\nabla^2 p_W=\nabla\left(2\rho_\infty \mathbf{V}_T\cdot\nabla\mathbf{V}_W+2\frac{a_T}{a_\infty}\nabla p_W\right) \tag{1}$$

where nonlinear terms in p_W have been neglected for the present. We note that this equation is linear in $(\ )_T$ as well, so we are able to speak of scattering of Fourier components of $(\ )_W$ by Fourier components of the inhomogeneity field $(\ )_T$. Defining ϵ as the small parameter characterizing the magnitude of $(\ )_T/(\ )_W$, the solution to equation (1) is expressed in terms of a series

$$p_W=p_0+\epsilon p_1+\epsilon^2 p_2+\cdots$$

Then it is easy to see that p_0 satisfies the homogeneous wave equation

$$\frac{1}{a_\infty^2}\frac{\partial^2 p_0}{\partial t^2}-\nabla^2 p_0=0 \tag{2}$$

and p_1 is governed by

$$\begin{aligned}\frac{1}{a_\infty^2}\frac{\partial^2 p_1}{\partial t^2}-\nabla^2 p_1&=\nabla\left(2\rho_\infty \mathbf{V}_T\cdot\nabla\mathbf{V}_0+2\frac{a_T}{a_\infty}\nabla p_0\right)\\&=f(\mathbf{x},t)\end{aligned} \tag{3}$$

The truncation of the series after p_1 is called the Born approximation. One can interpret p_1 as waves scattered once by inhomogeneities; p_2 then contains a second scattering from p_1 being scattered again as well as the energy loss due to the first scattered waves. The solution to equation (3) is formally given in terms of retarded times by

$$p_1=\frac{1}{4\pi}\int\frac{f\left(\mathbf{y},t-\dfrac{|\mathbf{x}-\mathbf{y}|}{a_\infty}\right)}{|\mathbf{x}-\mathbf{y}|}d^3\mathbf{y} \tag{4}$$

where f is a random function of space through its dependence on $\mathbf{V}_T$ and a_T, which are given statistically. Thus only statistical properties of p_1, such as $\langle p_1^2\rangle$, can be found ($\langle\ \rangle$ denotes the ensemble average). Complete treatments for harmonic waves can be found, for example, in the monographs by Chernov (ref. 19) and Tatarski (ref. 10), while Crow (ref. 18) has treated the case of a step-function incident wave.

Although arbitrary values of the diffraction parameter $\lambda D/L_0^2$ can sometimes be handled, in many cases the analyses are carried out for large or small values of $\lambda D/L_0^2$ to simplify the mathematics.

IMPLICATIONS OF SCATTERING THEORY

We will next discuss some of the results from harmonic wave scattering theory for $\lambda \ll L_0$ to illustrate the influences of inhomogeneity scale, wavelength, and propagation distance. As the phenomena are linear in the inhomogeneities, we can use results found for special models of turbulence that have essentially one scale (correlation functions of the form $\exp[-r^2/L_S^2]$). In the geometric acoustics limit $(\lambda D/L_S^2) \ll 1$, the mean-square perturbations can be shown to be (ref. 19, p. 34; ref. 10, p. 148)

$$\frac{\langle p_1^2 \rangle}{|p_0|^2} = \frac{8\sqrt{\pi}}{3} \epsilon^2 \frac{D^3}{L_S} \tag{5}$$

In this limit the perturbations are essentially due to focusing and defocusing. From equation (5), we see that for a given D the perturbations are greater for smaller L_S. (Smaller scale inhomogeneities have a shorter focal length.) Of course, we can only consider smaller values of L_S as long as $(\lambda D/L_S^2) \ll 1$, indicating that the maximum perturbations will be caused by the minimum L_S such that $(\lambda D/L_S^2) \approx 1$. Similarly, for the opposite case $(\lambda D/L_S^2) \gg 1$, scattering theory for $\lambda \ll L_S$ results in (ref. 19, p. 75; ref. 10, p. 149)

$$\frac{\langle p_1^2 \rangle}{|p_0|^2} = \frac{\sqrt{\pi}}{2} \epsilon^2 D L_S k^2 \tag{6}$$

where the wave number $k = 2\pi/\lambda$. The perturbations from equation (6) increase for increases in L_S until $(\lambda D/L_S^2) \simeq 1$, where the equation is invalid. Thus from either case we see that the maximum perturbations are caused by inhomogeneities of size $L_S \approx \sqrt{\lambda D}$. This result is derived using an analysis valid for arbitrary $\lambda D/L_S^2$ in Tatarski's book (ref. 10, secs. 7.4 and 7.6). For sonic booms, λ is in the range of 1 to 100 ft and D ranges from say one to several thousand feet. Thus we see that L_S's of interest cover the range from 1 ft to thousands of feet, which can include both the inertial and energy bearing ranges of atmospheric turbulence. For $\sqrt{\lambda D}$ less than L_0, the macroscale or integral scale of the turbulence, results depend on the details of the spectrum. For $\sqrt{\lambda D}$ much greater than L_0, results depend primarily on L_0 and the turbulent intensity ϵ^2.

Equation (6) for $(\lambda D/L_S^2) \gg 1$ shows that scattering is strongest for large k (small λ). If we look more closely at the results of scattering theory, we find that for $\lambda \ll L_S$, the major portion of the energy scattered

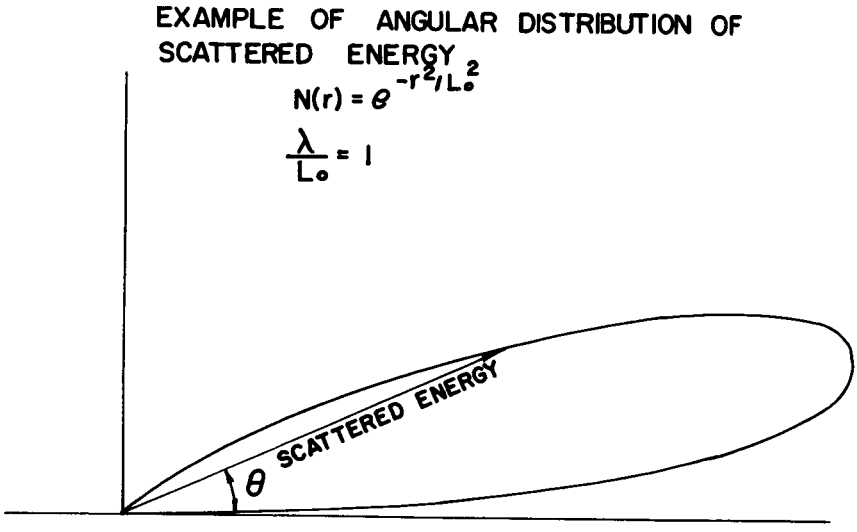

FIGURE 10.—Polar plot of energy scattered at angle θ.

propagates at an angle to the incident wave of $\theta \approx (\lambda/\pi L_S)$. For example, for scattering from sound speed fluctuations with correlation function $\exp[-r^2/L_S^2]$, the energy scattered at an angle θ to the incident wave's direction is proportional to

$$\sin\theta \exp\left[-\left(2\pi L_S \lambda^{-1} \sin\frac{\theta}{2}\right)^2\right]$$

(ref. 19, sec. 11). This factor is plotted for $\lambda = L_S$ in figure 10. We see that for $\lambda \leqslant L_S$, the scattered energy primarily propagates at a small angle to the incident wave's direction. To interpret the physical significance of the scattered perturbations, it is of interest whether the scattered perturbations are distinct from the remaining incident wave. Figure 11 shows a hypothetical example where a "perturbation" that initially merely changes the effective location of the incident step function propagates at an angle to the incident wave and thus eventually lags behind it. It then shows up as a distinct perturbation pulse behind the incident wave. To determine when harmonic waves propagating at an angle θ are distinct from an incident harmonic wave, we calculate when they have lagged at least one-half wavelength behind the incident wave. From figure 12 we obtain $D/(\cos\theta - D) \geqslant \lambda/2$ or for small values of $\theta = \lambda/\pi L_S$, $\lambda D/L_S^2 \geqslant \pi^2$. This gives us another view of the difference between geometric acoustics and far-field diffraction theory for $\lambda \ll L_0$. For small $\lambda D/L_S^2$, the scattered energy stays closely in phase with the incident wave and primarily gives overall amplitude fluctuations. For

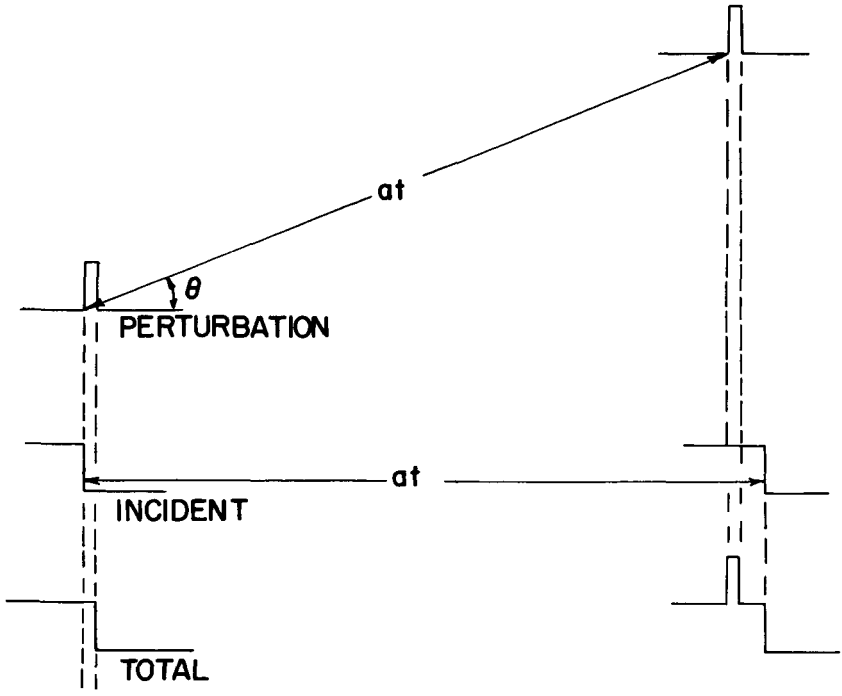

FIGURE 11. — Distinctness of a pulse propagating at an angle to the incident wave.

large $\lambda D/L_S^2$, the scattered energy is out of phase with the incident wave and appears as random fluctuations behind it. In this case, the initial part of the wave has its energy decreased by that scattered. As this damping is stronger for high frequencies, this leads to a smoothing of the wave structure and is the origin of shock thickening (refs. 20 to 22).

As atmospheric turbulence contains a spectrum of inhomogeneities ranging down to small fractions of an inch in size, there is always a range of inhomogeneities small enough to randomly scatter high-frequency wave components. Even accounting for the strong decrease in turbulent amplitude with wavelength in the inertial range, it is easy to show that scattering to any angle increases with incident wave frequency. Thus in experimental measurements, the very high frequencies will not appear either in the basic wave or in the perturbations due to strong multiple scattering. These multiply scattered waves will have had their propagation directions randomized and thus will be left behind the remaining part of the incident wave. The highest frequency perturbations will be largely those scattered once from the highest frequencies left in the smoothed signature shape.

To calculate how much the incident wave is damped by loss of first scattered waves, one can either carry scattering theory to second

order (ref. 23) or use an energy balance based on the first-order quantities (ref. 19). If the amplitude of the wave traveling in the original direction is A, then one finds for $\lambda \ll L_0$ (refs. 10 and 19)

$$A = A_0 e^{-\alpha D/2} \tag{7}$$

where

$$\alpha = \epsilon^2 L_0 k^2$$

Comparing with equation (6), we see that when the propagation distance is large enough so that $(\langle p_1^2 \rangle / |p_0|^2) \approx 1$, the original wave is reduced to e^{-1} of its original amplitude. Thus the maximum perturbations that can occur are approximately of the order of the incident wave amplitude. From equation (7), we also see that the maximum wave number expected can be found from $\alpha D \approx 1$ to be

$$k_{\max} \approx (\epsilon^2 D L_0)^{-1/2}$$

in the absence of nonlinear steepening effects.

Bringing these considerations together, we have the following physical picture of the effects of inhomogeneities on sonic boom propagation.

(1) Only the largest scale atmospheric inhomogeneities can result in overall geometric focusing and defocusing of N-waves.

(2) Somewhat smaller scale inhomogeneities can focus and defocus the higher frequency components of the wave (parts near the shock), but diffraction for $(\lambda D / L_S^2) \geqslant \pi^2$ makes lower frequency scattered waves appear as random perturbations about the N-wave shape. The lowest frequencies with $(\lambda D / L_0^2) \gg 1$ are only weakly affected and propagate essentially unchanged.

(3) The energy lost in the scattered waves results in a decay in amplitude of the high-frequency components of the signature that is eventually balanced by nonlinear steepening effects. As the signature loses its high-frequency components, geometric focusing becomes less important.

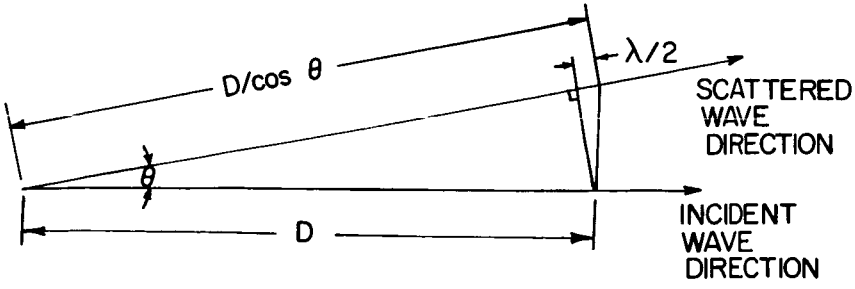

FIGURE 12.—Phase lag for distinctness of scattered waves.

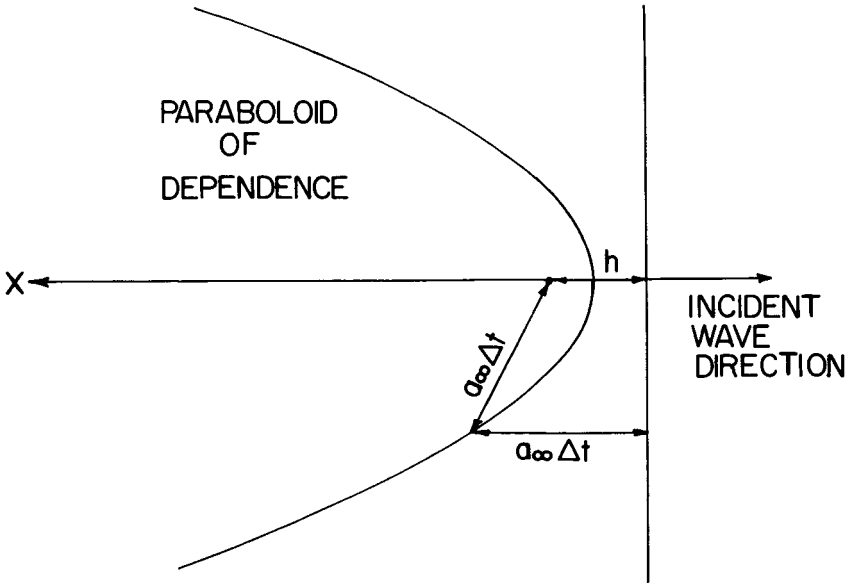

FIGURE 13.—Locus of points emitting scattered waves to $(h, 0)$.

(4) As the diffraction parameter $\lambda D/L_0^2$ increases with propagation distance or wavelength, there is a progressive shift from geometric focusing to diffraction-dominated random perturbations and shock thickening.

(5) Because of the decay of the high-frequency components of the original wave, the maximum nondimensional random perturbation can be only of order 1. These perturbations will have frequencies of the order of the maximum frequencies left in the signature.

FIRST-ORDER SCATTERING AND PERTURBATIONS

A complete treatment of the first-order perturbation of a step-function model of a shock has been presented by Crow in reference 18. He applied the first-order scattering approximation to equation (1) for a discontinuous incident wave $p_0 = \Delta p H(x + a_\infty t)$. He considers the scattered waves that arrive at a point a distance h behind the incident shock. Referring to figure 13, in cylindrical coordinates x, r, we see that the signal arriving from a point that was produced by the shock at time Δt will arrive at the point $(h, 0)$ if $x^2 = (a_\infty \Delta t)^2 = (x-h)^2 + r^2$. Thus the points that have radiated perturbations to $(h, 0)$ lie on the paraboloid

$$r = [2h(x - h/2)]^{1/2} \cong (2hx)^{1/2}$$

Crow then shows that the retarded time solution (eq. (4)) is reduced from a volume integral to a surface integral over the paraboloid. Then in his

solution for p_1, the maximum effect is felt from inhomogeneities of size $L_S \approx \sqrt{hx}$, which is analogous to the maximum effect from $L_S \approx \sqrt{\lambda D}$ from harmonic wave theory. Crow shows that his solution includes both geometrical acoustics and diffraction phenomena. To be able to evaluate $\langle p_1^2 \rangle$, he assumes $\sqrt{hx} \ll L_0$, where L_0 is the integral scale or macroscale. This implies that the eddies contributing most strongly to the scattering lie in the inertial range of the turbulence. This assumption allows him to evaluate the solution assuming a Kolmogorov inertial range and allowing variation of turbulent dissipation with height. He obtains the final result

$$\langle S_1^2 \rangle = \frac{\langle p_1^2 \rangle}{|p_0|^2} = \frac{1}{h^{7/6}} \int_0^\infty x^{5/6} A \mathscr{E}^{2/3}(x)\, dx \tag{8}$$

where A is a constant and $\mathscr{E}(x)$ is the turbulent dissipation. For any particular $\mathscr{E}(x)$ defined over a finite thickness layer, this reduces to

$$\frac{\langle p_1^2 \rangle}{|p_0|^2} = \left(\frac{h}{h_c}\right)^{-7/6}$$

where h_c is a length depending on the parameters characterizing the turbulent layer through which the step function has propagated.

As these results do not account for thickening of the shock, the perturbations become very large directly behind the shock. Outside of this region, however, the agreement with experiment is quite satisfactory within the limits of uncertainty of knowledge of the atmospheric turbulence and the accuracy of experimental evidence for $\langle p_1^2 \rangle$.

SECOND-ORDER EFFECTS AND SHOCK THICKENING

Crow's theory is linear. Thus the perturbations due to p_0's that are different from the step-function incident wave that he treated can be obtained by superposition. As shown in references 20 to 22, the turbulent medium can be considered as a series of layers in which the incident p_0 on each layer is the thickened wave emerging from the previous layer. For a step function passing through a given layer, equation (8) gives

$$\langle S_1^2 \rangle = A h^{-7/6} x^{5/6} \mathscr{E}^{2/3}(x)\, \Delta x$$

or

$$\langle S_1^2 \rangle^{1/2} = \left(\frac{h_t(x)}{h}\right)^{7/12} (\Delta x)^{1/2}$$

where

$$h_t^{7/6}(x) = A x^{5/6} \mathscr{E}^{2/3}(x)$$

Now if the incident wave is given by $p_0(\xi, x)$, where $\xi = x - a_\infty t$, then using a convolution and

$$\langle S_1(h) S_1(h') \rangle \leq \langle S_1^2(h) \rangle^{1/2} \langle S_1^2(h') \rangle^{1/2}$$

(ref. 21), one obtains

$$\langle S_1^2 \rangle^{1/2} \leq (\Delta x)^{1/2} \int_{-\infty}^{h} \left(\frac{h_t(x)}{h - \xi} \right)^{7/12} \frac{dp_0}{d\xi} (\xi, x)\, d\xi$$

Squaring and integrating to account for all layers, we have

$$\langle S_1^2 \rangle \leq \int_0^\infty \left[\int_{-\infty}^{h} (h - \xi)^{-7/12} \frac{dp_0}{d\xi} (\xi, x)\, d\xi \right]^2 A x^{5/6} \mathscr{E}^{2/3}(x) dx \qquad (9)$$

which gives an upper bound for the mean-square perturbations accounting for a varying p_0.

At this point however an important question still must be discussed: What is a proper definition of p_0 to use in equation (9)? A mathematically convenient choice would be $\langle p \rangle$, the ensemble average of the wave shape. If n are integers that characterize the particular realizations of the turbulence, then in terms of the individual deterministic solutions $p(\xi, x; n)$ the ensemble average is defined as

$$\langle p(\xi, x) \rangle = \lim_{N \to \infty} \frac{1}{N} \sum_{n=1}^{N} p(\xi, x; n)$$

However, as is seen with the aid of figure 14, the ensemble average is unsatisfactory for our purposes. The figure shows an ensemble of slightly thickened waves, each having propagated to slightly different positions at the given time due to randomly varying propagation speed. The ensemble average then shows a wave with an apparent extra thickness due only to the different positions of the individual waves. Consider the case where any particular wave is given by $p(\xi, x; n) = p_0(\xi + \epsilon(n), x)$, where $\epsilon(n)$ is a random variable with zero ensemble average. Then if ϵ is sufficiently small, we can write

$$p(\xi, x; n) = p_0(\xi, x) + \frac{\partial p_0}{\partial \xi} \epsilon(n) + \frac{\partial^2 p_0}{\partial \xi^2} \frac{\epsilon^2(n)}{2!} + \ldots$$

and taking the ensemble average

$$\langle p(\xi, x) \rangle \cong p_0(\xi, x) + \frac{\langle \epsilon^2 \rangle}{2!} \frac{\partial^2 p_0}{\partial \xi^2}$$

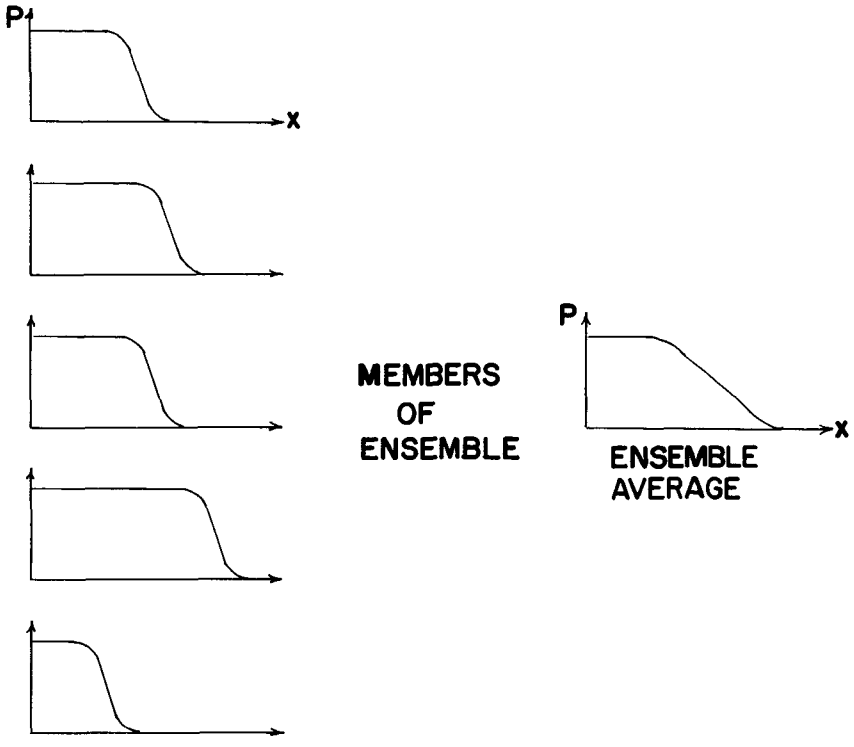

FIGURE 14.—Example of ensemble average for slightly thickened shocks.

showing a fictitious "thickening" of the $\langle p \rangle$ structure. Clearly this extra thickening is not related to the characteristics of any individually measured wave (given n). Also it is clear that the perturbations scattered for any given n will not depend on $\langle p \rangle$ but rather $p(\xi, x; n)$. In particular, $\langle p \rangle$ contains significantly less high-frequency energy than a particular $p(\xi, x; n)$, and the high frequencies are the most strongly scattered. Thus we need a more suitable choice for $p_0(\xi, x)$.

A suitable choice for p_0 has been analyzed in references 20 to 22. The analyses include both the second-order energy loss due to scattering and the counteracting effect of nonlinear steepening. The wave quantities are expanded in two small parameters: ϵ, the strength of the inhomogeneities, and δ, the incident wave strength giving

$$p_W = \delta p_{10} + \delta\epsilon p_{11} + \delta^2 p_{20} + \delta\epsilon^2 p_{12} + \ldots$$

The terms on the right-hand side represent, respectively, the incident wave, first scattering, lowest order nonlinear steepening, and second-

order scattering including energy lost in p_1. The series truncation requires $\delta^2 \ll \epsilon^2$, and to keep nonlinear effects from letting a significant portion of the scattered energy catch back up with the shock, $\delta \ll (k_{max} L_0)^{-2}$. To consider the wave shape without the effects of the random fluctuations, the wave is treated after subtracting the first scattered perturbations. Thus an approximate equation for $P = p_W - \delta\epsilon p_{11}$ is derived using the concept of a series of layers of turbulence. For P to correspond to the measured wave shape and thickness, the first scattered waves that are not included in P must have propagated far enough to have become distinct as discussed previously. Thus for predicting shock thicknesses or rise times, it is required that $(\lambda D/L_0^2) \gg 1$, which is only valid for long distance propagation through turbulence. However, for predicting the first-order perturbations, P can always be used. This is because, to second-order in ϵ, P corresponds to the part of the wave propagating in the original direction. The $\delta\epsilon p_{11}$, which has been subtracted to get P, has already been counted as scattered perturbations, and any rescattering of it should not be counted again. Rescattering can only serve to reduce the total scattered waves propagating along following the initial front as discussed previously. (The case when this reduction is important is discussed by K. J. Plotkin in these proceedings.)[1] Thus P is a satisfactory estimate for $p_0(\xi, x)$ in equation (9) for calculating the first-order perturbations due to turbulence.

For conditions typical of weak sonic booms propagating through locally homogeneous isotropic turbulence, the wave structure P has been shown (refs. 20 to 22) to be governed by the Burgers' equation:

$$\frac{\partial P}{\partial x} + \frac{\gamma + 1}{2\gamma p_\infty} P \frac{\partial P}{\partial \xi} = \epsilon^2 L_0 \frac{\partial^2 P}{\partial \xi^2}$$

where ϵ^2 and L_0 can be slowly varying with x (compared to L_0). The dissipative second-derivative scattering term is typically much larger than the analogous viscous dissipation term that could be included. This is because much more energy is scattered out of the incident wave's direction than is converted directly into heat.

In the case of $\epsilon^2 L_0 =$ constant, both unsteady and steady (equilibrium) solutions of this equation can be easily obtained. Using rough estimates for ϵ^2 and L_0, the results give shock thicknesses agreeing with those observed for sonic boom and weak explosion waves within the wide limits of uncertainty characterizing the atmospheric and thickness data. Figure 15 taken from reference 21 compares various sonic boom and explosion wave thicknesses to the theory. Using the P solutions as p_0

[1] See p. 59.

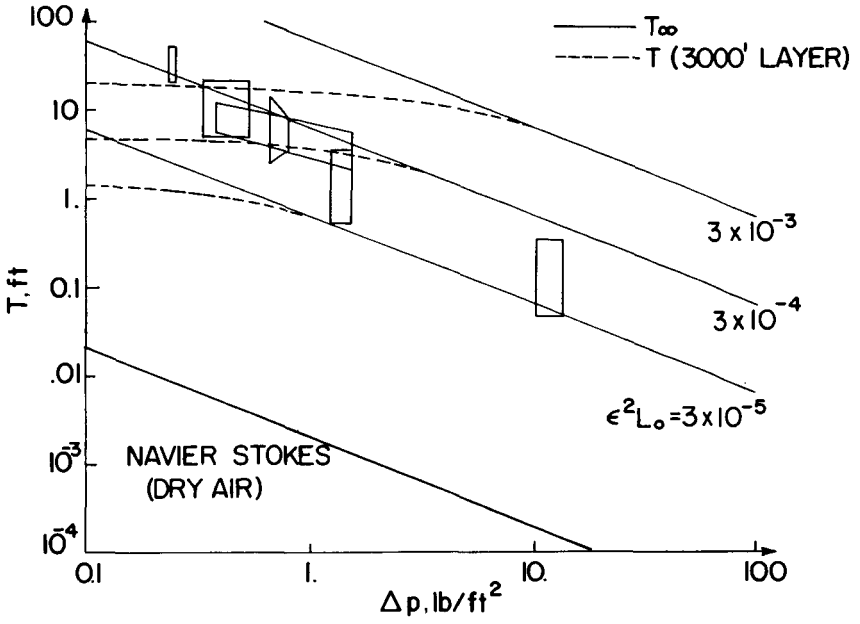

FIGURE 15.—Comparison of calculated shock thicknesses T to range of various sonic boom and explosion measurements.

in equation (9) gives results for $\langle p_1^2 \rangle$ that are also quite reasonable, although it is difficult to make precise comparisons with experiments.

The conclusions of the analysis that the high-frequency wave components are strongly and multiply scattered into random directions and eventually left behind is in accordance with the high-frequency decay observed in power spectral density measurements of sonic booms (refs. 7 and 13). For example, Young et al. in annex F of reference 13 have shown that there is an observed change from a 6- to a 12-dB/octave rolloff in energy spectral density above the frequency associated with the observed shock thicknesses (rise times). The model experiments of Bauer and Bagley (ref. 24) also help to verify various features of the model. For example, the shadowgraphs shown in figures B9 and B10 of their report clearly show the lagging scattered waves originating from a limited region of turbulent scattering. The associated pressure measurements show the resulting shock thickening as well. For waves passing through more extended turbulence, they conclude that their shadowgraphs only registered features associated with wrinkles on the nominally conical shock fronts. However, their pressure measurements clearly show the scattered waves in this case as well.

A quite different analysis has been proposed by Pierce to explain shock thickening (ref. 25). He bases his analysis on the behavior pre-

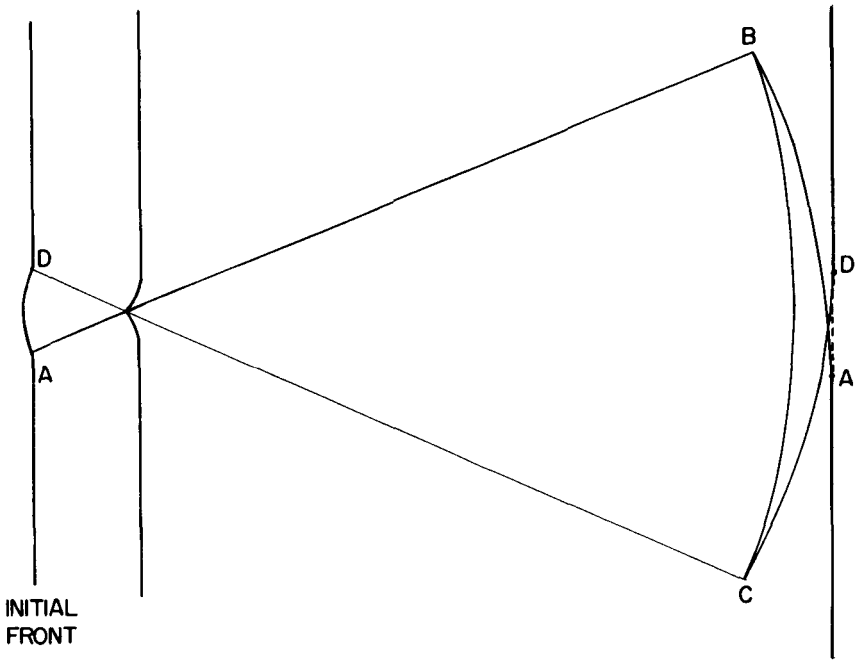

FIGURE 16. – Sketch of phenomena for wavefront passing through a focus.

dicted by geometric acoustics for wavefronts passing through a focus. As shown in figure 16, an initially concave portion of a geometric acoustic front will eventually focus and form a so-called "folded" front. However, we note that geometric acoustics applies only for the wave number $k \to \infty$ and that for finite k, diffraction should be accounted for. We thus consider the wave pattern after a long distance of propagation and see the picture as sketched on the far right of the figure. For $(\lambda D/L_S^2) \ll 1$, the geometric acoustics result would be valid and we find that the fronts AB, BC, and CD locate the high-frequency portions of the energy originally in the portion of the front AD. Because these fronts are convex, their ray tube areas have greatly increased and the strength of these fronts is, therefore, small. Meanwhile, for the low-frequency wave components with $(\lambda D/L_S^2) \gg 1$, diffraction effects will have filled in the "shadow" AD (shown as a dashed line). Thus we see that at some distance from a focus, the wave system will consist of a thickened wave AD made up of the lower frequency wave components followed by geometrically attenuated high-frequency scattered waves. This picture agrees with the more detailed picture supplied by scattering theory (which treats intermediate values of $\lambda D/L_S^2$ as well).

Pierce, however, bases his analysis only on the high-frequency geometric acoustics limit. He ignores all diffraction effects and con-

structs a heuristic model of many shocks arriving at random times. He constructs his assumed solution to include the parameter $t_c = h_c/a_\infty$ used by Crow. This is done by forcing the assumed solution to have certain similarities to Crow's scattering solution. After an involved analysis, he predicts waves made up of a multitude of "microshocks." His predictions of rise times of the order of t_c are not surprising because the assumed solution was constructed in such a manner as to contain t_c. Experimental evidence shows no evidence of microshocks in the shock structure, and the 12-dB/octave decay of high-frequency spectral energy density also implies they are not present. The analysis used an incomplete model for wave propagation and is based on a large number of tenuous approximations, as the author himself points out (ref. 25). As both the phenomena treated in the model as well as those left out are included in the more comprehensive scattering theory, there seems to be little incentive to refine further the "microshock" approach.

CONCLUSIONS

The mechanisms by which atmospheric irregularities distort sonic boom signatures from the stratified atmosphere predictions are individually reasonably well understood, at least on a semiquantitative basis. Precise predictions are still far from our grasp because of both lack of knowledge of atmospheric structure and some approximations in the available analyses. However, approximate predictions based on estimated atmospheric structures should be possible with some further development.

Geometric acoustics calculations can be carried out in a straightforward manner if the large-scale inhomogeneity structure is known; however, the large-scale structure is perhaps the least well known. For smaller scale inhomogeneities, if the turbulent structure can be approximated as isotropic and locally homogeneous, then Crow's theory with modifications for finite L_0 and multiple scattering can be applied. The value of p_0 is taken as P, which can be found by solving the Burgers' equation (9) with slow spatial variation of $\epsilon^2 L_0$ where appropriate. The shock thickness is predicted by P only if the scattered waves are distinct; i.e., for $(\lambda D/L_0^2) \gg 1$.

For predictions of annoyance due to sonic booms it would also be desirable to be able to predict probability distributions and their dependence on atmospheric conditions for quantities such as $p_{1,\,\max}$. The available experimental distributions are averages over a variety of atmospheric conditions. No analyses have yet grappled with this problem, and probability data for atmospheric turbulence are even less accessible than statistical data. However, some effort should be expended in this direction because of its importance.

REFERENCES

1. HAYES, W. D.; HAEFELI, R. C.; AND KULSRUD, H. E.: Sonic Boom Propagation in a Stratified Atmosphere with Computer Program. NASA CR–1299, 1969.
2. GEORGE, A. R.; AND PLOTKIN, K. J.: Sonic Boom Waveforms and Amplitudes in a Real Atmosphere. AIAA J. vol. 7, no. 10, Oct. 1969, pp. 1978–1981.
3. HILTON, D. A.; HUCKEL, V.; AND MAGLIERI, D. J.: Sonic-Boom Measurements during Bomber Training Operations in the Chicago Area. NASA TN D–3655, 1966.
4. MAGLIERI, D. J.: Sonic Boom Flight Research. Sonic Boom Research, NASA SP–147, 1967, pp. 25–48.
5. HERBERT, G. A.; HASS, W. A.; AND ANGELL, J. K.: A Preliminary Study of Atmospheric Effects on the Sonic Boom. J. Appl. Meteorol., vol. 8, no. 4, pp. 618–626.
6. HERBERT, G. A.: Sonic Boom Metamorphosis. Proc. Conf. Aerosp. Meteorol., 4th, 1970.
7. GARRICK, I. E.: Atmospheric Effects on the Sonic Boom. Second Conference on Sonic Boom Research, NASA SP–180, 1968, pp. 3–17.
8. MAGLIERI, D. J.; HUCKEL, V.; HENDERSON, H. R.; AND MCLEOD, N. J.: Variability in Sonic-Boom Signatures Measured along an 8000-Foot Linear Array. NASA TN D–5040, 1969.
9. MAGLIERI, D. J.: Sonic Boom Ground Pressure Measurements for Flights at Altitudes in Excess of 70,000 Feet and at Mach Numbers up to 3.0. Second Conference on Sonic Boom Research, NASA SP–180, 1968, pp. 19–27.
10. TATARSKI, V. I.: Wave Propagation in a Turbulent Medium. McGraw-Hill Book Co., Inc., 1961. Also Dover Pubs. Inc., 1967.
11. LANDAU, L. D.; AND LIFSHITZ, E. M.: The Classical Theory of Fields. Pergamon Press, Inc., 1968, sec. 58.
12. JOHNSON, W. B.: The Effect of Inversion Waves upon Sonic-Boom Propagation. Rept. IERTM–ATDL 2, Environmental Science Services Administration, Mar. 1967.
13. STANFORD RES. INST.: Sonic Boom Experiments at Edwards Air Force Base. Rept. NSBEO–1–67, National Sonic Boom Evaluation Office, ASTIA No. AD 655 310, 1967.
14. PAN, Y. S.: Propagation of an N Wave across a Nonuniform Medium. AIAA J., vol. 7, no. 4, Apr. 1969, pp. 788–790.
15. KANE, E. J.; AND PALMER, T. Y.: Meteorological Aspects of the Sonic Boom. SRDS Rept. RD64–160, Federal Aviation Agency, AD–610 463, 1964
16. PIERCE, A. D.: Spikes on Sonic Boom Pressure Waveforms. J. Acoust. Soc. Amer., vol. 44, no. 4, 1968, pp. 1052–1061.
17. BATCHELOR, G. K.: Wave Scattering Due to Turbulence. Symp. Naval Hydrodyn., Nat. Acad. Sci.-Nat. Res. Counc. Publ. 515, 1957, ch. 16.
18. CROW, S. C.: Distortion of Sonic Bangs by Atmospheric Turbulence. J. Fluid Mech., vol. 37, 1969, pp. 529–563.
19. CHERNOV, L. A.: Wave Propagation in a Random Medium. McGraw-Hill Book Co., Inc., 1960. Also Dover Pubs. Inc., 1967.
20. GEORGE, A. R.; AND PLOTKIN, K. J.: Propagation of Sonic Booms and Other Weak Nonlinear Waves through Turbulence. Phys. Fluids, vol. 14, no. 3, Mar. 1971, pp. 548–554.
21. PLOTKIN, K. J.; AND GEORGE, A. R.: Weak Shock Waves in Turbulent Media. AIAA Paper no. 70–54, 1970.
22. PLOTKIN, K. J.: The Effect of Atmospheric Inhomogeneities on the Sonic Boom. Ph. D. thesis, Cornell Univ., 1971.
23. KELLER, J. B.: Wave Propagation in Random Media. Hydrodyn. Instabil. Proc. Symp. Appl. Math. 13th, 1962, pp. 227–246.

24. BAUER, A. B.; AND BAGLEY, C. J.: Sonic Boom Modeling Investigation of Topographical and Atmospheric Effects. Rept. no. FAA–NO–70–10, Department of Transportation, July 1970.
25. PIERCE, A. D.: Statistical Theory of Atmospheric Turbulence Effects on Sonic Boom Rise Times. To be published in J. Acoust. Soc. Amer.

Perturbations Behind Thickened Shock Waves

KENNETH J. PLOTKIN
Cornell University

One of the most significant effects of turbulence on sonic boom signatures is the appearance of random spikes and wiggles behind the shock waves. The maximum of these spikes generally appears immediately behind the shock and may be positive or negative. This may be considered to represent a variation in the shock overpressure, which is psychologically one of the most important factors in annoyance. It has been pointed out by Ferri that some acceptable overpressure should be determined from psychoacoustic studies and that supersonic transports be designed within the constraint of such a limit.[1] A means of predicting the range of variation in shock overpressure due to meteorological conditions is necessary so that this variation can be accounted for in setting this constraint.

FIRST-ORDER SCATTERING

The first successful attempt at predicting the perturbations due to turbulence was performed by Crow (refs. 1 and 2). He applied first-order acoustic scattering theory (refs. 3 to 6), modeling the shock wave as a step-function acoustic wave.

Scattering theory is a perturbation scheme in which ϵ, the strength of the turbulence, is the expansion parameter. A solution is sought in the form

$$p = p_0 + \epsilon p_1 + \epsilon^2 p_2 + \cdots \tag{1}$$

The term p_0 is the incident wave and satisfies the mean conditions. The term ϵp_1 represents first-order scattered waves. Truncating the series at this point is called the Born approximation. In principle, the scheme may be carried through to higher orders.

The use of a step-function incident wave leads to delta functions in the usual retarded time integral (ref. 7) for the scattered waves so that the volume integral collapses into a surface integral. The physical meaning of the retarded time integral is that a scattered wave is emitted only as the incident wave passes an element of turbulence. An observer

[1] See p. 255.

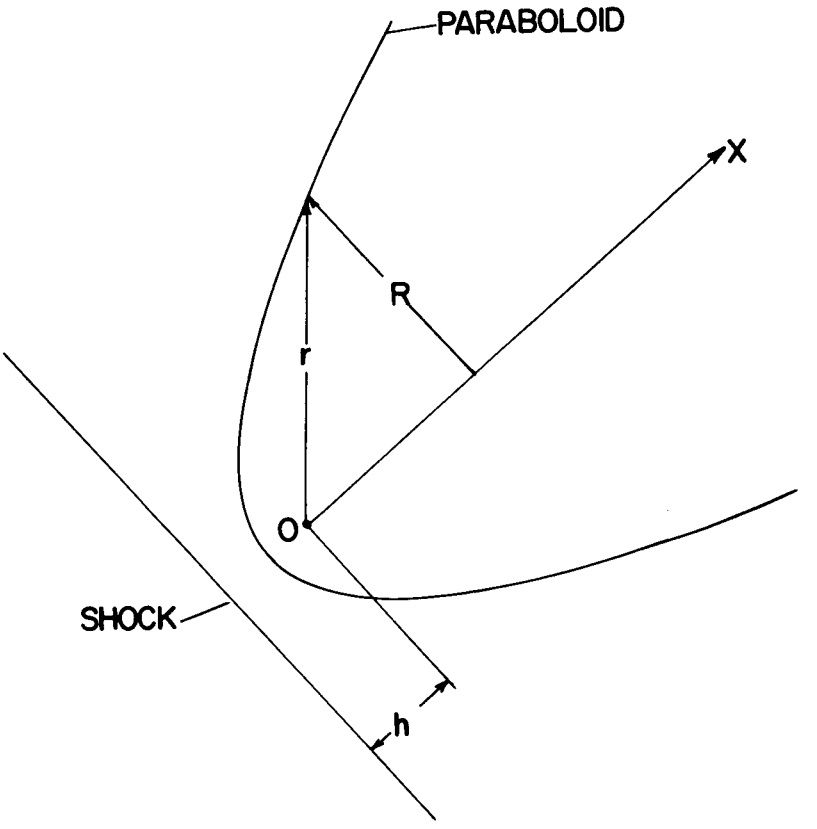

FIGURE 1.—Paraboloid of dependence.

at a given time "sees" a point on the scattering surface, which is equidistant from the observer and the shock front. The surface is thus a paraboloid of revolution with the observation point its focus and the shock front its directrix. Crow's paraboloid of dependence is illustrated in figure 1. After making several quite reasonable simplifying approximations, he obtained an expression for the mean-square perturbations, which may be expressed as

$$\left\langle \left(\frac{\epsilon p_1}{\Delta p} \right)^2 \right\rangle = \int_0^\infty \frac{x^2}{R^3} F(R)\, dx \tag{2}$$

where x and R are as shown in figure 1, and $F(R)$ represents an integral over a cylinder of radius R locally fitted to the paraboloid. This integral contains the statistical properties of the turbulence. For turbulence of the form of the Kolmogorov inertial subrange (refs. 4 and 8), $F(R) \propto R^{2/3}$ and equation (2) takes the form

$$\left\langle \left(\frac{\epsilon p_1}{\Delta p} \right)^2 \right\rangle = \frac{1}{h^{7/6}} \int_0^\infty x^{5/6} A \mathscr{E}^{2/3}(x)\, dx$$

$$= \left(\frac{h_C}{h} \right)^{7/6} \tag{3}$$

(eq. (6.3) of ref. 1 and eq. (7.3) of ref. 2) where A is a constant ($A = 0.383$ for thermal scattering) and $\mathscr{E}(x)$ is the turbulent dissipation function. This form is only valid when the diameter of the paraboloid is within the inertial subrange. Because the paraboloid grows with x, this means that equation (3) applies only for a finite layer of turbulence. Crow calculated h_C for a reasonable model of a finite turbulent atmospheric boundary layer and found that h_C was on the order of 1 ft. This gives reasonably good agreement between equation (3) and observed perturbations, except close to the shock front, where equation (3) predicts infinite perturbations.

The unreasonably large perturbations near the shock predicted by Crow's analysis are due to the modeling of the shock as a step function. A step contains very-high-frequency components, which are very strongly scattered in the forward direction. A shock with finite thickness may be divided into many infinitesimal steps with equation (3) applied to each, and the perturbations from each superposed. The upper bound for the root-mean-square perturbations is then given by a convolution integral over the shock thickness with equation (3) as the kernel (ref. 9). As long as the slope of the shock structure is finite, the maximum perturbations are finite. For example, figure 2 shows the upper bound of $\langle (\epsilon p_1/\Delta p)^2 \rangle^{1/2}$ for a possible thickened shock of thickness $T = h_C$ and $(h_C/h)^{7/12}$ for a step (ref. 10).

PERTURBATIONS BEHIND A STEADY SHOCK

The structure of a weak shock wave in a turbulent medium is governed by a balance between nonlinear steepening and a dissipative mechanism based on energy being scattered out of the incident wave direction by turbulence (refs. 9 to 11). Under conditions representative of weak sonic booms propagating through locally homogeneous isotropic turbulence, the shock structure is governed by the following Burgers' equation:

$$\frac{\partial P}{\partial t} + \frac{\gamma + 1}{2\gamma} \frac{a_\infty}{p_\infty} P \frac{\partial P}{\partial \chi} = \epsilon^2 L_0 a_\infty \frac{\partial^2 P}{\partial \chi^2} \tag{4}$$

where P is the wave structure with first scattered waves removed, a_∞ and p_∞ are mean ambient sound speed and pressure, χ is the wave fixed coordinate, ϵ^2 is the turbulent intensity, and L_0 is the turbulent macroscale length. This equation predicts a steady-state shock structure for long propagation distances through turbulence. This is an important

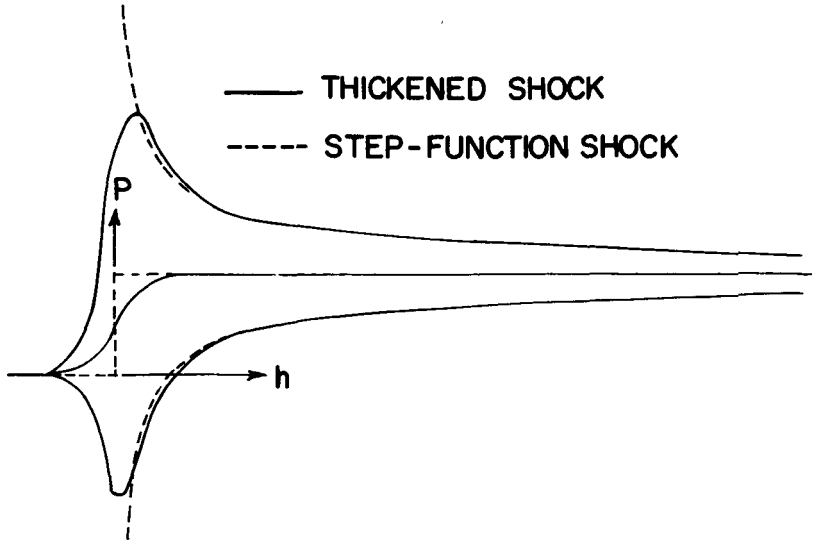

FIGURE 2.—Root-mean-square perturbations for a thickened shock of thickness $T = h_c$ and $(h_c/h)^{7/12}$.

case, as it corresponds to sonic booms near cutoff, conditions of high-altitude atmospheric turbulence, and blast waves from explosions near ground level. It is therefore desirable to calculate the perturbations behind a steady thickened shock. This means applying equation (2) to an unbounded region of turbulence.

The integral represented by $F(R)$ is proportional to $R^{2/3}$ only for the diameter $2R$ of the paraboloid less than the correlation length (maximum eddy size) $\mathscr{L}_0$. ($\mathscr{L}_0 \cong \frac{5}{2} L_0$ for turbulence obeying the Kolmogorov $\frac{2}{3}$-power law in the inertial subrange.) For $2R \gg \mathscr{L}_0$, it can be shown that $F(R) \sim$ constant. For homogeneous turbulence, then, equation (2) may be approximated (ref. 10) as

$$\left\langle \left(\frac{\epsilon p_1}{\Delta p} \right)^2 \right\rangle = \frac{1}{h^{7/6}} \int_0^{\mathscr{L}_0^2/8h} A \mathscr{E}^{2/3}(x) x^{5/6}\, dx + \frac{1}{h^{3/2}} \int_{\mathscr{L}_0^2/8h}^{\infty} C x^{1/2}\, dx \tag{5}$$

where A and $\mathscr{E}$ are as defined previously and C is a constant.

$$(\mathscr{E}^{2/3} = 2\epsilon^2 \left(\frac{2}{5L_0} \right)^{2/3}$$

for homogeneous turbulence, and $C = \epsilon^2$ for thermal scattering.)

It is clear that equation (5) predicts infinite perturbations everywhere for an infinite layer of turbulence. This is due to the failure of the Born approximation for long distances. Physically, scattered waves are

scattered many times until their propagation direction is completely randomized and they are left behind. As a first approximation, this may be allowed for in equation (5) by noting that a wave decays exponentially with distance due to scattering (refs. 10 and 12). A decay factor $e^{-\beta x}$ is thus used in the integrals in equation (5), where β is the decay coefficient. For conditions corresponding to those for which the Burgers' equation (eq. (4)) is applicable,

$$\beta = 2\epsilon^2 L_0 k^2 \tag{6}$$

where k is the wave number of the incident wave. The question of distinctness of scattered waves, as discussed in references 10 and 11, is not considered here. Equation (5) gives the scattered waves in terms of the location h at which they are observed and the location x from which they are scattered, not in terms of k. It is necessary to examine the frequency spectrum of the scattered waves at h from x to estimate β as a function of x and h for use in equation (5).

The angular distribution of scattered energy from a single component harmonic wave by isotropic turbulence (refs. 3 and 4) is

$$\langle |p_1|^2 \rangle \propto k^4 E\left(2k \sin \frac{\theta}{2}\right) \tag{7}$$

where E is the three-dimensional turbulence spectrum and θ is the scattering angle. This formula has been experimentally confirmed for small angles (refs. 13 and 14), which are of interest here. By considering the energy spectrum of the step-function acoustic wave, the spectrum of first scattered waves scattered at an angle θ (ref. 10) is

$$\langle |p_1|^2 \rangle \propto \begin{cases} \alpha_1 k^2 & k \leq \dfrac{\pi}{5L_0\theta} \\ \alpha_2 k^{-5/3}\theta^{-11/3} & k > \dfrac{\pi}{5L_0\theta} \end{cases} \tag{8}$$

where α_1 and α_2 are constants. The scattering angle θ may be matched to the geometry of the paraboloid of dependence to give equation (8) as a function of h and x. As a simplifying assumption so that β will be a function of x and h only, β is based on $\bar{k}$, where $\bar{k}$ is a median value such that half the energy in equation (8) is for $k < \bar{k}$ and half is for $k > \bar{k}$. This gives (ref. 10)

$$\beta(h, x) = \epsilon^2 \left(\frac{18}{11}\right)^3 \frac{\pi^2 x}{25 L_0 h} \tag{9}$$

Using equation (9) for the decay correction to equation (5),

$$\left\langle\left(\frac{\epsilon p_1}{\Delta p}\right)^2\right\rangle = \frac{1}{h^{7/6}}\int_0^{\mathscr{L}_0^{3}/8h} A\mathscr{E}^{2/3}x^{5/6}\exp\left\{-\epsilon^2\left(\frac{18}{11}\right)^3\frac{\pi^2x^2}{25L_0h}\right\}dx + \frac{1}{h^{3/2}}\int_{\mathscr{L}_0^{3}/8h}^{\infty} Cx^{1/2}\exp\left\{-\epsilon^2\left(\frac{18}{11}\right)^3\frac{\pi^2x^2}{25L_0h}\right\}dx \qquad (10)$$

This expression has asymptotic (ref. 10) behavior:

$$\left\langle\left(\frac{\epsilon p_1}{\Delta p}\right)^2\right\rangle \sim \left(\frac{0.00454\epsilon^{2/3}L_0}{h}\right)^{1/4} \qquad h \ll 0.796\epsilon^{2/3}L_0 \qquad (11a)$$

$$\left\langle\left(\frac{\epsilon p_1}{\Delta p}\right)^2\right\rangle \sim \left(\frac{1.43\epsilon^{2/3}L_0}{h}\right)^{3/4} \qquad h \gg 0.796\epsilon^{2/3}L_0 \qquad (11b)$$

It is seen that the perturbations depend on the factor $\epsilon^{2/3}L_0$, while shock thickness from equation (4) depends on the factor ϵ^2L_0. Shock thickness and the perturbations thus depend on the turbulent parameters in different ways.

Figure 3 shows the upper bound for the maximum root-mean-square perturbations behind a steady thickened shock whose structure is governed by the Burgers' equation (eq. (4)) for a range of ϵ^2 typical of atmospheric turbulence. The curves are based on equations (11a) and (11b) and are shown solid where these approximate forms are applicable and dashed otherwise. A calculation based on equation (10) would fall between the two curves. It is interesting that the maximum perturbation varies little with ϵ^2 over this range, which is consistent with much of the experimental data. For very small ϵ^2, the approximation used for β

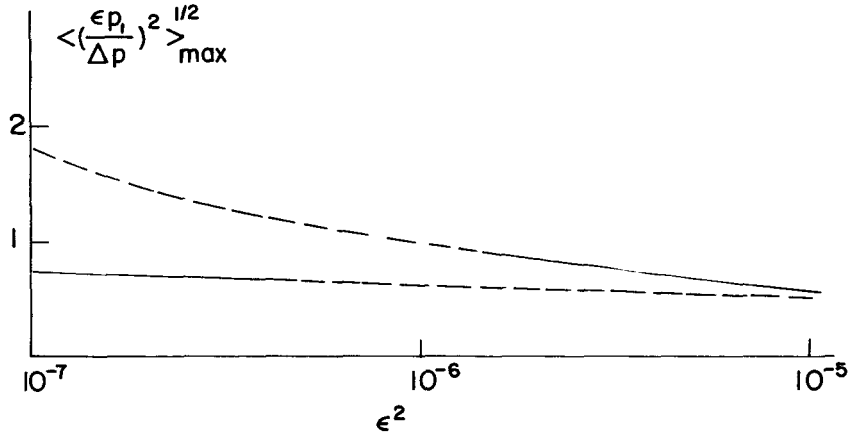

FIGURE 3.—Upper bound for maximum root-mean-square perturbations behind a shock.

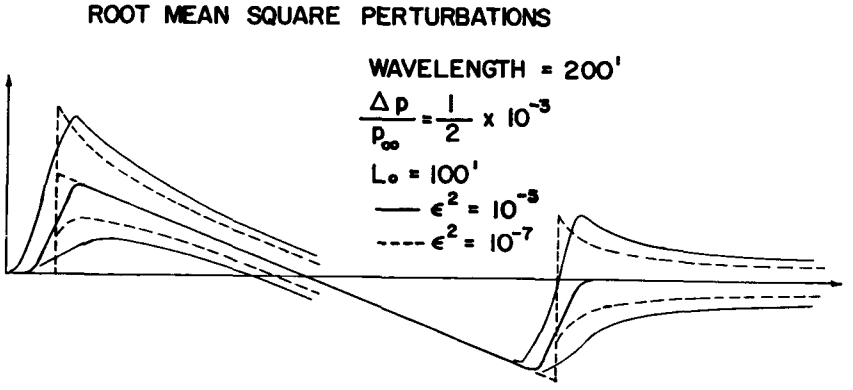

FIGURE 4.—Root-mean-square perturbations on an N-wave.

here based on $\bar{k}$ is not expected to be valid, and the maximum perturbation goes to zero as ϵ^2 goes to zero (ref. 10).

Figure 4 shows envelopes of perturbations on a 200-ft N-wave with $\Delta p/p_\infty = 0.5 \times 10^{-3}$ and $L_0 = 100$ ft for $\epsilon^2 = 10^{-7}$ and 10^{-5}. The change in the envelopes is relatively small, with the maximum perturbation almost identical for both cases.

CONCLUSIONS

It has been shown that the perturbations behind a steady shock wave in a turbulent medium have a finite maximum near the shock front and that this maximum is of the same order as the shock overpressure. The calculation was based on the decay of first scattered waves through further scattering. A number of approximations were employed, the most serious being that the question of the distinctness of the multiply scattered waves, as discussed in detail in references 10 and 11, was not considered. However, it is felt that the present calculation provides a reasonably good estimate of the physical situation. The maximum perturbations immediately behind the shock were found to vary only moderately with turbulent intensity, which is consistent with much experimental data.

The shock thickness has previously been shown to depend on the factor $\epsilon^2 L_0$, so that measurement of shock thickness should provide a good indication of the intensity of the turbulence if L_0 is known. The envelopes of the perturbations were shown here to depend on $\epsilon^{2/3} L_0$ and therefore reflect mainly the scale of the turbulence. With further refinement of this theory, it is possible that the measurement of perturbations and shock thicknesses may be a useful diagnostic technique in the determination of the form of atmospheric turbulence.

It appears at this point that the theory for the perturbations on N-waves due to turbulence is fairly well understood, if not worked out in complete detail. What is lacking is a good understanding of atmospheric turbulence. If the connection between atmospheric turbulence and the usual meteorological measurements could be made accurately, then the variability of sonic boom signatures could be predicted in terms of meteorological measurements and predictions.

REFERENCES

1. CROW, S. C.: Distortion of Sonic Bangs by Atmospheric Turbulence. NPL Aero Rept. 1260, 1968.
2. CROW, S. C.: Distortion of Sonic Bangs by Atmospheric Turbulence. J. Fluid Mech., vol. 37, 1969, pp. 529–563.
3. CHERNOV, L. A.: Wave Propagation in a Random Medium. McGraw-Hill Book Co., Inc., 1960. Also Dover Pub., Inc., 1967.
4. TATARSKI, V. I.: Wave Propagation in a Turbulent Medium. Dover Pub., Inc., 1961.
5. BATCHELOR, G. K.: Wave Scattering by Turbulence. Symp. Naval Hydrodyn., Nat. Acad. Sci.-Nat. Res. Counc. Pub. 515, 1957.
6. LIGHTHILL, M. J.: On the Energy Scattered from the Interaction of Turbulence with Sound or Shock Waves. Proc. Cambridge Phil. Soc., vol. 49, 1953, pp. 531–551.
7. BORN, M.; AND WOLF, E.: Principles of Optics. Second ed., The Macmillan Co., 1964.
8. LIN, C. C.: Statistical Theories of Turbulence. Princeton Univ. Press, 1951.
9. PLOTKIN, K. J.; AND GEORGE, A. R.: Weak Shock Waves in Turbulent Media. AIAA Paper No. 70–54, 1970.
10. PLOTKIN, K. J.: The Effect of Atmospheric Inhomogeneities on the Sonic Boom. Ph. D. thesis, Cornell Univ., 1971.
11. GEORGE, A. R.; AND PLOTKIN, K. J.: Propagation of Sonic Booms and Other Weak Nonlinear Waves Through Turbulence. Phys. Fluids, vol. 14, 1971, pp. 548–554.
12. KELLER, J. B.: Wave Propagation in Random Media. Hydrodyn. Instabil., Proc. Symp. Appl. Math. 13th, 1962, pp. 227–246.
13. KALLISTRATOVA, M. A.: An Experimental Investigation Into the Scattering of Sound in a Turbulent Atmosphere. Acad. Dokl. Sci. USSR Earth Sci. Sect., vol. 125, 1959, pp. 314–316.
14. KALLISTRATOVA, M. A.; AND TATARSKI, V. I.: Accounting for Wind Turbulence in the Calculation of Sound Scattering in the Atmosphere. Soviet Phys. Acoust., vol. 6, 1960, pp. 503–504.

Analysis of the Multiple Scattering of Shock Waves by a Turbulent Atmosphere

W. J. COLE
Columbia University and Bell Telephone Laboratories
AND
M. B. FRIEDMAN
Columbia University

Experimental observations of sonic boom pressure signatures exhibit random fluctuations superimposed on the basic N-shape pattern. In addition, a thickening of the shock front is observed that is many orders of magnitude larger than can be attributed to viscosity effects. Crow (ref. 1) has shown that the presence of the fluctuations can be explained by a first-order theory of turbulent scattering applied to a plane shock. However, his prediction of their intensity is unrealistically large in the neighborhood of the shock fronts (e.g., infinite at the front) and his single scattering analysis is incapable of predicting any shock thickening.

Plotkin and George (ref. 2) have shown that shock thickening can be attributed to higher order scattering effects. They recognize the importance of this thickening in producing finite values for the intensity of the fluctuations near the shock front, but the modified form of perturbation analysis they employ does not allow for a direct determination of the intensity. Their procedure for obtaining an upper bound on the fluctuation intensity does not take into account the continuously thickened nature of the plane shock profile as it propagates through the turbulent medium; i.e., they use Crow's first-order scattering theory for the fluctuation intensity as it applies to an arbitrary initial shock profile, but they substitute the final thickened shock profile computed from their shock thickening theory. Within the context of Crow's theory, Plotkin and George's intensity calculation is equivalent to assuming that the observed fluctuations are caused by scattering from this final thickened profile instead of the actual continuously thickened shock profile.

In this paper, it is shown that the shock thickening can be derived within the framework of a nonperturbative multiple-scattering theory that avoids the "several" hypothesis used in reference 2, and, most importantly, provides for a direct evaluation of the fluctuation intensity. This procedure inherently incorporates the coupling between the in-

tensity of the fluctuations and the continuously thickened shock profile. This more general analysis predicts values for the fluctuation intensity that are an order of magnitude smaller [1] than those predicted in reference 2 for a given set of turbulence parameters. In addition, the nature of the analysis permits the treatment of more general wave configurations.

The analysis is based on the method of "smoothing" previously used by Frisch (ref. 3) in studying the multiple scattering of single-frequency waves. In the course of this research, an effort has been made to study the accuracy of this method by utilizing a Monte Carlo computer experiment described in reference 4. The one-dimensional Helmholtz equation with a particular class of random functions describing the phase velocity was treated in this experiment. A comparison of the approximate solution obtained using the smoothing method and an "exact" numerical solution showed the smoothing method predicts accurately the behavior of high frequencies, whereas the single-scattering approximation of the type employed by Crow develops inaccuracies at high frequencies. Because a sonic boom has a considerable amount of high-frequency content, it is apparent that Crow's theory for the intensity is inadequate near the shock front; one has confidence, however, that the smoothing method will accurately predict the intensity uniformly both away from and, more importantly, at the front.

The properties of the atmosphere depend in a complicated way on both position and time. As a consequence, the propagation of an acoustic wave is effected by scattering from the local variations in the medium properties. The complexity of these variations makes it difficult to analyze these effects in a direct way and is of little interest even if it could be obtained because the behavior of the wave would be different at a neighboring point. Consequently, only the statistical properties of the wave as a function of the statistical properties of the random medium are of interest.

As a result, the mathematical concept of a random medium is introduced. A random medium is an ensemble of media, each designated by a parameter ω together with a probability distribution $p(\omega)$. The study of wave propagation in a turbulent medium leads, in general, to a family of partial differential equations:

$$L_0 u(\omega; \underline{x}, t) + V_1(\omega; \underline{x}, t) u(\omega; \underline{x}, t) = L_1[u(\omega; \underline{x}, t)] L_2[u(\omega; \underline{x}, t)] \quad (1)$$

where L_0 is a deterministic operator, $V_1(\omega; \underline{x}, t)$ is the random operator depending on the parameter ω that characterizes the effects of turbulence

[1] This conclusion is based on the assumption that $h_c = T$ as stated in reference 2. In a private communication, the authors indicate that h_c can be considerably smaller than T so that their result can, in some cases, be smaller than those presented here.

in scattering the wave, L_1 and L_2 are deterministic linear operators that describe the nonlinear steepening of the wave, and $u(\omega)$ is the random solution field. The average or mean value of u is defined by

$$\langle u\rangle = \int u(\omega)p(\omega)\,d\omega \tag{2}$$

The smoothing method involves the separation of the solution field into its coherent and incoherent (fluctuating) parts,

$$u(\omega;\underline{x},t) = u_c(\underline{x},t) + u_i(\omega;\underline{x},t)$$

where

$$\begin{aligned} u_c &= \langle u(\omega)\rangle = Pu \qquad \text{coherent field} \\ u_i &= u(\omega) - u_c = (I-P)u \qquad \text{incoherent field} \end{aligned} \tag{3}$$

where $P = \langle\ \rangle$ denotes the ensemble-averaging operation in equation (2).

Substituting equation (3) in equation (1), averaging, and assuming $\langle V_1\rangle = 0$ results in

$$u_c = -L_0^{-1}P(V_1u_i) + L_0^{-1}\{L_1(u_c)L_2(u_c) + P[L_1(u_i)L_2(u_i)]\} \tag{4}$$

Subtracting equation (4) from equation (1) gives

$$\begin{aligned} u_i = -L_0^{-1}V_1u_c + L_0^{-1}(I-P)[V_1u_i + L_1(u_i)L_2(u_i)] \\ + L_0^{-1}[L_1(u_c)L_2(u_i) + L_1(u_i)L_2(u_c)] \end{aligned} \tag{5}$$

The first-order smoothing approximation is equivalent to assuming that the second and third terms in equation (5) are small compared to the first. This implies that the principal contribution to the fluctuations is the single scattering of the coherent field instead of the incident undistorted field, as assumed by Crow. As a result,

$$L_0u_i + V_1u_c = 0 \tag{6}$$

Substituting equation (6) into equation (4) and assuming $P[L_1(u_i)L_2(u_i)]$ to be negligible yields

$$L_0u_c - \langle V_1L_0^{-1}V_1\rangle u_c = L_1(u_c)L_2(u_c) \tag{7}$$

To apply the above scattering theory to the sonic boom problem, it is assumed that the turbulence that distorts the sonic boom N-wave is concentrated in the 3000-ft boundary layer near the ground. It is further assumed that the shock front is essentially planar and that the scattering

experienced by the shock is associated with the sharp pressure rise across the shock and is insensitive to the rate of expansion behind the shock so that only a step-function shock need be considered. Therefore, the canonical problem of interest is a plane step shock incident on a random half space $z > 0$, with uniform statistical properties. For this canonical problem, the equation satisfied by the coherent field is

$$\frac{\partial^2\langle\rho_s\rangle}{\partial z^2}-\frac{1}{c_0^2}\frac{\partial^2}{\partial t^2}\langle\rho_s\rangle+\frac{\partial}{\partial z}\left\langle u(\underline{x})\frac{\partial\delta\rho_s}{\partial z}\right\rangle=-\frac{\partial}{\partial z}\left(\frac{2\langle\rho_s\rangle}{\rho_0}\frac{\partial\langle\rho_s\rangle}{\partial z}\right) \tag{8}$$

and that satisfied by the incoherent field is

$$\nabla^2\delta\rho_s-\frac{1}{c_0^2}\frac{\partial^2}{\partial t^2}\delta\rho_s+\frac{\partial}{\partial z}\mu(\underline{x})\frac{\partial\langle\rho_s\rangle}{\partial z}=0 \tag{9}$$

where $\langle\rho_s\rangle$ is the coherent acoustic fluid density, $\delta\rho_s=\rho_s-\langle\rho_s\rangle$, and

$$\mu(\underline{x})=\frac{2[v_3(\underline{x})-c_\theta(\underline{x})]}{c_0}$$

The term v_3 is the component of the turbulent velocity fluctuations in the direction of the normal to the wavefront and c_θ is the fluctuation in the sound speed due to temperature inhomogeneities. Solving equation (9) for ρ_s and substituting into equation (8) gives an equation for the coherent density analogous to equation (7). Under the assumption of small shock thickness compared to the turbulent correlation length, this nonlinear integro-differential equation for the coherent field reduces to the Burgers' equation:

$$\frac{\partial\psi(\xi,z)}{\partial z}-\frac{\psi(\xi,z)}{\rho_0}\frac{\partial\psi(\xi,z)}{\partial\xi}=n^2l_0\frac{\partial^2\psi}{\partial\xi^2}(\xi,z) \tag{10}$$

where

$$\xi=c_0t-z,\ \langle\rho_s\rangle(z,t)=\psi(\xi,z),\ n^2\doteq\left(\frac{\langle v_3^2\rangle}{c_0^2}+\frac{\langle c_\theta^2\rangle}{c_0^2}\right)$$

and l_0 is the correlation length of the turbulence. This equation is similar to that in reference 2 except the derivation is direct from first principles and does not require additional heuristic arguments. For an initial step-function shock, $\langle\rho_s\rangle(z=0,t)=(\Delta\rho)H(t)$, the solution of this Burgers' equation is obtained using the results of J. D. Cole (ref. 5). When the inequality $[(\Delta\rho)^2z]\ (4\rho_0^2l_0n^2)^{-1}<0.1$ is satisfied (a condition obtained for most sonic boom shock strengths of interest and for most parameter values that model atmospheric turbulence), this exact nonlinear solution reduces to the linear solution

$$\langle \rho_s \rangle (z, t) = \frac{\Delta\rho}{2}\left[1 + \operatorname{erf}\left(\frac{c_0 t - z}{\sqrt{4n^2 l_0 z}}\right)\right] \tag{11}$$

The coherent shock front, then, is increasingly smoothed out as a function of the propagation distance z, with $\langle \rho_s \rangle (x, t)$ approaching $(\Delta\rho)$ for $|c_0 t - z| > \sqrt{4n^2 l_0 z}$.

The intensity of the fluctuations is evaluated using equation (9) in conjunction with the solution for the coherent field in equation (10), which has been approximated by equation (11) under the above restriction. The resulting expression is

$$\delta\rho_s = (\mathrm{I}) + (\mathrm{II}) \tag{12}$$

where

$$(\mathrm{I}) = \frac{\Delta\rho}{2\sqrt{\pi}} \int_0^z dy_3 \, \mu(\rho = 0, y_3) \frac{\exp\left\{-\dfrac{(c_0 t - z)^2}{4n^2 l_0 y_3}\right\}}{\sqrt{4n^2 l_0 y_3}}$$

$$(\mathrm{II}) = \frac{1}{4\pi}\left(\frac{\Delta\rho}{\sqrt{\pi}}\right) \int_0^{2\pi} d\theta \int_0^z dy_3 \int_0^\infty d\rho \, \frac{(z - y_3)}{\sqrt{\rho^2 + (z - y_3)^2}} \left[\frac{\partial \mu(\rho, \theta, y_3)}{\partial y_3}\right] \frac{\exp\left\{-\dfrac{(c_0 t - y_3 - \sqrt{\rho^2 + (z - y_3)^2})^2}{4n^2 l_0 y_3}\right\}}{\sqrt{4n^2 l_0 y_3}}$$

The incoherent field $\delta\rho_s$ represents the difference between the observed or measured realization and the coherent field, which travels at the average speed of sound c_0 and arrives at the observer located at a distance z into the random medium at time $t = z/c_0$. Each realization arrives at a slightly different time because of the turbulence. The "phase shift" (see ref. 1) of each realization is accounted for by integral (I) in equation (12), whereas the actual fluctuations caused by scattering in the neighborhood of Crow's paraboloid of dependence (obtained by setting the argument of the exponential equal to zero) is given in integral (II). This decomposition permits the calculation of the intensity of the observed fluctuations. For the step-function shock considered above, the incoherent intensity was evaluated using the Kolmogorov turbulence model. The determination of this intensity reduces, after a series of reasonable assumptions, to the evaluation of a complicated integral along the axis of Crow's paraboloid of dependence. This integral can be computed accurately using numerical integration techniques. For values of t such that $\xi = (c_0 t - z) > \sqrt{4n^2 l_0 z}$, this integral reduces to the result of Crow:

$$\langle \delta\rho_s^2 \rangle = (\Delta\rho)^2 \, (h_c/\xi)^{7/6}$$

where h_c is proportional to z, l_0, and the parameter $I = c_0^{-2}\left(\langle v_3^2\rangle + \frac{3}{22}\langle c_\theta^2\rangle\right)$ for the case of a turbulent medium with uniform statistical properties. The effect of the continuously thickened coherent shock profile manifests itself for $\xi < \sqrt{4n^2 l_0 z}$ as illustrated in figure 1, where the intensity is plotted as a function of $\tau = t - z/c_0$ for three different values of I. The intensity becomes a continuous function of ξ, attaining a maximum value at some $\xi_1 > 0$ and then merging with Crow's result for $\xi > \sqrt{4n^2 l_0 z} > \xi_1$. The maximum value predicted by Plotkin and George (ref. 2) is an order of magnitude larger (see ref. 1) than the results presented in figure 1, so that the continuously thickened nature of the shock profile has a significant effect on the predicted fluctuation intensity. In addition, figure 2 illustrates the fluctuation intensity as a function of time for three different turbulence correlation lengths. It appears that the intensity is much more sensitive to the local correlation length than to the turbulence fluctuation intensity.

An important aspect of the above theory is the decomposition of each realization $u(\omega)$ of the solution field into its coherent and incoherent parts. It is of interest to determine whether the characteristics of each

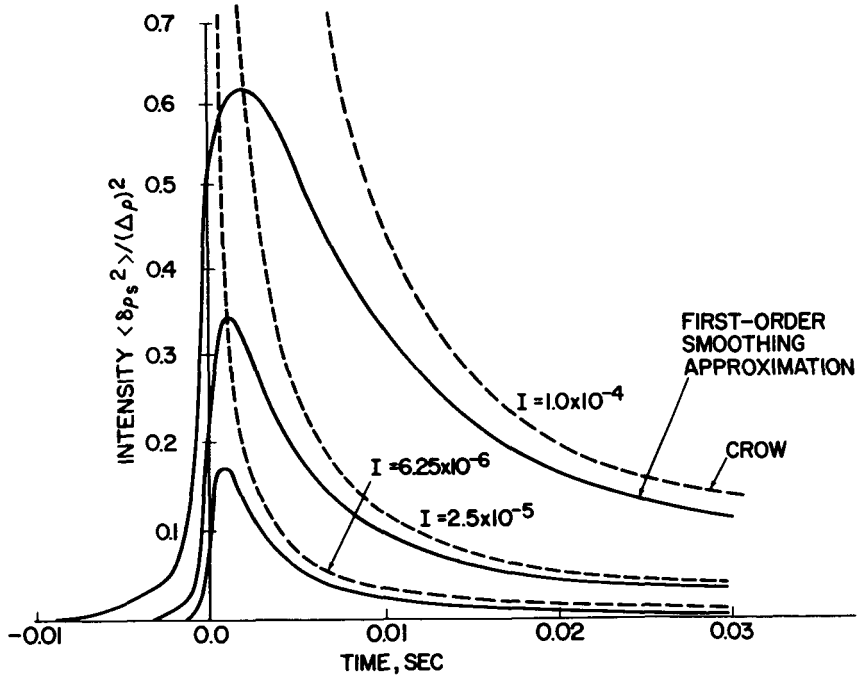

FIGURE 1.—Fluctuation intensity plotted as a function of τ for three different values of I. $I = v_3^2/c_0^2 + (3/22)(\langle T^2\rangle/T_0^2)$, $l_0 = 50$ m, $z = 1000$ m, and $\tau = t - z/c_0$.

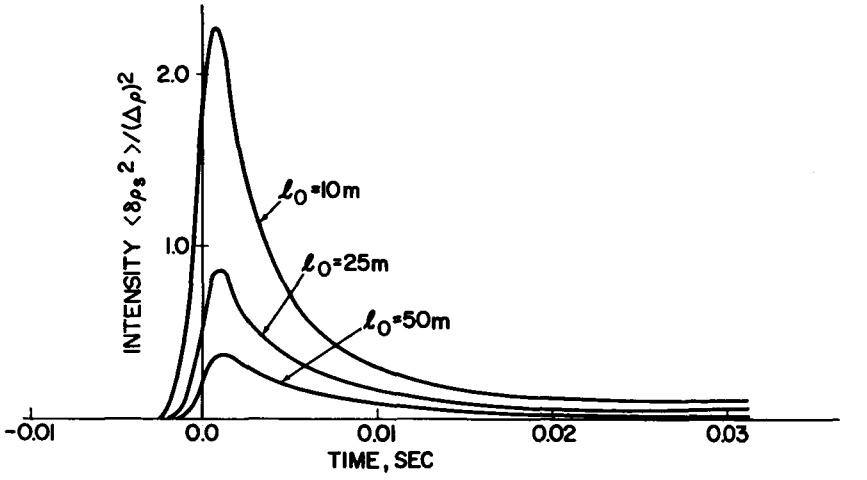

FIGURE 2. – Fluctuation intensity plotted as a function of time for three different turbulence correlation lengths. $z = 1000$ m, $I = 2.5 \times 10^{-5}$, and $\tau = t - z/c_0$.

measured sonic boom pressure signature is described by the corresponding thickened coherent shock profile and the predicted fluctuation intensity. The ensemble-averaging formulation considered above does not introduce any increased thickening of the shock profile that is not related to the scattering of energy out of the wave. Keller (ref. 6) computes the propagation constant of a single-frequency wave based on an energy conservation analysis of the type employed by Plotkin and George (ref. 2) and also by using the first-order smoothing approximation. He obtains the same result by each approach. Because the linear version of equations (8) and (9) could be solved by using a superposition of all of the frequency components in the initial shock wave, it is clear then that the smoothing method should yield exactly the same shock thickening as that predicted by the energy conservation analysis in reference 2 as is apparent from the derivation of equation (10). Furthermore, in the determination of the incoherent field, it was possible to separate the phase-shift contribution (which is not measured in practice) and the actual measured fluctuation contribution. Consequently, the ensemble average or smoothing approach should yield accurate estimates of actual measured shock thickening and fluctuation intensities.

The influence of more realistic nonhomogeneous turbulence models on the magnitude of the fluctuation intensity is being investigated by an application of the techniques described above. In addition, because pressure signatures can differ significantly from N-shapes particularly near focal points, some analysis of the effect of turbulence on more general waveforms is also being considered.

REFERENCES

1. CROW, S. C.: Distortion of Sonic Bangs by Atmosphere Turbulence. J. Fluid Mech., vol. 37, pt. 3, pp. 529–563.
2. PLOTKIN, K. J.: AND GEORGE, A. R.: Weak Shock Waves in Turbulent Media. AIAA Paper no. 70–54, 1970.
3. FRISCH, U.: Wave Propagation in Random Media. Probabilistic Methods in Applied Mathematics, A. T. Bharucha-Reid, ed., Academic Press, Inc., pp. 75–198.
4. COLE, W. J.: A Monte Carlo Experimental Verification of the Smoothing Method. To be published.
5. COLE, J. D.: On a Quasi-Linear Parabolic Equation Occurring in Aerodynamics. Quart. Appl. Math., vol. 9, no. 3, 1951, pp. 225–236.
6. KELLER, J. B.: A Survey of the Theory of Wave Propagation in Continuous Random Media. Proc. Symp. Turbulence Fluids Plasmas, Polytech. Inst. Brooklyn Microwave Res. Inst. Symp. Ser. 18. Polytechnic Press, 1968, pp. 131–142.

Uniform Wavefront Expansions for Diffracted and Focusing Waves

M. K. MYERS
Columbia University

The general objective of the present research is to develop theoretical descriptions of the propagation of shock waves in certain types of multidimensional problems of interest to sonic boom technology. In particular, the effort centers on two classes of problems: the first includes problems with diffracted wave systems; the second comprises problems involving focusing of waves. In each class, the dominant feature is the existence of a singularity in the surface forming the wavefront of the disturbance field calculated from a linearized theory. For problems involving diffraction, the wave surface is formed by two or more segments tangent to one another along curves analogous to shadow boundaries in optical diffraction problems. In the focusing case, the wavefront is cusped, and the surface traced by the cusp on the wavefront is a caustic of the associated system of rays.

The fundamental objective of determination of shock waves in these problems is approached in two separate stages. The first stage, which underlies the entire study, consists of determining satisfactory approximations to the linearized solution of problems of interest, especially in the vicinity of the linear wavefronts. While the linear solutions are easily written in exact form as integral expressions, these are generally too complex to be useful in practice. Hence, it is valuable to seek asymptotic approximations to the linear solutions valid near the wavefront appropriate to the problem being studied. A satisfactory approximation is one free of anomalous singularities that arise as a result of the process of approximation and that generally exist neither in the full linear solution nor in the exact solution to the problem.

The second stage of the study is to develop methods, analogous to those of Lighthill and Whitham, that correct the linearized solution by means of a straining of coordinates to yield a first approximation to the exact solution to the problem. The appropriate straining of coordinates required in a given problem is determined largely by the behavior of the linear solution near its wavefronts; i.e., by the information obtained in the first stage of the study described above. The present discussion

is confined to the first, or linear, stage of the work. Progress in application of the linearized results to the determination of nonlinear effects is described in the paper by Friedman and Davis.[1]

Any attempt to generalize the available methods for correcting linear solutions to include a first approximation to nonlinear effects must begin with a clarification both of the asymptotic nature of the Whitham theory relative to exact solutions and of the asymptotic nature of the approximate linear results used as input for the process relative to corresponding complete linear solutions. It is therefore important to examine the detailed structure of the linear potential fields for various problems of the two types indicated previously. Especially important is a study of the nature and mode of propagation of the singularities on the wavefronts of the fields because the subsequent generalization to nonlinear effects depends heavily upon the construction of a set of equations of motion in which the separate terms are known to be nonsingular throughout the field. The independent variables in which such equations must be written are suggested by the results of a linearized analysis.

SINGLE WAVE SYSTEMS: PROGRESSING WAVE THEORY

We review briefly the asymptotic form of linearized fields near wavefronts in cases in which a single wave system is propagating. In general, the linearized potential in such cases can be explained in a progressing wave of the form

$$\varphi=\sum v^n(r, s)F^n(T) \tag{1}$$

where the F^n are subjected to the condition

$$\frac{dF^{n+1}}{dT}=F^n \tag{2}$$

The expansion (1) is expressible in terms of a ray theoretical analysis; r is a parameter measuring distance along a ray from the appropriate source and s is the parameter denoting a particular ray. T is the phase of the wave, $T=0$ represents the wavefront, and the functions $F^n(T)$ are the waveforms or phase functions. If equations (1) and (2) are substituted into the wave equation, $\Box\varphi=0$, it is found that equation (1) is a formal solution if T is a solution of the characteristic equation for the wave equation

$$(\nabla T)^2-k^2(T_t)^2=0 \tag{3}$$

while the successive amplitudes v^n satisfy a set of transport equations associated with the phase T:

[1] See p. 123.

$$2(\nabla v^n \cdot \nabla T - k^2 v^l T_t) + v^n \Box T = -\Box v^{n-1} \tag{4}$$

where $v^{-1} \equiv 0$. Equations (4) are easily shown to be ordinary differential equations along any ray s equal to a constant. (See ref. 1.) In equations (3) and (4), k^2 stands for $1/c^2$ or $M^2 - 1$, depending on whether the problem is one for unsteady flows in space-fixed coordinates x, y, z or steady flows in body axes x, y, z. In the latter case, x takes the place of t in equations (3) and (4).

Expansions of the form of equation (1) can always be determined for a problem involving a single wave system. The simplest progressing wave expansions are those in which $F^0(T)$ is $H(T)$ or $T^{1/2}H(T)$, where H is the unit step function; then equation (1) becomes a series in powers of T or $T^{1/2}$ on the disturbed side of the wavefront. The leading term of such a series is often called the geometric acoustics approximation to the solution φ.

With φ in the form of a progressing wave, it is possible to interpret the asymptotic nature of the leading term of equation (1) relative to the full linear potential φ. In general it is found that, for a single wave system and physically real boundary data, the approximation to φ afforded by $v^0 F^0(t)$ is uniformly valid in the parameters s and r, but only for T sufficiently small; i.e., $T/L \ll 1$, where L is some characteristic time or length in the problem. Such an approximation to the linear solution is generally not useful as input for the nonlinear correction process (refs. 2 and 3). However, if the data of the problem are sufficiently simple, then a progressing wave expansion can be developed in which the $F^n(T)$ are, in fact, integrals over the timelike direction of the boundary data for the problem. In these cases, it can be shown that the amplitudes v^n decay rapidly enough with r so that the leading term of equation (1) is in reality an asymptotic approximation to φ for small T/r, uniformly in s.

As examples of problems involving single wave systems, three cases of steady flow are cited. First, for plane flow past a symmetric airfoil,

$$\varphi = -\beta^{-1} F^0(T) \qquad T = x - \beta y \qquad F^0(T) = m(T) \tag{5}$$

where $m(x)$ is the half thickness of the airfoil and $\beta = (M^2 - 1)^{1/2}$. In this case the full linear solution is itself in the form of a progressing wave.

For flow past a body of revolution,

$$\varphi = -(2\beta r)^{-1/2} F^0(T) + \ldots \qquad T = x - \beta r \qquad 2\pi F^0(T)$$
$$= \int_0^T \frac{A'(\xi)\, d\xi}{(T-\xi)^{1/2}} \tag{6}$$

where $A(x)$ is the cross-sectional area of the body. In this case, the progressing wave expansion involves waveforms that are integrals over the

body shape, and it can be shown that equation (6) approximates φ uniformly in r for $(T/r) \ll 1$.

A third example is for steady flow past a symmetric nonlifting wing with smooth leading edge $x=x_0(y)$ and streamwise slope $m(x, y)$. In this case,

$$\begin{aligned} \varphi &= [2\beta(r+r_0)]^{-1/2}F^0(T)+\ldots \\ T &= x-x_0(s)-\beta r \\ F^0 &= \left[\frac{2m\ (x_0\ (s),\ s)}{x_0''\ (s)}\right]^{1/2} TH(T) \end{aligned} \tag{7}$$

(See ref. 3.) The approximation in equation (7) for this problem is valid only in the limit $T/L \ll 1$, where L is, for example, the maximum chord length of the wing. Whitham (ref. 3) has made use of an extended result for this problem that, although it is not the first term of a progressing wave expansion, does involve the same amplitude function as in equation (7) and is an asymptotic expression valid for T/r sufficiently small:

$$\begin{aligned} \varphi &\sim [2\beta(r+r_0)]^{-1/2}G(s, T) \\ 2\pi G(s, T) &= \int_0^T \frac{S'(x)\,dx}{(T-x)^{1/2}} \end{aligned} \tag{8}$$

Here $S(x)$ is the cross-sectional area of the body of revolution in each plane s equal to the constant to which the wing is equivalent at large r as first demonstrated by Hayes (ref. 4).

DIFFRACTED WAVE SYSTEMS

A situation involving multiple wave systems arises in steady flow past a nonlifting wing with a supersonic leading edge having discontinuities in spanwise slope $x_0'(y)$. One of the simplest examples of this type is shown in figure 1, with the wavefront configuration in a plane x equal to a constant shown in figure 2. If T is the phase variable relative to the main, or envelope, portion of the wavefront and $T_\pm$ are the phases relative to the diffracted, or tip cone, portions of the front, then it is natural to seek a composite progressing wave expansion of φ in the form

$$\varphi = \Sigma v^n(r, s)F^n(T)+v_+^n(r_+, \alpha_+)F_+^n(T_+)+v_-^n(r_-, \alpha_-)F_-^n(T_-) \tag{9}$$

In such a multiple wave situation, however, it happens that the expansion (9) is always nonuniform in the ray parameters s and $\alpha_\pm$, regardless of its behavior in the parameters r and $r_\pm$. That is, the amplitude v_+^0 becomes infinite as $\alpha_+ \to \alpha_+^*$, and v_-^0 becomes infinite as $\alpha_- \to \alpha_-^*$. These are the rays of the families associated with the phases $T_\pm$ that coincide

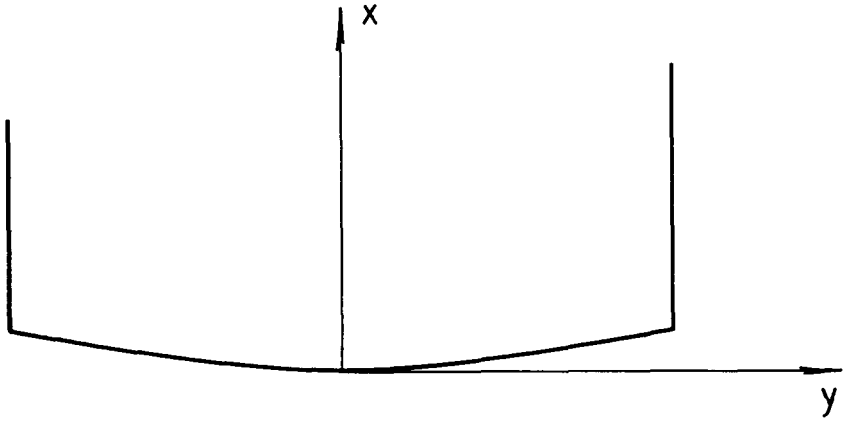

FIGURE 1. – Diffracting wing planform.

with a ray of the family associated with the main phase T. (See fig. 2.) These rays are analogous to shadow boundaries in optical diffraction problems.

A major aspect of the present research has been the development of a wavefront expansion for diffracted wave problems in which the anomalous singularities that plague the cruder analysis of equation (9) are not present. To simplify the discussion, consider a case in which only one shadow boundary exists. For example, for the problem depicted in figures 1 and 2, we confine attention to points in the range of influence of only the one wingtip at $y=L$; then $F_{-}^{n}(T_{-}) \equiv 0$ in equation (9). Detailed analysis of numerous special cases has established that near the wavefront $T=0$ or $T_{+}=0$, the potential is expressible in the form

$$\varphi = \Sigma v^{n}(r, s) F_{7}^{n}(T, \theta) + w^{n} F_{\theta}^{n}(T, \theta) \tag{10}$$

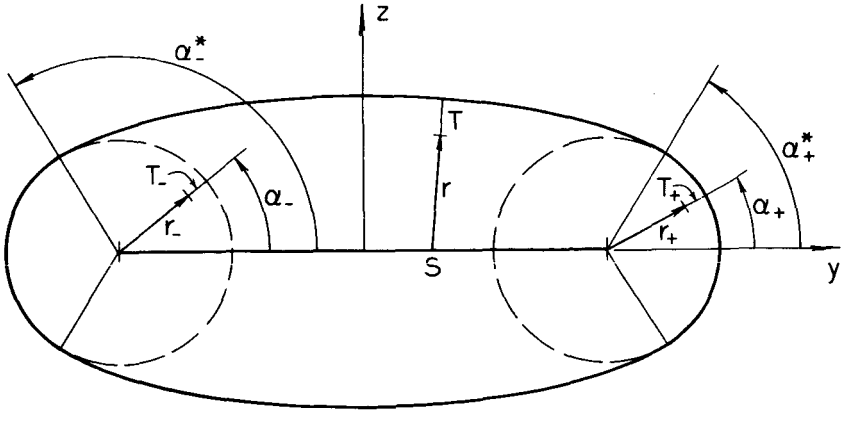

FIGURE 2. – Wavefront configuration in plane x = constant for diffracting wing.

where

$$w^n = v_+^n(r_+, \alpha_+) + \frac{v^n(r, s)}{2\theta} \tag{11}$$

$$\theta^2 = T - T_+ \tag{12}$$

and the generalized waveforms $F^n(T, \theta)$ satisfy

$$2\theta F^n_{T\theta} + F^n_{\theta\theta} = 0 \tag{13}$$

Substitution of equations (10) through (13) into $\Box\varphi = 0$ shows that such an expansion is a formal solution if T and T_+ satisfy equation (3), the v^n satisfy equation (4), and the v_+^n and T_+ satisfy equation (4) with a modified inhomogeneous term given by

$$-\Box v_+^{n-1} + \frac{1}{2}\left[\frac{1}{\theta}\Box v^{n-1} - \Box\left(\frac{v^{n-1}}{\theta}\right)\right] \tag{14}$$

In the uniform theory, both v^n and w^n are smooth functions throughout the field, with the v_+^n coupled to the v^n for $n \geq 1$ as shown by equation (14). The shadow boundary is given by $\theta = 0$, and the second term on the right in equation (11) exactly balances the singularity in v_+^n that arises in equation (9).

Just as for the cases involving single wave systems, the leading term, $n = 0$, of equation (10) affords a small T approximation to φ uniformly in the ray parameters s and $\alpha_\pm$. For a wing with general spanwise slope variation and arbitrarily curved leading edge, the successive amplitude factors do not decrease strongly enough with r to be useful in the straining process. An extended result, asymptotically valid for small T/r, has been developed and represents the counterpart to equation (8) for the smooth wing. At very large distances, the extended approximation goes over to the so-called cutting plane approximation, which effectively ignores the singular behavior of the solution across the diffracted fronts $T_\pm = 0$. Work is currently in progress to derive the approximate nonlinear solution using this extended result as a basis.

The uniformly valid linear approximation as represented by equation (10) and its asymptotic extension are sufficiently complicated that it is of value to consider whether, for simple enough shapes, the uniform expansion equation (10) is in fact asymptotic for small T/r, now necessarily uniform in the ray parameters s and $\alpha_\pm$. Perhaps the simplest case where this can be proved is that of a rectangular wing of constant cross section. This case has been studied in detail by Davis, who has given experimental confirmation of the nonlinear results derived by straining of coordinates from a linearized wavefront approximation essentially of

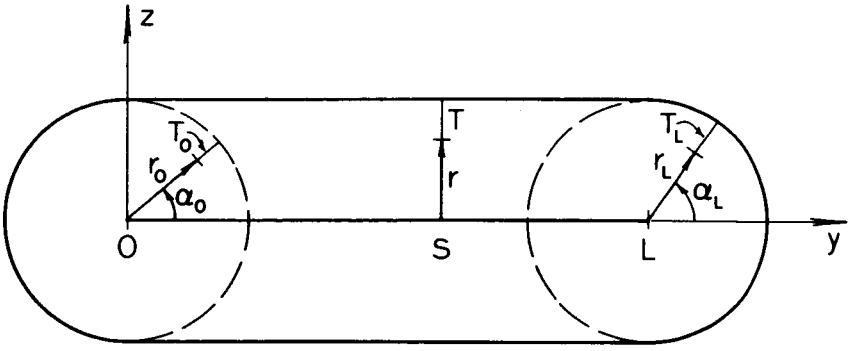

FIGURE 3.—Wavefront configuration for rectangular wing.

the form of the leading term $n=0$ of equation (10). (See the paper by S. Davis.)[2] As an illustration of the general theory represented by equations (10) through (13), consider the rectangular wing problem for which the wavefront geometry is shown in figure 3. For this case

$$\varphi=-\frac{1}{\pi}\iint \frac{m\ (\xi)\ d\xi d\eta}{[(x-\xi)^2-\beta^2\ (y-\eta)^2-\beta^2 z^2]^{1/2}} \tag{14}$$

where the region of integration is the area between the leading edge of the wing on $\xi=0$ and the hyperbola of intersection of the upstream Mach cone from (x, y, z). Let $\rho(\eta)=[(y-\eta)^2+z^2]^{1/2}$ and write

$$\varphi=-\frac{1}{\pi}\iint \frac{m(\xi)\ d\xi d\eta}{[2\beta\rho(\eta)+\Psi\ (\eta)-\xi]^{1/2}\ [\Psi(\eta)-\xi]^{1/2}}$$

where

$$\Psi\ (\eta)=x-\beta\rho\ (\eta) \tag{15}$$

Assuming $(\Psi/2\beta\rho) \ll 1$, the leading term of φ can be written

$$\varphi \sim -\mathrm{Re}\int_0^L \frac{m_{1/2}\ [\Psi\ (\eta)]\ d\eta}{[2\pi\beta\rho\ (\eta)]^{1/2}} \tag{16}$$

where $m_{1/2}$ is the fractional integral of order 1/2 of the slope function for the wing:

$$\pi^{1/2}\ m_{1/2}\ (\Psi)=\int_0^{\Psi} m\ (\xi)\,(\Psi-\xi)^{-1/2}\ d\xi \tag{17}$$

The symbol Re in equation (16) denotes "real part of" and gives the correct behavior for φ when $\Psi(0)$ or $\Psi\ (L)$ are negative.

---

[2] See p. 219.

The behavior of equation (16) near the wavefronts is governed by the function $\Psi(\eta)$; Ψ is stationary at $\eta = s$ where $s = y$, and this point defines a mapping from parameters (x, y, z) to ray parameters (r, s, T), where $r = \rho(s) = z$ and $T = \Psi(s) = x - \beta z$. Introduce a transformation $\eta(u)$ into equation (16) where

$$u^2 = T - \Psi(\eta) \qquad u = \text{sgn}\,(\eta - s)[T - \Psi(\eta)]^{1/2} \tag{18}$$

so that

$$\varphi \sim -\text{Re} \int_{u(0)}^{u(L)} h(u)\, m_{1/2}(T - u^2)\, du \tag{19}$$

where

$$h(u) = [2\pi\beta\rho(\eta)]^{-1/2} \frac{d\eta}{du} \tag{20}$$

It is convenient for the purpose of this discussion to confine attention to points in the range of influence of only one wingtip, $y = 0$. The finite wing is then easily handled by a superposition of two expansions of the form to be derived. In this case, $\Psi(L)$ is negative so that the upper limit in equation (19) can be replaced with $+T^{1/2}$. Then $h(u)$ is written as $h(0) + u\bar{h}(u)$, and the integral in equation (19) becomes, after an integration by parts,

$$-h(0) \int_{\theta}^{T^{1/2}} m_{1/2}(T - u^2)\, du - \frac{\bar{h}(\theta)}{2} m_{3/2}(T - \theta^2) - \frac{1}{2} \int_{\theta}^{T^{1/2}} \frac{d\bar{h}}{du} m_{3/2}(T - u^2)\, du \tag{21}$$

where

$$\theta = u(0) = \text{sgn}\,(-s)[T - \Psi(0)]^{1/2} \tag{22}$$

and the integral of m of order 3/2 is

$$m_{3/2}(\Psi) = 2\pi^{-1/2} \int_0^{\Psi} m(\xi)(\Psi - \xi)^{1/2}\, d\xi \tag{23}$$

It is readily verified that the last term in equation (21) is of the same order in Ψ/ρ as terms already neglected in equation (16). Thus, if $F(T, \theta)$ is defined as

$$F(T, \theta) = \text{Re} \int_{\theta}^{T^{1/2}} m_{3/2}(T - u^2)\, du \tag{24}$$

then the leading term of φ becomes

$$\varphi \sim -h(0) F_T(T, \theta) + \frac{\bar{h}(\theta)}{2} F_{\theta}(T, \theta) \tag{25}$$

which is of the form of equation (10) because equation (24) satisfies equation (13).

The amplitudes in equation (25) are easily computed in terms of ray parameters. First, note that the endpoint of integration θ introduces another set of such parameters into equation (25):

$$r_0 = \rho(0) = (y^2 + z^2)^{1/2}$$

$$\alpha_0 = \tan^{-1} \frac{z}{y} \tag{26}$$

$$T_0 = \Psi(0) = x - \beta(y^2 + z^2)^{1/2}$$

Then from equations (15) and (18),

$$\frac{d\eta}{du} = \frac{-2u\rho(\eta)}{\beta(y-\eta)} \qquad \left(\frac{d\eta}{du}\right)^2_{u=0} = \frac{2r}{\beta}$$

Hence,

$$h\ (0) = \frac{1}{\beta\pi^{1/2}}$$

$$\bar{h}\ (\theta) = \frac{1}{\theta}\left[h\ (\theta) - h\ (0)\right] = -\left[\frac{2}{(2\pi\beta^3 r_0)^{1/2}} \cos\alpha_0 + \frac{1}{\beta\pi^{1/2}\theta}\right] \tag{27}$$

In the main wave region, where $(T - \theta^2) = T_0 < 0$, the lower limit in equation (24) can be replaced with $-T^{1/2}$. F is then independent of θ:

$$F = 2\int_0^{T^{1/2}} m_{3/2}\ (T - u^2)\ du = \int_0^T \frac{m_{1/2}\ (\xi)\ d\xi}{(T-\xi)^{1/2}} \equiv \pi^{1/2}\ m\ (T)$$

and equation (25) reduces to the form of equation (5) for plane flow.

FOCUSING WAVE SYSTEMS

Here the situation is analogous to the case of diffraction. Any simple progressing wave expansion is such that the amplitude functions become infinite at the cusps on the appropriate wavefronts. For focusing systems, the general theory of uniformly valid expansions has been treated in detail in reference 5, in which expansions analogous to equations (10) through (13) are discussed and related to corresponding composite progressing wave expansions of the form of equation (9). For each particular problem in which focusing occurs, the appropriate canonical functions and amplitude coefficients must be determined in terms of the data of the problem. This has been carried out in the present research for a variety of cases in connection with sonic boom propagation. In

particular, the cases of an accelerating airfoil and an accelerating body of revolution have been studied in detail. The derivation of the nonlinear counterparts to these results is the subject of research currently in progress.

It is convenient here, however, to consider what is perhaps the simplest prototype of a problem involving focusing of waves. This is the case of steady flow past a nonlifting wing of constant cross section with a leading edge concave to the stream direction as depicted in figure 4. If the influence of the ends of the wing is ignored, then the wavefront configuration is as shown in figure 5. The origin of coordinates is taken at the point on the leading edge whose slope is just sonic. The envelope of Mach cones from the supersonic portion of the edge is the cusped figure shown, and the field is disturbed outside the sonic Mach cone, shown as a broken line. The potential here is again given near the wavefronts by equation (16), except that now there exist in general two ranges of η over which $\Psi(\eta)$ is positive and the integration must include both of these. In this case, $\Psi(\eta)$ is stationary at two points $s_\pm$ that define two mappings from parameters (x, y, z) to ray parameters $(r_\pm, s_\pm, T_\pm)$, where $T_\pm$ are the phase variables relative to the front and rear portions of the cusped envelope shown in figure 5. A transformation $\eta(u)$ is introduced by

$$\Psi(\eta) = A + Bu - \frac{1}{3}u^3 \tag{28}$$

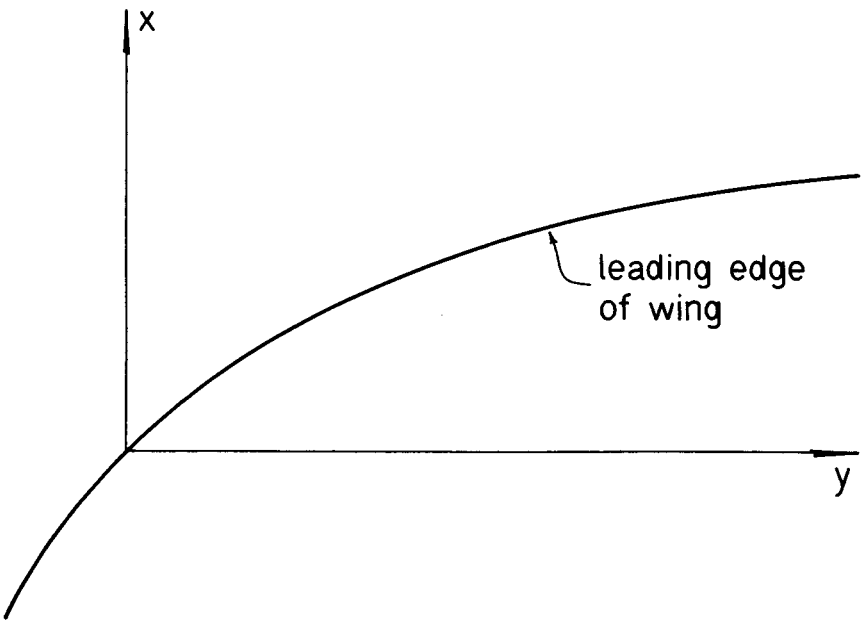

FIGURE 4.—Concave wing planform.

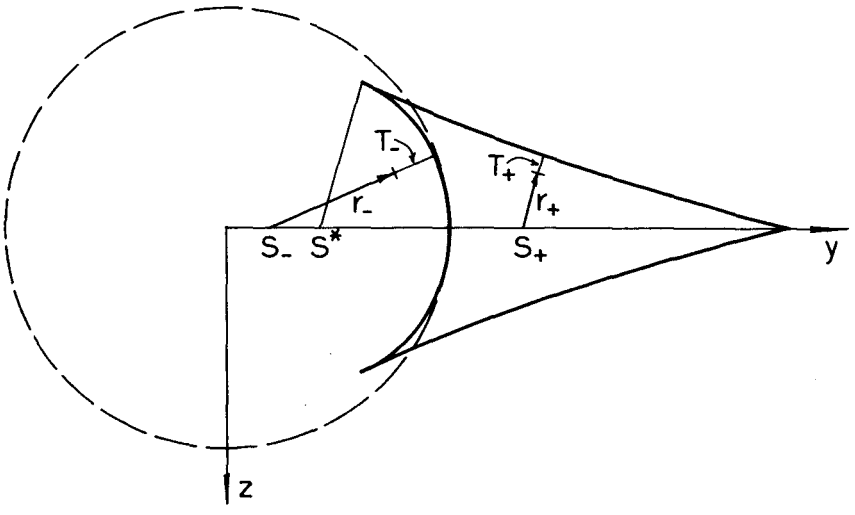

FIGURE 5.—Envelope portion of wavefront configuration for concave wing.

so that

$$\varphi \sim -\mathrm{Re} \int h(u)\, m_{1/2}(A+Bu-\tfrac{1}{3}u^3)\, du \tag{29}$$

Here,

$$A=\tfrac{1}{2}\,(T_+ + T_-)$$

and

$$B=[\tfrac{3}{4}\,(T_+ - T_-)]^{2/3}$$

and $T_\pm$ are the phases $\Psi(s_\pm)$ referred to above; $h(u)$ is given by equation (20) where $d\eta/du$ is now defined by equation (28). The points $\eta = s_\pm$ correspond to the points $u=\pm B^{1/2}$. Then, $h(u)$ is written as

$$h(u)=h_0+uh_1+(B-u^2)\,H(u)$$

so that

$$\begin{aligned} h_0&=\tfrac{1}{2}\,[h(B^{1/2})+h(-B^{1/2})] \\ h_1&=\frac{1}{2B^{1/2}}\,[h(B^{1/2})-h(-B^{1/2})] \end{aligned} \tag{30}$$

and the integral in equation (29) becomes

$$\begin{aligned} h_0 \int m_{1/2}(A+Bu-\tfrac{1}{3}u^3)\, du + h_1 \int m_{1/2}(A+Bu-\tfrac{1}{3}u^3)\, u\, du \\ + \int H(u)\, \frac{d}{du}\,[m_{3/2}(A+Bu-\tfrac{1}{3}u^3)]\, du \end{aligned} \tag{31}$$

The portion of φ that is singular across the envelopes $T_\pm = 0$ is represented by the integral in equation (29) between the two largest roots

u_2 and u_3 of the cubic argument. If this is denoted by φ_s, then the last term in equation (31) can be integrated by parts. The endpoint contributions vanish because $m_{3/2}$ vanishes at u_2 and u_3, and the remaining integral is small compared to the first two terms near the wavefront. If $F(A, B)$ is defined as

$$F(A, B) = \int_{u_2}^{u_3} m_{3/2}(A + Bu - \tfrac{1}{3} u^3)\, du \tag{32}$$

then equation (31) yields for the leading term of φ_s

$$\varphi_s \sim h_0 F_A(A, B) + h_1 F_B(A, B) \tag{33}$$

Equation (33) is a uniformly valid representation of the singular part of φ near the cusped wave envelope. The functions h_0 and h_1 can be written in terms of the ray parameters $r_\pm$ and $s_\pm$ from equation (30), and it is readily shown that h_0 and h_1 are smooth functions everywhere in the field including the ray $s = s^*$ to the cusp along which $A = T_+ = T_-$ and $B = 0$. The generalized waveform $F(A, B)$ is seen from equation (32) to satisfy the Tricomi equation

$$BF_{AA} - F_{BB} = 0$$

as required by the general theory discussed in reference 5.

REFERENCES

1. LEWIS, R. M.: The Progressing Wave Formalism. Proc. Symp. Quasi-Optics, Polytech. Inst. Brooklyn. Microwave Res. Inst. Symp. Ser. 14. Polytechnic Press, 1964, pp. 71–103.
2. LIGHTHILL, M. J.: Higher Approximations in Aerodynamic Theory. General Theory of High Speed Aerodynamics, sec. E, W. R. Sears, ed., Princeton Univ. Press, 1954.
3. WHITHAM, G. B.: On the Propagation of Weak Shock Waves. J. Fluid Mech., vol. 1, Sept. 1956, pp. 290–318.
4. HAYES, W. D.: Linearized Supersonic Flow. Rept. AL-222, North American Aviation, Inc., 1947.
5. LUDWIG, D.: Uniform Asymptotic Expansions at a Caustic. Commun. Pure Appl. Math., vol. 19, 1966, pp. 215–250.

Nonlinear Acoustic Behavior at a Caustic

R. SEEBASS
Cornell University

The basic theory that underlies the prediction of sonic booms was developed long before their occurrence became commonplace. With the era of commercial transport at supersonic speeds upon us, this theory is now used routinely to predict the pressure signature anywhere that it is desired for an aircraft in unsteady supersonic flight in a horizontally stratified atmosphere with steady winds (refs. 1 and 2). Fundamental contributions to the basic theory were made by Friedrichs, Hayes, Landau, and Whitham (refs. 3 to 8). A derivation of one of the results needed from linear theory, given first by Hayes (ref. 4) and implicit in Whitham's derivation (ref. 8), due to Lomax (ref. 9) should also be noted. The adequacy of this basic theory, never in question on theoretical grounds, has been demonstrated in wind-tunnel and flight tests (refs. 10 and 11).

Recent research on the sonic boom has been directed either at extending the conditions under which we may adequately predict the sonic boom or at various means of reducing or eliminating its impact. For aircraft slender enough that the product of their flight Mach number and their slenderness ratio is much smaller than one, there are two failures of this basic theory. First, it cannot predict the pressure levels that occur in the neighborhood of a caustic; second, it does not take into account the effects of atmospheric turbulence on the sonic boom pressure signature.

This paper is concerned with modifying the basic theory to include nonlinear effects not properly accounted for in the neighborhood of a caustic. The basic theory accounts for nonlinear effects on the propagation of the pressure signal down a ray tube (refs. 1 and 12), but the concept of ray tubes is a linear one. In regions where the differential ray tube area becomes small, the pressure becomes correspondingly large and the concept of a ray tube fails. The envelope of the rays is a caustic surface; this surface is the locus of cusps in the acoustic wavefronts.

Aircraft maneuvers and atmospheric refraction, separately or in conjunction with one another, cause successively emitted rays to have an envelope. The rate at which the ray tube area tends toward zero depends upon the maneuver performed and the acoustic environment

into which the rays are propagated. Analytic expressions for the variation of ray tube area with altitude for various maneuvers have been calculated by Haefeli (ref. 13) for a uniform atmosphere. For steady, level flight in an atmosphere in which the sound speed decreases with altitude, a caustic surface will occur at which the aircraft's speed is equal to the local sound speed. The pressure field in the neighborhood of a caustic is often referred to as a superboom. Such superbooms are an unavoidable consequence of supersonic flight. Whenever an aircraft accelerates to supersonic speeds, a caustic surface is formed. Unless the aircraft never achieves a speed that is greater than the speed of sound at the ground, the caustic will intersect the ground and a superboom will occur. It seems preferable to refer to the pressure field that is sensed at the ground in the neighborhood of a caustic as a superboom. It is a different pressure field than we would sense with a small probe in the absence of a plane surface such as the ground.

The mathematical formulation of the behavior of the pressure signature near a caustic has been given by Guiraud (ref. 14) and Hayes (ref. 15). A linear approximation to this problem was formulated and solved by Lighthill (ref. 16) in his study of the reflection of a weak steady shock wave at a laminar boundary layer. Our interest is not in the effect of the shock wave on the boundary layer, but in the detailed structure of the wavefront as it reflects at a caustic surface. Here the nonlinearity is an essential part of the problem. Lighthill, in the paper cited, proposed to extend his investigation to include nonlinear effects. Evidently other duties and problems intervened. However, aside from determining the maximum pressure amplitude and other details of the flow near the caustic, the linear theory accurately predicts the waveform shapes observed in the careful flight-test experiments, "Operation Jericho," conducted by French investigators (refs. 17 and 18). Thery (ref. 19) has studied the behavior of a shock wave in a sound speed gradient by the method of characteristics. His results are in accord with the similitude of Guiraud and Hayes. Because Thery's results do not account for the influence of the pressure rise through the shock wave communicated upstream by the subsonic portion of the flow, they must be viewed as a qualitative indication of the amplification of the pressure rise across the shock away from the point on the shock where the flow behind the shock is sonic. Naturally Thery's calculations must terminate at such a point.

With the proviso that the wavelength of the incoming signal λ is small compared to the radius of curvature of the wavefront at the caustic, a local irrotational analysis is permissible. In this case Hayes (ref. 15) has shown that the local solution near the caustic is governed by

$$\Phi_{yy} - \left[\frac{\gamma}{R} + 2\Gamma\,\Phi_x\right]\Phi_{xx} = 0 \tag{1}$$

where R^{-1} characterizes the relative curvature of a ray with respect to that of the caustic. Here x and y are distances along and normal to the caustic surface. This local coordinate system has been chosen in a way that changes with time and the other physical coordinate are of higher order. To complete the problem we must specify the initial disturbance at large negative x and positive y; this is properly done by matching the solution to equation (1) to a prescribed incoming signal. This signal is that determined by geometric acoustics with the appropriate quasi-linear correction. Such a description is consistent with equation (1) for large y. Because the signal determined by equation (1) approaches the solution to Tricomi's equation for large y, we follow Hayes (ref. 15) and prescribe an initial signal determined by the asymptotic behavior of the solution to the linear Tricomi equation:

$$\frac{p'(x, y)}{\rho a_0^2} = -\Phi_x(x, y) = -\epsilon \left(\frac{y}{R}\right)^{-1/4} F\left[\frac{x}{\lambda} + \frac{2}{3}\left(\frac{\lambda}{R}\right)^{1/2}\left(\frac{y}{\lambda}\right)^{3/2}\right]$$

We also require that p' approach zero at infinity in the lower half plane. Here p' is the perturbed pressure, ρ the density, a_0 the sound speed at the caustic, and 2Γ is the usual generalization of $\gamma+1$. The characteristic length R is prescribed by the behavior of the linear wavefronts

$$\frac{y}{R} = \left[\frac{3}{2}\frac{|c-x|}{R}\right]^{2/3}$$

or the rays

$$\frac{y}{R} = \left(\frac{c-x}{2R}\right)^2, \qquad c = \text{constant}$$

FORMULATION

Although the behavior at a caustic is locally steady in the appropriate coordinate system and governed by the simple equation introduced above, it is conceptually advantageous to investigate an equivalent aerodynamic problem. Consider steady flow of uniform speed U and varying free-stream sound speed $a_0(y)$ past a slender airfoil. Choose a coordinate system (x, y) such that x is in the direction of the flow and require $a_0(0) = U$. Here the initial flow is taken to be at constant pressure with a nonuniform entropy distribution; body forces are neglected. In this case the velocity perturbation is irrotational and derivable from a velocity potential Φ, which satisfies

$$[M^2(y) - 1 + 2\Gamma M^2 U^{-1}\Phi_x]\Phi_{xx} - \Phi_{yy} = 0$$

where $M^2(y) = U^2/a_0^2(y)$. We consider an incoming signal of length λ and amplitude A prescribed along a linear characteristic; this signal can

be thought of as being generated by an airfoil of specified length, thickness, and shape at some height $y=$ constant. No useful generality is achieved by considering an unspecified $M^2(y)$, and we replace $M^2(y)$ by $1+M^{2\prime}(0)y+\cdots$ and rewrite the equation for the velocity potential as

$$[M^{2\prime}(0)y+2\Gamma U^{-1}\Phi_x]\,\Phi_{xx}-\Phi_{yy}=0$$

With $M^2(y)$ specified, we introduce the linear characteristics

$$\tilde{r},\ \tilde{s}=x\pm\tfrac{2}{3}\sqrt{M^{2\prime}(0)}\,y^{3/2}$$

and express the incoming signal in terms of the pressure coefficient

$$C_p=-\frac{2}{U}\frac{\partial\Phi}{\partial x}=A\left(\frac{y}{S}\right)^{-1/4}f(\tilde{r})\qquad\text{on }\tilde{s}=S\gg 1$$

with $f(\tilde{r})=0$ for $\lambda<\tilde{r}<0$.

We must also require

$$(\Phi_x^2+\Phi_y^2)^{1/2}\to 0$$

as $x^2+y^2\to\infty$ for $y<0$.

The formulation is completed by the transformation

$$\Phi=US^{5/3}[M^{2\prime}(0)]^{2/3}\Phi/2\Gamma$$
$$x=S\xi$$
$$y=[M^{2\prime}(0)]^{-1/3}S^{2/3}\eta$$

which gives the simple canonical description

$$(\eta+\phi_\xi)\,\phi_{\xi\xi}-\phi_{\eta\eta}=0 \tag{2}$$

with the incoming signal specified by

$$-\frac{\partial\phi}{\partial\xi}(p,-1)=\frac{\Gamma C_p(p,-1)}{[SM^{2\prime}(0)]^{2/3}}=\frac{A\Gamma}{[SM^{2\prime}(0)]^{7/12}}\eta^{-1/4}F(p)\equiv\mu\eta^{-1/4}F(p) \tag{3}$$

for

$$0\leqslant p\leqslant\lambda/S$$

and

$$\frac{\partial\phi}{\partial\xi}(p,-1)=0$$

for

$$0>p>\frac{\lambda}{S}$$

on the linear characteristics $p,\ q=\xi\pm\frac{2}{3}\eta^{3/2}$. Only the parameter $\mu\equiv A\Gamma[SM^{2\prime}(0)]^{-7/12}$ remains in such a description. Specifying the

boundary conditions on the characteristics of Tricomi's equation requires that $\mu \ll 1$. In place of the length R, which characterizes the wavefront shape or ray tube area variation in a general formulation, we have the length $M^{2\prime}(0)^{-1}$. For conditions typical of troposphere, the latter length is about 10^{-5} ft.

Equation (2) is nonlinear and admits discontinuous solutions corresponding to shock waves. A straightforward application of the divergence theorem to the divergence form of equation (2) shows that such discontinuities have a local slope

$$\pm \frac{d\eta}{d\xi}\bigg|_{sh} = \left[\eta + \frac{(\phi_{\xi 2} + \phi_{\xi 1})}{2}\right]^{-1/2} \tag{4}$$

The subscripts refer to values on either side of the discontinuity. Across such discontinuity, the components ϕ_ξ, ϕ_η must satisfy

$$(\phi_{\xi 2} - \phi_{\xi 1})^2 \left[\tfrac{1}{2}\,(\phi_{\xi 1} + \phi_{\xi 2}) + \eta\right] = (\phi_{\eta 2} - \phi_{\eta 1})^2 \tag{5}$$

To complete our formulation, we note that the characteristics of equation (2) are given by

$$\xi + \phi_\eta = \pm \tfrac{2}{3}\,(\eta + \phi_\xi)^{3/2} + \text{constant} \tag{6}$$

and that along these characteristics

$$\pm \sqrt{\eta + \phi_\xi}\; d\phi_\xi = d\phi_\eta$$

This last equation was used in the quadrature that provides the characteristics.

A FORMAL SOLUTION

A formal expression for the solution to equation (2) can be derived by changing from the dependent variables ξ, η to $s = \xi + \phi_\eta$ and $t = \eta + \phi_\xi$. Such a change is suggested both by the form of the characteristic relation (6) and by the equation and boundary conditions for the Legendre transformation of the pseudo-potential $\xi\eta + \phi$. If we write

$$\phi_\xi(\xi, \eta) = f(s, t)$$

then the ξ derivative of equation (2) implies

$$tf_{ss} - f_{tt} = 0 \tag{7}$$

provided that the Jacobian of the map

$$J = \frac{\partial(s, t)}{\partial(\xi, \eta)} = (1 + \phi_{\xi\eta})^2 - (\eta + \phi_\xi)\phi_{\xi\xi}^2 \tag{8}$$

is not zero. The same approximation that we invoked to prescribe the incoming signal in terms of the linear solution to equation (2) provides the simple prescription equivalent to equation (3):

$$f \sim -\mu t^{-1/4} F(s + \tfrac{2}{3} t^{3/2}) \tag{9}$$

for $-s$ and t having large positive values.

The solution to the linear equation (7), subject to the condition $\partial(\xi,\eta)/\partial(s, t) = 1/J \neq 0$, then gives $\phi_\xi(\xi + \phi_\eta, \eta + \phi_\xi)$. Clearly, further information is required to determine either ϕ_ξ or ϕ_η. To this end, we write

$$\phi_\eta(\xi, \eta) = g(s, t)$$

and use the η derivative of equation (2) to conclude that

$$t g_{ss} - g_{tt} + \frac{g_t}{t} = 0 \tag{10}$$

again provided that $J \neq 0$. The appropriate prescription for the incoming signal in this case is

$$g \sim -\mu t^{1/4} F(s + \tfrac{2}{3} t^{3/2}) \tag{11}$$

The solution to equation (10) subject to equation (11) provides $\phi_\eta(\xi + \phi_\eta, \eta + \phi_\xi)$ which, when combined with the solution $\phi_\xi(\xi + \phi_\eta, \eta + \phi_\xi)$ to equation (7) gives implicit solutions for $\phi_\xi(\xi, \eta)$ and $\phi_\eta(\xi, \eta)$. These results are somewhat analogous to the implicit solution $u = f(x - ut)$ to the inviscid Burgers' equation $u_t + uu_x = 0$, and the same difficulties obtain. In particular, the solutions become multivalued, and the appropriate shock waves must be introduced to render the solution unique.

We note that f and g are related to one another through ϕ, and consequently we may replace equation (7) or equation (10) with the system

$$t f_s - g_t = 0 \qquad f_t - g_s = 0 \tag{12}$$

The potential implied by the last equation satisfies Tricomi's equation.

The linear problems of equations (7) and (10) or the equations (12) are solved by means of a Fourier transform on the s coordinate. The results, when inverted, can be written in the form

$$t - \phi_\xi = \eta = t - \frac{1}{\sqrt{2\pi}} \int_{-\infty}^{\infty} \alpha(\omega) e^{-is\omega} Ai(-|\omega|^{2/3} t)\, d\omega$$

$$s - \phi_\eta = \xi = s + \frac{i}{\sqrt{2\pi}} \int_{-\infty}^{\infty} |\omega|^{-1/3} \alpha(\omega)\, \operatorname{sgn} \omega e^{-is\omega} Ai'(-|\omega|^{2/3} t)\, d\omega \tag{13}$$

where $\alpha(\omega)$ is determined by the prescribed incoming signal $F(p)$

$$a(\omega) = -\mu|\omega|^{1/6}(1 - i \operatorname{sgn} \omega) \int_{-\infty}^{\infty} F(p)e^{i\omega p}\, dp \tag{14}$$

For a prescribed incoming signal $F(p)$ and with $\alpha(\omega)$ determined from equation (14), equations (13) determine ϕ_ξ and ϕ_η implicitly:

$$\begin{aligned} \phi_\xi &= \hat{\phi}_\xi(\xi + \phi_\eta,\ \eta + \phi_\xi) \\ \phi_\eta &= \hat{\phi}_\eta(\xi + \phi_\eta,\ \eta + \phi_\xi) \end{aligned} \tag{15}$$

The map from the s, t plane to the ξ, η plane will be singular when the Jacobian J^{-1} vanishes. A general study of this mapping is not very informative. For the functions of concern here, we know that our primary interest is in the solution for which $F(p)$ contains one or two step functions. With a discontinuity in the incoming signal, f and g will be discontinuous on one characteristic in the s, t plane, logarithmically infinite on another characteristic, and singular at the origin as the $-1/4$ power of t and the $-1/6$ power of s. This discontinuous and singular behavior dictates the main features of the mapping.

SOLUTION FOR A DISCONTINUOUS SIGNAL

We consider the signal $f \sim -\mu t^{-1/4}F(p)$ where

$$F(p) = H(p) - H(p + \delta) \tag{16}$$

and $H(p)$ is 0 for $p < 0$ and 1 for $p \geq 0$; that is, we consider the signal of uniform strength μ when $t = 1$ and of length δ. With the signal specified by equation (16), the integrals (13) can be evaluated explicitly in terms of hypergeometric functions. The solution can also be obtained by analytic continuation of basic self-similar solutions; for a single discontinuity, the results were given by Germain and Bader (ref. 20). Hayes has also carried out the analytic continuations, reproducing the results of Germain and Bader. Our formulation requires explicit formulas for both $f(s, t)$ and $g(s, t)$; these results are somewhat complex and are relegated to the appendix.

For the incoming signal, equation (16), our solution takes the form of equation (15), where the functions $\hat{\phi}_\xi$ and $\hat{\phi}_\eta$ are discontinuous on $\xi + \phi_\eta = -\frac{2}{3}(\eta + \phi_\xi)^{3/2}$ and logarithmically infinite on $\xi + \phi_\eta = \frac{2}{3}(\eta + \phi_\xi)^{3/2}$. Thus the physical plane map is not a simple one. First, because f and g are discontinuous across $s = -\frac{2}{3}t^{3/2}$, this characteristic maps into two distinct lines in the physical plane. These lines do not overlap one an-

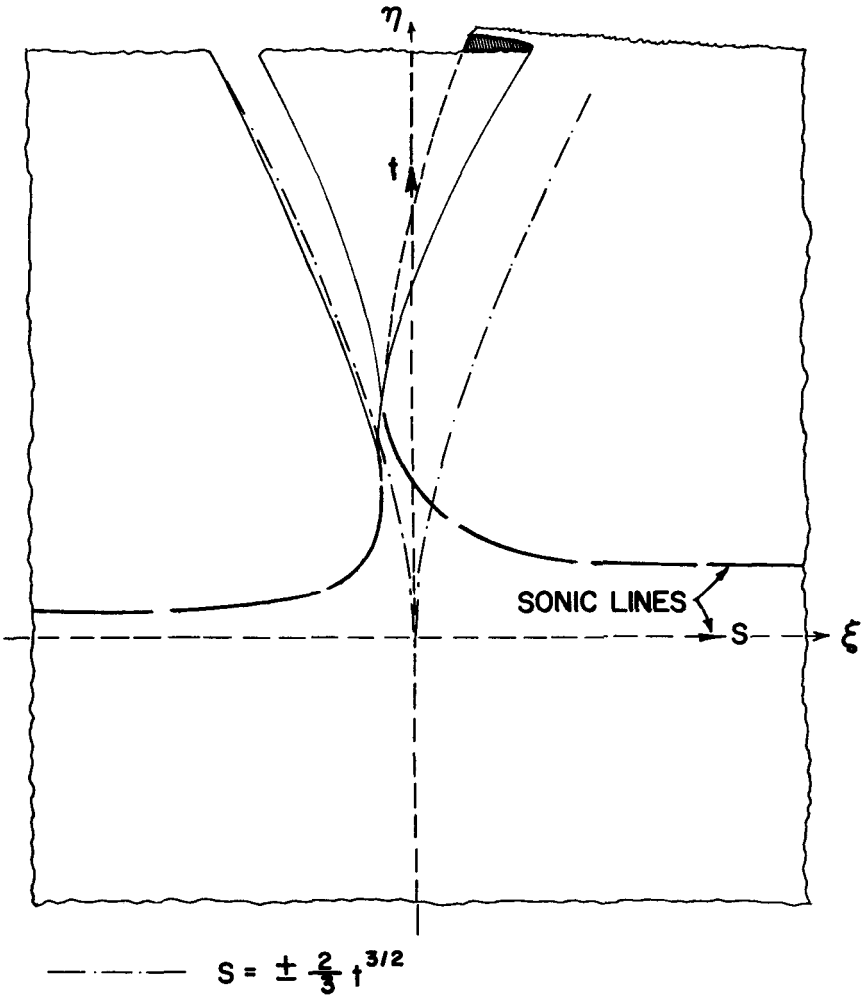

FIGURE 1.—Sketch of an overlay of the ξ, η plane on the s, t plane.

other, and there is a "gap" in the physical plane where the solution is yet to be determined. Second, in the neighborhood of the logarithmic singularity, the solution in the physical plane is multivalued. This behavior is indicated in figure 1 by a sketch that shows an overlay of the s, t and ξ, η planes. To complete the solution, we must determine the solution in the "gap" region as well as specify the correct procedure for rendering the solution single-valued in the folded region.

THE SIMPLE WAVE REGION

The solution that fills the "gap" must, of course, be a simple wave because it must map into a single characteristic. We can clarify the oc-

currence of the "gap" by examining the asymptotic behavior of our solution for large $-\xi$ and η, with $\xi+\frac{2}{3}\eta^{3/2}$ not too large. In this case, it is a simple matter to show that $s=-\frac{2}{3}t^{3/2}$ maps onto the two curves $\xi=-\frac{2}{3}\eta^{3/2}$ and $\xi=-\frac{2}{3}\eta^{3/2}+2\mu\eta^{1/4}$; and our signal, which was discontinuous in the s, t plane, now has a rise time proportional to its strength, namely $2\mu\eta^{1/4}$. The condition that

$$\xi+\phi_\eta=-\tfrac{2}{3}(\eta+\phi_\xi)^{3/2}$$

and equation (2) require that the solution in the "gap" be a simple wave of the form

$$\xi-\eta(\eta+\phi_\xi)^{1/2}=f^*(\eta+\phi_\xi)$$

where the arbitrary function f^* is determined from the known behavior of ϕ_ξ and ϕ_η on each edge of the "gap." For example, we may write for large $-\xi$ and η

$$t\sim\eta-\mu t^{-1/4}H(s+\tfrac{2}{3}\,t^{3/2})$$

and

$$s\sim\xi-\mu t^{1/4}H(s+\tfrac{2}{3}\,t^{3/2})$$

Eliminating H from these two equations and using $s=-\frac{2}{3}t^{3/2}$, we find

$$\xi-\eta(\eta+\phi_\xi)^{1/2}\sim-\tfrac{5}{3}\,(\eta+\phi_\xi)^{3/2}$$

for the asymptotic behavior in the "gap." The generalization of this procedure, using the full equations for ϕ_ξ and ϕ_η (eqs. (A–1) to (A–3)), provides the solution everywhere in the "gap."

SHOCK WAVES

The resolution of the multivalued nature of the solution is clear. All branches of the multivalued solution satisfy the basic inviscid equations. However, the "reflection" of the incident signal at the caustic gives rise to a reflected wave. The incident signal steepens as it approaches the caustic and is essentially discontinuous there. This gives rise to a reflected signal that, in our inviscid treatment, is multivalued. A shock wave must be introduced to render the solution single-valued but discontinuous. The jump in derivatives of ϕ across the discontinuity must satisfy equation (5), whereas its path must obey equation (4).

We note that even with shock waves present, the potential and the stream function defined by $\psi_\xi=\phi_\eta$, $\psi_\eta=\frac{1}{2}\,(\eta+\phi_\xi)^2$ are continuous. Both may be written in two ways; for example,

$$\phi=\int_a^\xi \phi_\xi(t,\,b)\;dt+\int_b^\eta \phi_\eta(\xi,\,t)\;dt=\int_a^\xi \phi_\xi(t,\,\eta)\;dt+\int_b^\eta \phi_\eta(a,\,t)\;dt \tag{17}$$

Assuming that ϕ_ξ and ϕ_η are discontinuous at ξ_s, η_s and differentiating either definition of ϕ with respect to ξ and η, we find

$$(\phi_{\eta_1}-\phi_{\eta_2}) \pm (\phi_{\xi 1}-\phi_{\xi 2}) \frac{d\xi_s}{d\eta_s}=0$$

The same procedure applied to ψ gives

$$(\phi_{\eta_1}-\phi_{\eta_2}) \frac{d\xi_s}{d\eta_s} \pm (\phi_{\xi 1}-\phi_{\xi 2}) \left(\eta+\frac{\phi_{\xi_1}+\phi_{\xi_2}}{2}\right)=0$$

Consequently, we can make either ϕ_ξ or ϕ_η single valued by introducing a discontinuity so that any one of the four integrals

$$\int_a^\xi \phi_\xi(t, \eta)\, dt, \qquad \int_b^\eta \phi_\eta(\xi, t)\, dt,$$

$$\int_a^\xi \phi_\eta(t, \eta)\, dt, \qquad \text{or} \qquad \int_b^\eta [t+\phi_\xi(\xi, t)]^2\, dt$$

is continuous. Such a discontinuity will propagate at the mean of the characteristic speeds ahead of and behind it (equation (4)) and satisfy equation (5).

The behavior of the multivalued solution near $s=\frac{2}{3}t^{3/2}$ is sketched in figures 2 and 3. Figure 2 depicts $\phi_\xi(\xi, \eta)$ as a function of ξ for a fixed η and a specified incoming signal. Figure 3 is a sketch of the locus of $\eta=$ constant in the s, t plane. From a practical point of view, the only multivalued portion of ϕ_ξ in figure 2 that makes any contribution to $\int_{-\infty}^\xi \phi_\xi(t, \eta)\, dt$ occurs when $\xi > 0.05$. This multivalued function is made single-valued but discontinuous at $\xi=\xi_s$ through

$$\int_{-\infty}^{\xi_s} \phi_{\xi_1}(t, \eta)\, dt+\int_{\xi_s}^{\xi} \phi_{\xi_2}(t, \eta)\, dt=\int_{-\infty}^{\xi} \phi_\xi(t, \eta)\, dt$$

Here ϕ_{ξ_1} corresponds to that branch of ϕ_ξ that originates at $\xi=-\infty$ and ϕ_{ξ_2} corresponds to the branch that ends at $\xi=+\infty$. A simple procedure for locating the points ξ_s where discontinuities are to be introduced is to calculate the running integral $\int_{-\infty}^\xi \phi_\xi(t, \eta)\, dt$ or one of its counterparts. This integral is then made continuous and single-valued by discarding spurious branches that cause it, too, to be multivalued. Such branches occur when the graph of the function represented by this integral intersects itself. The intersection points correspond to those values of ξ where ϕ_ξ is to be made discontinuous; that is, they are the shock positions ξ_s for the given value of η.

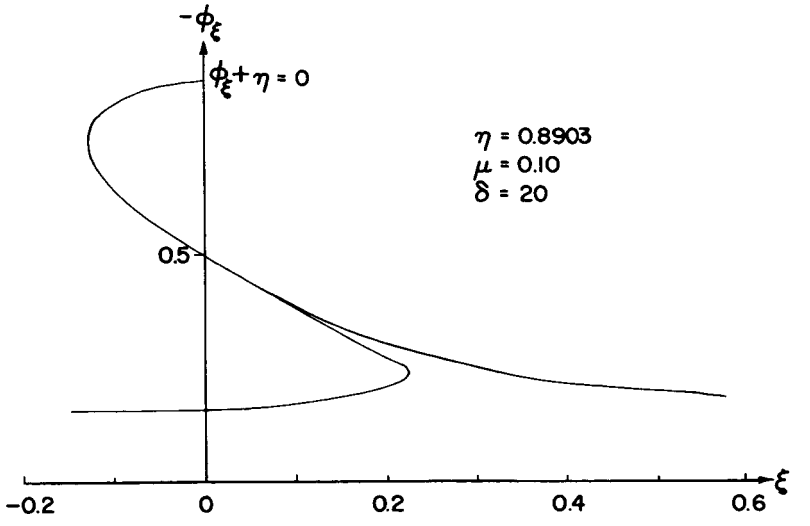

FIGURE 2.—Sketch of $\phi_\xi(\xi, \eta)$ as a function of ξ for fixed η.

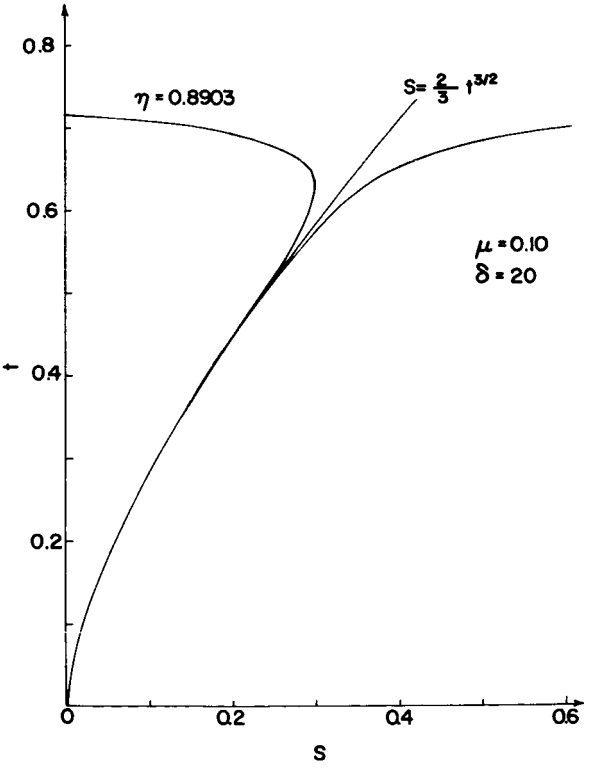

FIGURE 3.—Locus of points in s, t plane that correspond to $\eta =$ constant.

NUMERICAL EVALUATION

The nature of the solution near the caustic and near $s=\pm\frac{2}{3}t^{3/2}$ can be expressed analytically. From these analytical expressions it should be possible to determine the precise behavior of the solution in the neighborhood of its maximum amplitude. Here we pursue a more straightforward numerical evaluation of the solution. The solution is given in terms of hypergeometric functions. These functions are easily evaluated on a digital computer provided use is made of various alternate expressions for them (ref. 21). For this reason it is a simple matter to evaluate the solution in the s, t plane; i.e., to evaluate the linear solution.

Because of the implicit nature of the solution in the physical plane, it is necessary to solve a transcendental equation to obtain results that are easy to interpret. We can represent the solution given in the appendix by

$$t-\eta-F_1(s, t)=0 \tag{18}$$

and

$$s-\xi-F_2(s, t)=0 \tag{19}$$

where F_1 and F_2 are combinations of hypergeometric functions that are discontinuous on $s=-\frac{2}{3}t^{3/2}$ and logarithmically infinite on $s=\frac{2}{3}t^{3/2}$. We evaluate $\phi_\xi=t-\eta$ and $\phi_\eta=s-\xi$ as functions of ξ for a fixed value of η. To do this, we calculate the value of t that satisfies the first equation for given s and η; i.e., we solve the transcendental equation (18) for t. This is done numerically using Newton's method revised to account for the fact that the function F_1 is both discontinuous and singular. The numerical procedure was refined to the point where it was possible to find a root t, if one existed at all, to within one part in 10^4 within 20 iterations. A special routine sought multiple roots where they might exist. Equation (19) was then used to determine ξ. The running integrals

$$\int_a^\xi \phi_\xi(t, \eta)\, dt \qquad \int_a^\xi \phi_\eta(t, \eta)\, dt \tag{20}$$

were evaluated as well to provide the shock location and a check on that location. Values for s were taken in steps ranging from 0.10 to 0.01 in the range $-2.0 \leq s \leq 2.0$. The smallest increments were taken near $|s|=\frac{2}{3}\eta^{3/2}$ because t was not known a priori. This procedure did not always provide enough values for s when $s \leq \frac{2}{3}t^{3/2}$ and needs to be revised.

At this stage of development, our computer procedure does not incorporate the simple wave solution that provides the values of ϕ_ξ and ϕ_η between the two physical plane images of $s=-\frac{2}{3}t^{3/2}$. Our output is both digital and graphical. For simplicity, we allow the computer to plot continuous curves. Thus the results all display an incorrect

linear variation across the simple wave. From the graphical output the points of intersection of the two running integrals are determined and indicated by tick marks on the ξ axes (they are the same point). Whenever such a tick occurs at a ξ that is contained in the simple wave, it has been located with an incorrect linear variation for ϕ_ξ or ϕ_η. Although this error may not be serious, clearly a more sophisticated evaluation is needed. Also, in many instances we have, as mentioned above, not taken a sufficient number of points for s near but slightly less than $\frac{2}{3}t^{3/2}$. This, too, can affect the accuracy of our numerical quadratures. Equation (6) can be used to provide a graphical sketch of the characteristics once ϕ_ξ and ϕ_η have been calculated.

All calculations were performed on Boeing Scientific Research Laboratories' IBM 360/44 computer; graphical output was obtained using a Cal Comp plotter. Digital output for a single η and about 60 values of ξ averaged 1 min. When most or all of the solution was elliptic, times were substantially less than 1 min. Conversely, when the solution was hyperbolic, substantially more iterations were required to find the root of equation (18), and the evaluation could take several minutes for a single value of η.

RESULTS

Numerical evaluation of the solution was carried through for a range of signal strengths μ and lengths δ. While the absolute magnitude of the solution depends on the length of the signal, local variations in magnitude from the essentially ambient values were independent of δ. This is to by expected; the extent of the alteration of the sonic line shape depends on δ, but the rapid variation in signal strength as the signal approaches the caustic is essentially a local phenomenon and independent of signal length. Thus we view our results as indicating, in general, local behavior of a single shock wave approaching a caustic. However, it should be noted that the scale on which they are plotted may encompass several signature lengths for a real signal. For example, for threshold operation with the tropospheric sound speed gradient giving rise to a caustic, single units of our ξ and η coordinates correspond to roughly 750 and 2500 ft, respectively. Also, for the particular solution given here, the rise time of the incident signal is proportional to its strength. Regardless of its strength, the incoming signal becomes essentially discontinuous at the sonic line. Thus, while the nonlinear distortion of the reflected signal depends on μ, the maximum amplitude was found to be insensitive to the signal strength.

Figure 4 depicts the sonic line, characteristics, and incoming and reflected signals for $\mu = 0.05$ and $\delta = 5.0$. The shaded region represents the incoming simple wave. Figure 5 presents the corresponding plots of $\phi_\xi \equiv U$ and $\phi_\eta \equiv V$ as functions of ξ for prescribed values of η. The

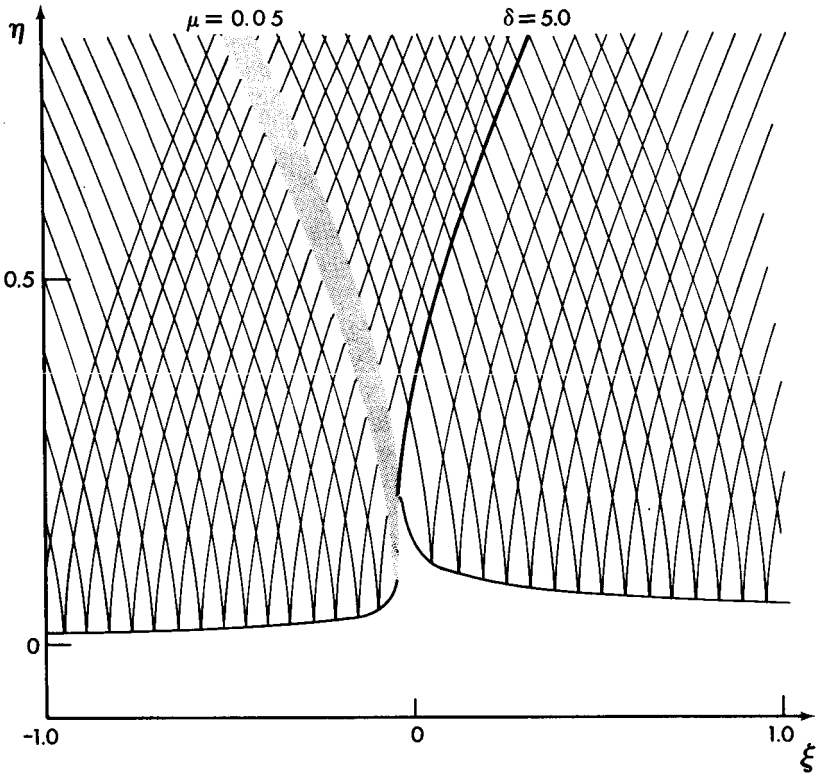

FIGURE 4.—Sonic line and characteristics for $\mu = 0.05$ and $\delta = 5.0$.

arrows mark the value of ξ, determined by the integrals of these functions, where a shock wave should be introduced to make the functions discontinuous but single valued. Fewer ξ values were used for flows that were essentially subsonic. As we have mentioned above, the linear variation shown for the incoming signal is spurious. The linear results for this case are given in figure 6. Here the $X \equiv s$ and $Y \equiv t$. Similar results are given for the nonlinear case with $\mu = 0.1$ and $\delta = 20$ in figures 7 and 8.

SUMMARY, CONCLUSION, AND RECOMMENDATIONS

Through a simple transformation we have been able to describe the nonlinear acoustic behavior at a caustic in terms of a linear equation. Using this result we have written, in implicit form, an analytical solution for a special incoming signal with a finite rise time. This solution has been studied by numerical evaluation and graphical presentation with a digital computer. Improvements in this digital evaluation are possible and probably warranted. But the essential features of the solution should be obtainable from the analytic expressions presented here. More important,

it should be possible to construct a multivalued solution in the transformed plane where the equation is linear that will correspond to a discontinuous signal in the physical plane. Except for the maximum amplitude of the reflected signal, the simple linear solution gives an adequate description of pressure signatures and does not differ greatly from the distorted nonlinear solution. For values of μ ranging from 0.05 to 0.15, the numerical results indicate that the amplification factors $\phi_\xi(\xi, \eta)_{\max}/\phi_\xi(\xi, 1)$ are less than five.

420-093 O - 71 - 8

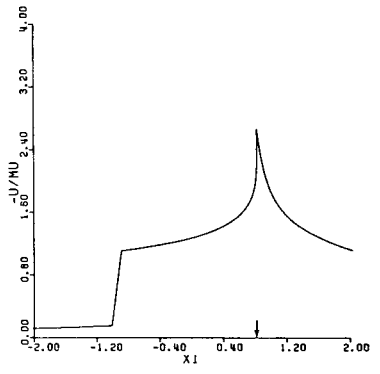

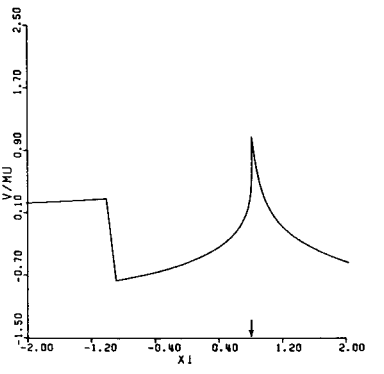

(*a*) $\eta = 1.310$.

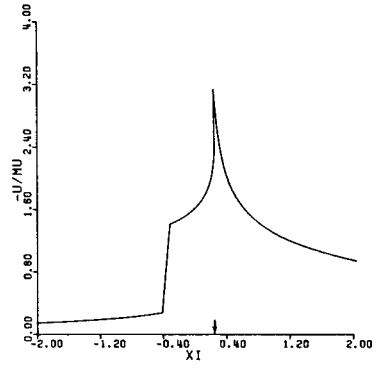

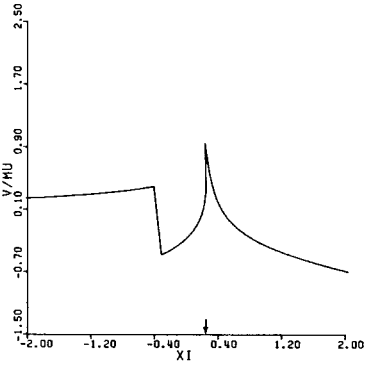

(*b*) $\eta = 0.711$.

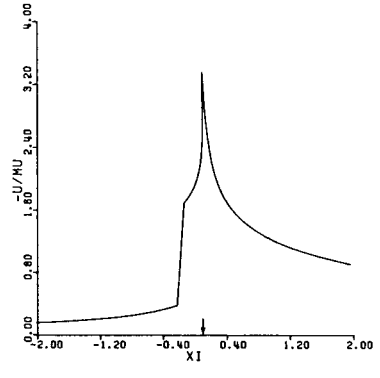

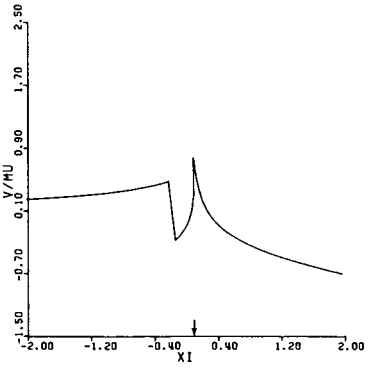

(*c*) $\eta = 0.478$.

FIGURE 5.—Computer-drawn graphs for $\phi_\xi = U$ and $\phi_\eta = V$ as functions of ξ for $\mu = 0.0500$ and $\delta = 5.000$.

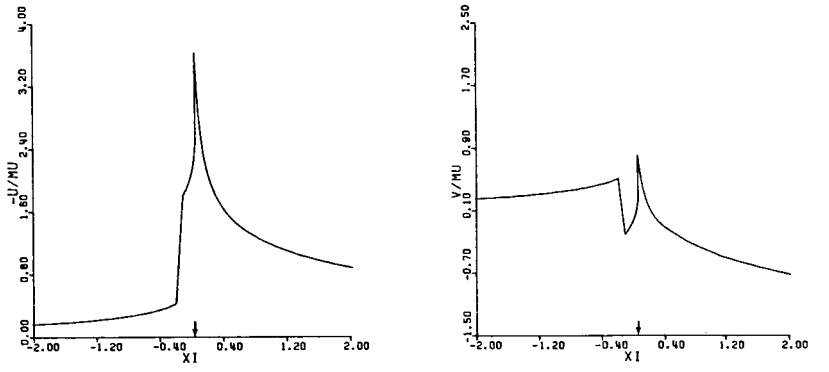

(*d*) $\eta = 0.418$.

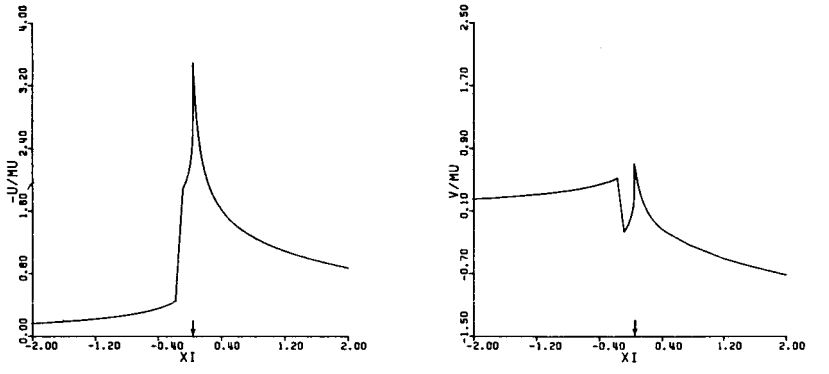

(*e*) $\eta = 0.386$.

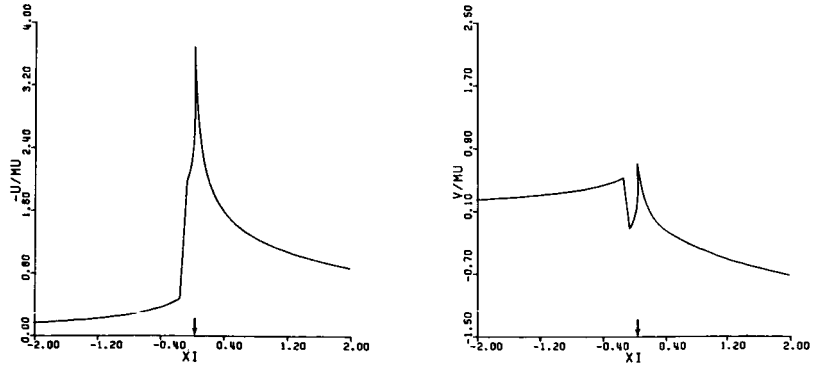

(*f*) $\eta = 0.353$.

FIGURE 5 (continued).—Computer-drawn graphs for $\phi_\xi = U$ and $\phi_\eta = V$ as functions of ξ for $\mu = 0.0500$ and $\delta = 5.000$.

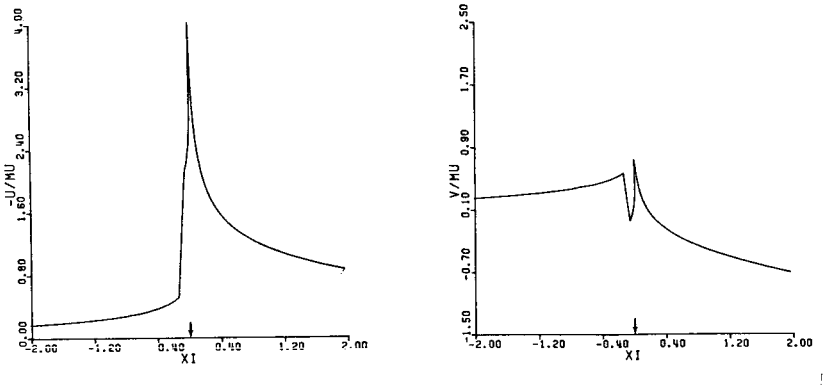

(*g*) $\eta = 0.319$.

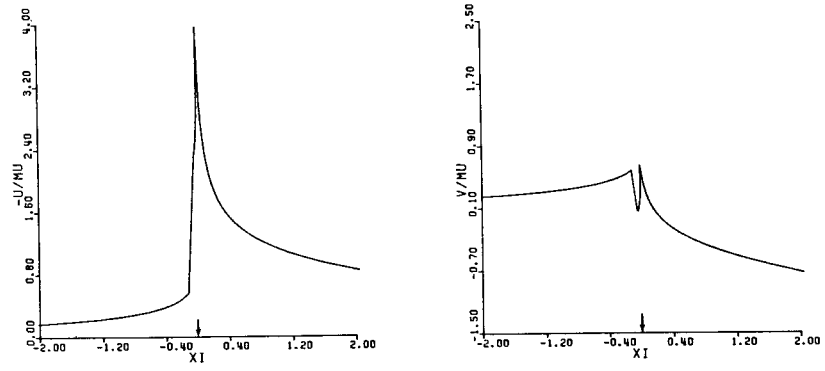

(*h*) $\eta = 0.282$.

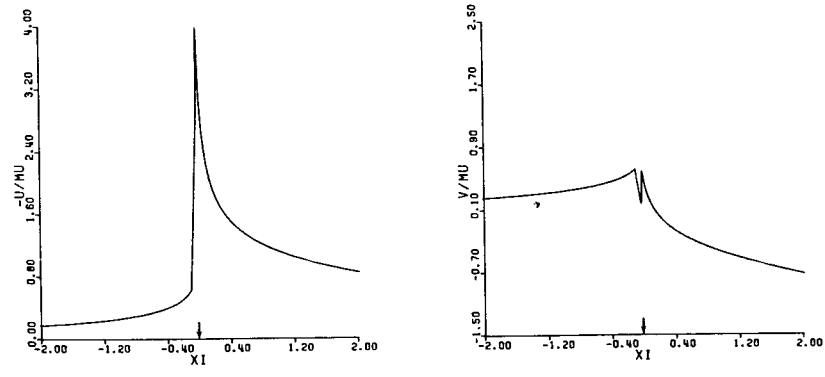

(*i*) $\eta = 0.243$.

FIGURE 5 (continued).—Computer-drawn graphs for $\phi_\xi = U$ and $\phi_\eta = V$ as functions of ξ for $\mu = 0.0500$ and $\delta = 5.000$.

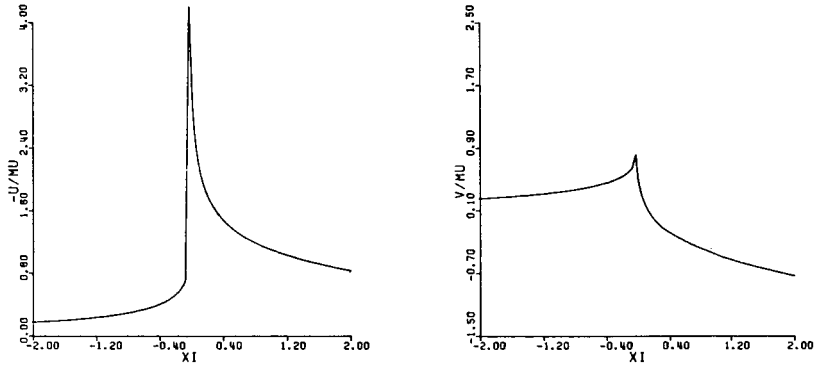

(*j*) $\eta = 0.201$.

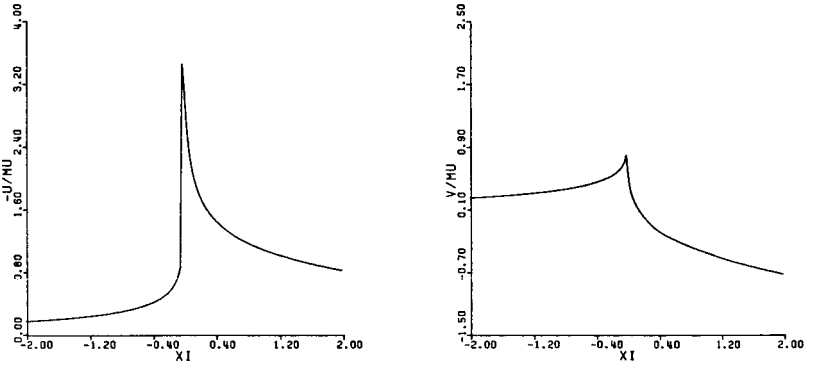

(*k*) $\eta = 0.153$.

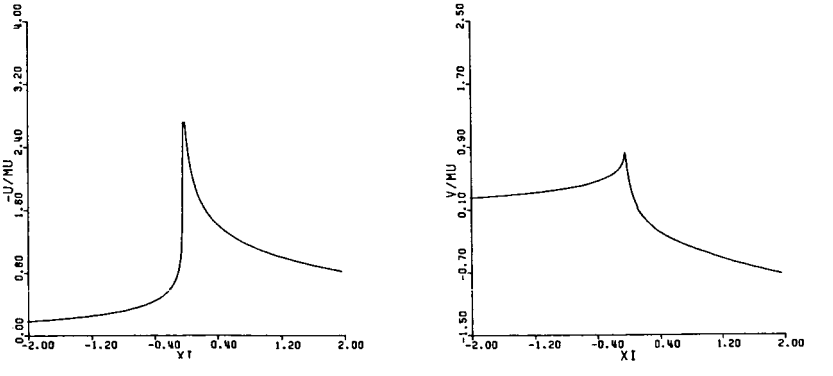

(*l*) $\eta = 0.097$.

FIGURE 5 (continued).—Computer-drawn graphs for $\phi_\xi = U$ and $\phi_\eta = V$ as functions of ξ for $\mu = 0.0500$ and $\delta = 5.000$.

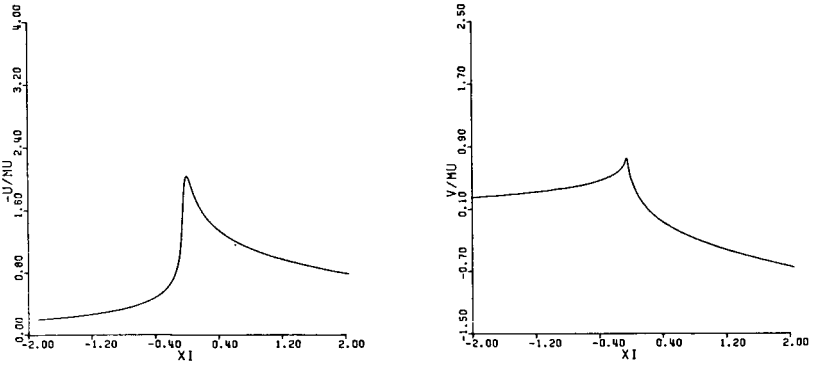

(m) $\eta = 0.000$.

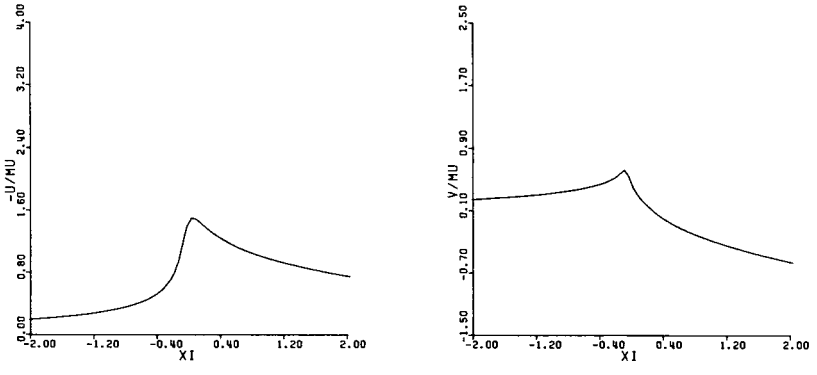

(n) $\eta = -0.153$.

FIGURE 5 (concluded). — Computer-drawn graphs for $\phi_\xi = U$ and $\phi_\eta = V$ as functions of ξ for $\mu = 0.0500$ and $\delta = 5.000$.

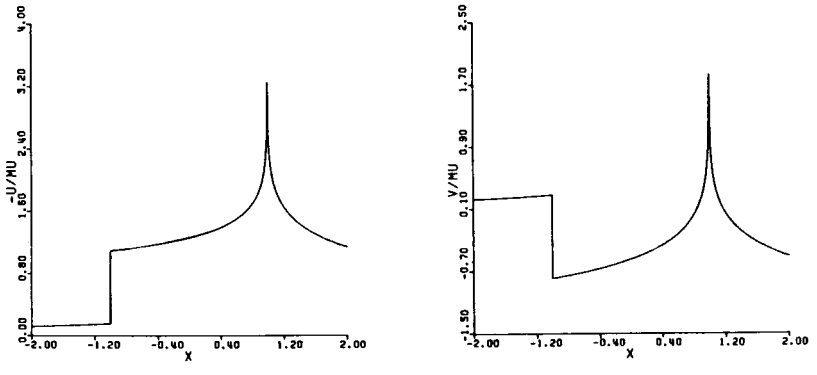

(a) $Y = t = \eta = 1.310$.

FIGURE 6. — Computer-drawn graphs of $f = \phi_\xi = U$ and $g = \phi_\eta = V$ for Tricomi's equation as functions of $X = s = \xi$ for $\delta = 5.000$.

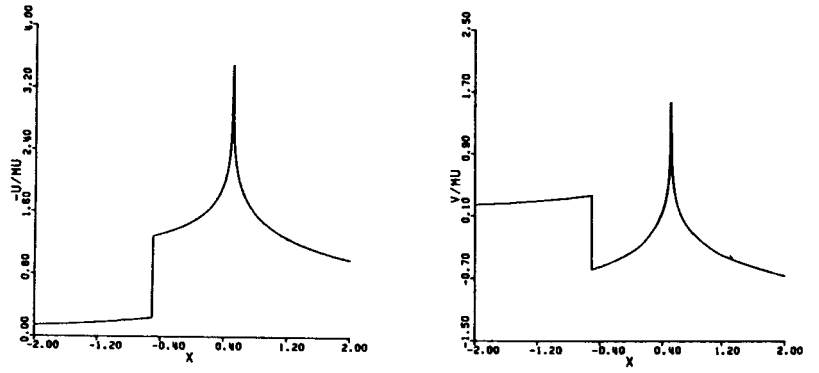

(*b*) $Y = t = \eta = 0.825$.

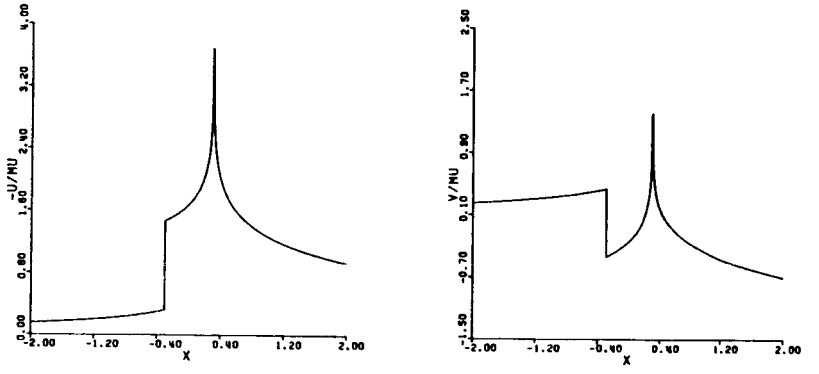

(*c*) $Y = t = \eta = 0.587$.

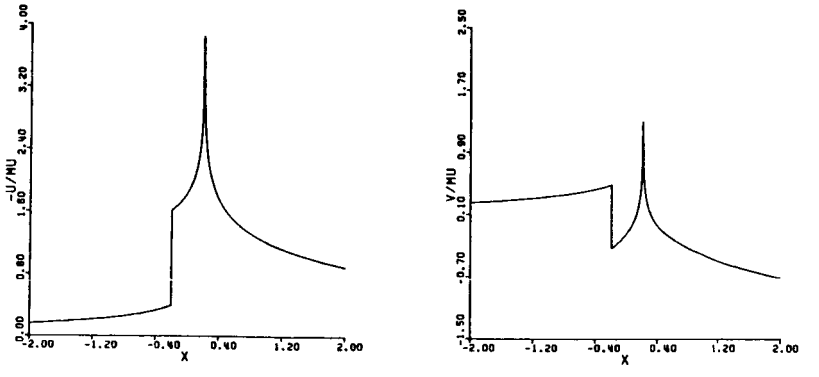

(*d*) $Y = t = \eta = 0.448$.

FIGURE 6 (continued).—Computer-drawn graphs of $f = \phi_\xi = U$ and $g = \phi_\eta = V$ for Tricomi's equation as functions of $X = s = \xi$ for $\delta = 5.000$.

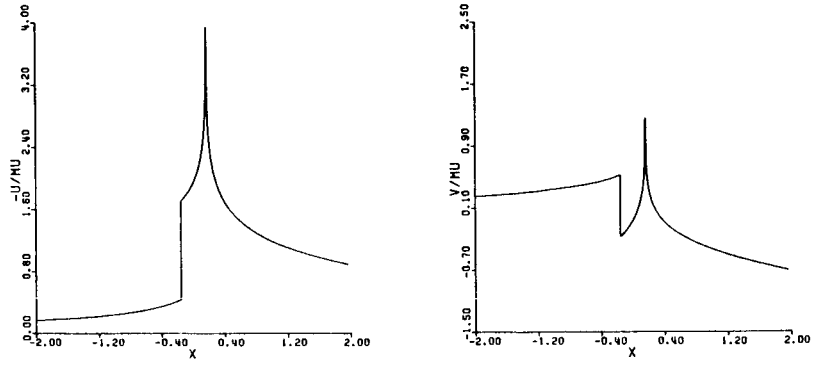

(*e*) $Y = t = \eta = 0.386$.

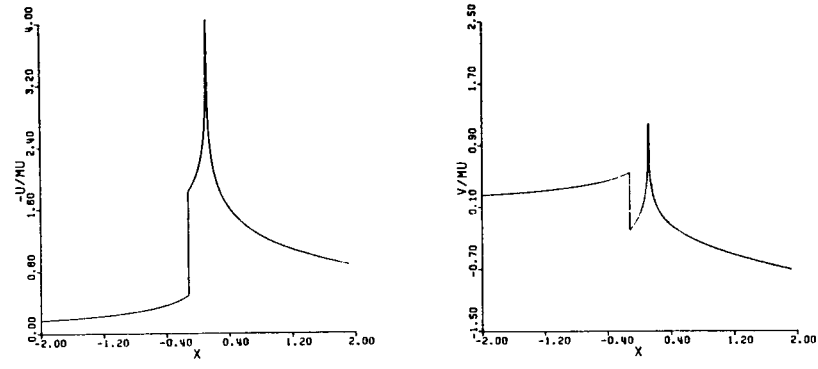

(*f*) $Y = t = \eta = 0.319$.

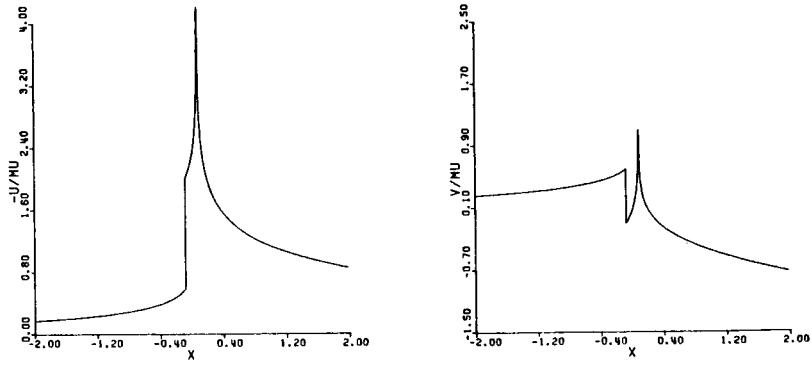

(*g*) $Y = t = \eta = 0.243$.

FIGURE 6 (continued). — Computer-drawn graphs of $f = \phi_\xi = U$ and $g = \phi_\eta = V$ for Tricomi's equation as functions of $X = s = \xi$ for $\delta = 5.000$.

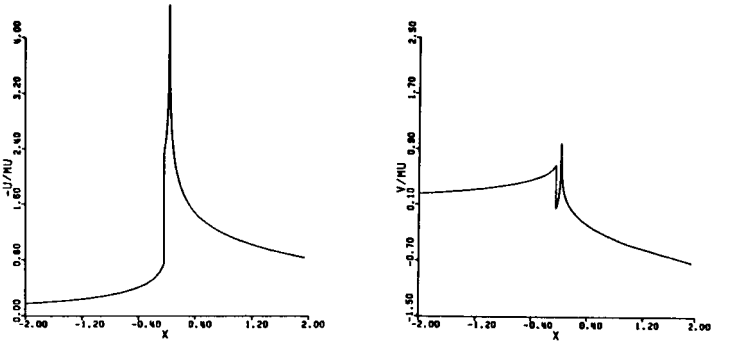

(*h*) $Y = t = \eta = 0.153$.

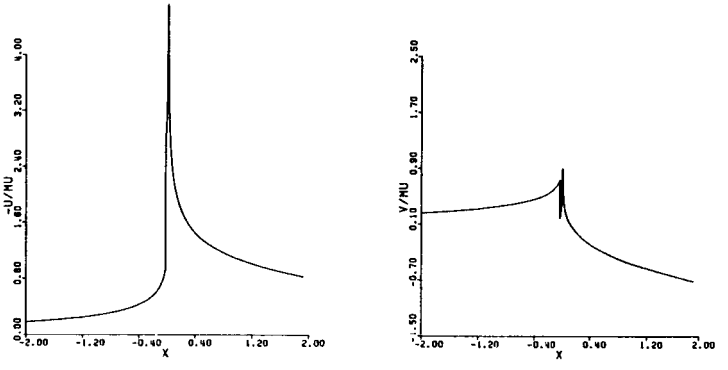

(*i*) $Y = t = \eta = 0.097$.

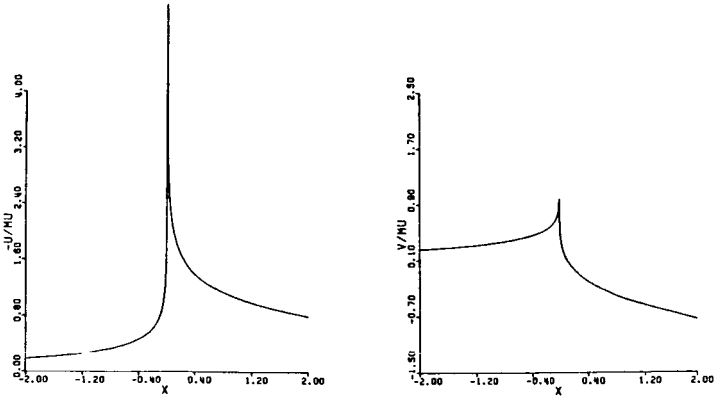

(*j*) $Y = t = \eta = 0.000$.

FIGURE 6 (continued).—Computer-drawn graphs of $f = \phi_\xi = U$ and $g = \phi_\eta = V$ for Tricomi's equation as functions of $X = s = \xi$ for $\delta = 5.000$.

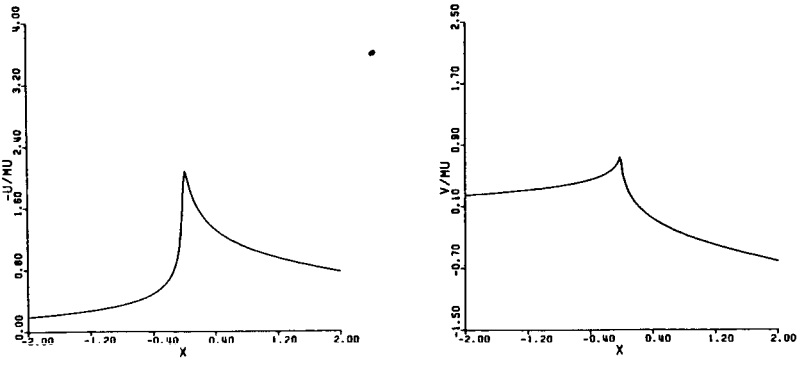

(*k*) $Y=t=\eta=-0.097$.

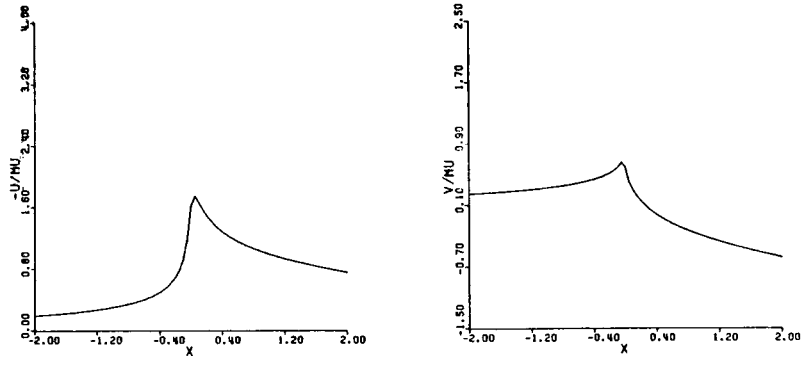

(*l*) $Y=t=\eta=-0.153$.

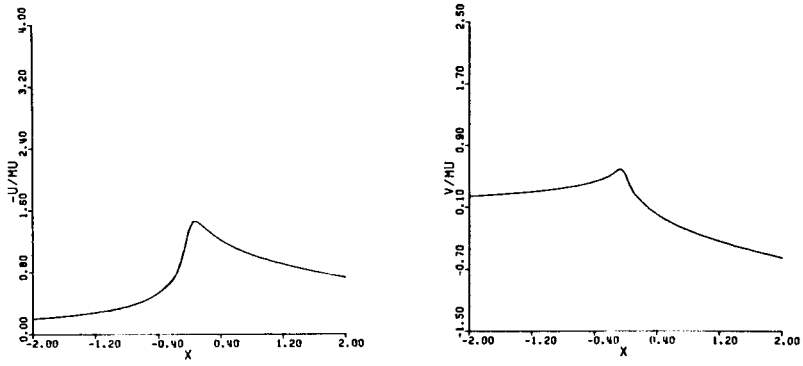

(*m*) $Y=t=\eta=-0.243$.

FIGURE 6 (continued).—Computer-drawn graphs of $f=\phi_\xi=U$ and $g=\phi_\eta=V$ for Tricomi's equation as functions of $X=s=\xi$ for $\delta=5.000$.

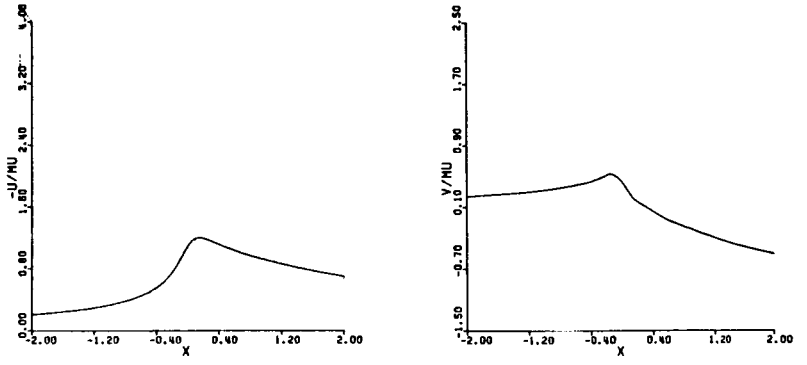

(*n*) $Y=t=\eta=-0.386$.

FIGURE 6 (concluded).—Computer-drawn graphs of $f=\phi_\xi=U$ and $g=\phi_\eta=V$ for Tricomi's equation as functions of $X=s=\xi$ for $\delta=5.000$.

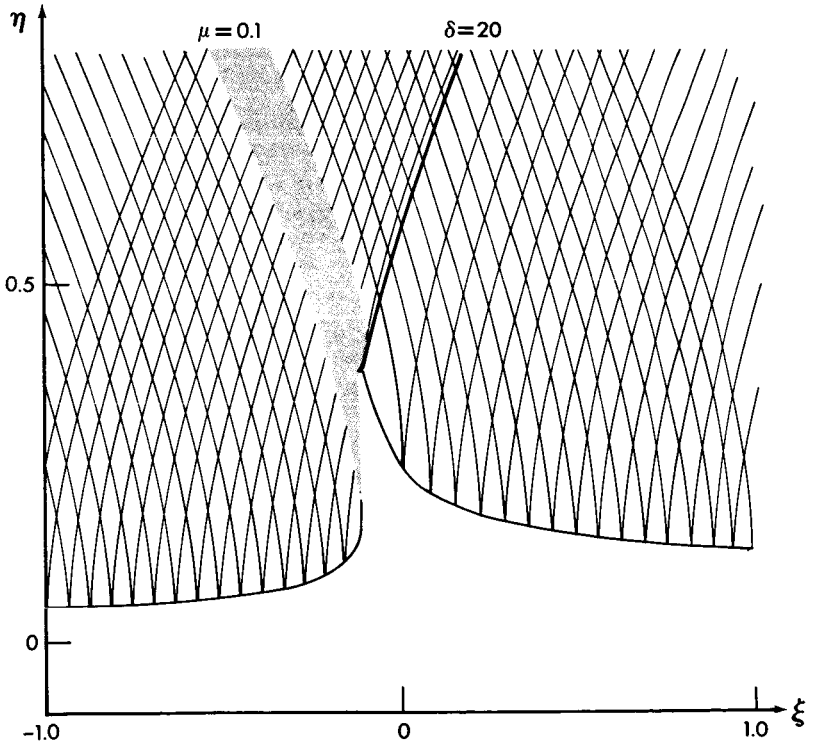

FIGURE 7.—Sonic line and characteristics for $\mu=0.10$ and $\delta=20.0$.

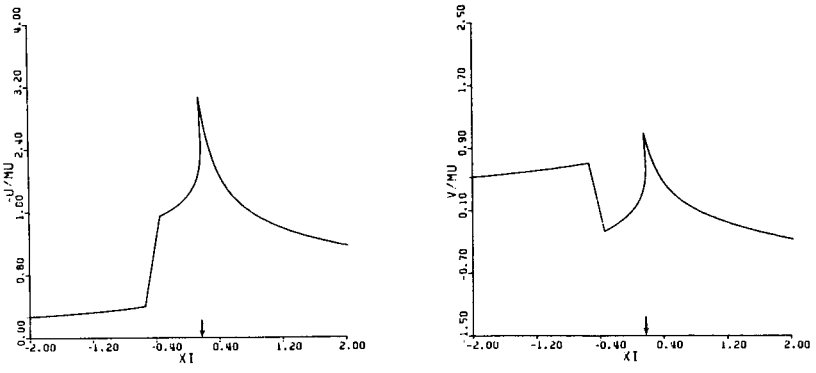

(*a*) $\eta = 0.825$.

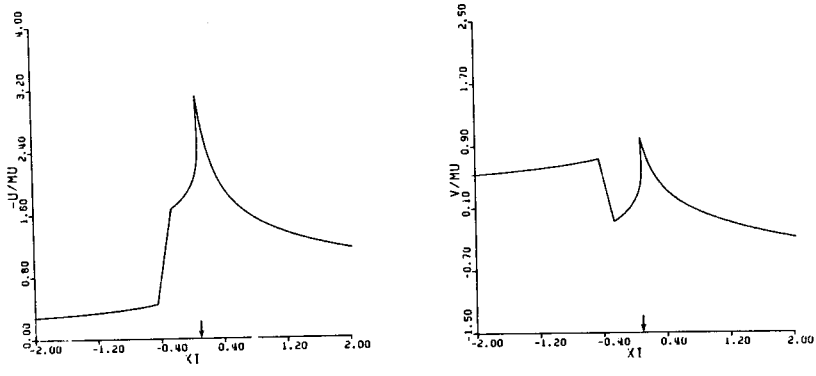

(*b*) $\eta = 0.711$.

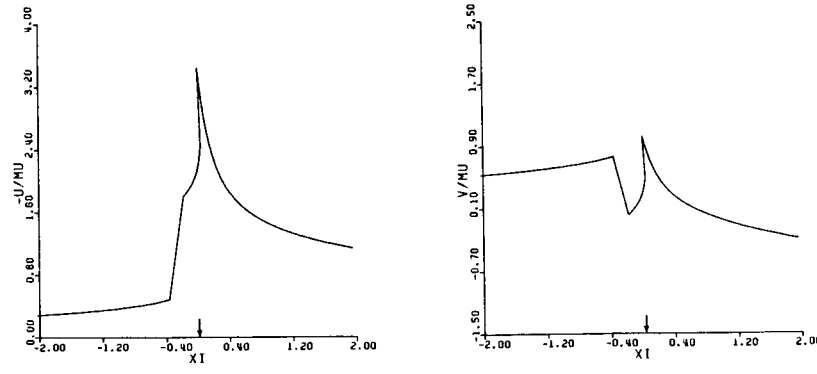

(*c*) $\eta = 0.613$.

FIGURE 8. – Computer-drawn graphs of $\phi_\xi = U$ and $\phi_\eta = V$ as functions of ξ for $\mu = 0.1000$ and $\delta = 20.000$.

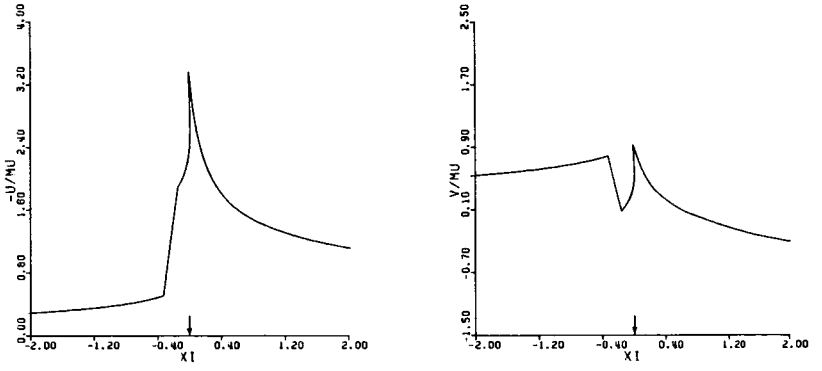

(*d*) $\eta = 0.561$.

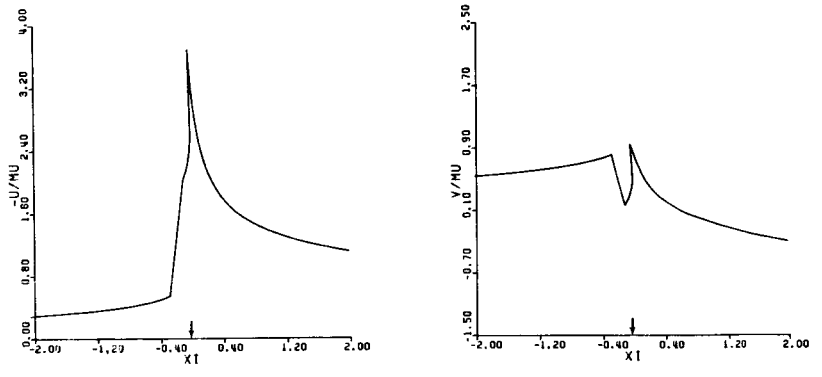

(*e*) $\eta = 0.506$.

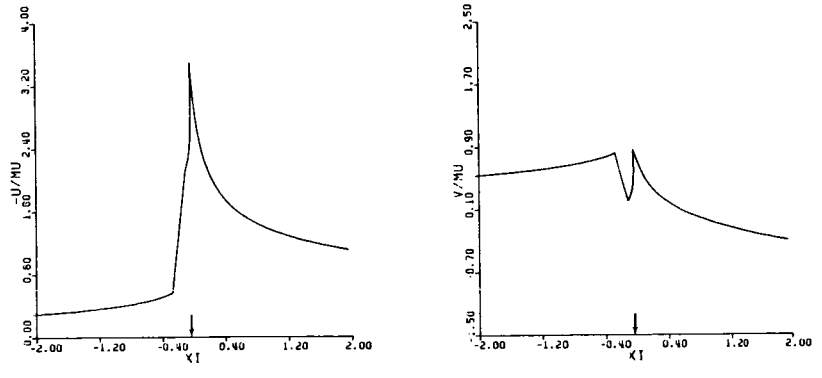

(*f*) $\eta = 0.478$.

FIGURE 8 (continued). — Computer-drawn graphs of $\phi_\xi = U$ and $\phi_\eta = V$ as functions of ξ for $\mu = 0.1000$ and $\delta = 20.000$.

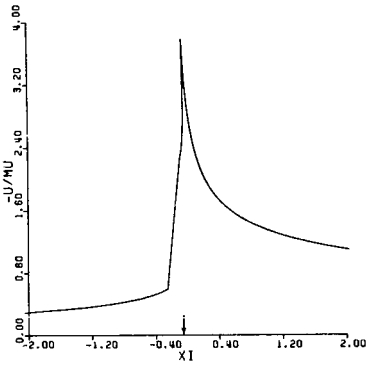

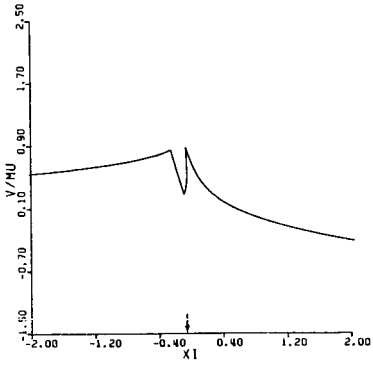

(g) $\eta = 0.448$.

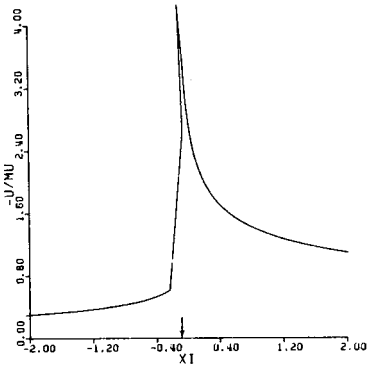

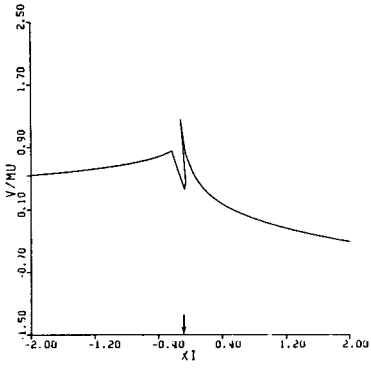

(h) $\eta = 0.418$.

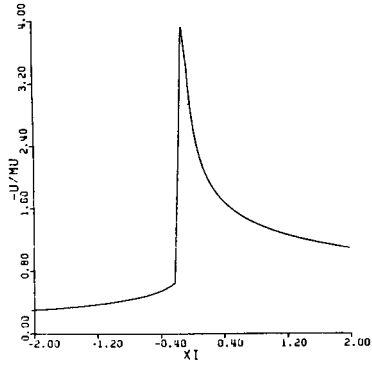

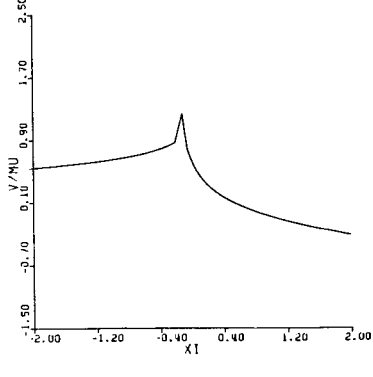

(i) $\eta = 0.386$.

FIGURE 8 (continued). — Computer-drawn graphs of $\phi_\xi = U$ and $\phi_\eta = V$ as functions of ξ for $\mu = 0.1000$ and $\delta = 20.000$.

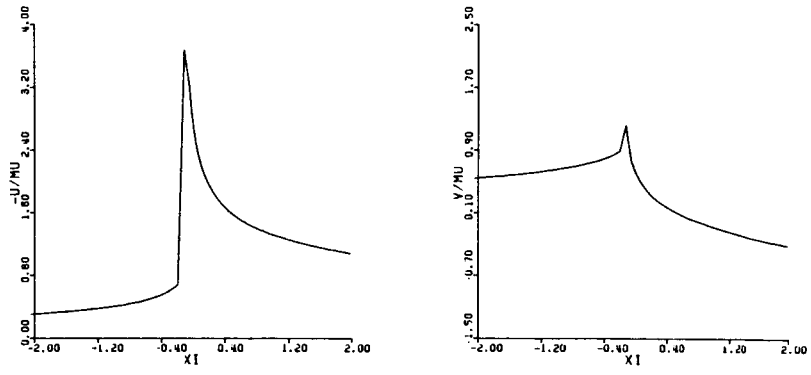

(*j*) $\eta = 0.353$.

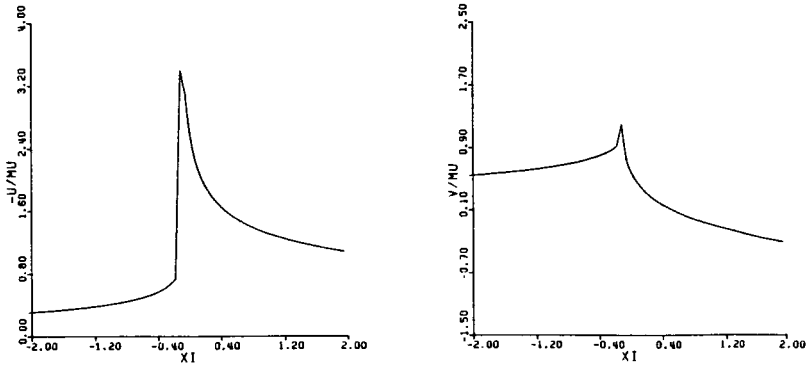

(*k*) $\eta = 0.319$

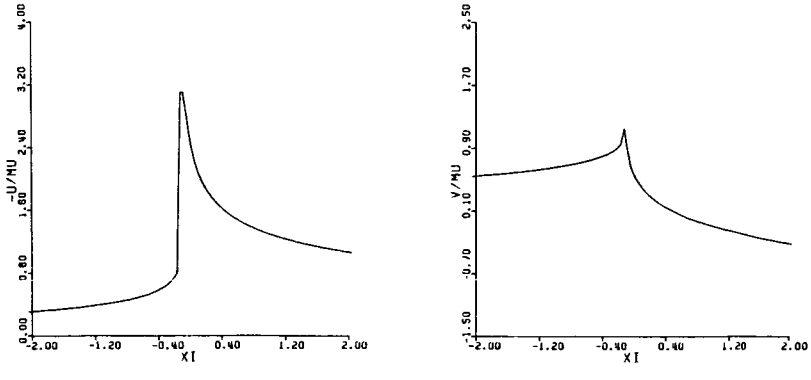

(*l*) $\eta = 0.282$.

FIGURE 8 (continued).—Computer-drawn graphs of $\phi_\xi = U$ and $\phi_\eta = V$ as functions of ξ for $\mu = 0.1000$ and $\delta = 20.000$.

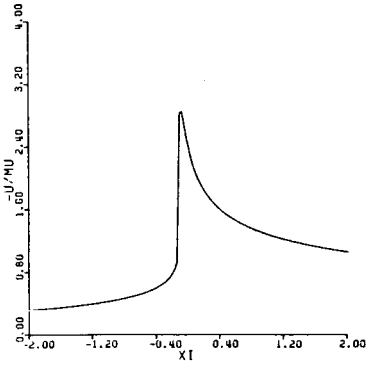

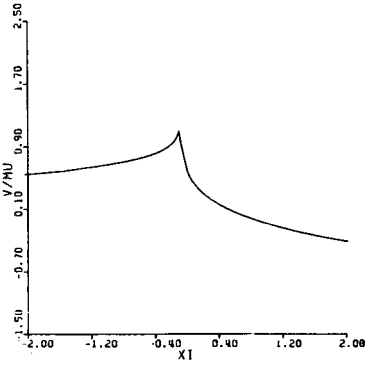

(m) $\eta = 0.243$.

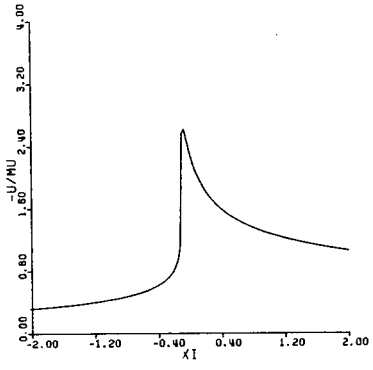

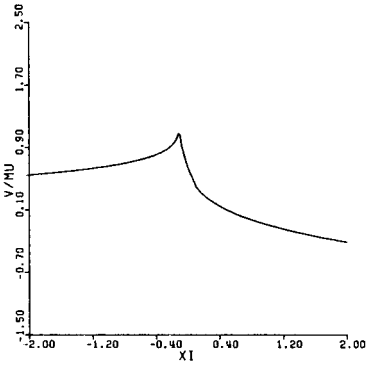

(n) $\eta = 0.201$.

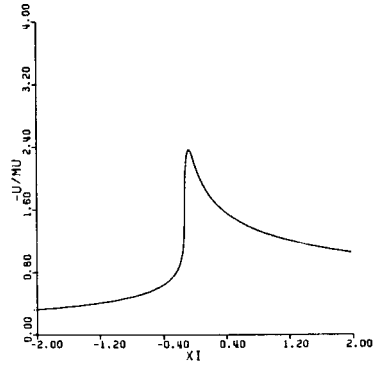

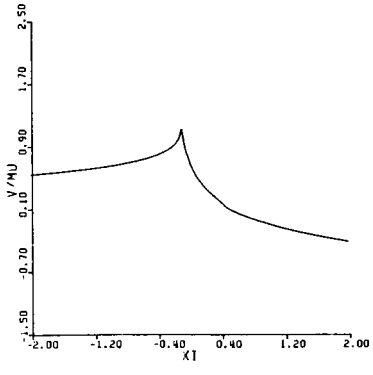

(o) $\eta = 0.153$.

FIGURE 8 (continued).—Computer-drawn graphs of $\phi_\xi = U$ and $\phi_\eta = V$ as functions of ξ for $\mu = 0.1000$ and $\delta = 20.000$.

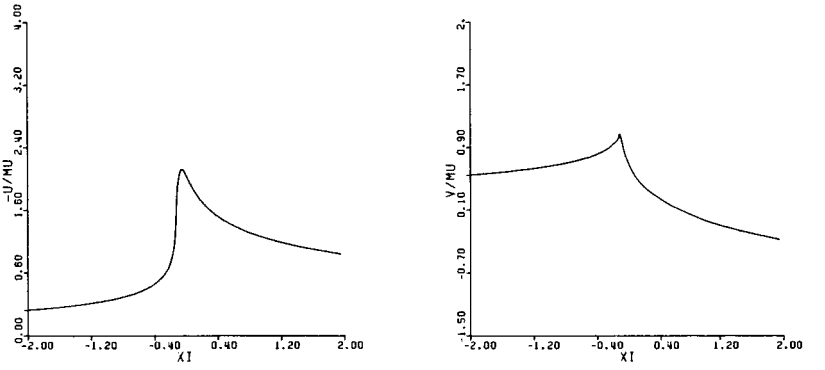

(*p*) $\eta = 0.097$.

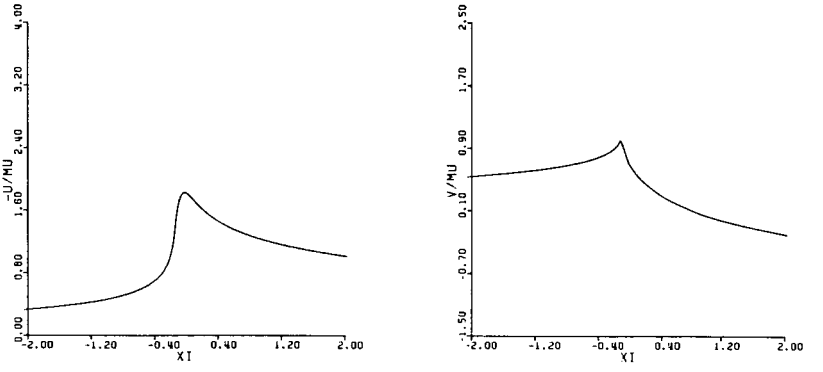

(*q*) $\eta = 0.000$.

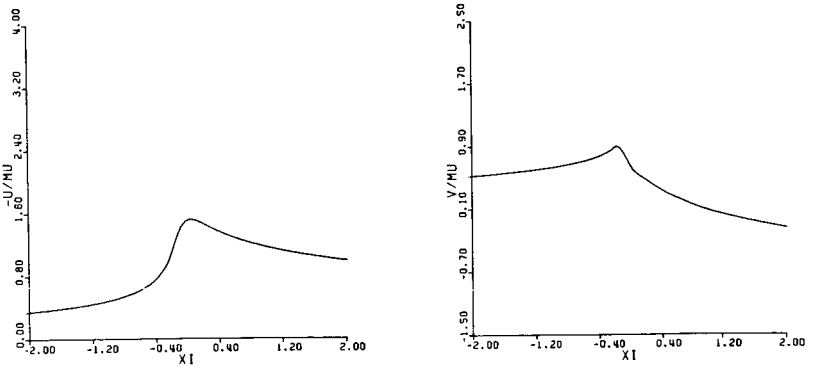

(*r*) $\eta = -0.153$.

FIGURE 8 (concluded).—Computer-drawn graphs of $\phi_\xi = U$ and $\phi_\eta = V$ as functions of ξ for $\mu = 0.1000$ and $\delta = 20.000$.

420-093 O - 71 - 9

ACKNOWLEDGMENTS

Much of the research was initiated while the author was a Faculty Associate of the Boeing Scientific Research Laboratories. The author is indebted to Dr. Arnold Goldburg for arranging his visit to BSRL. The artful programing that provided the numerical evaluation in the section with that title was the craftsmanship of Gordon Thomas. Finally, Dr. S. C. Crow and Dr. W. D. Hayes provided many instructive comments during this research. In particular, the author wishes to thank Dr. Crow for access to his solution to the linear problem in terms of integrals of the Bessel functions, which provided a useful check of equation (12), and Dr. Hayes for suggesting a less cumbersome interpretation of the transformation discussed here.

APPENDIX

For the incoming signal equation (16), equation (14) gives

$$\alpha(\omega) = -\frac{\mu|\omega|^{1/6}(1 - i\ \mathrm{sgn}\ \omega)(e^{i\omega\delta} - 1)}{i\omega}$$

When this result is substituted into equation (13), the quadratures can, with perseverance, be carried through. The simplest result is for ϕ; however, our procedure utilizes the derivatives $f = \phi_\xi$ and $g = \phi_n$; we give both below:

For $t > 0$:

$$\begin{aligned} f &= -\mu t^{-1/4}[U(Z) - U(Z')] \\ g &= \mu t^{1/4}[V(Z) - V(Z')] \end{aligned} \tag{A-1}$$

For $t = 0$:

$$f = \frac{\mu}{\sqrt{\pi}} \frac{3^{-2/3}}{2} \frac{\Gamma(1/6)}{\Gamma(2/3)} \{(\sqrt{3} + 1)(|s - \delta|^{-1/6} - |s|^{-1/6}) + (\sqrt{3} - 1) \cdot [\mathrm{sgn}\ (s - \delta)|s - \delta|^{-1/6} - \mathrm{sgn}\ s|s|^{-1/6}]\} \tag{A-2}$$

$$g = \frac{\mu}{\sqrt{\pi}} 3^{2/3} \frac{\Gamma(5/6)}{\Gamma(1/3)} \{(\sqrt{3} + 1)(|s - \delta|^{1/6} - |s|^{1/6}) + (\sqrt{3} - 1) \cdot [\mathrm{sgn}(s - \delta)|s - \delta|^{1/6} - \mathrm{sgn}\ s|s|^{1/6}]\}$$

For $t < 0$:

$$\begin{aligned} f &= -\mu(-t)^{-1/4}[R(Z) - R(Z')] \\ g &= \mu(-t)^{1/4}[S(Z) - S(Z')] \end{aligned} \tag{A-3}$$

Here $Z = 3s/2|t^{3/2}|$ and $Z' = 3(s-\delta)/2|t^{3/2}|$ and the functions U, V, R and S are given in equations (A-4) through (A-7) for $Z < 1$. For brevity, we omit the appropriate continuations for $Z > 1$.

$$U(Z) = (2\pi)^{-1/2}\left[\frac{\Gamma(5/12)}{\Gamma(11/12)}(\sqrt{3}+1)F(1/12, 5/12; 1/2; Z^2) + 2Z\frac{\Gamma(11/12)}{\Gamma(5/12)}(\sqrt{3}-1)F(7/12, 11/12; 3/2; Z^2)\right] \quad \text{(A-4)}$$

$$V(Z) = (2/\pi)^{1/2}(\sqrt{3}-1)\frac{\Gamma(11/12)}{\Gamma(5/12)}\left[Z^2F(7/12, 11/12; 3/2; Z^2) - 6F(-5/12, -1/12; 1/2; Z^2) + \frac{6\sqrt{\pi}}{\Gamma(11/12)\Gamma(7/12)} + \frac{\Gamma(13/12)\Gamma(5/12)}{\Gamma(7/12)\Gamma(11/12)}ZF(5/12, 13/12; 3/2; Z^2)\right] \quad \text{(A-5)}$$

$$R(Z) = (2\pi)^{-3/2}\{\Gamma(5/12)\Gamma(1/12)F(1/12, 5/12; 1/2; -Z^2) + 8\pi^2[\Gamma(5/12)\Gamma(1/12)]^{-1}ZF(7/12, 11/12; 3/2; -Z^2)\} \quad \text{(A-6)}$$

$$S(Z) = -\pi^{-1}(2\pi)^{-1/2}\{\Gamma(7/12)\Gamma(11/12)[Z^2F(7/12, 11/12; 3/2; -Z^2) + 6F(-5/12, -1/12; 1/2; -Z^2)] + \Gamma(13/12)\Gamma(5/12)ZF(5/12, 13/12; 3/2; -Z^2)\} \quad \text{(A-7)}$$

REFERENCES

1. HAYES, W. D.; HAEFELI, R. C.; AND KULSRUD, H. E.: Sonic Boom Propagation in a Stratified Atmosphere with Computer Program. NASA CR-1299, 1969. Also HAYES, W. D.; AND HAEFELI, R. C.: The ARAP Sonic Boom Computer Program. Second Conference on Sonic Boom Research, NASA SP-180, 1968, pp. 151-158.
2. RANDALL, D. G.: Sonic Bang Intensities in a Stratified Still Atmosphere. TR 66002, Royal Aircraft Establishment, 1966.
3. FRIEDRICHS, K. L.: Formation and Decay of Shock Waves. Commun. Pure Appl. Math., vol. 1, 1948, pp. 211-245.
4. HAYES, W. D.: Linearized Supersonic Flow, Ph. D. Thesis, Cal. Inst. Tech., 1947. Also available as AMS Rept. 052, Princeton Univ.
5. HAYES, W. D.: Pseudotransonic Similitude and First-Order Wave Structure. J. Aeronaut. Sci., vol. 21, 1954, pp. 721-730.
6. LANDAU, L. D.: On Shock Waves at Large Distances From the Place of Their Origin. Prik. Mat. Mekh., vol. 9, 1945, pp. 286-292. Also J. Phys., Academy of Sciences USSR, vol. 6, 1942, p. 242.
7. WHITHAM, G. B.: The Behavior of Supersonic Flow Past a Body of Revolution Far From the Axis. Proc. Roy. Soc., Ser. A, vol. 201, 1950, pp. 89-109.
8. WHITHAM, G. B.: On the Propagation of Weak Shock Waves. J. Fluid Mech., vol. 1, 1956, pp. 290-318.
9. LOMAX, H.: The Wave Drag of Arbitrary Configurations in Linearized Flows as Determined by Areas and Forces in Oblique Planes. NACA RM A55A18, 1955.
10. CARLSON, H. W.: Correlation of Sonic Boom Theory With Wind Tunnel and Flight Measurements. NASA TR R-213, 1964.

11. MAGLIERI, D. J.: Sonic Boom Flight Research—Some Effects of Airplane Operations and the Atmosphere on Sonic Boom Signatures. Sonic Boom Research, NASA SP-147, 1967, pp. 25-49.
12. SEEBASS, R.: Sonic Boom Theory. J. Aircr., vol. 6, 1969, pp. 127-184.
13. HAEFELI, R. C.: Sonic Boom Propagation From Maneuvering Aircraft. AIAA Paper no. 69-1134, Oct. 20-24, 1969.
14. GUIRAUD, J. P.: Acoustique Géométrique, Bruit Ballistique des Avions Supersonic et Focalisation. J. Méc., vol. 4, 1965, pp. 215-267.
15. HAYES, W. D.: Similarity Rules for Nonlinear Acoustic Propagation Through a Caustic. Second Conference on Sonic Boom Research, NASA SP-180, 1969, pp. 165-171.
16. LIGHTHILL, M. J.: Reflection at a Laminar Boundary Layer of a Weak Steady Disturbance due to a Supersonic Stream, Neglecting Viscosity and Heat Conduction. Quart. J. Mech. Appl. Math., vol. 3, 1950, pp. 303-325.
17. DEMAISTRE, A.; THERY, C.; VALLÉE, J.; VIVIEV, C.; AND WANNER, J.-C.: Bang Sonique, Théorie et Experimentation du Phénomène de Focalisation. Paper presented at the 1969 meeting of Assoc. Techn. Maritime Aéronaut.
18. VALLÉE, J.: Operation Jericho-Virage. Rapport d'Etude no. 277, Centre d'Essais en Vol Annexe d'Istres, 1969.
19. THERY, C.: Refraction Atmospherique et Reflexion en Sol des Bangs. Aircraft Noise and the Sonic Boom, AGARD Conf. Proc., May 1969.
20. GERMAIN, P.; AND BADER, R.: Sur Quelques Problems Relatifs a l'Equation de Type Mixte de Tricomi. Off. Nat. Etud. Rech. Aeronaut. Publ. 54, 1952.
21. ABRAMOWITZ, M.; AND STEGAN, I. A., EDS.: Handbook of Mathematical Functions. Nat. Bur. Stand. Applied Math. Ser. 55, 1964.

II

PREDICTION OF SONIC BOOM GENERATION AND PROPAGATION—THEORY AND EXPERIMENT

Chairman: I. E. GARRICK

Uniform Approximations for Shocks Generated by Thin Nonlifting Rectangular Wings

M. B. FRIEDMAN
Columbia University
AND
S. DAVIS
NASA Ames Research Center

The works of Lighthill and Whitham provide a methodology for developing uniform approximations for the flow fields and shocks encountered in a number of aerodynamic problems. These have been primarily problems in which variations in flow quantities are most significant in one direction only. However, realistic aerodynamic configurations generate flows in which variations can be of equal importance in more than one direction in some locations. The geometry of the configuration, the history of the motion, and the properties of the medium can all contribute to produce such situations. A study was initiated to assess the influence of these factors on the validity and feasibility of the methods and the consequences to the computed flows.

One phase of this study described in this paper (see ref. 1 for more details) dealt with the determination of the shock produced by the leading edge of an almost planar thin wing of rectangular planform and symmetrical airfoil section at zero angle of attack. This thickness problem was investigated for wings moving at a steady supersonic speed through uniform, unbounded atmosphere. The presence of sharp corners in the planform and the finite span produce diffractionlike effects from the wingtips and an asymmetrical disturbance field with regions of rapid variation in more than one direction at several locations.

The commonly employed methods for calculating sonic boom overpressures for arbitrary configurations assume that the flow field is, to a sufficiently accurate approximation, described by means of a family of F-functions appropriate to the configuration. However, this notion (equivalent body method) is dependent upon the flow "propagating" approximately as families of cylindrical waves. But this is not the case in the vicinity of a rectangular wing. The flow behaves like planar waves in some regions and like cylindrical waves in other regions, and contains transition regions in which the flow does neither. Thus the quasi-cylin-

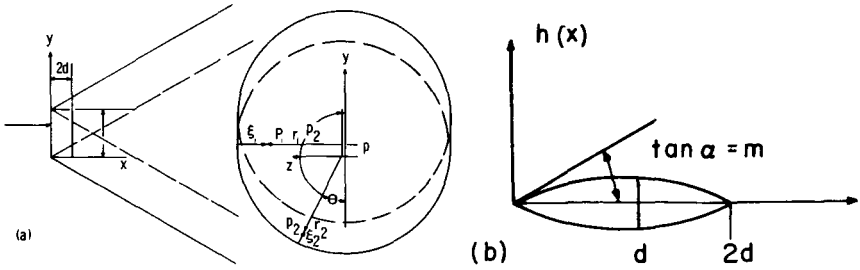

FIGURE 1.—The rectangular wing. (*a*) Wing planform, wave geometry, and ray geometry. (*b*) Detail of airfoil section.

drical approach utilizing the F-function must be replaced by a full three-dimensional approach. At sufficiently large distances, of course, it is to be expected that the flow is approximately cylindrical in nature. But because the behavior of the shock is dependent upon the history of the linear solution, the shock will be incorrectly described by the F-function procedure for some distance out from the wing.

METHOD OF ANALYSIS

In principle, the full linear solution might be employed because it can be expressed in closed form for the case of the rectangular nonlifting wing. But this would necessitate an almost wholly numerical treatment, if at all feasible, in which it would be difficult to assess the essential features of interest, and which is likely to be even less feasible for more general configurations. Consequently, it is preferable to proceed by ray tube analysis by a uniformly valid asymptotic approximation to the linear solution in the neighborhood of its wavefronts that would replace the nonuniform cylindrical F-function approximation. For the rectangular wing, a uniform approximation in the ray form can be derived readily.[1] Figure 1 illustrates the geometry of the wing and the wavefronts of linear theory.

The perturbation potential for the nonlifting rectangular wing in a free stream of Mach number M is given by

$$\varphi(x, y, z) = -\frac{V}{\pi} \int\int_{A} \frac{m(1 - x_1/d)\, dx_1 dy_1}{\sqrt{(x - x_1)^2 - \beta^2 (y - y_1)^2 - \beta^2 z^2}}$$

where $m(1 - x_1/d)$ represents the slope distribution in the streamwise direction of the parabolic airfoil, V is the free-stream velocity, and A is the area in the plane of the wing intercepted by the Mach fore cone from the field point (x, y, z).

[1] A more formal development by M. K. Myers valid for general configurations may be found on p. 75.

A set of ray coordinates associated with the plane front can be introduced for $z > 0$ and $0 < y < l$:

$$x = \xi_1 + \beta r_1$$
$$y = p_1$$
$$z = r_1$$

where ξ_1 is the phase variable, r_1 is distance along a ray, and p_1 identifies the ray. A set of ray coordinates associated with the tip cones ($z > 0$, $y < 0$; $z > 0$, $y < l$) is

$$x = \xi_2 + \beta r_2$$
$$y = r_2 \cos p_2$$
$$z = r_2 \sin p_2$$

Near the plane front (ξ_1/r_1 small), the potential may be approximated uniformly by

$$\varphi \sim -\frac{V}{\pi} \int\int_{A_1} \frac{m(1 - x_1/d)\, dx_1\, dy_1}{\sqrt{2\beta r_1(\xi_1 - x_1) - \beta^2 (p_1 - y_1)^2}}$$

where A_1 represents the area in the plane of the wing bounded by $2\beta r_1(\xi_1 - x_1) - \beta^2(-p_1 - y_1)^2 = 0$. Near the tip cones ($\xi_2/r_2$ small), the potential may be approximated uniformly by

$$\varphi \sim -\frac{V}{\pi} \int\int_{A_2} \frac{m(1 - x_1/d)\, dx_1 dy_1}{\sqrt{2\beta r_2(\xi_2 - x_1 + \beta y_1 \cos p_2 - \beta^2 y_1^2}}$$

where A_2 represents the area in the plane of the wing bounded by $2\beta r_2(\xi_2 - x_1 + \beta y_1 \cos p_2) - \beta^2 y_1^2 = 0$.

In these approximations, the intersection of the plane of the wing and the Mach fore cone is represented by a parabola instead of a hyperbola. If the quadratic terms were completely neglected, the intersection would be approximated by a straight line parallel to the leading edge and would yield the corresponding F-function. The uniform asymptotic representation does not occur in the geometric acoustics form of the product of an amplitude function and a phase function. The distortion of the waveform as it propagates along a ray tube because of interactions between neighboring tubes is neglected in the geometric acoustics approximation. This interaction is particularly important in the neighborhood of the wingtips. However, for $r_{1,2}$ sufficiently large, the uniform representation does approach the equivalent body approximation. But the construction of the shock is dependent upon the history of the linear solution in the neighborhood of its fronts, and the cutting plane approximation will describe the shock incorrectly for some distance out from the wing.

The axial perturbation velocity is the quantity of interest and may be obtained from the potential:

I: $z>0$, $0<y<l$:

$$\frac{u}{V}\sim-\frac{m}{\pi\beta}\left[(1-\xi_1/d)(\pi-\tan^{-1}A_0-\tan^{-1}A_l)-\beta\frac{p_1^2A_0}{2r_1d}-\beta\frac{(l-p_1)^2}{2r_1d}A_l\right] \tag{1}$$

where

$$A_0=\mathrm{Re}\left[\frac{2\xi_1r_1}{\beta p_1^2}-1\right]^{1/2}$$

$$A_l=\mathrm{Re}\left[\frac{2\xi_1r_1}{\beta(l-p_1)^2}-1\right]^{1/2}$$

II: $z>0$, $y<0$ (case $y>l$ follows from symmetry):

$$\frac{u}{V}\sim-\frac{m}{\pi\beta}\left[\left(1-\frac{\xi_2}{d}-\frac{\beta r_2\cos^2\theta}{2d}\right)(\tan^{-1}B_0-\tan^{-1}B_l)+\frac{\beta r_2\cos^2\theta B_0}{2d}-\frac{\beta(r_2\cos\theta+l)^2}{2r_2d}B_l\right]$$

where

$$B_0=\mathrm{Re}\left[\frac{2\xi_2}{\beta r_2\cos^2\theta}\right]^{1/2}$$

$$B_l=\mathrm{Re}\left[\frac{2\xi_2r_2/\beta-2r_2l\cos\theta-l^2}{(r_2\cos\theta+l)^2}\right]^{1/2}$$

and $\theta=\pi-p_2$.

To account uniformly to a first approximation for the nonlinear effects, in each ray tube the bicharacteristics of linear theory are replaced by the following approximation to the bicharacteristics of nonlinear theory:

$$\frac{dx}{dr_i}=\beta+\frac{(\alpha+1)M^4}{2\beta^2}\frac{u}{V}(\xi_i,\ r_i,\ p_i)-M^2\left\{\beta\frac{u}{V}+\frac{u_{r_i}}{V}\right\}+O\left(\frac{u^2}{V^2}\right) \tag{2}$$

where u_{r_i} is the perturbation velocity in the r_i direction, and the quantity $\beta(u/V)+u_{r_i}/V$ depends on the curvature of the bicharacteristics and is small compared to u. Thus the corrected characteristics may be approximated by

$$x=\beta r_i-G(\xi_i,\ r_i,\ p_i)+\xi_i$$

where

$$G=-\frac{(\alpha+1)M^4}{2\beta^2}\int_0^{r_i}\frac{u}{V}(\xi_i,\ t,\ p_i)dt$$

Equations (1) and (2) represent the uniform first approximation to the velocity field. To complete the solution, a shock must be inserted to separate the regions of disturbed and undisturbed flow and eliminate the regions of multivaluedness implied by equations (1) and (2). The shock is positioned according to the bisection rule that the direction of the shock wave to a first approximation bisects the characteristic directions that meet at a point. In the undisturbed flow, the characteristic direction is the free-stream Mach direction β. In the disturbed flow, the appropriate characteristic depends upon the region. In the region ahead of the corrected tip cone characteristics, the family of corrected planar characteristics are employed, while in the influence domain of the corrected tip cone, the trace of the corrected tip cone characteristic is used. Each family may be expressed as $\xi_0=\xi_i-f(r_i)$, where ξ_0 is the family to be used in the bisection rule with $f(r_1)=0$, $\xi_0=\xi_1$ for one family, and $f(r_2)=\beta(l/2)^2/2r_2$, $\xi_0=\xi_2-f(r_2)$ for the other.

If the position of the shock is expressed as

$$x_{sh}=\beta r_i-H(r_i)$$

then by the bisection rule

$$\frac{dx_{sh}}{dr_i}=\beta-\frac{dH}{dr_i}=\beta-\frac{1}{2}\frac{\partial G}{\partial r_i}+\frac{1}{2}\frac{\partial f}{\partial r_i}$$

so that

$$\frac{dH}{dr_i}=\frac{1}{2}\frac{\partial G}{\partial r_i}-\frac{1}{2}\frac{\partial f}{dr_i} \tag{3}$$

and

$$h=G-\xi_0-f \tag{4}$$

Equations (3) and (4) can be integrated numerically as a pair of equations for the functions $H(r_i)$ and $\xi(r_i)$ for several values of p_i. Initial values for the shock in the plane region are given by the wedge solution and are provided by the conical solution for $r_2\to 0$ for the tip cone.

RESULTS

Computations were carried out for $M=1.4$, $m=0.125$, and several aspect ratios and are summarized in figures 2 to 4. Figure 4 shows how the far-field predictions of the shock strength based on the uniform approximation compare with those based upon the equivalent body approximation. Directly below and to the side of the wing, the two predictions agree. In the former region, the tip cone interactions occur at relatively small values of r/d and the flow is approximately cylindrical for larger values of r/d. Directly to the side, the flow is approximately cylindrical for all values of r/d.

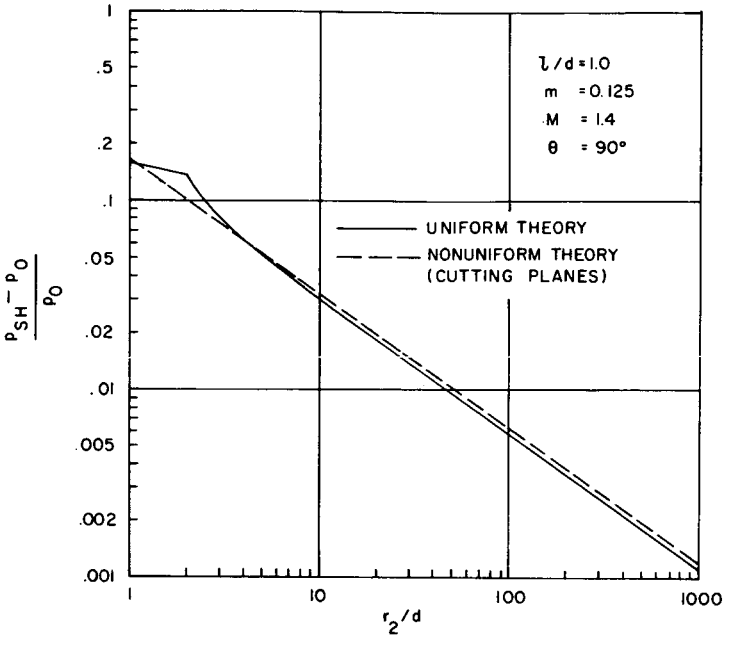

FIGURE 2.—Shock wave overpressure for $l/d = 1$ and $\theta = 90°$.

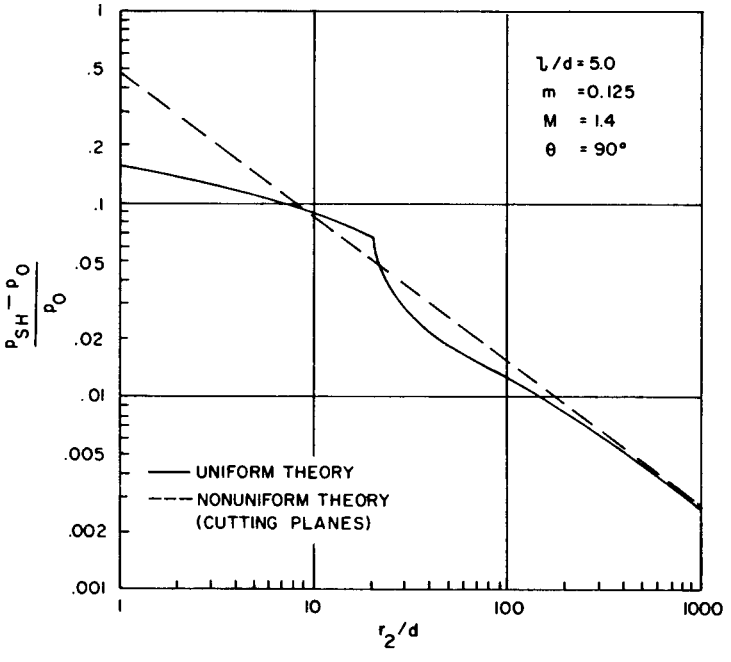

FIGURE 3.—Shock wave overpressure for $l/d = 5$ and $\theta = 90°$.

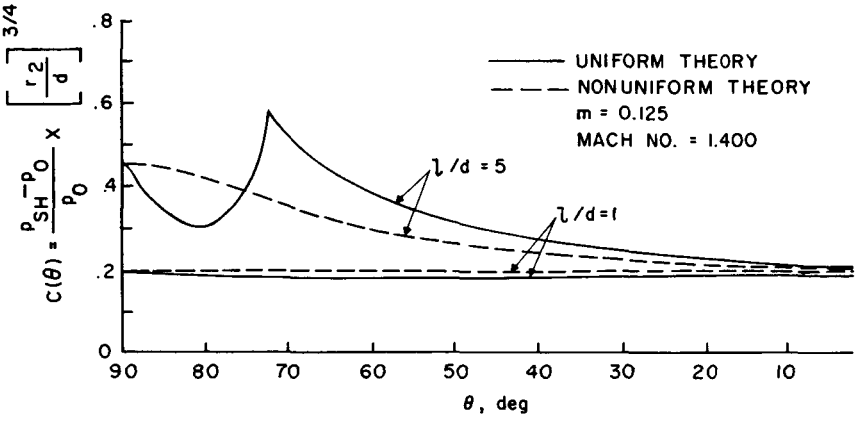

FIGURE 4. — Asymptotic far-field distribution of the shock wave overpressure.

On the other hand, in various meridional planes, the predictions may differ by as much as a factor of 2 for the larger aspect ratio wings, although both methods predict the 3/4-power-law decay. The nonuniform approximation always results in a monotone meridional distribution with a maximum occurring directly below the wing. However, for the larger aspect ratio wings, the uniform approximation shows a meridional distribution with both a maximum and a minimum occurring in some other meridional plane. This asymmetry tends to disappear as the aspect ratio decreases.

In the near-field region directly below the wing where the plane shock dominates, the two predictions differ for the larger aspect ratio as indicated in figure 4. However, for l/d on the order of unity, the equivalent body approximation is valid within a few chord lengths since the extent of the two-dimensional region is limited to small values of r/d. This is in agreement with some of the experimental results of reference 2.

The magnitude of the difference between the two predictions is dependent upon the scale distance r/d at which the near-field effects have tended to disappear because of the tip cone interactions; the larger the aspect ratio, the larger the value of r/d at which this occurs. This indicates that care must be taken in extrapolating experimental data by the equivalent body method. For if the measurements come from the near-field region, the extrapolation will be inaccurate. These conclusions appear to be in agreement with experimental results obtained by S. Davis.[2] The experimental results described in reference 3 suggest that for more complex configurations with sweepback and lift taken into account, the inaccuracies of the F-function approximation may be even more pronounced.

[2] See p. 133.

MATHEMATICAL FORMALISM

Although the experiments cited tend to confirm some features of the analysis, it may be of value to examine the work in the context of a more formal mathematical development. Such an approach is presently being explored for the case of the rectangular wing to assess the limitations of ray tube analysis. It is based on the notion that the techniques of Lighthill and Whitham imply that in problems of the kind being considered, there may exist coordinate systems in which uniformly valid approximations can be obtained directly by a formal perturbation procedure in which the successive perturbation solutions remain small everywhere. The corresponding first-order solution should coincide with linear theory in the transformed coordinates. The essence of the development can be seen in the case of the body of revolution, which is so well understood from the work of Whitham.

Consider the equations of motion appropriate for the body of revolution in a coordinate system in which the linear phase $x - \beta r$ is taken as the coordinate A and $\beta r = \rho$:

$$\frac{a_0^2}{V}\left[v_\rho + \frac{v}{\rho} - \beta u_\rho\right] + [-(\alpha+1)u - (\alpha-1)\beta u + 2\beta v + O(u^2, v^2)]u_A$$
$$+ [(\alpha-1)\beta^2 u + 2\beta v + (u^2, v^2)]u_\rho + [-(\alpha-1)\beta u + O(u^2, v^2)]v_\rho$$
$$+ [-(\alpha+1)\beta u + O(u^2, v^2)]\frac{v}{\rho} = 0 \qquad (5)$$

$$-\beta u_A + \beta u_\rho - v_A = 0 \qquad (6)$$

The classical perturbation series

$$u = \epsilon^2 u^{(2)}(A, \rho) + \epsilon^4 u^{(4)}(A, \rho) + \cdots$$
$$v = \epsilon^2 v^{(2)}(A, \rho) + \epsilon^4 v^{(4)}(A, \rho) + \cdots \qquad (7)$$

produces the well-known result that $u^{(2)}$ and $v^{(2)}$ represent linear theory and have singular derivatives at the Mach cone $A = 0$, while the higher approximations themselves diverge. The propagation of singularities into the higher orders is typical of nonuniform expansions. The nonuniformity of the perturbation series is evidenced more directly by an attempt to construct a wavefront expansion (of the geometric acoustics type) in fractional powers of A/ρ for the equations of motion. The result is a formal series

$$u = \sum_{n=1}^{\infty} a_n (A/\rho)^{1-n/2}$$

$$v = \sum_{n=1}^{\infty} b_n (A/\rho)^{1-n/2}$$

that diverges in the vicinity of $A=0$. However, an expansion of the geometric acoustics type is valid for linear theory despite the singular derivatives in the first approximation because derivatives with respect to A appear in such a way that there is no propagation into the higher approximations and the singularity is fully described by the leading term. This suggests that for the nonlinear equations, a new independent variable be introduced (corresponding to the phase of linear theory) which is a priori unknown. It is to be chosen so that equation (5) is independent of derivatives with respect to this variable, which should insure no propagation of a singularity. If the variable is denoted by $S(A,\rho)$, the equations of motion become (with $R=\rho$)

$$\begin{aligned}(a-\beta\lambda)u_R+bv_R+c\frac{v}{R}&=0\\ \beta u_S+v_S-\beta u_R+\lambda u_S-\beta u_R\int\lambda_S\,dR&=0\end{aligned}\tag{8}$$

provided $S(A,\rho)$ satisfies the first-order differential equation, which is precisely the condition that S be a characteristic surface of the equations of motion:

$$\begin{aligned}&\left[-(\alpha+1)\frac{u}{\beta}-(\alpha-1)\beta u+2v+(u^2,v^2)\right]\\ &\quad+2\left[-\beta\frac{a_0^2}{V}+(\alpha-1)\beta u-v+O(u^2,v^2)\right](S_\rho/S_A)\\ &\quad+\left[\beta\frac{a_0^2}{V}-(\alpha-1)\beta u+O(u^2,v^2)\right](S_\rho/S_A)^2=0\end{aligned}\tag{9}$$

It follows that

$$\lambda(u,v)=-(S_\rho/S_A)$$

is a root of the quadratic equation implied by equation (9). Consequently

$$A=S+\int\lambda(u,v)\,d\rho\tag{10}$$

defines $S(A,\rho)$. The coefficients a, b, and c are given by

$$a=\beta\left(\frac{a_0^2}{V}\right)+\beta(\alpha-1)u-2v+O(u^2,v^2)$$

$$b=\left(\frac{a_0^2}{V}\right)-(\alpha-1)u+O(u^2,v^2)$$

$$c=\left(\frac{a_0^2}{V}\right)-(\alpha-1)u+O(u^2,v^2)$$

The cumulative nonlinear terms in the equations of motion that are essential for a uniform approximation have been absorbed into the defining equation for S. The nonlinear system (eqs. (5) and (6)) is uniform in (S, R) in the sense that it admits of a geometric expansion of the form

$$u = \sum a_n \left(\frac{S}{R}\right)^{n/2}$$

$$v = \sum b_n \left(\frac{S}{R}\right)^{n/2}$$

in contrast to the original nonlinear system in (A, ρ). In addition, it also admits of the more general expansion of the form

$$u = a_1 \frac{F(S)}{\sqrt{R}} + a_2 \frac{F^2(S)}{R} + \cdots$$

$$v = b_1 \frac{F(S)}{\sqrt{R}} + b_2 \frac{F^2(S)}{R} + \cdots \tag{11}$$

determined by Whitham to be the uniformly valid expansion for the body of revolution. If, further, the perturbation series of the type in equations (7) in S and R is introduced, then $u^{(2)}$ and $v^{(2)}$ satisfy in S and R the differential equations of linear theory. But in the coordinates (S, R), they do not generate higher order singularities in the successive perturbations and are uniformly valid approximations to the exact solution. To express these approximations in the physical variables (x, r), it is necessary to expand also the coordinate relation equation (10). If this is done, the first approximation is just the Whitham theory. It might be noted that the geometric expansion is a progressive wave expansion, whereas the more general expansion equation (11) is not, as opposed to the case in linear theory where both are progressive wave expansions. It is interesting to speculate whether there exists a slight distortion of the coordinate R that might, in fact, reduce the system to precisely linear theory so that in the new coordinates, an expansion of the progressive wave type might be valid for all R. The fact that coefficients b and c agree to the first order in u and v and almost agree to that order with the coefficient $a - \beta\lambda$ tends to suggest this possibility and remains to be explored.

REFERENCES

1. DAVIS, S.; AND FRIEDMAN, M. B.: Uniform Approximations to the Shocks Generated by Thin Nonlifting Wings of Rectangular Planform. To be published as NASA CR.
2. RUNYAN, H. L.; AND HENDERSON, H. R.: Current Research in Sonic Boom. Second Conference on Sonic Boom Research, NASA SP–180, pp. 47–55.
3. HUNTON, L. W.: Current Research in Sonic Boom. Second Conference on Sonic Boom Research, NASA SP–180, 1968, pp. 57–66.

A Preliminary Investigation of Sonic Boom Waveforms Near Focusing Ray Systems

SANFORD S. DAVIS
NASA Ames Research Center

The characteristics of the sonic boom at the sonic cutoff altitude are extremely difficult to measure accurately. The major obstacles to full-scale experimental investigations are (1) in the case of sonic cutoff due to acceleration, the cusp location is unsteady and difficult to locate and follow; (2) in the case of sonic cutoff due to atmospheric inhomogeneities, these inhomogeneities cannot be determined precisely. Wind-tunnel tests are also hampered by the complexities involved with accelerated models and the difficulties encountered with the modeling of atmospheric inhomogeneities.

It is proposed to investigate the characteristics of cusped shock waves by using the well-known analogy between steady supersonic flows and unsteady two-dimensional flows. In this analogy, a thin wing will be used to induce a cusped shock wave in the flow field. The characteristics of the shock wave in the vicinity of the cusp will then be investigated both analytically and experimentally.

A fundamental difficulty with the linearized, analytical approach to the cusping problem is that the solution satisfies the mixed Tricomi equation. This difficulty is bypassed in the wing problem because the solution can be expressed directly as an integral over a distribution of elementary sources on the wing planform. Furthermore, the behavior of the singularities of this linear solution at and near the cusp can be inferred directly by the confluence of the three neighboring roots corresponding to the intersection of the leading edge of the wing and the trace of the Mach forecone from the field point (x, y, z). *This transparent form of the linearized solution, when expressed in a geometrical acoustics coordinate system, can be used in conjunction with Whitham's hypothesis to obtain a uniformly valid first approximation to the exact nonlinear disturbance field.*

For the proposed experimental phase of this study, a wing with a convex leading edge, inboard subsonic and outboard supersonic, is used to induce a steady-state cusped shock wave in the disturbed region below the wing. A static pressure rake will then be used to measure the shock wave signature in this steady-flow analogy to the sonic cutoff problem. The results of this experiment would serve as an ideal test case for the numerous studies that are now underway concerning sonic boom propagation near the sonic cutoff altitude.

420-093 O - 71 - 10

SYMBOLS

A	area on the plane of the wing in the dependence domain of the upstream Mach cone from (x, y, z)
B	wing sweep factor, $\sqrt{1-\tan^2 \chi^*}$
$K(k)$	complete elliptic integral of the first kind with respect to the modulus k
$m(x_1, y_1)$	streamwise slope distribution of the airfoil
p_0	static pressure in the undisturbed stream
Δp_1	perturbation pressure rise due to the supersonic portion of the wing
$\mathbf{q}$	total velocity vector $= V\mathbf{e}_x + \nabla\Phi$
s	distance along the ray in a crossflow plane measured from the wing trace
V	free-stream velocity
(x^*, y^*)	coordinates of a point on the leading edge of the wing
(x_1, y_1)	integration variables in the plane $z = 0$
(x, y, z)	cartesian coordinate system, the wing occupies part of the plane $z = 0$ and the free stream flows in the direction of increasing x
(y_e, z_e)	coordinates of a point on the envelope curve in a crossflow plane
α	integration variable, $\alpha = x_1 - \tan \chi^* y_1$
α^*	$x^* - \tan \chi^* y^*$
ξ	distance along the ray in a crossflow plane measured from the envelope curve
Φ	perturbation velocity potential
χ^*	local sweep of the wing leading edge, $\cot \chi^* = dy^*/dx^*$

INTRODUCTION

The two most well-known examples of cusped shocked waves in supersonic flight are due to the propagation of shock waves through the real inhomogeneous atmosphere and due to accelerated flight (fig. 1). At the present time, many investigators are examining the mathematical details of sonic boom propagation near these cusping regions. To test these theories, it would be desirable to have some experimental evidence available on the behavior of cusped shock waves. Unfortunately, full-scale experimental investigations are difficult to control because: (1) in the case of atmospheric refraction, the exact location of the cusp is difficult to determine because it is dependent on a precisely determined distribution of the atmospheric inhomogeneities; and (2) in the case of cusping due to acceleration, the unsteady cusp location is difficult to

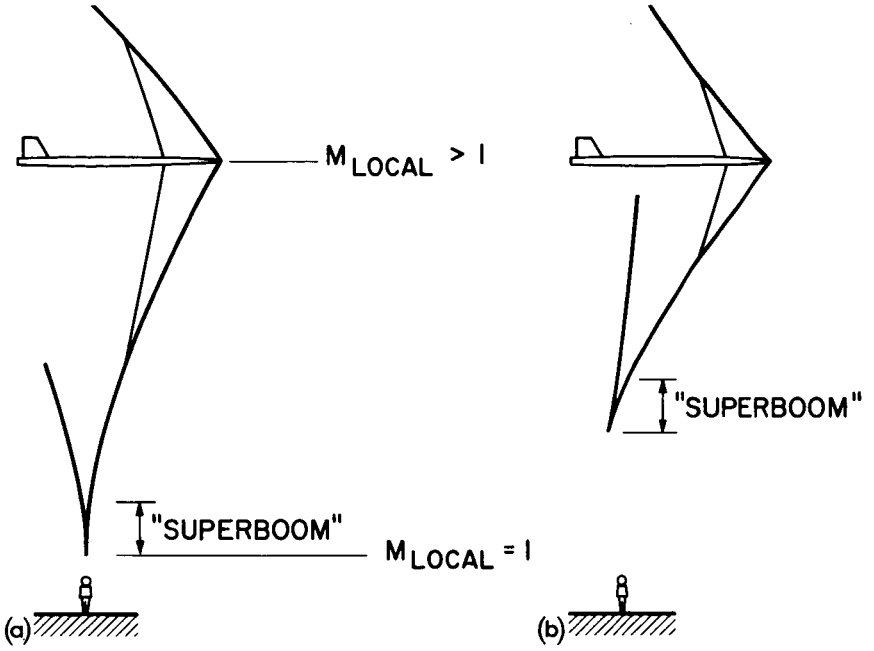

FIGURE 1.—Examples of cusping in supersonic flight. (*a*) Nonhomogeneous atmosphere. (*b*) Accelerated flight.

follow and measure. Wind-tunnel tests are similarly hampered by the difficulties involved with modeling atmospheric inhomogeneities and/or operating accelerated models.

To avoid these complications, the characteristics of a shock wave in the vicinity of a cusp can be studied experimentally (and analytically) by resorting to an analogous problem in the theory of steady supersonic flows. It is well known that the small-perturbation equations of steady supersonic three-dimensional flow is completely analogous to the equations of unsteady two-dimensional flow. In this analogy, the axial (streamwise) independent variable plays the role of a time variable. With the choice of a proper shape for the leading edge of a thin wing, a cusped shock wave (similar to the one found in the atmosphere) can be induced in the disturbed flow field beneath the wing. This scheme has an obvious advantage because the cusp is fixed in space and its properties can be fully explored in the wind tunnel with a simple rake of static pressure probes. For the analytic investigation of this cusped shock wave analogy, a linearized solution is immediately available in integral form and a complicated boundary-value problem for the Tricomi equation does not have to be solved.

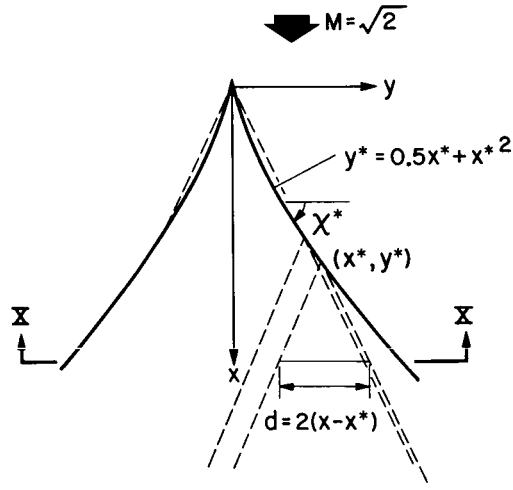

FIGURE 2. — Leading edge Mach cone at (x^*, y^*) is represented by $(x-x^*)^2-(y-y^*)^2-z^2=0$.

GEOMETRY OF THE CUSPED SHOCK WAVE

Consider a steady supersonic flow at Mach number $M = \sqrt{2}$ past a thin, nonlifting wing in the (x, y)-plane of a cartesian (x, y, z) coordinate system. The flow is taken in the direction of increasing x, and the wing has a concave leading edge as shown in figure 2. Using linearized, small-perturbation theory, the disturbance due to the presence of the wing is first communicated to the undisturbed flow along the surface of the family of free-stream Mach cones emitted by the leading edge of the wing. If (x^*, y^*) represents a point on the leading edge, a typical Mach cone can be written as

$$(x - x^*)^2 - (y - y^*)^2 - z^2 = 0 \tag{1}$$

In any crossflow plane x = constant, the Mach cone trace of equation (1) is represented by a circle of radius $(x - x^*)$ and centered at $y = y^*$, $z = 0$. As x^* varies in the range $0 \geqslant x^* \geqslant x$, a family of circles is generated in the crossflow plane. Figure 3 shows such a family (for the region $y > 0$) in the plane $x = 0.5$ for a wing with a concave leading edge given by

$$y^* = 0.5x^* + x^{*2} \tag{2}$$

The form of equation (2) has been specially chosen so that the inboard portion of the leading edge is subsonic and the outboard portion is supersonic. Figure 3 shows that the supersonic portion of the leading edge emits a family of Mach cone traces that form an envelope curve. Because each

point of the envelope is formed by the confluence of two neighboring elementary Mach cones, the envelope defines a locus of enhanced disturbances. This envelope differs from the envelope obtained from a wing possessing a straight supersonic leading edge in two important respects. First, the envelope is not straight, but consists of two distinct branches: a concave branch and a convex branch. These branches meet at a cusp that delineates the maximum extent of the envelope. This cusping behavior is the supersonic flow analogy of the atmospheric cusp. Second, the envelope does not separate the regions of disturbed and undisturbed flow because, in this case, the envelope forms in the domain of dependence of the Mach cone emitted by the vertex of the wing.

The cusp location and the envelope curve are obtained analytically. The envelope is a surface in the cartesian space, and the cusp is a curved line in cartesian space. The intersection of these quantities with a plane $x=$ constant define a curve and a point, respectively. A point (x, y, z) is on the envelope surface if equation (1) and its derivative with respect to x^* are simultaneously satisfied.

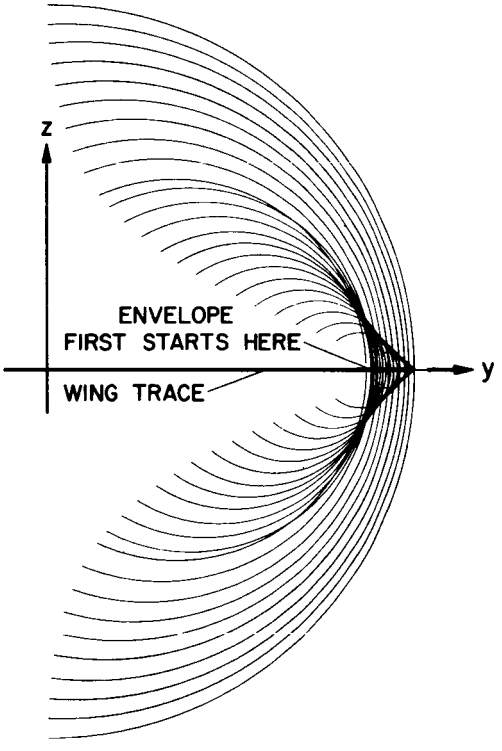

FIGURE 3.—Mach cone envelopes in the plane $x=0.5$ for a wing planform given by $y^*=0.50x^*+(x^*)^2$, $y^*>0$.

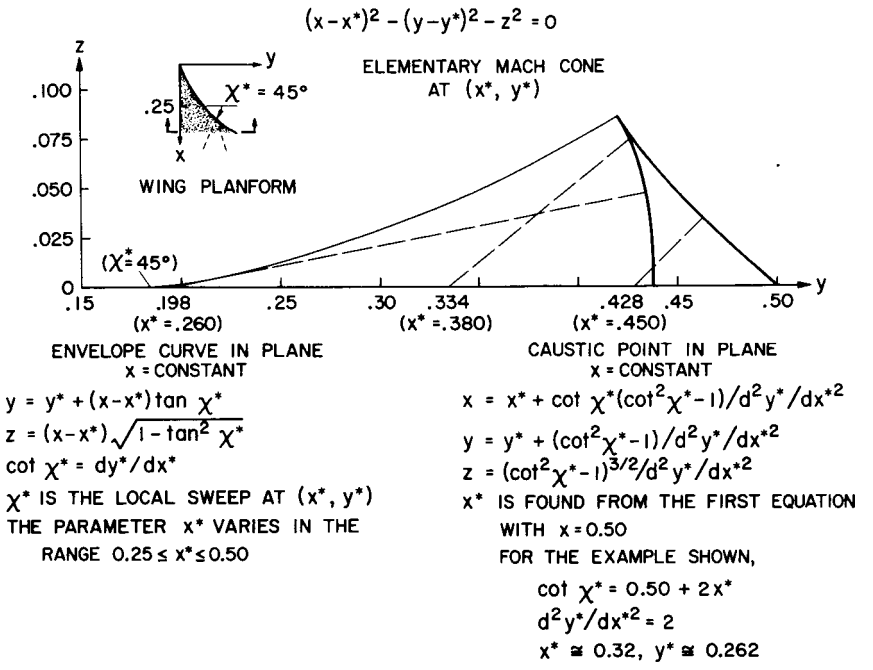

FIGURE 4. – Envelope curve in the plane $x = 0.50$.

$$(x-x^*)^2-(y-y^*)^2-z^2=0$$

$$-2(x-x^*)+2(y-y^*)\cot\chi^*=0 \tag{3}$$

$$\cot\chi^*=\frac{dy^*}{dx^*}$$

The quantity χ^* is the local sweep of the leading edge at (x^*, y^*). In the crossflow plane $x =$ constant, the envelope curve is given with respect to the parameter x^* by

$$\begin{aligned} y &= y^*+(x-x^*)\tan\chi^* \\ z &= (x-x^*)\sqrt{1-\tan^2\chi^*} \end{aligned} \tag{4}$$

where y^* and χ^* are given functions of x^*. Note that equations (4) show that only those values of the parameter x^* greater than the value of x^* defined by $\tan\chi^* = 1$ contribute to the envelope surface. This behavior is a confirmation of the well-known fact that only the supersonic portion of the leading edge emits Mach cones that coalesce to form envelopes. Figure 4 shows an example of the envelope in the plane $x = 0.5$.

A point (x, y, z) is on the cusp if it satisfies equations (3) and the second derivative of equation (1) with respect to x^* simultaneously.

$$\begin{aligned} &(x-x^*)^2-(y-y^*)^2-z^2=0 \\ &-2(x-x^*)+2(y-y^*)\cot\chi^*=0 \\ &2-2\cot^2\chi^*+2(y-y^*)d^2y^*/d(x^*)^2=0 \end{aligned} \tag{5}$$

or

$$\begin{aligned} x&=x^*+\frac{\cot\chi^*\,(\cot^2\chi^*-1)}{d^2y^*/d(x^*)^2} \\ y&=y^*+\frac{(\cot^2\chi^*-1)}{d^2y^*/d(x^*)^2} \\ z&=\frac{(\cot^2\chi^*-1)^{3/2}}{d^2y^*/d(x^*)^2} \end{aligned} \tag{6}$$

In a given plane $x =$ constant, the first of equations (6) is used to solve for the value of x^* (and y^* and χ^*) at the cusp. The remaining two formulas are used to find the cusp point y and z. Again, reference to figure 4 will show the cusp in the plane $x = 0.5$.

RAYS IN THE CROSSFLOW PLANE

In the region surrounding the wing, the envelope is generated by a family of straight lines. Each one of these lines represents a particular generator of one of the free-stream Mach cones emitted by the leading edge of the wing. These envelope generators are the bicharacteristics of the wave equation, and the parameter y^* (or x^* or χ^*) may be used to identify each member of the bicharacteristic family. In the crossflow plane, the rays are defined as the projection of a particular bicharacteristic into the plane $x =$ constant. This definition of the ray is consistent with ray concepts introduced in geometrical acoustics, the only difference arises in replacing the time variable t by a space variable x.

In the crossflow plane, the family of rays are everywhere orthogonal to the envelope curve, and the family of envelopes and rays form a mutually orthogonal family of curves. Some representative rays are shown in figure 4 for the concave and convex portions of the envelope. Also depicted in figure 4 is the caustic curve that corresponds to an envelope of the ray system.

The ray geometry is most useful in studies of the behavior of the solution near the envelope curves. A ray coordinate system will be introduced to replace the cartesian coordinates (x, y, z). The three parameters to be chosen will be denoted by (y^*, s, ξ), where y^* is the ray labeling parameter, s represents distance along the ray to the field

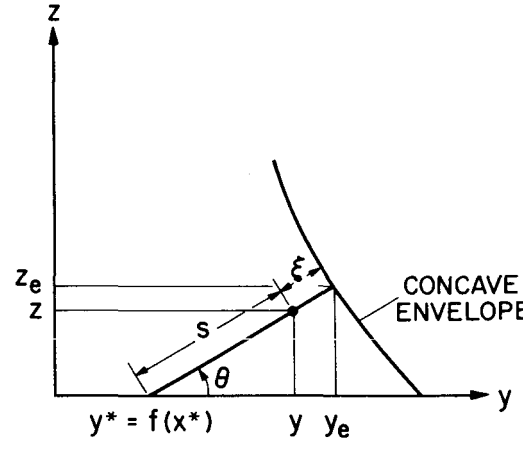

FIGURE 5.—Ray coordinate system.

point, and ξ represents the distance behind the envelope to the field point. From figure 5, the distance from the envelope (y_e, z_e) to the origin of the ray is obtained as

$$(s+\xi)^2 = (y^* - y_e)^2 + z_e^2$$

or with the help of equations (4)

$$s + \xi = x - x^* \tag{7}$$

Because $\cos\theta = (y_e - y^*)/(s+\xi) = \tan\chi^*$, the variables (y, z) are related to (y^*, s) by

$$\begin{aligned} y &= y^* + s\tan\chi^* \\ z &= s\sqrt{1-\tan^2\chi^*} \end{aligned} \tag{8}$$

Equations (7) and (8) give the required transformation from (x, y, z) to (y^*, s, ξ) (recall that y^* is a given function of x^* as well as $\tan\chi^*$).

SOME QUALITATIVE ASPECTS OF THE LINEARIZED SOLUTION

One of the major difficulties with the theory of cusping shock waves is due to the problems arising with the simplest linearization of the equations of motion. In the vicinity of the cusp, the perturbation quantities satisfy a mixed partial differential equation of the Tricomi type. Although particular solutions to this equation are known, they are difficult to work with because they are expressed in terms of nonelementary hypergeometric functions. One of the major simplifications with the wing problem is that the linearized perturbation quantities can be expressed directly in the form of an indefinite integral.

The well-known solution for the perturbation potential for a steady flow at $M=\sqrt{2}$ past a thin, nonlifting wing can be written as

$$\Phi=-\frac{V}{\pi}\int_A \frac{m(x_1, y_1)}{\sqrt{C(x_1, y_1)}}\,dx_1 dy_1 \tag{9}$$

where

$$C(x_1, y_1)=(x-x_1)^2-(y-y_1)^2-z^2$$

To simplify the analysis, the airfoil slope $m(x_1, y_1)$ will be assumed to be constant.

The characteristic form C can be reexpressed in terms of the ray coordinates as

$$C(x_1, y_1)=[\xi+(x^*-\tan\chi^* y^*-x_1+\tan\chi^* y_1)]^2+2\tan\chi^*(y^*-y_1)$$
$$[\xi+(x^*-\tan\chi^* y^*-x_1+\tan\chi^* y_1)]+2s[\xi+(x^*-\tan\chi^* y^*-x_1$$
$$+\tan\chi^* y_1]-(1-\tan^2\chi^*)(y^*-y_1)^2 \tag{10}$$

The area of integration in equation (9) can have one or more segments, depending on the location of the field point $P(y^*, s, \xi)$. As an example of this behavior, figure 6 shows the sequence of intersected areas for a wing with a leading edge given by

$$y_1=\pm(0.5x_1+x_1^2) \qquad y_1 \lesssim 0$$

At point a on the ray, the disturbance field is due to the subsonic portion of the leading edge only. This is shown in sketch (a) by the small shaded area near the origin. At point b, inside the concave envelope, two regions are shown shaded in sketch (b). The Mach cone intercept in the (x_1, y_1)-plane intersects the wing leading edge in three distinct places.

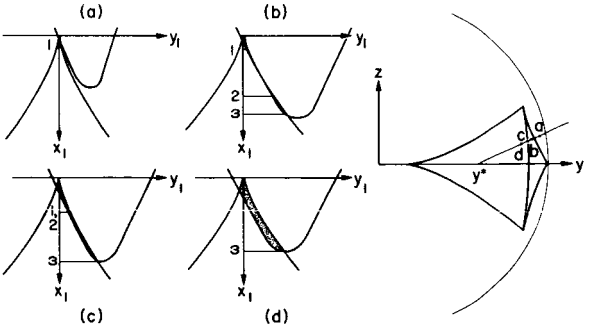

FIGURE 6.—*Left:* Areas of integration shown shaded; *right:* Variation of intercepted areas along a ray.

The singular part of the solution across the envelope is introduced by the first appearance of the roots 2 and 3. With increasing distance behind the envelope, roots 1 and 2 approach one another. When roots 1 and 2 are coincident, the rear, convex branch of the envelope is first reached. This case is shown in sketch (*c*). A further increase in distance relegates roots 1 and 2 to complex values and only root 3 remains. This integration area is shown in sketch (*d*). This example clearly shows how the envelopes are intimately related to the behavior of the points of intersection between the Mach trace and the leading edge of the wing.

An envelope with two branches (and a cusp) can only occur when the intersection of the Mach forecone and the leading edge has three real roots (1, 2, 3). One envelope corresponds to $2=3$, the other to $1=2$, and the cusp to $1=2=3$. Clearly, no cusp can form in the case of a wing with a straight leading edge because only two real roots appear.

THE ASYMPTOTIC FORM OF THE LINEARIZED SOLUTION ATTRIBUTED TO THE SUPERSONIC PORTION OF THE LEADING EDGE

Formulation of the Potential

The exact linear potential, equation (9), will now be cast in an asymptotic form that can be integrated explicitly. Instead of the variable x_1, let a new integration variable α be defined by $\alpha=x_1-y_1\tan\chi^*$. The family of straight lines $\alpha=$constant are coincident with and parallel to the line tangent to the leading edge at (x^*, y^*). In particular, the line $\alpha=\alpha^*=x^*-y^*\tan\chi^*$ is the leading edge tangent at (x^*, y^*). With this reinterpretation, the quantity C becomes

$$C(\alpha, y_1)=(\xi+\alpha^*-\alpha)^2+2\tan\chi^*(y^*-y_1)(\xi+\alpha^*-\alpha) +2s(\xi+\alpha^*-\alpha)-B^2(y^*-y_1)^2 \qquad (11)$$

where $B^2=1-\tan^2\chi^*$.

An asymptotic approximation to equation (11) is desired in the region where ξ/s is small (i.e., in the vicinity of the envelope curve). The quantity α has been chosen because it varies in the approximate range $0\leq\alpha^*-\alpha\leq\xi$. Consequently, when ξ/s is small, the quantity $(\xi+\alpha^*-\alpha)^2$ is small compared with the remaining terms. If this quadratic term in $\xi+\alpha^*-\alpha$ is neglected, the characteristic quantity C becomes

$$C(\alpha, y_1)=2\tan\chi^*(y^*-y_1)(\xi+\alpha^*-\alpha) +2s(\xi+\alpha^*-\alpha)-B^2(y^*-y_1)^2 \qquad (12)$$

Note that the usual cutting plane approximation used by Whitham would also neglect the terms in y^*-y_1 in equation (12). However, in this uniformly valid approximation, no such restriction is placed on the

spanwise variations. The desired portion of the velocity potential at the envelope is expressed as

$$\Phi_1 = \frac{-Vm}{\pi} \int_{A_1} \frac{d\alpha dy_1}{\sqrt{C}} \tag{13}$$

where C is given by the expression (12) and A_1 represents the area depicted in figure 7. The contribution to the potential from equation (13) corresponds to the change in the solution as the envelope curve is crossed.

Calculation of the Perturbation Pressure

Equation (13) for the potential must be obtained by integrating $1/\sqrt{C}$ over the area bounded by the curve $C = 0$ and the leading edge of the wing. Let the leading edge be given by the expression:

$$y_1 = 0.5x_1 + x_1^2 \tag{14}$$

If x_1 is replaced by $y_1 \tan \chi^* + \alpha$, and the resulting formula is expanded in a Taylor series about $y_1 = y^*$, the quadratic approximation to $\alpha(y_1)$ is

$$\alpha(y_1) = \alpha^* - \tan^3 \chi^* (y^* - y_1)^2 \tag{15}$$

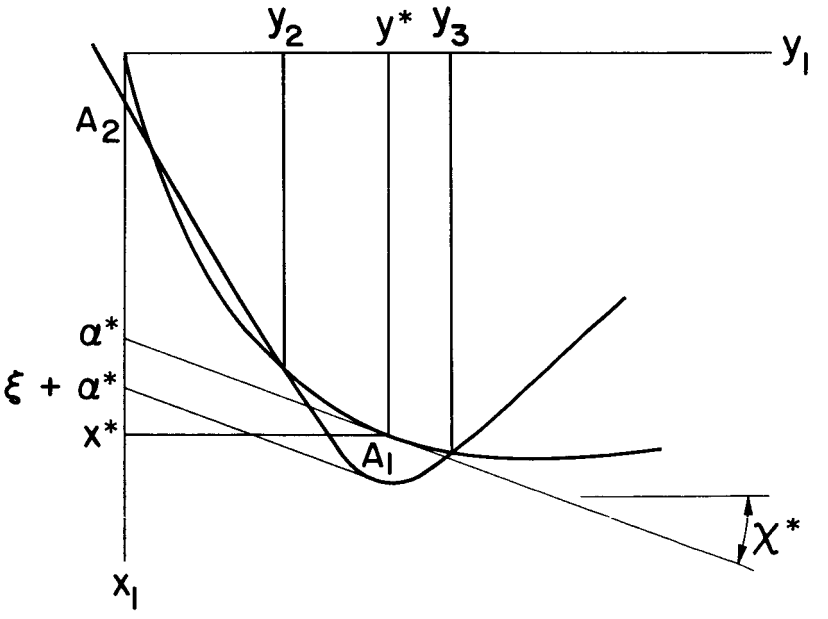

FIGURE 7.—Asymptotic form of potential due to the supersonic portion of the wing leading edge.

For this smooth wing, only a quadratic approximation to the wing leading edge is necessary for the evaluation of the potential. The explicit expressions for the potential become

$$\Phi_1 = -\frac{Vm}{\pi}\int_{y_2}^{y_3} dy_1 \int_{\alpha^* - \tan^3\chi^*(y^*-y_1)^2}^{\xi+\alpha^*-B^2(y^*-y_1)^2/(2\tan\chi^*(y^*-y_1)+2s)} d\alpha \frac{1}{\sqrt{C}} \tag{16}$$

where C is the expression given in equation (12) and y_2 and y_3 are the intersections of $C(\alpha, y_1) = 0$ and the wing leading edge. (See fig. 7.) After performing the α integration and differentiating with respect to x, the perturbation pressure is expressed as

$$\frac{\Delta p_1}{p_0} = \frac{2\gamma m}{\pi\sqrt{2}\tan^2\chi^*}\int_{r_2}^{r_3} d\eta \frac{1}{\sqrt{r_3-\eta)(\eta-r_2)(\eta-r_1)}} \tag{17}$$

where $\gamma = \frac{c_p}{c_v}$, $\eta = y_1 - y^*$, and $r_3 > r_2 > r_1$ are the three real roots of

$$s\xi\cot^4\chi^* - \xi\cot^3\chi^*\eta - \frac{1}{2}\cot^4\chi^*(B^2 - 2s\tan^3\chi^*)\eta^2 - \eta^3 = 0$$

Equation (17) can be expressed directly in terms of the roots r_3, r_2, and r_1 as

$$\frac{\Delta p_1}{p_0} = \frac{2\gamma m}{\pi}\frac{\sqrt{2}\,K(\sqrt{r_3-r_2}/\sqrt{r_3-r_1})}{\tan^2\chi^*\sqrt{r_3-r_1}} \tag{18}$$

or

$$\frac{\Delta p_1}{p_0} = \frac{2\gamma m}{\pi}\frac{\sqrt[4]{12}\,K(k)/\sqrt{\sin\frac{1}{3}(\theta+\pi)}}{[(B^2-2s\tan^3\chi^*)^2 - 12\tan^5\chi^*\xi]^{1/4}} \tag{19}$$

and θ satisfies

$$\cos\theta = -\frac{b}{2}\Big/\sqrt{\frac{-a^3}{27}}$$

$$a = \frac{12\tan^5\chi^*\xi - (B^2-2s\tan^3\chi^*)^2}{12\tan^8\chi^*}$$

$$b = \frac{1}{27}\left[-\frac{(B^2-2s\tan^3\chi^*)^3}{4\tan^{12}\chi^*} + 9\frac{(B^2-2s\tan^3\chi^*)\xi}{2\tan^7\chi^*} + \frac{27s\xi}{\tan^4\chi^*}\right]$$

where $K(k)$ is the complete elliptic integral of the first kind and

$$k^2 = \frac{\sin\frac{1}{3}\theta}{\sin\frac{1}{3}(\theta+\pi)}$$

Examination of the Perturbation Pressure

The formula given in equation (19) is valid for the region between the concave and convex envelope curves. Along a ray, the angle θ varies from 0 at the concave branch to π at the convex branch.

Away from the focus, but near the concave branch, $(B^2-2s\tan^3\chi^*)^2 \gg (12\tan^5\chi^*\xi)$ and $\theta \to 0$. In this region, the pressure becomes

$$\frac{\Delta p_1}{p_0}=\frac{2\gamma m}{\sqrt{B^2-2s\tan^3\chi^*}} \tag{20}$$

The quantity $(B^2-2s\tan^3\chi^*)$ may be identified with the ray tube area ratio $A(s)$ of geometrical acoustics. Equation (20) can be obtained directly from the usual geometrical acoustics formulas. For points far from the focus, equation (20) is a good approximation to the pressure jump. However, in the region near the focus, $(A(s)\to 0)$ and the uniformly valid representation of equation (19) must be used for the perturbation pressure.

In the case of a wing with a straight leading edge, the term in equation (20) that is proportional to the leading edge curvature vanishes. In this instance, the pressure formula becomes

$$\frac{\Delta p_1}{p_0}=\frac{2\gamma m}{\sqrt{1-\tan^2\chi^*}} \tag{21}$$

which is the well-known formula for the pressure rise across an infinite wing yawed at an angle χ^* with respect to the free stream.

At the convex branch, the angle $\theta \to \pi$. When $\theta \to \pi$, the modulus k of the elliptic integral in equation (19) approaches unity. In this case the value of the elliptic integral approaches a logarithmic infinity. This corresponds to the behavior indicated by Lighthill (and others) for a step discontinuity reflecting from a caustic as a logarithmic infinity.

SUMMARY OF PROPOSED RESEARCH

The preceding paragraphs have described the main features of the analogy between atmospheric cusping and the steady cusped shock waves emitted by certain thin wings in supersonic flow. The results of an experimental investigation into this wing-induced cusping phenomenon should serve as an ideal "first cut" for the variation in strength of a shock wave near a caustic. By varying the thickness distribution of the wing, any desired shock wave signature (i.e., an N-wave) could be induced in the vicinity of the cusp. In this manner, a variety of sonic boom signals could be studied experimentally as they propagate through a caustic.

This paper has also demonstrated the feasibility of obtaining the

most important part of the linear solution (as far as shock waves are concerned) in closed form. This linear solution can be used as the basis of a characteristic correction scheme to correct for weak nonlinear effects. However, the usual one-dimensional characteristic correction formulas must be modified to include the effects of large pressure gradients normal to the ray directions.

Some Attempts To Theorize About the Anomalous Rise Times of Sonic Booms

ALLAN D. PIERCE
Massachusetts Institute of Technology

The material presented at the conference was based to a large extent on two recent papers, both of which are scheduled to appear in the *Journal of the Acoustical Society*. The first (ref. 1) gives a comprehensive development of the author's theory of the anomalous rise times of sonic booms, while the second (ref. 2) is a review by the author and Domenic J. Maglieri of the present status of research on the effects of atmospheric turbulence on sonic boom waveforms. The present paper is essentially a condensation of a portion of the latter paper. It is hoped that this additional airing of the author's views will help to stimulate future research aimed at resolving the current controversy that exists concerning the physical origin of the anomalous rise times.

SOME RELEVANT EXPERIMENTAL DATA

The plots of rise time relative probabilities shown in figure 1 are based on data taken during tests in Oklahoma City and are similar to other rise time histograms given in the literature (refs. 3 to 5). This particular figure illustrates the general observation that larger rise times may be expected when the distance from the ground track is increased. (Both the mean rise time and the relative probability of larger rise times increase.) The figure also is intended to give some indication of the effect the definition of rise time may have on the form of the histograms. (The half rise time $\tau_{1/2}$ (time from onset to time when the overpressure first reaches $(1/2)\Delta p_0$ was also measured for the same set of data.) In the figure, the relative probabilities of $\tau_{1/2}$ and τ are plotted simultaneously. The qualitative variation of both sets of relative probabilities with lateral distance is similar. Furthermore, one should note that the mean $\tau_{1/2}$ is very nearly one-half the mean τ.

As is evident from the figure, measured rise times of sonic booms generally range from 1 to 10 msec. It has been known for some time (in particular, it was pointed out by Lilley (ref. 6) in his 1965 review) that such values are anomalously large (by factors of the order of 500) com-

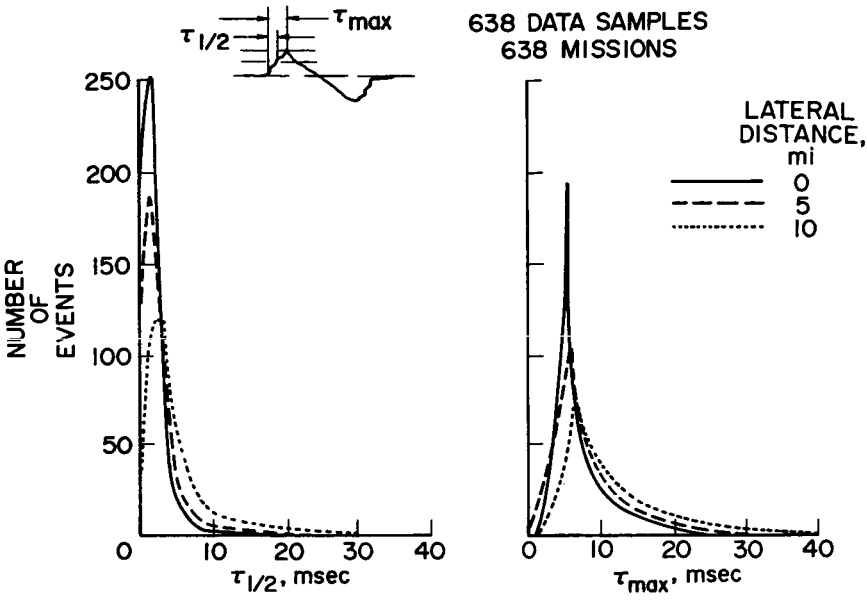

FIGURE 1.—Relative probabilities (proportional to probability density functions) of obtaining a given value of rise time τ or half rise $\tau_{1/2}$ within a given interval for various distances from the ground track, derived from data taken at Oklahoma City.

pared to what might be expected for a plane shock in a homogeneous atmosphere with realistic dissipation mechanisms. While the larger rise times of the order of 10 msec clearly correspond to rounded-type signatures, one should note that even the spiked waveforms have anomalously large rise times.

Although it has been generally agreed for some time that the variability of sonic boom signatures is largely due to atmospheric turbulence, the physical mechanisms by which the turbulence creates spiked or rounded waveforms or anomalously large rise times remain somewhat controversial. In spite of the fact that a rich and impressive literature exists that is concerned with the interaction of waves and turbulence, the direct application of this literature to sonic boom propagation phenomena is somewhat less than obvious. Among the distinctions of the problems typically treated in the literature and those of interest here are (1) that the sonic boom cannot be regarded as a narrowly collimated beam, out of which turbulence scatters energy; (2) that the boom is a transient disturbance rather than a narrow bandwidth signal; (3) that the criteria for applying either of the two standard approximations, the ray approximation or the first-order scattering approximation, may not strictly be satisfied in the case of sonic booms; and (4) that nonlinear effects may be of importance in the description of the accumulative

effect of turbulence on the waveform when the boom propagates over relatively large distances.

Regardless of just what mechanism is responsible for the rise times, it would seem that it should be similar to that which causes the type *R* (rounded) waveforms. A crucial question in this respect is whether or not the turbulence is causing higher frequency energy to be extracted from the waveform (either by scattering or by some other process). In an attempt to answer this question, it is of interest to reexamine Garrick's comparison (ref. 7) of the relative energy spectra of signatures having rounded and peaked shapes. In figure 2, the energy spectra of the two waveforms shown in figure 3 are simultaneously plotted. Although the two spectra do not exactly agree, one should note that there is a remarkable agreement in the gross shape of the two curves at higher frequencies. The interpretation given by Garrick to this fact is that turbulence leads to a phase-scrambling process taking place for the higher frequencies. In the following we examine the possible mechanisms that may account for such phase scrambling.

SCATTERING THEORIES

The first attempt to give a theory of the anomalous rise times was apparently made by Crow (ref. 8), who conjectured that energy "is beaten out of the shock front by the intense interactions that give rise to scattering." He estimated the average energy density of the scattered wave on the basis of first-order scattering theory as a function of the dis-

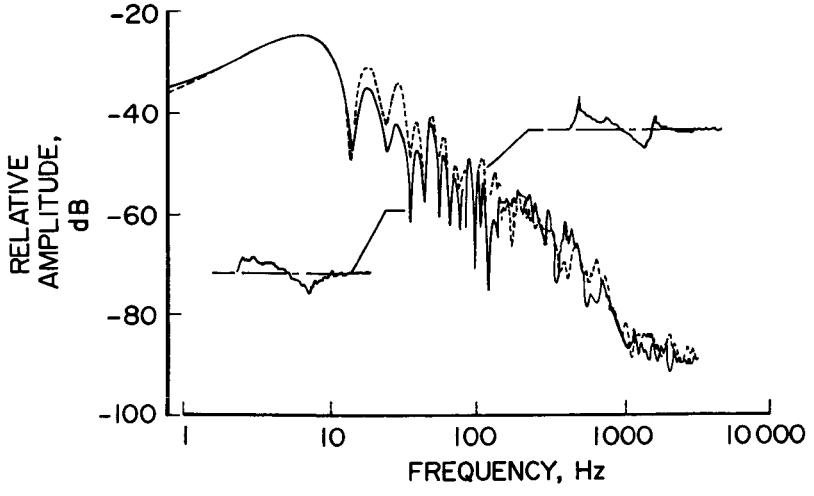

FIGURE 2.—Energy spectra for the two different sonic boom pressure signatures in figure 3. The relative amplitude is defined as $10 \log_{10} |f(\omega)|^2$, where $f(\omega)$ is the Fourier transform of the acoustic pressure.

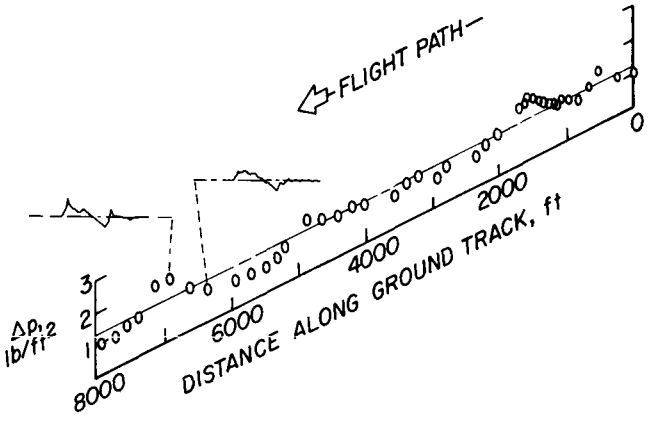

FIGURE 3.—The peak overpressure Δp_0 measured at microphones along an 8000-ft array on the ground track of an F–104 airplane flying at 30 500 ft, with two sample signatures.

tance h behind the front. The integral of the resulting expression over values of h greater than the shock thickness h_s was then equated to the energy of the undisturbed shock within a thickness of the order of h_s. (This is not exactly Crow's phrasing, but our interpretation of the sense of his discussion.) The result is that h_s should be of the order of $c_0 t_c$, and thus that the rise time should be of the order of t_c. The argument, although persuasive, is somewhat tenuous. It does, however, demonstrate the fact that a first-order scattering theory by itself is insufficient to explain the anomalous rise times. (Here t_c is Crow's characteristic time, which is a function of the height profile of the rate of turbulent energy dissipation per unit mass, which is estimated to be of the order of 1 msec. The quantity c_0 is the sound speed.)

One should note that the point of view that the rise times are caused by scattering, if given too literal an interpretation, is in apparent conflict with some well-known properties of shock propagation through an inhomogeneous medium. In an inviscid fluid, once a discontinuity is formed, it tends to stay a discontinuity (ref. 9), even though it may propagate through an inhomogeneous medium. Furthermore, the magnitude of the discontinuity (if sufficiently weak) tends to adjust (in a reversible manner) so as always to conserve wave action (ref. 10). The results derived from first-order scattering theory should therefore only give at best, an approximate description of the deformation in shape of the front and of the adiabatic adjustment of the discontinuity induced by the presence of inhomogeneities. The scattered wave cannot be construed as a description of energy extracted from the actual shock. While the above argument may be modified somewhat by viscosity and nonlinear effects, the modification would appear to be relatively small, when one considers the fact that viscosity by itself is far too small to account for

the actual rise times and that nonlinear effects should, if anything, cause the rise time to decrease. Thus, the view that scattering causes a gradual erosion of a shock front would seem to have no physical basis.

A basic theoretical difficulty in the problem of estimating a numerical value for the mean rise time is that one would generally want to take such an estimate as the rise time of an average signature. The average signature as a function of time, on the other hand, is strongly dependent on the choice of time origin in individual signatures. It is well known, for example, that if each individual waveform had zero rise time, but the time of shock onset is random, then the average waveform will have a finite rise time.

George and Plotkin (refs. 11 and 12) have recently proposed a theory of the anomalous rise times in which nonlinear effects play a dominant role. Their basic assumptions are that the rise times are created by a scattering of high frequencies out of the front and that this erosion process is partly or totally offset by nonlinear steepening. The implication is apparently that, for propagation over sufficiently large distances, the rise time eventually attains an equilibrium value characteristic of the net shock overpressure Δp_0 and of the parameters describing the state of turbulence, such that there is a balance between scattering and nonlinear steepening. In general, their analysis predicts that the overpressure p at a distance $-\xi$ behind the nominal location of the front should approximately satisfy Burgers' equation

$$\frac{\partial p}{\partial t}+\left[\frac{c(\gamma+1)}{2\gamma}\right]\left(\frac{p}{p_0}\right)\frac{\partial p}{\partial \xi}=\left(\frac{L_0}{c}\right)\langle(\Delta c+\Delta u_{||})^2\rangle\frac{\partial^2 p}{\partial \xi^2} \tag{1}$$

where $\Delta u_{||}$ is the turbulent fluid velocity component in the nominal direction of propagation. The quantity γ ($=1.4$, for air) is the specific heat ratio.

The general initial-value solution (refs. 13 and 14) to Burgers' equation was used to study the gradual evolvement of the signatures of an initial step-function shock of overpressure Δp_0. At large times, the resulting waveform asymptotically approaches a characteristic shape with a rise time

$$\tau=\left(\frac{32\gamma}{\gamma+1}\right)\frac{p_0}{\Delta p_0}\frac{\langle(\Delta u_{||}+\Delta c)^2\rangle L_0}{c^3} \tag{2}$$

The inverse dependence on Δp_0 should particularly be noted.

Although a substitution of representative values into the above expression gives a value of τ that is of the general order of magnitude of the experimentally observed rise times, one finds it difficult to accept the George-Plotkin theory without a closer examination of its major premises. One particular problem, mentioned earlier in this section, is that of the distinction between the average rise time of a collection of

signatures and the rise time of the average signature. The pressure $p(\xi, t)$ in equation (1) clearly must be interpreted as an average, perhaps an ensemble average in which ξ and t should be kept fixed during the averaging process. If this is the case, then the function $p(\xi, t)$ obtained from a solution of equation (1) represents an average signature of an ensemble of signatures that do not necessarily all begin at the same time. In this event, the computed rise time of the average signature could be strongly affected by the spread in arrival times of the sample signatures. In fairness, it should be stated that the authors believe p to be defined such that this difficulty is avoided. However, in perusing their paper, the present author can see no reason for accepting this to be the case. In particular, the present author questions the argument whereby they replace (ref. 12)

$$\frac{\delta\epsilon^2\,\partial p_{12}}{\partial t} = D(\delta p_{10})$$

by

$$\frac{\delta\epsilon^2\,\partial p_{12}}{\partial t} = \langle D(\delta p_{10})\rangle$$

where the brackets denote an ensemble average. The remaining symbols are defined in the paper by Plotkin and George.

THE WAVEFRONT FOLDING MECHANISM

The remarks in the previous section concerning the intrinsic conflict between the concept of scattering and what is known concerning the propagation of discontinuities hold, strictly speaking, only in the absence of caustics, which are surfaces in space along which the ray tube areas of geometrical acoustics rays vanish. However, even in the presence of caustics, linear acoustics predicts that weak discontinuities should propagate according to the laws of geometrical acoustics along any ray segment where the ray tube area is nonzero. Thus any alteration of shock fronts caused by the presence of caustics is a discrete rather than a continuous process.

A theory to explain the anomalous rise times in terms of processes occurring at caustics has been recently proposed by one of the authors (ref. 1). The basic mechanism for creation of the rise times is considered that of wavefront folding at a caustic. If an abrupt shock advances into a turbulent atmosphere, the rippling due to refraction or travel speed (fig. 4) variations along the front can result in the formation of caustics. (See fig. 5.) As the rippled wavefront approaches the cusp of a caustic (the line joining two caustic surfaces) the radius of curvature of the front becomes progressively smaller. After it reaches the cusp, the linear theory (refs. 15 and 16) predicts a wavefront folding (fig. 6), such that at

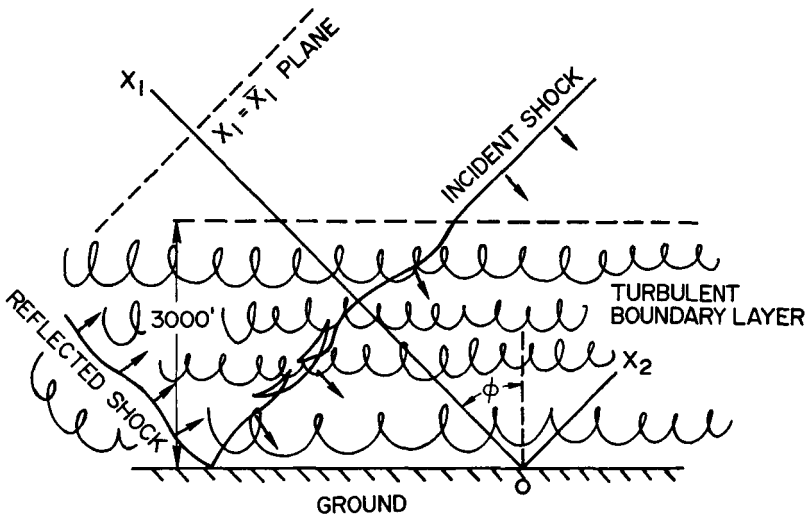

FIGURE 4.—A sketch illustrating the rippling and folding of an incident sonic boom shock by the turbulence in the lower atmosphere. The common theoretical assumption that only the lowest 3000 ft of the atmosphere has appreciable turbulence is also indicated. The choice of coordinate system is that used by Crow and by Pierce in recent theoretical studies.

points between the legs of the caustic, three wavefronts rather than one arrive. If the incident wave is a weak shock, two of the wavefronts will also be weak shocks, whereas the third will formally be a logarithmic singularity (which one may expect to be limited in amplitude due to nonlinear effects and viscosity).

The viewpoint was advanced that such wavefront folding occurs on a small scale many times as a wavefront propagates through a turbulent atmosphere. The net effect as observed at a single far-field point would then be that in which many segments of the multifolded front pass by (fig. 7(*a*)). The resulting overpressure signature would accordingly be composed of a number of discrete pressure jumps (microshocks) and logarithmic singularities (fig. 7(*b*)), with the latter whittled down to finite size and with the individual microshocks smoothed out by viscosity. The net effect would appear to be a wavefront with an anomalously large rise time.

The one principal uncertainty in the application of the wavefront-folding mechanism to sonic booms is the role of nonlinear effects. In this regard, it could conceivably be argued that when a shock approaches a caustic, the portion of the front with the smallest radius of curvature will have the highest overpressure and will therefore tend to speed up relative to other portions of the front. The net effect could then be that the ripple straightens itself out and thus that wavefront folding does not

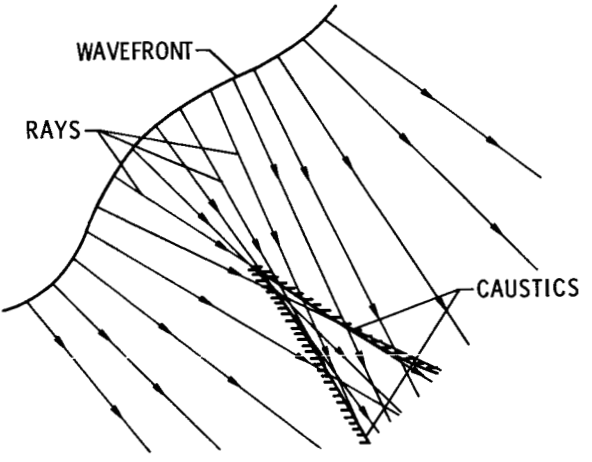

FIGURE 5.—Ray paths describing the subsequent propagation of a rippled wavefront. The caustics are formed by the locus of points where neighboring rays intersect. The sketch indicates that rippling may lead to either focusing or defocusing.

occur. (This point of view is implicit in one of Whitham's earlier papers, ref. 17.) This general question of nonlinear effects on weak shocks near caustics is currently one of great interest in connection with the superboom generated by a maneuvering aircraft. Recently, Beasley, Brooks, and Barger (ref. 18) have experimentally studied the behavior of weak shocks at a focus (which may be considered a degenerate case of a cusped caustic) using spark-generated N-waves reflected from parabolic mirrors. They found their results tended to conform to concepts derived from linear acoustics, particularly as regards the phase shift at the focus. More recently, Kuo (ref. 19) has sought to demonstrate explicitly wavefront folding by repeating Beasley, Brooks, and Barger's experiment, but with aberrated mirrors. The results are somewhat ambiguous because of the limited resolution of the microphone but do tend to support the folding hypothesis.

Perhaps the most intriguing experimental evidence obtained to date concerning the wavefront-folding theory of the anomalous rise times are the shadowgraphs taken by Bauer and Bagley (ref. 20) of shocks propagating through a turbulent boundary layer during their ballistic-range experiments. Figure 8 is typical of those appearing in their report. This should be compared with the sketch in figure 7(*a*). While there is considerable latitude in the subjective interpretation of the myriad of lines (evidently microshocks) in figure 8, the overall pattern would appear to support the hypothesis that the turbulence induced the wavefront folding.

The distinction between the refraction-focusing-diffraction process described as a means of producing spikes in a previous paper by the

author (ref. 21) and the wavefront-folding process is evidently one of scale. The folding mechanism requires a relatively short focal length of the ripples and may occur many times before the shock reaches the ground. The composite front may be viewed as a more or less tightly packed bundle of separate fronts. The more pronounced spikes are presumed to be caused by the larger scale turbulence, which refracts and focuses the composite front as a unit.

The expected number of microshocks in a sonic boom by the time it reaches the ground may be estimated as the expected number of rays that connect the near-field shock front with a given point on the ground. With the adoption of the same turbulence model as used by Crow, the result turns out to be directly proportional to Crow's expression for $\langle \psi^2(0) \rangle$, which was estimated (ref. 8) to be of the order of 10^8. Thus the number of microshocks is expected to be enormous. However, this value will certainly be reduced (just how much is an unsolved problem) because of the tendency of nonlinear effects to cause individual shocks to coalesce with increasing propagation distance. A similar calculation (which also ignored nonlinear effects) of the probability distribution of pressure jumps in the individual microshocks shows that the vast majority of the microshocks are extremely small.

The statistical model proposed to explore the quantitative implications of the wavefront-folding mechanism on sonic boom signatures was that

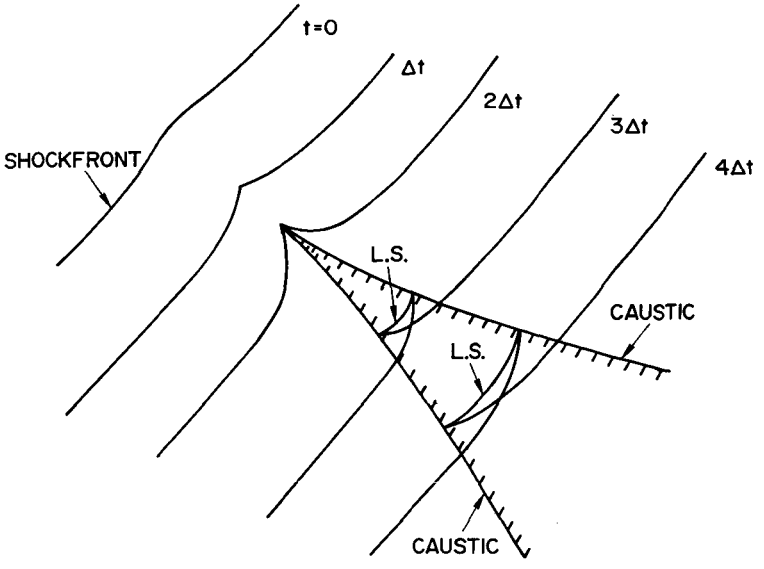

FIGURE 6.—Sketch showing the phenomenon of wavefront folding at a caustic. The symbol L.S. denotes the logarithmic singularities predicted by linear acoustics when the incident shock has an ideal jump.

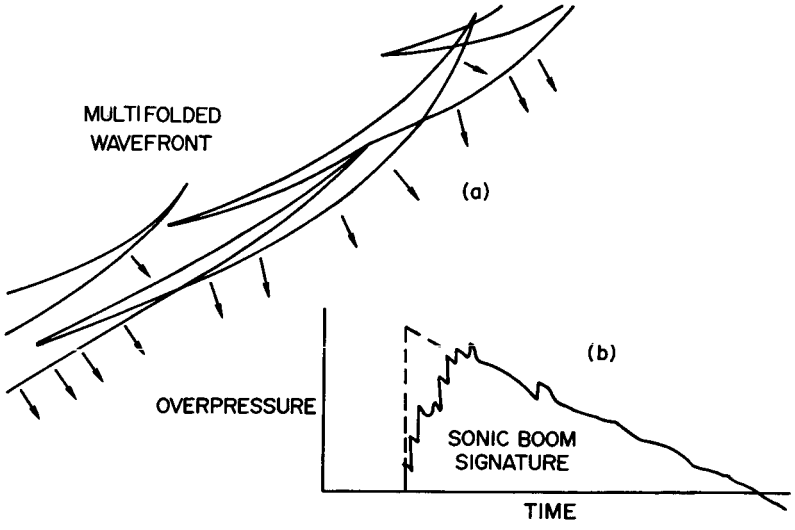

FIGURE 7.—(*a*) Sketch of a multifolded shock front. (*b*) Possible sonic boom signature corresponding to the passage of a multifolded shock.

represented by the Kirchhoff-Fresnel diffraction formula (ref. 22), whose use in the present context may be explained as follows.

The actual signature of the boom at any given point may be regarded as a function of the time history of the acoustic pressure on a surface at some intermediate altitude separating the flightpath and the microphone location. In the geometrical acoustics approximation, only the time history at one particular point (which lies on the ray connecting the surface and the microphone) governs the time history at the microphone. In general, this is not the case and it may be more appropriate to regard the signature as being affected by the time history of points within an extended region of the surface. In the simple case, for example, when the intervening medium is homogeneous, the acoustic pressure p at $\mathbf{r}$ is given by the Kirchhoff-Fresnel diffraction formula

$$p(\mathbf{r}, t) = \frac{1}{2\pi c} \frac{\partial}{\partial t} \iint_{S_0} \frac{p(\mathbf{r}_0, t_{\text{ret}}) \cos \theta}{|\mathbf{r} - \mathbf{r}_0|} d^2 S_0 \tag{3}$$

where the integral extends over all points $\mathbf{r}_0$ on the surface S_0. The angle θ is that between the surface's normal and the nominal propagation direction. Here the acoustic pressure $p(\mathbf{r}_0, t_{\text{ret}})$ in the integrand should be evaluated at the retarded time

$$t_{\text{ret}} = \frac{t - |\mathbf{r} - \mathbf{r}_0|}{c} \tag{4}$$

A relation similar to equation (3) may be derived for the case when the intervening medium is inhomogeneous. An approximate relation for this case would be that where the retarded time is regarded as

$$t_{\text{ret}} = t - t_{\text{tr}}(\mathbf{r}_0, \mathbf{r}) \tag{5}$$

where $t_{\text{tr}}(\mathbf{r}_0, \mathbf{r})$ is the acoustic travel time between $\mathbf{r}_0$ and $\mathbf{r}$. Equation (3) ignores the presence of the ground, but this is easily taken into account for the case of a microphone on the ground if equation (3) is multiplied by a ground reflection factor $K_r \approx 2$ and if the pressure $p(\mathbf{r}_0, t_{\text{ret}})$ in the integrand is interpreted as that due only to the incident shock. (Just how eq. (3) should be modified to take into account nonlinear effects is at present not understood, although it is expected that many of its predictions should not be appreciably altered by nonlinear effects.)

If the incident pressure $p(\mathbf{r}_0, t_{\text{ret}})$ at each point $\mathbf{r}_0$ on the surface has a definite onset time $t_{\text{on}}(\mathbf{r}_0)$ (which should be the case for sonic booms), then the earliest time a disturbance is received at $\mathbf{r}$ will be

$$t_{\text{min}} = \min \{t_{\text{on}}(\mathbf{r}_0) + t_{\text{tr}}(\mathbf{r}_0, \mathbf{r})\} \tag{6}$$

For times t shortly after t_{min}, the domain of points $\mathbf{r}_0$ for which the integrand in equation (3) is nonzero may be expected to be relatively small.

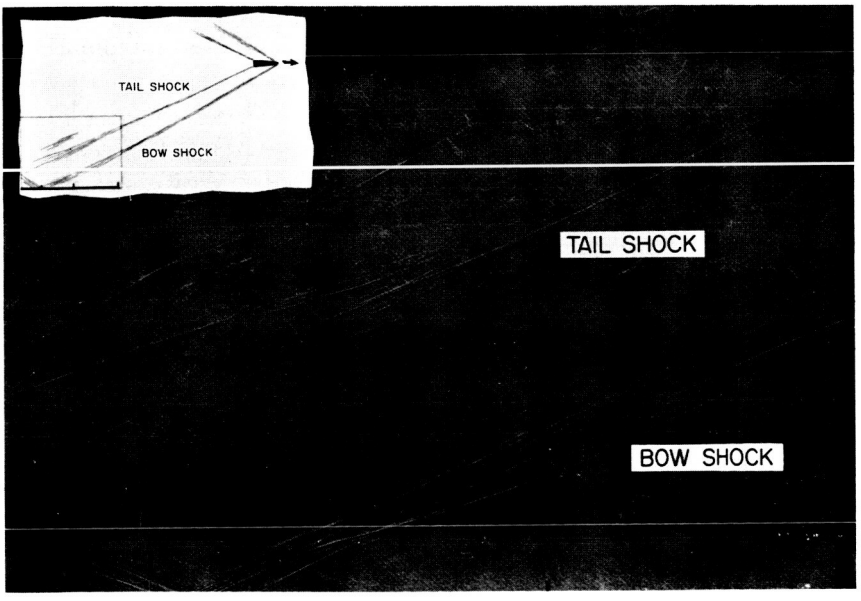

FIGURE 8.—Shadowgraph taken by Bauer and Bagley of a ballistic-range-generated shock wave advancing through a turbulent boundary layer. (The wall is on the right and the shock is moving toward the upper right-hand corner.) The projectile (a sharp-nose machined projectile of 0.457-in. diameter) was moving at a Mach number of 2.55.

In this case, the integral gives just the geometrical acoustics result (to the same approximation as is implied by the adoption of equation (3)). The later arrivals are affected, however, by progressively larger domains of the surface S_0 and thus tend to average out any effects caused by small-scale variations of $p(\mathbf{r}_0, t_{\text{ret}})$ along the surface S_0.

In the subsequent development of a statistical theory, the travel time t_{tr} was interpreted as a random variable that could in principle be calculated were the detailed state of turbulence known. The surface S_0 was selected sufficiently high in altitude that the incident pressure waveform $p(\mathbf{r}_0, t_{\text{ret}})$ could be considered as undisturbed by turbulence and consequently considered as a known function. To make the mathematics tractable, the travel time fluctuations were taken as first order in $\Delta\mathbf{u}$ and Δc. The appropriate expression for Δt_{tr} was determined by the requirement that the total integral, equation (3), should agree with first-order scattering theory in the limit of infinitesimal $\Delta\mathbf{u}$ and Δc. The resulting expression for $p(\mathbf{r}, t)$ then turned out, for arbitrary Δu and Δc, to be independent of the choice of the surface S_0, providing that it was at an altitude above the turbulent boundary layer. Since $p(\mathbf{r}_0, t_{\text{ret}})$ is not necessarily linear in t_{ret}, the adiabatically perturbed expression for $p(\mathbf{r}, t)$ was not necessarily of first order (or of second order, etc.).

A computation based on this model was undertaken of the ensemble-averaged waveform signature, the average being taken with the time origin of individual sample signatures shifted so that each sample first becomes nonzero at $t = 0$. The surprising result of this computation was a relatively long precursor (with a duration of the order of $12t_c$), which preceded the main arrival. The rise time of the main arrival (based on maximum slope) turned out to be of the order of $2t_c$ or $3t_c$. This would appear to substantiate Crow's conjecture concerning the rise times, although there is very little basis for supposing the average rise time of sample signatures to be the rise time of the averaged sample signature, even with the time origin shifted as described above. In retrospect, the computation would appear to give more information about the time duration of the precursor. Nevertheless, the model is sufficiently complete that improved calculations with time origin selected so that all sample signatures attain (1/2) Δp_0 at the same time can be made. It may be necessary to resort to Monte Carlo calculations, however.

CONCLUDING REMARKS

At present, there appears to be little widespread agreement on the details of sonic boom distortion by atmospheric turbulence, although an extensive catalog of systematic empirical knowledge has been obtained in field tests. Each of the phenomena of refraction, focusing, and of wavefront folding would appear to be an integral part of the distortion proc-

ess. Each of these effects have apparently been observed, either in field tests or in laboratory simulation studies. On the other hand, there is some question as to whether the concept of scattering is a viable concept for the description of sonic boom distortion. Although it is clear that any distortion process may formally be attributed to scattering, it would appear unnecessarily awkward to describe travel time deviations, refraction, or focusing in terms of scattering.

Although the theoretical development is currently in a state of flux, it seems at present that the one meteorological parameter that best summarizes the atmosphere's gross state of turbulence, insofar as sonic boom distortion is concerned, is Crow's characteristic time t_c. Techniques for measuring t_c should therefore be given some consideration. As for the general prediction that t_c governs waveform variability, an experimental check is still lacking.

Another question that remains unresolved is the extent of the role of nonlinear effects in waveform distortion.

In conclusion, one cannot state at this time that the topic of sonic boom interaction with turbulence is well understood. Instead, it is an active area of current research in which progress is rapidly being made.

REFERENCES

1. PIERCE, A. D.: Statistical Theory of Atmospheric Turbulence Effects on Sonic Boom Rise Times. J. Acoust. Soc. Amer., vol. 49, 1971, pp. 906–924.
2. PIERCE, A. D.; AND MAGLIERI, D. J.: Effects of Atmospheric Irregularities on Sonic Boom Propagation. To be published in J. Acoust. Soc. Amer.
3. MAGLIERI, D. J.; HUCKEL, V.; HENDERSON, H. R.; AND MCLEOD, N. J.: Variability in Sonic-Boom Signatures Measured Along an 8000-Foot Linear Array. NASA TN D–5040, 1969.
4. GARRICK, I. E.; AND MAGLIERI, D. J.: A Summary of Results on Sonic Boom Pressure-Signature Variations Associated With Atmospheric Conditions. NASA TN D–4588, 1968.
5. MAGLIERI, D. J.: Sonic Boom Ground Pressure Measurements for Flights at Altitudes in Excess of 70,000 Feet and at Mach Numbers Up to 3.0. Second Conference on Sonic Boom Research, NASA SP–180, 1968, pp. 19–27.
6. LILLEY, G. M.: The Structure of Shock Waves at Large Distances From Bodies Travelling at High Speeds. Congr. Int. Acoust. 5th. Vol. II. Daniel E. Commins, ed., 1965, pp. 109–162.
7. GARRICK, I. E.: Atmospheric Effects on the Sonic Boom. Second Conference on Sonic Boom Research, NASA SP–180, 1968, pp. 3–17.
8. CROW, S. C.: Distortion of Sonic Bangs by Atmospheric Turbulence. J. Fluid Mech, vol. 37, 1963, pp. 529–563.
9. KELLER, J. B.: Geometrical Acoustics I. The Theory of Weak Shock Waves. J. Appl. Phys., vol. 25, 1954, pp. 938–947.
10. BRETHERTON, F. P.; AND GARRETT, C. J. R.: Wavetrains in Inhomogeneous Moving Media. Proc. Roy. Soc. Ser. A, vol. 302, 1968, pp. 529–576.
11. GEORGE, A. R.; AND PLOTKIN, K. J.: Propagation of Sonic Booms and Other Weak Nonlinear Waves Through Turbulence. Phys. Fluids, vol. 14, 1971, pp. 548–554.

12. PLOTKIN, K. J.; AND GEORGE, A. R.: Weak Shock Waves in Turbulent Media. AIAA Paper no. 70–54, 1970.
13. HOPF, E.: The Partial Differential Equation $u_t + uu_x = \mu u_{xx}$. Commun. Pure Appl. Math., vol. 3, 1950, pp. 201–230.
14. COLE, J. D.: On a Quasi-Linear Parabolic Equation Occurring in Aerodynamics. Quart. Appl. Math., vol. 9, 1951, pp. 225–236.
15. FRIEDLANDER, F. G.: Sound Pulses. Cambridge Univ. Press, 1958.
16. LUDWIG, D.: Uniform Asymptotic Expansions at a Caustic. Commun. Pure Appl. Math., vol. 19, 1966, pp. 215–250.
17. WHITHAM, G. B.: On the Propagation of Weak Shock Waves. J. Fluid Mech., vol. 1, 1956, pp. 290–318.
18. BEASLEY, W. D.; BROOKS, J. D.; AND BARGER, R. L.: A Laboratory Investigation of N-Wave Focusing. NASA TN D-5306, 1969.
19. KUO, F., JR.: A Laboratory Investigation of Shock Folding at a Caustic. M.S. thesis, MIT, 1970.
20. BAUER, A. B.; AND BAGLEY, C. J.: Sonic Boom Modeling Investigation of Topographical and Atmospheric Effects. Rept. no. FAA–NO–70–10, Department of Transportation, July 1970.
21. PIERCE, A. D.: Spikes on Sonic Boom Pressure Waveforms. J. Acoust. Soc. Amer., vol. 44, 1968, pp. 1052–1061.
22. LINDSAY, R. B.: Mechanical Radiation. McGraw-Hill Book Co., Inc., 1960.

Studies in the Diffraction of a Pulse by a Three-Dimensional Corner*

LU TING AND FANNY KUNG
New York University

The present investigation is motivated by the study of the effect of sonic boom on structures. The pressure wave created by a supersonic airplane is three dimensional in nature. However, the radius of curvature of the wavefront is usually much larger than the length scale of a structure. Therefore, the incident waves can be approximated by progressing plane waves with an N-shape waveform and are referred to as N-waves as shown in figure 1.

For two-dimensional structures in the shape of a rectangular block, the diffraction of a plane pulse by the first corner is given explicitly by the two-dimensional conical solution of Keller and Blank (ref. 1). The solution for each subsequent diffraction by the next corners can be obtained by the use of Green's function for a wedge (ref. 2). For right-angle corners, the diffraction solutions can be obtained by the solution of an Abel-type integral equation (ref. 3). By means of the integral of Duhamel, the solution for the diffraction of a plane pulse by a two-dimensional structure was used to construct the solution for the diffraction of an N-wave by the same structure (ref. 4).

For the three-dimensional problem of the diffraction of sonic boom by structures, the first step is the construction of the solution for the diffraction of a plane pulse by a corner of a structure. By the decomposition of an N-wave to plane pulses, the solution for the diffraction of an N-wave by a corner will then be constructed.

The results presented here contain the highlights of two reports (refs. 5 and 6). One deals with the construction of a three-dimensional conical solution (ref. 5), and the other deals with the use of the conical solution for the computation of pressure distributions on the surfaces due to a N-wave of any waveform and at any incident angle (ref. 6). Both reports contain detailed analyses and the relevant numerical programs.

---

*This research has been carried out under NASA grant NGL-33-016-119.

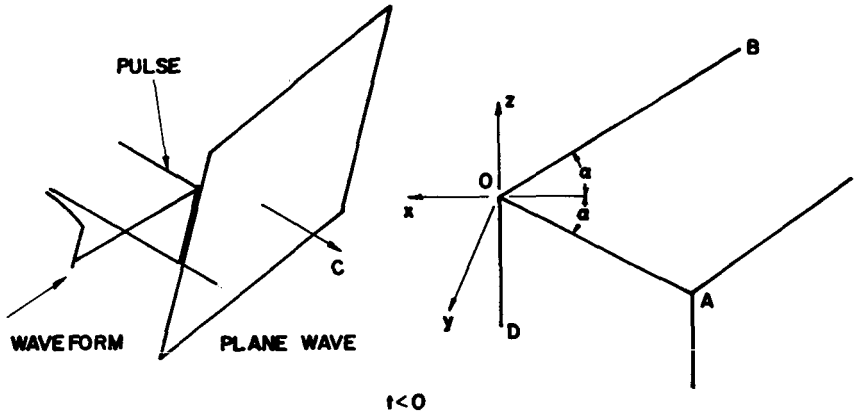

FIGURE 1.—Incidence of a plane wave on a corner.

REFLECTION AND DIFFRACTION BY A CORNER

For a plane pulse incident on a three-dimensional corner, the disturbed regions behind the incident plane wave are a simple reflection from the surface of the corner, a two-dimensional diffraction by an edge, or the three-dimensional diffraction by the vertex. The last region is confined by a sonic sphere centered at the vertex.

Figure 2 shows a normal incidence of a plane pulse on a corner *OABD*. The plane is moving parallel to edge *OB*; i.e., normal to face *OAD*. The incident wave is therefore reflected by face *OAD* with double intensity. The diffraction by edge *OA* or *OD* is confined by a circular cylinder of radius Ct from the edge, where C is the speed of sound. Outside the sonic sphere around the vertex O, the disturbance is two-dimensional conical with respect to time. The cross section of the wave patterns normal to the edge is shown in figure 3 together with the boundary conditions. The solution is given explicitly in reference 5, based on the analysis of reference 1. The boundary data on the sonic sphere $r=Ct$ about the vertex are thereby obtained, and the three-dimensional conical solution with respect to time inside the unit sphere $\zeta=r/Ct=1$ can be constructed.

Figure 4 shows an oblique incidence of a plane pulse on a corner *OABC*. On each face there is a reflected plane wave (shown for face *OAD* only). On each edge there is a diffracted wave confined inside a cone, with vertex located at the intersection of the plane pulse with the edge, and tangential to the adjacent reflected plane wave and the sonic sphere about the vertex of the corner (not shown for edge *OB*). The solution inside the cone and outside the sonic sphere is again given by the two-dimensional conical solution with respect to the distance from the vertex of the cone (ref. 1). Figure 5 shows the wave pattern at a cross section of the cone and

the boundary conditions. Explicit solutions are given in reference 6. The boundary data on the unit sphere $\zeta = r/Ct$ are again prepared. The numerical program in reference 6 is capable of defining the various regions for any incident angle and carrying out the computation of disturbance pressure accordingly. In the next section the essential procedures for the determination of the three-dimensional conical solution inside the unit sphere $\zeta = 1$ are described.

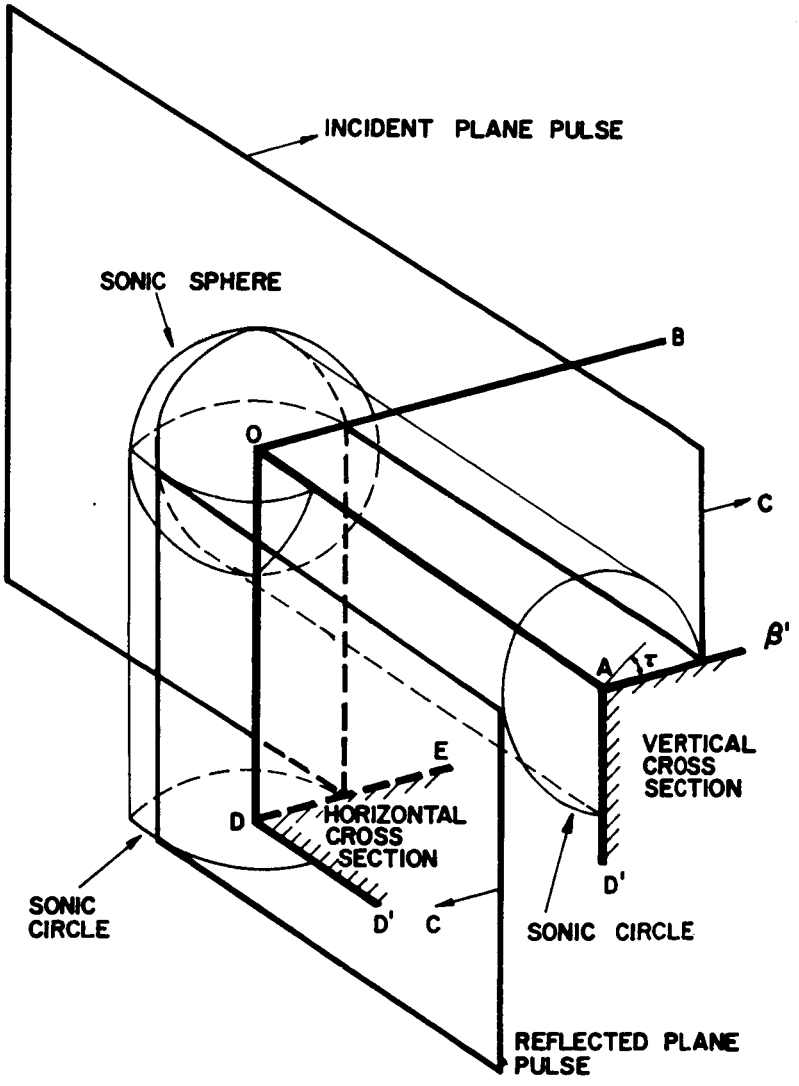

FIGURE 2.—Plane pulse incidence head on to face *OAD*, the reflected plane pulse, and the diffracted fronts around edges *OA*, *OD*, and vertex *O*.

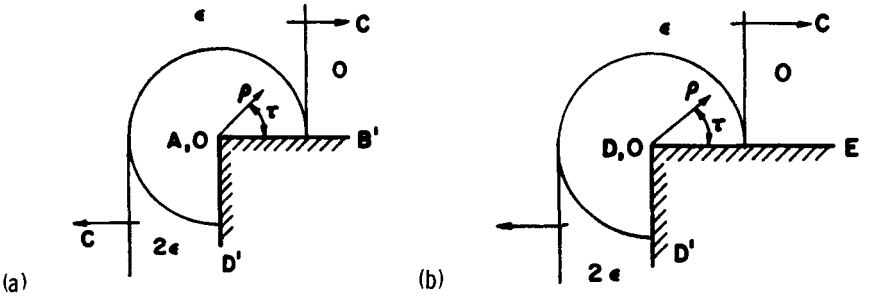

FIGURE 3. — Two-dimensional conical solutions around edges OA and OD. (a) Section normal to edge OA. (b) Section normal to edge OD.

THREE-DIMENSIONAL CONICAL SOLUTION

For the acoustic disturbance pressure p, the governing differential equation is the simple wave equation

$$p_{xx}+p_{yy}+p_{zz}-C^{-2}p_{tt}=0 \tag{1}$$

in the region outside a trihedron simulating the corner of a structure. As shown in figure 1, two edges, OA and OB, of the trihedron are in the x, y-plane and are bisected by the negative x-axis with half angle α and the third edge OD, which is the negative z-axis with the vertex O as the origin. Let $t=0$ be the instant when the pulse front hits the vertex. The boundary condition on the three faces of the trihedron is

$$\partial p/\partial n=0 \tag{2}$$

The three-dimensional disturbance due to the vertex is confined inside the sonic sphere $r=Ct$, where $r=(x^2+y^2+z^2)^{1/2}$. On the sonic sphere, the pressure distribution is given as described in the preceding section.

Because of the absence of a time scale and a length scale, the disturbance pressure p nondimensionalized by the strength of the incident pulse should be a function of the three-dimensional conical variables, x/Ct, y/Ct, and z/Ct or be given in terms of the spherical coordinates by $\zeta=r/Ct$, θ, and φ. The simple wave equation for $p(\zeta,\theta,\varphi)$ becomes

$$\zeta^2(1-\zeta^2)\frac{\partial^2 p}{\partial\zeta^2}+2\zeta(1-\zeta^2)\frac{\partial p}{\partial\zeta}+\frac{1}{\sin\theta}\frac{\partial}{\partial\theta}\left(\sin\theta\frac{\partial p}{\partial\theta}\right)+\frac{1}{\sin^2\theta}\frac{\partial^2 p}{\partial\varphi^2}=0 \tag{3}$$

inside the unit sphere $\zeta=1$ and exterior to the trihedron. The boundary conditions are

$$\partial p/\partial\theta=0 \qquad \text{on surface } OAB,\ \theta=\pi/2,\ -(\pi-\alpha)<\varphi<\pi-\alpha \tag{4}$$

$\partial p/\partial \varphi = 0$ on surface OAD, $\varphi = \pi - \alpha$, $\pi/2 < \theta < \pi$ (5a)

$\partial p/\partial \varphi = 0$ on surface OBD, $\varphi = -\pi + \alpha$, $\pi/2 < \theta < \pi$ (5b)

and $p = F(\theta, \varphi)$ on unit sphere $\zeta = 1$ outside of the trihedron.

To construct the solution by the method of separation of variables, the usual trial substitution $p(\zeta, \theta, \varphi) = Z(\zeta)G(\mu, \varphi)$ is introduced where $\mu = \cos\theta$ and equation (3) becomes

$$\zeta^2(1-\zeta^2)Z''(\zeta) + 2(1-\zeta^2)\zeta Z'(\zeta) - \lambda(\lambda+1)Z(\zeta) = 0 \tag{6}$$

for $1 > \zeta \geq 0$, and

$$\frac{\partial}{\partial \mu}\left[(1-\mu^2)\frac{\partial G}{\partial \mu}\right] + \lambda(\lambda+1)G + \frac{1}{1-\mu^2}\frac{\partial^2 G}{\partial \varphi^2} = 0 \tag{7}$$

Differential equation (7) and the boundary conditions, equations (4) and (5), define an eigenvalue problem.

The solution of the eigenvalue problem itself can be formulated for a wider class of corners as shown in figure 6. The surface OAB is a conical surface with $\theta = \beta$, and the two surfaces OAD and OBD are planes with

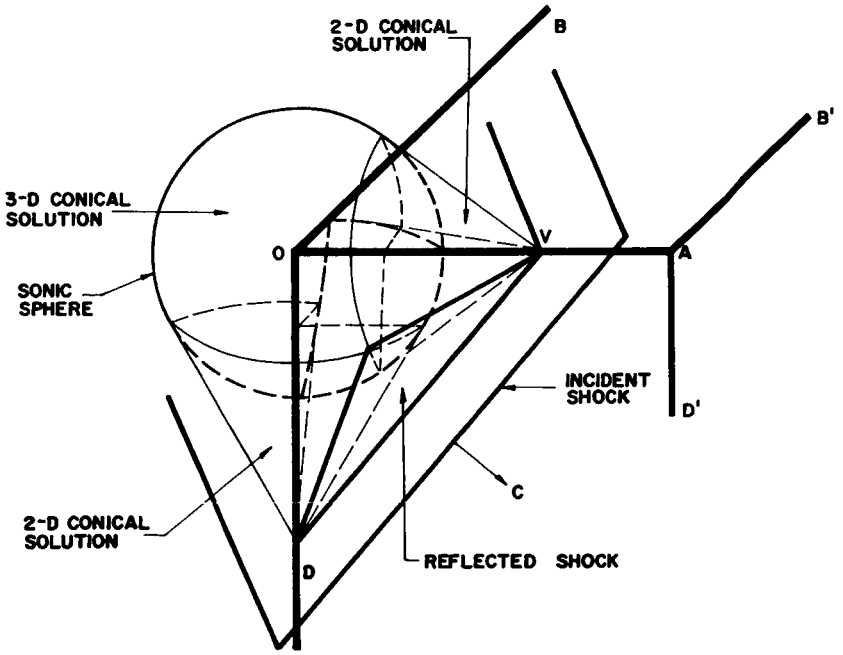

FIGURE 4.—Oblique incidence on a corner.

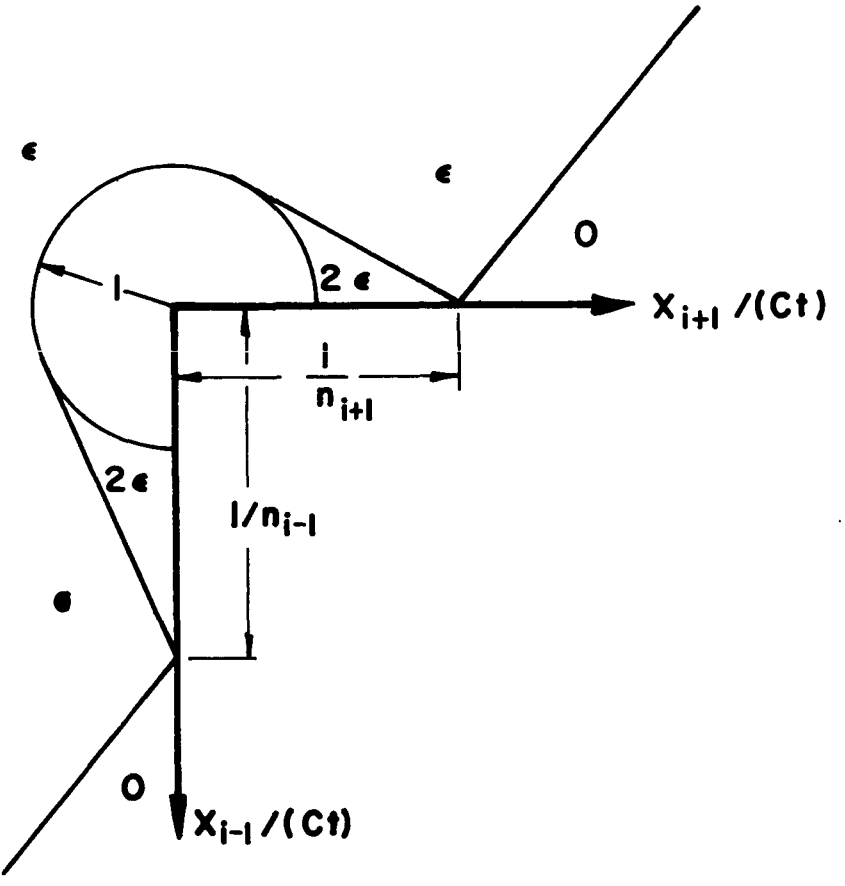

FIGURE 5. – Two-dimensional conical solution around *i*th edge.

$\varphi = \pi - \alpha$ and $\varphi = -\pi + \alpha$, respectively. The boundary conditions for the solution of equation (7) are

$$\partial G/\partial \mu = 0 \qquad \text{along } \mu = \mu_0 = \cos\beta \text{ with } \pi - \alpha < |\varphi| \leq \pi \tag{8a}$$

$$\partial G/\partial \varphi = 0 \qquad \text{along } \varphi = \pm(\pi - \alpha) \text{ with } -1 \leq \mu < \mu_0 \tag{8b}$$

$$|G| < \infty \qquad \text{at } \mu = \pm 1 \tag{8c}$$

$$G(\mu, \pi) = G(\mu, -\pi),\ G_\varphi(\mu, \pi) = G_\varphi(\mu, -\pi) \qquad \text{for } \mu_0 \leq \mu \leq 1 \tag{8d}$$

The eigenvalue problem is now defined by differential equation (7) and the boundary conditions of equations (8a) through (8d). To reduce the problem to that for a set of algebraic equations, two representations of the eigenfunction $G_\lambda(\mu, \varphi)$ associated with the eigenvalue λ will be sought, one for the region R^+ with $\mu > \mu_0$ and the other for R^- with $\mu < \mu_0$

(fig. 7). These two solutions and their normal derivatives will be matched across the dividing line $\mu=\mu_0$ for $|\varphi|<\pi-\alpha$.

For the upper region R^+, the eigenfunction $G_\lambda^+(\mu, \varphi)$, which is periodic in φ because of equations (8c) and (8d), can be represented by the Fourier series in φ with period of 2π:

$$G_\lambda^+(\mu, \varphi)=\sum_{m=0, 1, \ldots} A_m P_\lambda^{-m}(\mu) \cos m\varphi+\sum_{m=1, 2, \ldots} B_m P_\lambda^{-m}(\mu) \sin m\varphi \quad (9)$$

For each m, equation (7) yields the Legendre equation for $P_\lambda^{-m}(\mu)$

$$\frac{d}{d\mu}\left[(1-\mu^2)\frac{d}{d\mu}P_\lambda^{-m}(\mu)\right]+\left[\lambda(\lambda+1)-\frac{m^2}{1-\mu^2}\right]P_\lambda^{-m}(\mu)=0 \quad (10)$$

Because equation (9) is defined for $1\geq\mu\geq\mu_0>-1$, P_λ^{-m} should be finite at $\mu=1$. P_λ^{-m} is therefore identified as the generalized Legendre function defined by

$$P_\lambda^{-m}(\mu)=\left(\frac{1-\mu}{1+\mu}\right)^{m/2} F\{-\lambda, \lambda+1, 1+m; (1-\mu)/2\} \quad (11)$$

where F denotes the gaussian hypergeometric function.

For the lower region R^-, i.e., $-1\leq\mu<\mu_0$, the eigenfunction G_λ^-, which fulfills the boundary conditions of equations (8b) and (8c), can be expressed as

$$G_\lambda^-(\mu, \varphi)=\sum_{j=0, 1, \ldots} C_j P_\lambda^{-\nu}j(-\mu) \cos \nu_j\varphi+\sum_{j=1, 2, \ldots} D_j P_\lambda^{-\bar{\nu}}j(-\mu) \sin \bar{\nu}_j\varphi \quad (12)$$

where $\Phi=2(\pi-\alpha)$, $\nu_j=2j\pi/\Phi$, and $\bar{\nu}_j=(2j-1)\pi/\Phi$.

Equations (10) and (12) fulfill the differential equation (7) and the boundary conditions (8b) and (8c) appropriate for regions R^+ and R^-, respectively. The remaining boundary conditions, equation (8a) and the matching condition across the dividing line of R^+ and R^-, can be written as

$$G_\lambda^+(\mu_0^+, \varphi)=G_\lambda^-(\mu_0^-, \varphi) \qquad \text{for } |\varphi|\leq\pi-\alpha \quad (13)$$

$$\partial G_\lambda^+(\mu_0^+, \varphi)/\partial\mu=\begin{cases}\partial G_\lambda^-(\mu_0^-, \varphi)/\partial\mu & \text{for } |\varphi|<\pi-\alpha \\ 0 & \text{for } \pi-\alpha<|\varphi|\leq\pi\end{cases} \quad (14)$$

Equations (13) and (14) can be reduced to a system of linear homogeneous algebraic equations for the unknown constants A_m, B_m, and E_n by Fourier analysis, and the uncoupling of the even and odd solutions will also come about automatically as follows.

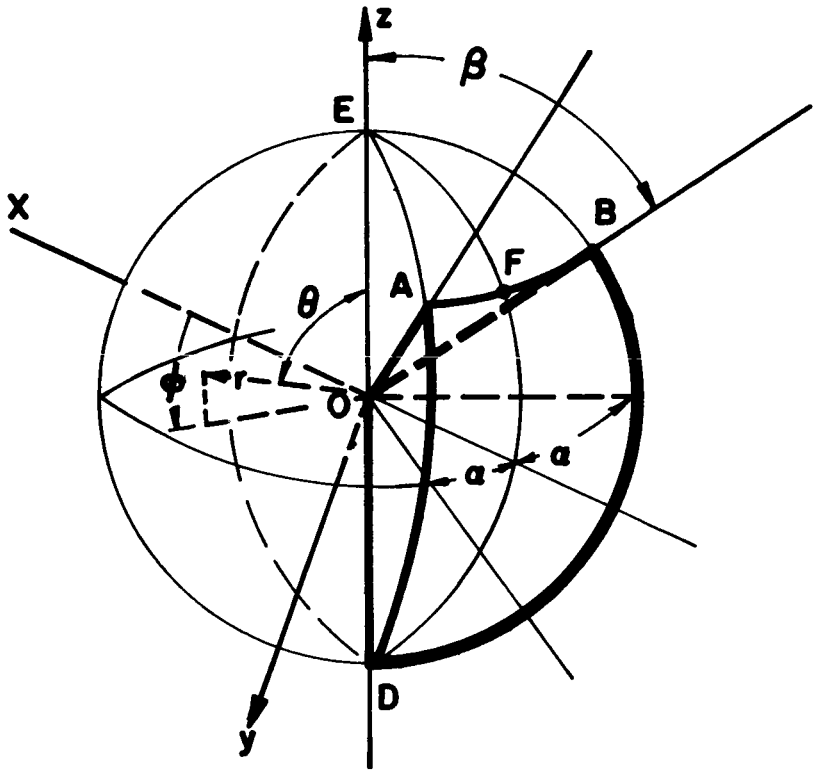

FIGURE 6. — Sonic sphere and the three-dimensional corner.

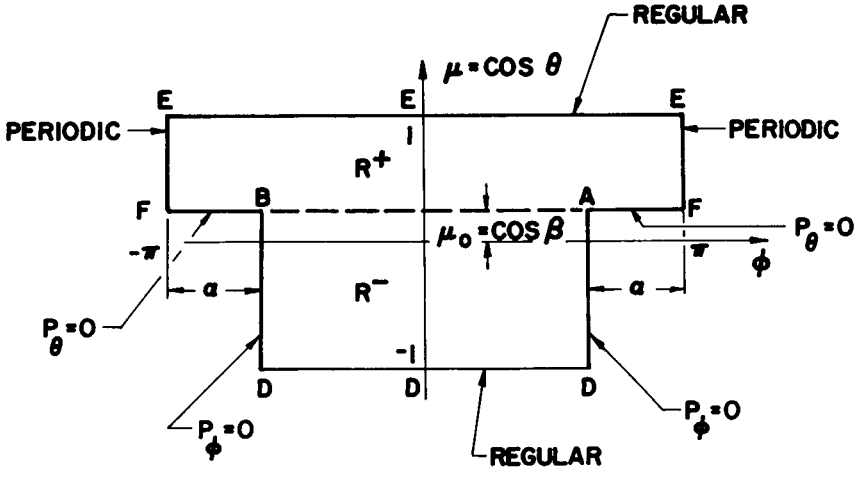

FIGURE 7. — Eigenvalue problem in ϕ, μ plane.

Equation (14) defines $\partial G_\lambda^+(\mu_0, \varphi)/\partial\mu$ for the interval $-\pi < \varphi < \pi$. It will be multiplied by $\cos n\varphi$ and will be integrated over the interval. Equations (14) then become the linear algebraic equations for the coefficients of the even terms involving coefficients A_m and C_j.

Similarly, equation (13), which holds for the interval $|\varphi| \leq \pi - \alpha/2 = \Phi/2$, will be multiplied by $\cos \nu_k\varphi$ with $\nu_k = 2k\pi/\Phi$ and will be integrated over the interval $-\Phi/2 < \varphi < \Phi/2$. The resulting algebraic equations contain again only the coefficients A_m and C_j. They are linear and homogeneous equations for A_m and C_j; therefore, the eigenvalues are the roots of the determinant $D_e(\lambda) = 0$.

The algebraic equations for the coefficients B_m and D_j associated with the odd parts can also be obtained from equations (13) and (14). Equations (14) should be multiplied by $\sin n\varphi$ and integrated over the interval $-\pi < \varphi < \pi$, and equation (13) should be multiplied by $\sin \bar{\nu}_k\varphi$ and integrated over the interval $-\Phi/2 < \varphi < \Phi/2$ with $\bar{\nu}_k = (2k-1)\pi/\Phi$. The determinant D_0 for the algebraic equations for B_m and D_j defines the eigenvalues for the odd solution as the roots of $D_0 = 0$.

The detailed procedures and a numerical program are presented in reference 5 for the determination of the eigenvalues, the roots of $\Delta_e(\lambda)=0$ and $\Delta_0(\lambda)=0$, their associated eigenfunctions $G_\lambda^+(\mu, \varphi)$, $G_\lambda^-(\mu, \varphi)$ and the function $Z_\lambda(\zeta)$ of equation (6). For each corner they are determined once. They are tabulated in reference 5 for the corner of a cube ($2\alpha - \pi/2$ and $\beta = \pi/2$).

Figures 8 and 9 show the pressure distribution on the surface due to the normal incidence of the plane pulse sketched in figure 2 (detailed analysis given in ref. 5).

Figure 10 shows the pressure distribution on the surface due to the oblique incidence of a plane pulse at an equal inclination to the edges.

It should be noted that the nondimensionalized pressure distribution at the vertex is always 8/7, and the value along the portion of the edge lying outside the sonic sphere is always 4/3. These values are independent of the incident angle of the plane wave.

This phenomenon can be explained and predicted by the theorems stated in the next section.

MEAN-VALUE THEOREMS FOR DIFFRACTION BY A CONICAL SURFACE AND APPLICATIONS

In this section, two theorems will be stated, the conditions under which the theorems are valid are emphasized, and their applications will be explained in detail. Proofs for the theorems are presented in reference 5.

Let $t = 0$ be the instant when an acoustic incident wave $\varphi^{(i)}$ hits the vertex of the cone located at the origin. Let T be the finite time interval such that for $t \leq -T$ the incident wave does not hit the conical surface.

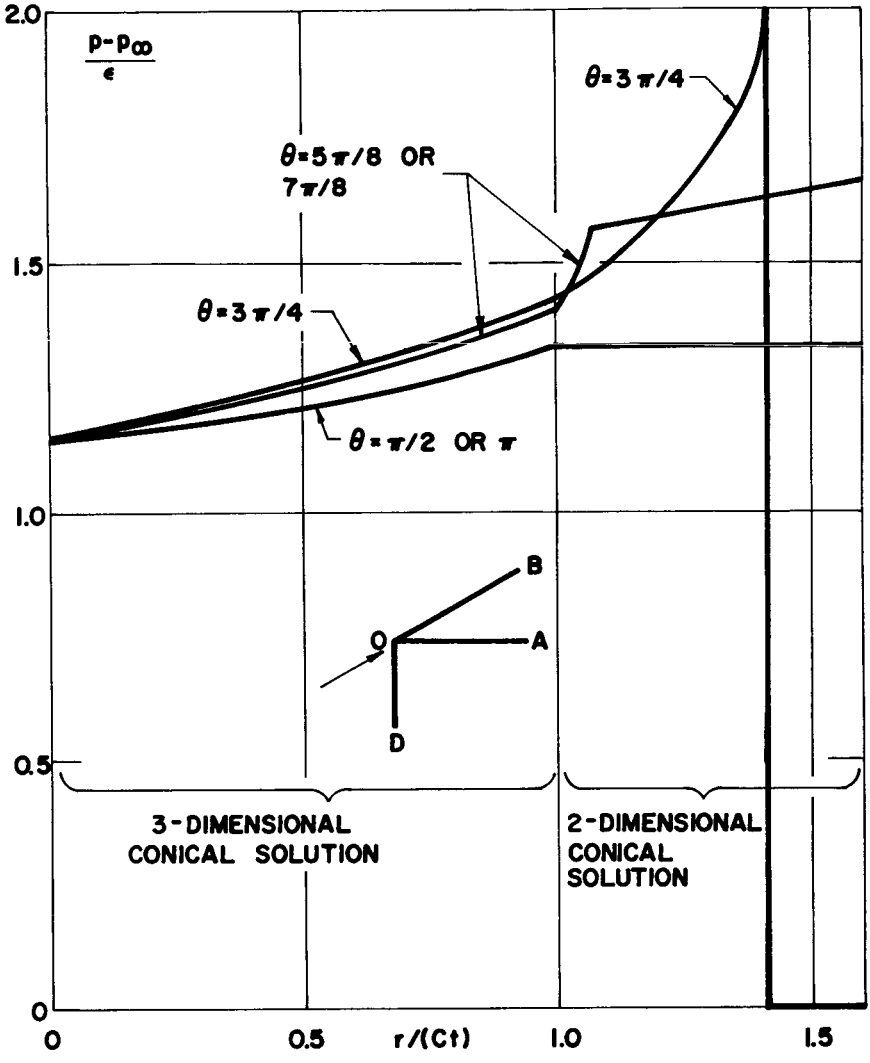

FIGURE 8.—Overpressure along constant θ lines on face OAD ($\phi = 3\pi/4$), shock advancing along OB.

Let $D(t)$ denote the domain outside of which the incident wave vanishes at the instant t; e.g., $\varphi^{(i)}(x, y, z, -T) = 0$ for (x, y, z) not in $D(-T)$. Domain $D(t \leqslant -T)$ does not intersect the cone G with solid angle Ω, as shown in figure 11.

In the absence of the cone, the incident wave $\varphi^{(i)}$ at the origin can be related to the initial data at an instant $t = t_0 < -T$ by the Poisson formula (ref. 7),

$$\varphi^{(i)}(0, 0, 0, t) = \frac{1}{4\pi C}\left[\frac{\partial}{\partial t}\iint_S \frac{f}{r}\,dS + \iint_S \frac{g}{r}\,dS\right]$$

where r is the distance from the origin, $f(x, y, z) = \varphi^i(x, y, z, -t_0)$, $g(x, y, z) = \varphi_t^{(i)}(x, y, z, -t_0)$, and S is the sphere with radius $R = C(t+t_0) > C(t+T)$ and with its center at the origin.

In the presence of the cone, the incident wave will be reflected and diffracted by the conical surface. The resultant pressure at the vertex $\varphi(0, 0, 0, t)$ is related directly to the incident wave by the relationship

$$\varphi(0, 0, 0, t) = \frac{4\pi}{4\pi - \Omega}\,\varphi^{(i)}(0, 0, 0, t) \qquad \text{for } t > -T \qquad (15)$$

as a consequence of theorem I, which is discussed in the following section.

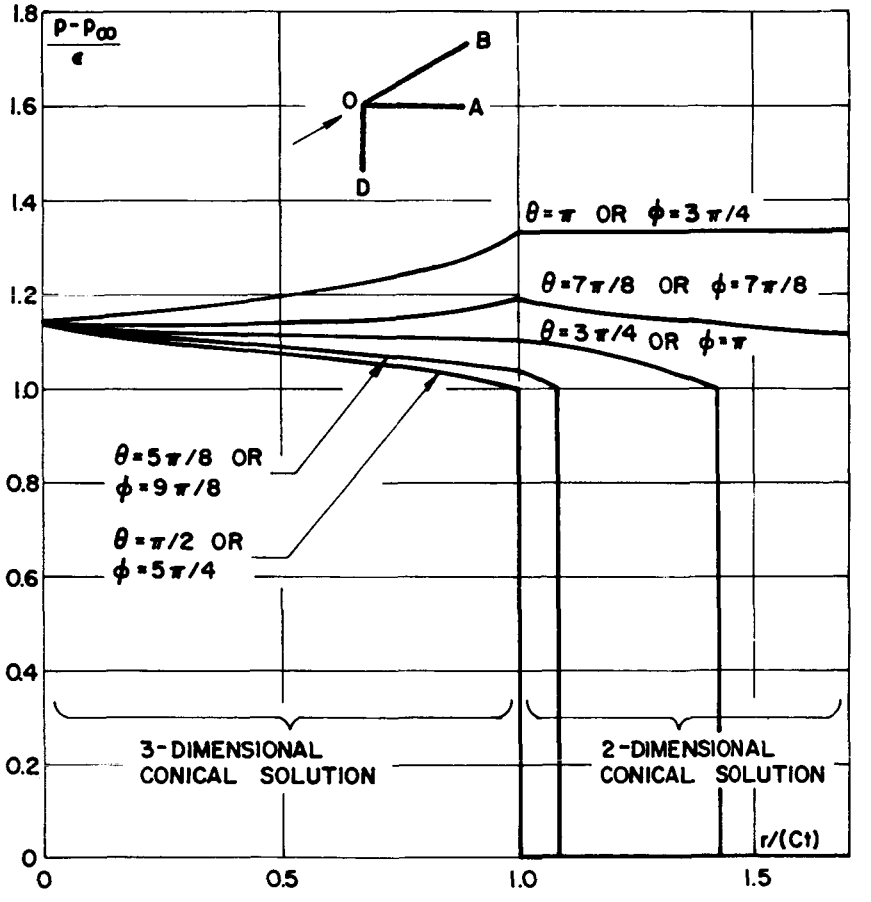

FIGURE 9. – Overpressure along constant ϕ lines on face OAB ($\theta = \pi/2$) and along constant θ lines on face OBD ($\phi = -3\pi/4$), shock advancing along OB.

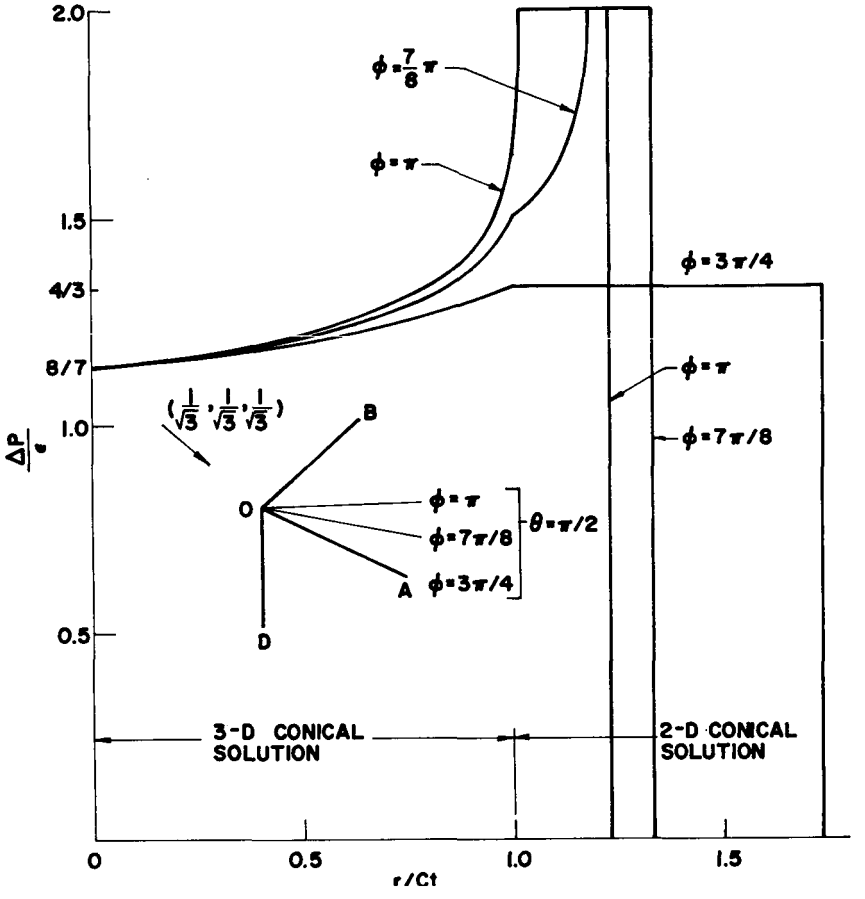

FIGURE 10. — Overpressure due to oblique incidence at equal inclination to the edges of the corner.

Theorem I

Theorem I states that the resultant value at the vertex of a cone with solid angle Ω is equal to $4\pi/(4\pi-\Omega)$ times the incident wave at the vertex if a finite T can be found such that the incident wave hits the conical surface within the time interval T prior to its encounter with the vertex of the cone.

In a practical problem, the conical surface, which forms a part of the surface of an obstacle, has a finite length L. In applying the theorem, it is essential that the part of the obstacle inside the sphere S with radius $C(t+T)$ is conical; i.e.,

$$C(t+T) < L \tag{16}$$

This defines an upper bound for T. On the other hand, for a given T with $CT < L$, the inequality defines an upper bound for t for which equation (15) holds.

With theorem I, the numerical results obtained in the preceding section for the overpressure at the vertex and along the portion of the edges outside the sonic sphere can be explained.

Figure 12(a) shows a wave incident on a two-dimensional right corner. As in a cone, the solid angle Ω at the corner P is 1/4 of the whole space; i.e., $\Omega = \pi$. Theorem I yields

$$\frac{\varphi(p, t)}{\varphi^{(i)}(p, t)} = \frac{4\pi}{4\pi - \pi} = \frac{4}{3} \tag{17}$$

With $\varphi^{(i)} = 1$ in the preceding section, $\varphi(B, t) = 4/3$. It holds for any incident angle at any point P on the edges of the three-dimensional corner $OABD$ of a cube prior to the arrival of the disturbances from the vertex; i.e., P lies outside the sonic sphere, or equation (17) holds for $t \leqslant |OP|/C$.

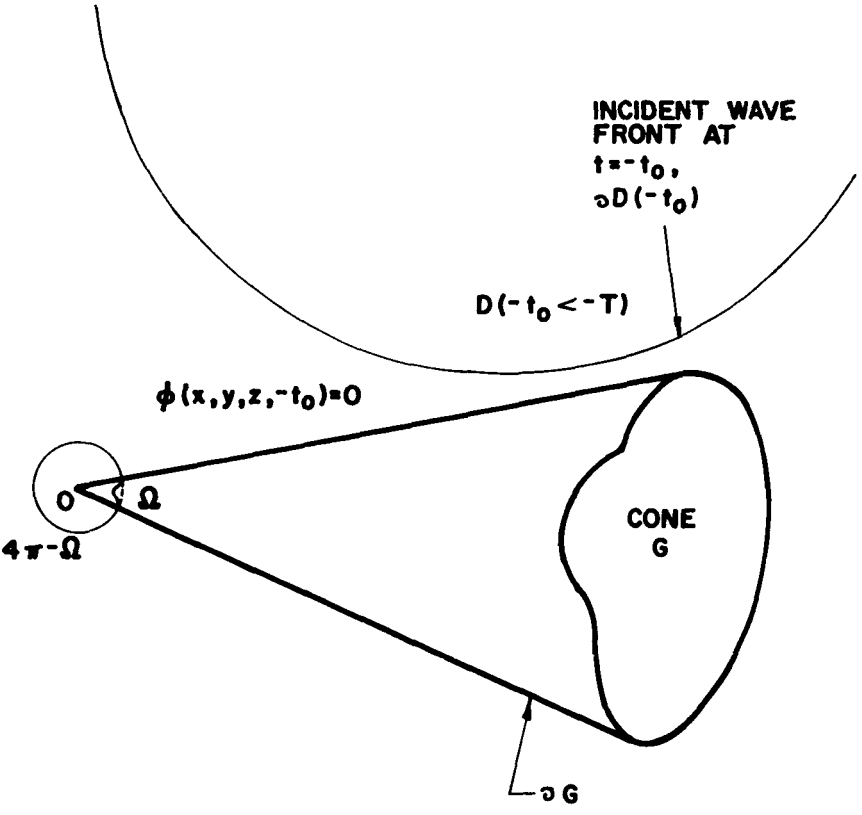

FIGURE 11.—Incidence on a cone.

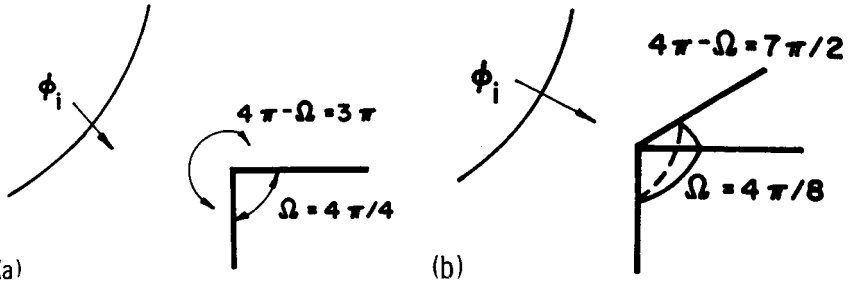

FIGURE 12.—Application of theorem II. (*a*) Intensification fa tor for two-dimensional corner $= 4\pi/3\pi = 4/3$. (*b*) Intensification factor for three-dimensional corner $= [4\pi/(7\pi/2)] = 8/7$.

Figure 12(*b*) shows a wave incident on the corner of a cube *OABD*. The solid angle at *O* is 1/8 of the whole space; i.e., $\Omega = \pi/2$. Theorem I yields the value at point *O*,

$$\frac{\varphi(O,t)}{\varphi^{(i)}(O,t)} = \frac{4\pi}{4\pi - \pi/2} = \frac{8}{7} \tag{18}$$

With $\varphi^{(i)} = 1$ in the preceding section, $\varphi(O, t) = 8/7$. This value holds for any incident angle until the arrival at point *O* of its diffracted waves from the adjacent corners of the cube. Let $n_j, j = 1, 2, 3$, denote the directional cosine of the normal of the plane pulse with the three edges *OA*, *OB*, and *OD* and L_j denote their lengths. The time of arrival at *O* of diffracted waves from an adjacent corner is $(1 + n_j)L_j/C$. Therefore equation (18) is valid for $t <$ minimum of $(1 + n_j)L_j/C$, $j = 1, 2, 3$.

When an incident wave is diffracted first by a part of the surface of the obstacle other than the conical surface of finite length *L*, condition (16) cannot be fulfilled. Even for a cone of infinite length, the incident pulse may be in contact with a part of the conical surface all the time. Consequently, the finite time interval *T* assumed in theorem I does not exist. For both examples, the value at the vertex of the cone cannot be related directly to the incident wave by theorem I. Therefore, a theorem relating the value at the vertex of one cone to that of another cone will be presented.

Figure 13(*a*) shows the relative orientations of two cones, G_1 and G_2, with solid angles Ω_1 and Ω_2. Their vertices coincide at the origin, and their boundaries ∂G_1 and ∂G_2 have a common region *OAB* as shown.

Let $\varphi_1(x, y, z, t)$ denote the resultant of an incident wave $\varphi^{(i)}$ and its reflected and diffracted waves by the cone G_1 along with $\partial\varphi_1/\partial n = 0$ on the surface of the cone ∂G_1. $D_1(t)$ denotes the domain outside of which $\varphi_1 = 0$ at the instant *t*. At $t = 0$, the origin lies on the boundary of $D_1(t)$ and $D_1(t)$ does not contain the origin for $t < 0$.

It will be assumed that there exists a finite time interval T such that the domain $D(t \leqslant -T)$ is in partial contact with the cone G_1 only over the surface OAB as shown in figure 13(b).

Figure 13(c) shows the same resultant wave $\varphi_1(x, y, z, t)$ being diffracted by cone G_2. The domain $D_1(t \leqslant -T)$ is in contact with cone G_2 only over the surface OAB. The values at the vertex of the cone in both cases (figs. 13(b) and 13(c)) are related by theorem II, which is discussed in the following section.

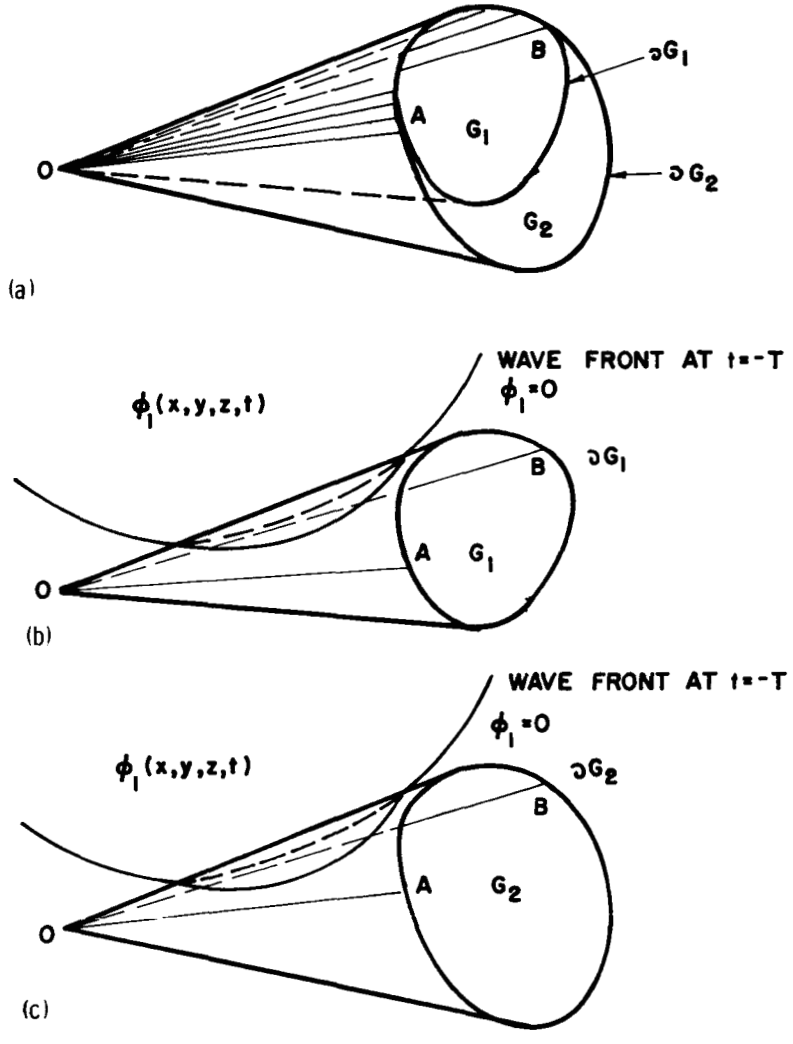

FIGURE 13.—Comparison of two cones. (a) Relative orientation of two cones. (b) Wave ϕ_1 incident on cone G_1. (c) Wave ϕ_1 incident on cone G_2.

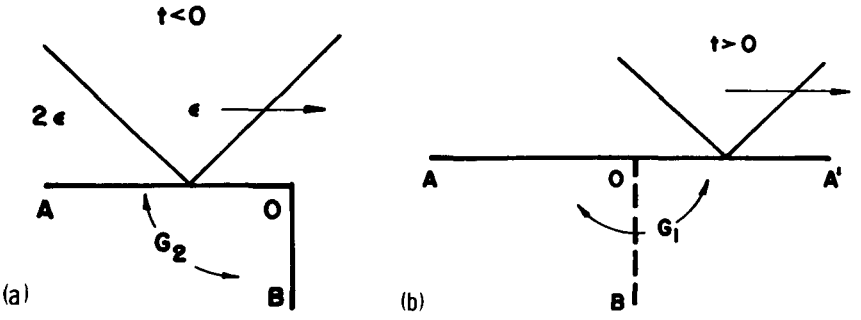

FIGURE 14.—Application of theorem II. (*a*) Two-dimensional corner. (*b*) Extension of side OA.

Theorem II

Theorem II states that for two conical surfaces ∂G_1 and ∂G_2, with the same location for the vertices and with the same initial data $\varphi = f(x, y, z)$ and $\varphi_t = g(x, y, z)$ at the instant $t = -T < 0$, the resultant disturbance at the vertex for each cone alone is inversely proportional to the exterior solid angle of the cone if the support D of f and g does not intersect either one of the cones and if the part of the boundary ∂D that is common to one of the conical surfaces is also common to the other.

This theorem will now be applied to a simple two-dimensional problem. Figure 14(*a*) shows an incident plane pulse of strength ϵ and its reflected wave from the horizontal surface OA advancing over a right convex corner O. Point O can be considered as the vertex of cone G_2 with solid angle $\Omega_2 = 4\pi/4$. Figure 14(*b*) shows the same incident and reflected wave advancing over the same horizontal surface OA and extended beyond point O. In this case there is no disturbance when the waves pass over point O at $t = 0$. The pressure at point O is $2\epsilon H[t]$, where H is the Heaviside function. Point O can be considered as the vertex of cone G_1 (fig. 14(*b*)) with solid angle $\Omega_1 = 4\pi/2$. According to theorem II, the pressure p_2 at the vertex O of cone G_2 in figure 14(*a*) is

$$p_2(O, t) = p_1(O, t)\left[\frac{4\pi - \Omega_1}{4\pi - \Omega_2}\right] = \frac{4}{3}\epsilon H[t]$$

Figure 4 shows another example in which theorem II can be useful. The diffraction by the edge OA is confined in the cone tangential to the sonic sphere with vertex V. The distance OV is Ct/n, where n is the direction cosine of the normal to the plane pulse with edge OA.

In the absence of a corner at point A, the surfaces OAB and OAD will be extended beyond AB' and AD', respectively. The conical solution p_c developed in the section on the three-dimensional conical solution is not diffracted at point A and remains valid when point V passes over

A; i.e., for $t > |OA|n/C$. Point A in this case can be considered as the vertex of a cone G_1 with solid angle $\Omega_1 = 4\pi/4 = \pi$.

With a corner at point A, the conical solution p_c is diffracted at A when point V passes over A. Point A can now be considered as the vertex of the cone G_1 with solid angle $\Omega_2 = 4\pi/8 = \pi/2$. The resultant pressure at vertex A due to the diffraction of the conical solution from O is given by theorem II as

$$p_2(A, t) = p_1(A, t)(4\pi - \Omega_1)/(4\pi - \Omega_2) = (6/7)p_c(A, t) \qquad (19)$$
$$\text{for } t > |OA|n/C$$

In particular, before the arrival of the sonic sphere at point A, it is known from theorem I or equation (17) that

$$p_c(A, t) = (4/3)\epsilon$$

Hence

$$p_2(A, t) = (8/7)\epsilon \qquad \text{for } |OA|/C > t > |OA|n/C$$

Of course, this result for $p_2(A, t)$ should be modified whenever an additional diffracted wave from another corner arrives at A.

It is obvious that when the wave equation has an inhomogeneous term $h(x, y, z, t)$ that represents an interior source distribution, similar conclusions can be obtained.

Corollary

The corollary of these two theorems states that they will also be valid for solutions of inhomogeneous wave equations $\Delta\varphi - C^{-2}\varphi_{tt} = h(x, y, z, t)$ if the support $E(t)$ of h ($h \equiv 0$ outside E) does not intersect the cone or both cones, respectively.

An interesting application for theorem I and the corollary is the initial- and boundary-value problem for an inhomogeneous wave equation in the interior of a conical surface ∂G_c with solid angle Ω_c (or the exterior of a cone G with solid angle $\Omega = 4\pi - \Omega_c > 2\pi$). The mathematical problem consists of the following differential equations (D.E.), boundary conditions (B.C.), and initial conditions (I.C.):

(D.E.) $\Delta\varphi - C^{-2}\varphi_{tt} = h(x, y, z, t)$ inside the cone G_c for $t > 0$

(B.C.) $\varphi_n = 0$ on ∂G_c

(I.C.) $\varphi = f(x, y, z)$, $\varphi_t = g(x, y, z)$ at $t = 0$

From the definition of the problem both the support E of h and the support D of f and g lie in G_c and therefore do not intersect G. Theorem I and the corollary state that the value at the vertex, $\varphi(0, 0, 0, t)$, is related to the initial-value problem $\varphi_{3D}(0, 0, 0, t)$ for the inhomogeneous wave

equation in three-dimensional (3D) space with the removal of the conical surface by an amplification factor equal to the local enlargement in solid angle $4\pi/\Omega_c$; i.e.,

$$\varphi(0,0,0,t)=\frac{4\pi}{\Omega_c}\{\varphi_{3D}(0,0,0,t)\}$$
$$=\frac{4\pi}{\Omega_c}\left\{\frac{1}{4\pi C}\left(\frac{\partial}{\partial t}\int\int_{S^*_{Ct}}\frac{f}{r}\,dS+\int\int_{S^*_{Ct}}\frac{g}{r}\,dS\right)\right.$$
$$\left.+\frac{1}{4\pi}\int_0^{Ct}dr\int\int_{S^*_r}\frac{[h]}{r}\,dS\right\}$$

where [ ] denotes the retarded value, S^*_{Ct} is the part of the spherical surface inside the support D of f and g, and S^*_r is the part of the spherical surface inside the support of $[h]$. The spheres are centered at the origin, and the subscript denotes the radius.

It is of interest to note that the value at the vertex of the cone is independent of the geometry of the cone G_c and does not depend on the distribution of f, g, and h and their supports D and E with respect to the spherical angles θ and φ so long as the integrals of f, g, and h over the spherical surface are invariant as functions of r and t. This corollary is useful in determining the noise intensity along corners or edges of a cavity or of a room with interior acoustic source distribution.

GENERAL INCIDENT WAVE

The incident wave due to the sonic boom can be locally represented as a plane wave because the length of a structure is usually much smaller than the radius of curvature of the wavefront. The waveform Ψ is in general a sequence of a weak shock wave and an expansive wave or a compression wave as shown in figure 1.

The conical solutions developed earlier in this paper for an incident plane pulse now will be employed to construct diffraction solutions for an incident wave of a more general type by superposition of plane pulses. In particular, when the incident wave is a plane wave of the type

$$p_i=\Psi(\eta)$$

with

$$\eta=Ct-(n_1x+n_2y+n_3z)$$

where the waveform Ψ is an arbitrary function of its phase η, and n_1, n_2, and n_3 are the direction cosines of the normal to the plane wave.

If the waveform is a Heaviside function, the diffraction due to the three-dimensional corner is given by the preceding conical solution and

will be designated as $p^*(r/Ct, \theta, \varphi)$. The solution of the diffracted wave corresponding to a general waveform of a sonic boom is

$$p(r, \theta, \varphi, t) = \sum_i \left[(\Delta p)_i p^* \left(\frac{r}{Ct - \eta_i}, \theta, \varphi \right) + \int_{\eta_i}^{\eta_{i+1}} p^* \left(\frac{r}{Ct - \eta}, \theta, \varphi \right) \frac{d\psi}{d\eta} \, d\eta \right] \tag{20}$$

where η_i is the phase of the ith shock wave with strength $(\Delta p)_i = \psi(\eta_i + O) - \psi(\eta_i - O)$. Note that η increases in the direction opposite to the normal of the plane wave.

A numerical program is presented in reference 6. For given input data of the direction cosines and the waveform $\psi(\eta)$ of the incident plane wave, the numerical program automatically defines the various regions of diffraction, as illustrated in figures 2 and 4, and computes the corresponding conical solution for a unit pulse at each phase η and then computes the resultant pressure by carrying out the supposition of the plane pulse by equation (20). Several numerical examples are also presented in reference 6 to illustrate the use of the numerical program.

CONCLUSIONS

This paper presents the main points of references 5 and 6:

(1) The conical solution for the diffraction of a plane acoustic pulse by a three-dimensional corner of a cube is obtained by separation of variables, as outlined in this paper. The detailed analysis, the eigenvalues, and eigenfunctions are presented in reference 5.

(2) A complete numerical program is presented in reference 6 to yield the resultant pressure distribution on the surfaces of the three-dimensional corner due to an incident plane wave with any incident angles and waveform.

(3) Mean-value theorems are derived in reference 5 for solutions of wave equations so that the resultant value at the vertex of a cone can be related to the incident wave or the value at the vertex of a different cone. These theorems are useful to extend the knowledge of the conical solutions to the adjacent corners or edges. Their applications have been presented in this paper, and additional ones can be found in reference 5.

REFERENCES

1. KELLER, J. B.; AND BLANK, A.: Diffraction and Reflection of Pulses by Wedges and Corners. Commun. Pure Appl. Math., vol. 4, no. 1, June 1951, pp. 75–94.

2. FRIEDLANDER, F. G.: Sound Pulse. Cambridge Univ. Press, 1958.
3. TING, L.: Diffraction of Disturbances Around a Convex Right Corner With Applications in Acoustics and Wing-body Interference. J. Aerosp. Sci., vol. 24, no. 11, Nov. 1957, pp. 821–831.
4. TING, L.; AND PAN, Y. S.: Incidence of N-Waves on Structures. Second Conference on Sonic Boom Research, NASA SP–180, 1968, pp. 89–98.
5. TING, L.; AND KUNG, F.: Diffraction of a Pulse by a Three-Dimensional Corner. NASA CR–1728, Mar. 1971.
6. TING, L.; AND KUNG, F.: Diffraction of a Plane Wave of General Wave Form by a Three-Dimensional Corner. Rept. AA–70–28, New York Univ., May 1971.
7. TYCHONOW, A. N.; AND SAMARSKI, A. A.: Partial Differential Equations of Mathematical Physics. Vol. II. Holden-Day, Inc., 1967, pp. 381–392.

Preliminary Numerical Investigation of Sonic Boom at Threshold Mach Numbers

THOMAS J. COAKLEY
NASA Ames Research Center

It is widely held that sonic boom constitutes a major obstacle to the successful implementation of supersonic air transport. Over the past decade since sonic boom was first recognized to be a serious problem, no absolutely conclusive design concept has been proposed that will reduce the boom to publicly acceptable levels. The current philosophy with regard to the supersonic transport (SST) under development at the Boeing Co. is to fly it supersonically over water but subsonically over populated land areas. A variation of this concept is the so-called threshold operation in which the airplane is permitted to fly supersonically over land but at Mach numbers only slightly in excess of unity. In this case, the shock system or sonic boom created by the aircraft does not propagate to the ground, but instead is reflected in the atmosphere because of a positive temperature gradient toward the ground. (See fig. 1.) The principal advantage of threshold operation as compared with subsonic operation is an increased ground speed of about 25 percent.

The aircraft Mach number at which the sonic boom just reaches the ground is called the threshold Mach number (fig. 1). Because of local and uncertain variations in atmospheric winds and temperatures, the threshold Mach number is not constant but varies (e.g., between 1.1 and 1.2) over a typical transcontinental flight track. Because it is desirable to fly the airplane at a relatively constant speed, as close as possible to the estimated threshold Mach number, there generally will be locations on the flight track where the sonic boom propagates to the ground. If the threshold Mach number drops substantially below the aircraft Mach number, the reflection at the ground will be simple. The maximum sonic boom overpressure can then be predicted by linear theory as schematically illustrated in the lower sketch of figure 1. On the other hand, if the threshold Mach number becomes equal to or slightly less than the flight Mach number, there will be an irregular ground reflection, the details of which are largely unknown. Sonic boom overpressure characteristics that might be considered favorable and unfavorable for flight in this regime are shown by the dashed curves in the lower sketch of

420-093 O - 71 - 13

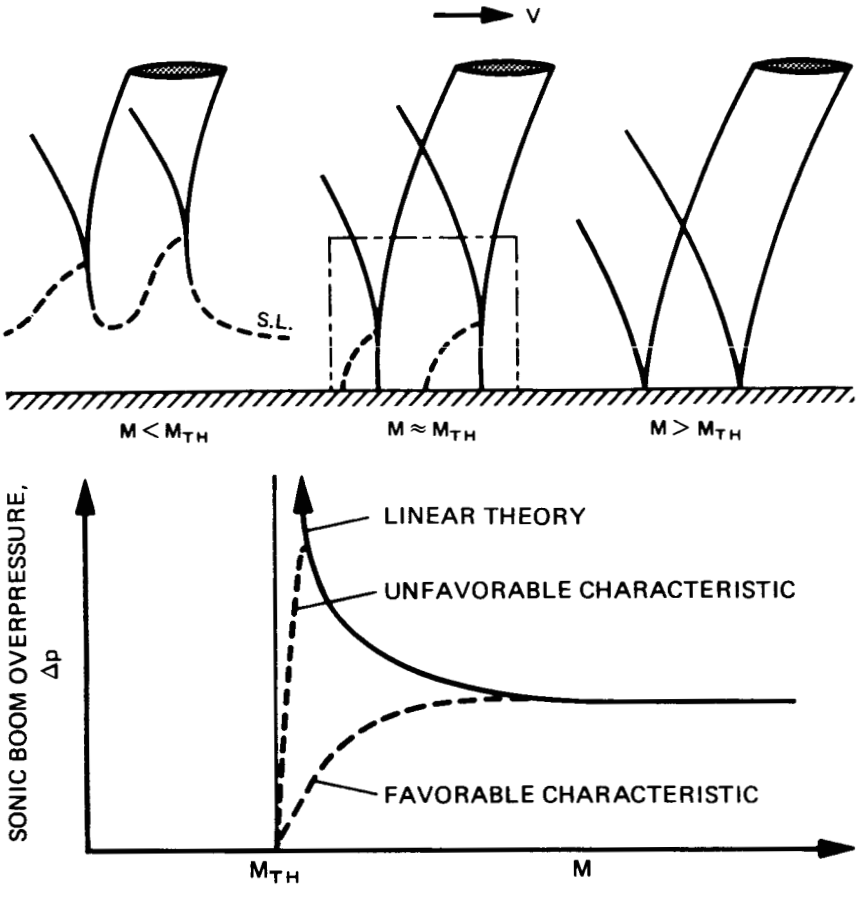

FIGURE 1. – Sonic boom characteristics for flight near the threshold Mach number.

figure 1. It is possible that the overall feasibility of threshold operation may depend on the unknown details of these curves, and it is these details that we propose to investigate by applying the methods of computational fluid dynamics.

FORMULATION

In mathematically modeling a real flow problem, one must make simplifying assumptions. The assumptions pertinent to this investigation are as follows: First, we restrict our attention to a vertical plane of symmetry containing the airplane, for it is in this plane that maximum

sonic boom overpressures occur for aircraft in steady level flight. Second, we consider only a relatively small rectangular region in the vicinity of the ground where the reflection takes place. (See upper center sketch of fig. 1.) We assume that the region is large enough that the incoming or incident wave can be predicted by linear theory. These assumptions appear to be sufficient to reduce the problem to plane or two-dimensional channel flow of a compressible perfect gas.

The physical flow model is depicted in figure 2. The frame of reference has been taken fixed with respect to the airplane, and the flow configuration has been turned upside down from that of figure 1. This has been done strictly for convenience in presenting results. The incoming wave or disturbance is represented by a given flow deflection angle $\theta(x)$ at the lower streamwise boundary of the channel.

The upstream boundary conditions are taken to be uniform steady parallel flow with given velocity and temperature distributions in the y-direction. In addition, gravitational forces are ignored so that the upstream pressure may be assumed constant. The boundary condition at the upper wall is that the normal component of velocity v be zero, while at the lower wall the ratio of this component to the tangential component u is given by the tangent of the local flow deflection angle $\theta(x)$. The dividing streamline is specified by the function $y(x)$, with y' approximately equal to $\tan \theta(x)$ for small disturbances. For the tangential velocity, pressure, and temperature at the two streamwise boundaries, one-sided or inward differencing is used, which is the same as using the so-called reflection principle. These boundary conditions are equivalent to assuming that the normal gradient of the relevant variables at the two walls be zero. At the outflow boundary, a number of extrapolative boundary conditions have been used, the simplest of which is shown in figure 2. It is the simple shift condition in which the values of all flow variables on the outflow boundary are set equal to the values one mesh line in from the boundary. For initial conditions we use an impulsive start, that is, a uniform flow is assumed to exist in the channel initially at which time the incoming disturbance or flow deflection angle is introduced impulsively. The resulting wave system propagates to the upper wall where it is reflected. In discussing results this wall will be referred to as the ground plane.

The governing flow equations and the finite difference scheme used to solve them are discussed here. The flow equations are Euler's inviscid equations expressed in conservation law form. The perfect-gas law is assumed and the total energy e is expressed as a function of pressure, density, and velocity.

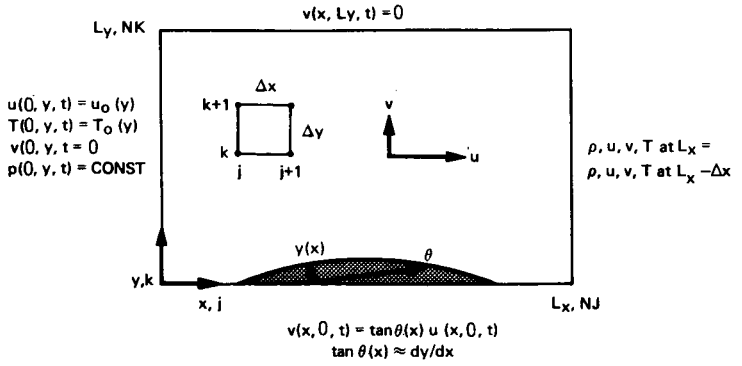

FIGURE 2.—Problem definition.

$$W_t + F_x + G_y = 0$$

where

$$W = \begin{bmatrix} \rho \\ \rho u \\ \rho v \\ e \end{bmatrix}$$

$$F = \begin{bmatrix} \rho u \\ \rho u^2 + p' \\ \rho uv \\ (e+p)u \end{bmatrix}$$

and

$$G = \begin{bmatrix} \rho v \\ \rho uv \\ \rho v^2 + p \\ (e+p)v \end{bmatrix}$$

where

$$p = \rho RT$$

$$e = p/(\gamma - 1) + \rho(u^2 + v^2)/2$$

and

$$W(x, y, t) = W_0(y) + U(x, y, t)$$

In setting up this problem, a perturbation form of the differential equations is actually used in which the flow variables are expressed in terms of perturbations about their constant free-stream values. The result is a modified (but still exact) form of Euler's equations in which all unknown variables are small (assuming the incident disturbance to be small). The procedure avoids differencing two very nearly equal numbers and improves accuracy without resorting to double precision.

$$U(x, y, t) \rightarrow U^n_{j,k};\ t = n\,\Delta t,\ x = j\,\Delta x,\ y = k\,\Delta y$$

$$\bar{U}^{n+1}_{j,k} = U^n_{j,k} - \frac{\Delta t\,(F^n_{j,k} - F^n_{j-1,k})}{\Delta x} - \frac{\Delta t\,(G^n_{j,k+1} - G^n_{j,k})}{\Delta y}$$

$$\bar{U}^{n+2}_{j,k} = \bar{U}^{n+1}_{j,k} - \frac{\Delta t\,(\bar{F}^{n+1}_{j+1,k} - \bar{F}^{n-1}_{j,k})}{\Delta x} - \frac{\Delta t\,(\bar{G}^{n+1}_{j,k} - \bar{G}^{n+1}_{j,k-1})}{\Delta y}$$

$$U^{n+1}_{j,k} = \frac{(U^n_{j,k} + \bar{U}^{n+2}_{j,k})}{2}$$

The second group of equations are the difference equations. They are given by MacCormack in reference 1 and constitute a variant of the second-order two-step Lax-Wendroff scheme described by Richtmeyer in references 2 and 3. In this method the continuous vector function $U(x, y, t)$ is replaced by a net function $U^n_{j,k}$ defined at the net points in space and time with $t = n\Delta t$, $x = j\Delta x$, and $y = k\Delta y$. Assuming a solution at the time step n is known, a conditional solution $\bar{U}^{n+1}_{j,k}$ at $n+1$ using one-sided differences is first found. Using this solution, a conditional solution $\bar{U}^{n+2}_{j,k}$ at $n+2$ is then obtained, reversing the one-sided differencing in j and k. The final solution at the time step $n+1$ is obtained by averaging $U^n_{j,k}$ and $\bar{U}^{n+2}_{j,k}$. We note that this procedure must be modified somewhat if time appears explicitly in the functions F and G or if undifferentiated variables appear in the equations, as happens when curvilinear coordinates are used.

$$D^{n+1}_{j,k} = Q_1(U^n_{j+1,k} - U^n_{j,k}) - Q_2(U^n_{j,k} - U^n_{j-1,k})$$
$$+ R_1(U^n_{j,k+1} - U^n_{j,k}) - R_2(U^n_{j,k} - U^n_{j,k-1})$$

The final expression is an artificial viscosity term, which may be used to smooth or stabilize solutions that otherwise would exhibit undesirable features such as precursor oscillations or overshoots near shocks. The

coefficients in this expression generally are functions of the flow variables U, but in our limited use we have given them relatively small constant values, $O(10^{-2})$. In applications the artificial viscosity term is simply added to $U_{j,k}^{n+1}$ before proceeding to the next time step.

RESULTS

Some preliminary results using the method just described are shown in figures 3 and 4. In figure 3 we compare numerical solutions for a parabolic arc profile with linearized supersonic flow theory. The upstream conditions for this example are uniform isentropic flow at a Mach number $M=\sqrt{2}$. The thickness-to-chord ratio of the disturbing profile is $t/c=0.005$, where t is the maximum value of $y(x)$. The numerical solutions are obtained on the relatively coarse net of $36\times 11=396$ points with mesh ratio $\Delta y/\Delta x=1.0$. The curves, shown in the upper half of the

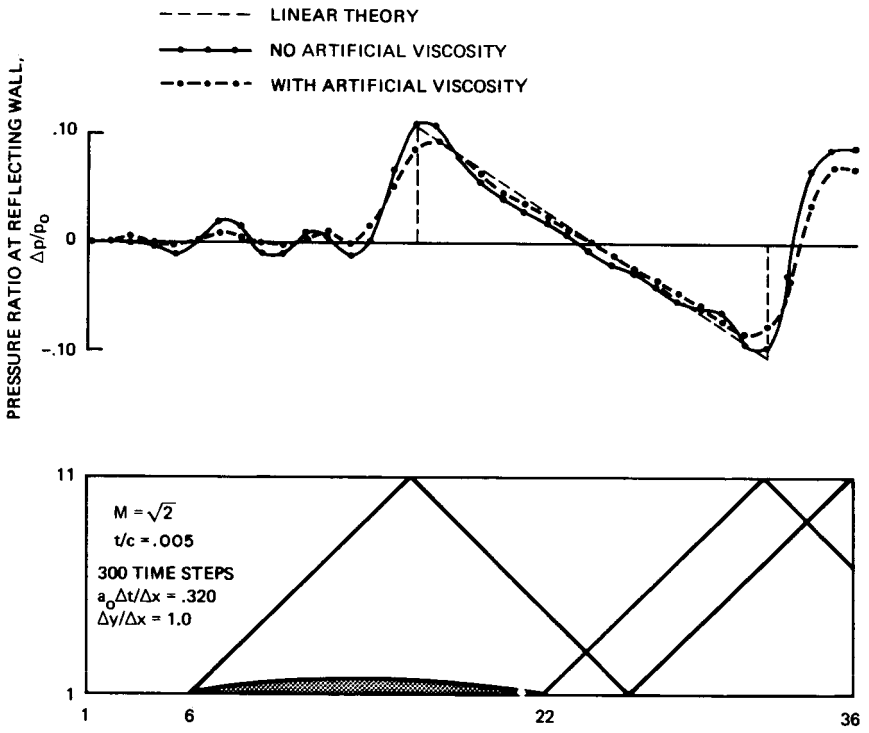

FIGURE 3.—Numerical solution for parabolic arc disturbance at Mach number $\sqrt{2}$.

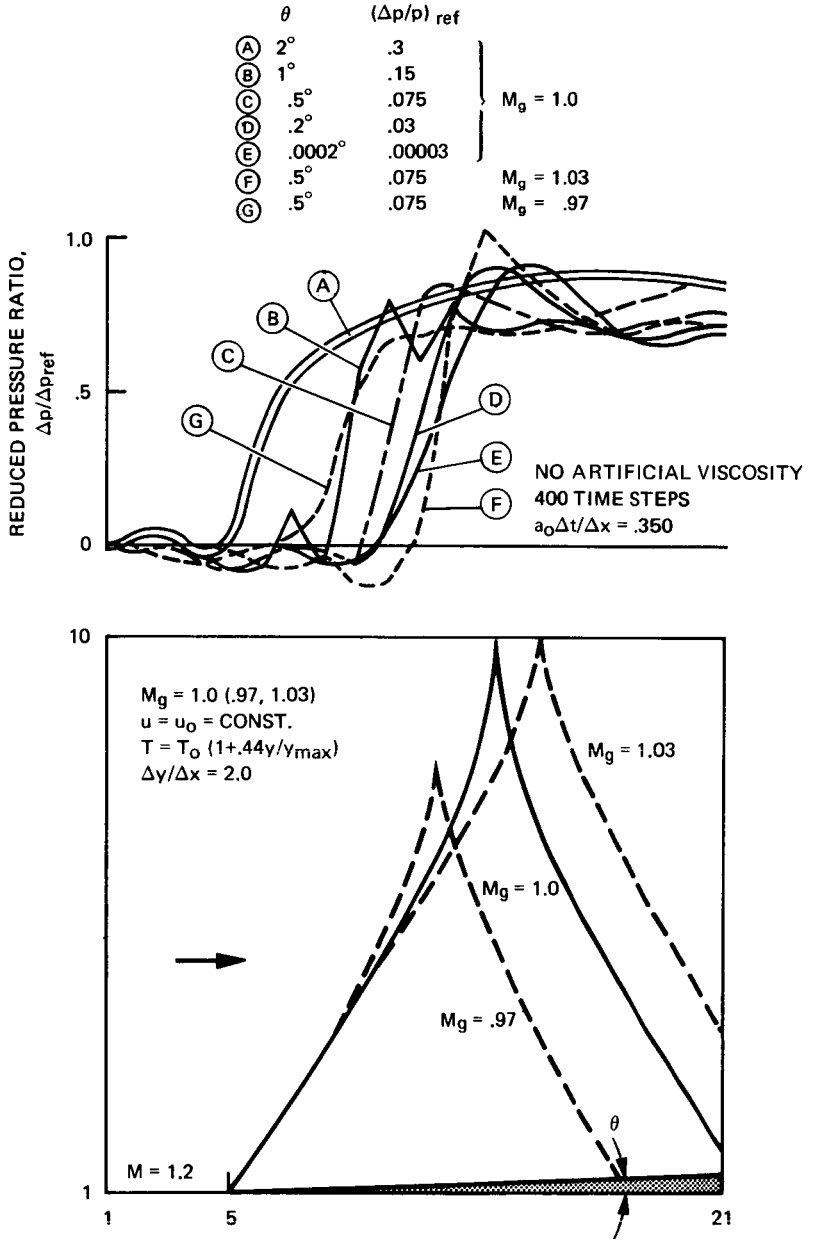

FIGURE 4.—Effects of incident wave intensity and ground Mach number variations on ground pressure signatures.

figure, are for the pressure ratio at the reflecting wall or ground plane. The total number of time steps taken to advance the solutions was 300, and at this time the solutions had essentially converged to their steady-state values. The computing time for each solution was approximately 8 min on an IBM 360–67 computer.

The two numerical solutions shown in figure 3 illustrate some of the difficulties encountered in applying numerical finite-difference methods to flow problems involving discontinuities such as shocks. Consider first the solution for which artificial viscosity was not included (solid curve). In this case, there are relatively large precursor oscillations in front of the bow shock wave that compromise the quality of the solution. These oscillations appear to depend in a complicated way on many factors chosen in the formulation and application of the difference method. A widely used remedy for this difficulty, which avoids numerical experimentation to determine optimal values of parameters (such as $\Delta t/\Delta x$ and $\Delta y/\Delta x$), is the use of artificial viscosity. A typical solution using artificial viscosity is also shown in figure 3 (heavy dashed curve). From this result it can be seen that although the use of artificial viscosity does indeed reduce precursor oscillations and generally smooths solutions, it has the adverse effects of smearing out the shock wave over a larger number of net points (i.e., from two to three points) and reducing the maximum jump of the shock pressure ratio from its true value. From this, it appears that artificial viscosity does not improve solution quality to the extent that would warrant its use, at least in the simple formulation chosen for this investigation.

The second example, shown in figure 4, is a more relevant application to the prediction of sonic boom at threshold Mach numbers. It represents a parametric study of the effects of incident wave intensity and ground Mach number variations on the pressure signature at the ground plane. The physical flow model is illustrated in the lower sketch of figure 4. It consists of a nonuniform upstream flow with a linear temperature gradient adjusted so that the Mach number at the disturbance boundary is 1.2, while at the ground plane it is given the values 1.0, 0.97 and 1.03. The upstream velocity is assumed constant across the channel width, and the mesh ratio is 2.0. The disturbance is assumed to be generated by a simple wedge with angle θ, which is the parameter defining the incident wave intensity. The solid and dashed curves shown in the lower sketch are linearized characteristics of the flow at the three different Mach numbers and identify the theoretical positions of incident and reflected shock waves of vanishingly small intensity.

The numerical solutions for the pressure signature at the ground plane are shown in the upper curves of figure 4. For these solutions, a

reduced pressure ratio is used that is given by the ratio of the computed pressure ratio to a reference pressure ratio proportional to the incident wave intensity or wedge angle. This implies that for waves of very small intensity, the curves for different values of θ should be identical. This in fact was observed in the numerical solutions for θ less than about 0.02°.

The solutions for a ground Mach number $M_g = 1.0$ are shown by the solid curves (with the exception of the curve for $\theta = 0.5°$). No artificial viscosity was used, and the solutions were each advanced 400 time steps. It must be noted that to this state of advancement, the solutions have not yet fully converged to a steady-state condition. The solutions do, however, correspond to the same state in real time because of the constancy of the time step used in each case (i.e., $\Delta t = 0.350\ \Delta x/a_0$, where a_0 is the speed of sound in the undisturbed flow at the lower boundary). Solutions for the case where $\theta = 0.5°$ were continued to 1000 time steps. The solution curves in these cases were practically the same as the one at 400 steps, except for a region four or five net points in from the exit boundary. In this region the solution rose from the values shown in figure 3 to about twice these values and, furthermore, was continuing to rise very slowly. The cause of this slow convergence or drift in solutions at large n is not clear but appears to be due, in part, to a second reflection off the wedge surface of the wave reflected at the ground plane. Another factor is the possibility of improper boundary conditions primarily for subsonic outflows, which will be discussed later.

It should be noted that the quality of solutions in which the incident wave intensity is strong is inferior to the quality of weak wave solutions. This is indicated by the jagged nature of the curve for $\theta = 1°$ in the vicinity of the shock. This jaggedness (in about the same degree) was also observed for the case where $\theta = 2°$. The double-line curve shown for this case represents a faired curve through the actual solution points.

The solutions representing the effect of varying ground Mach number are shown by the dashed curves in figure 4. The solution shown for $M_g = 1.03$ is almost fully converged after 400 time steps; the only difference between this curve and those obtained after 600 steps (up to 1000 steps) is a small and uniform rise of the solution, in the disturbed flow region, of about 10 percent. A more drastic change occurs for the case of subsonic upstream flow at the ground plane; i.e., $M_g = 0.97$. In this case, the solution near the outflow boundary continues to rise slowly as the number of time steps is increased from 400 to 1000. At 1000 time steps, the solution at the outflow boundary has risen to nearly three times the values attained at 400 steps. The shape of the signature upstream of the sharp pressure rise remains essentially the same however.

An additional run, not shown in figure 4, was made for uniform upstream flow at a Mach number of 1.2 with $\theta = 0.5°$. The solution, which was fully converged after 400 time steps, had practically the same appearance and maximum pressure jump as the solution for $M_g = 1.03$, but the location of the jump had shifted downstream.

CONCLUSIONS AND FUTURE RESEARCH PLANS

Because of the tentative and preliminary nature of our results, there are no firm conclusions to be reached concerning sonic boom signatures at threshold Mach numbers. The solutions shown in figure 4 are very crude but indicate some trends to study and difficulties to be overcome in future work. One trend is that there appears to be no substantial change in magnitude of the reduced or relative pressure ratio as the absolute value of the wave intensity is changed, at least at a ground Mach number of unity. The principal effect of increasing wave intensity appears to be an upstream or forward movement of the signature which is known to occur for an irregular or Mach-type reflection with a uniform upstream flow. A second trend is that there does not seem to be a substantial difference in peak overpressures as the ground Mach number is varied from 0.97 to 1.2, which is the prediction of linearized theory. Whether this effect is due to the relatively strong incident wave strength used (i.e., 0.5°), or to the coarseness of the mesh, or to some other cause, remains to be determined. It seems that an essential requirement for the numerical method be that it give reasonable predictions in those cases where linear (or exact) theory is applicable (or nearly applicable); this requirement will be respected in any final results.

One area of considerable concern is the question of boundary conditions, especially at the upstream and downstream ends of the channel. It appears that the conditions used in this investigation are satisfactory in those cases in which the flow is wholly supersonic. In those cases in which the inflow or upstream flow is dominantly supersonic but contains a small region of subsonic flow at the reflecting wall, the solutions appear to be reasonable at least up to the position of the leading pressure wave. However, we have found that flows that are wholly subsonic at the upstream boundary are unstable. Similarly, for flows that are predominantly supersonic at the exit boundary but contain small regions of subsonic flow, the solutions are stable but take a relatively long time to converge (in the region of the exit boundary). For the case in which the outflow contains substantial subsonic regions (i.e., the $M_g = 0.97$ case), the solutions either take an extremely long time to converge (i.e., greater than 1000 time steps) or are ultimately unstable. Clearly, our boundary conditions for subsonic and mixed flows must be improved.

REFERENCES

1. MacCormack, R. W.: The Effect of Viscosity in Hypervelocity Impact Cratering. AIAA Paper no. 69–354, 1969.
2. Richtmeyer, R. D.: A Survey of Difference Methods for Non-Steady Fluid Dynamics. NCAR Technical Note 63–2, National Center for Atmosphere Research, 1963.
3. Richtmeyer, R. D.: Difference Methods for Initial Value Problems. Second ed., Interscience Pubs., Inc., John Wiley & Sons, Inc., 1967.

Experimental Studies of Sonic Boom Phenomena at High Supersonic Mach Numbers

ODELL MORRIS
NASA Langley Research Center

The Langley Research Center has been engaged in research studies dealing with sonic boom generation and propagation phenomena for a number of years. Most of the past studies were concerned with sonic boom overpressures in the low or moderate supersonic Mach number range. For this Mach number range, substantial experimental data have been obtained and have been used to verify and refine current sonic boom estimation techniques (refs. 1 to 3). Results of these studies show existing theoretical methods to be effective in providing reasonably accurate predictions of sonic boom characteristics for Mach numbers up to about 3.0.

However, current interest in hypersonic aircraft configurations has created a need for information about sonic boom characteristics at higher Mach numbers for which, at present, very little experimental data are available. Therefore, several experimental investigations have been conducted in the Langley Unitary Wind Tunnel to obtain sonic boom data over a wider range of Mach numbers. This paper reviews some of the more recent research, which includes wind-tunnel and theoretical studies of a complex configuration in the moderate Mach number range and of simplified basic model shapes at high supersonic Mach numbers. First to be discussed will be results of an investigation of a complex airplane model for a Mach number range from 1.5 to 2.5. Then, results of tests on several slender bodies of revolution at zero lift covering a Mach number range from 1.4 to 4.63 will be presented. Finally, studies on two lifting wing-body models that deal primarily with the high supersonic Mach number range from 2.3 to 4.63 will be presented.

SYMBOLS

A effective cross-sectional area
C_L lift coefficient
h perpendicular distance from model
l model reference length

M Mach number
p reference pressure (free-stream static)
Δp incremental pressure due to flow field of model
Δx distance from bow shock to point on pressure signature measured parallel to free-stream direction
α angle of attack

MODELS AND APPARATUS

Photographs of the models used for the tunnel tests are shown in figure 1. The complex model configuration, shown at the top of the figure, was relatively large with an overall length of 6 in. The two slender bodies of revolution are shown on the left side of the figure; one model had a sharp-nose conical body, and the other model had a relatively blunt-nose body. The simple lifting wing models are shown on the lower right side of the figure. The slender delta-wing model (above) and the double delta-wing model (below) both had a length of 3 in.

The measurement of sonic boom overpressures in the wind tunnel require special tunnel equipment and testing techniques that have been developed and used over a period of years for tests in the moderate Mach number range from about 1.2 to 2.0. Figure 2 shows a sketch of the wind-tunnel apparatus used for the present tests, which is basically the same as previously used except for some modifications that were found necessary for tests in the higher Mach number range. The model is sting supported by a remotely controlled actuator that permits longi-

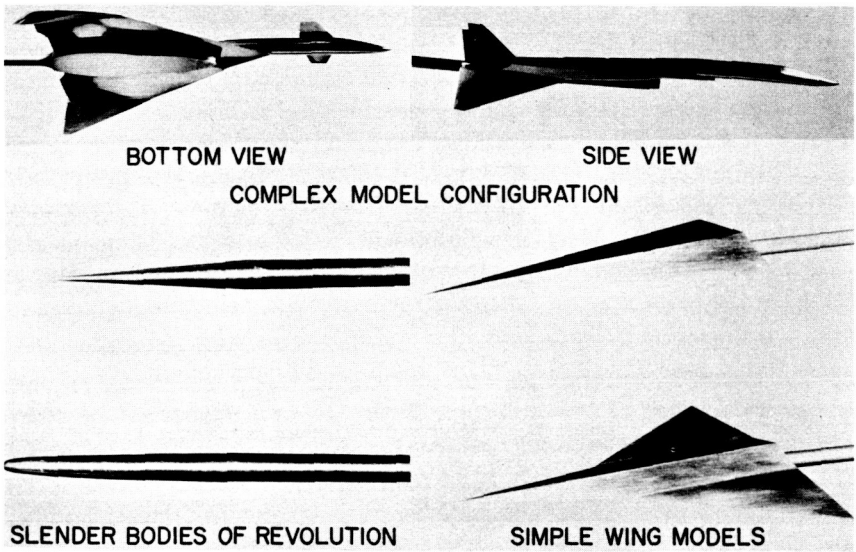

FIGURE 1. – Photographs of models.

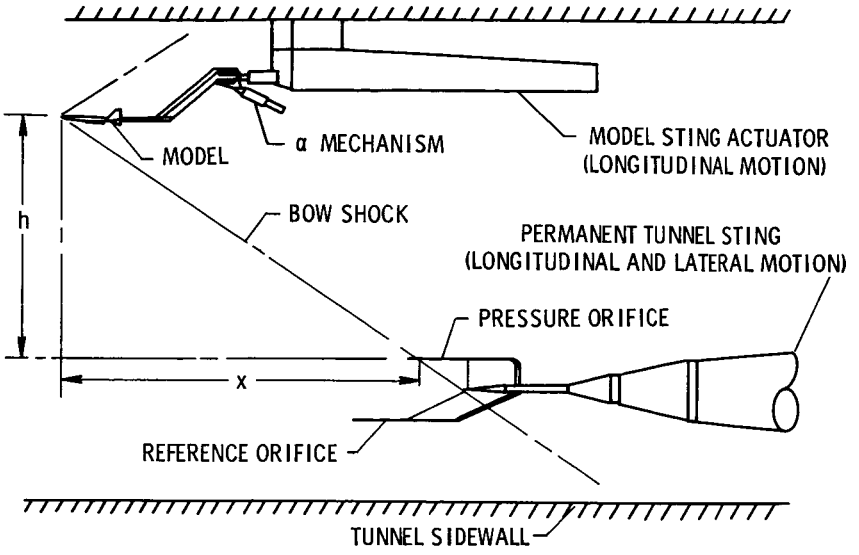

FIGURE 2. — Wind-tunnel apparatus.

tudinal positioning of the model. The α mechanism provides angle-of-attack variation of the model-strut combination. The pressure wave generated by the model is measured by the pressure probe assembly, which is mounted on the permanent tunnel sting. The tunnel sting provides both longitudinal and lateral motion of the pressure probes. This motion coupled with the movement of the model provides for a wide range of survey positions. For the series of tests at high Mach numbers, it was found that the model-mounting equipment, which allowed for the measurement of interference-free sonic boom signatures at the lower Mach number range, would produce interference pressures that tended to blanket out a large portion of the model signature at the high Mach numbers. To separate the model signatures from the pressure field produced by the α mechanism, an offset strut was employed, as shown in figure 2.

For measurement of a particular signature, the probe position is fixed and the model is moved. A complete signature is built up point by point as the model is moved to successive positions. A complete signature usually may require from about 15 to 30 min of tunnel testing time.

THEORETICAL CONSIDERATIONS

For each of the measured wind-tunnel signatures to be shown in the following figures, comparisons have been made with calculated theoretical pressures. The estimation techniques used for these calculations employ a number of machine computing programs that have been in

use for some time at Langley and consequently will be outlined only briefly as illustrated in figure 3. First, the geometry of the model is obtained from the model drawings, and numerical coordinates are used to define the model shape. With these inputs, the wave drag computer program is used to determine the area development of the models defined by supersonic area-rule Mach planes. Then the development of the wing lift is obtained using the wing lift computer program. With these input data, the sonic boom generation program may then be employed to determine theoretical pressure signatures for a given set of model conditions such as Mach number, separation distance, lift coefficient, etc.

The F-function generated by the boom generation may be used as input data for the Hayes propagation program to calculate signatures in a nonuniform atmosphere. This program is quite useful in the prediction of airplane-generated signatures but is not required for the present wind-tunnel tests. A more complete description of these computer techniques is given by Carlson in reference 4.

DISCUSSION

Results of a comparison between the theoretical and experimental sonic boom pressure signatures are shown in figure 4 for a complex configuration at moderate supersonic Mach numbers. The test model

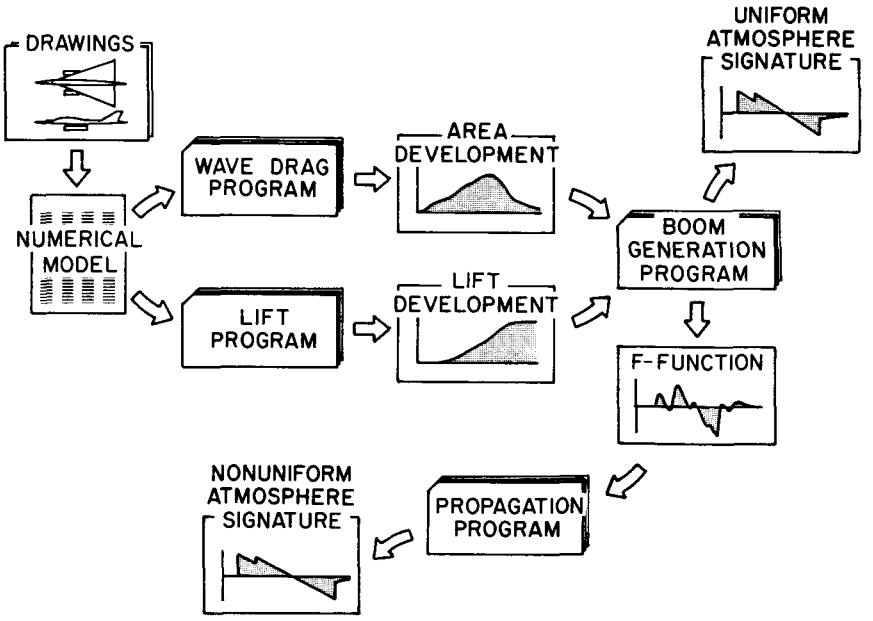

FIGURE 3. — Computer employment in sonic boom analysis.

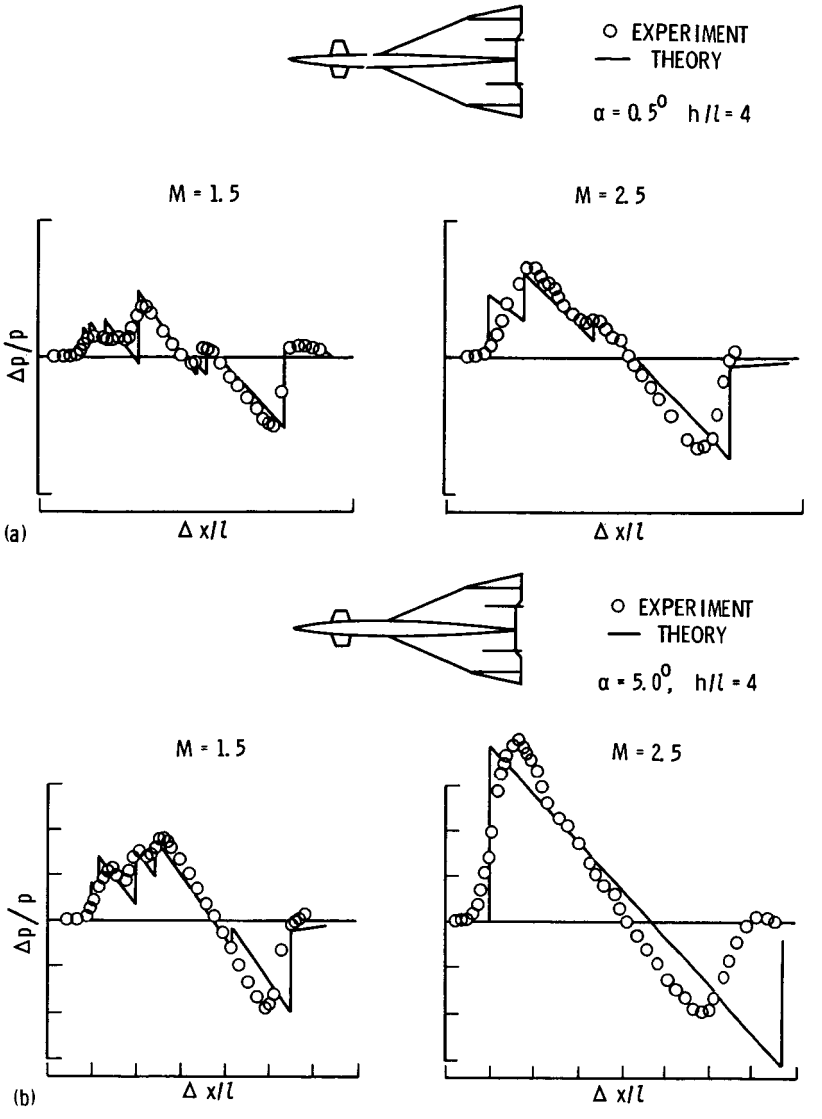

FIGURE 4.—Complex configuration at moderate supersonic Mach numbers. (*a*) Low lift. (*b*) High lift.

was made relatively large to determine whether reasonable correlation could be obtained between the theoretical and experimental results for the near-field sonic boom signatures of a complex model. The model design incorporated a number of details of a large airplane configuration such as wing camber and twist, engine package installation, movable canards, and trailing edge controls.

420-093 O - 71 - 14

Data are shown in figure 4(*a*) for an angle of attack of $\frac{1}{2}°$ and a distance of four body lengths below the model. The signatures are plotted as a function of the pressure ratio $\Delta p/p$ versus the distance ratio $\Delta x/l$ for Mach numbers of 1.5 and 2.5. Comparison of the experiment and theory show very good correlation at $M = 1.5$. For a Mach number of 2.5, the correlation is still reasonably good for the forward part of the signature. Some differences, however, are seen in the region of the tail shock.

Figure 4(*b*) shows the comparison of the model signatures for the high-lift case, in which all conditions are the same for the model, except that the model angle of attack has been increased to 5.0°. For this comparison it can be seen that the characteristic near-field signature shape is still present at $M = 1.5$ with good correlation shown between the measured and the theoretical sonic boom overpressures. At $M = 2.5$, the measured signature is more fully developed and approaches a typical far-field N-shape signature. For this signature, it can be seen that the differences between the experiment and theory are larger, with the greatest difference shown in the region of tail shock. Comparison with signatures obtained even closer to the model shows that the correlation of the theory and experiment improve with increased distance and indicates that good correlation would be expected at large distances comparable to flight altitudes. For this speed range, good correlation between experiment and theory has also been shown in other wind-tunnel tests and in flight-test programs.

As the first step in an extension of the Langley wind-tunnel program to higher supersonic Mach number, tests were conducted on a systematic series of body shapes at zero lift. Figure 5(*a*) shows a comparison of the signatures for one of these models, a sharp nose body of revolution. The test model has a slender, cone-shape body with an area development that is representative of the equivalent body of a supersonic transport configuration for the transonic region of flight. For this model, the signatures were measured at zero lift and at five body lengths below the model. Again the signatures are plotted as a function of the pressure ratio versus the distance ratio for Mach numbers of 1.41, 2.96, and 4.63. At $M = 1.41$, the agreement between the experiment and theory is shown to be very good. This example is typical of the correlation between theory and experiment that has been shown for a number of test models in the low Mach number range from about $M = 1.2$ to $M = 2.0$. However, with the increase in Mach number to 4.63, it can be seen that the theory tends to depart from the measured signatures, with the largest differences shown in the region of the tail shock.

Figure 5(*b*) shows results of the test for a blunt-nose body of revolution for the same Mach number range and separation distance. Even though the theory would not be expected to show good results for a blunt-nose body of this type, agreement with the measured signatures was good at

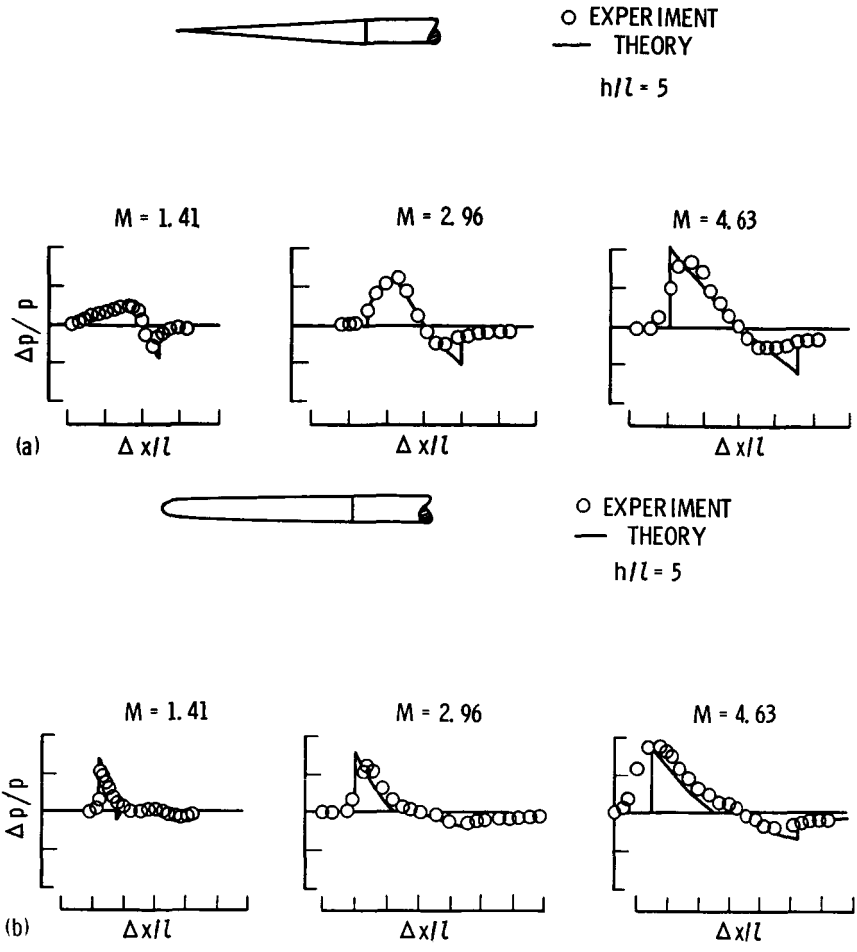

FIGURE 5.—Bodies of revolution for a wide range of supersonic Mach numbers at $\alpha = 0°$. (*a*) Sharp-nose conical body. (*b*) Blunt-nose body.

$M = 1.41$. However, at the higher Mach numbers, larger discrepancies are shown between the theory and experiment, as was previously noted to be the case for the sharp-nose body of revolution. From these signatures it can also be seen that the maximum sonic boom overpressure tend to increase with increasing Mach numbers and that the signature impulse, which is the integrated area under the bow-shock overpressure region, shows an even more pronounced increase in magnitude with increasing Mach number.

As a second step in the extension of the Langley wind-tunnel program to higher supersonic Mach number, tests were performed on two simple wing models at various angles of attack. These tests were conducted to provide experimental data, which would be useful in studying lift-

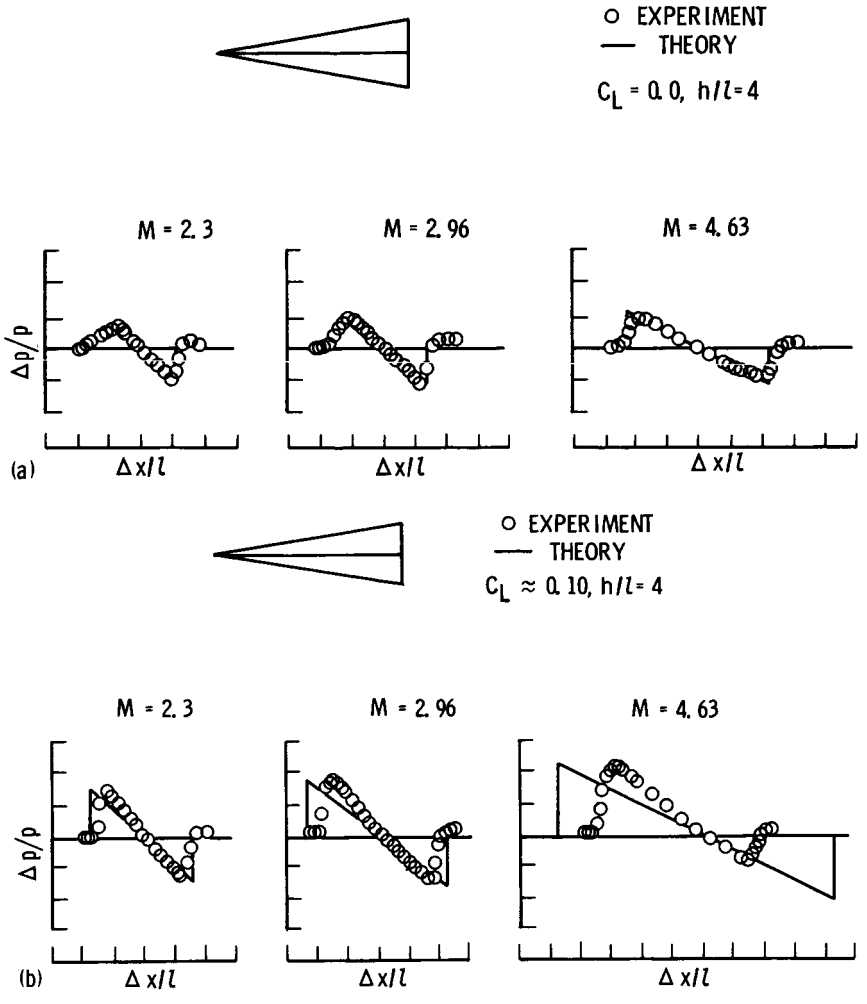

FIGURE 6.—Simple slender delta-wing model at high supersonic Mach numbers. (*a*) Low lift. (*b*) High lift.

induced sonic boom characteristics in the high-Mach-number speed range. Figure 6 shows a sample of the sonic boom measurements for one of these models, the slender delta-wing model. The overall model design was purposely kept simple to facilitate analysis. The delta-wing model had a subsonic wing leading edge with a sweep angle of 80° and an overall length of 3 in. The model was sized and built to accommodate a miniature strain-gage balance for accurate measurement of the model lift. For the sonic boom overpressures presented in figure 6(*a*), the measurements were made for a lift coefficient of zero at four body lengths below the model. The data for the overpressure plots show that reason-

ably good agreement between the experiment and theory is obtained for each Mach number. However, the good correlation shown for this model at low lift does not hold for higher lift conditions.

The signatures of the slender delta wing for high-lift conditions are shown in figure 6(*b*). For these plots, everything is the same as shown before, except that the model angle of attack was increased to about 7° to obtain a lift coefficient of 0.10. For these sonic boom signatures, it is seen that the theory predicts the signature shape fairly well at $M = 2.30$, but as the Mach number is increased to $M = 4.63$, the agreement between theory and experiment becomes progressively worse. However, in spite of the large differences in signature shape, the maximum values of sonic boom overpressures are predicted very well by the theory.

A sample of data for the second model in this test series, a simple double delta wing, is shown in figure 7. This model had the same overall length as the slender delta-wing model but had a larger wing area with considerably more volume. The wing had a supersonic wing leading edge on the outer panel (a sweep angle of 60°). Signatures are shown for a lift coefficient of zero at four body lengths below the model in figure 7(*a*). For this model, it can be seen that the agreement between the theory and experiment is not as good as shown for the slender delta wing, and the agreement tends to become poorer with increasing Mach number.

Figure 7(*b*) presents data for the double delta wing for the high-lift case. For these overpressure signatures, the lift coefficient was approximately 0.10. For this comparison, large differences are shown between the theory and experiment, particularly at $M = 4.63$, where it can be seen that the theory does not adequately describe the signature shape. For this signature, not only is there a large difference in the shape of the pressure decline in positive pressure region, but there is an appreciable discrepancy in the signature positive area. There are several possible reasons why the theoretical estimate shown for this model tends to break down at $M = 4.63$ for high lift. First, the model has a low fineness ratio. Then, the equivalent body fineness ratio is reduced even further for lifting conditions. As a result, for the close-in position shown here, the model-induced pressure variations are about 10 percent of the ambient pressure, a magnitude that may be too large to meet the small-disturbance assumptions of linearized theory. At larger distances, some improvement in correlation might be expected as the overall pressure field disturbances become weaker and as the large distance approximations of the theory become more applicable. However, in any case, the results indicate shortcomings in the present theory for the high Mach number range at lifting conditions and suggest that further study is needed in this area.

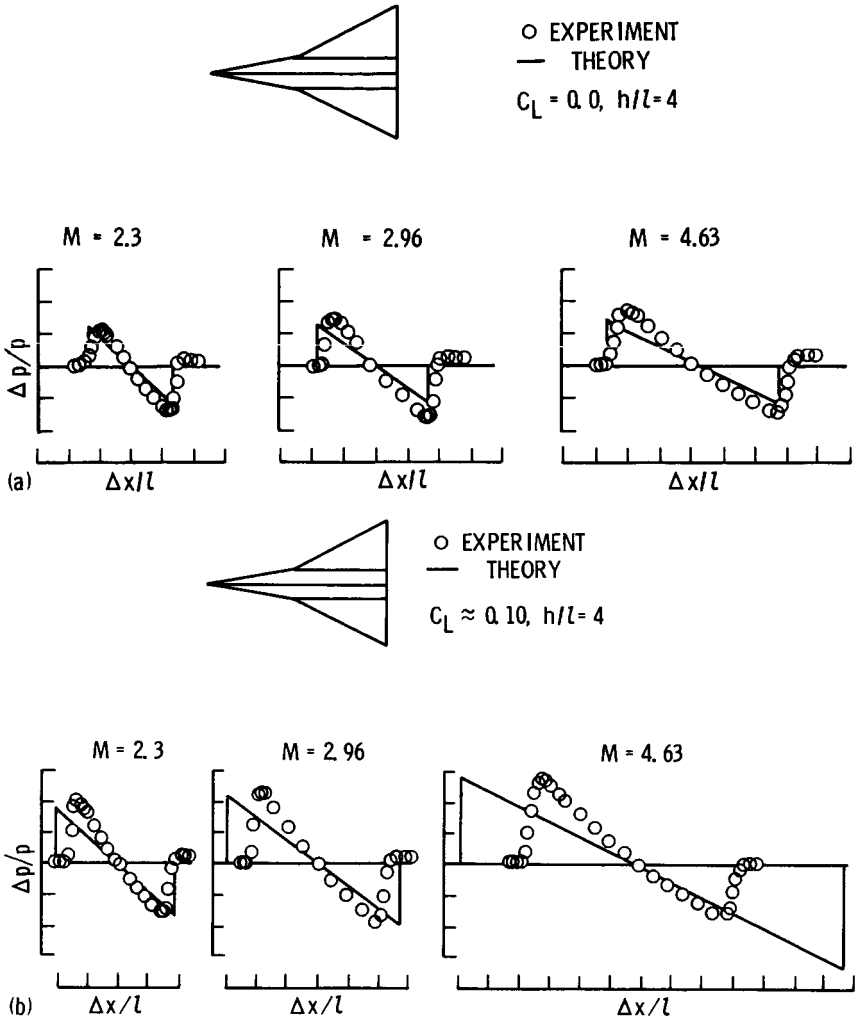

FIGURE 7.—Simple double delta-wing model at high supersonic Mach numbers. (*a*) Low lift. (*b*) High lift.

CONCLUDING REMARKS

In summary, results of recent sonic boom wind-tunnel studies have been reviewed for several model configurations over a wide Mach number range. Comparisons of experimental and theoretical pressure signatures calculated by use of techniques derived from the work of Whitham and Hayes show good agreement for the complex airplane model configuration as well as for the simple body shapes in the lower Mach number and lower lift range. However, results of the high-Mach-number tests for

the simple body and wing model configurations show that the theoretical methods for predicting the pressure signatures appear to be only qualitatively correct at the high Mach numbers. In general, it is shown that the agreement between theory and experiment decreases with both increasing Mach number and increasing lift coefficient, and it is indicated that further research is needed in this area.

REFERENCES

1. CARLSON, HARRY W.: Correlation of Sonic-Boom Theory With Wind-Tunnel and Flight Measurements. NASA TR R–213, 1964.
2. CARLSON, HARRY W.; MACK, ROBERT J.; AND MORRIS, ODELL A.: A Wind Tunnel Investigation of the Effect of Body Shape on Sonic-Boom Pressure Distributions. NASA TN D–3106, 1965.
3. CARLSON, HARRY W.; MCLEAN, F. EDWARD; AND SHROUT, BARRETT L.: A Wind-Tunnel Study of Sonic-Boom Characteristics for Basic and Modified Models of a Supersonic Transport Configuration. NASA TM X–1236, 1966.
4. CARLSON, HARRY W.: Experimental and Analytic Research On Sonic Boom Generation at NASA. Sonic Boom Research, NASA SP–147, 1967, pp. 9–23.

Extrapolation of Wind-Tunnel Sonic Boom Signatures Without Use of a Whitham *F*-Function

CHARLES L. THOMAS
NASA Ames Research Center

Use of the wind tunnel to predict sonic boom characteristics of airplane configurations began at Langley Research Center about 10 yr ago. Most of the early work in this field was done by Carlson and Morris (refs. 1 to 8). The first method used tested very small models in fairly large tunnels so that far-field signatures could be obtained in the wind tunnel. Then, with the use of Whitham's far-field theory, sonic boom signatures at greater distances could be predicted. In 1967, a method was devised by Hicks and Mendoza (ref. 9) for extrapolating near-field wind-tunnel signatures out to the far field. The near-field signature is used to obtain a Whitham F-function, which is then used to obtain signatures at greater distances. The near-field extrapolation method eliminated the requirement for very small models. Sharper experimental signatures are possible with larger models because of the reduced effect of model vibration. Also, with larger models, lift coefficients can be measured directly with an internal balance, rather than estimated from model angle of attack. The F-function extrapolation method also has the advantage that signatures are measured in the near field where the pressure disturbance is stronger and therefore easier to measure. The main restriction on use of the Whitham theory in extrapolation of sonic boom signatures is that steady flight in a uniform atmosphere without winds is assumed. A uniform-atmosphere extrapolation can be corrected to account for the atmospheric temperature, pressure, and wind gradients by the use of an atmospheric correction factor (refs. 10 and 11). However, an atmospheric correction factor only adjusts the amplitude of the wave and does not account for the effect that the atmosphere has in determining the amount of nonlinear waveform distortion that occurs. A better method to account for atmospheric effects is the "age variable" method. This approach has been used in a sonic boom computer program developed by Hayes, Haefeli, and Kulsrud (ref. 12). The age variable, which is calculated from the atmospheric properties, is used to determine the amount that an F-function is skewed before applying the area balancing technique for locating shocks. The age variable method accounts for

the atmospheric effects on both the waveform shape and waveform amplitude.

In this paper a method is presented for extrapolating near-field signatures out to the far field, without use of an F-function to account for nonlinear waveform distortion. Effects of aircraft acceleration and atmospheric temperature, pressure, and wind gradients are included in the theory. The approach used is to describe the waveform of the sonic boom wave by several waveform parameters and then to obtain equations for the parameters as functions of time. This approach has the advantages that (1) the theory is simpler and more intuitive than the Whitham theory, (2) it provides a more convenient method for extrapolating experimental signatures because the signature is dealt with directly, rather than through the use of an F-function, and (3) shock locations are determined by a much neater method than the classical area balancing technique used in F-function extrapolations.

THE WAVEFORM PARAMETERS

To describe the waveform of the sonic boom wave at any instant of time, we approximate the waveform by an arbitrary number of linear segments and define the waveform parameters Δp_i, m_i, and λ_i of each segment as follows: Δp_i is the pressure rise across the shock at the juncture of segments i and $i-1$. Often there will be no shock at the juncture, in which case Δp_i is zero. m_i is the slope of segment i, which may be positive or negative. Finally, λ_i is the length of segment i. A completely general waveform can be described using these waveform parameters.

To determine the waveform parameters as functions of time, it is assumed that the time rate of change of any waveform parameter can be obtained by superposition of the rate of change assuming the wave propagates as a linear, nonplane wave and the rate of change assuming the wave propagates as a nonlinear, plane wave; that is, for example

$$\left(\frac{d\Delta p_i}{dt}\right)_{\substack{\text{nonlinear}\\\text{nonplane}}} = \left(\frac{d\Delta p_i}{dt}\right)_{\substack{\text{linear}\\\text{nonplane}}} + \left(\frac{d\Delta p_i}{dt}\right)_{\substack{\text{nonlinear}\\\text{plane}}}$$

The linear wave term accounts for the effects of changing ray tube area and changing atmospheric properties. The nonlinear, plane wave term, which is also influenced by the atmospheric properties, accounts for the nonlinear distortion of the waveform.

THE LINEAR, NONPLANE WAVE

The waveform parameter rates of change for a linear, nonplane wave propagating through a nonuniform atmosphere with winds are determined

from conservation of the Blokhintsev energy invariant (ref. 13, eq. (1.12)), which states

$$\frac{p^2 c_n^2 A}{\rho_0 a_0^3} = \text{constant along a ray tube}$$

and also from (ref. 13, eq. (3.9))

$$\frac{\lambda_i}{c_n} = \text{constant along a ray tube}$$

where, in the above two equations:

p = acoustic pressure
ρ_0 = ambient density
a_0 = ambient sound speed
$c_n = a_0 + \mathbf{V}_0 \cdot \mathbf{N}$
$\mathbf{V}_0$ = wind velocity
$\mathbf{N}$ = wavefront unit normal
A = ray tube area as cut by the wavefront

It can easily be shown from the conservation of the above quantities that

$$\frac{dm_i}{dt} = \frac{m_i}{2}\left[\frac{3}{a_0}\frac{da_0}{dt} + \frac{1}{\rho_0}\frac{d\rho_0}{dt} - \frac{4}{c_n}\frac{dc_n}{dt} - \frac{1}{A}\frac{dA}{dt}\right]$$

$$\frac{d\Delta p_i}{dt} = \frac{\Delta p_i}{2}\left[\frac{3}{a_0}\frac{da_0}{dt} + \frac{1}{\rho_0}\frac{d\rho_0}{dt} - \frac{2}{c_n}\frac{dc_n}{dt} - \frac{1}{A}\frac{dA}{dt}\right]$$

$$\frac{d\lambda_i}{dt} = \frac{\lambda_i}{c_n}\frac{dc_n}{dt}$$

where the fractional rates of change of the ambient properties a_0, ρ_0, and c_n and of the ray tube area A are understood to be the rates of change as seen by an observer moving down the ray tube with the wave.

THE NONLINEAR, PLANE WAVE

The waveform parameter rates of change for a nonlinear, plane wave are determined from the assumption that the wave propagates as a finite-amplitude, isentropic wave. This is a valid assumption because the shocks in a sonic boom wave are very weak. The propagation speed of each point of the wave is therefore $u + a$, where u is the local fluid particle speed (+ means in the direction of propagation) and a is the local sound speed. A shock propagates at a speed equal to its average value of $u + a$. It can be shown that

$$u + a = a_0\left(1 + \frac{\gamma + 1}{2\gamma}\frac{p}{p_0}\right)$$

where p_0 is the ambient pressure. Using these results, the waveform parameter rates of change for a nonlinear, plane wave can be shown by the following expressions:

$$\frac{dm_i}{dt} = km_i^2$$

$$\frac{d\Delta p_i}{dt} = \frac{1}{2} k\Delta p_i(m_i + m_{i-1})$$

$$\frac{d\lambda_i}{dt} = -\frac{1}{2} k(\Delta p_i + \Delta p_{i+1}) - km_i\lambda_i$$

where

$$k = \frac{\gamma+1}{2\gamma} \frac{a_0}{p_0}$$

The effect of the atmosphere enters the above equations in the parameter k. As the sonic boom wave propagates down through the atmosphere, p_0 increases and, therefore, k decreases. This causes a reduction in the rate of nonlinear waveform distortion. As a result, shocks do not coalesce as rapidly and signatures do not lengthen as rapidly as predicted by uniform-atmosphere extrapolations.

THE NONLINEAR, NONPLANE WAVE

The expressions obtained in the last two sections are now combined to obtain the parameter rates of change for a nonlinear, nonplane wave. The following equations describe the waveform deformation of the sonic boom wave.

$$\frac{dm_i}{dt} = km_i^2 + c_1 m_i$$

$$\frac{d\Delta p_i}{dt} = \frac{1}{2} k\ \Delta p_i\ (m_i + m_{i-1}) + c_2\ \Delta p_i$$

$$\frac{d\lambda_i}{dt} = -\frac{1}{2} k(\Delta p_i + \Delta p_{i+1}) - km_i\lambda_i + c_3\lambda_i$$

where

$$c_1 = \frac{1}{2}\left(\frac{3}{a_0}\frac{da_0}{dt} + \frac{1}{\rho_0}\frac{d\rho_0}{dt} - \frac{4}{c_n}\frac{dc_n}{dt} - \frac{1}{A}\frac{dA}{dt}\right)$$

$$c_2 = c_1 + \frac{1}{c_n}\frac{dc_n}{dt}$$

$$c_3 = \frac{1}{c_n}\frac{dc_n}{dt}$$

$$k = \frac{\gamma+1}{2\gamma}\frac{a_0}{p_0}$$

In these equations, the waveform parameters are understood to correspond to a waveform defined perpendicular to the wavefront. To solve these equations, the quantities c_1, c_2, c_3, and k will be assumed to be constant over small time increments. The first step in the solution of these equations is therefore to determine the values of c_1, c_2, c_3, and k at many points along the ray path.

RAY-PATH CALCULATION

If the atmospheric properties, namely the temperature or sound speed, the winds in the x-direction, and the winds in the y-direction, are given, all as functions of altitude, then the ray path vector $\mathbf{R}(I)$, defined in figure 1, and the wavefront unit normal vector $\mathbf{N}(I)$ can be determined from the following set of equations:

$$\mathbf{R}(I+1) = \mathbf{R}(I) + \Delta\mathbf{R}(I)$$

$$\mathbf{N}(I+1) = \mathbf{N}(I) + \Delta\mathbf{N}(I)$$

$$\Delta\mathbf{R}(I) = [a_0(I)\mathbf{N}(I) + \mathbf{V}_0(I)]\Delta t$$

$$\begin{bmatrix}\Delta N_1(I)\\ \Delta N_2(I)\\ \Delta N_3(I)\end{bmatrix} = F(I)\begin{bmatrix}N_1(I)N_3(I)\\ N_2(I)N_3(I)\\ -N_1^2(I)-N_2^2(I)\end{bmatrix}\Delta t$$

$$F(I) = N_1(I)\frac{dV_{0_1}}{dz}(I) + N_2(I)\frac{dV_{0_2}}{dz}(I) + \frac{da_0}{dz}(I)$$

where Δt is the time increment between points, which is chosen. The derivation of this expression for the three components of $\Delta\mathbf{N}(I)$ is based upon the assumption that the time rate of change of the wavefront unit normal $\mathbf{N}$ is equal to the component of $\nabla(-a_0 - \mathbf{V}_0\cdot\mathbf{N})$ perpendicular to $\mathbf{N}$. Using this procedure one can calculate as many points as necessary along the ray path, and at each point, the value of k and the fractional rates of change of the ambient properties a_0, p_0, and c_n can be determined.

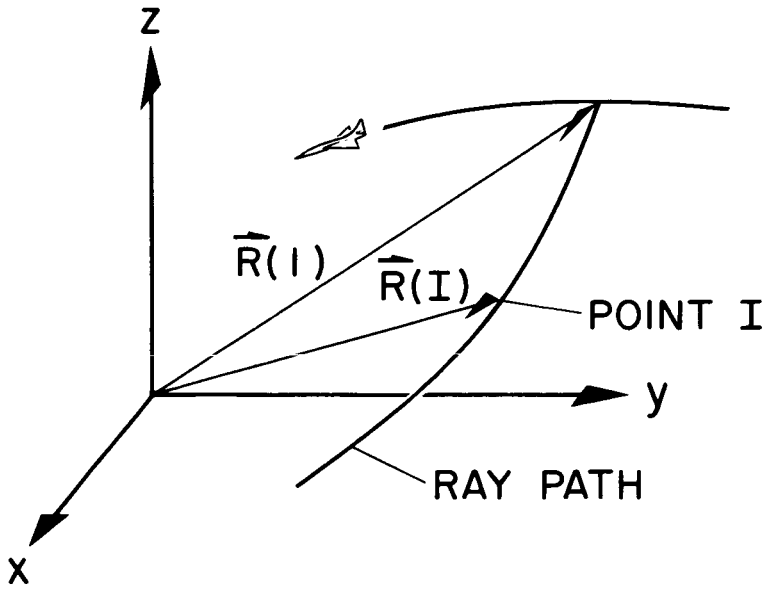

FIGURE 1. – Definition of the ray path vector.

RAY TUBE AREA CALCULATION

The quantities c_1 and c_2 depend upon the fractional rate of change of ray tube area. The ray tube is defined by four rays. Ray 1 emanates from the flightpath at time t with azimuth angle ϕ. The azimuth angle is defined to be the angle between the vertical plane through $\mathbf{V}$ (the velocity of the aircraft relative to the air) and the plane that passes through both $\mathbf{N}(1)$ and $\mathbf{V}$. Ray 2 is defined by $(t, \phi + d\phi)$, ray 3 by $(t + dt, \phi)$, and ray 4 by $(t + dt, \phi + d\phi)$. The ray tube will have a cross section that is very nearly a parallelogram, and therefore the ray tube area is determined by any three rays. To determine points along ray 2 and ray 3, points along ray 1 being known, the assumption is made that all rays which compose an infinitesimal ray tube are essentially the same spatial curve; therefore, if one ray is known, any other ray can be obtained by a simple translation and rotation of the known ray. Let ray 1 be the known ray. For each point on ray 1, there corresponds a point on ray 2 and a point on ray 3, as determined by the translation and rotation of ray 1. If $\mathbf{L}_1$ is a vector that joins corresponding points on rays 1 and 3 and $\mathbf{L}_2$ is a vector that joins corresponding points on rays 1 and 2, then the ray tube area at point I, as cut by the wavefront, can be calculated from

$$A(I) = \frac{\mathbf{L}_1(I) \times \mathbf{L}_2(I) \cdot \Delta\mathbf{R}(I)}{\Delta\mathbf{R}(I) \cdot \mathbf{N}(I)}$$

where

$$\mathbf{L}_1(I) = \mathbf{V}_r + \mathbf{V}_{of} + \dot{\psi}\mathbf{D}(I) \times \mathbf{k} + \frac{\dot{\gamma}(\mathbf{V} \times \mathbf{k}) \times \mathbf{D}(I)}{|\mathbf{V} \times \mathbf{k}|} + \frac{\dot{M}}{M\sqrt{M^2-1}} \frac{[\mathbf{V} \times \mathbf{N}(1)] \times \mathbf{D}(I)}{|\mathbf{V} \times \mathbf{N}(1)|}$$

$$\mathbf{L}_2(I) = (\mathbf{k} + F[\Delta\mathbf{R}(1) \times \mathbf{k}]) \times \mathbf{D}(I)$$

$$\mathbf{D}(I) = \mathbf{R}(I) - \mathbf{R}(1)$$

$$F = \frac{[\mathbf{V} \times \mathbf{N}(1)]_3}{[\mathbf{V} \times \mathbf{N}(1)]_2 \Delta R_1(1) - [\mathbf{V} \times \mathbf{N}(1)]_1 \Delta R_2(1)}$$

$$\mathbf{V}_r = \mathbf{V} - \frac{V_3 \Delta\mathbf{R}(1)}{\Delta R_3(1)}$$

$\mathbf{V}$ = aircraft velocity (relative to air)

The first two terms of $\mathbf{L}_1(I)$ correspond to a horizontal translation of ray 1. The other three terms of $\mathbf{L}_1(I)$ are aircraft acceleration terms, which correspond to rotations of ray 1. The aircraft acceleration is specified by $\dot{\gamma}$, $\dot{\psi}$, and $\dot{M}$, where $\dot{\gamma}$ is the rate of change of flightpath angle in radians per unit of time; $\dot{\psi}$ is the rate of change of heading, or turning rate, also in radians per unit of time; and $\dot{M}$ is the rate of change of Mach number. The vector $\mathbf{L}_2(I)$ is due solely to rotation of ray 1. The rotation is chosen so that if ray 1 lies in a vertical plane, as it does in an atmosphere without winds, then ray 2 will also lie in a vertical plane.

It is felt that this relatively simple-minded approach for determining the fractional rate of change of ray tube area along a ray path provides a good approximation to what is predicted using more elegant methods, especially when the ray tube lies nearly beneath the flightpath. Extrapolations of N-waves through a standard atmosphere for flight Mach numbers between 1.2 and 3 have been found to agree within about 2 percent of what is predicted using the atmospheric correction factor of Kane and Palmer (ref. 11) indicating that ray tube areas provided by the above method are quite satisfactory, at least in the simple case of steady flight in an atmosphere without winds.

It should be pointed out that the method being employed to obtain solutions for the waveform parameters is not dependent upon use of the above ray tube area calculation method. Other ray tube area calculation methods may be used.

SOLUTION OF THE WAVEFORM DEFORMATION EQUATIONS

With the fractional rates of change of the ambient properties and of the ray tube area determined by the methods discussed in the last two sections, or by any other methods, the values of c_1, c_2, c_3, and k are now known at all points along the ray path. Assuming c_1, c_2, c_3, and k are constant between points, the waveform deformation equations can now be solved in closed form. The solutions are found to be

$$m_i = \frac{m_i^\circ e^{c_1 \Delta t}}{1 - k m_i^\circ T}$$

$$\Delta p_i = \Delta p_i^\circ e^{c_2 \Delta t} [(1 - k m_i^\circ T)(1 - k m_{i-1}^\circ T)]^{-1/2}$$

$$\lambda_i = e^{c_3 \Delta t}[1 - k m_i^\circ T] \left[\lambda_i^\circ - \frac{\Delta p_i^\circ}{m_i^\circ - m_{i-1}^\circ} \left(\sqrt{\frac{1 - k m_{i-1}^\circ T}{1 - k m_i^\circ T}} - 1 \right) - \frac{\Delta p_{i+1}^\circ}{m_i^\circ - m_{i+1}^\circ} \left(\sqrt{\frac{1 - k m_{i+1}^\circ T}{1 - k m_i^\circ T}} - 1 \right) \right]$$

where

$$T = \frac{e^{c_1 \Delta t} - 1}{c_1}$$

The above solutions for m_i, Δp_i, and λ_i are used to determine the values of the waveform parameters at some point on the ray path, given m_i°, Δp_i°, and λ_i°, which are the values of the parameters at the preceding point. The waveform at any point of interest along the ray path can now be determined, if the waveform near the aircraft is known.

The above expressions for the waveform parameters are valid only as long as all the λ_i's remain greater than zero. When one of the λ_i's does go to zero somewhere between two points on the ray path, which is often the case, the above expression for λ_i can be used to determine the value of Δt at which it goes to zero. The waveform parameters are then incremented using this value of Δt. The waveform segment that goes to zero is replaced by a shock, and then the waveform parameters can be incremented the rest of the way to the next point on the ray path.

The above expression for λ_i cannot be used when $m_i^\circ = m_{i-1}^\circ$ or when $m_i^\circ = m_{i+1}^\circ$. In the case when $m_i^\circ = m_{i-1}^\circ$ or, in general, when

$$\left| \frac{k(m_i^\circ - m_{i-1}^\circ)T}{1 - k m_i^\circ T} \right| < 0.001$$

we can use the approximation

$$\frac{\Delta p_i^\circ}{m_i^\circ - m_{i-1}^\circ} \left(\sqrt{\frac{1 - k m_{i-1}^\circ T}{1 - k m_i^\circ T}} - 1 \right) \approx \frac{\Delta p_i}{2} \frac{kT}{1 - k m_i^\circ T}$$

A similar expression can be obtained when $m_i^\circ = m_{i+1}^\circ$.

Consider now the special case of steady flight in a uniform atmosphere without winds. In this case, c_3 is zero and c_1 and c_2 are just equal to $\frac{-1}{2r}\frac{dr}{dt}$, where r is the distance from the flightpath. In this case the waveform deformation equations can be written with r as the independent variable rather than time and then can easily be integrated to obtain the following closed-form solutions for the waveform parameters:

$$m_i = \frac{m_i^\circ}{(R+1)(1-km_i^\circ R)}$$

$$\Delta p_i = \frac{\Delta p_i^\circ}{(R+1)[(1-km_i^\circ R)(1-km_{i-1}^\circ R)]^{1/2}}$$

$$\lambda_i = [1-km_i^\circ R]\left[\lambda_i^\circ - \frac{\Delta p_i^\circ}{m_i^\circ - m_{i-1}^\circ}\left(\sqrt{\frac{1-km_{i-1}^\circ R}{1-km_i^\circ R}}-1\right) - \frac{\Delta p_{i+1}^\circ}{m_i^\circ - m_{i+1}^\circ}\left(\sqrt{\frac{1-km_{i+1}^\circ R}{1-km_i^\circ R}}-1\right)\right]$$

where

$$R = \sqrt{\frac{r}{r_0}} - 1$$

$$k = \frac{(1+\gamma)M^2 r_0}{\gamma(M^2-1)^{1/2} p_0}$$

In the above equations m_i°, Δp_i°, and λ_i° are the values of the waveform parameters at $r = r_0$. Also, the waveform parameters are now assumed to correspond to waveforms defined at constant r, rather than normal to the wavefront. The above expressions for the waveform parameters are valid only as long as all the λ_i's remain greater than zero. When some of the λ_i's do go to zero, which is the usual case, the above expression for λ_i can be used to determine the value of r at which the first λ_i goes to zero, and then the initial waveform parameters can be redefined to be those at that value of r. Extrapolations of near-field signatures using the above uniform atmosphere expressions have been found to agree exactly with extrapolations using the Whitham F-function method of reference 9, indicating that the two methods are actually equivalent.

The waveform deformation equations can also be solved in closed form for plane waves and spherical waves propagating in a uniform medium by letting $\frac{1}{A}\frac{dA}{dt}$ equal zero and $\frac{2}{r}\frac{dr}{dt}$, respectively.

420-093 O - 71 - 15

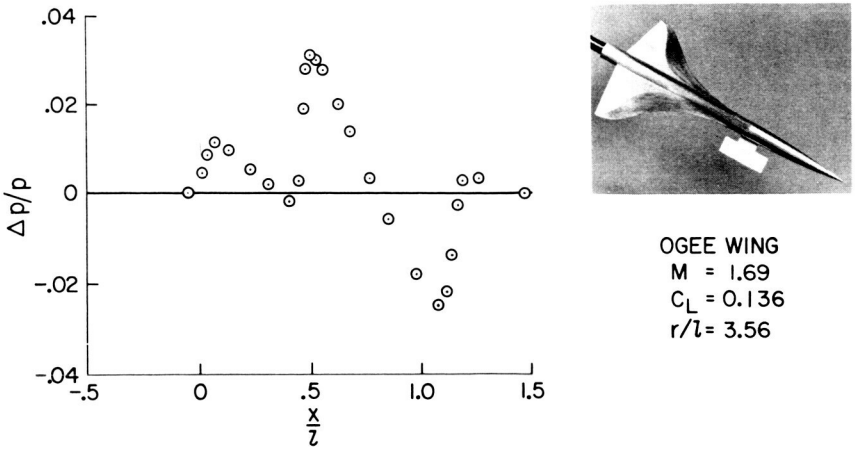

FIGURE 2. – Near-field pressure signature for the ogee wing.

APPLICATION OF THE THEORY

An extrapolation program, based upon the theory presented in this paper, has been used to investigate the effect of the atmospheric gradients on the propagation of the sonic boom wave. The experimental near-field signature that has been extrapolated is shown in figure 2. This signature was extrapolated through a standard atmosphere without winds. The aircraft was assumed to be in steady flight at a constant altitude of 60 000 ft. The results of this extrapolation are shown in figures 3 and 4. Figure 3 shows the effect of the atmospheric gradients on the rate of coalescence of the front shock and wing shock. It is seen that the effect of the atmosphere is to reduce the rate of coalescence over what is predicted by extrapolation in a uniform atmosphere. The uniform-atmosphere extrapolation predicts that the two shocks will run together at an altitude of about 31 000 ft, whereas the standard-atmosphere extrapolation shows that the two shocks are still slightly apart at the ground. This reduction in the nonlinear waveform distortion also affects the wavelength of the entire signature, which as a result increases less rapidly in the standard atmosphere than in a uniform atmosphere. The signature wavelength at the ground turns out to be about 21 percent longer in the uniform atmosphere. It is seen from the results of figure 3 that predictions of the waveform shape at the ground using the atmospheric correction factor approach will normally be incorrect. However, as it turns out, the amplitude of the waveform at the ground, as predicted with an atmospheric correction factor, is usually fairly good.

Figure 4 shows the effect of the atmospheric gradients on the amplitude of the wave. Below about 35 000 ft in the standard atmosphere, the

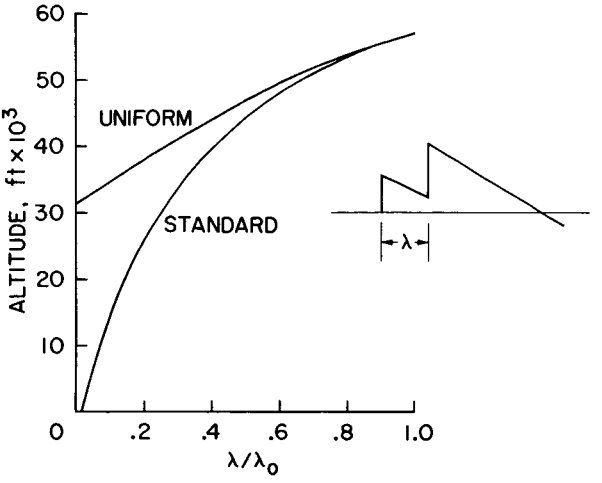

FIGURE 3. — Effect of atmospheric gradients on shock coalescence for an ogee wing at $M = 1.69$ and $C_L = 0.136$.

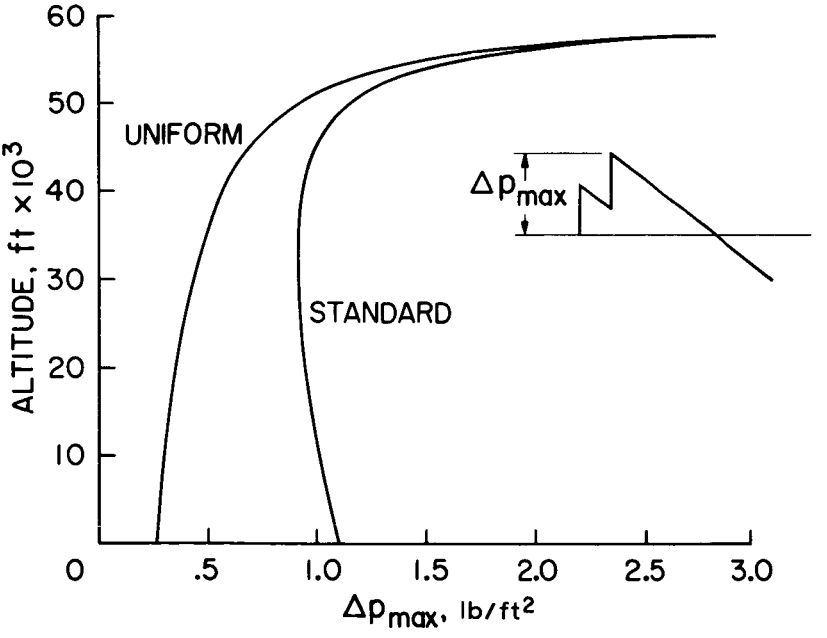

FIGURE 4. — Effect of atmospheric gradients on wave amplitude for an ogee wing at $M = 1.69$ and $C_L = 0.136$.

amplitude of the wave stops decreasing and actually increases slightly before the wave reaches the ground; whereas in the uniform-atmosphere extrapolation the wave amplitude continues to decrease, approaching the $r^{-3/4}$ rate of attenuation. At the ground, the wave amplitude for the standard atmosphere is about 4.2 times the wave amplitude for the uniform atmosphere, which agrees very well with what is predicted using an atmospheric correction factor.

The program has been applied to cases with atmospheric winds and with aircraft accelerations and has been found to give reasonable results in all cases. The only restriction on the use of the program is that the experimental signature that is extrapolated must be consistent with the flight conditions specified. For example, if the effect of $\dot{\gamma}$ is to be investigated, then an increase in $\dot{\gamma}$ must be accompanied by an increase in the aircraft lift coefficient. This means that a different signature will have to be extrapolated for each value of $\dot{\gamma}$. Therefore, if general accelerated flight of a particular aircraft configuration is to be considered, near-field signatures should be obtained in the wind tunnel at several lift coefficients and in several azimuthal planes of the model.

SUMMARY

A method for extrapolating near-field sonic boom pressure signatures through a variable atmosphere with winds has been presented. The effects of aircraft acceleration and flightpath angle are accounted for in the theory. Deformation of the waveform is described by the use of waveform parameters rather than through the use of a Whitham F-function. It is felt that this approach provides for a simpler, more intuitive, and more compact theory for the propagation of weak pressure waves.

REFERENCES

1. CARLSON, HARRY W.: An Investigation of the Influence of Lift on Sonic-Boom Intensity by Means of Wind-Tunnel Measurements of the Pressure Fields of Several Wing-Body Combinations at a Mach Number of 2.01. NASA TN D–881, 1961.
2. CARLSON, HARRY W.: Wind-Tunnel Measurements of the Sonic-Boom Characteristics of a Supersonic Bomber Model and a Correlation with Flight-Test Ground Measurements. NASA TM X–700, 1962.
3. MORRIS, ODELL A.: A Wind Tunnel Investigation at a Mach Number of 2.01 of the Sonic Boom Characteristics of Three Wing-Body Combinations Differing in Wing Longitudinal Location. NASA TN D–1384, 1962.
4. CARLSON, HARRY W.; AND MORRIS, ODELL A.: Wind Tunnel Investigation of the Sonic-Boom Characteristics of a Large Supersonic Bomber Configuration. NASA TM X–898, 1963.
5. CARLSON, HARRY W.: Correlation of Sonic-Boom Theory with Wind-Tunnel and Flight Measurements. NASA TR R–213, 1964.
6. CARLSON, HARRY W.; MACK, ROBERT J.; AND MORRIS, ODELL A.: A Wind Tunnel Investigation of the Effect of Body Shape on Sonic-Boom Pressure Distributions. NASA TN D–3106, 1965.

7. MORRIS, ODELL A.: Wind Tunnel Investigation of Sonic Boom Characteristics of a Delta-Wing-Body Combination at Mach Numbers of 1.41 and 2.01. NASA TN D-3455, 1966.
8. CARLSON, HARRY W.; AND MORRIS, ODELL A.: Wind-Tunnel Sonic-Boom Testing Techniques. J. Aircr., vol. 4, no. 3, May–June 1967, pp. 245–249.
9. HICKS, R. M.; AND MENDOZA, J. P.: Prediction of Aircraft Sonic Boom Characteristics From Experimental Near Field Results. NASA TM X-1477, 1967.
10. PIERCE, ALLAN D.; AND THOMAS, CHARLES L.: Atmospheric Correction Factor for Sonic-Boom Pressure Amplitudes. J. Acoust. Soc. Amer., vol. 46, no. 5, Nov. 1969, pp. 1366–1380.
11. KANE, E. J.; AND PALMER, T. Y.: Meteorological Aspects of the Sonic Boom. SRDS Rept. No. RD64-160, Federal Aviation Agency, AD 610 463, 1964.
12. HAYES, W. H.; HAEFELI, R. C.; AND KULSRUD, H. E.: Sonic Boom Propagation in a Stratified Atmosphere, with Computer Program. Rept. no. 116, Aeronautical Research Associates of Princeton, Inc., Dec. 1968.
13. RYZHOV, O. S.; AND SHEFTER, G. M.: On the Energy of Acoustic Waves Propagating in Moving Media. Prikl. Mat. Mekh., vol. 26, 1962, pp. 1293–1309.

A Near- and Far-Field Analysis of the Sonic Boom Emitted by Nonlifting Rectangular Wings

SANFORD S. DAVIS
NASA Ames Research Center

The theory discussed in this paper describes a procedure to be used to obtain a sonic boom pressure signature that is uniformly valid from the surface of a nonlifting rectangular wing to infinity. The purpose of this study was to determine if near-field effects, which could not be correctly accounted for in the usual equivalent body approach, could influence the far-field sonic boom pressure signature in a favorable manner. The method is based on a procedure developed by Whitham for obtaining an approximate solution to the exact potential equation of gas dynamics by refitting the linearized solution to a first-order set of characteristics. The basic linearized solution that is used in this new theory does not correspond to an equivalent body of revolution (i.e., no F-function interpretation) but must be obtained as a uniformly valid asymptotic solution to the wave equation.

Results of the theory have been compared to wind-tunnel tests in the Ames 2- by 2-ft wind tunnel on a series of rectangular planform wings. Conclusions based on these tests are: (1) the uniformly valid theory correctly predicts the behavior of the sonic boom signature at all distances from the wing; (2) the equivalent body theory does not predict the correct signature shape in the region near the wing ("near the wing" means distances on the order of the wing span); and (3) at large distances below the wing, the equivalent body theory and the uniformly valid theory agree with one another. This last result shows that near-field effects cannot affect the far-field signature below the wing in a radical manner and that the equivalent body theory can be expected to give a good approximation to the flow at these large distances.

The purpose of this investigation was to determine the effect of the near-field region on the sonic boom emitted by thin, nonlifting rectangular wings. In this near-field region, the flow is complicated by the appearance of contiguous regions of two- and three-dimensional flow patterns. Far away from the wing, these complicated flow regions are washed out by the smoothing effect of the tip cone interactions. At very large distances, the flow can be described adequately by a one-dimensional distribution of singularities; i.e., the equivalent body of revolution. The breakdown of the equivalent body of revolution in the near-field region can be traced to the appearance of a square-root singularity in the F-function for the field directly below the wing. This behavior indicates that the

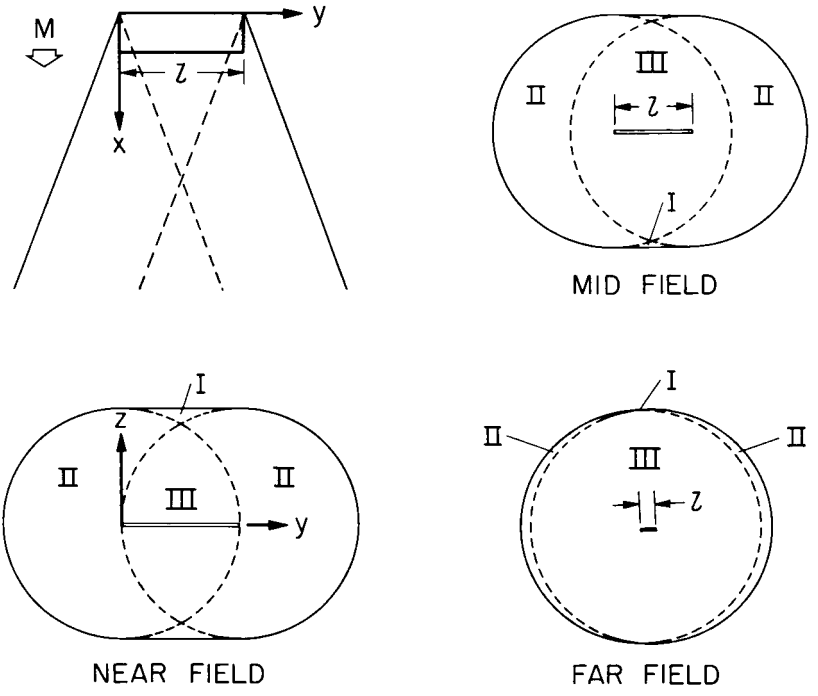

FIGURE 1.—Coordinate system and wave geometry for the rectangular wing.

equivalent body of revolution has a blunt nose, which violates the underlying assumptions of small disturbances. To avoid this difficulty, a new theory was developed that describes the flow correctly from the near to the far field. The basis of this theory is the development of a uniformly valid asymptotic representation to the linearized potential equation.

The evolution of the linearized flow field from the near to the far field is shown in figure 1 for a rectangular wing of span l. The rectangular wing occupies part of the plane $z = 0$, and the free stream flows in the direction of increasing x. The characteristic Mach surfaces that are emitted by the leading edge of the wing separates the flow into the disturbed and undisturbed regions. This surface is described by the equation

$$\begin{aligned} x-\beta z=0 \qquad & 0<y<l \\ x-\beta\sqrt{y^2+z^2}=0 \qquad & y<0 \\ x-\beta\sqrt{(y-l)^2+z^2}=0 \qquad & y>l \end{aligned}$$

where $\beta=\sqrt{M^2-1}$.

As depicted in figure 1, the tip cones also separate the flow into the two- and three-dimensional regions. Region I contains a two-dimensional flow that is unaffected by the presence of the wingtips, region II contains a three-dimensional flow that is influenced by one or the other of the wingtips, and region III encloses the interactions between the two tip cones. Figure 1 shows how these regions redistribute themselves in the near to far field. In the far-field sketch, note that the Mach surface can be approximated quite readily by a circular elementary Mach cone. This approximation would correspond to an equivalent body interpretation.

In reality, the Mach surfaces are replaced by shock waves. These shock waves are determined by obtaining a uniformly valid first-order expression to the flow field by refitting the linearized, uniformly valid asymptotic representation to a first-order set of characteristics.

Figure 2 shows in flowchart form how the uniformly valid first-order pressure rise is obtained from the linearized uniformly valid asymptotic representation. The shock waves are then inserted in the region of intersecting characteristics by satisfying the Rankine-Hugoniot shock relations to first order (ref. 1).

To explore the characteristics of the sonic boom emitted by rectangular wings, an experimental test program was conducted in the Ames 2- by 2-ft transonic wind tunnel on a series of three nonlifting rectangular planform wings (ref. 2). All the wings had a parabolic airfoil section with a chord of 5.08 cm (2 in.), a maximum thickness of 0.318

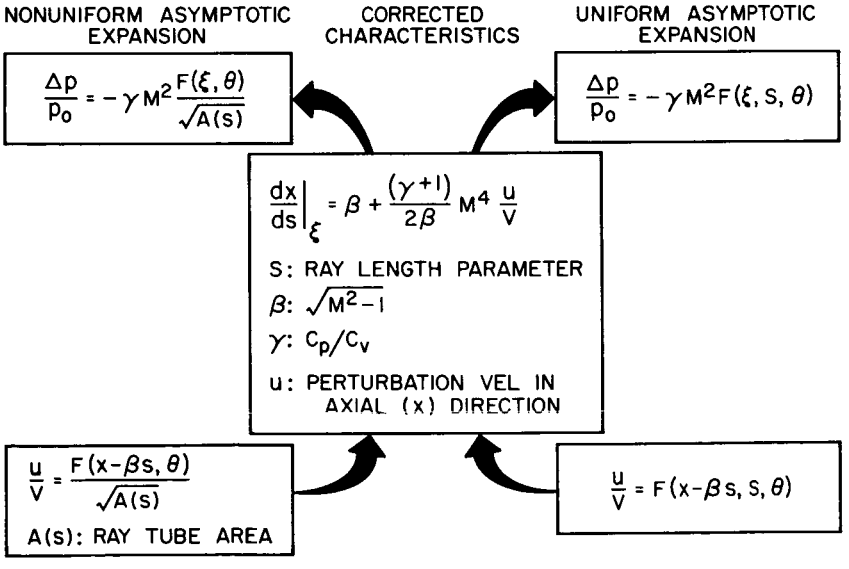

FIGURE 2. — Uniformly valid first-order solution.

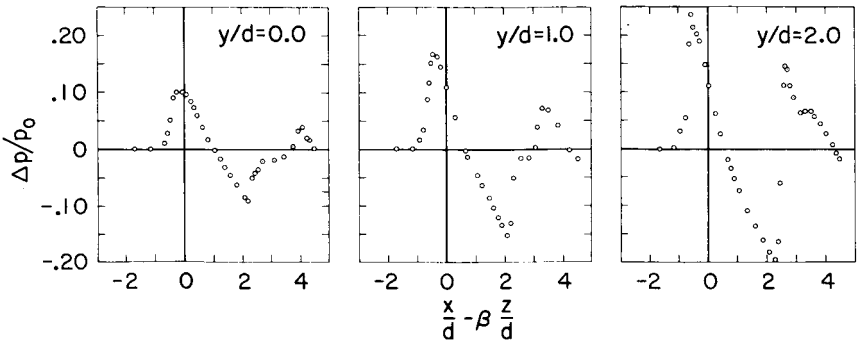

FIGURE 3.—Shock wave signature measured at $z/d=2.2$ for three spanwise stations, $l/d=4.0$ and $M=1.4$.

cm, and an initial slope $m=0.125$. The wing spans were 2.54 cm (1 in.), 10.16 cm (4 in.), and 15.24 cm (6 in.), respectively. The tunnel was run at a Mach number of 1.40, a total pressure of 67.5 kN/m^2, and a total temperature of 296° K.

One of the most important effects to be measured in this experiment was the interaction of the wingtip Mach cone with the two-dimensional flow region. The shock wave signatures illustrating this behavior are shown in figures 3 and 4. The pressure signatures are shown as pressure perturbations normalized with respect to p_0 (the static free-stream pressure) against an abscissa based on the free-stream characteristics. All geometrical dimensions have been normalized with respect to $d=2.54$ cm (1 in.), which represents the distance from the leading edge to the point of maximum airfoil thickness.

Figure 3 shows signatures at $z/d=2.2$ for three spanwise stations for the wing $l/d=4$. The strength of the shock wave at span station $y/d=0$ is about one-half of the value at the plane of symmetry $y/d=2.0$. This ratio of 2:1 is consistent with linear theory if the higher shock strength is calculated for a two-dimensional flow and the lower shock strength is calculated in the tip cone region. But the magnitudes given by linear theory are $\Delta p/p_0=0.34$ and $\Delta p/p_0=0.17$, respectively; values that are greatly in error. Note that the strongest shock wave has propagated farthest ahead of the linearized shock wave position $x/d-\beta z/d=0$.

In figure 4, similar signatures are shown farther below the wing at $z/d=8$. At this distance, the tip cones have completely overwhelmed the shock waves and both signatures are similar in shape and magnitude. This figure clearly shows that the smoothing effect of the tip cones has caused a redistribution of the pressure that cancels any spanwise variations. At a distance of only two spans, all two-dimensional characteristics of the wing have disappeared and the configuration could be treated as an equivalent body from this station out to infinity. This

does not necessarily mean that an equivalent body calculated from the wing geometry (i.e., supersonic cutting planes) would be adequate, but that extrapolation techniques (based on equivalent body concepts) from the data shown in figure 4 would give consistent results.

A comparison of the shock wave signature for this 4-in. wing as calculated for both the uniformly valid theory and the equivalent body theory based on supersonic cutting planes is shown in figure 5 for the region directly below the wing. At $z/d = 2.2$, the signature is completely two-dimensional, and it is surprising that the equivalent body theory, which assumes three-dimensional flow, comes as close as it does. At higher miss distances, the experimental data and the uniform theory show adequate agreement, but the equivalent body overpressure signatures are very bad in predicting the expansion slopes behind the shock. Because the overpressures predicted by the equivalent body theory and the experiment are of the same order, the impulse is grossly overestimated. This deviation in the predictions is present even at four or more spans from the wing, but calculations show that the signatures based on the equivalent body theory and the uniform theory do agree with one another at infinite distances from the wing. That is, the uniform theory reduces to the equivalent body theory in the very far field. This asymptotic behavior is illustrated in figure 6, which shows the shock pressure rise decay with distance. The break in the uniform curve shows the first influence of the tip cone on the shock strength. (If the tip cone did not interfere with the shock wave, the solid curve would approach a slope of $-1/2$, which is characteristic of the decay of two-dimensional shock waves.) The uniform curve now undergoes a quick change in curvature and approaches a $-3/4$ slope asymptotically. The equivalent body curve lies very close to and just above the uniform curve. Beyond 25 to 30 spans, they are effectively coincident.

A similar comparison for the 1-in. wing is shown in figures 7 and 8. In figure 7 the signatures are quite close for all of the distance ratios

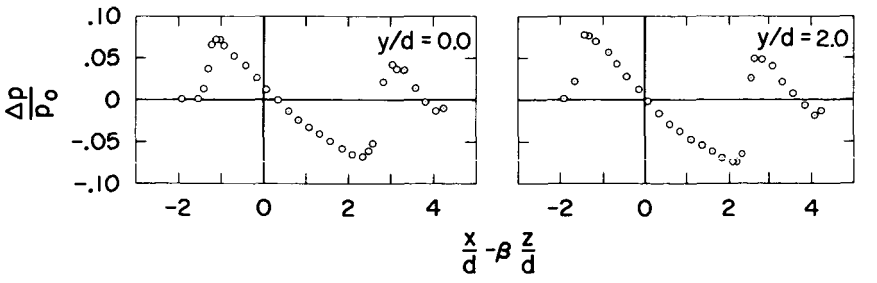

FIGURE 4. – Shock wave signature measured at $z/d = 8.0$ for two spanwise stations, $l/d = 4.0$ and $M = 1.4$.

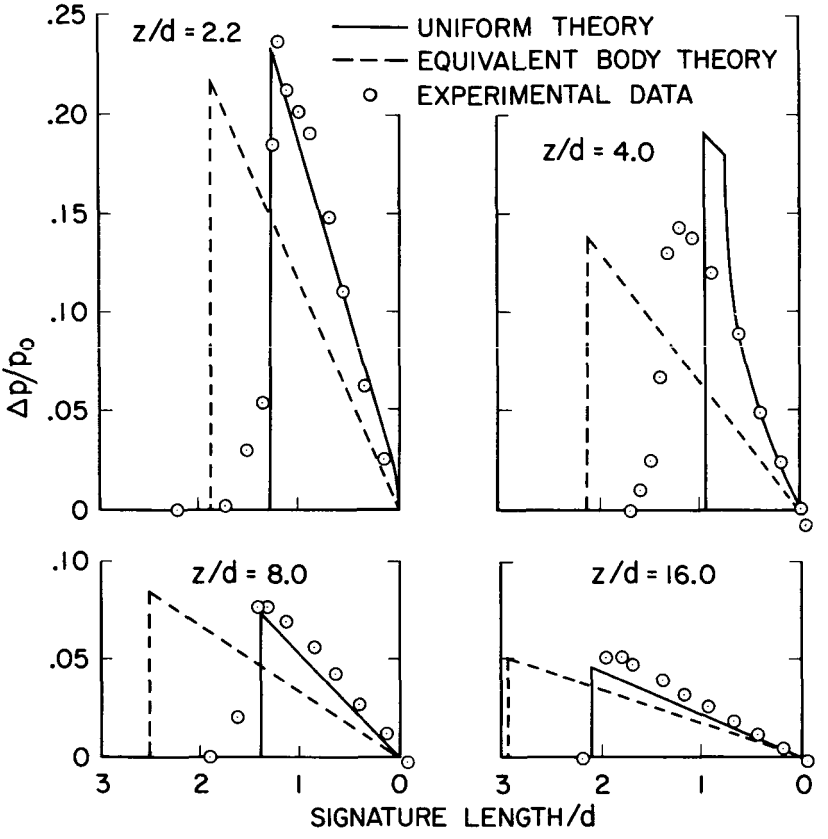

FIGURE 5.—Overpressure signatures directly below the wing, $l/d = 4.0$ and $M = 1.4$.

shown. Note that a slight underestimation in the expansion slope is also apparent in this case of the low-aspect-ratio wing. The pressure decay curve in figure 8 shows much closer agreement between the two theories in the mid to the far field.

CONCLUSIONS

The results of an experimental investigation into the shock wave characteristics of a finite, rectangular wing have generally confirmed the predictions of the uniform theory. The existence of rapid variations in near-field spanwise strengths and the subsequent smoothing effect of the tip cone interactions have also been verified by the experiment. The equivalent body theory, while giving erroneous results in the near field, predicts the characteristics of the far-field sonic boom below the wing quite well. In fact, the predictions of the uniformly valid theory reduce to the equivalent body theory in the far-field region below the wing.

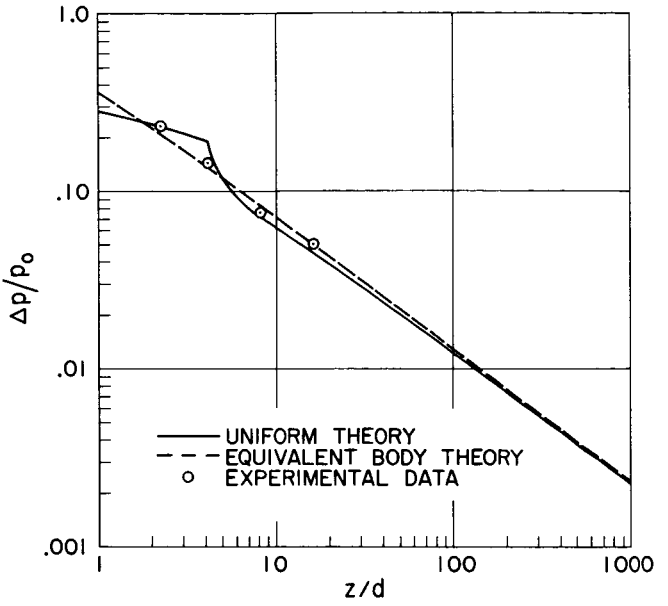

FIGURE 6. – Decay of peak pressure rise with distance below the wing, $l/d = 4.0$, $M = 1.4$, and $m = 0.125$.

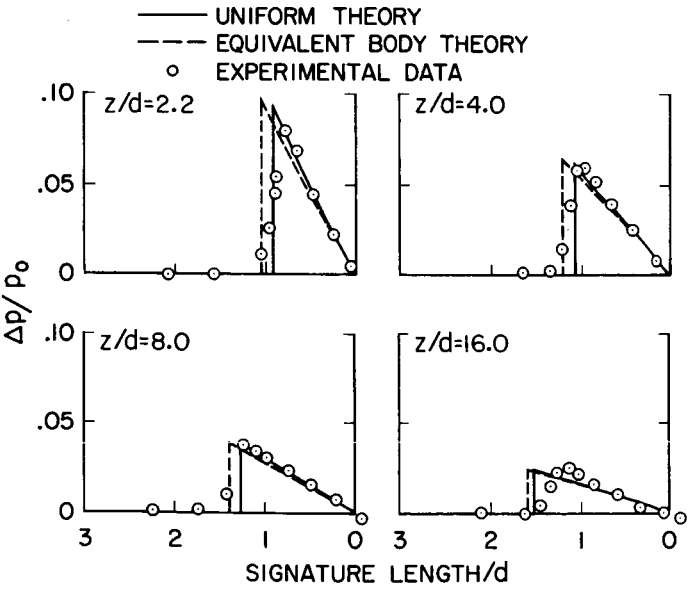

FIGURE 7. – Overpressure signatures directly below the wing, $l/d = 1.0$ and $M = 1.4$.

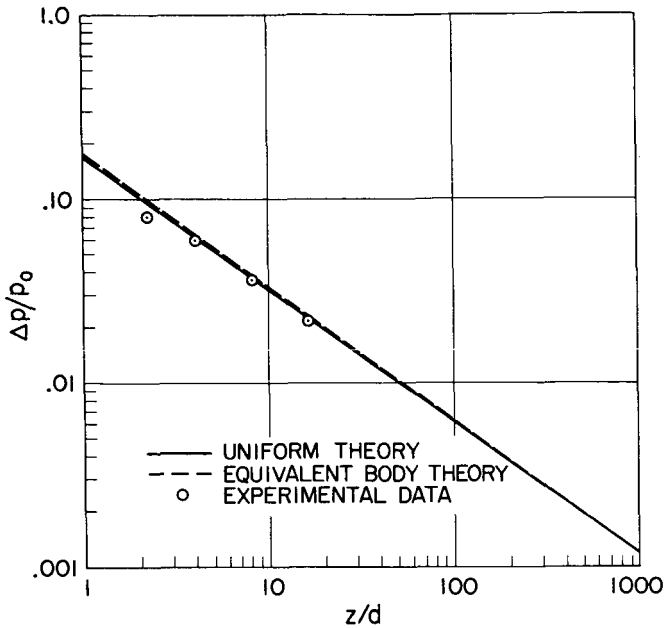

FIGURE 8.—Decay of peak pressure rise with distance below the wing, $l/d = 1.0$, $M = 1.4$, and $m = 0.125$.

An important conclusion that may be reached from this analysis is that the far-field sonic boom below a rectangular wing is not affected by details of the flow in the near-field region. At large distances from the wing, only the simplest axial distribution of sources (as given by the equivalent body theory) is necessary in order to give good results. However, in the mid-field region the situation may be quite different. The shock pressure decay graphs show that the uniformly valid theory approaches the equivalent body theory from below. This result shows that the effects of a planar distribution of singularities acts in a favorable manner and persists into the mid-field region. It may be possible to choose exotic wing thickness distributions (or in the lifting case, exotic lift distributions) by which the plane wave contribution significantly reduces the mid-field shock strength. These plane wave effects are not given correctly by the equivalent body approach, and the uniformly valid theory must be used for such a comparative study.

REFERENCES

1. DAVIS, S.; AND FRIEDMAN, M.: A Uniform Approximation to the Shock Generated by Thin, Nonlifting Wings of Rectangular Planform. To be published as NASA CR.
2. DAVIS, S.: An Investigation Into the Sonic Boom Generated by Thin, Nonlifting Rectangular Wings. To be published as NASA TN.

Coupled Elastic and Acoustic Response of Room Interiors to Sonic Boom*

S. SLUTSKY AND L. ARNOLD
New York University

A study was initiated whose purpose was to determine and predict the time history of acoustic response within architectural structures due to sonic boom transients and to investigate aspects of signature that strongly influence undesirable internal acoustic response.

The procedure was based upon the use of the convolution integral to relate the forcing signature-response relationship in terms of the system transfer function. This transfer function was determined experimentally using scaled models as well as analytically. An inexpensive sonic boom generator was constructed, and input-output responses were recorded and converted to digital data. Transfer functions were computed and used to calculate responses to modified forcing signatures. Measured and calculated responses agreed very well. It was concluded that this technique could be used to investigate a large variety of transient response problems as well as the coupled elastic-acoustic systems studied in the present program.

Results of special relevance to the interior response of structures include the following: (1) high-frequency transmission of open windows can be correlated with the ratio of signature rise time to a retarded time from window edge scattered waves, (2) interior acoustic response of buildings with closed windows is insensitive to outdoor signature rise time, and (3) high frequency wall acceleration response is sensitive to signature rise time.

This paper is a review of some results that were recently obtained for the Federal Aviation Administration concerning the interior response of architectural structures. More complete details are reported in reference 1.

The first purpose of this work was to determine and predict the time history of acoustic response in the interior of architectural structures due to sonic booms. The second purpose was to determine aspects of sonic boom signature that influence undesirable internal acoustic response and to examine the effect of changes in free-field waveform on interior response.

*This work was supported by the Federal Aviation Administration of the Department of Transportation, Washington, D.C.

FIGURE 1.—Basic system for use of the convolution integral.

The procedure included the development of the following principal steps:

(1) A study of techniques for determining the impulsive response of a complex system by application of the convolution concept
(2) Construction of a suitable sonic boom generator
(3) Experimental and analytical study of a two-dimensional fence configuration
(4) Analog and digital data processing
(5) Analytical approach

CONVOLUTION

The basic ideas behind use of the convolution are summarized in figure 1 and in the defining equation

$$y_x^{(1)}(t) = \int_0^t H_{x,\xi}(\tau)\, P_\xi^{(1)}(t-\tau)\, d\tau \tag{1}$$

We interpret the transfer function $H_{x,\xi}(t)$ as the impulse response of point x of the system of figure 1 due to a unit impulse applied at point ξ at time $t=0$. If, by means of some appropriate experiment, we could determine $H_{x,\xi}(t)$, then we could use it to find the response $y_x^{(2)}(t)$ at point x due to any different force history $P_\xi^{(2)}(t)$ applied at point ξ:

$$y_x^{(2)}(t) = \int_0^t H_{x,\xi}(\tau)\, P_\xi^{(2)}(t-\tau)\, d\tau \tag{2}$$

The kind of system we are interested in is somewhat more complicated and is represented diagramatically by the structure in figure 2. It is clear that a transfer function relating the pressure response within the room to a sonic boom signature varies with the detailed geometry of the building, the elastic characteristics of the wall, the window geometry, the position of the microphone, and the direction of the sonic boom relative to the structure. It does not, however, depend on the pressure versus time history of the boom signature.

One of the results of the present work was to demonstrate that transfer functions for this type of complex structure (and theoretically for any linear structure) could be determined from measurements of the free-field sonic boom signature and the interior response. Two numerical procedures were investigated: one is based on the properties of the Fourier transform, the other is a direct inversion of the convolution relationship. Thus, if our input-output data are obtained as two sequences of points y_α and P_β, we can write equation (1) as a summation:

$$y(\alpha)=\sum_{\beta=0}^{N-1} P(\alpha-\beta)H(\beta) \qquad \alpha=0, 1, 2, \ldots, N-1 \tag{3}$$

We can then use the discrete Fourier transform relation

$$\hat{Y}(n)=\sum_{\alpha=0}^{N-1} y(\alpha)e^{2\pi i \frac{\alpha h}{N}} \qquad n=0, 1, \ldots, N-1 \tag{4a}$$

and

$$y(\alpha)=\frac{1}{N}\sum_{n=0}^{N-1} \hat{Y}(n)e^{-2\pi i \frac{\alpha n}{N}} \qquad \alpha=0, 1, \ldots, N-1 \tag{4b}$$

to obtain the transform relation

$$\hat{H}(n)=\frac{\hat{Y}(n)}{\hat{P}(n)} \tag{5}$$

and thence

$$H(\alpha)=\frac{1}{N}\sum_{n=0}^{N-1} \hat{H}(n)e^{-2\pi i \frac{\alpha n}{N}} \tag{6}$$

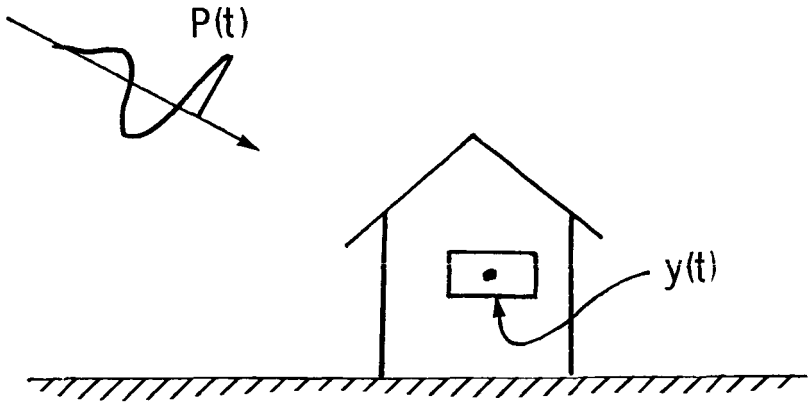

FIGURE 2.—Basic system for transfer function within a house.

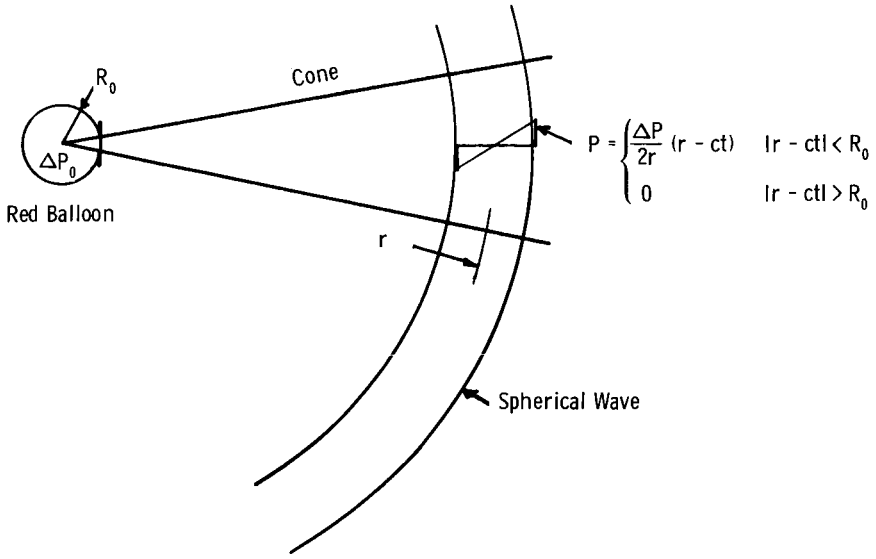

FIGURE 3. – Principle of the sonic boom generator.

An alternative procedure is based on the direct inversion of equation (3):

$$H(\alpha) = [P_{\alpha\beta}]^{-1} y(\beta) \tag{7}$$

wherein we require $P_{00} = P(0) > 0$.

It was found that while both methods worked well, the sensitivity to random noise of the direct method was far superior; thus the latter method was finally adopted.

SONIC BOOM GENERATOR

The principle of the sonic boom generator used in the current tests is described diagrammatically in figure 3. Thus Lamb (ref. 2) shows that if a spherical balloon of radius R_0 with overpressure $\Delta p \ll p_0$ is burst symmetrically, then at a point p in the field, an N-wave of overpressure $\Delta p/2$ and duration $2R/c$ will be experienced. The presence of a cone with apex located at the center of the balloon will not change the spherical symmetry of the wave field. Therefore if we burst a diaphragm within the cone, we should obtain an N-wave within the cone, and nothing outside (until the wave propagates beyond the end of the cone). Figure 4 is a photograph of the reinforced wooden cone and aluminum driver section at an early stage when the construction could still be seen. It was subsequently extended to 20 ft with a 6-ft square opening. The flanges at the vertex end permit placement of diaphragms at $R_0 = 3, 6,$

or 30 in. The waves generated are N-waves if the diaphragm material is brittle and tears suddenly (carbon paper or cellophane) and more sinusoidal if the diaphragm tears slowly (polyethylene or other soft plastics).

The models to be investigated are placed on the floor to represent Mach 1 flyby, or on an incline for larger Mach numbers.

TWO-DIMENSIONAL CONFIGURATION

To verify that the experimental configuration was operating as anticipated, the two-dimensional analysis of Lu Ting (ref. 3) was used to compute the pressure history at several positions of a fence (fig. 5). The calculated and measured results are drawn as solid and dashed lines, respectively, in figure 6. The input wave shape was approximated by that drawn in figure 6(*a*). The ordinate is the ratio of the measured pressure to the peak overpressure of the incident N-wave. Agreement was found to be good considering that the data reduction procedures at the time of this experiment were still fairly crude.

Considerably better results were obtained subsequently (as noted below) when the data handling was improved in connection with computation of the convolution.

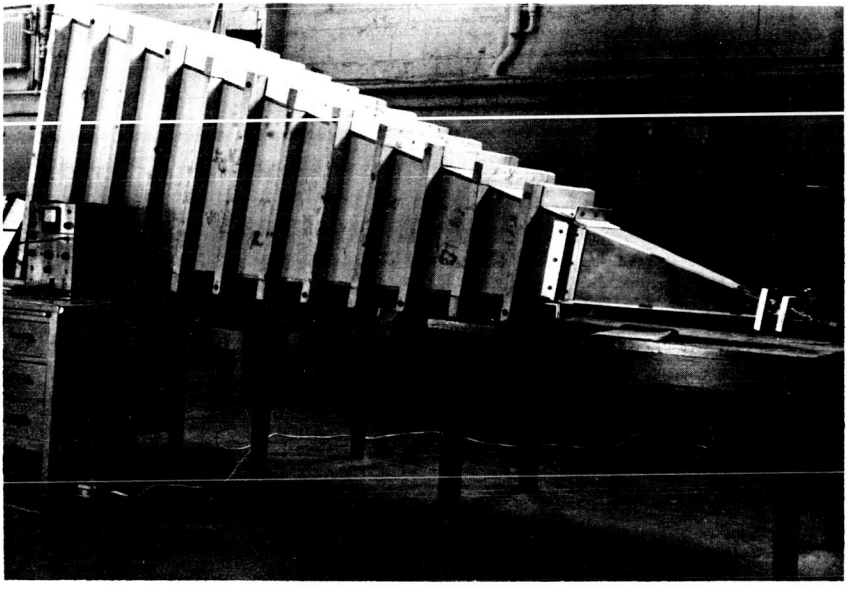

FIGURE 4. — Inner face and ribs of the sonic boom generator before addition of 4-in. concrete shell.

ANALOG AND DIGITAL DATA PROCESSING

To carry out the subsequent experimental program as planned, it was necessary to obtain the input-output data in digital form, i.e., on digital tape or punched cards. The procedure used was to record input, output, and a trigger signal on three channels of an FM tape recorder (bandwidth 0 to 80 kHz). The signals were recorded at 120 in./sec and played back into an analog-to-digital converter at reduced speed, ranging from 15 to 3 3/4 in./sec. The conversion rate of the ADAGE computer used for the purpose was 32 000 words/sec so that resolutions of from 2.5 to 10 μsec were obtained for traces containing about 4000 samples. Figure 7 is an example of several traces played back on an oscilloscope from digitally stored data and illustrates that the oscilloscope has insufficient resolution to display discrete data steps at this kind of point density. Figures 7(b) and 7(c) are examples of a slowly rising N-wave and the interior acoustic response to it, whereas figure 7(a) is the interior response to a fast rise N-wave such as that of figure 11(b). The radical behavior difference is characteristic and is discussed later. The ADAGE computer (operated by the Electrical Engineering Department and adapted to our needs by Professor Thumim of that department) stores its data on magnetic disks. These data were transferred to digital tape for processing on the NYU UNIVAC 1108.

The deconvolution program described in reference 1 was then tested on a number of problems. The first was the fence configuration of figure 5. In this case the transfer function was generated by processing a fast rise N-wave generated by means of the 6-in. radius driver (approximately 1 msec duration) and the response at the bottom of the forward face of the fence. This transfer function was then convolved with a wave generated with the 3-in. radius driver (approximately 1/2 msec). The result is drawn as dots in figure 8. The experimentally measured response was also digitized and stored and is noted for comparison as the plus marks in figure 8. (Note that only every fourth point was drawn.)

The second configuration was that of a 12- by 12- by 6-in. box with a flexible wall (12 by 6 in.) and a 4- by 2-in. window in the center. An approximately 1-msec fast rise N-wave was used to excite the system.

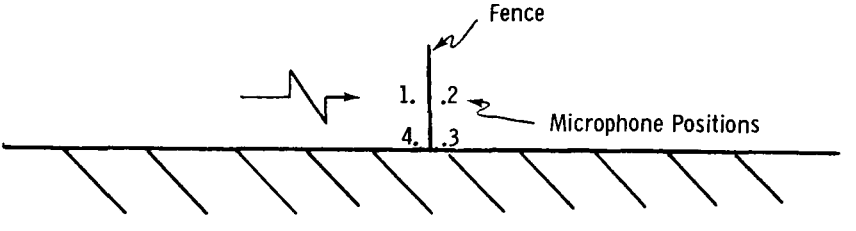

FIGURE 5. – Two-dimensional fence and microphone reading positions.

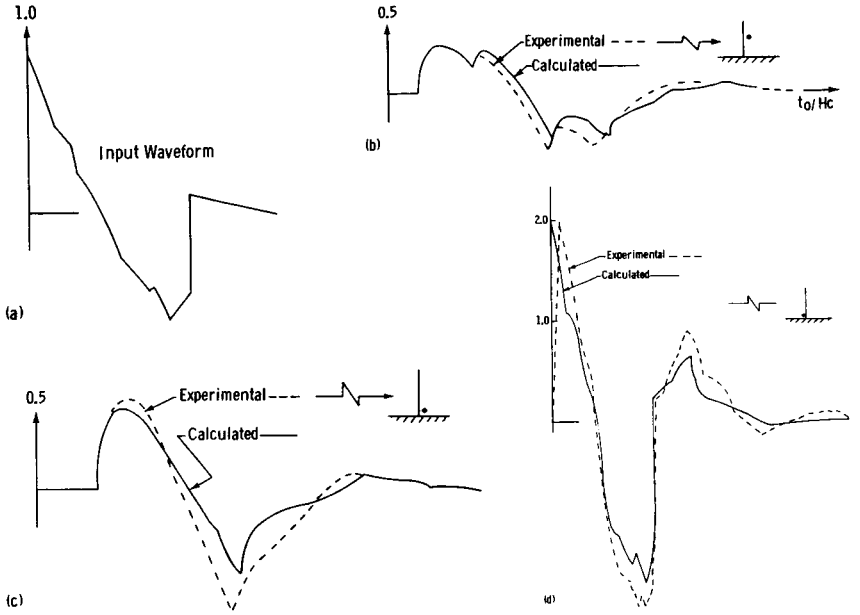

FIGURE 6. — Comparison of calculated and measured fence pressure responses. (*a*) Approximate input wave shape. (*b*) Microphone in position 2. (*c*) Microphone in position 3. (*d*) Microphone in position 4.

Free-field and interior microphones were used to measure the input and response, and the transfer function was computed. Then a slow rise wave of about 1 msec was generated, recorded, digitized, and used in the convolution to calculate a response, drawn as dots in figure 9. The experimentally measured response is also drawn for comparison using plus marks.

Another case was that of a model one-room house built using very light bungalow-type construction (studded wall and sheet rock). The windows (modeled in steel shimstock, although aluminum would have provided a better impedance match) were sealed shut. The transfer function for the pressure in the middle of the house interior was determined using a fast rise 1-msec N-wave as above and then was convolved with a slow rise wave. The calculated response (plus marks) and experimental response (dots) are plotted in figure 10.

It is seen from the foregoing figures that the convolution is very accurate at short response times (corresponding to the high frequencies of specific concern). The measured and computed results appear to diverge slowly. Although this type of discrepancy should be studied and improved, it is probably not important for audio response purposes.

A very striking difference in response of the models to fast rise waves and to slow rise waves was noted in the experiments. These differences

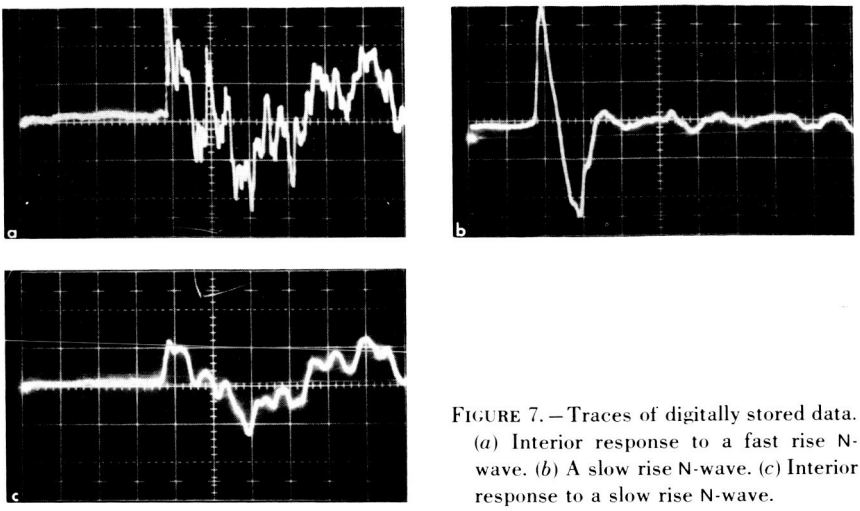

FIGURE 7.—Traces of digitally stored data. (*a*) Interior response to a fast rise N-wave. (*b*) A slow rise N-wave. (*c*) Interior response to a slow rise N-wave.

are shown in figure 11 for the case of a 12- by 12- by 6-in. box, with all walls rigid and with an open 4- by 2-in. window in the middle of one of the 12- by 6-in. walls. The interior microphone was placed in the center of the chamber, and the box was oriented so that the sonic boom wave struck normal to the wall and window and microphone face. The upper trace of figure 11(*a*) is that of the free-field 1-msec wave recorded upstream of the model. The lower trace shows the interior response. Figure 11(*b*) is a larger scale detail of the incident wave, and 11(*c*) is a similar detail of the response. The upper trace of figure 11(*d*) is a slow rise wave produced by bursting a polyethylene diaphragm, and the lower trace is the interior response. It will be noted that figure 11(*c*) shows extremely short initial pulses and subsequent high-frequency responses superimposed on a low-frequency oscillation, whereas the lower trace of figure 11(*d*) shows little more than the low-frequency oscillation (apparently the Helmholtz cavity mode).

Responses resembling figure 11(*d*) can also be obtained with a fast rise N-wave if the model is rotated so that the incident wave no longer strikes the window wall normally, but instead approaches grazing incidence. In these cases the effective wave rise time is equal to the time to traverse the window opening, about 0.3 msec.

Experiments carried out with flexible walls and closed windows show very little difference in interior pressure response to either fast or slow rise waves. However, when the acceleration response of a flexible wall (with closed windows) is measured, the response is qiute striking and resembles the pressure response through an open window. Thus the lower trace of figure 12(*a*) represents a fast rise free-field signature, and the upper trace is that of the acceleration response (obtained using

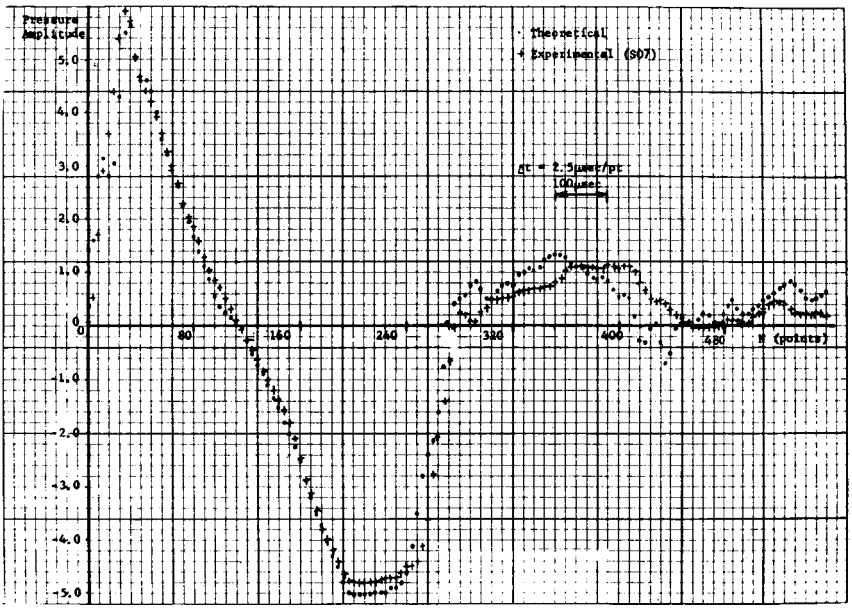

FIGURE 8. – Results of testing of transfer function on fence configuration of figure 5.

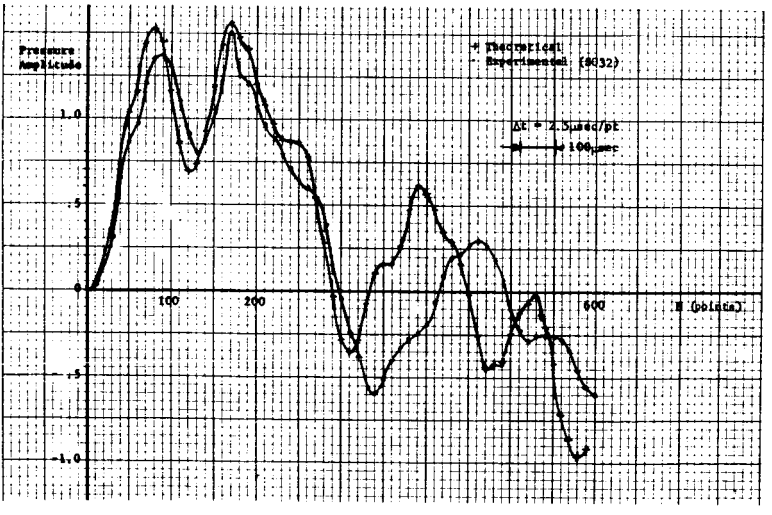

FIGURE 9. – Results of testing of transfer function on box with window.

an unshielded accelerometer weighing 0.1 g). Figure 12(*b*) shows a slow rise incident pressure wave trace and the wall acceleration response thereto (the large wavelength curvature is due to unshielded 60-cycle stray fields). It must be concluded that noise produced by rattling of small objects coupled to the wall would be much more intense for the fast rise input than for the slow rise case.

ANALYTICAL CONSIDERATIONS

An important consideration of the present study was the high-frequency behavior of the interior acoustic field and the effect of open windows on that behavior. As a consequence, we were not able to make use of the procedures of Craggs (ref. 4) and Pretlove (refs. 5 and 6), which treat the interior volume as well as the walls by means of a finite number of degrees of freedom and do not treat the case of an open window. A procedure to circumvent these limitations was formulated by dividing the flexible wall into rectangular panels and treating the open window as a panel of zero mass and zero rigidity. The external pressure loads acting on the panels are assumed known (from measurements over a rigid body) and concentrated at the center of each panel. These are assumed to produce a motion of each of the panels, which is constant on each panel. These motions generate a pressure field inside and outside the structure as well as inertial and damping forces in the structure that tend to modify or resist the original motions. This interaction between wall motion and acoustic fields is expressed by a pair of coupled

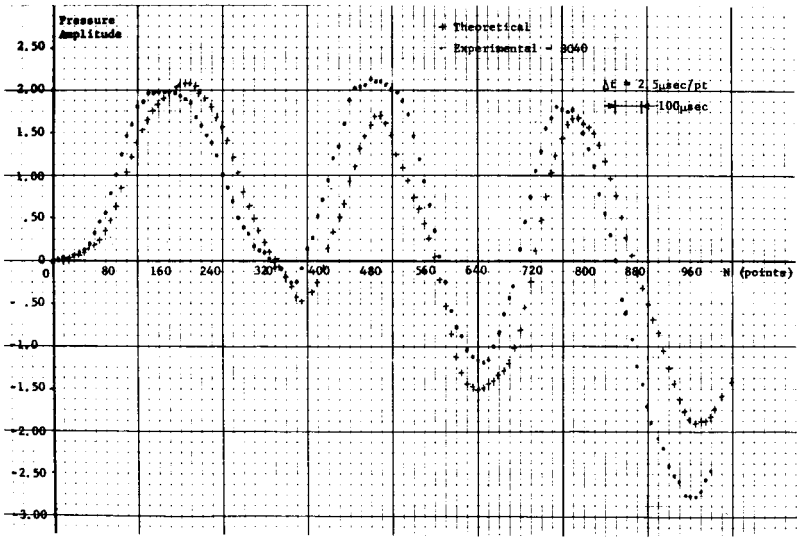

FIGURE 10.—Results of testing of transfer function on model one-room house.

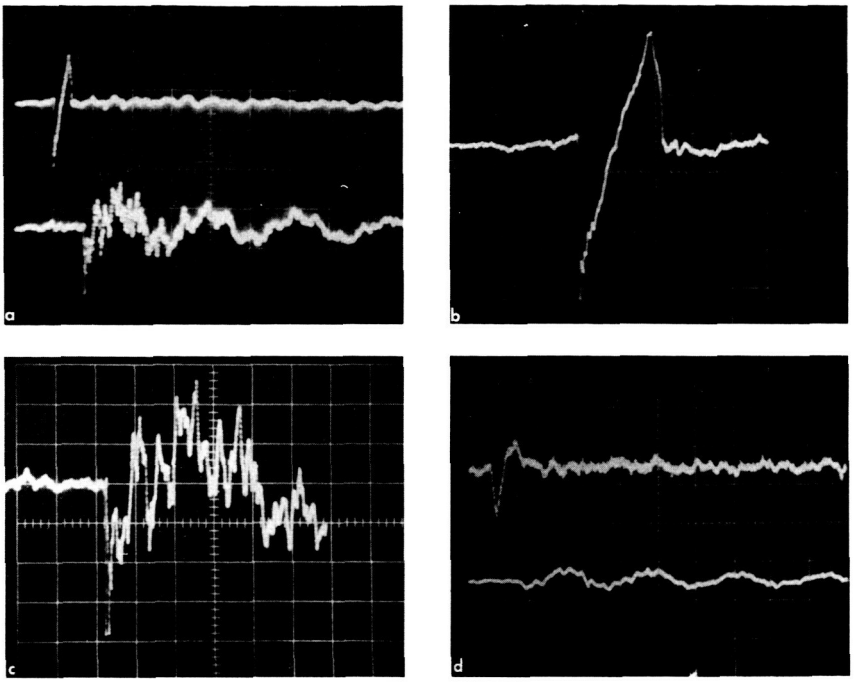

FIGURE 11.—Response of box with rigid wall and window to fast rise and slow rise waves. (*a*) Fast rise wave and response. (*b*) Detail of incident wave. (*c*) Detail of pressure response. (*d*) Slow rise wave and response.

integral equations for the wall deflection and the induced pressure difference. These equations are of the form

$$w(\tilde{x}, t) = \int_A G^s(\tilde{x} \mid \tilde{x}_0 \mid t) * [P(\tilde{x}_0, t) + \pi(\tilde{x}_0, t)] \, dA_0 \tag{8}$$

$$\pi(\tilde{x}, t) = \int_A G^a(\tilde{x} \mid \tilde{x}_0 \mid t) * w(\tilde{x}_0 \mid t) \, dA_0 \tag{9}$$

The symbol $*$ represents the convolution with respect to time; $\tilde{x}$ and $\tilde{x}_0$ are shorthand for (x, y, z) and (x_0, y_0, z_0), respectively; dA_0 is the surface element for the source distribution; and $G^s(\tilde{x} \mid \tilde{x}_0 \mid t)$ represents the structural Green's function that describes the displacement at point x and time t due to a unit impulse applied at point $\tilde{x}_0$ at time zero. The function $P(\tilde{x}_0, t)$ represents the known external pressure that would exist over the structure at points $\tilde{x}_0$ and time t if the structure were rigid. The function $\pi(\tilde{x}_0, t)$ is defined as the pressure difference between the outside and the inside induced by the motion $w(\tilde{x}_0, t)$ of the wall.

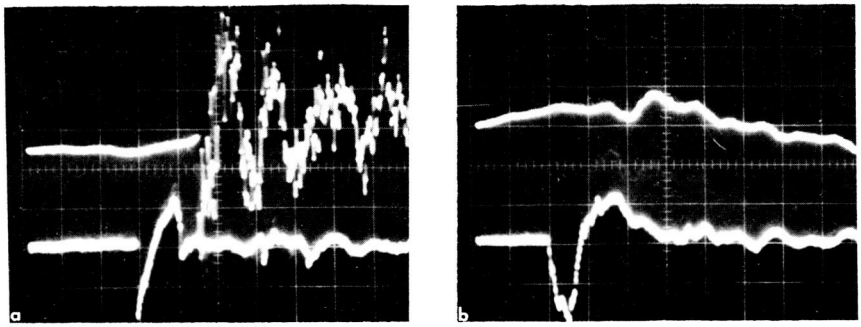

FIGURE 12. – Accelerometer response of flexible wall with no window. (*a*) Fast rise wave. (*b*) Slow rise wave.

The function $G^a(\tilde{x}\,|\,x_0\,|\,t)$ is the pressure difference induced at point $\tilde{x}$ at time t due to a unit impulsive displacement applied at point $\tilde{x}_0$ at time zero.

The structural Green's function is constructed from a knowledge of the normal modes and frequencies of the structure. Powerful programs that can be applied to quite complicated three-dimensional structures are commercially available for the analysis of structures built up out of plates, beams, and rods.

The resulting Green's function is expressible in the form

$$G^s(\tilde{x}_j|\tilde{x}_k|t) = \sum_{n=1}^{N} \frac{\Phi_j^n \Phi_k^n}{M_n} e^{-b_n t} \frac{\sin \Omega_n t}{\Omega_n} \tag{10}$$

where b_n is a viscous damping, $\Omega_n = \sqrt{\omega_n^2 - b_n^2}$, Φ_j^n is the nth normal mode deflection at the center of the jth panel, and M_n is the generalized mass corresponding to the nth mode.

The interior pressure response due to excitation of a wall panel and of the open window panel was treated using the method of images rather than the method of normal modes. The expressions are very complicated, and the reader is referred for details to reference 1. However, when the wave field enters normal to the wall and the microphone is located along the centerline of the window, if we simplify the window to be circular, then the initial pressure field p_{10} sensed by the microphone is relatively simple:

$$p_{10}(x,\,t) = \rho_0 c\left[u_0\left(t - \frac{|x|}{c}\right) - u_0\left(t - \frac{|x| + D_0}{c}\right)\right] + \text{wall reflection terms} \tag{11}$$

$$D_0 \cong \frac{A_0}{2\pi|x|} \tag{12}$$

where $u_0(t)$ is the *free-field* velocity perturbation produced by the sonic boom, A_0 is the area of the window, and x is the distance from the window to the microphone. The consequence of equation (11) is that an incident wave is severely distorted in passing through an open window so that an N-wave comes through essentially as two pulses, which then undergo internal reflections. This state of affairs can be discussed with the help of figure 13. The first sketch shows a fast rise wave hitting a large window, so that the rise time t_R is much smaller than $\Delta t = D_0/c$. We see that the first term of equation (11) is a wave having the same form as the free-field pressure and a time delay corresponding to the normal distance x between the *center* of the window and the microphone. The second term also has the same form but arrives at a slightly later time, $\Delta t = D_0/c$, from the *edge* of the window. The second term does not have any cancellation effect until after the incident wave has reached its peak amplitude and is decreasing. The second sketch shows a slowly rising wave and a small edge delay value, $\Delta t = D_0/c$, so that $\Delta t < t_R$. In this case the second (window edge) term of equation (11) begins to have its canceling effect before the first (window center) term has reached its peak. The resulting interior response is much smaller than in the previous case.

Computer calculations with a program based on the foregoing analysis were initiated and showed promise. Additional exploratory study is

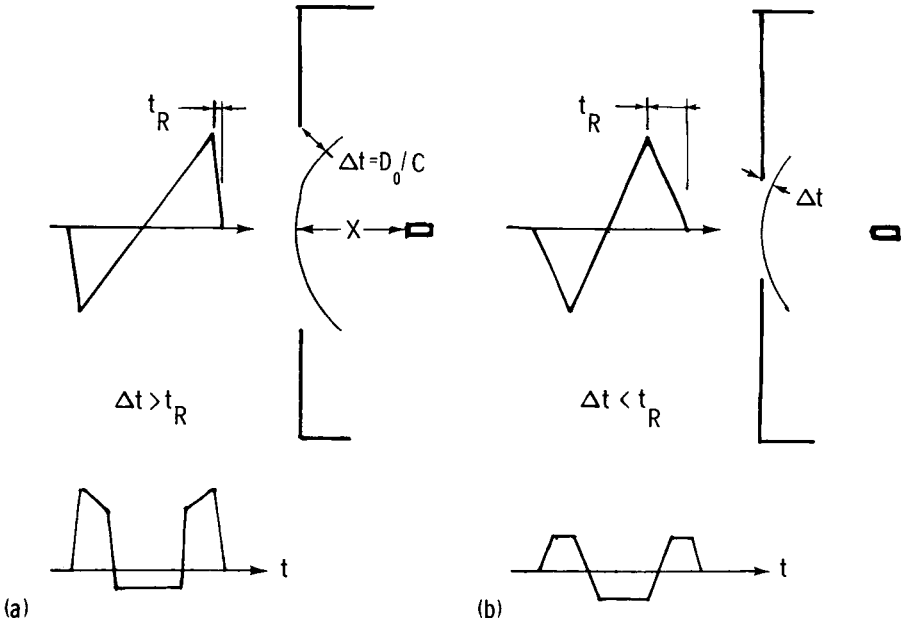

FIGURE 13.—Distortion of an incident wave. (*a*) Fast rise wave. (*b*) Slow rise wave.

indicated, however, and it is hoped that this may be possible at some future date.

CONCLUSIONS

A procedure was devised based on the use of the convolution integral to relate the input-response relationship in terms of the system transfer function. This transfer function was determined experimentally, using scaled models, as well as analytically. An inexpensive sonic boom generator was constructed, and input-output responses were recorded and converted to digital data. Transfer functions were computed and used to calculate responses to modified forcing signatures. Measured and calculated responses agreed very well. It was concluded that this technique could be used to investigate a large variety of transient response problems as well as the coupled elastic-acoustic systems studied in the present program.

Results of special relevance to the interior response of structures include the following: (1) high-frequency transmission of open windows can be correlated with the ratio of signature rise time to a retarded time from window edge scattered waves, (2) interior acoustic response of buildings with closed windows is insensitive to outdoor signature rise time, and (3) high-frequency wall acceleration response is sensitive to signature rise time.

REFERENCES

1. SLUTSKY, S.; AND ARNOLD, L.: Experimental-Analytic Dynamic Techniques for Application to Sonic Boom Structural and Acoustic Response Determination. FAA Rept., NYU–AA–70–19, New York Univ., 1970.
2. LAMB, H.: Dynamical Theory of Sound. Dover Pub., Inc., 1960, pp. 208–212.
3. TING, L.; AND PAN, Y. S.: Incidence of N-Waves on Structures. Second Conference on Sonic Boom Research, NASA SP–180, 1968, pp. 89–98.
4. CRAGGS, A.: The Transient Response of Coupled Acousto-Mechanical System. NASA CR–1421, 1969.
5. PRETLOVE, A. J.: Free Vibrations of a Rectangular Panel Backed by a Closed Rectangular Cavity. J. Sound Vib., vol. 2, no. 3, 1965, p. 197.
6. PRETLOVE, A. J.: Acousto-Elastic Effects in the Response of Large Windows to Sonic Bangs. J. Sound Vib., vol. 9, no. 3, 1969, p. 487–500.

III

CONFIGURATIONS FOR MINIMIZATION OF SONIC BOOM

Chairman: M. FRIEDMAN

Measurements of Sonic Boom Signatures From Flights at Cutoff Mach Number

DOMENIC J. MAGLIERI, DAVID A. HILTON, VERA HUCKEL, AND HERBERT R. HENDERSON
NASA Langley Research Center

AND

NORMAN J. MCLEOD
NASA Flight Research Center

Sonic boom is synonymous with supersonic flight. A considerable amount of experimental and theoretical information has been accumulated in recent years regarding this subject (for example, refs. 1 to 4); so that the sonic boom phenomena are to a large extent understood and predictable, although not necessarily avoidable. To illustrate this latter point, figure 1 (ref. 5) shows the proposed route structures for a fleet of about 500 supersonic transports (SST's) in the 1990's. The solid lines indicate routes that will be flown at cruise Mach numbers of 2.2 or 2.7. These routes are noted to exist over water and sparsely inhabited land areas to minimize public reaction to sonic boom. Overflight of land areas is represented by the dashed lines. Worldwide public opinion, backed by a proposed Federal ruling (ref. 6), dictates that these overland routes be flown so that sonic booms are not produced at ground level. These routes could be flown subsonically; however, for most effective aircraft utilization, they should be flown at as high a speed as possible. It has been suggested that these routes be flown at so-called "cutoff Mach numbers," that is, relatively low Mach numbers at which the booms do not reach the ground. This might be accomplished by operating the conventional SST at low supersonic speeds, by developing a low Mach number SST (ref. 7), or by an advanced sonic transport.

The purpose of this paper is to present results of a recent flight study aimed at investigating the sonic boom phenomena associated with low-Mach-number supersonic flight in which the sonic booms do not reach the ground because they are cut off or are at "grazing" angles to the ground.

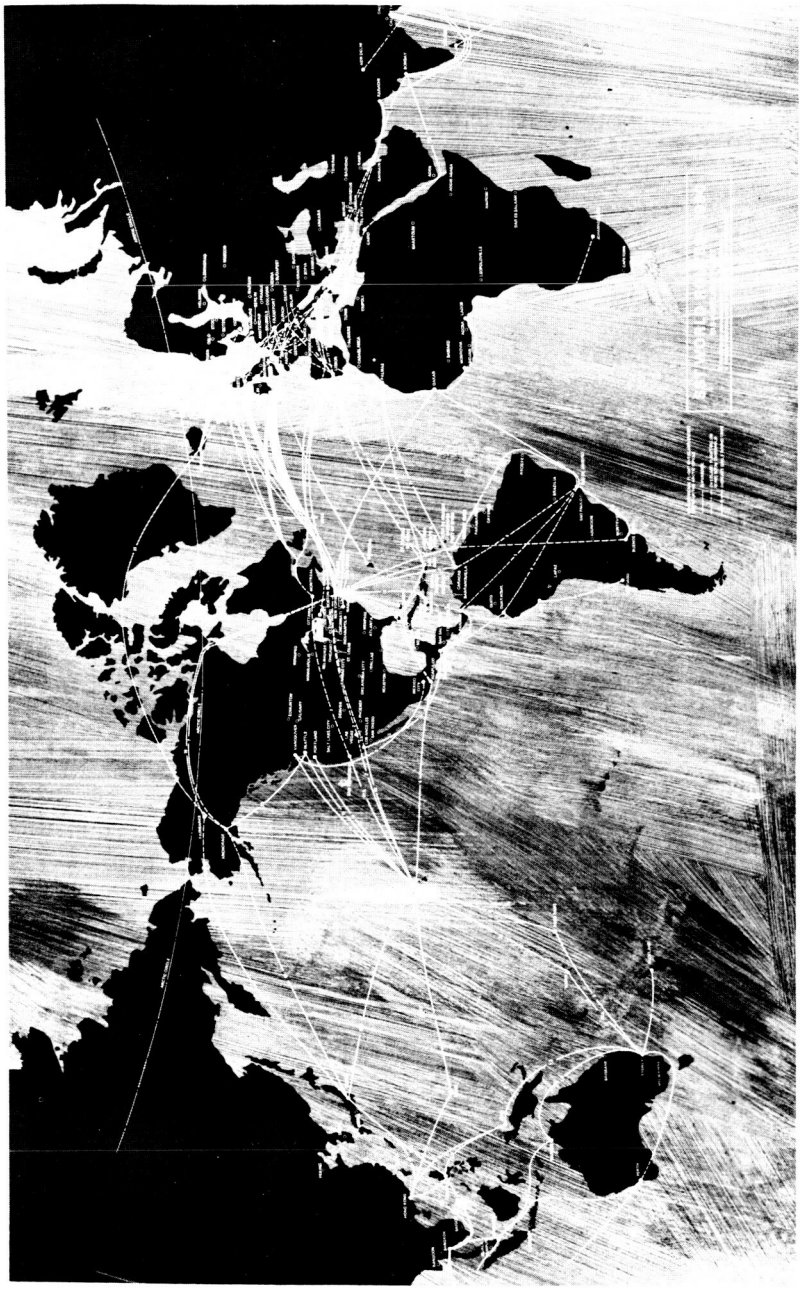

FIGURE 1.—Proposed SST routes for a fleet of 500 SST's around 1990.

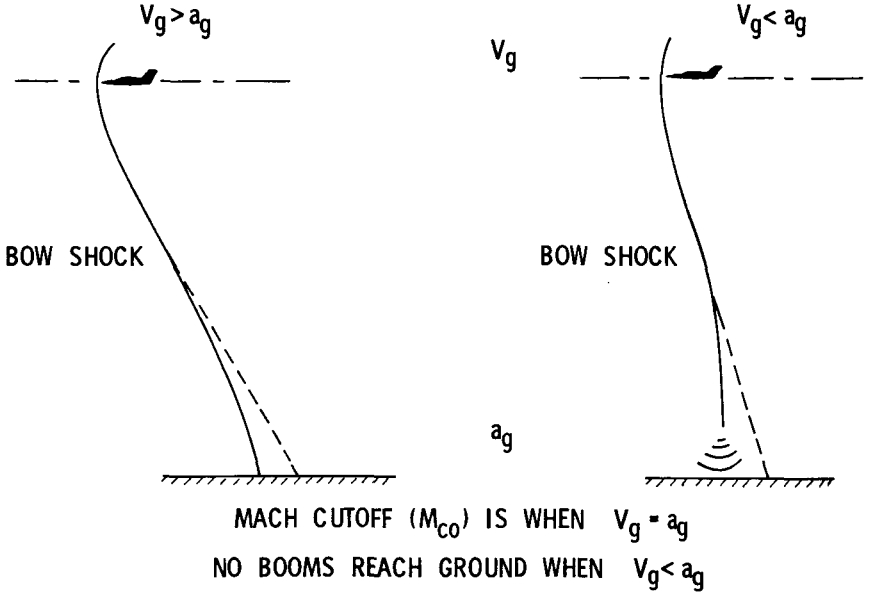

FIGURE 2. – Effect of sound speed gradient on bow wave propagation for two airplane Mach numbers.

EFFECTS OF THE ATMOSPHERE

The sonic boom cutoff phenomenon is attributable to the effects of the sound speed gradients that exist in the atmosphere. This effect is illustrated in figure 2. Shown on the left-hand side of the figure is an aircraft in supersonic flight where the speed of the aircraft over the ground V_g is greater than the speed of sound at the ground a_g. The example shown could correspond to a local airplane Mach number of about 1.5. For simplicity, only the bow shock is shown. If the sound speed were constant at all points between the aircraft and ground, the bow shock wave would be straight and would take the position of the dashed line. However, sound speed gradients are usually present in the atmosphere, the sound speed (temperature) at ground level being higher than at altitude. A sound speed gradient affects the shape of the wave because the lower extremities propagate faster than the upper extremities, thus resulting in a bending forward of the wave as shown by the solid line.

In the right-hand side of figure 2 is shown an aircraft in supersonic flight where the speed of the airplane over the ground V_g is less than the speed of sound at the ground a_g. The example shown could correspond to a local airplane Mach number of about 1.1. The bow shock, in this case, does not extend all the way to the ground. The bow wave has

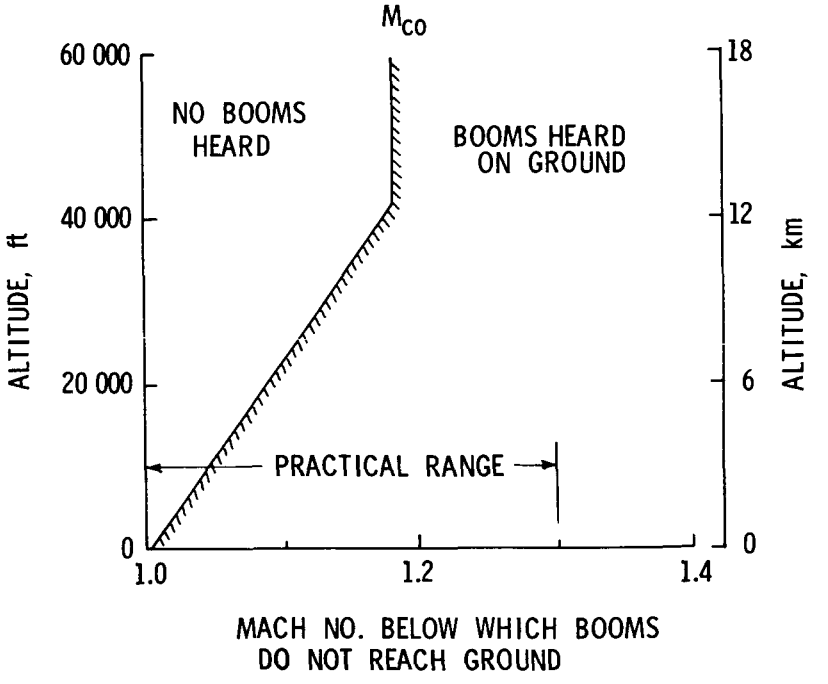

FIGURE 3. – Combinations of airplane Mach number and altitude for complete cutoff for steady, level flight in a standard atmosphere with no wind.

bent forward so that the lower extremity of the wave is traveling at the local speed of sound and has become essentially normal to the ground. For the case shown, the aircraft is said to be operating below "cutoff Mach number" (M_{co}).

The range of Mach numbers and altitudes over which M_{co} operations can be performed, assuming steady, level flight in a standard atmosphere with no wind, is shown in figure 3 (ref. 8). Flights at Mach numbers to the left of the hatched curve will result in no booms reaching the ground, whereas flights at Mach numbers to the right of the curve will result in booms reaching the ground. Figure 3 indicates that the highest speed at which the aircraft could operate in a standard atmosphere without producing booms at the ground is about $M = 1.15$. In the real atmosphere, variations in sound speed gradient do exist because of temperature and winds. Headwinds at altitude and higher temperatures at the surface would increase M_{co}; and conversely, tailwinds at altitude and colder temperatures at the surface would decrease M_{co}. The practical range of M_{co} for a fairly wide range of atmospheres (ref. 9) is shown to be from about 1.0 to 1.3.

Operation of aircraft below M_{co} has been used in the past by military and research pilots to fly at constant altitude supersonically without

having booms reach the ground. This was a particularly useful procedure with the earlier supersonic aircraft having $M = 1.2$ to 1.4 capability. In addition, these operations were performed for fairly short durations. Consideration of sustained flight at M_{co} is an entirely new and more complex operation. Before such sustained M_{co} operations are to be considered feasible, information is needed regarding (1) the practicality of these operations in terms of the required atmospheric information along the entire route, (2) the behavior of the shock waves near their extremities, and (3) the nature of the associated sonic boom exposures. This paper provides information from flight experiments that applies directly to the behavior of the shock wave near its extremity and the nature of the associated boom exposure. The information to be presented is in the form of a progress report to date on the results of these flight experiments.

EXPERIMENTAL SETUP

Previous attempts at experimentally defining the sonic boom pressure field at the shock wave extremities using ground-based microphones have been inadequate (refs. 2, 10, and 11). The present setup, however, involved the use of both ground-based microphones and microphones positioned at various heights above the ground to an altitude of 456 m (1500 ft). The test arrangement is shown schematically in figure 4. The aircraft were guided and tracked by ground-based radar, and all measured data were correlated with respect to time.

The tests were conducted at the AEC test site at Jackass Flats, Nev., in conjunction with NASA, AEC, NOAA, USAF, and DOT (FAA). Use

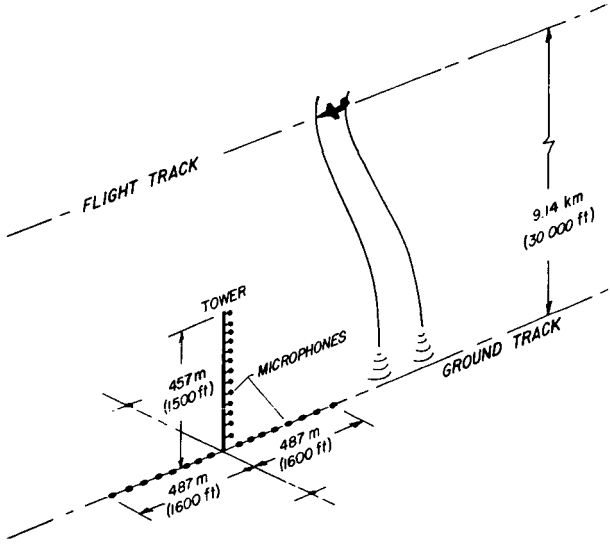

FIGURE 4. – Schematic diagram of experimental test arrangement used during M_{co} studies.

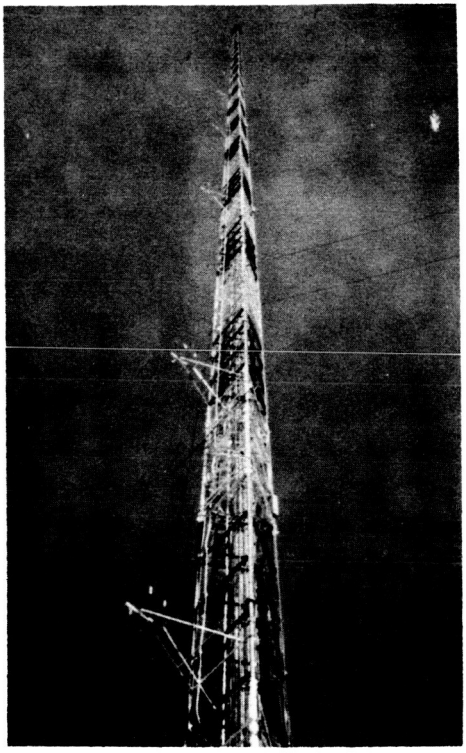

FIGURE 5. – The 456-m (1500-ft) Bren tower used for the flight tests.

was made of the 456-m (1500-ft) high Bren Tower located at the test site. A photograph of the tower is shown in figure 5. Microphones were positioned every 30.5 m (100 ft) on the tower along with appropriate meteorological instrumentation. The tower contained an elevator that permitted servicing and calibration of the instruments.

SONIC BOOM EXPOSURES

Flights Above M_{co}

In figure 6 are presented sketches of sonic boom signatures, as measured from various tower microphones, for steady, level flight condition of the aircraft where the airplane speed over the ground V_g is greater than sound speed at the ground a_g. This condition corresponds to a Mach number of about 1.3. As the incident bow and tail shocks propagate away from the aircraft, they extend down and intersect the ground and are then reflected upward. The intermediate shock that is shown is typical of an F–104 aircraft and originates from the inlet-wing junction (refs. 12 and 13). The sonic boom signatures that were observed as this

shock pattern moves past the tower microphones are illustrated in the figure.

At the top of the tower, both incident and reflected sonic boom signatures are observed. These two signatures are displaced in time according to the shock wave reflection angle. The incident and reflected signature are similar in shape and are about equal in amplitude. At ground level, these two signatures are coincident and only a single signature is observed having about twice the amplitude of the free air pressure signatures. To an observer at the top of the tower, therefore, four booms would be observed, whereas at ground level only two booms would be observed and they would be of twice the intensity of the free air booms.

In discussing shock wave propagation, it is helpful to make use of the ray-shock diagrams sketched in figure 7. The top part of figure 7 relates to the operating conditions of figure 6 in which V_g is greater than a_g. The aircraft is shown moving in a direction from right to left, and for simplicity only the bow wave is shown. The shock wave extends to the ground and is reflected upward. As the disturbances that form this shock wave are emitted from the aircraft, they travel toward the ground along ray paths indicated by the solid lines. These rays intersect the ground and are reflected upward, as illustrated by the dotted lines. Any number of such rays can be drawn from the aircraft at different times along the flightpath. It will be noted that two consecutive rays are essentially parallel and tend to converge only slightly as they approach the ground.

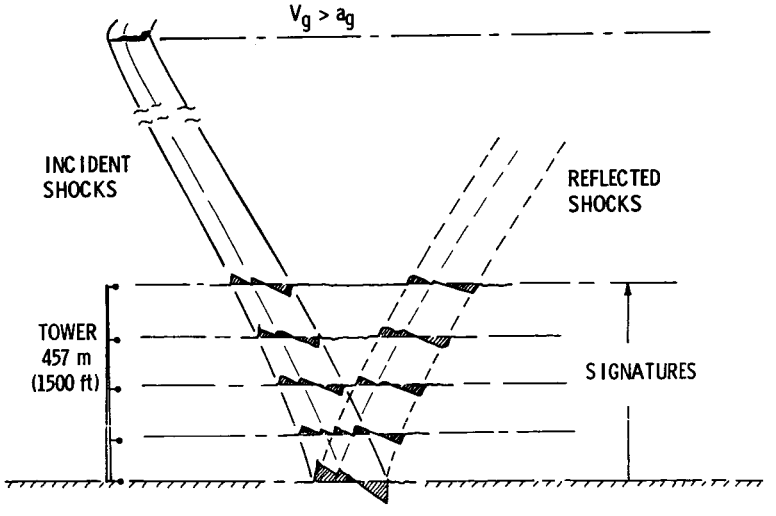

FIGURE 6.—Measured sonic boom signatures at various heights above the ground for an F-104 aircraft in steady, level flight at a Mach number above cutoff ($M = 1.3$) and at an altitude of 10.26 km (33 700 ft).

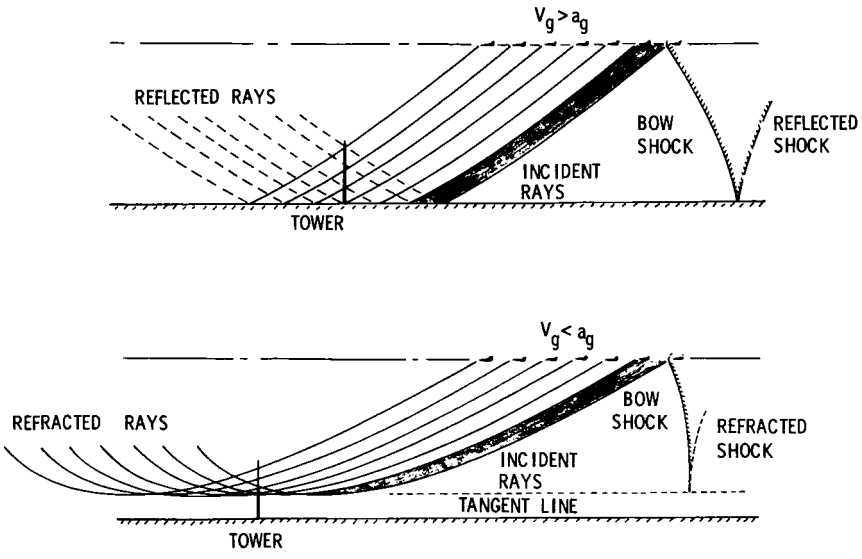

FIGURE 7. — Ray-shock diagram for aircraft operating at Mach numbers above and below the cutoff Mach number.

Flight Operations Near M_{co}

The bottom sketch shown in figure 7 relates to the conditions when the aircraft speed over the ground V_g is less than the sound speed at the ground a_g. These conditions would be associated with an aircraft flying below the cutoff Mach number. It will be noted that the rays have a greater curvature than those for the higher Mach number conditions and are totally refracted at an altitude above the ground. The rays, which have been drawn for various positions of the aircraft along the flight track, become tangent to each other at the cutoff altitude. The areas between adjacent rays, as indicated by the shaded region, decrease until they theoretically approach zero where the rays become tangent. The pressures are expected to markedly increase in regions of decreasing ray tube area. Thus, a caustic, or line focus, is formed where the rays become tangent at the cutoff altitude (for example, refs. 3 and 14 to 17).

A theoretical description of the bow shock near the cutoff altitude (ref. 14) is shown in figure 8. Altitude is plotted as a function of distance for an aircraft flight condition of V_g less than a_g. This could correspond to an aircraft Mach number of about 1.10. In the supersonic flow region, the bow wave is shown to propagate downward to the point where the sonic region is reached, at which point the shock refracts back on itself. Below the sonic region, subsonic flow exists. It is also noted in figure 8 that the depth of the region between supersonic and subsonic flow is suggested as being on the order of 304.8 to 609.6 m (1000 to 2000 ft), the

subsonic region being of the order of 914.4 to 1524 m (3000 to 5000 ft). It was expected, on the basis of analytical studies, that the pressure signatures on the region of the shock extremity would vary considerably in the three flow regimes. One of the main objectives of the flight tests was to define these pressure signatures by means of systematic measurements.

Measurements of the pressure field associated with the grazing condition shown in figure 8 are illustrated in figure 9. The aircraft is shown traveling in a direction from right to left on the figure at a ground speed slightly less than the sound speed at the ground. The shock waves are shown as solid lines, and the dashed lines are the refracted shocks. Also shown in the figure are the measured sonic boom signatures that were observed as the shock wave system moved across the microphones on the tower. In this particular experiment the shock extremity was positioned so that pressure disturbances in the supersonic, sonic, and acoustic regions were measured. At the top of the tower, a normal N-wave sonic boom signature was measured that included the incident bow and tail shocks and their refractions. At midtower, which was the approximate location of the shock extremity, it is noted that a U-shape (caustic) signature is measured for which the amplitudes are larger than

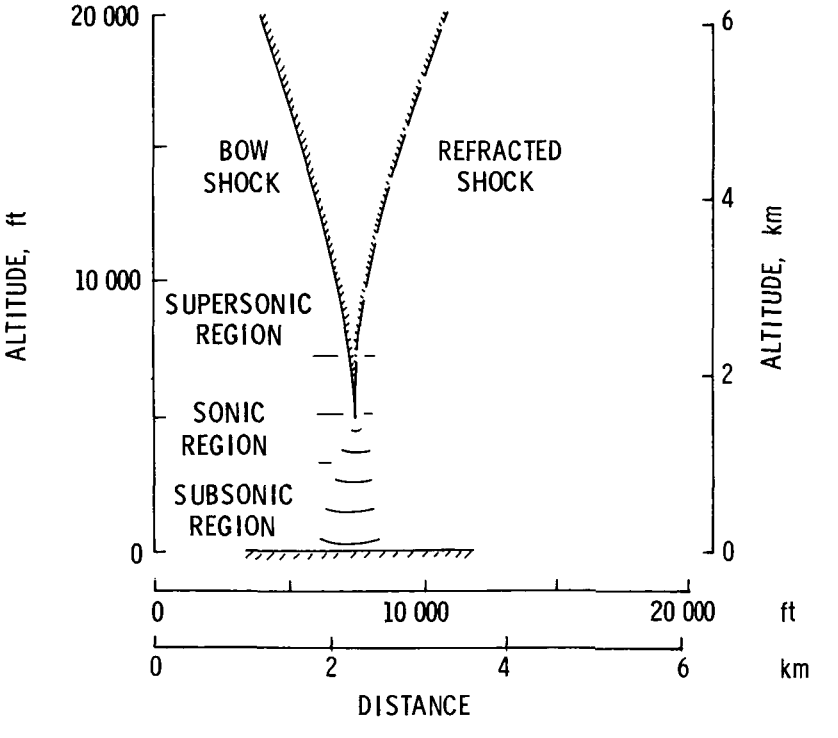

FIGURE 8. – Details of bow shock wave structure near Mach cutoff altitude.

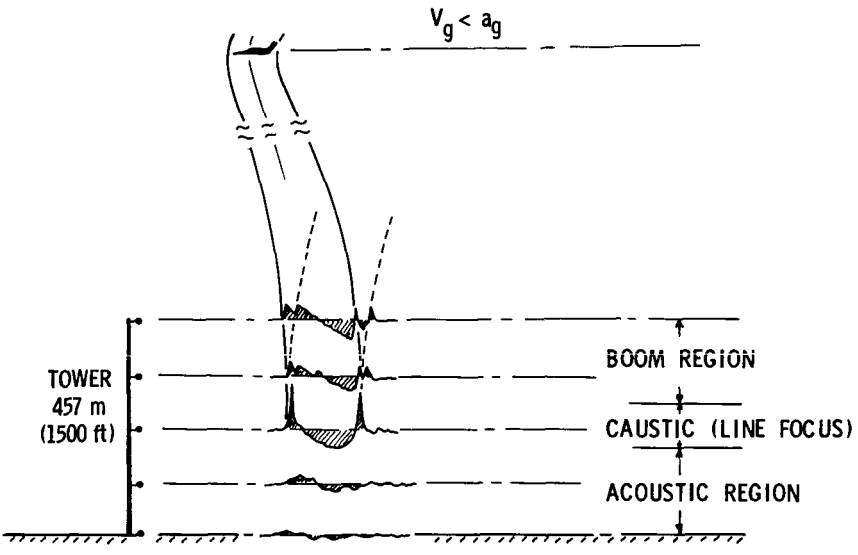

FIGURE 9.—Measured sonic boom signatures at various heights above the ground for an F–104 aircraft in steady, level flight at cutoff Mach number ($M = 1.095$) and at an altitude of 10.26 km (33 700 ft) mean sea level (msl).

those associated with N-wave signatures observed in the supersonic flow region. Near the base of the tower, below the shock extremity, the signatures are rounded or sinusoidal in shape and suggest acoustic disturbances.

The bow overpressure from signatures such as those shown in figure 9 for the flight operations near cutoff Mach number are presented in figure 10. The measurements, which represent the average values obtained from the ground and tower microphones, are from steady, level flights of F–104 aircraft at 9.13 km (30 000 ft) above the ground. The solid curve represents the overpressure variations suggested by theory (refs. 2, 8, and 14 to 17), and the symbols represent the measurements. Because M_{co} varied somewhat (from about $M = 1.08$ to 1.12) from flight to flight and over the 3-day test period because of variations in atmospheric conditions, the measured data have been normalized so that the overpressures associated with the caustic or U-shape signatures are located at an M_{co} of $M = 1.10$.

At Mach numbers below $M = 1.10$, very low overpressure levels were measured, and these were associated with the acoustic type of signature shown at the top left of figure 10. At Mach numbers above $M = 1.10$, normal N-wave types of signatures were observed from which the pressure increased gradually with increasing Mach number as predicted by theory. Near $M = 1.10$, U-shape waveforms were generally observed. The predicted overpressure values approach infinitely be-

cause of the presence of the caustic line. The measured caustic signatures generally indicate overpressure enhancement compared to those associated with the higher Mach numbers. The highest enhancement factor suggested by the data of figure 10 is 3.

SUMMARY REMARKS

Sonic boom measurements have been obtained from flight experiments of aircraft operating at cutoff Mach numbers to define the sonic boom pressure field at the shock wave extremity. The experimental results provide an indication of the depth and width of the focus region and a description of the pressure field near the shock extremity. U-shape or caustic signatures resulting in overpressure enhancement were observed at the shock wave extremities, and the highest measured levels are on the order of three times the nominal N-wave overpressures associated with operations at higher supersonic Mach numbers. The shock wave was found to be quite sensitive at its extremity to local atmospheric conditions (winds, turbulence, etc.). Good qualitative agreement with theory was obtained regarding the extent of the subsonic, sonic, and supersonic flow fields and their associated overpressure signature shapes.

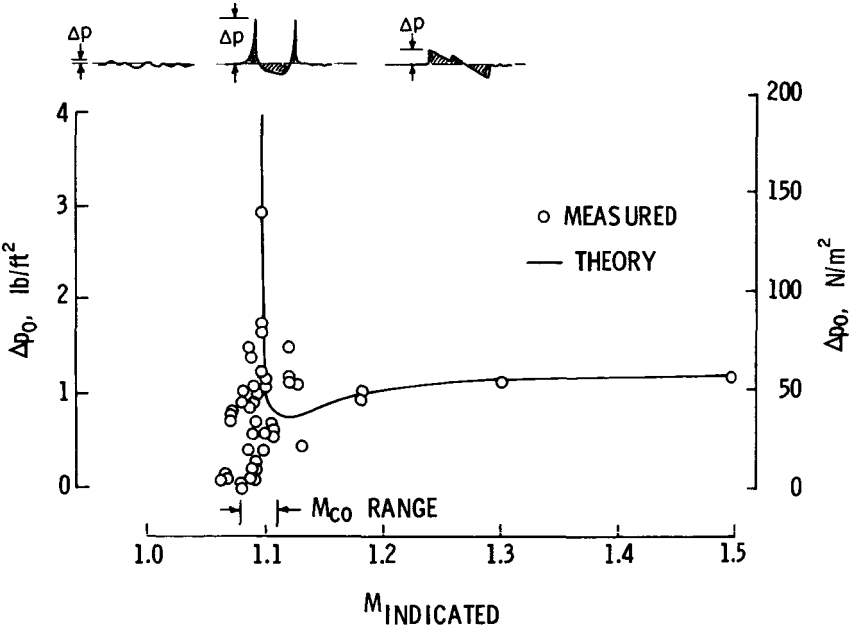

FIGURE 10.—Variation of overpressure with airplane Mach number for an F–104 in steady, level flight at 10.26 km (33 700 ft) msl. Data represent average of ground and tower overpressures.

REFERENCES

1. Proceedings of the Sonic Boom Symposium, pt. 2. J. Acoust. Soc. Amer., vol. 39, no. 5, May 1966, pp. S1–S80.
2. SEEBASS, A. R., ED.: Sonic Boom Research, NASA SP–147, 1967.
3. SCHWARTZ, IRA R., ED.: Second Conference on Sonic Boom Research, NASA SP–180, 1968.
4. Stanford Res. Inst.: Sonic Boom Experiments at Edwards Air Force Base. Rept. NSBEO–1–67, National Sonic Boom Evaluation Office, ASTIA no. AD 655 310, 1967.
5. SST Will Develop Global Route Patterns. Aviat. Week Space Technol., vol. 92, no. 1, Jan. 5, 1970, pp. 45–49.
6. Civil Aircraft Sonic Boom. Fed. Regist., vol. 35, no. 74, Apr. 16, 1970, pp. 6189–6190.
7. BRADLEY, E. S.; JOHNSTON, W. M.; AND VON KESZYCKI, C. H.: Passenger Transport at Low Supersonic Speeds. AIAA Paper no. 69–776, 1969.
8. RANDALL, D. G.: Methods for Estimating Distributions and Intensities of Sonic Bangs. R.&M. no. 3113, British A.R.C., 1959.
9. KANE, EDWARD J.; AND PALMER, THOMAS Y.: Meteorological Aspects of the Sonic Boom. SRDS Report no. RD 64–160, Federal Aviation Agency, ASTIA no. AD 610 463, 1964.
10. LINA, LINDSAY J.; AND MAGLIERI, DOMENIC J.: Ground Measurements of Airplane Shock-Wave Noise at Mach Numbers to 2.0 and at Altitudes to 60,000 Feet. NASA TN D–235, 1960.
11. MAGLIERI, DOMENIC J.; HILTON, DAVID A.; AND MCLEOD, NORMAN J.: Experiments on the Effects of Atmospheric Refraction and Airplane Accelerations on Sonic-Boom Ground-Pressure Patterns. NASA TN D–3520, 1966.
12. HUBBARD, HARVEY H.; MAGLIERI, DOMENIC J.; HUCKEL, VERA; AND HILTON, DAVID A.: Ground Measurements of Sonic-Boom Pressures for the Altitude Range of 10,000 to 75,000 Feet. NASA TR R–198, 1964.
13. MAGLIERI, DOMENIC J.; HUCKEL, VERA; AND PARROTT, TONY L.: Ground Measurements of Shock-Wave Pressure for Fighter Airplanes Flying at Very Low Altitudes and Comments on Associated Response Phenomena. NASA TN D–3443, 1966.
14. FRIEDMAN, MANFRED P.; AND CHOU, DAVID C.: Behavior of the Sonic Boom Shock Wave Near the Sonic Cutoff Altitude. NASA CR–358, 1965.
15. THERY, C.: Refraction Atmospherique et Reflection au Sol Des Bangs. AGARD Conf. Proc. no. 42, May 1969.
16. GUIRAUD, J. P.: On the Intensity Value of Sonic Boom in the Neighborhood of a Caustic. C. R. H. Acad. Sci., vol. 256, no. 8, Feb. 18, 1963. (A63–16929).
17. GUIRAUD, J. P.: Remarks on the Supersonic Boom in the Neighborhood of a Caustic. Rech. Aerosp. 3–13, Jan.–Feb. 1964. (A64–16179).

Airplane Configurations for Low Sonic Boom*

ANTONIO FERRI
New York University

Supersonic transport (SST) configurations selected from the point of minimizing sonic booms are investigated. It is indicated that for a total length of 300 ft and total initial weight of the same order as the present U.S. SST designs, sonic booms having shock pressure rise of the order of 0.5 lb/ft² can be obtained. Values as low as 0.3 lb/ft² are possible for airplanes designed for cross-country flights.

The introduction of supersonic airplanes for commercial aviation has encountered severe criticism and at the present time is opposed by many political and technical groups on the basis of several objections of different natures. Some of the furor generated against such steps is not completely justified because it is generated by superficial and incomplete information. However, the basic objection, related to the disturbances created by the sonic boom, is based on solid ground and presents one of the greatest obstacles in the practical development of future supersonic aviation.

Many of the present difficulties are the result of the fact that the problem of the sonic boom has been downgraded at the beginning of the planning of the development of the first generation of the SST. Therefore, programs for the first generation of these airplanes have been initiated without a complete understanding of the effects of the sonic boom on the population and their reaction against it. Only when strong objections have been raised against the use of such airplanes has the responsible technical community considered such problems to be of primary importance, and because of the lack of an acceptable solution, has been forced to limit the use of such means of transportation to overseas flights, at least for the first generation of airplanes.

The formation of sonic boom by supersonic airplanes is a physical

*This work was supported by the National Aeronautics and Space Administration under NASA grant NGL 33-016-119. The project monitor is Ira R. Schwartz. The work presented here is part of an investigation on sonic boom problems performed by a team at New York University under the direction of the author and Prof. Lu Ting. Participating in some phases of this work are Dr. Lu Ting, Dr. Huai-Chu Wang, F. Kung, A. Agnone, and M. Siclari.

phenomenon that cannot be eliminated when the airplane has lift and can only be reduced or modified; therefore, any technical effort in this field should be directed to answering the following basic questions:

(1) What is the level of minimum practical values that can be obtained if the airplane design is optimized for minimum boom?

(2) What is the minimum value acceptable if the airplane flies over a populated area?

If the answers to the first two questions give values that are of the same order of magnitude, then a third question should be answered:

(3) What are the penalties of performance, and what is a possible compromise if the airplane is designed for acceptable sonic boom?

This paper reviews an effort devoted to the first task; however, some remarks directed to the second and third questions are in order. Present regulations in the United States forbid the production by airplanes of sonic booms of any strength over the United States. Such a limitation is related only to airplanes; however, sonic booms and noise of some level and similar shapes are produced by many other human activities and are acceptable everywhere. Therefore, it must be assumed that such a regulation is of a preliminary nature. The strongly restrictive limitation is presently justified because of the lack of required information raised in question (2). It can be expected that better knowledge will permit changing such a restriction. It is interesting to recall indeed that similar objections (which were just as loud but not as well organized) were leveled against the introduction of the first generation of automobiles. They were also classified as too noisy, unnecessary, uneconomical, and dangerous. Today, the population has become used to car noise because of the practical advantages of the use of the automobile.

Although all the information is not available, it is very probable that all the objections related to possible damage to structures or buildings will be eliminated by better knowledge of the problem coupled with the reduction of the sonic boom level required to make the boom value acceptable to the people. The objection based on disturbances to humans is therefore the most serious objection to deal with at this stage of the problem. This objection is related strongly to the value of the discontinuous increase of pressure. Therefore, in the present discussion we will concentrate on minimizing this value.

It can be expected that the objection against supersonic flight will be overcome by a combination of several steps: limitation of the number of sonic booms over a given populated area on the basis of selection of appropriate routes, selection of airplane configurations that minimize the sonic boom effects on the ground, and adoption of provisions that minimize the disturbances due to local conditions.

The sonic boom on the ground depends on the details of the airplane design and flight conditions as well as on the focusing effects due to atmospheric conditions and to terrain configurations. Therefore, all aspects of the minimization should be considered. The presence of some atmospheric conditions can increase somewhat the intensity of the peak overpressures on the ground (refs. 1, 2, and 3). Control of atmospheric conditions is impossible; however, some knowledge is already available that permits the reduction of such effects by carefully selecting time of flight and flightpaths. It is probable that for very low values of sonic boom, the sporadic increase of sonic boom overpressure due to special atmospheric conditions would not make it impossible to fly supersonic planes over land.

The problem of focusing due to terrain configurations is more serious because these conditions will exist all the time for every given flightpath. In addition, such effects can produce large increases of sonic boom effects. Fortunately, such effects, once detected, can be reduced or eliminated by correct selection of flightpaths and by introducing special precautions in the vicinity of the focusing.

LOCAL REDUCTION OF SONIC BOOM BY MANEUVERING OF THE AIRPLANE

The sonic boom of an airplane, according to the Whitham theory (ref. 4), depends on the distribution of the lift and volume along the length. Following the approach suggested by Carlson (ref. 5), the lift and volume can be combined in a single equation. The F-function that defines the sonic boom can then be expressed in terms of an integral that combines lift and volume. (The function is determined by transforming the lift into an equivalent cross-sectional area.) The cross-sectional area due to volume reduces to zero at the end of the airplane; therefore, a cross-sectional area of the airplane at zero lift is equal to the difference in area due to the streamtubes of the engines plus the cross section of the wake. The equivalent area due to the lift reaches the value of $\beta/2\ C_L S$ [1] at the end of the wing and then remains roughly constant downstream. Then for a given distribution of equivalent cross-sectional area, which produces a given sonic boom signature, many airplane configurations can be obtained because a change in the division of equivalent cross-sectional area between volume and lift that does not change the total area distribution does not change the sonic boom. However, when a given design is selected, the sonic boom on the ground depends on the lift of the airplane. The signal generated by the air-

[1] $\beta = \sqrt{M_\infty^2 - 1}$, C_L is lift coefficient, S is wing area, and M_∞ is flight Mach number. This value is increased by nonlinear effects because the overpressure side of the wing produces more than one-half of the lift. This effect can be evaluated and is included in the results presented here.

plane and modified by the atmosphere is reflected and amplified by the ground, depending on the shape of the ground. If the ground is absolutely flat and rigid, the coefficient of amplification at high Mach numbers is 2. In practical conditions some decay takes place because of the nonuniformity and thickness of the ground. Therefore, usually a coefficient less than 2 is assumed for the reflection for a rough flat ground. In this paper a coefficient of 1.8 is used. However, if the ground has some special type of shapes, larger amplifications are also possible (refs. 4 and 5). It can be expected, for example, that larger amplifications could be obtained locally at the beginning of a chain of mountains or at some points at the end of a valley if the airplane flies parallel to the valley.

In addition, it would be useful to reduce substantially the sonic boom when airplanes fly in the proximity of cities. This could be done if the airplane reduces its lift by means of a maneuver. An airplane flying at high velocity could perform a pullup maneuver of a few degrees before reaching the point where the sonic boom peak value should be reduced and then fly a lower lift trajectory over the selected point. The airplane could then fly for several miles producing a signal that is substantially reduced.

Figure 1 gives the range obtainable for different values of C_L at a constant speed and constant C_L trajectory as a function of the Mach number. The maneuver starts at an altitude of 40 000 ft where the airplane makes a pullup maneuver of α degrees and then flies a trajectory at constant C_L equal to N times the C_L for cruise, with constant velocity. The airplane

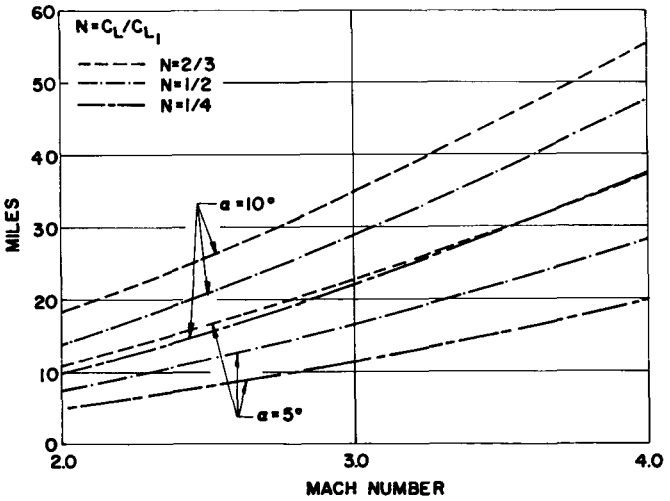

FIGURE 1.—Range as a function of flight Mach number for a constant C_L, constant speed trajectory, starting at 40 000 ft and angle α and terminating at the same altitude.

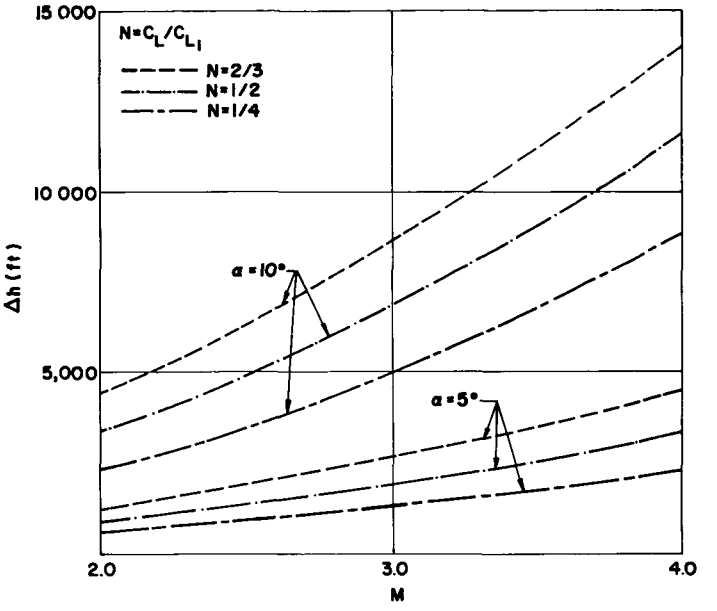

FIGURE 2.—Maximum Δh reached for an airplane during a trajectory corresponding to ranges given in figure 1.

first increases altitude, then descends, and reaches 40 000 ft again at the same angle α. The maximum altitude reached is given in figure 2. Two values of initial angle of the trajectory have been considered; one corresponding to $\alpha = 5°$ and the second to $\alpha = 10°$. The maximum value of discontinuous Δp produced by the sonic boom decreases strongly when the flight altitude decreases and C_L decreases. The maneuver, therefore, can alleviate substantially the disturbances produced by sonic boom. For example, initial Δp for a C_L corresponding to two-thirds of the horizontal value at an altitude of 40 000 ft can be as low as 0.4 lb/ft^2 as shown in figure 3. The curve corresponds to an airplane having a weight of 460 000 lb and a length on the order of 300 ft. The takeoff weight of the airplane is between 650 000 and 700 000 lb.

DESIGN CRITERIA FOR MINIMUM BOOM DURING CRUISE

Optimum design criteria for supersonic airplanes have been discussed in detail by several authors for the case of far-field signatures. Jones (ref. 6) and Carlson (ref. 5) give expressions for minimum overpressures for the conditions of far-field signature. McLean (ref. 7) has shown that for the acceleration phase, near-field signature is possible. The author (refs. 8 and 9) has shown that near-field signature with sonic booms having values of Δp_{max} on the order of 0.8 lb/ft^2 can be

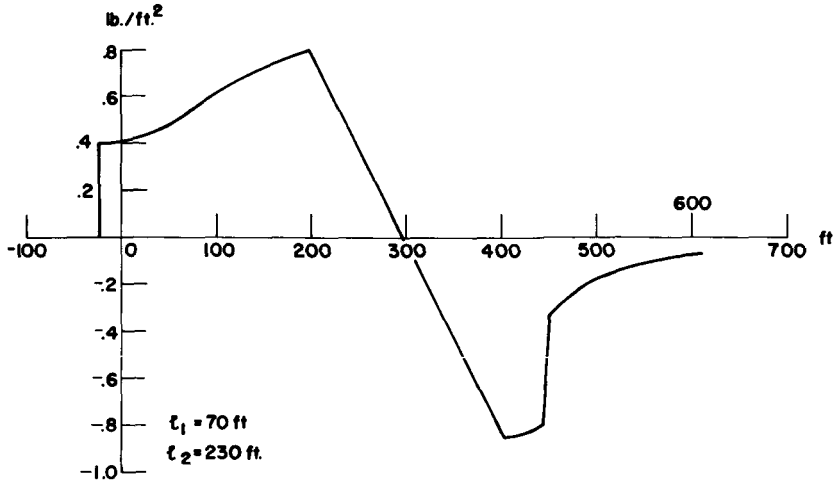

FIGURE 3. — Sonic boom signature corresponding to an airplane 300 ft long flying at $M = 2.7$ and 40 000-ft altitude at a lift equal to two-thirds of the lift required for horizontal flight. Airplane weight is 460 000 lb. The equivalent area of the front part is equal to one-ninth of the total.

obtained even for very large airplanes on the order of 500 000 lb during cruise at 60 000 ft and $M = 2.7$, provided that a large amount of equivalent cross-sectional area is placed near the front. Later Seebass (ref. 10) and George (ref. 11) obtained analytical expressions confirming such results. For the far-field signature, it is possible to obtain simple expressions relating the length, weight, and altitude of the airplane to peak sonic boom signature. The problem is more complex for the near field because the peak overpressure is not necessarily obtained at the beginning and even the maximum peak overpressure is not indicative of the disturbance because both criteria are important: the value of pressure discontinuities and the maximum overpressure. Both these quantities vary with weight of the airplane, length, flight altitude, and airplane configurations.

The analyses of references 10 and 11 indicate that especially for low-level flight, the discontinuous variation of pressure can be avoided completely when values of the length above what is considered acceptable today are considered. In the present work the investigation has been directed toward obtaining information on practical lower values obtainable when some of the practical constraints are retained. The important constraints are the length of the airplane, which, for practical operation, can vary only within limits; flight altitude, which is related to the possibility of flying at acceptable values of the L/D required for the range; and area distribution and volume of the fuselage, which is related to the possibility of utilization of the airplane. In addition, the

variation of the cross-sectional area of the fuselage in the front part is related to visibility requirements.

In the work presented here (which is a continuation of the work presented in ref. 8), details of the signature have been related directly to the airplane configuration. The results obtained have been derived by using two different numerical programs: (1) the program generated by Carlson at NASA Langley Research Center (required modifications have been introduced in the original program) with the assumption of constant atmospheric pressure averaged between the flight altitude and ground ($p = \sqrt{p_h p_{ground}}$), and (2) the additional program generated by W. Hayes (ref. 12). The latter program permits analyzing maneuvers, takes into account variable density for horizontal flight, and requires somewhat longer computing time. Some data have been obtained with both programs. The differences between the results of the two methods are small and not important for the conclusion reached here and therefore are not discussed.

The parameters investigated here are airplane configuration, weight, length, Mach number, and flight altitude. The criteria for the selection of the range of the parameters selected are briefly outlined below: Three different values of weight have been considered corresponding either to horizontal flight or to maneuvers: 460 000, 320 000, and 240 000 lb. The first weight assumed is representative of the first part of cruise for an airplane takeoff weight of 600 000 lb. A typical airplane weight distribution for such an airplane is

Total weight, 600 000 lb
Empty weight, 240 000 lb
Fuel weight, 310 000 lb

This airplane, with a payload of 50 000 lb, should be able to fly 4900 statute miles. In selecting these data, it has been assumed that because the airplane is a second-generation airplane, it will have improved structural design and better engines. Therefore, for the same total weight and range, it can be more complex than first-generation airplanes. For these airplanes, taking the fuel consumption for acceleration into account, the weight of the airplane at cruise speeds varies between 490 000 to 330 000 lb. Then a weight of 460 000 lb is close to the worst condition. Consistent with these data, an airplane having an initial gross weight of 400 000 lb will have a range of 2800 statute miles, with required reserve. This distance is typical of cross-country flights in the United States. Such an airplane at the beginning of cruise will weigh 330 000 lb and at the end 230 000 lb. The first two values assumed correspond to the initial and final phases of cruise for transatlantic airplanes of 600 000 lb; the second and third, to an airplane having smaller ranges usable for cross-country flights.

420-093 O - 71 - 18

The length of the airplane is a very important parameter to obtain near-field signatures; therefore, lengths on the order of 300 to 400 ft have been considered. Few calculations have been performed for shorter lengths to emphasize the difficulty of obtaining near-field signatures for short airplane lengths. In addition, the available height of the airplane has also been utilized to increase the effective length of the airplane. Present airplanes have vertical tails about 60 ft from the ground. The height can be used advantageously to decrease sonic boom in a biplane configuration as will be discussed later. In this case, the effective length can be increased roughly by h/M_∞ with respect to the physical length (h is the height of the airplane; M_∞, the flight Mach number). Therefore an effective length of 300 ft could be obtained with an airplane on the order of 200-ft actual length at $M=2.7$, while 450 ft can be obtained for an airplane 300 ft long. In a biplane configuration, the wing area is distributed in two wings. However, the wing thickness required by the structure probably will not increase substantially provided that the two wings are connected rigidly near the tip to form a box structure. Then, the system can be designed aerodynamically for low drag even at transonic speed.

In the analysis the presence of a vertical tail, the fact that the engine exhausts are usually placed near the trailing edge of the wings, and the presence of the wake have been taken into account. These factors tend to increase the effective length of the airplane and decrease slightly the strength of the second shock of the N-wave. In addition, nonlinear corrections have been introduced when required in the definition of the equivalent cross-sectional area.

The flight Mach numbers considered are 1.5, 2.7, and 4. An increase in cruise Mach number tends to decrease the fuel consumption per mile, and therefore for a given weight of the airplane, will permit a better compromise for the design from the sonic boom point of view because it will permit some degradation of aerodynamic performances.

Several flight altitudes have been considered between 40 000 and 80 000 ft. The altitude of 60 000 ft has been assumed as typical for the present SST design by Boeing because it corresponds to high values of L/D. The flight altitude is a very important parameter for the utilization of near-field effects. In addition, a decrease of flight altitude decreases proportionally the lateral spread of the disturbance. When far-field signature is present, the increase of altitude decreases the sonic boom overpressure; therefore, high altitudes have been considered desirable in the past. (For a given weight of airplane, the Δp_{max} decreases roughly proportionally to $h^{3/4}$). However, when near-field effects are utilized, such a conclusion is invalid, and lower altitudes of flight appear to be advantageous. A decrease of flight altitude simplifies the engine design and reduces engine weight and will permit using a somewhat more

efficient engine, thus canceling some of the penalties due to the decrease of L/D.

The parameter that has been investigated parametrically is the shape of equivalent cross-sectional area distribution. To obtain realistic equivalent area distribution that could correspond to a possible airplane design, the equivalent area distribution has been divided into two regions, the front and rear. The important characteristic of the front and rear regions is defined mainly by two parameters: the area of the equivalent cross-sectional area in the front region indicated by L_1 and the length of the front region indicated by l_1. The details of the distribution of the equivalent cross-sectional area in this region do not affect strongly the results provided that such a distribution is close to optimum. Therefore, in all of the analyses, the equivalent area distribution has been divided into two regions. The total value of the equivalent area and the length has been changed parametrically, while the form of the distribution has been kept constant.

RESULTS OF THE ANALYSIS

The distribution of an equivalent area along the length of the airplane is a very important parameter for the shape of the sonic boom. All of the results indicate that a minimum concentration of equivalent cross-sectional area is required in front to obtain near-field effects. Such a minimum depends on the Mach number and flight altitude. However, the details of such a distribution are not too important, provided that the distribution is not too different from the optimum shape.

As an indication of these effects, in figure 4 the sonic boom signature obtained for an airplane flying at 60 000 ft, with $M=2.7$, and having a weight of 460 000 lb is shown. The total equivalent area in each case is constant and corresponds to a weight of 460 000 lb. The total length of the airplane is 300 ft. For all cases, this length has been divided into two regions, $l_1=70$ ft and $l_2=230$ ft. The equivalent area at the end of the front part corresponds to 15.5 percent of the total. This value is also kept constant for all cases. The distribution of the equivalent area as a function of the length in the front part has been changed in the different diagrams as indicated in the figure. The distribution of the rear part has been kept constant and assumed in all cases to be linear. The figure indicates that for all cases, near-field effects are obtained and peak values of the order of 0.9 can be obtained for values of the exponents of the expressions between 1/3 and 1/5.

A change of either the l_1 or of the value of the equivalent area of the front $L_1=\int_0^{l_1} kx^n dx$ for a given length of the airplane changes the near-field region and the value of the initial Δp. In figure 5, sonic booms cor-

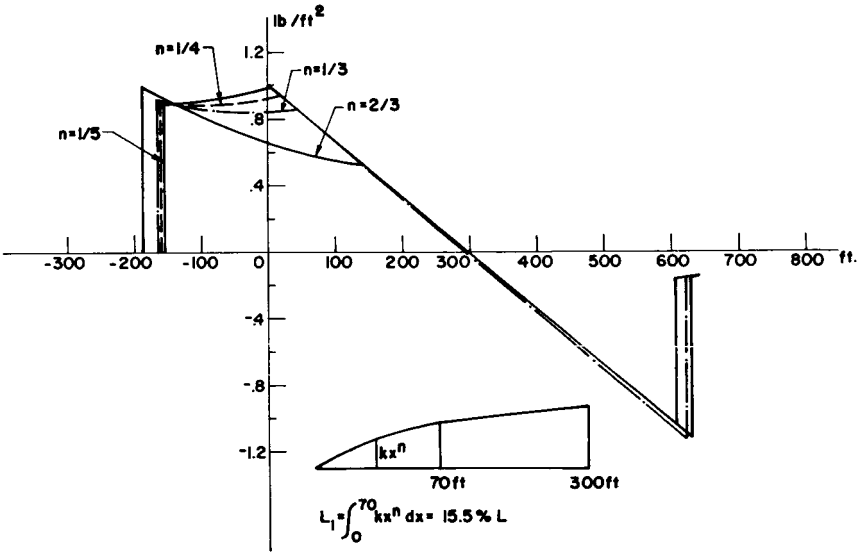

FIGURE 4.—Effect of distribution of equivalent area in the front part. Airplane characteristics are $L = 300$ ft, weight of 460 000 lb, $M = 2.7$, $h = 60\,000$ ft, L_1 frontal area 15.5 percent of total, and $l_1 = 70$ ft.

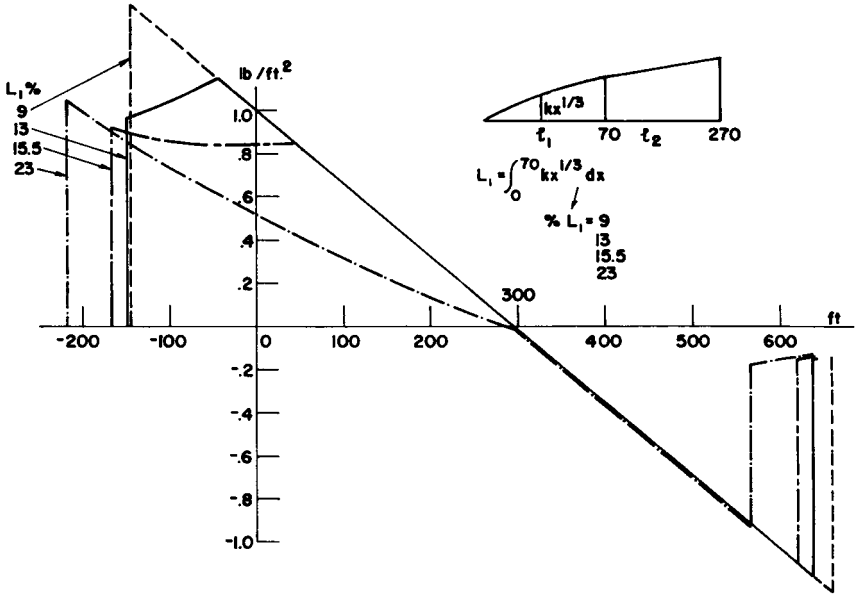

FIGURE 5.—Sonic booms corresponding to $M = 2.7$, $h = 60\,000$ ft, weight 460 000 lb, total length equal to 300 ft, different equivalent area in the front part, and $l_1 = 70$ ft.

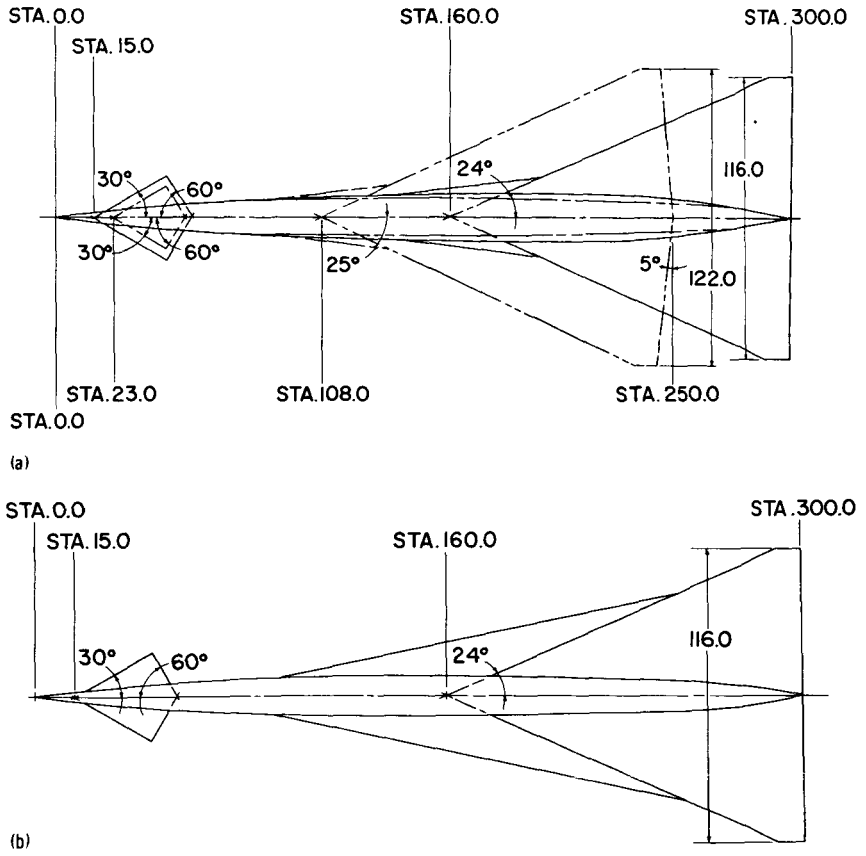

FIGURE 6.—(*a*) Possible airplane configuration corresponding to the sonic boom shown in figure 5 for $L_1 = 0.155\ L$. Actual configuration used for first-generation SST is shown by dotted lines. (*b*) A possible airplane configuration corresponding to the sonic boom shown in figure 5 for $L_1 = 0.155\ L$.

responding to a given value of l_1 equal to 70 ft and different values of L_1 are shown. Too small an amount of equivalent area in front, i.e., $L_1 \leq 9$ percent of the total, gives far-field signatures. The extent of the near-field signature increases with the increase of L_1; however, the initial Δp increases with L_1 when L_1 is larger than 16 percent. Similar results are obtained if the value of l_1 is changed and L_1 is kept constant.

It is interesting to observe that the peak sonic boom is of the order of 0.9 for the conditions selected, while configurations used for the first generation of supersonic transports have for corresponding conditions values of the order of 1.9. The difference is due to the distribution of lift along the airplane. In figures 6(*a*) and 6(*b*), two possible configurations are shown that correspond to the equivalent area distribution selected for the case of $n = 1/3$, $l_1 = 70$ ft, and $L_1/L = 15.5$ percent. For comparison, in

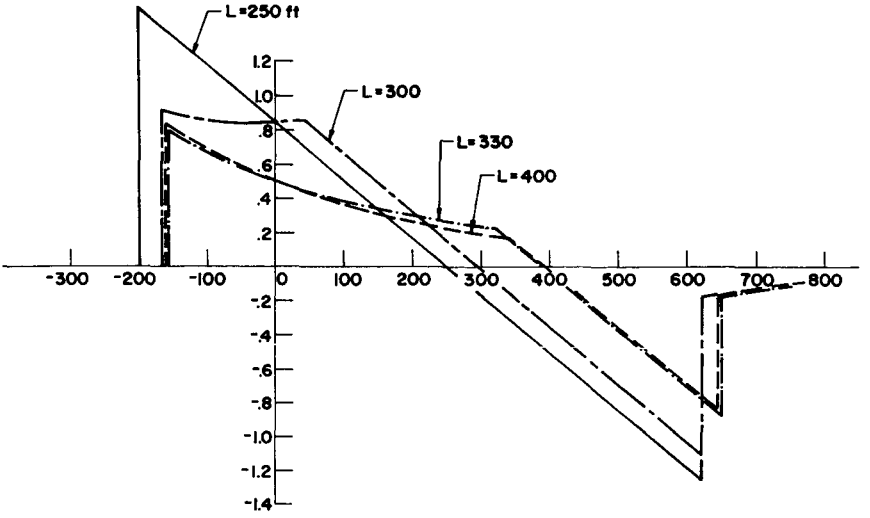

FIGURE 7.—Effect of airplane length on sonic boom signature at $M = 2.7$, $h = 60\,000$ ft, and weight of 460 000 lb.

figure 6(*a*) a configuration used for the first-generation airplane having a peak value of 1.9 is also shown in dotted lines. The configuration of figure 6(*a*) has a larger fuselage than the original one; therefore, the changes required are obtained by means of volume changes. In figure 6(*b*), the wing planform has been changed and a highly sweptback wing has been used, while the fuselage has been kept similar to the fuselage of the first generation of airplanes. The second configuration permits similar or better aerodynamic performances than the original airplane for cruise conditions; however, it probably will require more wing area for low-speed flight.

The other design parameter that is of extreme importance is the total length of the airplane. In figure 7, the effect of the total length of the airplane is indicated. In this comparison, the values of l_1 and L_1 are kept constant and equal to 70 ft and 15.5 percent of the total lift, and the total length has been changed. In figure 8 a similar comparison is shown; however, the values of L_1 and l_1 are optimized for each total length. An increase of length permits decreasing the Δp_{max} somewhat and permits the use of a slender fuselage. A possible configuration is shown in figure 9.

The required length of the airplane can be interchanged with the height of the airplane (ref. 13). This possible tradeoff suggests that a biplane having wings that do not interfere at supersonic speeds and do not choke at transonic speeds has some good possibilities from the point of view of reducing sonic boom. Examples of such a configuration are shown in figures 10(*a*) and 10(*b*). The wing area has been distributed on two wings, one placed on the fuselage and the other placed on top

of the vertical surface. The height of the vertical surface is the same as in present SST configurations of the same size. The two wings are staggered to avoid choking at transonic speed and are connected by the vertical tail and have two vertical reinforcing structures near the tip to decrease the bending stresses. The sonic boom of this configuration is shown in figures 11(*a*) and 11(*b*). Figures 11(*a*) and 11(*b*) indicate that without increasing the length and the height of the configurations considered, it is possible to reduce the jump in Δp due to the sonic boom for an airplane with a weight of 460 000 lb flying at 60 000 ft and with $M = 2.7$ to values of the order of 0.5 to 0.6. An alternate solution is a high-wing airplane as shown in figure 10(*c*). In this case, the perturbation of the design configuration is smaller, and smaller aerodynamic changes are required. However, the fuselage hangs underneath the wing as in the old hydroplanes. Therefore problems related to lateral stability and roll stability should be investigated. In figure 10(*c*), the use of the dihedral is introduced to reduce the length of the struts. From an aerodynamic point of view, this configuration has attractive characteristics as it produces favorable interference.

Let us consider now the variation of the total weight at the same Mach number and flight altitude. In figure 12, the sonic booms of three airplanes having the same length and the same distribution of cross-sectional area but different weights are shown. A decrease in weight decreases substantially the Δp_{max}.

In figure 13, the sonic boom for an airplane with a weight of 320 000 lb is shown for several values of L_1. The length of the front part is constant and equal to 70 ft, and the total length is also constant and equal to 300 ft.

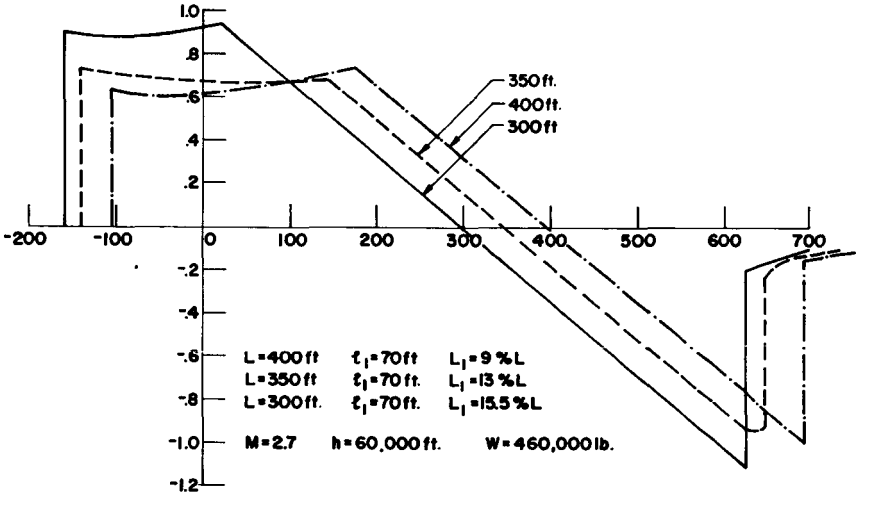

FIGURE 8.—Effect of length on sonic boom signature.

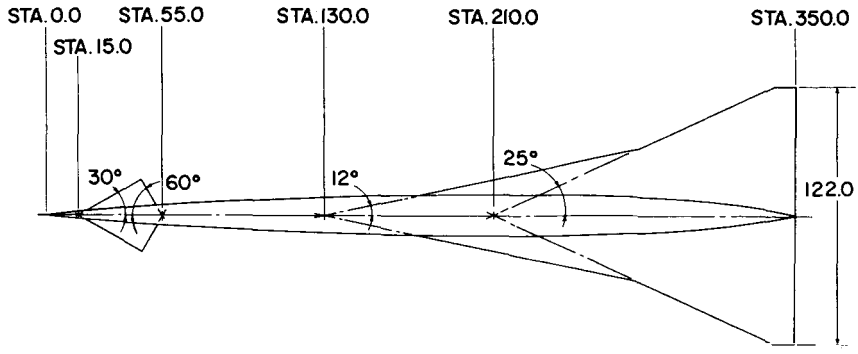

FIGURE 9. – Possible configuration of an airplane 350 ft long with Δp_{max} equal to 0.7 lb/ft².

Figure 13 indicates that shocks on the order of 0.6 lb/ft² can be obtained for an SST useful for a cross-country flight with a weight of 320 000 lb. The physical configuration of the airplane changes when the value of the lift changes even if the distribution of equivalent area is similar because the volume of the airplane must change in proportion. For a weight of 320 000 lb the pressure jump can be reduced to values as low as 0.4 lb/ft² if a biplane configuration is used.

Figure 14 gives the sonic boom configuration for a biplane flying at altitudes of 40 000 and 60 000 ft at $M = 2.70$. The airplane is 300 ft long. A possible configuration is similar in shape to the configurations shown in figure 15. The first and last discontinuous jumps have a value of the order of 0.28 to 0.40. After the initial jump, a gradual pressure rise takes place that is not objectionable from the point of view of disturbances to the population.

The altitude of flight is also a parameter. A change of flight altitude between 60 000 and 30 000 ft does not change strongly the value of the minimum intensity of the pressure jump unless the strength of the initial shock and the wave is decreased. When the altitude or Mach number of flight is changed for a given vehicle weight and total cross-sectional area distribution, the relation between cross-sectional area contribution due to lift and area due to volume changes because the equivalent cross section due to lift is proportional to the ratio between weight and dynamic pressure (the coefficient is $\beta/2$). Then an increase in Mach number or decrease of altitude for a given total weight increases the dynamic pressure and decreases the contribution of the lift with respect to the contribution of volume, and vice versa. Now if the equivalent area distribution selected on the basis of sonic boom optimization requires too large a fuselage in the front part of the vehicle, the requirement can be satisfied by using highly sweptback wings as shown in figure 6(*b*). However, if the flight Mach number increases at constant altitude or the flight altitude decreases for the same Mach numbers, then the maximum

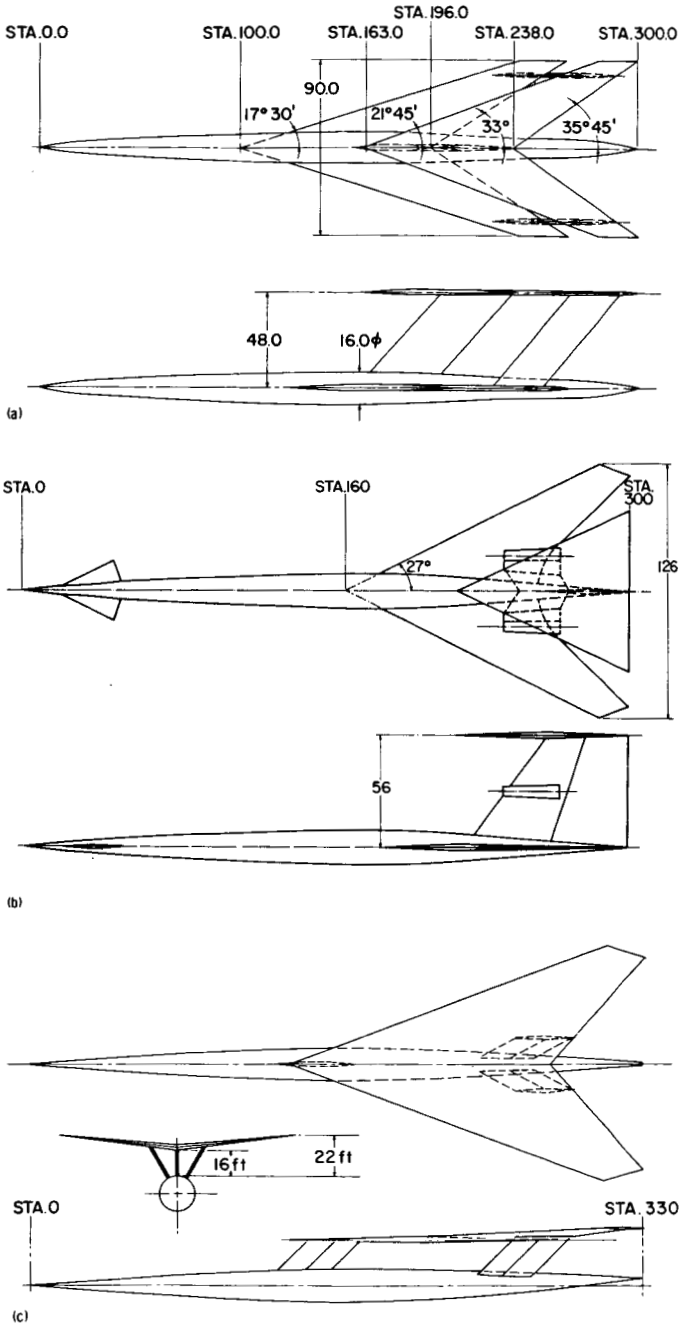

FIGURE 10.—(*a*) Schematic design of a biplane configuration 300 ft long having sonic boom signature shown in figure 11(*a*). (*b*) Schematic design of biplane configuration. (*c*) High-wing configuration.

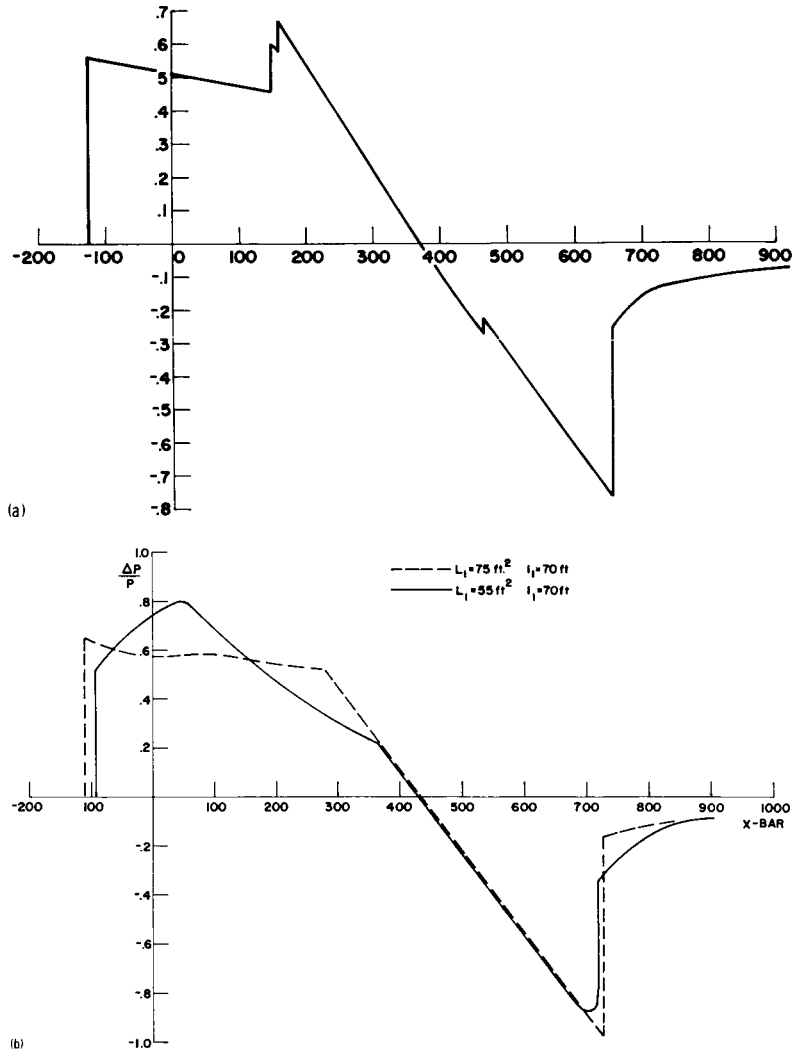

FIGURE 11.—(*a*) Sonic boom signature of the biplane shown in figure 10(*a*), $M = 2.7$, $h = 60\,000$ ft, weight of 460 000 lb, and $L = 300$ ft. (*b*) Sonic boom for biplane configuration $M = 2.7$, weight of 460 000 lb, and $h = 60\,000$ ft.

fuselage cross section permitted corresponding to the total area distribution selected decreases. As a consequence, solutions are obtained that do not have practical applications because the permissible fuselage is too small. Because the cross section and volume of the fuselage required for an SST are dictated by the mission, the apparent advantage from the point of view of reduced sonic boom of low-altitude flight (below 40 000 ft) as indicated by generalized optimization studies cannot be

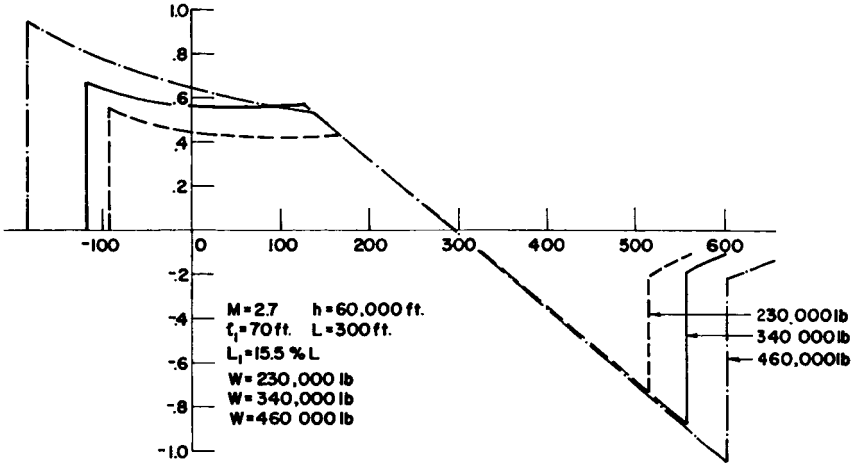

FIGURE 12.—Sonic boom signature as a function of airplane weight.

achieved when realistic requirements of volume, area, and length of the fuselage are introduced even if the large reduction of airplane performance due to the decrease of flight altitude could be accepted.

The last parameter considered is the Mach number. An increase in Mach number increases slightly the peak Δp for the same configuration for the same weight and altitude of flight, but the difference is very small (fig. 16). If the Mach number and altitude of flight decreases, then the near-field effects become very pronounced, and very low initial

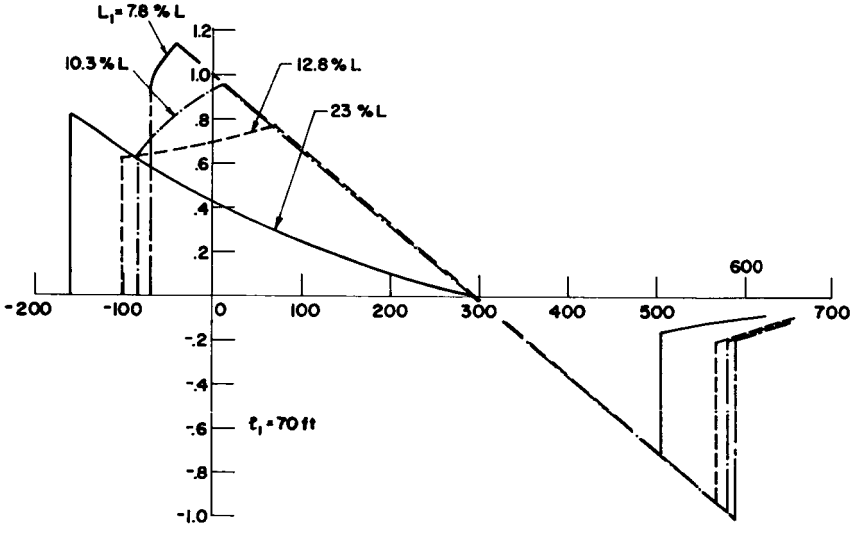

FIGURE 13.—Sonic boom configurations for airplanes 300 ft long with a weight of 320 000 lb, $M=2.7$, and $h=60\,000$ ft.

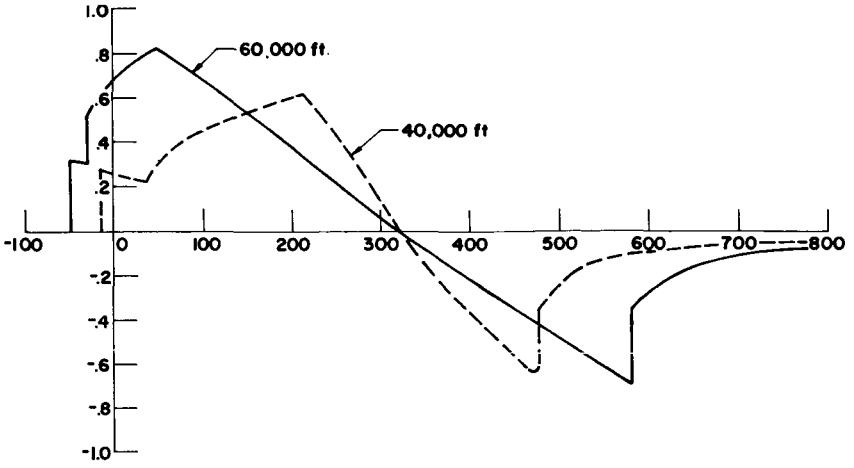

FIGURE 14.—Sonic boom signature of a biplane configuration at $M = 2.7$ and $h = 40\,000$ and $h = 60\,000$ ft, with a length of 300 ft, height of 45 ft, weight of 320 000 lb.

Δp can be obtained. For these conditions, initial pressure jumps as low as 0.3 are possible; however, the trailing shock does not decrease in the same proportion, and usually it increases, unless the equivalent airplane length is substantial. Again the biplane configuration can be used to advantage. A signature obtained for a biplane 290 ft long, flying at $M = 1.5$ and 40 000 ft is shown in figure 15. The peak pressure is less

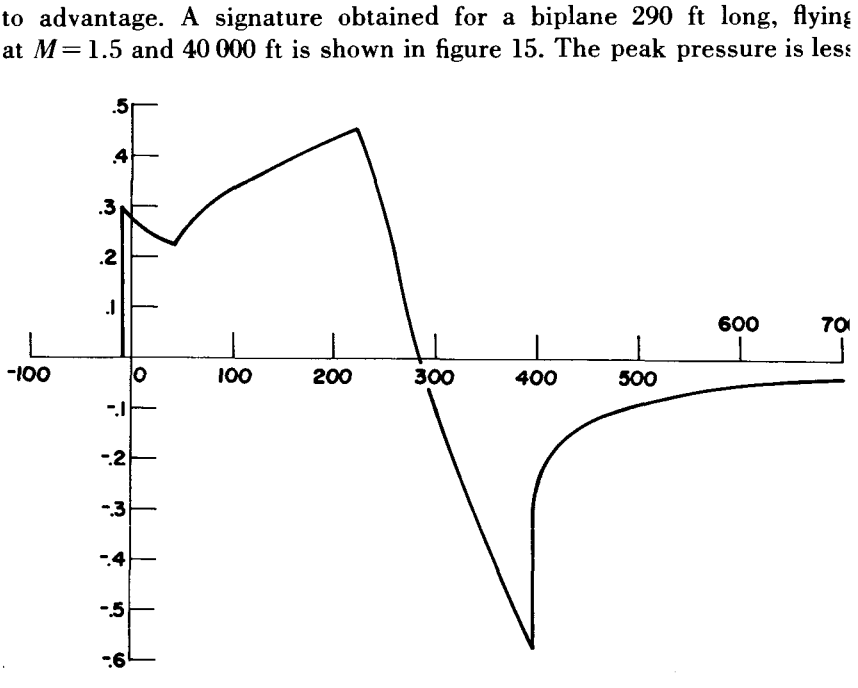

FIGURE 15.—Sonic boom signature of the biplane shown in figure 17 flying at $M = 1.5$ an 40 000-ft altitude, with a weight of 320 000 lb and length of 290 ft.

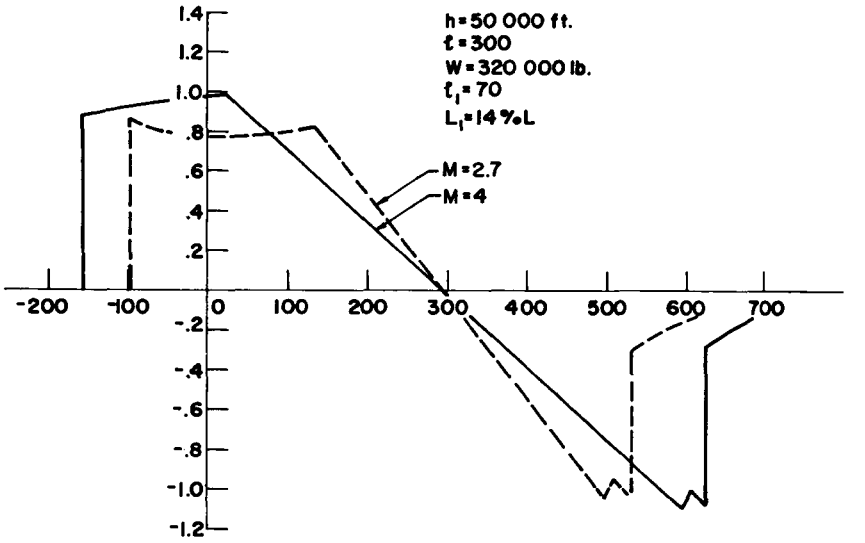

FIGURE 16.—Sonic boom for two airplanes flying at $M=4$ and $M=2.7$. The airplanes have the same weight and equivalent area distribution.

than 0.3 lb/ft^2. A possible corresponding configuration is shown in figure 17. It should be noted that the area of the fuselage in the front part is substantially reduced as mentioned before.

CONCLUSIONS

The results of the analysis presented here indicate that from an aerodynamic point of view, it is possible to generate airplane configurations that can reduce substantially the strength of the front and tail shocks of sonic booms for airplanes designed for transatlantic operations: values as low as 0.5 lb/ft^2 are possible. Values as low as 0.4 and 0.3 lb/ft^2 are possible when the weight is reduced for cross-country operations and the airplane is optimized for minimum sonic boom. These values are much lower than the values investigated in present flight tests and appear to be in the range of acceptable disturbance from extrapolation of present information on possible reaction to sonic boom. In addition, disturbances of the same order are presently accepted in normal operations in populated areas. The analysis presented here has analyzed only superficially the consequences of utilization of such concepts on airplane performances. The maximum L/D of the airplane at cruise should not be strongly affected by the change suggested. The structural weight, however, will probably increase with respect to simpler conventional solutions. Some increase in weight and decrease in L/D are acceptable for a shorter range airplane; in addi-

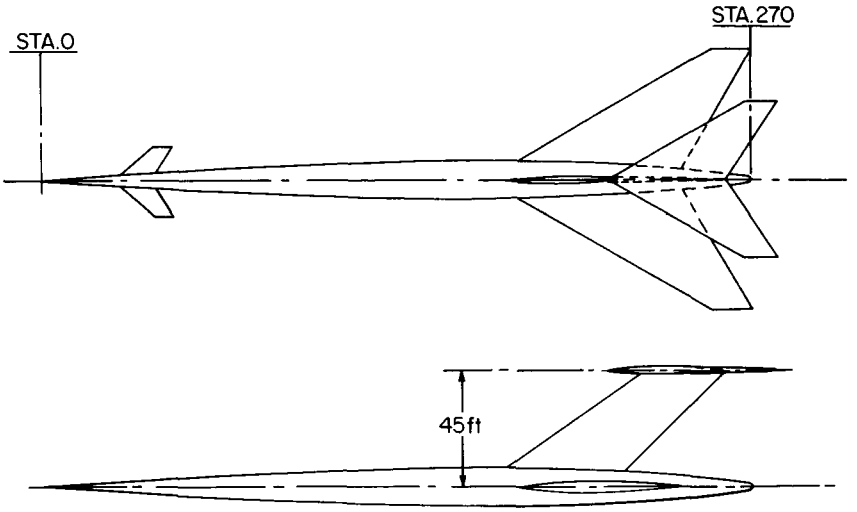

FIGURE 17. – Possible biplane configuration corresponding to sonic boom signature shown in figure 15.

tion, small improvements in engine performances could make such deterioration acceptable. Therefore, the work required to analyze such configurations is justified. Two steps are required to proceed further: (1) the acceptance of such levels of disturbances should be determined by measuring the shape and level of present disturbances currently generated in city operations and by additional flight tests; and (2) the incorporation of such concepts in practical, usable configurations for second-generation SST's should be investigated.

REFERENCES

1. SEEBASS, R., ED.: Sonic Boom Research. NASA SP–147, 1967.
2. SCHWARTZ, IRA R., ED.: Second Conference on Sonic Boom Research, NASA SP–180, 1968.
3. Aircraft Engine Noise and Sonic Boom. AGARD Conf. Proc. no. 42, May 1969.
4. WHITHAM, G. B.: The Propagation of Weak Spherical Shocks in Stars. Commun. Pure Appl Math., vol. 6, 1953, pp. 397–414.
5. CARLSON, H.: The Lower Bound of Obtainable Sonic Boom Overpressure and Design Methods of Approaching This Limit. NASA TN D–1494, 1962.
6. JONES, L. B.: Lower Bounds for Sonic Bangs. J. Roy. Aeronaut. Soc., vol. 65, 1961, pp. 433–436.
7. MCLEAN, F. E.: Some Nonasymptotic Effects on the Sonic Boom of Large Airplanes. NASA TN D–2877, 1965.
8. FERRI, A.; AND ISMAIL, A.: Report on Sonic Boom Studies. Part I. Second Conference on Sonic Boom Research, NASA SP–180, 1968, pp. 73–88.
9. FERRI, A.; AND ISMAIL, A.: Effects of Lengthwise Lift Distributions on Sonic Boom of SST Configurations. AIAA J., vol. 7, no. 8, Aug. 1969, pp. 1538–1541.

10. SEEBASS, R.: Sonic Boom Theory. J. Aircr., vol. 6, no. 3, June 1969, pp. 177–184.
11. GEORGE, A. R.: Lower Bounds for Sonic Booms in the Midfields. AIAA J., vol. 7, no. 8, 1969, p. 1542.
12. HAYES, W. D.: Second Conference on Sonic Boom Research. NASA SP–180, 1968, pp. 159–164. Also HAYES, W. D.; HAEFELI, R. C.; AND KULSRUD, H. E.: Sonic Boom Propagation in a Stratified Atmosphere. NASA CR–1299, 1969.
13. SIEGELMAN, DAVID: Sonic Boom Minimization by Use of a Multiwing Concept. Rept. AA–68–19, New York Univ., Aug. 1968.

Observations on Problems Related to Experimental Determination of Sonic Boom*

ANTONIO FERRI AND HUAI-CHU WANG
New York University

The determination of sonic boom signatures for complex models can be performed experimentally. Usually when the sonic boom is determined analytically, the strength of the disturbances that determine the signature is obtained on the basis of linear approximation. Even for linear theory, interference effects are sometimes difficult to analyze. On the contrary, an experimental determination of the sonic boom at some distance from the model, where disturbances are small, permits extrapolation of the signature at large distances from the model by means of the Whitham theory without the introduction of additional approximations above that given by this theory.

A correct method of extrapolation from one distance to another requires that the distribution of disturbance be determined either on a surface, for example, a cylinder that surrounds the model at some distance from the model, or at a surface that is a stream surface of the flow obtained by intersecting the flow field with an infinite plane parallel to the undisturbed velocity. The disturbances at these surfaces can be substituted for the body. At these surfaces the disturbances are small, thus the analysis can be applied correctly.

While this approach is the only theoretically correct one, it is difficult to use because it requires the determination of a complete stream surface; therefore, in many experiments the assumption that the flow around the body can be represented by an equivalent axially symmetric body placed at the position of the model is introduced. Then the signature needs to be determined only along a line. From this signature, the signature at other distances can be obtained. This approach is not completely satisfactory when supersonic leading edges are present. In addition, when large nonlinear effects are present, the signature does not lead to an F-function at the axis of the body. Often, other problems of a practical nature are present that affect strongly the precision of the results. The

*This work was supported by the National Aeronautics and Space Administration under grant NGL 33-016-119.

420-093 O - 71 - 19

purpose of this paper is to outline some of these practical problems. The effects discussed herein are

(1) Support interference
(2) Uniformity of flow
(3) Difficulties at high Mach numbers
(4) Reynolds number effects

SUPPORT INTERFERENCE

Usually the model is supported by a sting that connects the model to the mechanism that translates the model. The presence of the sting and support changes the distribution of the cross-sectional area of the vehicle and the wake. Figure 1 shows typical variation of cross-sectional area related to wing thickness, fuselage volume, and lift with sting and without sting. Usually the sting area is added without corrections. This produces large effects when near-field signature is present. A possible improvement is to correct the presence of the sting by changing the lift distribution locally, as shown in figure 1. Unfortunately, this correction changes for each lift coefficient.

In figures 2 and 3, the effect of the sting on the signature is shown for two configurations: one giving far-field signature and the second giving near-field effects. In the second case, the presence of the stings eliminates such effects.

The effect of the support is also important. In figure 4, several signatures are presented for vehicles having the same cross-sectional area but having different wakes. Signature *a* represents no interference from the support; signatures *b* and *c* represent different types of supports. The support can change the position and strength of the second shock.

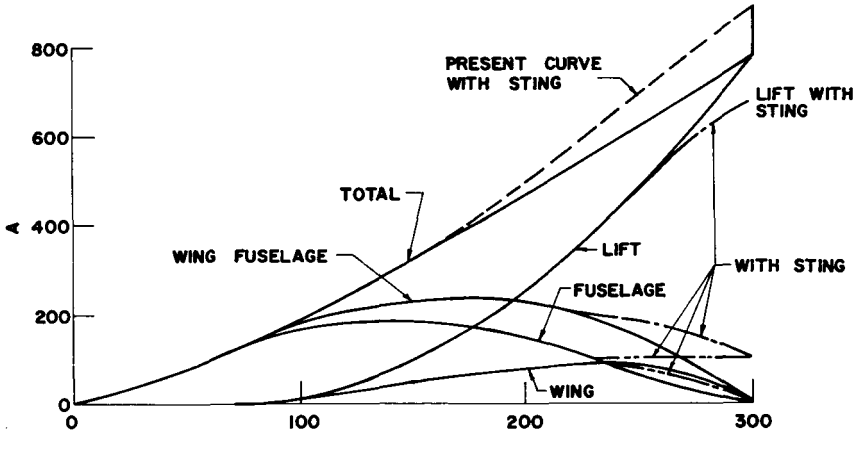

FIGURE 1.—Equivalent area distribution of the configuration with and without sting.

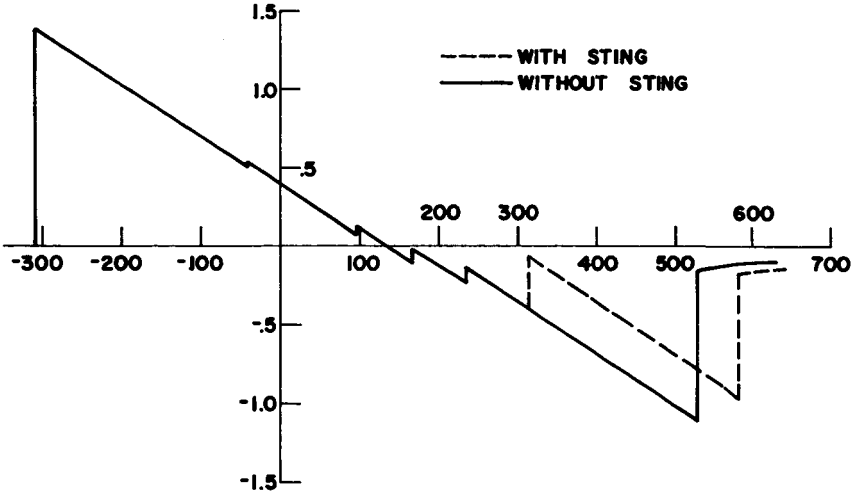

FIGURE 2.—Effect of sting for configuration with far-field signature.

UNIFORMITY OF FLOW

Supersonic wind tunnels are designed to obtain uniform flow in the test section; however, some nonuniformity exists in all wind tunnels. Usually, nonuniformities of the order of ± 0.01 or ± 0.005 in Mach numbers are considered acceptable. Such accuracy is difficult to obtain. These nonuniformities do not affect vehicle performances because the vehicle is usually placed in a region where the flow is quasi-uniform and where the gradients are small. However, such nonuniformities are important for the determination of the sonic boom signature, where all of the flow field between the model and the instrument is involved.

A variation of 0.01 in Mach number corresponds to $\Delta P/P = 0.011$ at $M = 2$, and 0.015 at $M = 4$. The corresponding angular deviation decreases with Mach number and goes from 16′ to 8′ as Mach number increases from $M = 2$ to $M = 4$. The deviations due to nonuniformity existing in the wind tunnels increase with Mach number; therefore, at high Mach numbers, these effects are of extreme importance. The wind-tunnel nonuniformities are carried by two opposite families of waves. The waves of the same family as the shock tend to modify the position and strength of the shock. A typical example is shown in figure 5. Here the calculated and measured signatures are shown in the physical position relative to the model. In figure 6, a correction for a possible nonuniformity is introduced. The correction required is of 6′ for the shock strength, plus an additional 14′ for the position. Such variations are of the same order of the disturbances existing in the tunnel.

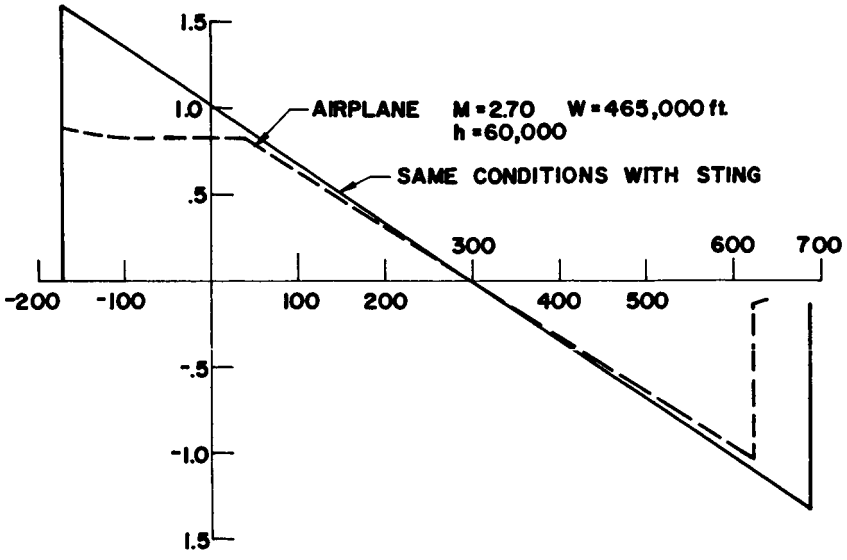

FIGURE 3.—Effect of the presence of sting.

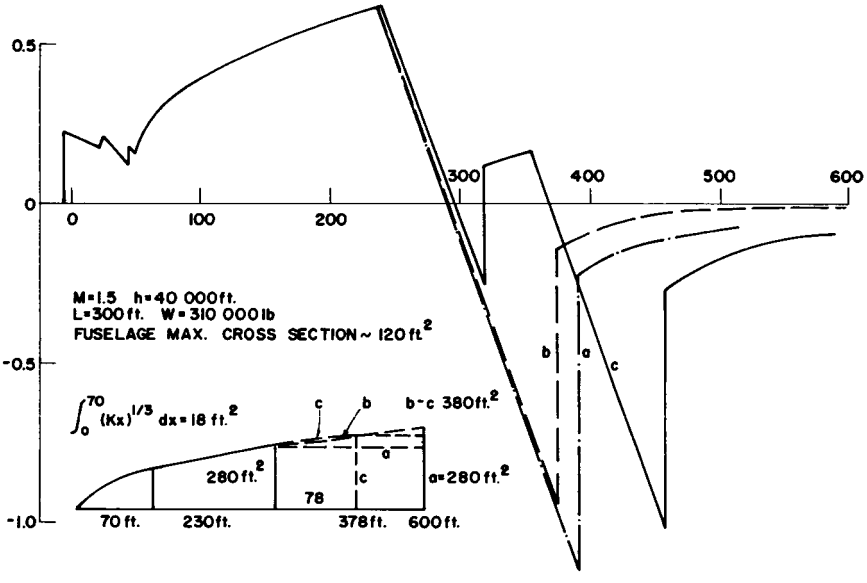

FIGURE 4.—Effect of model support.

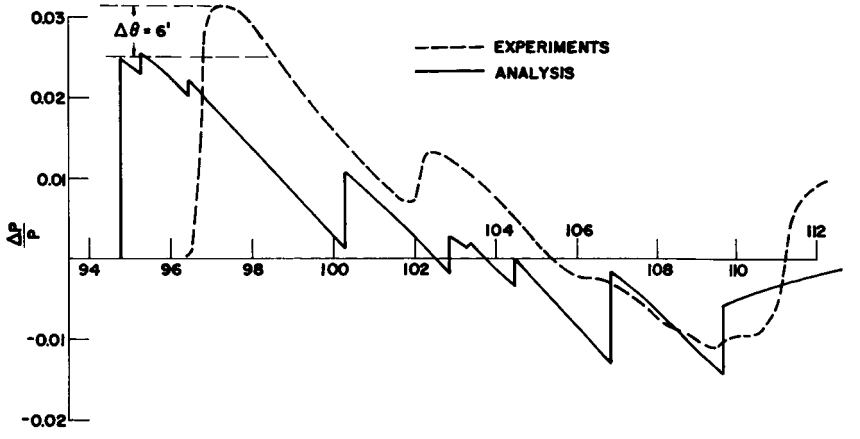

FIGURE 5.—Sonic boom for $h/L = 3.58$ and $M = 2.7$.

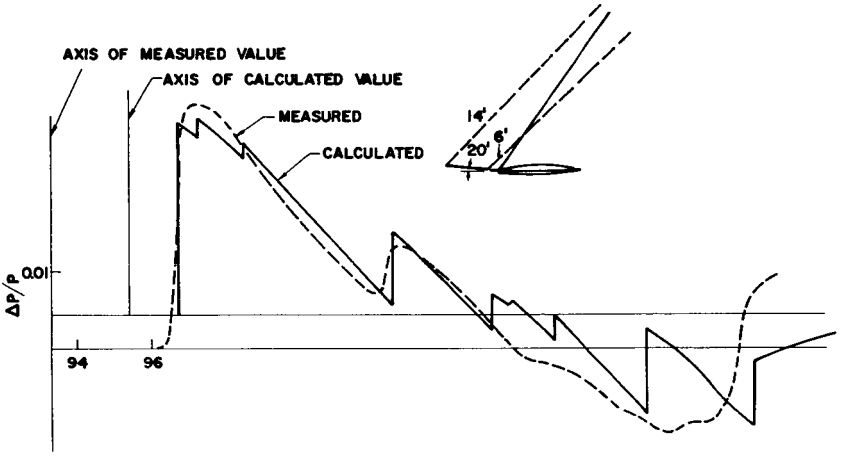

FIGURE 6.—Sonic boom for $h/L = 3.58$ and $M = 2.7$.

The waves of opposite families produce changes on the signature distribution after the shock. The signature changes because the waves are reflected at the surface of the body. This changes the pressure distribution. In figure 7, a comparison between analytical and experimental values is shown for two angles of attack. The front of the shock is placed at the same position. The difference between calculated and measured signature appears to be about the same for both cases, indicating the possibility of the presence of wind-tunnel nonuniformity. The problem becomes extremely serious when the $\Delta P/P$ produced is small and when the measurements are performed at large distances from the model. Then extremely uniform flow is required unless corrections are introduced. In figure 8 some of these effects are summarized.

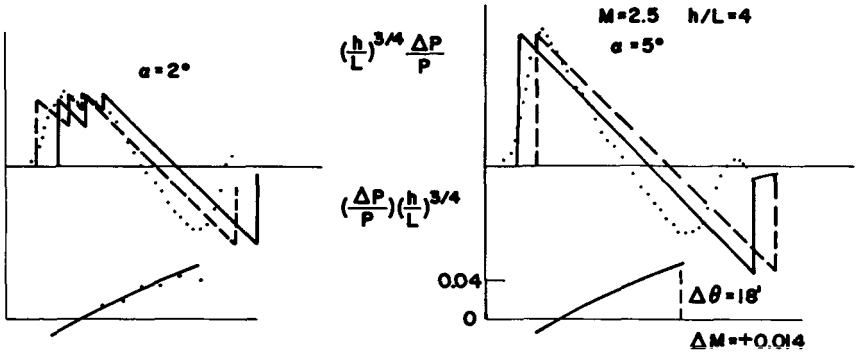

FIGURE 7.—Example of possible wind-tunnel nonuniformity.

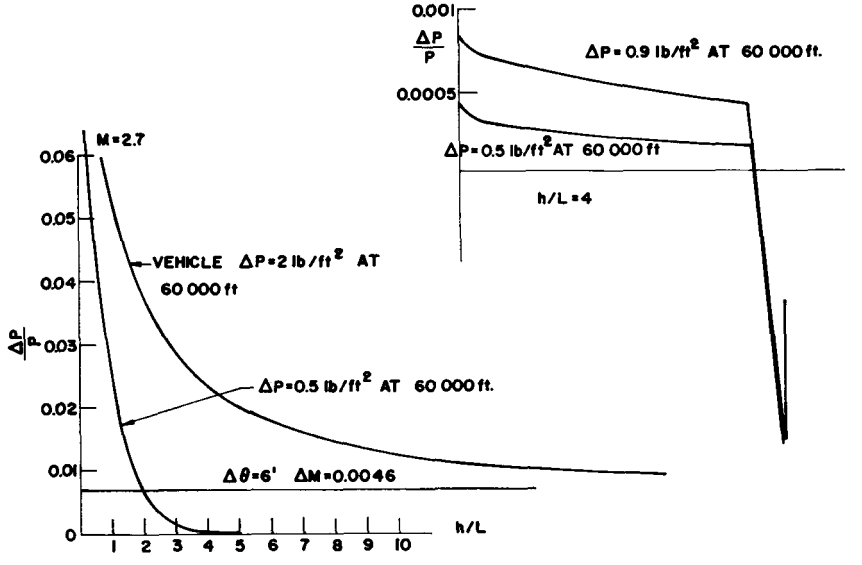

FIGURE 8.—Pressure variation as function of h/L in wind tunnel.

Here the $\Delta P/P$ as a function of h/L is shown (h/L is the distance of the axis of measurements referred to the length of the model L). Two cases are considered that refer to different values of $\Delta P/P$ for the full-scale airplane. The figure indicates that it will be very difficult to measure the sonic boom signature in wind tunnels at large values of h/L.

REYNOLDS NUMBERS

The sonic boom signature is very sensitive to the distribution of lift along the span of the wing. In sonic boom measurements, the Reynolds numbers of the tests are extremely low. Possibility of laminar separation

exists for the flow at the trailing and leading edges. Such separation will change the lift distribution for a given value of the lift. Therefore, some investigation of the flow in the upper surface of the wing is required for the analysis of the data.

THREE-DIMENSIONAL EFFECTS

It is difficult to obtain information on three-dimensional effects without performing a complex, detailed analysis. Usually, experimental data are extrapolated at large distances by assuming that the vehicle can be represented by an equivalent axially symmetric body placed at the same location. Some indication that this approach is not valid for supersonic leading edges can be obtained from the following considerations. Consider, for example, a cone cylinder (the cone has a 6° half angle and a length $l=10$). The signature at a distance $5l$ has been determined analytically (fig. 9 (position d)). This signature has been used to determine an axially symmetric body (body B) at a distance $2l$ from the axis of the cone cylinder (position b). Such a body is different from the first because of the different position as shown in figure 9. Body A and body B produce a deflection of the flow inside the area defined by the intersection between the shock and a plane at position $3l$ with respect to the cone (position c). If we consider the two stream surfaces produced by deflection due to the presence of the two bodies, each of these stream surfaces can be substituted by a solid surface that now represents a wing. The surface has the same pressure distribution in the lower surface as the pressure distribution produced by the corresponding body. The planform of the two

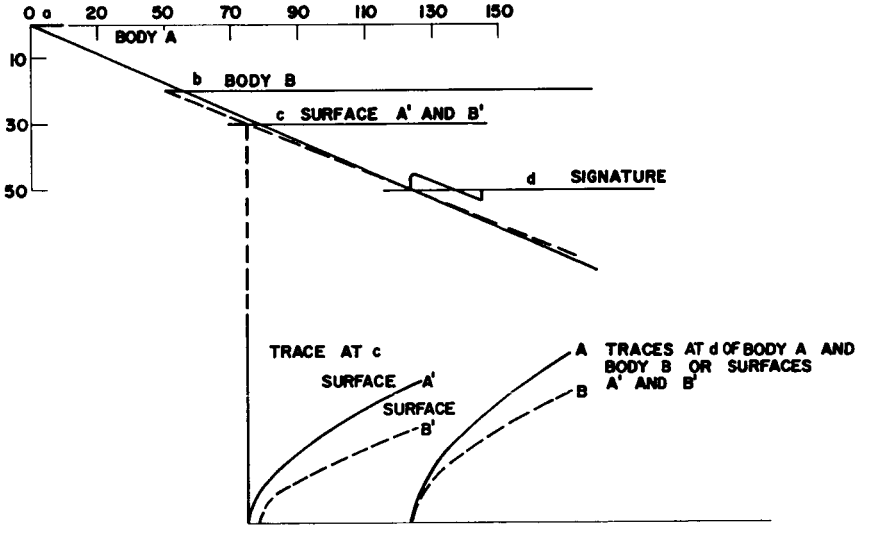

FIGURE 9.—Three-dimensional effects.

wings is different, as shown in figure 9; however, each surface produces the same sonic boom signature at position d. If we want to extrapolate the signature of the two wings at larger distances, for example, $200l$, by using equivalent axially symmetric bodies, the correct extrapolation is to determine first the position and shape of body A and body B, then to determine the signature corresponding to these bodies. The signature at a given distance different from d is not the same for the two bodies. These signatures are shown in figure 10. If we assume that the equivalent bodies corresponding to the two surfaces are located at c, and we determine the equivalent axially symmetric bodies at c from the surfaces, the two surfaces do not correspond to the same equivalent body in spite of the fact that they produce the same signature at d, and the signature at a distance of $200l$ from the axis of the cone is different for the two surfaces and is different from the signature of the two axially symmetric bodies. If we use the signature at d to determine an equivalent axially symmetric body at c, and then we determine the signature produced by this body at $200l$ from the axis of the cone, then we obtain a signature for both surfaces that is identical and is different from the two correct signatures. The differences are on the order of 20 percent.

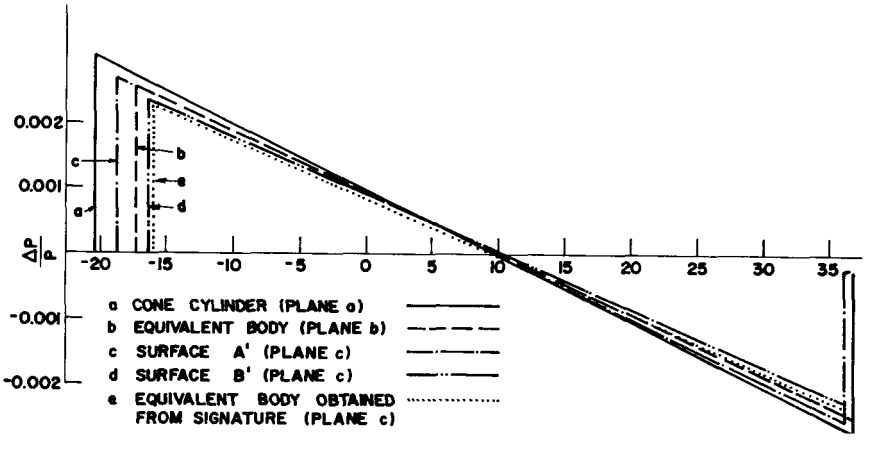

FIGURE 10.—Pressure signatures at $200l$ from the axis of the cone.

CONCLUSIONS

The use of experimental data permits obtaining sonic boom signatures at some distance from the body when the theory applies. However, wind-tunnel irregularities and support interference can influence the results unless these effects are taken into consideration. Three-dimensional effects can be important.

A New Method for Determining Sonic Boom Strength From Near-Field Measurements

M. LANDAHL, I. RYHMING, H. SORENSEN, AND G. DROUGGE
Aeronautical Research Institute of Sweden

In sonic boom research, the wind tunnel has until recently been used primarily as a tool to find the sonic boom signature many airplane lengths away from the flightpath. This kind of experimental research has involved the use of very small models in a large supersonic wind tunnel. Recently, however, the idea has been put forward to use the wind tunnel instead as a tool to measure the F-function directly (refs. 1 and 2). One can then use large models; and in order to grasp as much as possible of the details of the F-function, the measurements are performed close to the model. Usually, pressure readings are taken along a line directly underneath the model and parallel with the model axis (ref. 2). The acquired data are then reduced according to first-order theory to construct the F-function from the data.

However, an important conclusion in this respect has been reached in the analysis of nonlinear effects presented previously (ref. 1); namely, that these effects are confined primarily to the near field. Hence, to obtain an accurate determination of the F-function from wind-tunnel measurements in the near field, one has to correct for second-order effects.

A new method has therefore been developed in which, instead of pressure readings, the streamline inclination angles at the edge of the near flow field are measured along lines of constant distance from the model axis at different azimuthal locations. In other words, a careful mapping of the flow field is carried out along a cylindrical surface that circumscribes the model. This is necessary to evaluate to second order the three-dimensional effects on the F-function. The reason for measuring the streamline inclination angles is that it has been found possible to measure these angles very accurately.

As will be shown in this paper, this technique when applied to a simple body of revolution produces excellent results. A critical test of the method is offered by measuring the axisymmetric flow field produced by this body of revolution at two different radial locations. The F-curves produced at these two different radial locations must then coincide. As will

be shown, the evaluation to second order gives two F-curves that are very nearly identical. The F-curves determined from the tests according to first-order theory differ, however, significantly from each other and also from the first-order theory.

THEORETICAL BACKGROUND

According to Landahl, Ryhming, and Lofgren,[1] the perturbation velocity components at large distances from a three-dimensional body in supersonic flow are given to second order by

$$u_2 = \frac{\rho_\infty}{\rho} u(x_0, r_0, \theta_0) \tag{1}$$

$$v_2 = \frac{\rho_\infty}{\rho} \frac{r_0}{r} v(x_0, r_0, \theta_0) \tag{2}$$

$$w_2 = w(x_0, r_0, \theta_0) = \frac{1}{r_0} \varphi_\theta \tag{3}$$

where u_2, v_2, and w_2 are the second-order components referred to a cylindrical coordinate system

$$x = x_0 - Kr_0 v - M^2 \varphi + Kr_0 \frac{\partial w}{\partial \theta} \tag{4}$$

$$r = r_0 \left(1 - Ku - \frac{K}{\beta} \frac{\partial w}{\partial \theta}\right) \tag{5}$$

$$\theta = \theta_0 - 2K \frac{\partial u}{\partial \theta} \tag{6}$$

where

$$K = \frac{(\gamma+1)\, M^4}{2\beta^2}$$

$$\beta^2 = M^2 - 1$$

and u, v, and w are the corresponding values according to linearized theory and their potential is φ. For large distances, the following expansions were shown to hold:

$$F(y; \theta) = \sqrt{\frac{2r_0}{\beta}} \left[v + \frac{3\varphi}{8r_0} - \frac{\varphi_{\theta\theta}}{2r_0}\right] \tag{7}$$

[1] See p. 3.

Furthermore, equation (5) gives

$$r_0 \simeq r\left(1-\frac{K}{\beta}\epsilon\right) \tag{17}$$

We now have the quantities needed to calculate F from equation (7). The Mach line parameter y and the angle parameter θ_0, finally, can then be determined from equations (11) and (12).

For an axisymmetrical flow field, w is zero as are all θ derivatives. The measurements and the evaluation of the F-function are then simplified because it is only necessary to consider a single azimuthal plane. Hence, to evaluate the measurements for a simple body of revolution presented subsequently, we start by calculating the v and φ_2 distributions according to equations (16) and (15) from the measured ϵ distribution along r equal to a constant. Subsequently, the φ distribution is obtained from equation (10), where r_0 is obtained from equation (17). The F-function is now calculated from equation (7), and the corresponding y values are then obtained from equation (11).

MODEL AND APPARATUS

The test model, a parabolic spindle with a diameter $D=40$ mm and a length $L=282.84$ mm (the theoretical length $L_0=339.40$ mm), is constructed of brass and has pressure orifices over the whole length in one section.

The hemispherical differential pressure yaw meter employed for pressure measurements is shown in figure 1. The pressure probe has a diam-

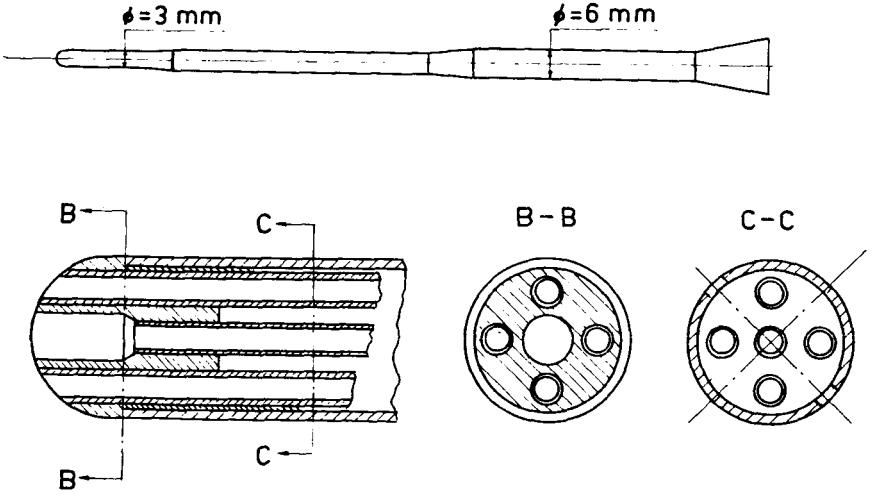

FIGURE 1.—Pressure yaw meter.

eter of 3.5 mm. Four static-pressure orifices are located circumferentially 90° apart on the hemispherical surface, and four on the cylindrical surface. A pitot-pressure orifice is located at the probe apex. The static-pressure orifice diameters are 0.5 mm and the pitot-pressure orifice diameter is 1.0 mm.

The model was mounted on a sting and could be moved back and forth (400 mm), making possible a complete survey of the flow field along a line parallel to the flow direction (fig. 2).

The pressure probe was mounted fixed on the top wall.

The tunnel total pressure was sensed in the stilling chamber, and the reference pressure in the test section with two 74-psia transducers. The probe and model pressures were measured with high-sensitivity pressure measurement devices. For the model pressure and the four static pressures on the hemispherical surface, pressure scanners were used. The pressure scanner for the model pressure was located in the movable sting, and the transducers and scanners for the probe were located outside the wind tunnel (fig. 2).

TEST CONDITIONS AND ACCURACY

The investigation was conducted in the Trisonic Tunnel FFA–TVM 500 facility at Mach number 3.0.

The tunnel has a square test section of 50×50 cm^2 with perforated walls for the transonic speed range and a flexible wall nozzle, which allows the Mach number to be varied continuously between 1 and 4. It is a blowdown tunnel, which may be operated with a stagnation pressure up to 12 atm and a stagnation temperature range of 300° to 400° K.

Pressure measurements were performed on the model at 0° angle of incidence and at three positions along the tunnel axis. In addition, the supersonic flow field along a line parallel to the flow direction was measured as the model moved 400 mm along the tunnel axis. These flow-field measurements were conducted at two radial distances from the model axis. The pressures were recorded almost simultaneously because the time between the individual measurements was 1×10^{-4} sec. Schlieren photographs were taken of the flow field generated by the model and the pressure probe.

The absolute level of accuracy of the results is very difficult to establish because of the combined effects of the many possible sources of error. A number of precautions were taken, however, to reduce the magnitude and probability of significant errors. The facility instrumentation consists primarily of high-sensitivity pressure measurement devices for determining both stagnation and reference pressures. These pressures were calibrated carefully before the investigation. The free-stream properties are considered accurate within the following limits: ± 0.01 for M_∞ and ± 0.1 percent for $p_{t,\infty}$.

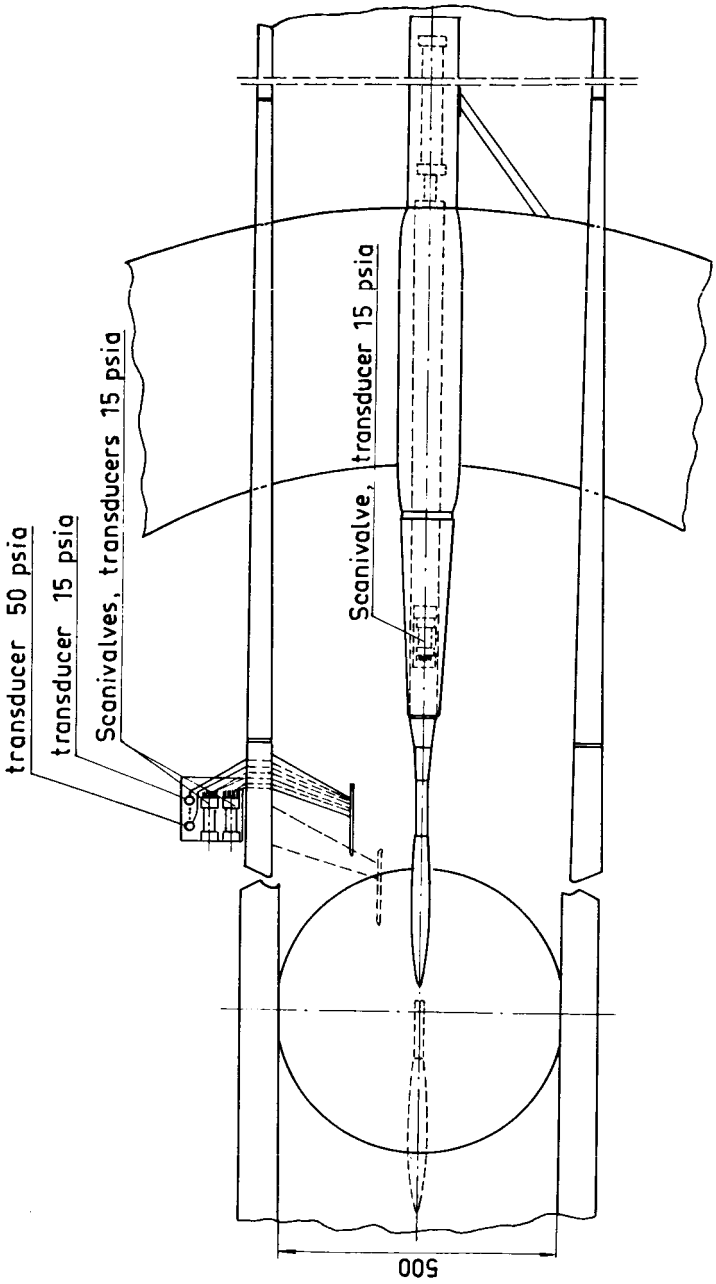

FIGURE 2.—Schematic view of test setup.

The precision with which local flow quantities for $M_\infty = 3.0$ can be determined is estimated to be ± 0.07 for M_1, ± 1.0 percent for $p_{t,1}$, and $\pm 0.10°$ for ϵ where M_1 is the local Mach number (Mach number ahead of shock wave at probe apex) and $p_{t,1}$ is the local total pressure.

RESULTS

Local flow-field parameters, determined from the probe-measured pressures, are presented together with a schlieren photograph in figures 3 to 6. The pressure distribution on the surface of the model is shown in figure 3 for three positions along the tunnel centerline. The downwash

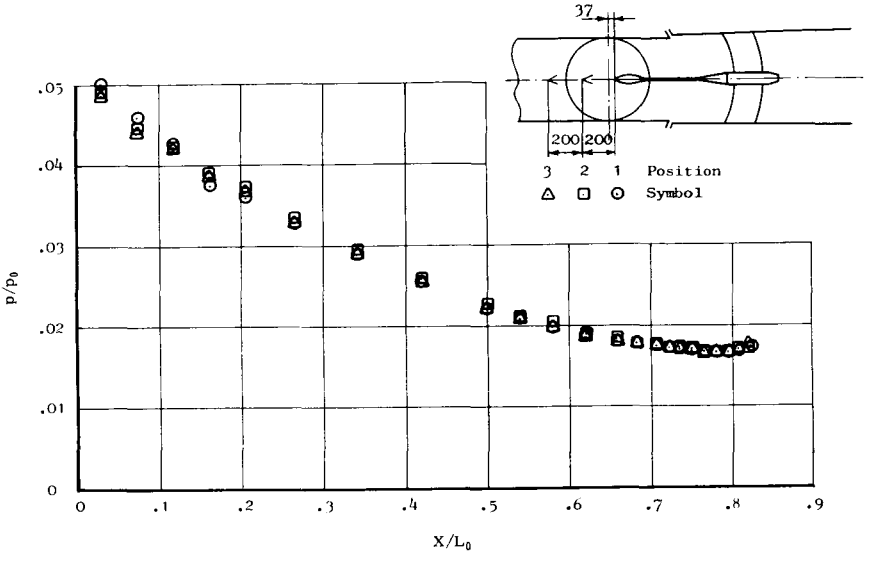

FIGURE 3. — Pressure distribution on the model.

angle ϵ for $(r/L_0) = 0.375$ is shown in figure 4 and for $(r/L_0) = 0.228$ in figure 5. To test reproducibility, several different traverses were made at the probe locations of $(r/L_0) = 0.375$ and $(r/L_0) = 0.228$. A schlieren photograph of the model and the pressure probe is shown in figure 6. Table I shows the tunnel pressure and Mach number variation during the time for a complete traverse of the flow field.

Inspection of figures 4 and 5 reveals a very good reproducibility of the various runs in the tunnel. The scatter in the measured points observed for the lower x-values is due to interference effects caused by the probe nose being in immediate contact with the almost conical shock wave emanating from the model apex. Similar effects occur as the probe nose traverses the rear shock system emanating from the model sting support.

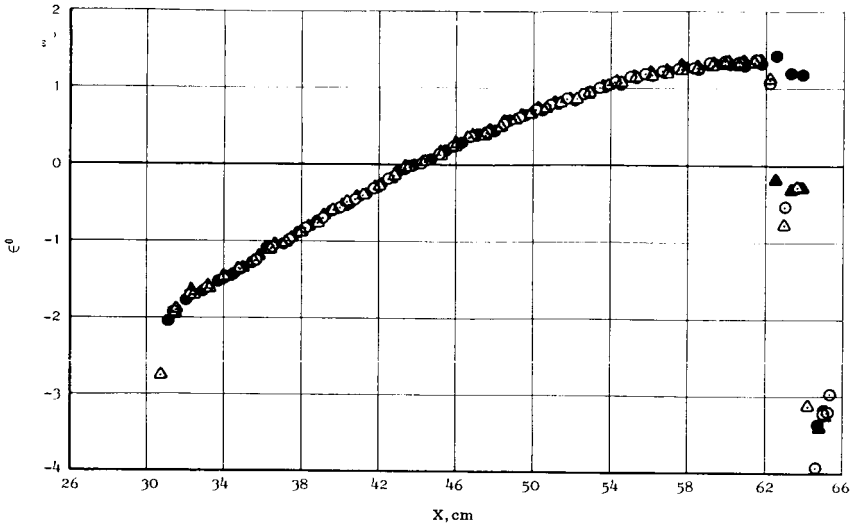

FIGURE 4. – Downwash angle ϵ as a function of x for $r/L_0 = 0.375$.

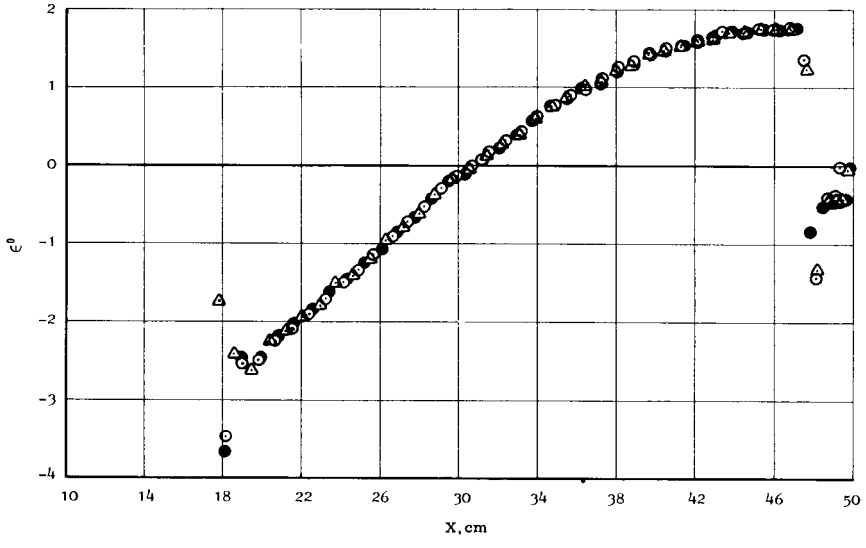

FIGURE 5. – Downwash angle ϵ as a function of x for $r/L_0 = 0.228$.

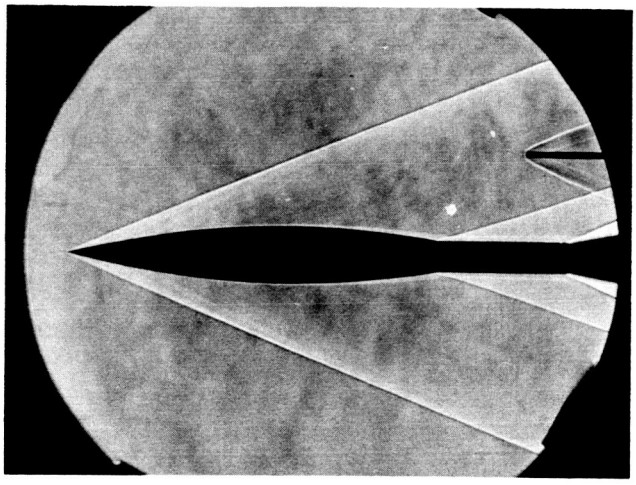

FIGURE 6.—Schlieren photograph of model and probe.

TABLE I.—*Variation of Total Pressure* p_0, *Reference Pressure* p_{ref} (*Tunnel Wall Pressure*), *and Mach Number as a Function of Time*

t, sec	p_0, mbar	p_{ref}, mbar	M_∞
0	4965	140	2.982
5	4973	138	2.993
10	4981	138	2.994
15	4987	139	2.990
20	4982	139	2.990
25	4991	139	2.991
30	4987	139	2.990
35	4988	139	2.990
40	4989	139	2.990
45	4989	139	2.990
50	4988	139	2.990
55	4989	139	2.990

420-093 O - 71 - 20

The distributions of the downwash angle ϵ measured at the two radial locations $(r/L_0) = 0.375$ and $(r/L_0) = 0.228$ have been used to calculate the F-function for the body using the method outlined earlier. Schlieren photographs have been used to determine the shock wave x-location for the evaluation of φ according to equation (15). The result is shown in figure 7. As can be seen, the two ϵ distributions produce almost identical

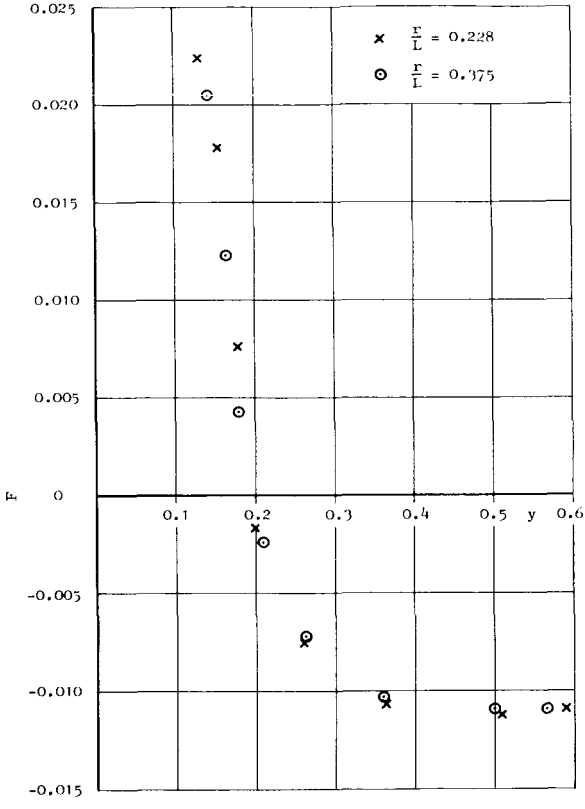

FIGURE 7. — Test results evaluated according to second-order theory.

F-curves. By comparison, the same ϵ distribution when reduced according to Whitham first-order theory produces two different F-functions. (See fig. 8.) There are also substantial differences between the second- and first-order predictions.

Calculations to second order from the body shape of the F-function are in progress. It has been found necessary to improve the slender-body theory for this case, and a new quasi-cylindrical solution has been developed.

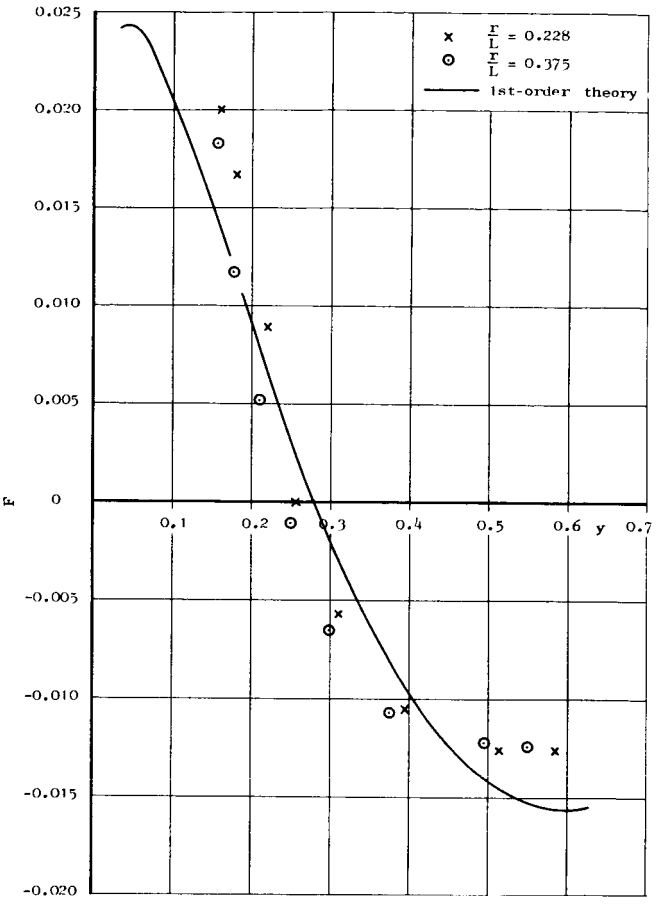

FIGURE 8.—Test results evaluated according to first-order theory.

CONCLUSION

A new method for determining the F-function based on accurate wind-tunnel measurements of the flow inclination angles along a cylindrical surface that circumscribes the wind-tunnel model has been presented. The new method seems to be quite feasible and has so far been used to predict the F-function to second order for a simple body of revolution.

Presently, the complete mapping of a three-dimensional flow field produced by an SST-like configuration is being carried out in the wind tunnel.

REFERENCES

1. LANDAHL, M. T.; RYHMING, I. L.; AND HILDING, L.: Nonlinear Effects on Sonic Boom Intensity. Second Conference on Sonic Boom Research, NASA SP-180, 1968, pp. 117-124.
2. HUNTON, L. W.: Current Research in Sonic Boom. Second Conference on Sonic Boom Research, NASA SP-180, 1968, pp. 57-66.

A Preliminary Report on Shock Coalescence

RAYMOND M. HICKS AND CHARLES L. THOMAS
NASA Ames Research Center

Aircraft with minimum sonic boom can be designed by two methods. The first, or direct, method consists of calculating the pressure signature from known configuration geometry (ref. 1). In the second, or indirect, method, the aircraft geometry is calculated from a given pressure signature (ref. 2). The study described in this paper has been done with the latter method in mind. The effect of six different pressure signature parameters on the rate of coalescence of the nose and wing shocks has been studied for a typical near-field, wing-body signature. No attempt has been made to calculate configurations from the pressure signatures developed during the investigation. However, the results of the analysis will permit the airplane designer to specify a near-field pressure signature with a better understanding of the subsequent development of the mid-field and far-field signatures as the waveform propagates through the atmosphere.

DISCUSSION

From extrapolation of experimental, near-field, wing-body pressure signatures it has been observed that, for certain configurations, the distance between the nose and wing shocks first increases and then decreases as the wave system propagates through a uniform atmosphere. (See fig. 1.) This appeared to be a shock propagation phenomenon that could produce a "sawtooth" pressure signature with an attendant decrease in sonic boom in the mid field. Hence, a systematic study was undertaken to determine which pressure signature parameters were most effective in producing this effect. The type of signature studied is shown in figure 2. The parameters studied were Mach number, nose and wing shock strengths, slopes behind nose and wing shocks, and initial distance from nose shock to wing shock. Only the positive part of the waveform was considered. However, the technique used in the analysis could be applied to the negative part without modification.

The distance λ from the nose shock to the wing shock for a uniform atmosphere is given by

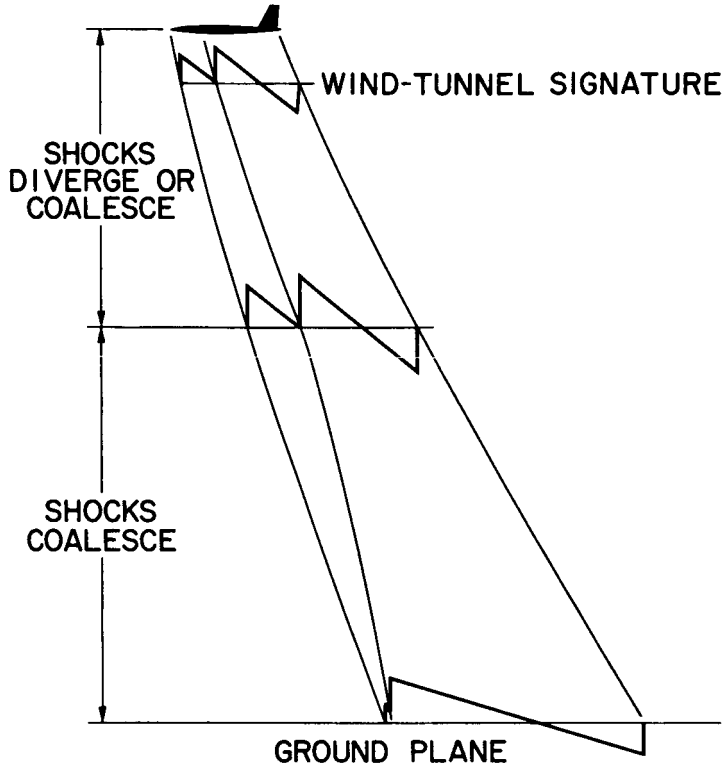

FIGURE 1.—Coalescence characteristics of nose and wing shocks in a uniform atmosphere.

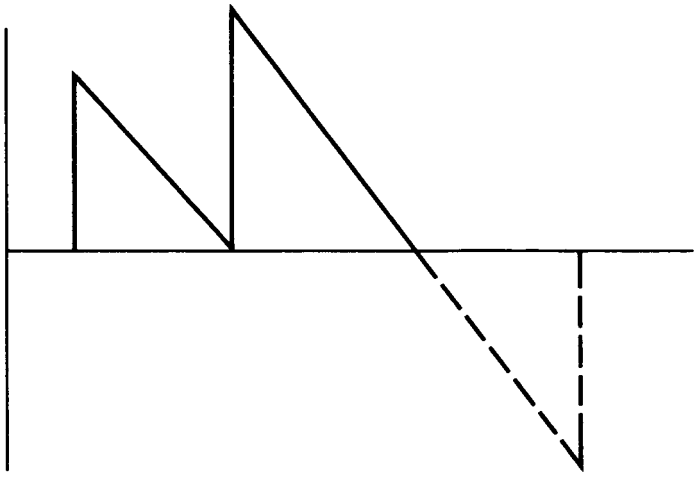

FIGURE 2.—Signature studied. Parameters studied are Mach number, nose and wing shock strengths, slopes behind nose and wing shocks, and initial distance from nose shock to wing shock.

$$\lambda=[1-20km_1\ (\sqrt{0.1r-1})]\left[\lambda_0-\frac{\Delta p_1}{m_1}\left(\sqrt{\frac{1}{1-20km_1\ (\sqrt{0.1r-1})}}-1\right)\right.$$
$$\left.-\frac{\Delta p_2}{m_1-m_2}\left(\sqrt{\frac{1-20km_2\ (\sqrt{0.1r-1})}{1-20km_1\ (\sqrt{0.1r-1})}}-1\right)\right]$$

where

$$k=\frac{1+\gamma}{2\gamma p_0 \sin\mu\cos\mu}$$

and

λ_0 = initial distance from the nose shock to the wing shock
m_1 = slope behind the nose shock
m_2 = slope behind the wing shock
Δp_1 = nose shock strength
Δp_2 = wing shock strength
r = distance from the axis of the aircraft
γ = ratio of specific heats
p_0 = ambient pressure
μ = Mach angle

The derivation of this equation will not be given here because it can be obtained from the equation for $\lambda(r)$ in the paper by C. L. Thomas,[1] in this document, by setting $r_0=10$. The use of a uniform atmosphere in this study does not restrict the results in any way because coalescence rates are lower in a standard atmosphere. The study could have been carried out by the method of reference 3 but would have required considerably more time and effort.

Each subsequent figure will show the effect of one of the six parameters studied on the rate of coalescence of the nose and wing shocks with the remaining five held constant. All figures will show graphs of the normalized distance from the nose shock to the wing shock versus distance from the aircraft; i.e., λ/λ_0 versus r.

The effect of Mach number on the rate of coalescence of the nose and wing shocks is shown in figure 3 for the initial signature shown at the top of the figure. Note that the lowest rate of coalescence is found at a Mach number of 1.4 with the rate increasing rapidly with increasing Mach number. The Mach number for minimum rate of coalescence can be shown mathematically to be $\sqrt{2}$. If a different initial signature had been used, the trend with Mach number would have been similar but the curves would be shifted according to values of the five parameters (Δp_1, Δp_2, m_1, m_2, and λ_0) used.

[1] See p. 205.

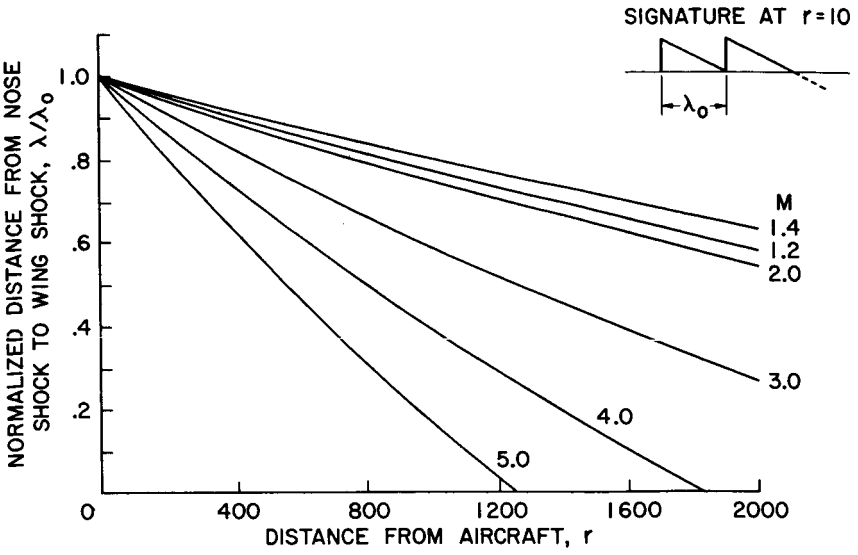

FIGURE 3. – Effect of Mach number on coalescence.

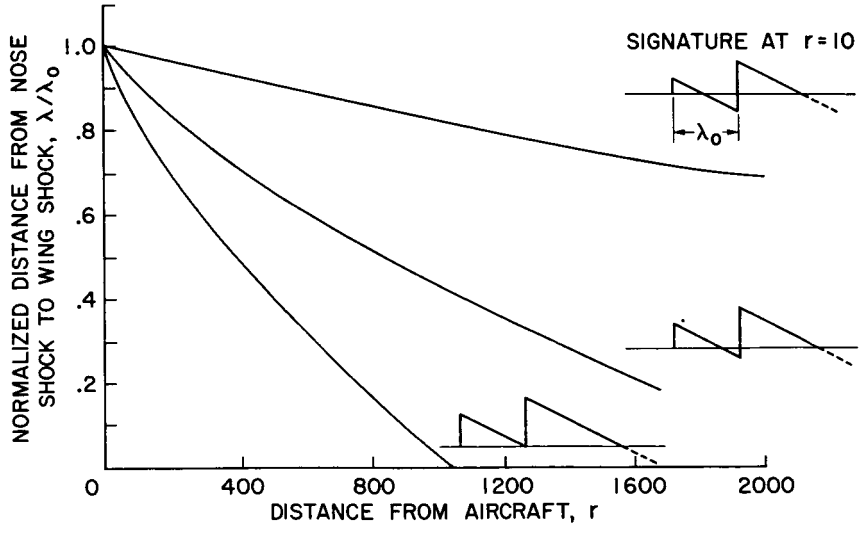

FIGURE 4. – Effect of nose shock strength on coalescence, $M = 3$.

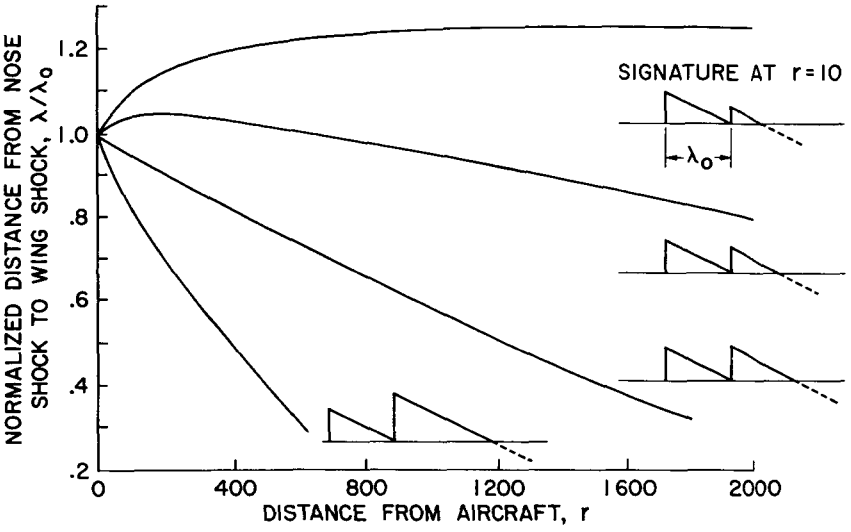

FIGURE 5. – Effect of wing shock strength on coalescence, $M = 3$.

The effect of nose shock strength on the rate of coalescence of the nose and wing shocks is shown in figure 4 for $M = 3.0$. Note that the nose and wing shocks remain separated to greater distances from the aircraft as the nose shock strength is decreased, with the remaining five parameters held constant. This reduced rate of coalescence is a result of a reduced pressure ahead of the wing shock for the smaller values of nose shock strength. One might surmise that lower coalescence rates can be achieved by decreasing the pressure ahead of the wing shock because this produces a lower average pressure for the wing shock and, therefore, a lower propagation speed. It should be pointed out that the equation for λ given earlier has been derived with the assumption that the propagation speed of any shock wave is the average of the propagation speeds immediately ahead and immediately behind the shock.

The effect of wing shock strength on the coalescence characteristics of the nose and wing shocks is shown in figure 5. As might be expected, lower coalescence rates are found for smaller values of wing shock strength. Note that for the initial signature shown second from the top of the figure, the nose and wing shocks diverge briefly before coalescing, while only divergence of the shocks is shown for the top signature. However, coalescence of the shocks for the top signature will begin at r greater than 2000.

The effect of slope (rate of expansion) behind the nose shock is shown in figure 6. Note the rapid decrease in rate of coalescence as the slope becomes more negative. The mechanism by which this parameter reduces the rate of coalescence is similar to that of figure 4; i.e., the

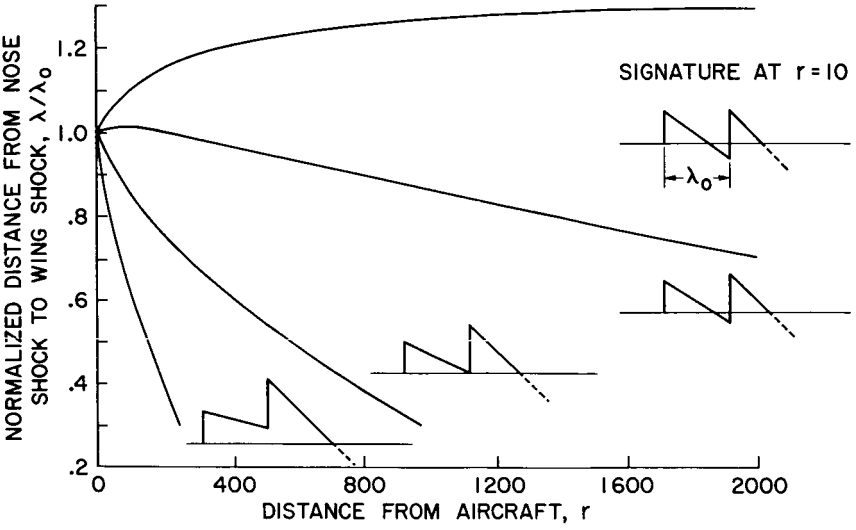

FIGURE 6.—Effect of slope behind nose shock on coalescence, $M=3$.

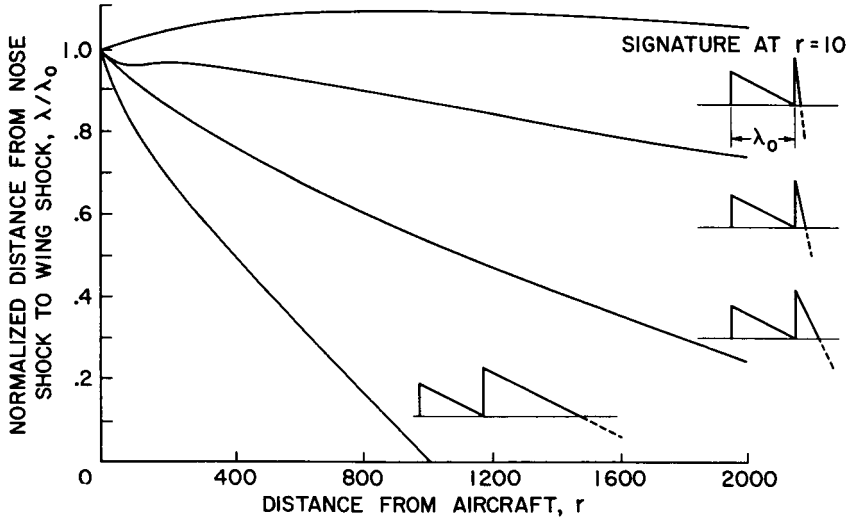

FIGURE 7.—Effect of slope behind wing shock on coalescence, $M=3$.

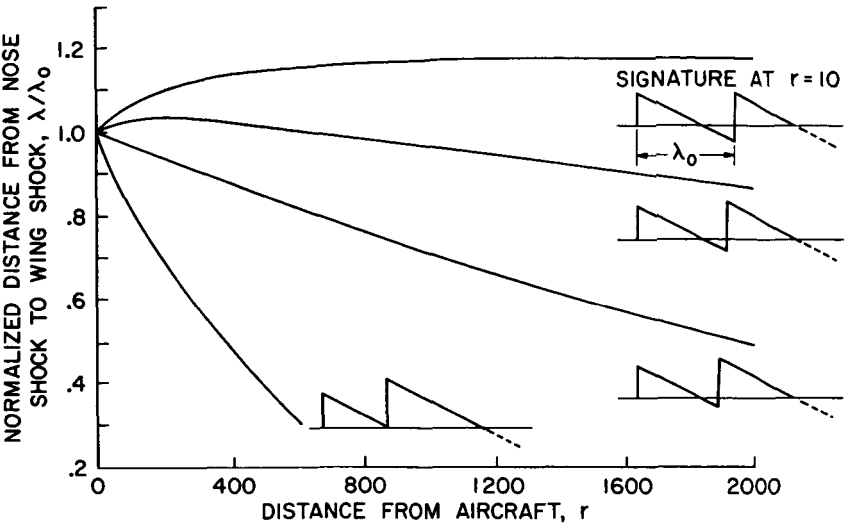

FIGURE 8. — Effect of initial distance from nose shock to wing shock on coalescence, $M = 3$.

average pressure of the wing shock, and hence the propagation speed, is reduced.

The effect of slope (rate of expansion) behind the wing shock is shown in figure 7. Note that as the slope becomes more negative, the rate of coalescence is reduced. This parameter decreases coalescence by producing a rapid decay of the wing shock, which reduces its propagation speed. It may be less practical to change the rate of expansion behind the wing shock than the other parameters that reduce the coalescence rate because the extreme expansion rates shown for the two signatures at the top of the figure may be difficult to achieve in reality. Large expansion rates, however, have been measured during tests of high-aspect-ratio, unswept wings, and blunt-nose bodies. The curve at the top of the figure does not show an initial decrease in λ/λ_0 because the step size in r was too large. It is obvious that there must be such an initial decrease because the average pressure of the wing shock is greater than the average pressure of the nose shock at $r = 10$.

The effect of the initial distance from the nose shock to the wing shock on shock coalescence is shown in figure 8. Note that increasing the initial distance between the nose and wing shocks while holding the other five parameters constant produces a decrease in rate of coalescence. Increasing λ_0 has a similar effect on the expansion behind the nose shock as was found for the parameters of figures 4 and 6; i.e., expanding to a pressure lower than free stream before the wing shock pressure rise begins. As before, this results in a decrease in the average value of the wing shock pressure and hence reduces the propagation

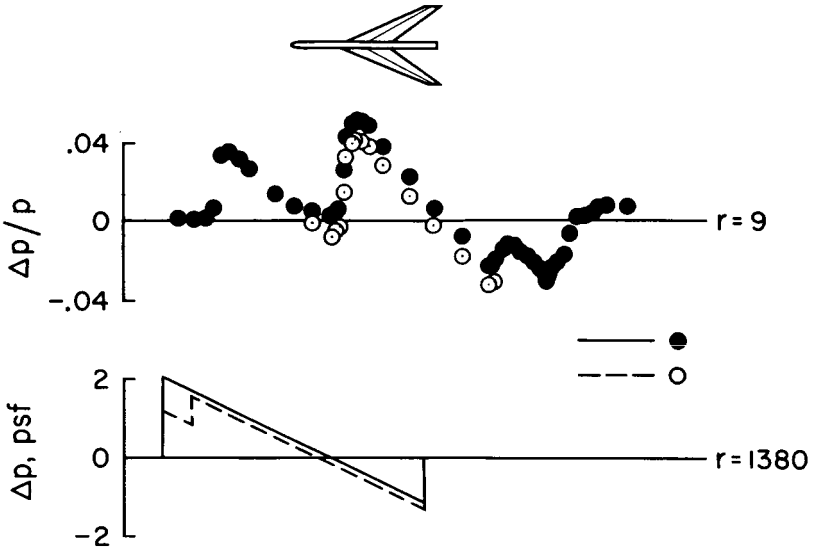

FIGURE 9. – Effect of pressure reduction ahead of wing shock, $M = 2.7$.

speed of the wing shock relative to the nose shock. This overexpansion could be achieved by a carefully located canard or forward wing or by use of a blunt nose followed by "coke-bottling" of the body in front of the wing. This type of radius distribution has been found to be beneficial for bodies of revolution by other investigators. (See the paper by D. S. Hague and R. T. Jones.)[2]

The results of this study have shown, among other things, that a reduction in pressure ahead of the wing shock may be the most practical method for reducing the coalescence of the nose and wing shocks. Hence, an application of this effect to an experimental signature is shown in figure 9. The solid symbols represent an experimental signature measured at a Mach number of 2.7 for the arrow-wing model shown. The open symbols show an arbitrary shift in the data to evaluate the effect of a greater expansion behind the nose shock. The solid and dashed curves shown at the bottom of the figure are extrapolations of the solid and open symbols, respectively, from $r = 9$ to $r = 1380$ (1.3 to 200 body lengths). Note the 50-percent reduction in bow shock strength and the 25-percent reduction in maximum overpressure. The use of even more negative pressure ahead of the wing shock than shown by the open symbols could produce a maximum wing shock less than or equal to the nose shock overpressure. This would reduce the maximum positive overpressure to approximately 1 lb/ft^2. (The signatures at $r = 1380$ have been calculated for a standard atmosphere and a reflection factor of 1.8.)

[2] See p. 307.

CONCLUDING REMARKS

A parametric study has been conducted to determine the effect of six pressure signature parameters on the rate of coalescence of the nose and wing shocks of a wing-body type of pressure signature. This has been a cursory investigation because many combinations of the six parameters were not considered. However, definite trends of shock coalescence with each parameter have been shown and it is clear that many combinations of the six parameters could be used to reduce sonic boom by retaining a near-field signature to large distances from the aircraft. One example has been given to show that a reduction in sonic boom can be realized by decreasing the pressure ahead of the wing shock. While no attempt has been made to develop configurations that produce the signatures discussed, a relation between certain signature parameters and aircraft geometry has been indicated.

Future effort will be devoted to investigation of the effect of the six pressure signature parameters on shock coalescence in the real atmosphere and to development of aircraft configurations that will generate shock systems with low rates of coalescence.

REFERENCES

1. WHITHAM, G. B.: The Flow Pattern of a Supersonic Projectile. Commun. Pure Appl. Math., vol. 5, no. 3, Aug. 1952, pp. 301–348.
2. BARGER, RAYMOND L.: Design of Bodies to Produce Specified Sonic-Boom Signatures. NASA TN D–4704, 1968.
3. HICKS, R. M.; AND MENDOZA, J. P.: Prediction of Aircraft Sonic Boom Characteristics From Experimental Near Field Results. NASA TM X–1447, 1967.

Application of Multivariable Search Techniques to the Design of Low Sonic Boom Overpressure Body Shapes*

D. S. HAGUE AND R. T. JONES
Aerophysics Research Corp.

Body shapes that minimize sonic boom overpressures in the near and far fields (refs. 1 and 2) have previously been obtained through application of the variational calculus. There are indications (ref. 3) that certain supersonic transport (SST) designs may fly at altitudes that lie in the mid-field region, where the pressure waves emitted from a vehicle have yet to coalesce into far-field N-wave form. This paper investigates body shapes or equivalent body shapes that provide low boom in the mid field.

Solutions are sought through the application of multivariable search techniques (refs. 4 and 5). This approach involves the construction of a finite, many parametric system model. Such models may vary in geometric and dimensional complexity. As the number of parameters increases, the approach tends to the variational calculus solution; however, for many design problems, it suffices to represent continuous systems by a relatively small number of parameters (ref. 6). In such cases, multivariable search represents an attractive alternative to the variational calculus formation. Of more significance in vehicle design is the ability of the multivariable search procedure to readily combine many system disciplines into a unified quantitative system optimization problem. Thus, the optimization program employed in this study (refs. 5 and 7) has been successfully applied to a variety of subsystem optimization problems in the areas of aerodynamics (ref. 6), communication systems (ref. 8), propulsion design (ref. 9), and trajectory shaping and combined aerodynamic-structural-propulsion mission shaping (refs. 10 and 11). Thus, it is conceivable that a complete SST synthesis involving technical-economic-environmental constraints could yield to the multivariable search procedures used here.

It should be noted that the variational calculus may also be used to obtain solutions to problems in which continuous control and finite

*Study undertaken under sponsorship of NASA Ames Research Center as part of contract NAS 2-4880.

parameters are intermixed. On problems of reasonable complexity, the variational calculus must be reduced to a numeric form. Generalized computer programs for the solution of such problems are available (refs. 12 and 13); however, computation time requirements tend to rise rapidly with problem complexity.

MULTIVARIABLE SEARCH

Multivariable search based on the gradual evolution of an optimal solution by iterative procedures has seen increasing uses throughout the sixties. This can be traced directly to increases in computational capacity during this period. To apply the method, a performance function $\phi = \phi(\alpha_i)$, which is to be minimized or maximized, is defined. Here, the vector $\boldsymbol{\alpha}$ has a finite number of components α_i, whose values are to be determined to satisfy the optimization criteria. Simultaneously, with the minimization of ϕ, a vector $\boldsymbol{\psi} = \boldsymbol{\psi}(\boldsymbol{\alpha})$ may be constrained to the null vector having components $\psi_j = 0$. Inequality constraints $\psi_k \leq 0$ or $\psi_k \geq 0$ may readily be incorporated into the constraint vector (ref. 5). In general, the constrained optimization problem may be replaced by an unconstrained problem by the device of a penalty function; e.g., by minimization of an augmented performance function $\phi^* = \phi + \sum_i W_i \psi_i^2$. It can be shown that if the constraint weights W_i are sufficiently large, minimization of ϕ^* is equivalent to minimization of ϕ, subject to the constraints $\boldsymbol{\psi} = \mathbf{0}$. When the constraint weighting factors approach infinity, such an approach defines an interior penalty function, and only designs that satisfy the constraints are retained in the search process. This approach is typified by the Fiacco-McCormick procedure (ref. 14). For problems involving straightforward constraints, an interior penalty function is satisfactory; for complex, nonconvex constraints, interior penalty function methods are inappropriate (ref. 15) and finite constraint weights should be employed. This leads to an exterior penalty function approach in which designs that do not satisfy all constraints may be temporarily retained in the optimization process.

A variety of iterative search strategies for solution of multivariable optimization problems has been proposed (ref. 4). The more popular methods include steepest descent and Fletcher-Powell methods (ref. 16). However, in general, any one strategy may encounter convergence difficulty, and the search strategy appropriate to one optimization problem may be quite inappropriate for another problem. It follows that search reliability may be enhanced by the adoption of a variety of search strategies for problem solution. This is the approach used in the present study, which employed the program of references 5 and 7 containing nine multivariable search algorithms that may be applied in an arbitrary sequential order. These nine searches include elementary single-pa-

rameter search strategies, organized multivariable search strategies, and random techniques as follows:

Sectioning search exhaustively searches the range of each parameter in turn for the one-dimensional optimum. The values of the parameters are fixed at their optimum as they are achieved. The procedure is repeated until no further gain is possible. The parameter order can be chosen by the user or selected at random. This search can be used for evaluating nonoptimum sensitivities about any point in the parameter space because each search essentially describes a one-dimensional cut through the multidimensional design parameter space.

Creeping search is similar to sectioning in that the parameters are perturbed in turn one at a time. In the creeping algorithm, however, the parameters initially undergo only small incremental changes in the favorable performance direction. On repetitive cycles the step size is increased independently in each parameter until further gain is impossible in either increasing or decreasing directions. An order-of-magnitude reduction in step size is then effected, and the process is repeated. At any given moment some parameter step sizes may be increasing, while others are decreasing. Ultimately, all step sizes are reduced to prespecified minimum values, and the search is discontinued.

Random point search is essentially a Monte Carlo technique that distributes points uniformly in the control parameter space. After a prespecified number of evaluations of the objective function, the control vector providing the best performance characteristics is retained.

Magnify search scales all the control parameters uniformly in the favorable direction until the local optimum is achieved.

Steepest descent search relies on partial derivatives of the objective function with respect to the control parameters to predict a favorable direction. In effect, a tangent plane is fitted to the objective function surface at the starting point. Numerical derivatives are computed by two-sided perturbation of each design parameter and are thus correct to second order. In its simplest form, the search proceeds in the gradient direction. Experience has shown that gradient direction search is often very inefficient. Ridge lines are rapidly located; from that point gradient search becomes a sequence of oscillatory perturbations along the ridge. Algorithm extensions have been incorporated that allow the search to proceed in a weighted gradient direction. The weighting matrix employed as a perturbation measure is adaptively determined within the program by nondimensionalization of the search hyperrectangle; local partial circularization of the payoff function contours, and, most important, by an adaptive learning mechanism based on previous search behavior.

Quadratic search fits a second-order surface to the payoff function at a nominal design point. The extremal of the approximating quadratic surface is predicted, and the search proceeds along the ray defined by

420-093 O - 71 - 21

(*a*) the initial point and (*b*) the predicted extremal point. This technique, although developed as a search procedure, is also useful for predicting optimal second-order sensitivities about the optimal design point.

Fletcher-Powell or Davidon search, or deflected gradient method, essentially combines features of steepest descent and quadratic searches. The procedure initially searches in the gradient direction. Recursive relationships permit development of approximate second-order information from successive ray searches. This information is used to develop a weighting matrix that provides quadratic convergence. The method can become ill-conditioned if the payoff response surface does not exhibit almost quadratic form in the search region.

Pattern search can be applied after successive applications of any combination of other searches. It uses the starting point from the first search and the final point from the last search to define a new search ray. This ray is searched in the favorable direction for the local optimum. It is essentially an acceleration technique exploring gross directions revealed by other organized search algorithms.

Random ray search proceeds on the basis of small randomly selected design parameter perturbations. Perturbation magnitude is adaptively determined on the basis of past performance characteristic behavior. This can be very efficient when used in conjunction with pattern search when there are many interacting design parameters.

In addition to these nine searches, which assume unimodality of the performance response surface, the program contains a method of locating more than one extremal. This multiple-extremal technique consists of design parameter space warping. A transformation is applied to the parameter space such that all the extremals of the performance response function are retained in the transformed space, but the relative locations are altered in an inverse exponential manner about an arbitrary point in the original space. In practice, the transformation is performed about some previously discovered extremal point. Subsequent searches in the transformed space then have a reduced probability of finding the same extremal. This probability depends on the exponential order of the transformation selected by the user.

OVERPRESSURE CALCULATION

Overpressure calculations are performed by the method of Lighthill (ref. 17). For smooth, pointed bodies having a longitudinal area distribution $S(t)$ and lift distribution $l(t)$, the equivalent area distribution

$$f(t)=\frac{1}{2\pi}\left[S'(t)+\frac{\beta l(t)}{2q}\right]$$

is utilized, and the F-function is obtained from

$$F(y)=\int_0^y \frac{f'(t)\,dt}{(y-t)^{1/2}}$$

For bodies having slope discontinuities in the equivalent area distribution, an additional term ΔF_i is added to $F(y)$ at each point of discontinuity t_i. The F-function becomes

$$F(y)=\left[\int_0^y \frac{f'(t)\,dt}{(y-t)^{1/2}}+\left(\frac{2}{\beta}\right)^{1/2}\sum_{k=1}^{i}\frac{h(z)\Delta S'(t_k)}{R_k}\right]$$

Here R_k is the equivalent radius at the kth discontinuity, and $h(z)$ is defined in reference 17 as a function of

$$z=\frac{y-t_k}{\beta R_k}$$

Typical pressure signatures emitted by a parabolic body of revolution as computed by the Lighthill method at three values of h/l are presented in figure 1. The gradual approach to a far-field N-signature is apparent from this figure. It should be noted that l is equal to twice the nose length throughout this paper. Shock positions are located by the Whitham method based on the definition of the hull or upper boundary of the F-function integral

$$I(y)=\oint_{-\infty}^{y} F(t)\,dt$$

This integration is performed numerically without smoothing, and a local parabolic representation of each subarc corresponding to the signature compression and expansion waves is employed to determine subarc intersections (fig. 2).

SINGLE-PARAMETER SOLUTIONS

A typical single-parameter family of body shapes can be defined by a radius distribution of the form

$$r(x)=Ax^N \qquad x\leq L$$
$$=R_B \qquad x>L$$

Here N is a free parameter and A is a constant determined by problem constraints. If base radius R_B and nose length L are constrained,

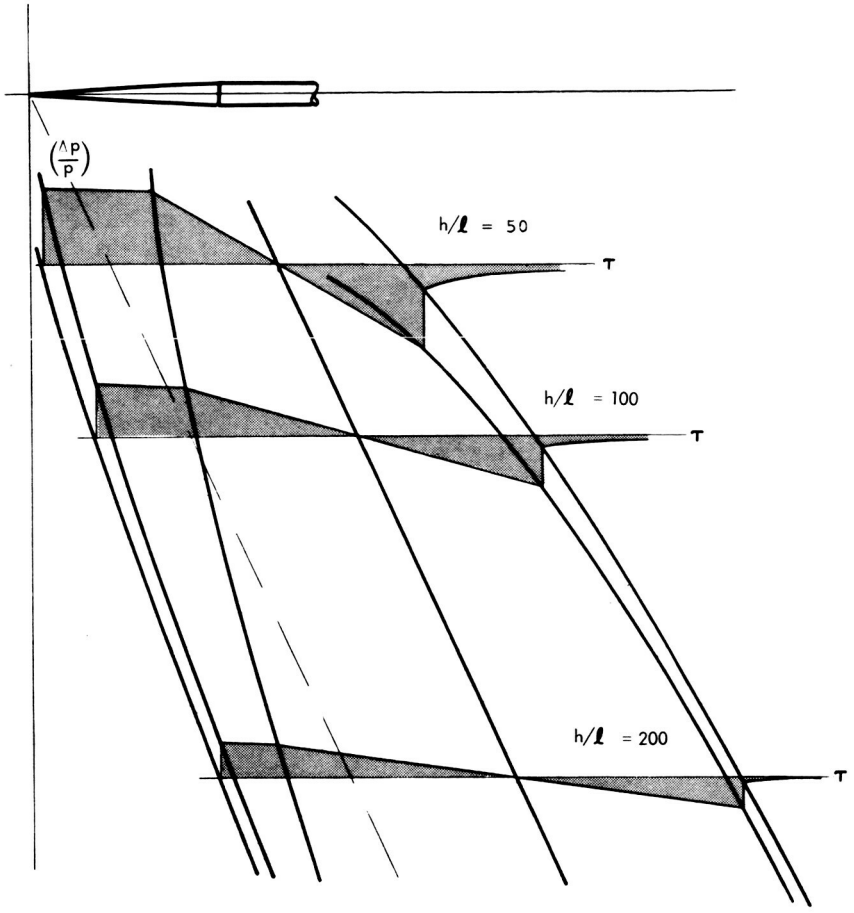

FIGURE 1. – Pressure waves from power body at three distances.

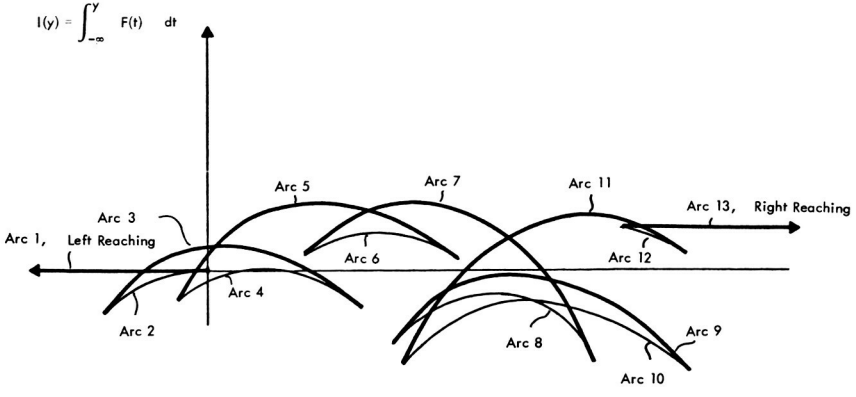

FIGURE 2. – Schematic of shock formations.

$$A=\frac{R_B}{L^N}$$

If the nose volume V is constrained,

$$A=\left[\frac{2(N+1)V}{\pi L^{(2N+1)}}\right]^{1/2}$$

Typical body shapes defined in this manner for the base radius and nose length constrained case are presented in figure 3. It may be noted that a local inequality constraint

$$\frac{dr}{dx}\leqslant\frac{1}{\beta}$$

is imposed on the body profile. This straightforward one-parameter family of bodies produces a fairly wide range of pressure signature types as illustrated by figure 4 for the case $L=4.0$, $R_B=0.25$, $M=1.414$, and $(h/l)=10$. For very low exponents, an N-wave with a zero-pressure point immediately aft of the nose results. For higher exponents, a semi-flat top signature with declining pressure results, until at an exponent of 0.79, a true flat top signature is attained. Increasing the exponent results again in a semi-flat top signature of increasing pressure until, for a sufficiently high exponent, a finite rise signature is obtained. Finally, for a sufficiently large exponent, an N-wave with a zero-pressure point at the shoulder $(x=4.0)$ is obtained.

If the maximum overpressure *at any point on the signature* is plotted, figure 5 is obtained. This is the quantity minimized in the present study. A single-parameter search for the minimum of a function having a slope discontinuity at the extremal point is best carried out by a "golden section" search (refs. 4 and 5). This is almost as efficient as the Fibonacci search but avoids the Fibonacci requirement of prespecification of the number of point evaluations to be made in the section search prior to search commencement. The actual points employed in a typical search are illustrated in figure 5. The minimum-maximum overpressure obtained by a series of such one-dimensional searches are presented in figure 6 for a range of h/l value between 10 and 700 with bodies of nose length $L=4.0$ and base radius $R_B=0.25$. It can be seen that in the near field, a $\frac{3}{4}$-power body provides the optimal solution and in the far field $N_{\text{optimum}}\rightarrow\frac{1}{4}$. In general, within the mid field, a transition from a $\frac{3}{4}$-power to a $\frac{1}{4}$-power body occurs gradually with optimal exponent varying with Mach number, slenderness, and h/l values. A family of volume-constrained solutions obtained in a similar manner at $M=2.7$ is presented in figure 7. All bodies have a nose volume equal to that of a cone having a nose length of 4.0 and a base radius of 0.25.

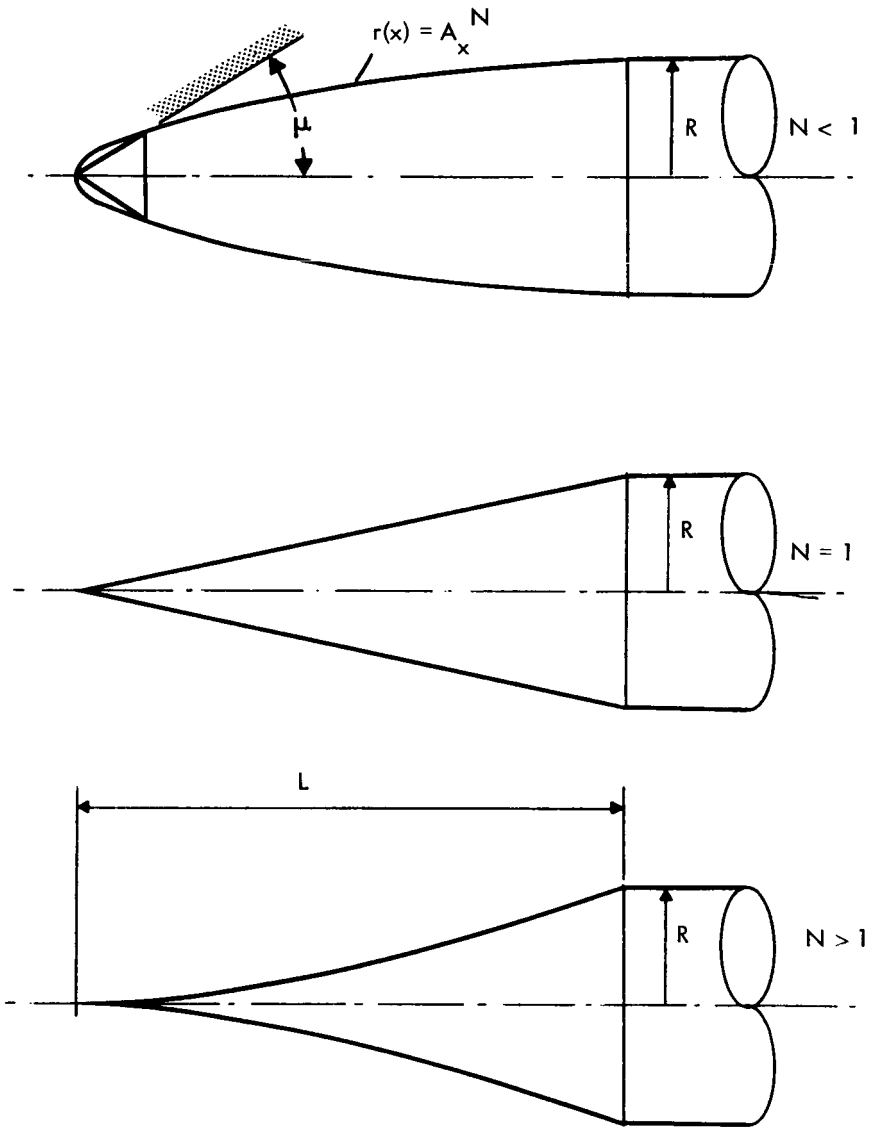

FIGURE 3. – Single-arc power bodies, with a fixed length and base radius.

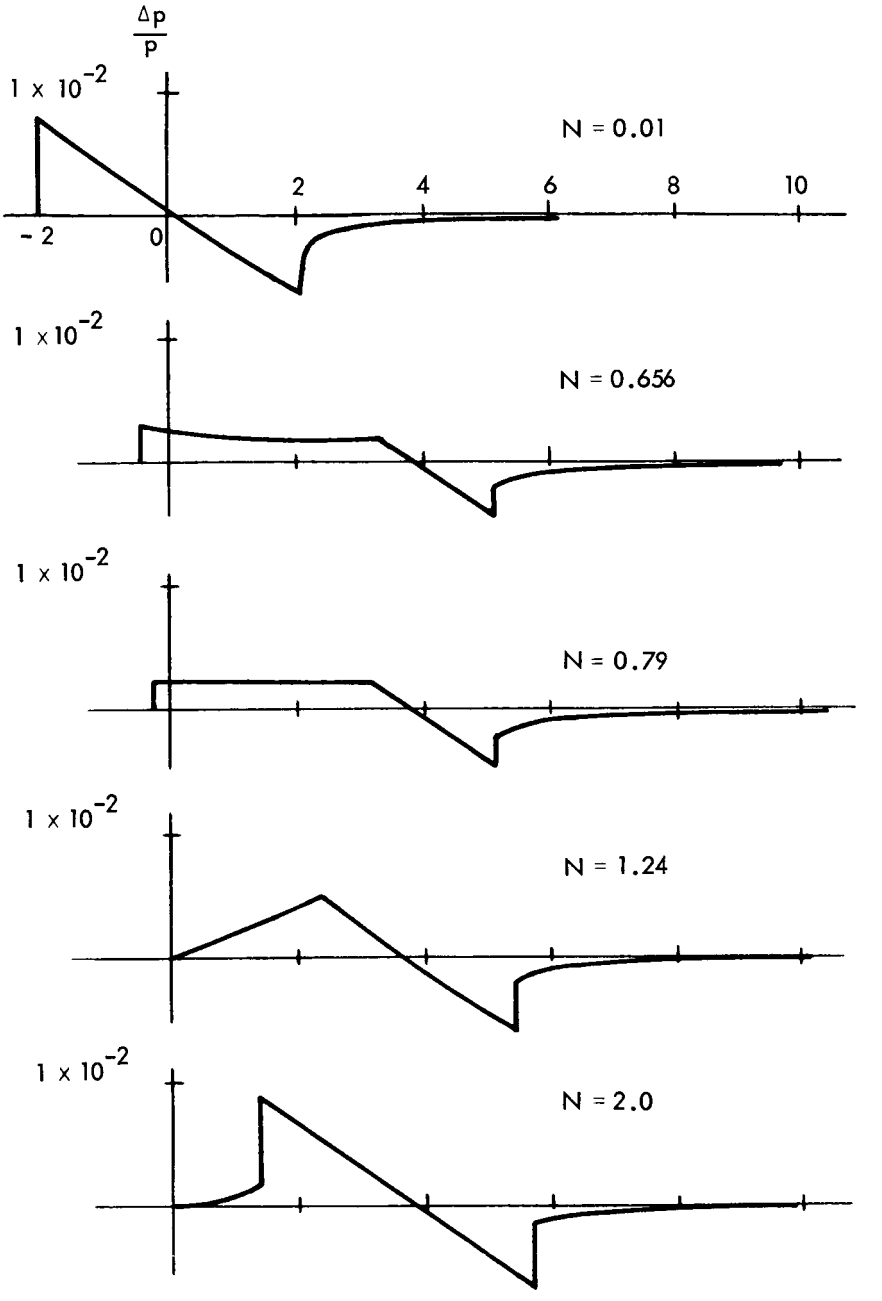

FIGURE 4.—Selected signatures for single-arc power bodies with base and length constrained, $M = 1.414$ and $h/l = 10$.

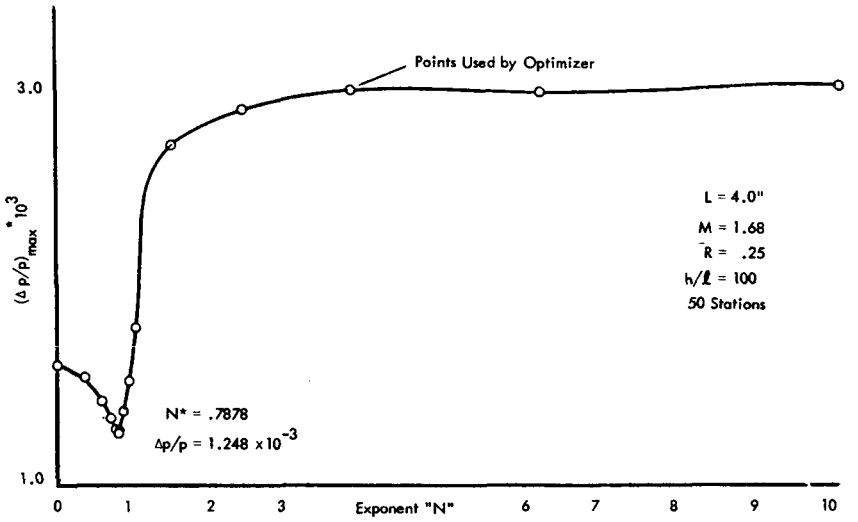

FIGURE 5. — Variation of maximum overpressure with power body exponent with radius and length constrained.

MULTIPLE-PARAMETER SOLUTIONS

A four-parameter family of bodies that consists of two successive power arcs is illustrated in figure 8(*a*). Free parameters α_i are

$\alpha_1 = R_1$, radius at power-arc intersection
$\alpha_2 = X_1$, location of power-arc intersection
$\alpha_3 =$ First arc exponent
$\alpha_4 =$ Second arc exponent

Optimization of this family of body shapes results in a typical signature of the form presented in figure 8(*b*). The signature is compared to that of a $\frac{3}{4}$-power body of the same base radius. The maximum overpressure is unchanged from that of the $\frac{3}{4}$-power body, although the signature is somewhat different in form. Clearly, the $\frac{3}{4}$-power body itself lies within this four-parameter family of shapes. Hence, it appears that the minimum overpressure shape is not unique. The body shape corresponding to this signature is given in figure 8(*a*) and is somewhat more bulbous than the $\frac{3}{4}$-power body.

Proceeding one step farther, a three-arc body can be defined by the use of seven parameters. Figure 9 illustrates the body geometry. With length and base radius constrained, seven convenient free parameters are

$\alpha_1 = X_1$
$\alpha_2 = K$, where $X_2 = X_1 + K(X_3 - X_1)$

$\alpha_3 = R_1$
$\alpha_4 = R_2$
$\alpha_5 = N_1$
$\alpha_6 = N_2$
$\alpha_7 = N_3$

Figure 10 presents an optimal solution obtained at $M = 1.68$ $h/l = 50$ employing this problem formulation. A distinct three-arc shape has been evolved. The solution was obtained by a combination of random ray,

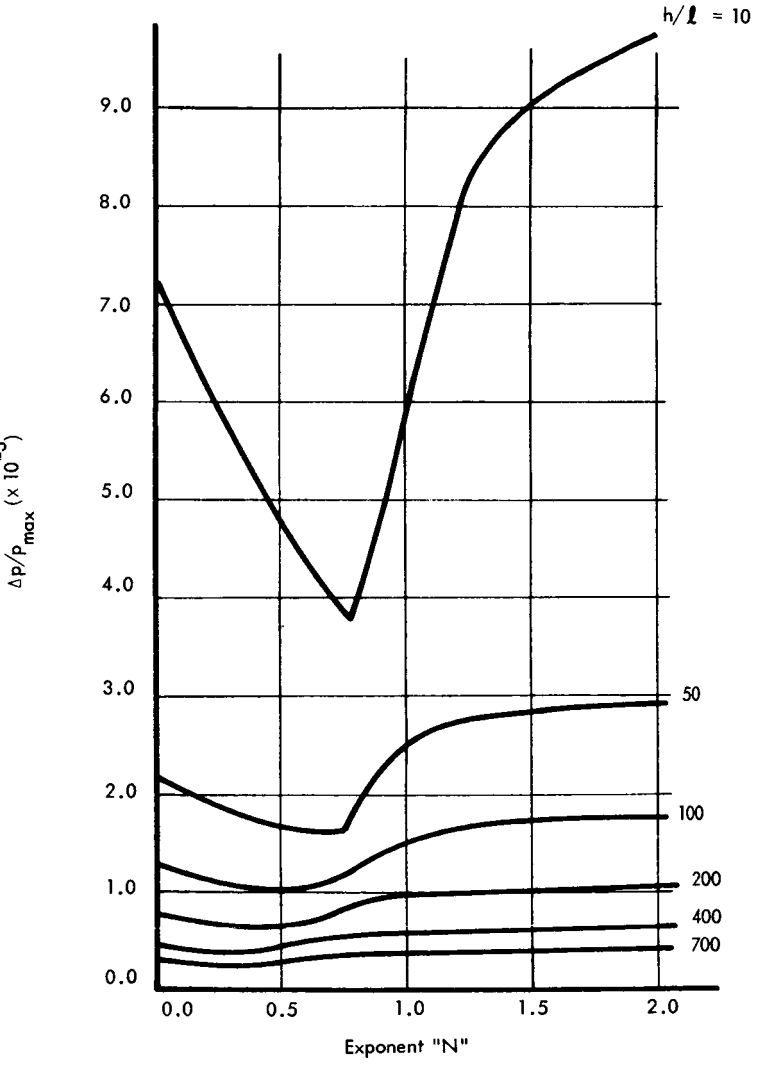

FIGURE 6.—Effect of distance on single power arc solutions with length and base constrained, $M = 2.2$.

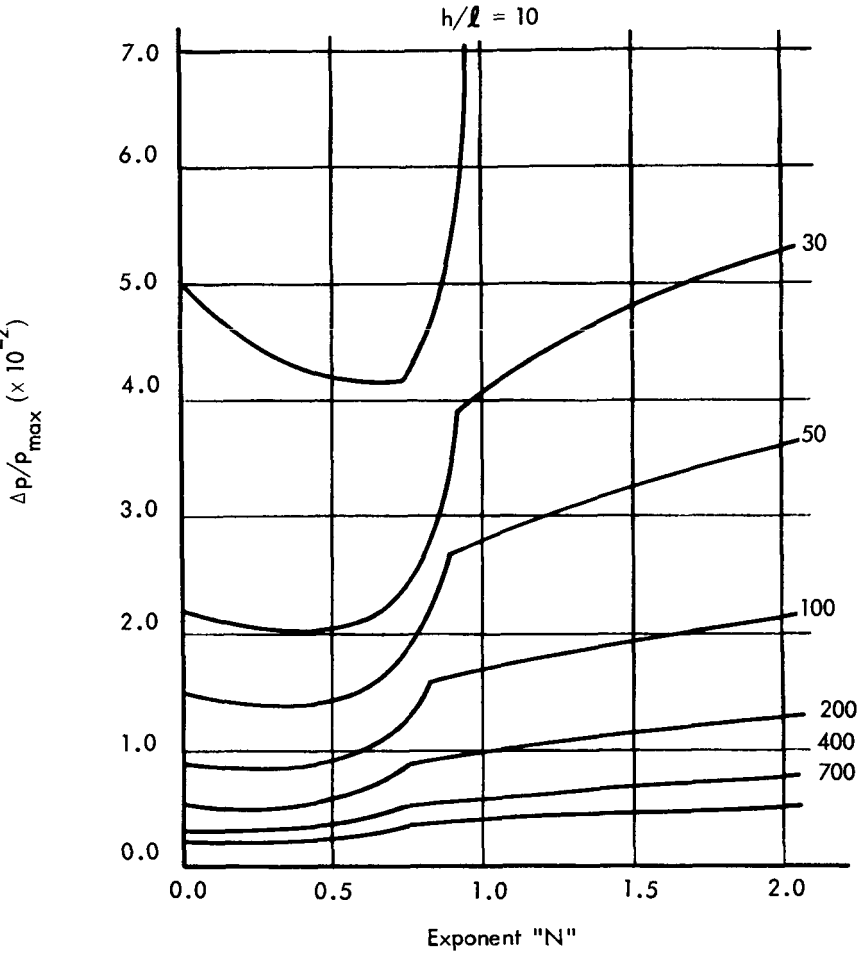

FIGURE 7.—Effect of distance on single power arc solutions with volume constrained, $M = 2.7$ and $V_F = 1.0$.

adaptive creeping, and pattern searches preceded by a random point (Monte Carlo) search. This optimal shape has a maximum overpressure ratio of 7.99×10^{-4}. For comparison, a $\frac{3}{4}$-power body of the same total nose length and base area would have a maximum overpressure ratio of 1.25×10^{-3}. The computed three-arc minimum-maximum overpressure is, therefore, 64 percent of the corresponding $\frac{3}{4}$-power body overpressure, the optimal single-arc solution for the conditions employed. This is a significant reduction in overpressure.

Computed pressure signature, including shock locations, is presented in figure 11; it is a modified flat top signature. The overpressure reduction mechanism is clear. A smooth forebody generates an initial flat top

signature. The forebody has a smaller terminal radius than that of the body base; hence, the flat top overpressure is less than that of a single-arc flat top signature. Aft of the forebody, the second arc necks inward, creating an expansion field that interacts with the compression field originating from the third arc as it achieves the base radius constraint. The resulting wave cancellations provide a signature that nowhere

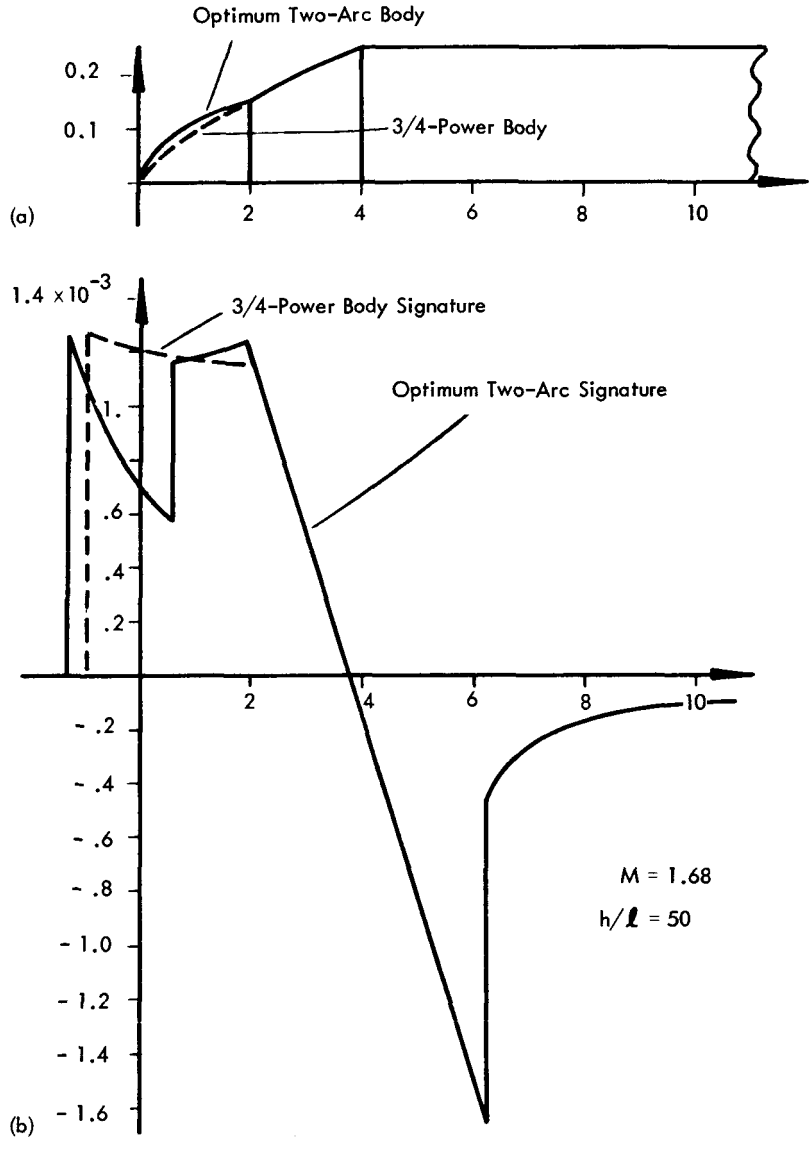

FIGURE 8.—(*a*) Two-arc body shape compared to that of a 3/4-power body. (*b*) Two-arc signature compared to that of a 3/4-power body.

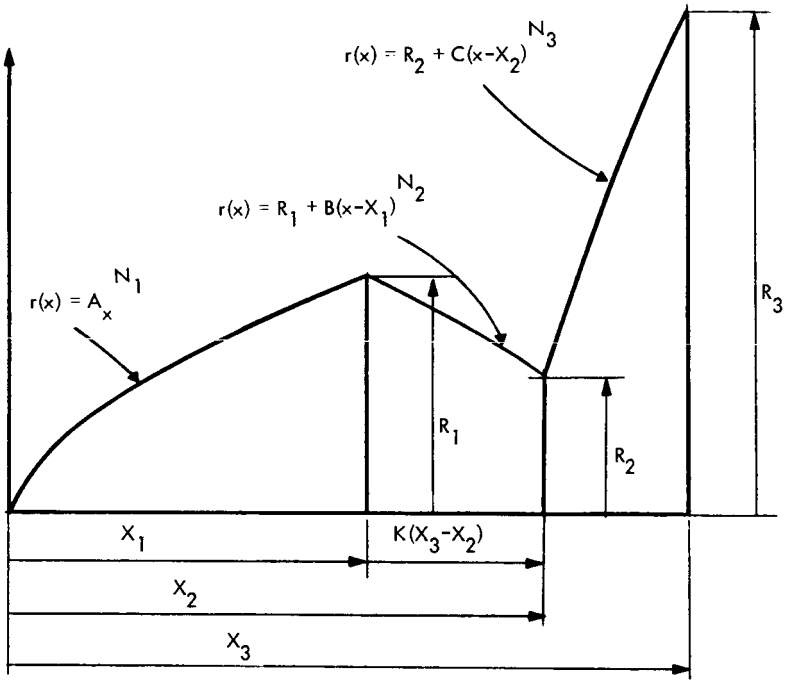

FIGURE 9. – Three-arc body parameters.

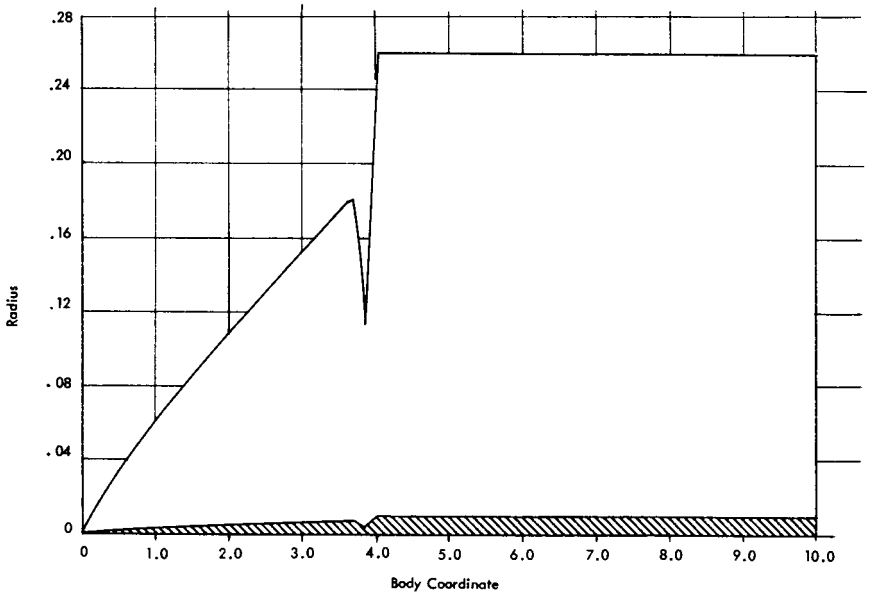

FIGURE 10. – Optimal three-arc body.

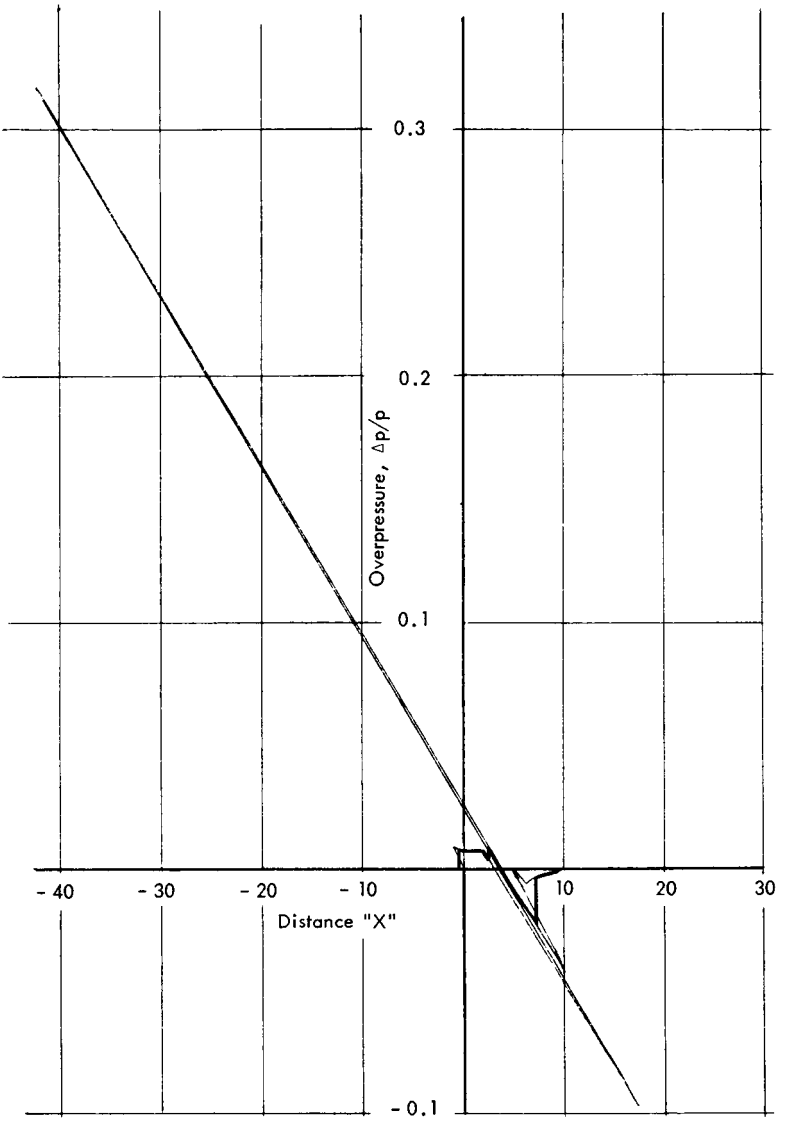

FIGURE 11.—Pressure signature of a three-arc body.

exceeds the initial flat top overpressure generated by the reduced base forebody.

CONFIGURATION IMPLICATIONS

The question arises, "What type of three-dimensional wing-body would create a low overpressure signature of the type obtained by the three-arc parametric model?" It seems clear that the dominant part of

the equivalent area distribution specified by the first two arcs would be due to volume. The equivalent area distribution specified by the third arc would probably consist largely of lift with a diminishing volume component toward the aft part of the distribution. The rapid rise in lift probably would require the use of a relatively unswept wing. Preliminary studies have indicated that some extension of the notch width is possible without destruction of the low overpressure signature. This widening was accompanied by a reduction in the slope of area in the region of the second and third arcs.

No attempt to reduce the magnitude of the trailing shock overpressures was made in the study. However, it would appear likely that an increase in the number of arcs would permit a similar reduction in the magnitude of the trailing pressures. This conceivably could be achieved by a boattail interaction with an underexpanded engine exhaust stream.

Questions of drag, stability, and control were not considered in this study. With regard to drag, it should be noted that an equivalent area distribution of the three-arc type is not necessarily incompatible with supersonic area-rule requirements. At the 0° angle, however, a high drag component area distribution would be contributed to the mean area.

CONCLUSION

It would appear that the use of relatively unconventional configurations might produce significant maximum overpressure reductions in the mid-field. These configurations would involve slope of area discontinuities in the configuration 0° equivalent area distribution and probably employ a canard arrangement.

The solutions discussed in this paper have been determined by the application of multivariable search techniques to a numerical model of the mid-field overpressure problem. Computation of mid-field signatures is a fairly sensitive process; hence, it is recommended that prior to further work in this area, methods for computing mid-field signatures be reexamined. Emphasis would lie in the adequacy of existing techniques when the body has slope of area discontinuities.

Finally, on verification of mid-field signature techniques, it is recommended that the feasibility of employing a multiple-arc distribution for an SST configuration be examined, possibly using the overall system design techniques developed by Petersen and Gregory in references 18 and 19. These configuration design techniques are also well suited to the multivariable search process (ref. 10).

REFERENCES

1. SEEBASS, A. R., ED.: Sonic Boom Research. NASA SP–147, 1967.
2. SCHWARTZ, IRA R., ED.: Second Conference on Sonic Boom Research. NASA SP–180, 1968.

3. MCLEAN, EDWARD F.: Configuration Design for Specified Pressure Signature Characteristics. Second Conference on Sonic Boom Research, NASA SP-180, 1968, pp. 37-45.
4. WILDE, D. J.: Optimal Seeking Methods. Prentice-Hall, Inc., 1964.
5. HAGUE, D. S.; AND GLATT, C. R.: An Introduction to Multivariable Search Techniques for Parameter Optimization (and Program AESOP). NASA CR-73200, 1968.
6. HAGUE, D. S.; ROZENDAAL, H. L.; AND WOODWARD, F. A.: Application of Multivariable Search Techniques to Optimal Aerodynamic Shaping Problems. J. Astronaut. Sci., vol. 15, no. 6, Nov.-Dec. 1968, pp. 283-296.
7. HAGUE, D. S.; AND GLATT, C. R.: A Guide to the *A*utomated *E*ngineering and *S*cientific *O*ptimization *P*rogram (AESOP). NASA CR-73201, 1968.
8. SANDRIN, W. A.; GLATT, C. R.; AND HAGUE, D. S.: Design Arrays with Unequal Spacing and Partially Uniform Amplitude Taper. IEEE Trans. Antennas Propagat., Sept. 1969.
9. Aerophysics Research Corp.: Application of Multivariable Search Techniques to Optimal Combustor Design. Contract NAS 3-13331, in progress.
10. HAGUE, D. S.; AND GLATT, C. R.: Application of Multivariable Search Techniques to the Optimal Design of Hypersonic Cruise Vehicle. NASA CR-73202, 1968.
11. HAGUE, D. S.; AND GLATT, C. R.: Computer-Aided Aerospace Vehicle Performance and Design Optimization. Paper presented at the Joint Conference on Mathematical and Computer Aids to Design, 1969.
12. SCHMIDT, H. E.; HELGASON, R. V.; WITHERSPOON, J.; AND BEIB, K.: Trajectory Optimization by the Method of Steepest-Descent. AFFDL-TR-67-108, vol. III, Apr. 1968.
13. HAGUE, D. S.: The Optimization of Multiple-Arc Trajectories by the Steepest-Descent Method. Recent Advan. Optimization Tech., Lavi and Vogl, eds., John Wiley & Sons, Inc., 1966, pp. 389-517.
14. FIACCO, A. F.; AND MCCORMICK, G. P.: Computational Algorithm for the Sequential Unconstrained Minimization Technique for Nonlinear Programming. Management Sci., vol. 10, no. 4, July 1964, pp. 601-617.
15. Aerophysics Research Corp.: Application of Multivariable Search Techniques to the Design of Optimal Aircraft Structures. Contract NAS 1-9936. To be published as NASA CR.
16. FLETCHER, R.; AND POWELL, M. J. D.: A Rapidly Convergent Descent Method for Minimization. Computer J. (British), vol. 6, 1963, pp. 163-168.
17. LIGHTHILL, M. J.: Higher Approximations in Aerodynamic Theory. Coleman Du P. Donaldson, ed., Princeton Aeronautical Paperbacks, Princeton Univ. Press, 1960.
18. GREGORY, T. J.; PETERSEN, R. H.; AND WYSS, J. A.: Performance Trade-Offs and Research Problems for Hypersonic Transports. J. Aircr., July-Aug. 1965.
19. PETERSEN, R. H.; GREGORY, T. J.; AND SMITH, C. L.: Some Comparisons of Turboramjet-Powered Hypersonic Aircraft for Cruise and Boost Missions. J. Aircr., Sept.-Oct. 1966.

Status of Research on Boom Minimization Through Airstream Alteration

DAVID S. MILLER
NASA Langley Research Center

A solution to the sonic boom problem would have a tremendous impact on the future of our air transport system. In fact, it has been estimated the potential market for worldwide supersonic transport (SST) sales would be more than doubled if supersonic flights were permitted over populated areas. Numerous studies have led to the development of reliable minimization techniques that employ aircraft shaping. There is no assurance, however, that these conventional minimization techniques will reduce the sonic boom to levels that would be unquestionably acceptable for routine overland operation of SST's. As a result there has been recently an increased interest in unique and somewhat unconventional approaches to the sonic boom problem. One such approach, the subject of this paper, involves the use of heat or force fields to alter the airflow in the vicinity of the airplane to produce more acceptable sonic boom signatures. In this paper, the basic concepts of this approach are formulated and are related to the well-established body of information on sonic boom generation and propagation. For the more promising heat-field concept, problems to be anticipated in practical application are explored by applying a simple analysis procedure to a typical SST configuration. Preliminary estimates of heat distribution and power requirements are presented, and a method of concept implementation is discussed.

SYMBOLS

A_E	effective cross-sectional area due to a combination of airplane lift, airplane volume, and the altered airstream
A_s	airplane flight altitude or perpendicular distance from model to measuring probe
A_0	initial phantom-body cross-sectional area
l	airplane or model reference length
l_p	phantom-body length
M	Mach number

420-093 O - 71 - 22

P power summation, $\int_0^x (dP/dx)\,dx$

dP/dx power distribution

Δp incremental pressure due to flow field of airplane or model

Δt_r rise time of sonic boom pressure signature

T_0 stagnation temperature

x distance measured along longitudinal axis from airplane nose, model nose, or initial change in phantom-body area (i.e., phantom-body nose)

β $\sqrt{M^2-1}$

Subscripts

max maximum

min minimum

CONVENTIONAL MINIMIZATION TECHNIQUES

Numerous studies have attacked the problem of defining configuration requirements for sonic-boom minimization under various constraints. Some general signature characteristics and airplane shaping considerations for sonic boom minimization are illustrated in figure 1. Currently operational supersonic military aircraft and present SST designs would by expected to produce a classical N-wave, as depicted at the left of the figure, for most flight conditions. For these aircraft, shaping for sonic boom minimization (refs. 1 to 3) could effect limited reductions in bow shock overpressure and signature impulse, but the basic N-wave signature shape would remain.

It was first pointed out by McLean (ref. 4) that for somewhat longer and more slender configurations, representative of some SST designs, a near-field signature may be expected to extend from the airplane to the ground. Under these circumstances the signature shape would depend on the airplane shape; and, as illustrated by the plateau signature, further reductions in overpressure could be achieved through airplane design modifications (refs. 5 to 8). Although the plateau signature achieves moderate reductions in bow shock overpressure, the shocks and the attendant sonic boom noise still exist.

Upon relaxation of all realistic restraints on airplane length and with a very carefully controlled effective area development, the shocks themselves could theoretically be eliminated (refs. 9 and 10) as depicted by the finite rise time signature shown at the right of the figure. However, theoretical calculations indicate that in order to implement this minimization technique, it would be necessary to increase the length of the SST now under development by a factor of 3 or more with no attendant increase in airplane weight. Thus, at the present time, a finite rise time signature appears to be a desirable but unobtainable goal. Alternate

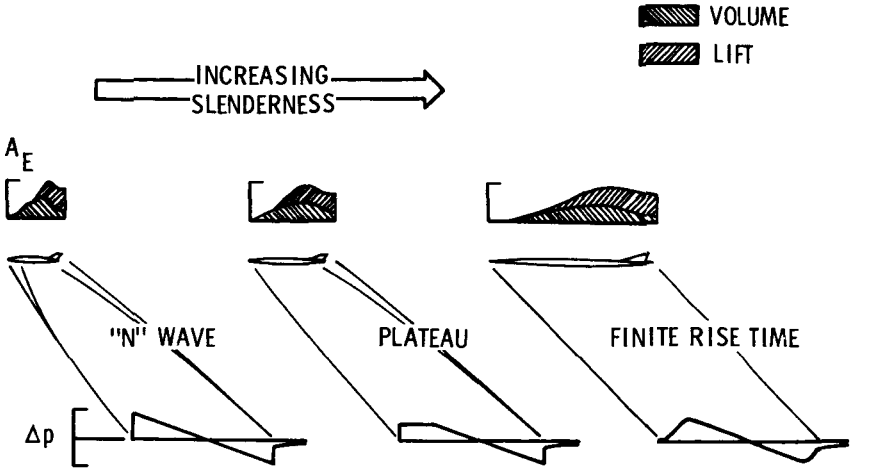

FIGURE 1. – Airplane design for sonic boom minimization.

methods for the generation of shockless signatures through the employment of heat or force fields will be the subject of further discussion in this paper; however, at this point it seems appropriate to present evidence of the applicability of present theoretical methods utilized in the prediction and minimization of sonic booms.

Based on the theoretical work of Hayes (ref. 11) and Whitham (ref. 12), numerical methods (ref. 13) have been developed for calculating both the near-field and far-field pressure signatures of complex aircraft configurations. Studies in which theoretically determined pressure signatures are compared with experimental data from wind-tunnel and flight-test programs indicate that present techniques provide reasonably accurate estimates of sonic boom characteristics for a wide variety of airplanes and operating conditions (refs. 14 to 17). The sample of wind-tunnel data given in figure 2 serves to substantiate the applicability of present prediction and minimization techniques to complex configurations. Pressure signatures were measured at a variety of flow-field positions and test conditions for the two 4-in.-long SST models shown in the figure. These particular signatures were obtained five body lengths below the models at a Mach number of 1.4 and a lift coefficient of 0.1. Effective area developments used in determining the theoretical signature are shown in the inset sketches. Although the signature for the basic model is quite complex, there is excellent agreement between experiment and theory. The signature shown at the right was obtained for a model that had fuselage modifications intended to result in plateau signature. Experimental data show that the desired plateau signature is not quite obtained, but a good approach is made. Differences between experiment and theory

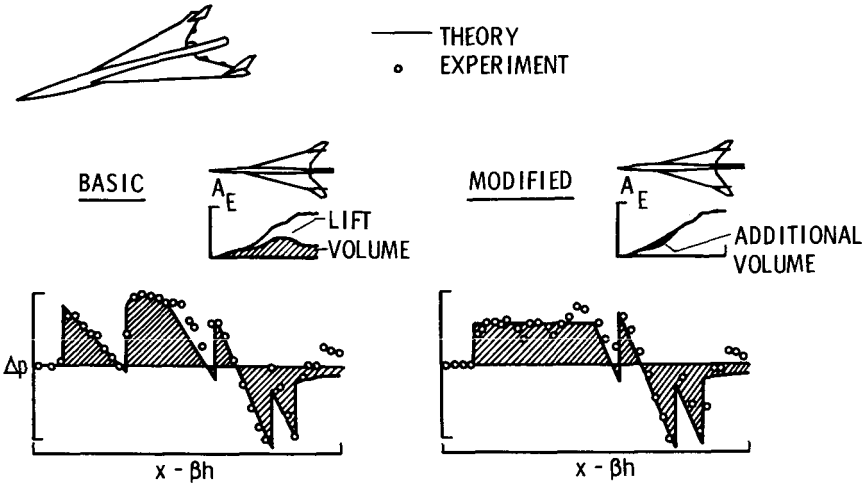

FIGURE 2. – Wind-tunnel verification of prediction and minimization techniques, $M = 1.4$ and $h/l = 5$.

are attributed to inaccuracies in model construction and illustrate the extreme sensitivity of signature shape to small changes in model shape. The same theory applied to a 400 000-lb airplane flying at an altitude of 40 000 ft and $M = 1.4$ indicates a maximum positive overpressure of 2.2 lb/ft^2 for the design at the left and a reduced value of 1.3 lb/ft^2 for the modified design. Application of these same design principles for cruise conditions results in only a small maximum overpressure reduction relative to that of the basic design.

THE PHANTOM-BODY CONCEPT

Changes in the physical shape of the airplane are required in the minimization techniques discussed thus far; however, it may be possible to create desired pressure signatures by employing heat or force fields to alter the airflow in the vicinity of the airplane without drastic changes in the airplane dimensions (refs. 10, 18, and 19). A phantom-body or airstream alteration concept for achievement of the highly desirable finite rise time signature is shown in figure 3. Depicted in the figure is an effective area development of an airplane that would produce an N-wave and a phantom-body effective area development, resulting from a combination of airplane and altered airstream, which would produce a shock-free signature on the airplane flight track. The difference between the area development of the phantom body and that of the airplane defines the required airstream alterations that must be created by a carefully controlled heat or force field extending well ahead of and well behind

the airplane. At ground positions away from the flight track, the airplane effective area development assumes a different shape and magnitude; thus, shock elimination at all ground positions would require a carefully controlled azimuthally as well as longitudinally altered airstream.

Illustrated in figure 4 are several alternate applications of the phantom-body concept that would be equivalent within the assumptions of area-rule considerations on which present sonic boom theory rests. The altered airstream whose boundary streamlines are represented by dashed lines can be located along the airplane axis as shown at the left or can be displaced below the airplane as shown at the center. The airstream alteration can also be the net result of many airstreams distributed in the manner shown at the right. The three methods illustrated are considered equivalent because they would produce identical sonic boom signatures on the flight track. The criterion for equivalence is that the area-rule-determined effective area developments of the airstreams and airplane combine to create the specified shape. For simplicity, the following analysis is restricted to the azimuth angle corresponding to the flight track and treats the on-axis case as shown at the left; however, it can be seen that analysis of the other systems would not be different in principle. The analysis is also restricted to the heat-field method, which appears to offer more hope for practical implementation. A treatment of both the heat-field and force-field methods is given in reference 18.

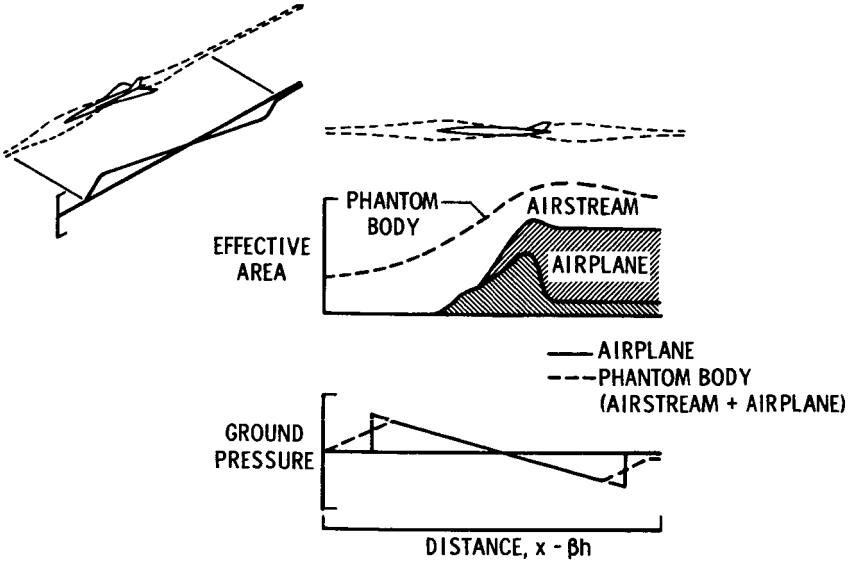

FIGURE 3. — Phantom-body concept.

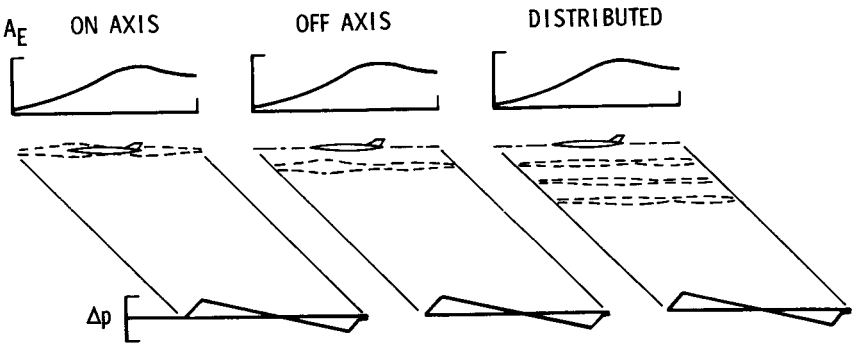

FIGURE 4. – Equivalent application of concept.

ANALYSIS

The theoretical method employed to analyze the altered airstream flow properties and to estimate the heat distribution and power requirements is based on the assumption that the flow within the airstream can be treated as the steady, one-dimensional, inviscid channel flow of a perfect gas.

The solution is found by defining the channel area development, establishing boundary conditions, and applying influence coefficients and iterating.

The assumptions included in this analysis are that the radial and azimuthal variations are ignored, that the heat transfer from the airstream is not considered, that the interaction of the airstream and the airplane is neglected, and that the shocks at the airplane surface are assumed to be weak.

To check the validity of the solution, the nature of the modified airstream flow properties is determined and a first estimate of minimum power requirements is made.

For a given airplane and given flight conditions, the phantom-body area development that completely envelops the airplane area development and produces a finite rise time sonic boom signature can be determined. The forepart of the area development has a $\frac{5}{2}$-power variation with length (an isentropic spike). The Whitham theory provides the length-diameter relationship to prevent bow shock formation for a specified Mach number and altitude. Prevention of a tail shock is accomplished by a design process for the remainder of the phantom-body area development, which involves trial-and-error application of a computing program solution of the Whitham equations (ref. 13). To take account of the favorable "freezing" effect of a real atmosphere through employment of the atmospheric propagation program of Hayes (ref. 20) requires further iteration to define phantom-body shape characteristics for a specified rise time.

The airstream channel is defined as the difference between the phantom-body cross-sectional area and the effective cross-sectional area of the airplane. The boundary condition of the longitudinal pressure distribution along the channel is established by calculating the surface pressure on the phantom body using small-disturbance theory (ref. 21) and by assuming the pressure to be constant across the channel. The governing differential equations written in terms of influence coefficients (ref. 22) are then solved by iteration for successive increments along the channel. A thorough description of the solution procedure is given in reference 18.

The applicability of the present simplified analysis procedure in treating practical problems of phantom-body concept implementation can be assessed by examining the assumptions and simplifications employed in its development. The complexity of the problem has been significantly reduced by ignoring radial and azimuthal variations that would be required for shock elimination at ground positions away from the flight track; however, this simplified treatment of the problem is not expected to significantly alter the results of this preliminary study.

Another basic assumption is that all of the distributed heat energy is confined within the boundaries of the airstream and is completely effective in creating the desired airstream alterations. A more realistic approach would consider heat transfer across the airstream boundaries, which would in turn influence the entire flow field in a different manner than does the heating with no heat transfer. The relationships between the heating rates and airstream variations for this case cannot be easily established and are beyond the scope of this preliminary analysis. Under the assumption of no heat transfer, the manner in which the local heating influences the flow is well defined.

It is also recognized that for strong shocks formed immediately at the airplane surfaces, the airstream expansions might not be fully effective in providing a cancellation. However, a typically pointed airplane nose or a subsonic leading edge wing need not form strong shocks, and cancellation should be possible. Other complicating factors are the effects that variations in the airstream flow properties will have in altering the aerodynamic performance and flow-field characteristics of the airplane and the effects that airplane-produced disturbances will have on the airstream. This interaction between the airstream and the airplane is neglected for results presented in this paper.

Subject to the previously discussed assumptions and simplifications, the present method of analysis is believed to be sufficient to indicate the nature of the altered airstream flow properties and to make preliminary estimates of the required heat distribution and minimum power requirements.

CONCEPT APPLICATION

Problems to be encountered in employing the phantom-body concept for sonic boom minimization can best be explored by applying the concept to an actual airplane configuration. The baseline configuration used in the following discussion is a typical proposed supersonic transport having a length of 300 ft and a cruise Mach number of 2.7 at an altitude of 60 000 ft. The cruise weight of the airplane is assumed to be 575 000 lb, and no account is taken of weight increase due to additional onboard equipment required to generate the altered airstream.

Illustrations of the results of the study as reported herein are restricted to the heat-field application, which at present appears to be of greater practical interest. In reference 18, attention is given to both the heat- and force-field methods.

As shown in figure 5, the creation of a finite rise time signature ($\Delta t_r = 0.03$ sec) required airstream modification extending over 200 ft ahead of and over 400 ft behind the 300-ft-long airplane. An initial airstream channel area of 500 ft^2 was selected for reasons that will be discussed later. It is seen that because a typical airplane configuration with

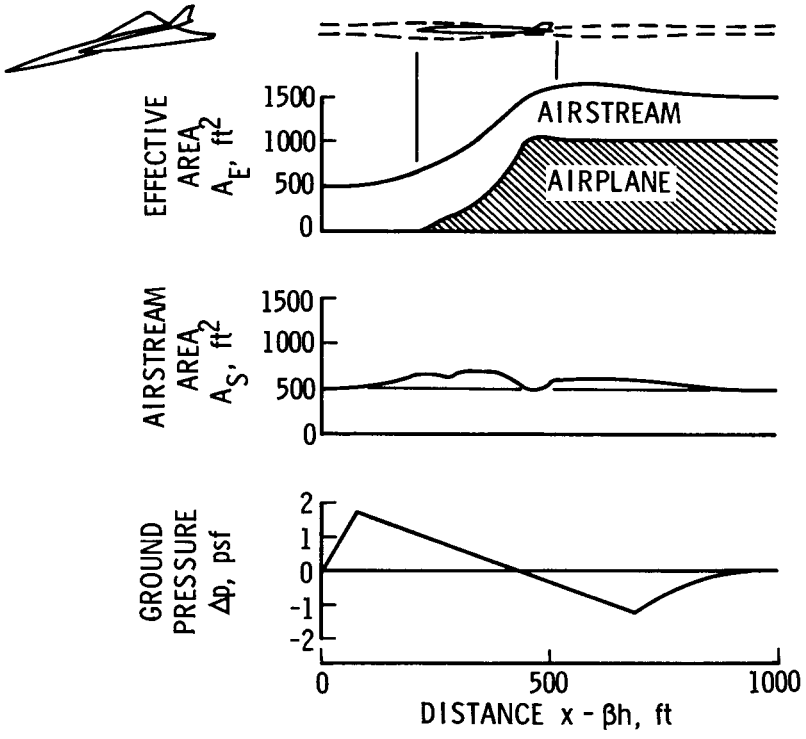

FIGURE 5. – Concept application for an SST, $M = 2.7$ and $h = 60\,000$ ft.

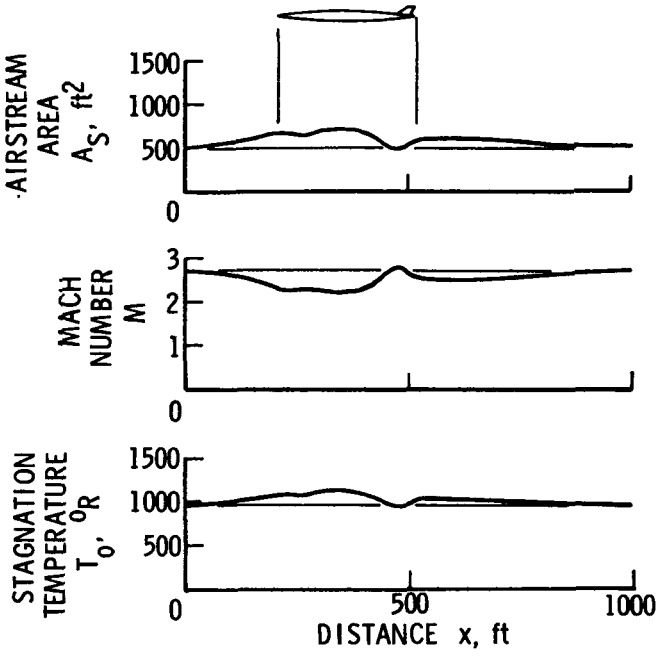

FIGURE 6. – Airstream flow properties.

irregularities in effective area development was chosen, the smooth effective area required for the phantom body can be created only with a modified airstream channel that also displays irregularities.

Local variations in the airstream channel area cause local variations in flow properties, as illustrated in figure 6. Extreme variations in Mach number and temperature could, of course, result in a degradation of aircraft aerodynamic performance and would intensify already severe heating problems. A very large initial channel area would minimize these problems but would make the task of insuring the proper distribution of heat that much more difficult.

The power requirements shown in figure 7 demonstrate the severity of the problems to be encountered in attempts at practical implementation of the phantom-body concept. Irregularities and extreme gradients in the local power distribution indicate that great care would be required in the selection and arrangement of heating devices. An even more difficult problem is posed by the necessity of power removal or refrigeration dictated by the presence of the negative values of local power. As will be explored in somewhat greater detail later, the power removal requirement could be avoided by reshaping of the airplane, but this in itself would be a rather drastic measure. From the power summation plot, it is seen that in the forepart of the airstream, it is necessary to

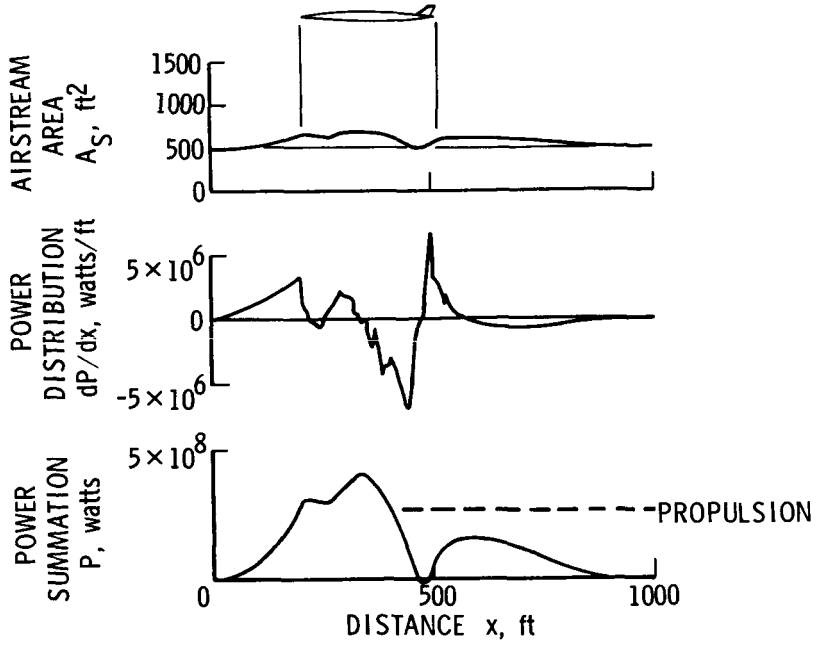

FIGURE 7. – Airstream power requirements.

add power to the airstream amounting to more than the propulsive power output supplied by engines producing an estimated 75 000 lb of thrust for the assumed flight conditions. Even if a reasonably efficient system for recycling heat energy could be devised to result in relatively low net power consumption, the equipment would be sized by the huge maximum power requirement of 400 million W.

It should be recognized that in the unlikely event of the development of efficient means of processing the airstream to drastically reduce cross-sectional area, the ideas of Dr. Resler (ref. 23) would be worthy of further consideration. His approach may be considered as an extreme application of the phantom-body concept in which a constant area body would be created by stream tube reduction only. If this could be accomplished, no disturbance of any kind would be felt outside the phantom-body boundaries.

An important factor in analyzing the phantom-body concept is the selection of the phantom-body capture area A_0. Variations in the flow properties and the maximum power requirements with changes of A_0 are shown infigure 8. As expected, the flow properties are very sensitive for small values of A_0; therefore, to avoid large changes in the flow properties, which in turn alter the airplane performance characteristics, a large initial area is desired. The maximum power is fairly insensitive

to changes in A_0 throughout the range considered; thus, an area of 500 ft^2 appears to be a reasonable selection. Larger values that do not significantly reduce flow property variations would create even greater problems of heat-field distribution.

The phantom-body length is the primary factor upon which the sonic boom signature characteristics as well as the power requirements depend. Figure 9 shows how the rise time Δt_r increases and the maximum ground overpressure Δp_{max} decreases as the phantom-body area development is stretched out. In selecting a reasonable body length, no values less than 900 ft were considered because lengths less than that produce no finite rise time. Allowance has been made for the somewhat reduced lengths that result from an exacting treatment of real atmosphere effects afforded by use of the Hayes computer program. As expected, the power requirements increase with increasing length. The desired rise time is the primary factor for defining the necessary phantom-body length and the maximum power requirements. A rise time of 30 msec and a corresponding body length of 975 ft were chosen for the example to provide a near minimum power requirement while offering significant noise benefits (ref. 24) and a margin against possible adverse effects of atmospheric distortion.

The results of the studies reported in reference 18 indicate that power requirements become less for lower Mach numbers, but not to the extent

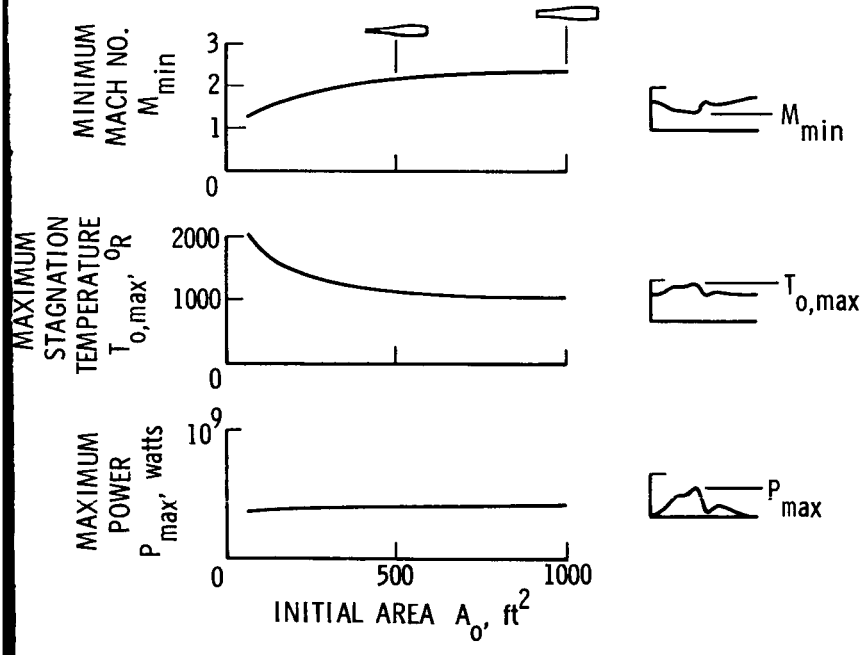

FIGURE 8. – Phantom-body initial area considerations.

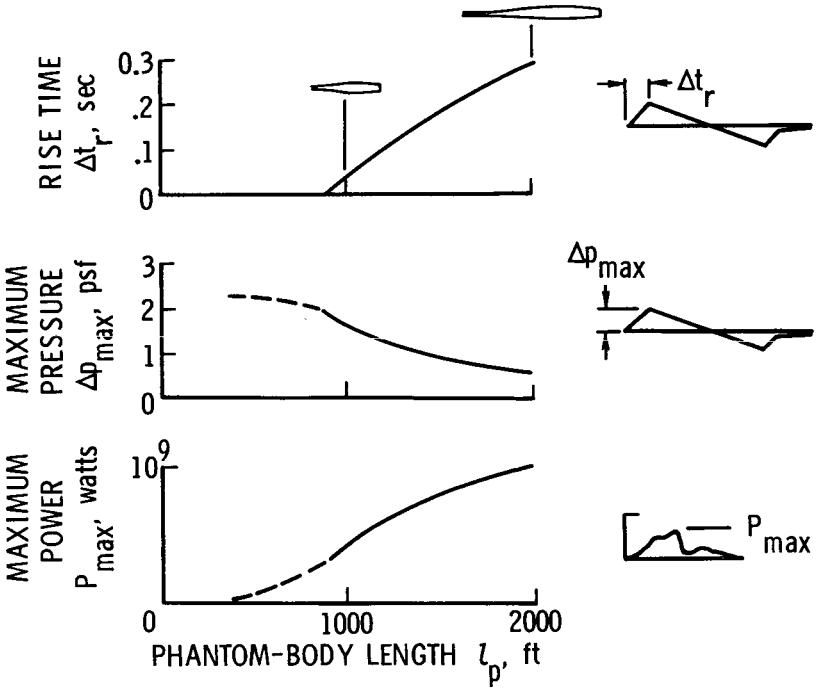

FIGURE 9. – Phantom-body length considerations.

that the scheme appears to be more practical. For high Mach numbers which are more attractive from an economic standpoint, the power requirements are greater. For a given Mach number, power requirements are not significantly less at altitudes above or below those normally selected for cruise economy.

THERMAL FIN CONCEPT

This discussion would not be complete without mention of recent studies of ingenious methods for concept implementation conducted by Dr. S. B. Batdorf (ref. 25) and Dr. R. J. Swigart (ref. 26) of Aerospace Corp. Of several methods considered, the thermal fin appears to be the more practical and will be described with the aid of figure 10. The unique features of the thermal fin are the direct burning of fuel to produce the heat field and the introduction of the heat below the airplane itself. Dr. Batdorf points out that with direct burning of jet fuel, the power requirements for bow shock elimination are not necessarily prohibitive and that locating the heat field below the airplane would be attractive from the standpoint of airplane thermal environment and safety.

The conceptual single thermal fin arrangement illustrated at the center of the figure is compared with the previously discussed unimplemented axial distribution of heating and cooling shown at the left. Because the thermal fin as presently conceived provides for heat addition only, the airplane must be reshaped and the phantom-body forepart must be extended an additional 27 ft to provide an airstream that requires no heat removal. For the single thermal fin, no significant increase in power over the basic axial concept is required. With direct burning during the supersonic portion of a coast-to-coast flight, it is estimated that power requirements can be met with about a 20-percent increase in onboard fuel. It should be noted that the single thermal fin would be effective in eliminating only the bow shock, and the tail shock would remain unless some means is provided for properly shaping the rear portion of the phantom body. The possibility of employing a second thermal fin for tail shock suppression was considered and is illustrated in the right of the figure. Estimates indicate that total shock elimination employing thermal fins would require about 60 percent additional onboard fuel, with no account being taken of the weight and performance penalties of the system.

It is obvious that the thermal fin that must extend about 80 ft below the airplane would pose severe if not insurmountable problems related to aircraft performance, stability, structure, and weight. However, because of the urgent need for a solution to the sonic boom problem and the fact that the power requirements, though large, are not necessarily prohibitive, a wind-tunnel test program is planned to provide a preliminary indication of the feasibility of the concept.

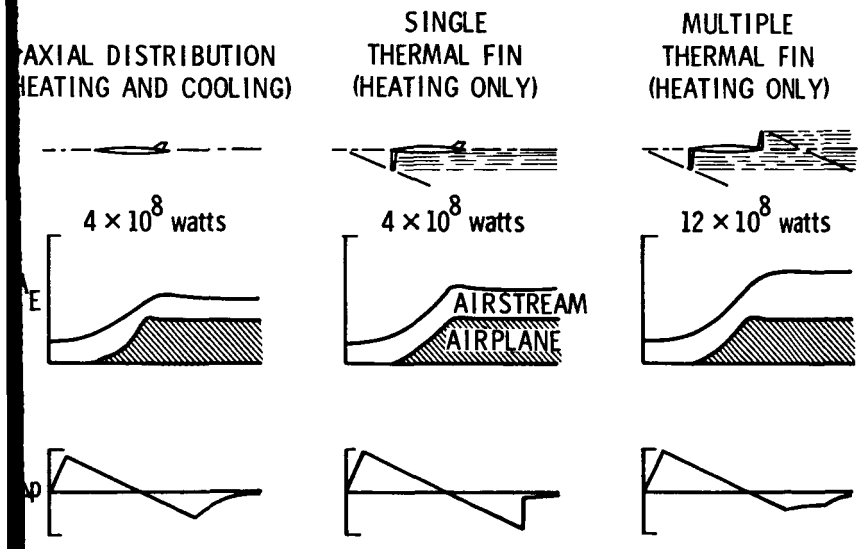

FIGURE 10. – Thermal fin implementation.

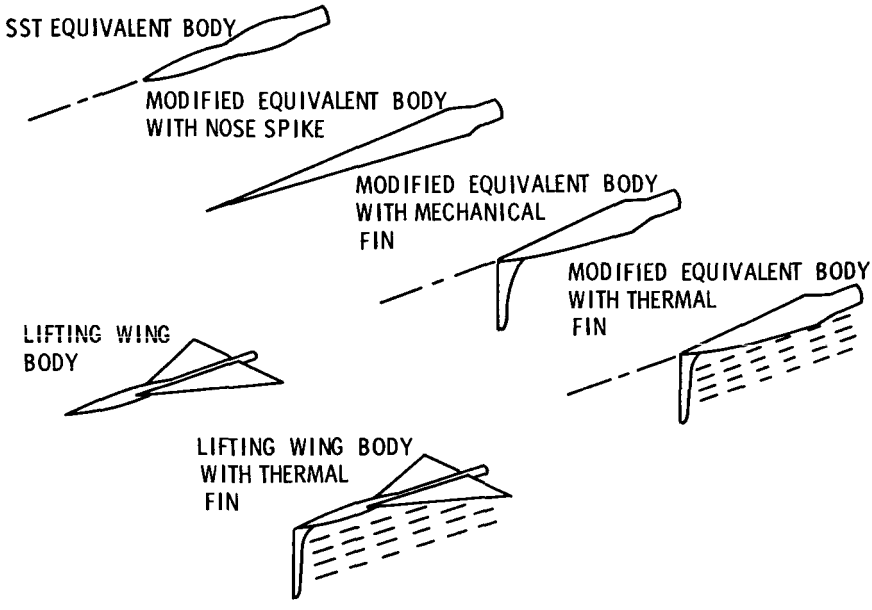

FIGURE 11.—Models for wind-tunnel test program.

The wind-tunnel test program will involve the testing of the six models illustrated in figure 11. The tests themselves will be conducted in the NASA Langley 4- by 4-ft supersonic wind tunnel, and the remainder of the program (design and construction of models, data reduction, analysis, and reporting) will be conducted by Aerospace Corp. under contract to NASA.

The test program can be divided into two parts. The first part consists of testing the four nonlifting bodies shown diagonally across the top of the figure. The basic model in this series is a 10-in.-long body of revolution having an effective area development representative of an SST at cruise speeds. The second model is essentially an isentropic spike modification of the basic model with an additional length of 6 in., which was designed to produce a finite rise time signature. Each of the remaining two models in this series have a vertical fin extending about 4 in. below the model nose. The fin models are designed to have identical effective area developments and thus produce identical signatures as the isentropic spike model. The solid mechanical fin is about 40 percent larger than the thermal fin; this difference will be simulated by means of hot-gas ejection. The second part of the test program involves the testing of two lifting wing-body models shown at the lower left of the figure. The basic wing body model will produce a lift-induced sonic boom pressure signature with shocks. The wing-body model with the thermal fin is designed to suppress the shocks.

For each of the models, signatures will be measured at $M = 2.0$ for a minimum of two model-probe separation distances. Both thermal fin model designs incorporate the instrumentation necessary for measuring the properties of the gas being emitted.

CONCLUDING REMARKS

A study has been made of the potential benefits to be gained, the problems encountered, and the power required in the application of heat-field concepts to the sonic boom minimization problem. Subject to the simplifying assumptions made in this study, the results indicate that finite rise time signatures are theoretically obtainable but require the creation of a carefully controlled heat field extending far ahead of and behind the airplane.

To assess problems to be encountered in practical application of the concept, an illustrative example for a representative SST configuration at cruise speed was treated. In order to create the proper airstream alterations, it was found that power amounting to more than the airplane's propulsion power output must be supplied to the forepart of the airstream and by some unknown means extracted from the aft part. Significant variations in the airstream flow properties and large gradients in the heat distribution were also encountered.

The thermal fin implementation of the phantom-body concept proposed by Aerospace Corp. can be extended to prevent formation of both the bow and tail shock without the necessity of heat extraction; however, airplane reshaping as well as thermal fin heat addition is required. For a typical SST at cruise speed, it is estimated that, with direct burning, the bow and tail shock elimination could be accomplished with 60 percent additional fuel.

Because of the tremendous impact that a solution to the sonic boom problem would have and in spite of the many problems associated with the airstream alteration approach for sonic boom minimization, it is believed that further study is warranted, and a wind-tunnel test program is planned. No other approach has yet been suggested for elimination of sonic boom shocks that is not directly contradictory to the accumulated knowledge of sonic boom phenomena or that does not require airplane lengths far beyond any present contemplations.

REFERENCES

1. JONES, L. B.: Lower Bounds for Sonic Bangs. J. Roy. Aeronaut. Soc., vol. 65, no. 606, June 1969, pp. 433–436.
2. CARLSON, H. W.: The Lower Bound of Attainable Sonic-Boom Overpressure and Design Methods of Approaching This Limit. NASA TN D–1494, 1962.
3. RYHMING, I. L.; AND YOLER, Y. A.: Supersonic Boom of Wing-Body Configurations. J. Aerosp. Sci., vol. 28, no. 4, 1961, pp. 313–320.

4. McLEAN, F. EDWARD: Some Nonasymptotic Effects on the Sonic Boom of Large Airplanes. NASA TN D-2877, 1965.
5. McLEAN, F. EDWARD; AND SHROUT, BARRETT L.: Design Methods for Minimization of Sonic-Boom Pressure-Field Disturbances. Proc. Acoust. Soc. Amer. (St. Louis, Mo.), Nov. 3, 1965, pp. S19–S25.
6. GEORGE, A. R.: Reduction of Sonic Boom by Azimuthal Redistribution of Overpressure. AIAA Paper no. 68-159, 1968.
7. FERRI, ANTONIO; AND ISMAIL, AHMED: Report on Sonic Boom Studies. Second Conference on Sonic Boom Research, NASA SP-180, 1968, pp. 73–88.
8. SEEBASS, R.: Minimum Sonic Boom Shock Strengths and Overpressures. Nature London, vol. 221, Feb. 15, 1969, pp. 651–653.
9. McLEAN, F. EDWARD; CARLSON, HARRY W.; AND HUNTON, LYNN W.: Sonic Boom Characteristics of Proposed Supersonic and Hypersonic Airplanes. NASA TN D-3587, 1966.
10. McLEAN, F. EDWARD: Configuration Design for Specified Pressure Characteristics. Second Conference on Sonic Boom Research, NASA SP-180, 1968, pp. 37–45.
11. HAYES, W. D.: Linearized Supersonic Flow. Rept. AL-222, North American Aviation, Inc., 1947.
12. WHITHAM, G. B.: The Flow Pattern of a Supersonic Projectile. Commun. Pure Appl. Math., vol. 5, 1952, pp. 301–348.
13. MIDDLETON, W. D.; AND CARLSON, H. W.: A Numerical Method for Calculating Near-Field Sonic-Boom Pressure Signatures. NASA TN D-3082, 1965.
14. CARLSON, H. W.: Correlation of Sonic-Boom Theory With Wind Tunnel and Flight Measurements. NASA TR R-213, 1964.
15. CARLSON, HARRY W.: Experimental and Analytic Research on Sonic Boom Generation at NASA. Sonic Boom Research, NASA SP-147, 1967, pp. 9–23.
16. HUNTON, LYNN W.: Current Research in Sonic Boom. Second Conference on Sonic Boom Research, NASA SP-180, 1968, pp. 57–66.
17. GARRICK, I. E.; AND MAGLIERI, D. J.: A Summary of Results on Sonic Boom Pressure-Signature Variations Associated With Atmospheric Conditions. NASA TN D-4588, 1968.
18. MILLER, DAVID S.; AND CARLSON, HARRY W.: A Study of the Application of Heat or Force Fields to the Sonic Boom Minimization Problem. NASA TN D-5582, 1969.
19. SIEGELMAN, DAVID: Sonic Boom Minimization Schemes. J. Aircr., vol. 7, no. 3, 1970, pp. 280–281.
20. HAYES, WALLACE D.; HAEFELI, RUDOLPH C.; AND KULSRUD, H. E.: Sonic Boom Propagation in a Stratified Atmosphere, With Computer Program. NASA CR-1299, 1969.
21. BROWN, CLINTON E.: Internal and External Aerodynamics of Ducted Bodies at Supersonic Speeds. NACA WR L-728, 1946. (Formerly NACA CB L6B26.)
22. SHAPIRO, ASCHER H.: The Dynamics and Thermodynamics of Compressible Fluid Flow. Vol. I. The Ronald Press Co., C. 1953, pp. 226–232.
23. RESLER, E. L., JR.: Lifting Aerodynamic Configurations With No Sonic Boom. AFOSR-UTIAS Symposium on Aerodynamic Noise, Univ. of Toronto Press, 1969.
24. KRYTER, K. D.: Laboratory Tests of Physiological Reactions to Sonic Booms. J. Acoust. Soc. Amer., vol. 39, no. 5, pt. 2, May 1966, pp. 565–572.
25. BATDORF, S. B.: On a New Approach to the Alleviation of the Sonic Boom. Rept. ATR-70 (S9990)-1, Aerospace Corp., Sept. 1969.
26. SWIGART, R.; AND LUBARD, S.: Sonic Boom Studies. Rept. ATR-69 (S8125)-1, Aerospace Corp., May 1969.

Measured and Calculated Sonic Boom Signatures From Six Nonaxisymmetric Wind-Tunnel Models

H. L. RUNYAN, H. R. HENDERSON, O. A. MORRIS, AND D. J. MAGLIERI
NASA Langley Research Center

A considerable amount of effort has been directed toward the establishment of adequate sonic boom prediction techniques, and various studies have related to the problem of minimization of the sonic boom through airplane design. Extensive wind-tunnel test programs, beginning about 10 yr ago, have investigated a variety of models including basic research shapes, airplane components, and complete airplanes (refs. 1 and 2). In addition, investigations in wind tunnels have provided data for evaluation of certain minimum boom and minimum drag shapes and for evaulation of a number of nonconventional airplane concepts as well.

The above studies have shown that linearized theory (with appropriate corrections) provides reasonably accurate predictions of the sonic boom pressure signatures. The fundamental concept in the theoretical treatment is the replacement of a three-dimensional aircraft or other complex shape by an equivalent body of revolution. It is presumed that the three-dimensional flow field can be adequately represented locally (within a specified sector of the flow field and at reasonably large distances) by the axially symmetric flow field of a properly defined body of revolution. Definition of the required body of revolution, which requires a consideration of both volume and lift effects, is provided by application of area-rule principles outlined by Hayes (ref. 3). The subsequent calculation of the flow field, including shocks, follows the method introduced by Whitham (ref. 4). The results of wind-tunnel programs indicate the applicability of the simplified approach at distances as close as one or two body lengths for shapes that approach axial symmetry and at somewhat larger ratios for more complex configurations.

The work of reference 2 extended these wind-tunnel studies and established the adequacy of the above theoretical methods for a body shape that departed drastically from a body of revolution. This particular configuration consisted of a rectangular planform with a flat upper surface alined to the airstream and with the lower surface made up of several steps. On the basis of two-dimensional flow concepts, lifting pressures

420-093 O - 71 - 23

are created on the lower surface for a small distance behind the shock wave. The flow is then turned to the original free-stream direction, thereby creating a shock-canceling expansion. These events are assumed to be repeated for each step on the model. The tests indicated that the lower surface two-dimensional flow pattern changes rapidly and becomes predominantly three-dimensional in character within about five body lengths for this nonaxisymmetrical configuration.

As part of the studies performed in reference 2, six other nonaxisymmetric model configurations were constructed and tested in the wind tunnel to study the growth of the pressure field as a function of distance from the models. The models consisted of two 40° delta and four rectangular planforms including one model with side plates that force two-dimensional flow to exist over the model.

The purpose of this paper is to present the results of these wind-tunnel tests in the form of measured sonic boom pressure signatures at three distances below the models at $M=2.7$. A comparison is made of these experimental data with theoretical signatures based on two- and three-dimensional theories.

MODELS

The six models used in the present studies are shown in figure 1. All models were constructed of stainless steel and had a width of from 2 to 4 in. (5.1 to 10.2 cm), a thickness of about 0.25 in. (0.635 cm), and an overall length of 12 in. (30.5 cm), 4 in. (10.2 cm) of which was considered to be effective body length. The remaining 8 in. (20.3 cm) of the model was of constant cross-sectional area to provide for the sting support. One sting support adapter was used for all models. The characteristics of the models are as follows:

Model 1 is a 40°-V-delta planform, with a wedge-shape profile, and a lower lifting surface angle of 5°.

Model 2 is a "stepped" version of the basic 40°-V-delta wedge (model 1). Three "steps" were incorporated and consisted of a 5° lifting surface angle followed by a straight portion (0°) that created compression and expansion shocks.

Model 3 is rectangular in planform and wedge shape in profile with a lower lifting surface angle of 5°.

Model 4 is a "stepped" version of the basic rectangular 5° wedge (model 3). Three "steps" were incorporated and consisted of a 5° lifting surface angle followed by a straight portion (0°). Model 4 was similar to the model tested in reference 2, except that the constant area sting support portion of the present model was lengthened from 4 in. to 8 in. (10.2 cm to 20.3 cm) in an attempt to minimize the effect of the sting adaptor support on the model flow field.

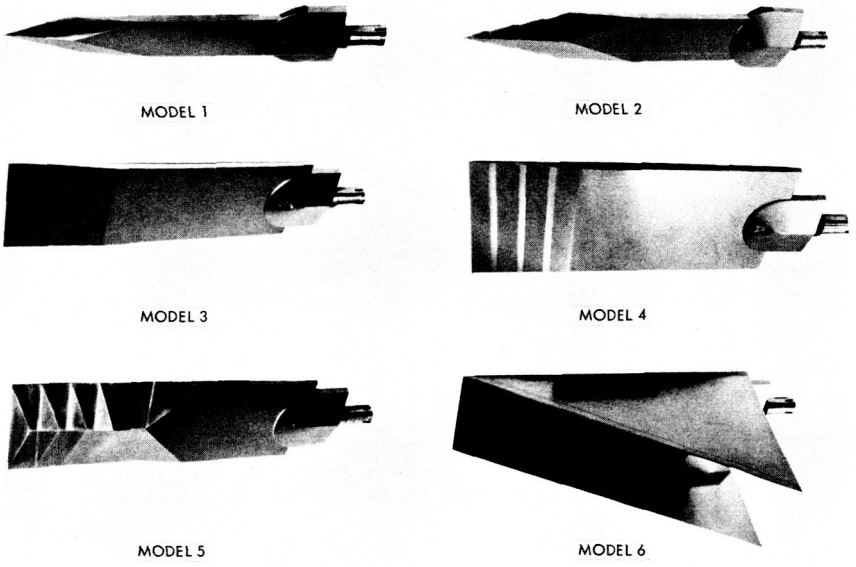

FIGURE 1.—Photographs of minimum sonic boom models with sting adaptor.

Model 5 is a rectangular "stepped V-shape" wedge having the same number of steps (three) and lifting surface angles (5° to 0°) as model 4.

Model 6 is a rectangular "stepped" wedge with side plates. In effect, it is model 4 with side plates attached. The side plate angle was established at 27° so that at $M = 2.7$, for which the Mach angle is about 22°, the bow shock and the flow behind the bow shock are contained between the side plates (within about a 6-in. (15.3-cm) radial distance from the model). In addition, these side plates were made thin and alined to the stream flow to reduce any distortion of the basic flow field from the "stepped model."

APPARATUS AND TEST

The six sonic boom models were tested in the Langley Unitary Plan Wind Tunnel (ref. 5) at a Mach number of 2.7, a stagnation pressure of 944 lb/ft^2 (45.2×10^3 N/m^2), and a Reynolds number per foot of 1×10^6 or 3.28×10^6/m. The test section is 4 by 7 ft long (1.2 by 2.13 m).

The model mount and the method of measurement of the pressure field below the model are the same as those given in references 6 and 7 and are shown schematically in the sketch of figure 2. The model and adaptor were mounted to a translating support from the tunnel sidewall. A reference probe and static measuring probe were mounted on a support attached to the main sting. Pressure measurements of the shock field of the model were obtained by translating the model and its associated shock field across the measuring probes. These flow-field surveys were

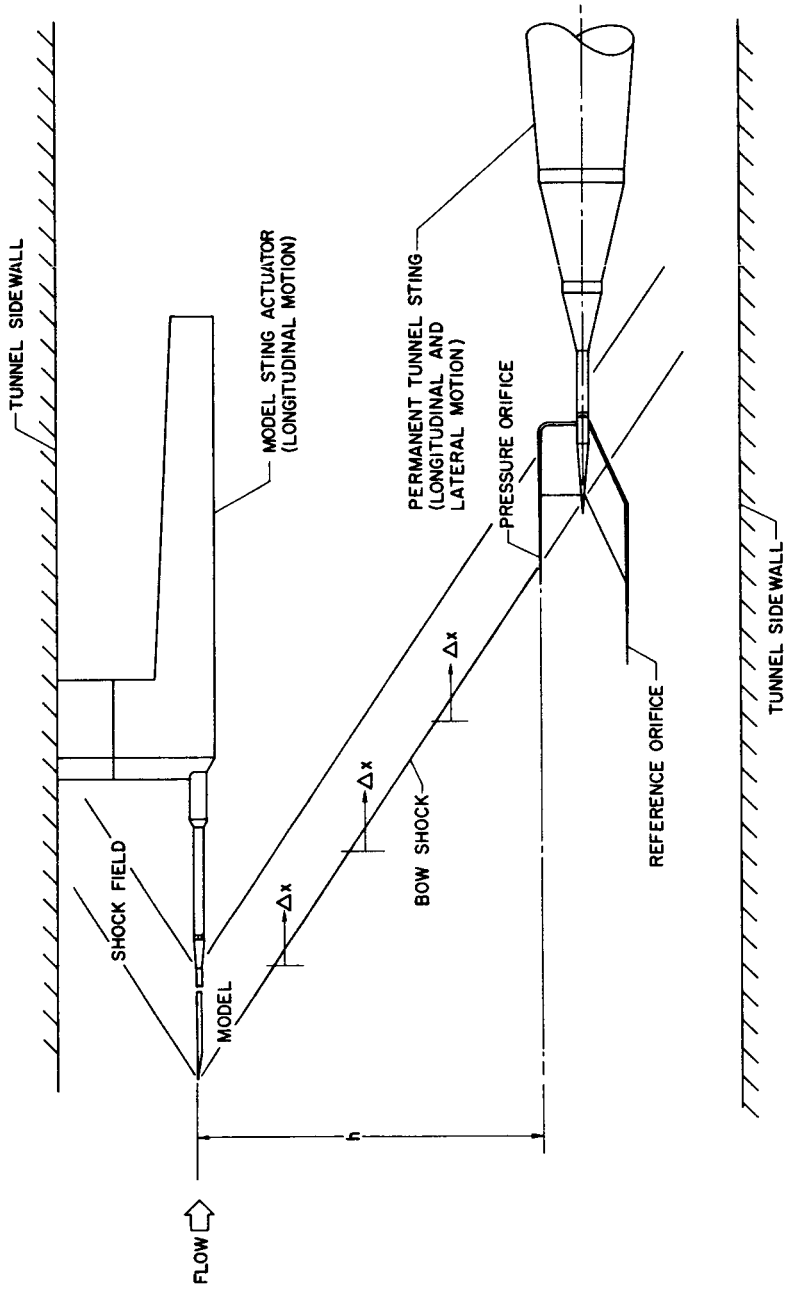

FIGURE 2. – Model arrangement in supersonic tunnel showing probe measurement technique.

obtained at distances h below the model of 5, 10, and 20 in. (12.7, 25.4, and 50.8 cm). The 5-in. (12.7-cm) distance represented the minimum distance, and 20 in. (50.8 cm) was the maximum distance from the model that could be obtained. The distances of 5, 10, and 20 in. (12.7, 25.4, and 50.8 cm) correspond to 1.25, 2.5, and 5 body lengths below the model, respectively. In addition to obtaining pressure measurements below the models, some schlieren photographs were taken of certain models for flow visualization.

RESULTS AND DISCUSSION

Figure 3 shows the schlieren photographs of model 4 for $M = 2.7$. The light lines indicate shock waves, and the dark areas indicate the expansion zones. The vertical dark lines are caused by the schlieren window supports, which are external to the flow. At the top of the figure, the plan view is shown, and it is significant that no discernible shock waves are seen to originate from the corners of the leading edge. The profile view of the lower photograph shows rather clearly the shocks and expansion patterns associated with each of the steps on the model. The remaining shocks emanate from the model adaptor and sting support.

The measured pressure distributions obtained below each of the six models at three distances for $M = 2.7$ flow are presented in figure 4. The data are presented in the form of overpressure Δp divided by free stream ambient pressure p, plotted against horizontal distance Δx parallel to the model longitudinal axis. Also shown in the figure are the calculated pressure signatures for each of the models at the three measuring distances using numerical methods (refs. 6 and 8) based on the equivalent body principle and accounting for lift and volume contributions. Because the influence of the model sting adaptor, located between the model and the sting support, was found to be rather strong (fig. 3), the above calculations were made with and without the inclusion of the adaptor. Calculations based on two-dimensional flow (ref. 9) for models 4 and 6 are also included.

The experimental pressure distributions of figure 4 at the close-in position ($h = 5$ in. or 12.7 cm) for each of the six models suggest the development of an N-wave. The data for the step models (2, 4, 5, and 6) show perturbations on the flow. As the distance from the model is increased to $h = 20$ in. (50.8 cm), an approach to an N-wave is noted to occur in all cases except for model 5 (fig. 4(*e*)), for which shock perturbations still persist.

Agreement of the experimental pressure signatures with those of the three-dimensional theory is good for models 1, 2, and 5 and is also fairly good for models 3 and 4. This reasonably good agreement with theory was not expected close to models of the type tested. In general, the agreement improves as the distance from the models increases, and

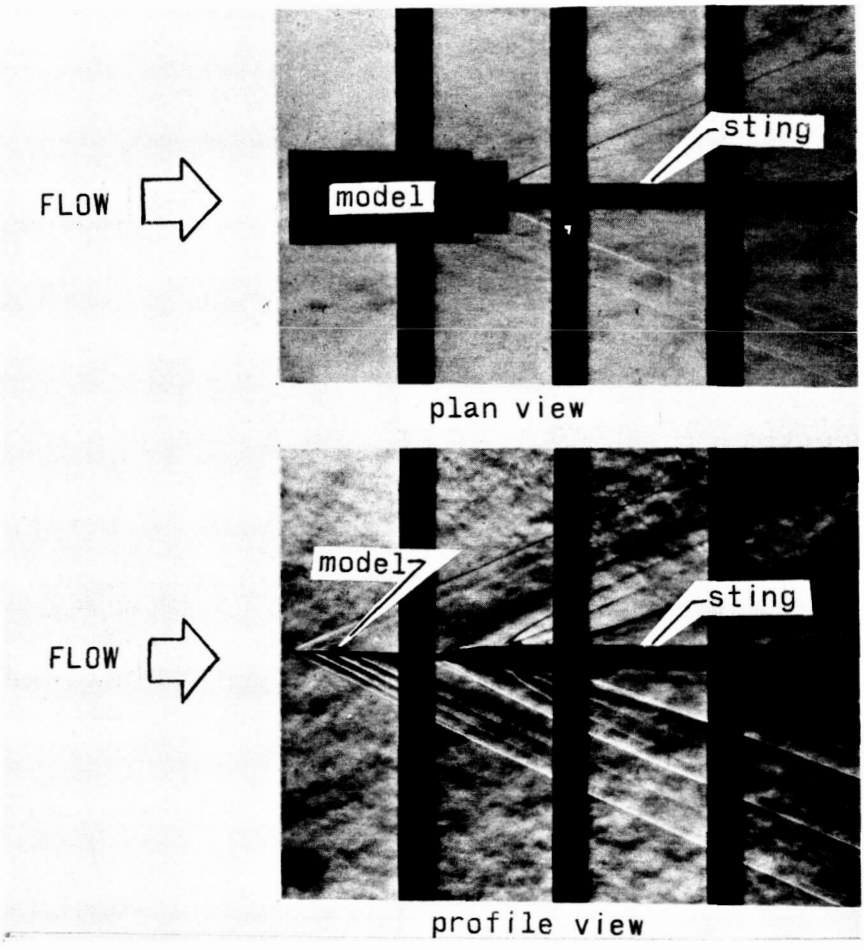

FIGURE 3.—Schlieren photographs of model 4 at a Mach number of 2.7.

although some rounding and smoothing of the experimental results are evident (due to the effects of model vibrations and probe boundary layer as discussed in ref. 6), fairly good agreement is obtained even to the number of shocks and their locations. The strong influence of the sting adaptor is apparent in the measured data and is also predicted by theory.

The results obtained using model 6, which had side plates to induce two-dimensional flow, are given in figure 4(*f*). It can be seen that the three-dimensional theory greatly underestimates the overpressure magnitude particularly at $h = 5$ in. or 12.7 cm. In this case, a much better estimate of the signature is obtained by using two-dimensional theory (ref. 9). This improved result would be expected particularly at the close-in distance ($h = 5$ in. or 12.7 cm) because the pressure survey was made

between the model side plates where two-dimensional flow was forced to exist.

The above results indicate a rapid transition from two- to three-dimensional flow for the six models tested. In some cases, the three-dimensional flow field is established within one body length; in all cases tested, in at least five body lengths.

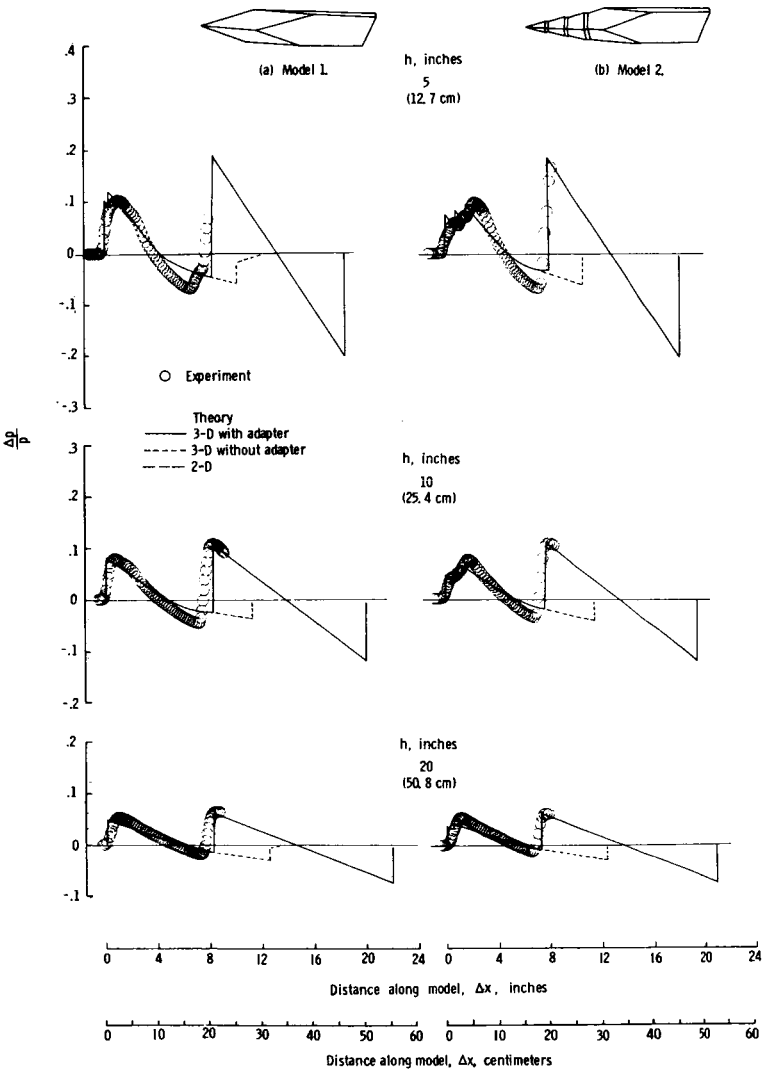

FIGURE 4.—Theoretical and experimental pressure distributions obtained at a Mach number of 2.7 and at distances of 5, 10, and 20 in. below the models. (*a*) Model 1. (*b*) Model 2.

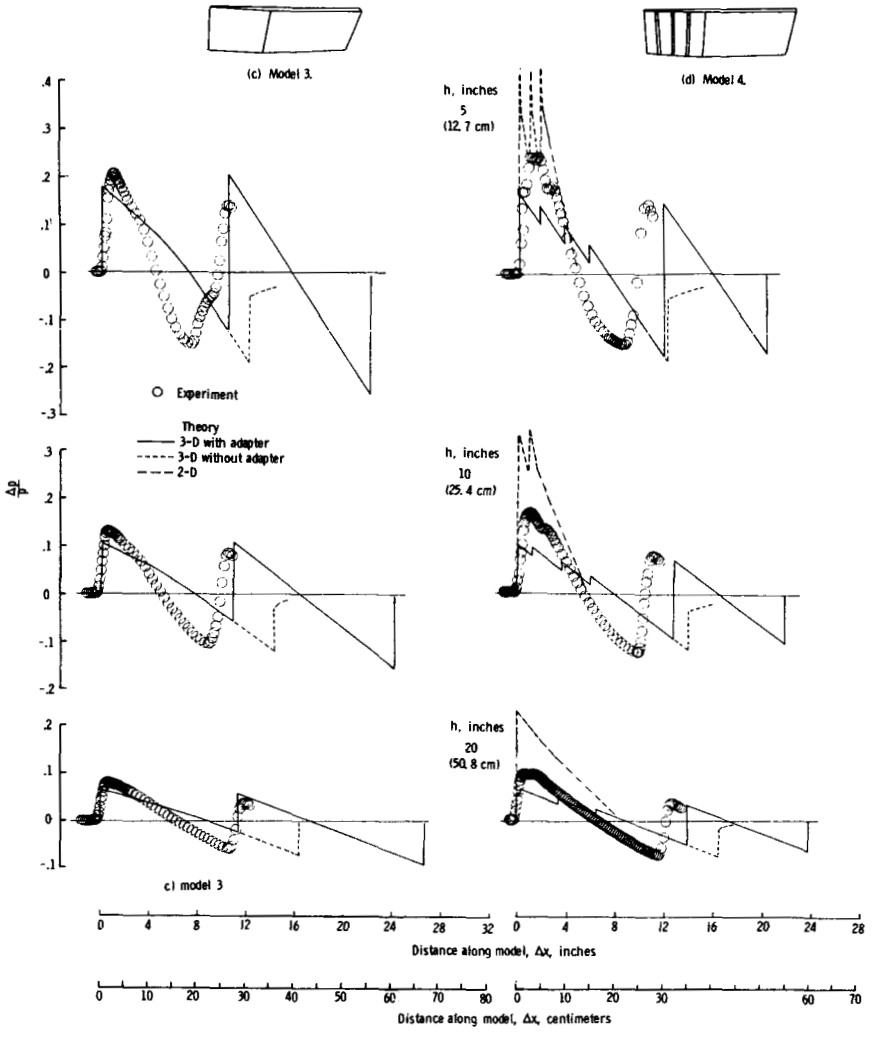

FIGURE 4 (continued).—(*c*) Model 3. (*d*) Model 4.

CONCLUDING REMARKS

A wind-tunnel experiment using six models has been conducted at $M=2.7$ to study the growth of the pressure field as a function of distance from the model. The models consisted of two delta and four rectangular planforms including one model with side plates. The measured sonic boom pressure signatures are compared with calculated signatures based on the two- and three-dimensional flow theories.

The results indicated a rapid transition from two-dimensional flow characteristics, known to exist near the model lower surfaces, to the

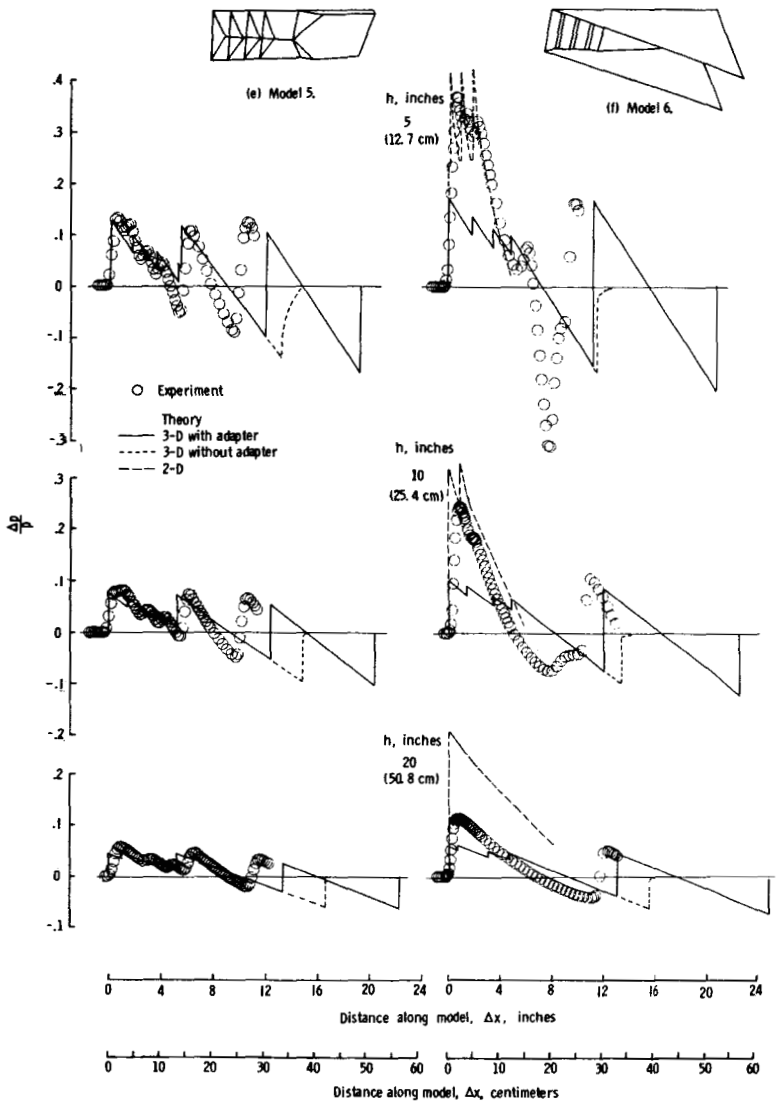

FIGURE 4 (concluded). — (*e*) Model 5. (*f*) Model 6.

three-dimensional characteristics measured in the tests. In general, good agreement was obtained between the measured and calculated pressure field using conventional techniques for three-dimensional flow analysis, especially at the larger distances. The notable exception occurred for a model for which two-dimensional flow was forced to exist within the confines of side plates. For that model, good agreement was obtained using two-dimensional flow theory, particularly at the smallest distance

of about one body length. At the farthest measurement point, five body lengths, better agreement was obtained using three-dimensional flow theory.

These results suggest that three-dimensional flow about the models is established very rapidly, in some cases, in about one body length. The results also serve as a reminder that minimum or zero sonic boom concepts based on two-dimensional reasoning can be very misleading and that the rapid development of three-dimensional flow is significant and must be taken into account.

REFERENCES

1. SEEBASS, A. R., ED.: Sonic Boom Research. NASA SP–147, 1967.
2. RUNYAN, HARRY L.; AND HENDERSON, HERBERT R.: Evaluation of Certain Minimum Boom Concepts. Second Conference on Sonic Boom Research. NASA SP–180, 1968, pp. 47–55.
3. HAYES, WALLACE D.: Long-Range Acoustic-Propagation in the Atmosphere. IDA Research Paper P–50, July 31, 1963.
4. WHITHAM, G. B.: The Flow Pattern of a Supersonic Projective. Commun. Pure Appl. Math., vol. 5, 1952, pp. 301–348.
5. SCHAEFER, WILLIAM T., JR.: Characteristics of Major Active Wind Tunnels at the Langley Research Center. NASA TM X–1130, 1965.
6. CARLSON, HARRY W.: Correlation of Sonic Boom Theory With Wind Tunnel and Flight Measurements. NASA TR R–213, 1964.
7. CARLSON, H. W.; AND MORRIS, O. A.: Wind Tunnel Sonic-Boom Testing Techniques. J. Aircr., vol. 4, no. 3, May–June 1967, pp. 245–249.
8. MIDDLETON, WILBUR D.; AND CARLSON, HARRY W.: A Numerical Method for Calculating Near-Field Sonic Boom Pressure Signatures. NASA TN D–3082, 1965.
9. FERRI, ANTONIO: Elements of Aerodynamics of Supersonic Flows. The Macmillan Co., 1949.

Variability of Sonic Boom Signatures With Emphasis on the Extremities of the Ground Exposure Patterns

HARVEY H. HUBBARD, DOMENIC J. MAGLIERI, AND VERA HUCKEL
NASA Langley Research Center

There is considerable concern about the nature of sonic boom exposure patterns near their lateral extremities, particularly with regard to atmosphere-induced variability. Lack of systematic measurements has left voids in our knowledge of the signature wave shapes and the overpressure gradients as a function of distance near the points of cutoff due to atmospheric refraction. The purpose of this paper is to review the pertinent published measurement results and to describe the unpublished results of some recent atmospheric refraction experiments that were performed to define better the physical phenomena involved.

PROBABILITY DISTRIBUTIONS

The overpressure measurements made to date indicate substantial variability, as illustrated in figure 1 (refs. 1 and 2). The probability of equaling or exceeding a given ratio of the measured overpressure value to the maximum predicted value (which occurs on the flight track) for particular flight conditions of the F–104 and XB–70 is shown. The data have been plotted on a log normal scale, and straight lines have been faired through the data points as an aid in interpretation. The data associated with lines having lesser slopes have the greater variability. On the left-hand side of figure 1, it can be seen that the data measured at a point 10 miles from the ground track for the F–104 at an altitude of about 9.15 km (30 000 ft) have markedly more variability than the data for the measuring point on the ground track. The net result is that at the lowest probability values, the lateral station data exceed in amplitude those measured on the track.

Data obtained for the XB–70 aircraft at an altitude of 18.3 km (60 000 ft) are plotted in a similar manner in the right-hand side of figure 1. Again, it is obvious that the measured data taken at a station 13 miles from the ground track have more variability than those on the ground track. The maximum values of overpressure measured off the track approach the maximum values of the on-track data. The variability for the high-Mach-

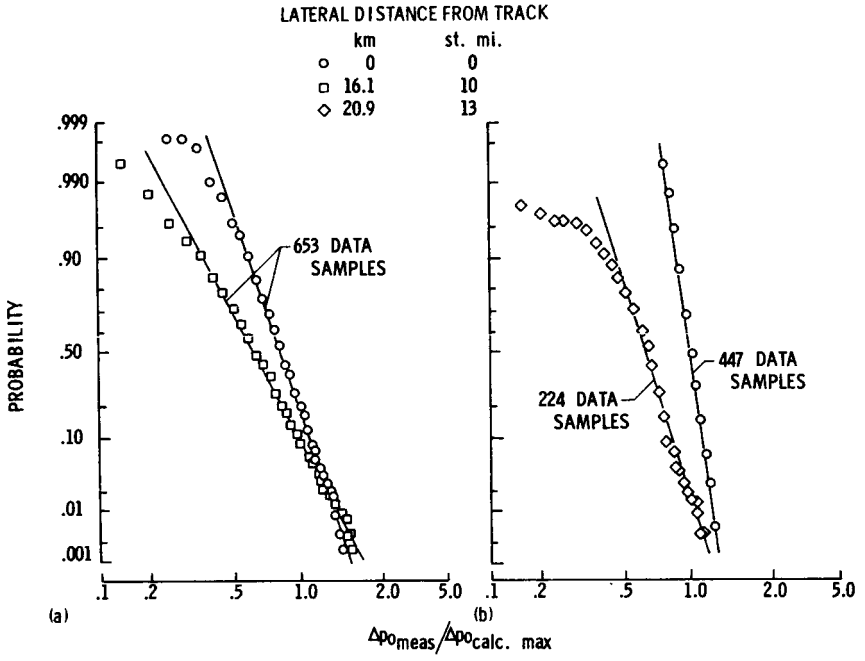

FIGURE 1.—Probability of equaling or exceeding a given value of the ratio of measured overpressure to maximum calculated overpressure. (*a*) F–104. (*b*) XB–70.

number, high-altitude data of the XB–70 is noted to be similar to that for the lower Mach number, lower altitude data of the F–104 airplane.

LATERAL SPREAD PATTERNS

The trends noted in the data of figure 1 have caused some concern about the situation that may exist at greater distances from the ground track for which there was, until recently, little experimental data. There has thus been some speculation about the validity of predictions of overpressures at the greater lateral distances where atmospheric focusing may be a very significant factor (refs. 3 to 6).

Sample measured ground overpressure data for the XB–70 aircraft over a range of lateral distances for two different flight conditions are given in figure 2 (refs. 1 and 7). Each of the data points shown represents averages of measured values for several microphones as indicated in the figure. The vertical lines through the data points indicate the extreme values of the data. It can be seen that the maximum measured values occurred on the track, values nearly as high occurred at points several miles off the track, and relatively small values were measured near the edge of the pattern.

Also shown are curves calculated by means of the method of Middleton and Carlson (ref. 8). The cutoff distances due to refraction are shown as dotted vertical lines according to the method of Randall (ref. 9). It can be seen that the average ground overpressure values from a large number of measurements are in general agreement with the calculated values on or near the ground track. As lateral distance from the ground track increases, however, the measured average values are generally lower than the calculated values. This trend appears to be valid out to the extreme distance of the measurements. The calculations indicate a sudden drop in pressure amplitude in the region of cutoff; however, this may result in part from the fact that only the Mach cutting plane corresponding to locations directly below the aircraft was used in the calculations.

The trend toward a gradual reduction of overpressure value as a function of lateral distance is also illustrated by the data of figures 3, 4, and 5, which apply to the SR–71 (ref. 10), B–58, and F–104 aircraft, respectively, but for operating conditions different from those of the XB–70. The B–58 and F–104 measurements were obtained within 15 minutes after the XB–70 data and used the same microphone arrays. For several aircraft and for a range of flight conditions, it is seen that pressure disturbances were measured at distances beyond the theoretically predicted cutoff points.

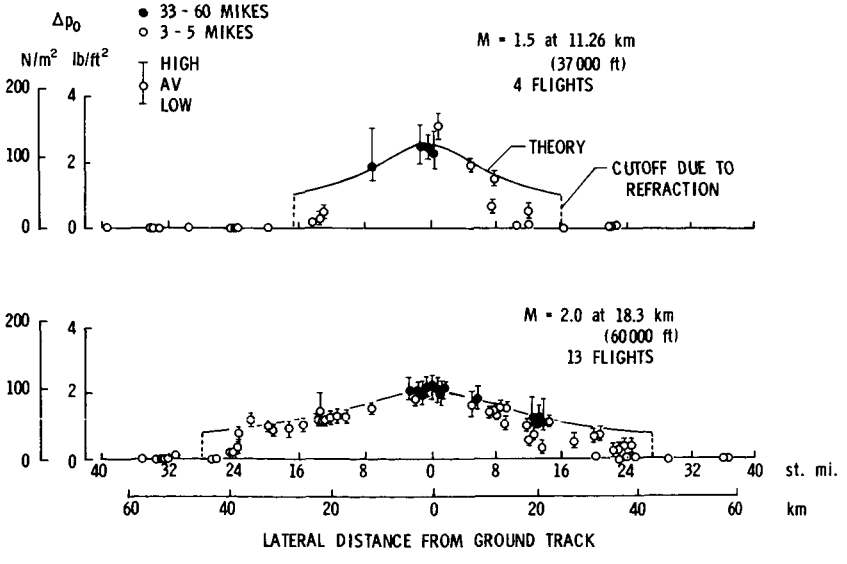

FIGURE 2.—Sonic boom overpressures for the XB–70 aircraft as a function of lateral distance for two different flight conditions.

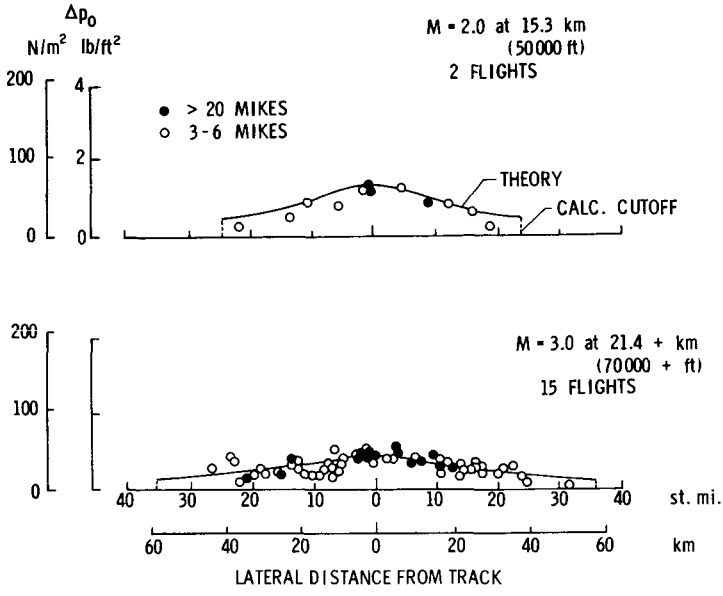

FIGURE 3.—Sonic boom overpressures for the SR–71 aircraft as a function of lateral distance for two different flight conditions.

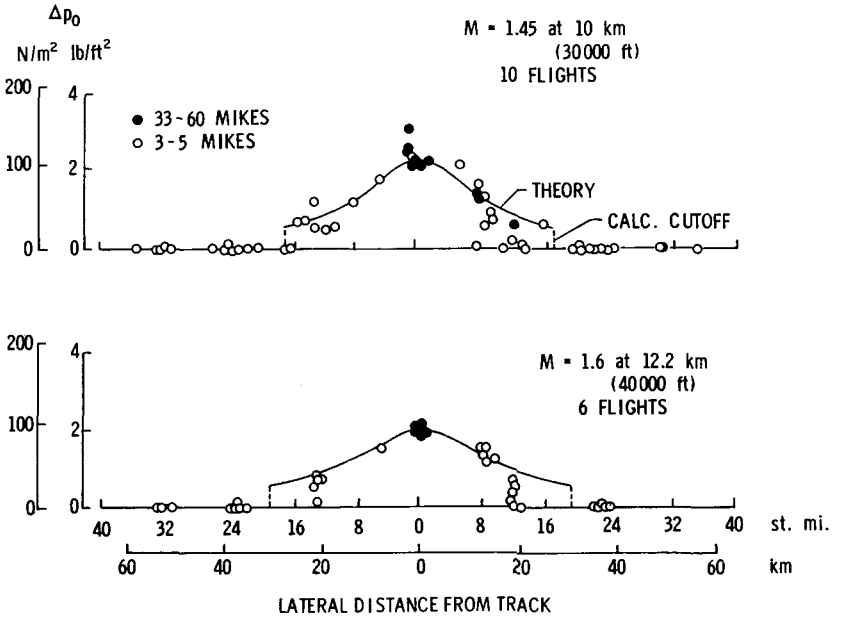

FIGURE 4.—Sonic boom overpressures for the B–58 aircraft as a function of lateral distance for two different flight conditions.

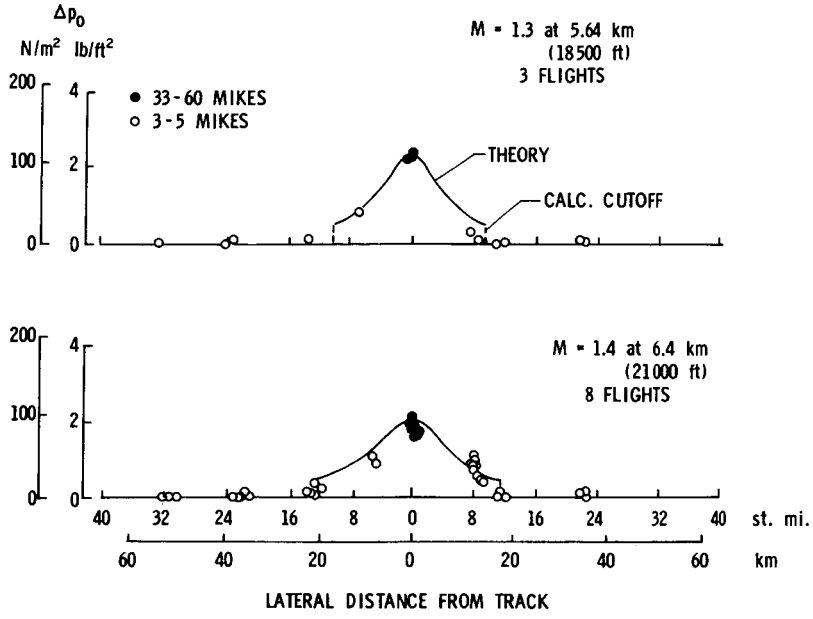

FIGURE 5. — Sonic boom overpressures for the F–104 aircraft as a function of lateral distance for two different flight conditions.

MEASUREMENTS NEAR LATERAL CUTOFF

To study the situation in this cutoff region, a series of definitive studies was conducted with an F–104 airplane for the conditions of figure 6 (refs. 1 and 11). Data at the top of the figure were obtained for flights at various lateral distances out to a distance of approximately twice the predicted cutoff distance with microphones spaced about 1 mile apart. The data of figure 6 also suggest a general decrease in the pressure amplitudes in the region of cutoff. The fact that valid measurements were made at large distances beyond the cutoff point is believed to be due to the fact that propagation phenomena at the near-grazing incidence condition are very sensitive to local changes in the atmosphere. A significant finding of these tests was that the wave shape changed in a systematic manner as a function of distance as indicated by the sketches on the figure. For instance, the waves associated with distances shorter than the predicted cutoff distance were N-shape, whereas those at the extreme edge of the pattern did not have any particular identifying features. Furthermore, the rise times of the waves generally increased with lateral distance.

Data for similar flight conditions, but for somewhat less stable atmospheric conditions, are plotted in the bottom part of figure 6. The trends of these latter data are similar to those at the top of the figure except that more scattering is evident in the measurements. In addition, a pres-

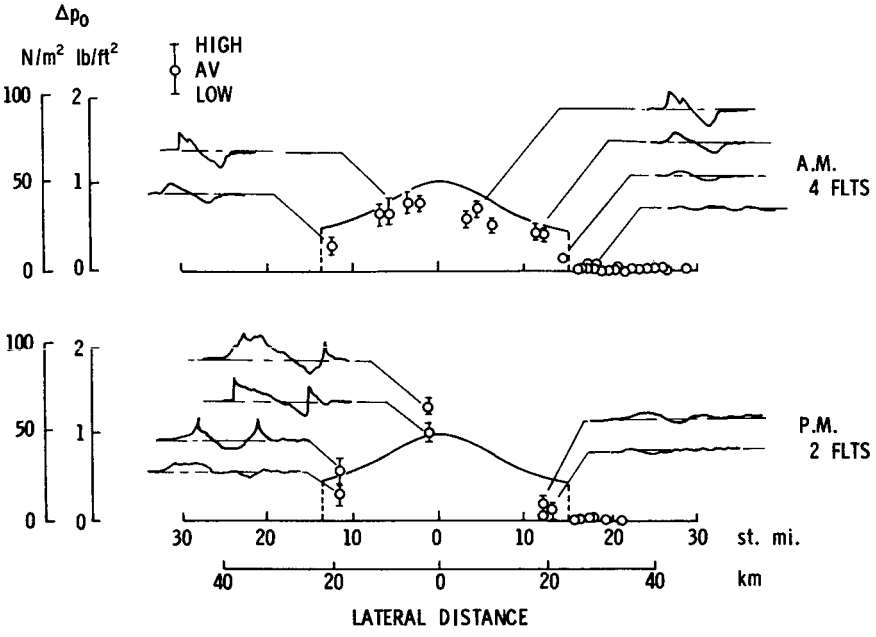

FIGURE 6.—Measured lateral spread patterns for an F–104 aircraft at $M = 1.5$ at an altitude of 11.35 km (37 200 ft) mean sea level (msl) and for two different times of day.

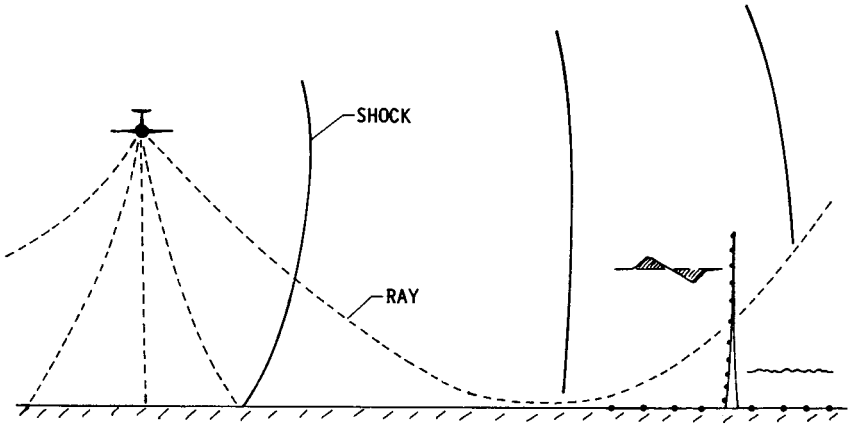

FIGURE 7.—Sketch of experimental test setup used to define sonic boom overpressures near the lateral cutoff.

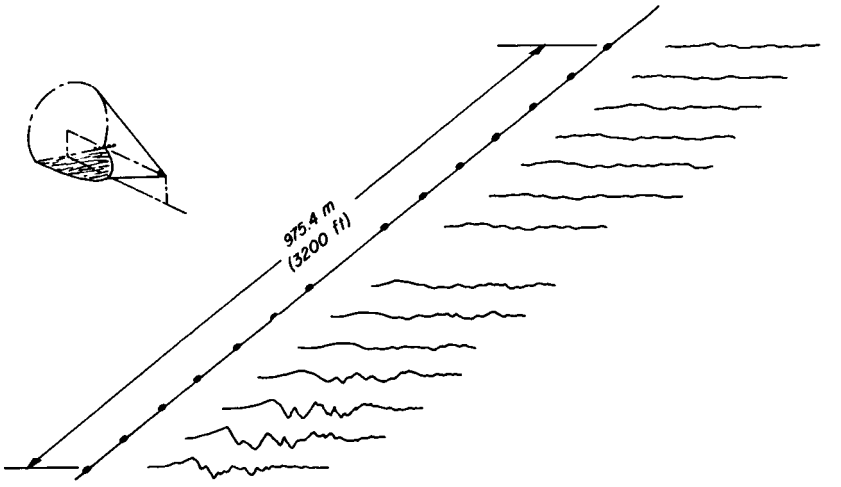

FIGURE 8.—Measured sonic boom signatures near lateral cutoff for an F–104 aircraft at $M = 1.3$ at 10.3 km (33 700 ft) msl.

sure signature is observed (second sketch from the bottom) which, according to some theoretical and experimental studies, suggests the presence of a caustic. A caustic condition is associated with ray convergence, with the result that stream tube area is substantially reduced. The associated U-shape pressure signatures represent focus conditions that may result in overpressure enhancement. (See ref. 12.)

To evaluate the overpressure patterns in the region of the caustic, overflight measurements were made with the use of special microphone arrays, the measuring stations being about 61 m (200 ft) apart. The setup is indicated schematically in figure 7. A 975.4-m (3200-ft) horizontal and a 45.8-m (1500-ft) vertical microphone array are indicated. The flights were accomplished so that the edge of the exposure pattern was placed in or near this array. The data of figure 8 are representative of those obtained from the 975.4-m (3200-ft) array during one aircraft flight. A definite trend in signature shape variation is evident.

By means of repeated flights offset in lateral distance from the tower, a large number of overpressure signatures were measured at the edge of the pattern. Some of these signatures and the associated peak overpressure data are presented in figure 9. It can be seen that there is a general decrease in overpressure as distance increases. There is also a corresponding trend from N-shape signatures, which are observed as booms, to signatures with no definite shape characteristics, which are observed as acoustic rumbles. Although U-shape waves are observed in the data records, there is no indication of large overpressure enhance-

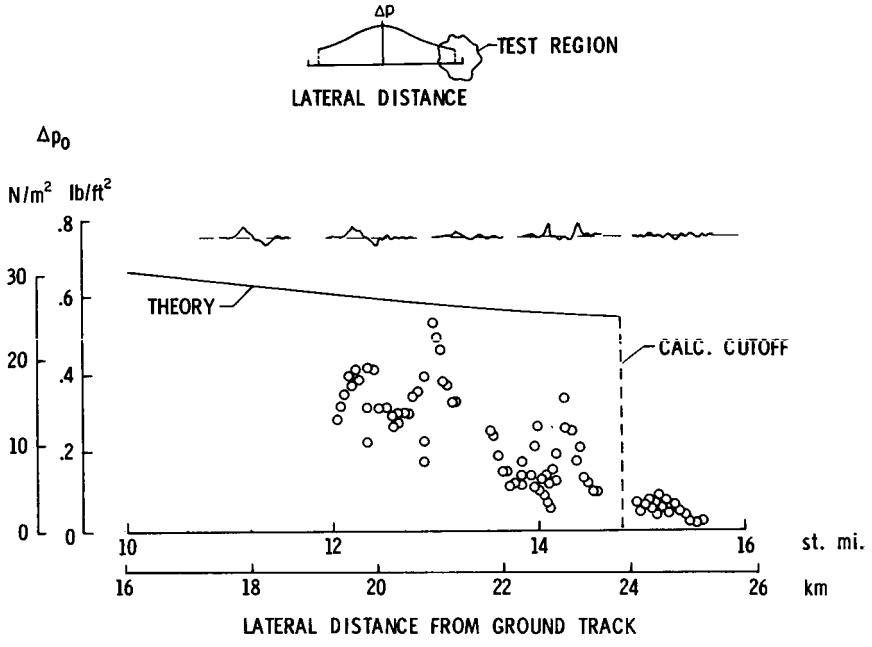

FIGURE 9.—Variation of sonic boom overpressure near lateral cutoff for an F–104 aircraft at $M = 1.3$ and at an altitude of 10.3 km (33 700 ft) msl.

ment as is observed at grazing incidence on the ground track (see paper by Maglieri, Hilton, Huckel, Henderson, and McLeod).[1]

CONCLUDING REMARKS

The following concluding remarks may be drawn from the data presented. The overpressures generally decrease and rise times are generally greater as lateral distance from the ground track increases. Overpressure variability is greater at locations 10 to 13 miles laterally from the ground track than for locations on the track for a range of Mach numbers and altitudes. The maximum measured overpressure values at 10 to 13 miles off the track for a range of altitudes and Mach numbers are of the same order of magnitude as those measured on the track. Although signatures representative of caustic conditions were observed near the edge of the pattern, there was no evidence of substantial overpressure enhancement.

[1] See p. 243.

REFERENCES

1. SEEBASS, A. R., ED.: Sonic Boom Research, NASA SP–147, 1967.
2. HILTON, DAVID A.; HUCKEL, VERA; STEINER, ROY; AND MAGLIERI, DOMENIC J.: Sonic-Boom Exposures During FAA Community-Response Studies Over a 6-Month Period in the Oklahoma City Area. NASA TN D–2539, 1964.
3. KANE, EDWARD J.; AND PALMER, THOMAS Y.: Meteorological Aspects of the Sonic Boom. SRDS Rept. RD 64–160, Federal Aviation Agency, ASTIA no. AD 610 463, 1964.
4. DRESSLER, ROBERT F.: Sonic-Boom Waves in Strong Winds. FFA Rept. 97, Aeronaut. Res. Inst. Swed., 1964.
5. DRESSLER, ROBERT; AND FREDHOLM, NILS: Statistical Magnifications of Sonic Booms by the Atmosphere. FFA Rept. 104, Aeronaut. Res. Inst. Swed., 1966.
6. LUNDBERG, BO K.; DRESSLER, ROBERT F.; AND LAGMAN, SVEN: Atmospheric Magnification of Sonic Booms in the Oklahoma Tests. FFA Rept. 112, Aeronaut. Res. Inst. Swed., June 1967.
7. GARRICK, I. E.; AND MAGLIERI, D. J.: A Summary of Results on Sonic-Boom Pressure-Signature Variations Associated With Atmospheric Conditions. NASA TN D–4588, 1968.
8. MIDDLETON, WILBUR D.; AND CARLSON, HARRY W.: A Numerical Method for Calculating Near-Field Sonic Boom Pressure Signatures. NASA TN D–3082, 1965.
9. RANDALL, D. G.: Methods for Estimating Distributions and Intensities of Sonic Bangs. R. & M. No. 3113, British A.R.C., 1959.
10. MAGLIERI, DOMENIC J.: Sonic Boom Ground Pressure Measurements for Flights at Altitudes in Excess of 70 000 Feet and at Mach Numbers up to 3.0. Second Conference on Sonic Boom Research, NASA SP–180, 1968, pp. 19–27.
11. MAGLIERI, DOMENIC J.; HILTON, DAVID A.; AND MCLEOD, NORMAN J.: Experiments on the Effects of Atmospheric Refraction and Airplane Accelerations on Sonic-Boom Ground-Pressure Patterns. NASA TN D–3520, 1966.
12. FRIEDMAN, MANFRED P.; AND CHOU, DAVID C.: Behavior of the Sonic Boom Shock Wave Near the Sonic Cutoff Altitude. NASA CR–358, 1965.

Finite Difference Calculation of the Behavior of a Discontinuous Signal Near a Caustic

R. SEEBASS, E. M. MURMAN, AND J. A. KRUPP
Boeing Scientific Research Laboratories

It is important, as was mentioned elsewhere in these proceedings, that we be able to predict sonic boom overpressure signatures in the vicinity of a caustic. And, in particular, we need to be able to calculate it when the caustic surface intersects, or when it is near, the ground. While the analytical formulation of this problem is a simple one (ref. 1), the solution by formal mathematical techniques presents great difficulties.[1] Consequently, there is great impetus for developing numerical techniques that can provide such predictions. Here we report on the extension to the caustic problem of a technique developed by Murman and Cole for transonic flows (ref. 2). This technique and some recent calculations are described in reference 3. The goal of such calculations, of course, is to be able to theoretically predict pressure signatures such as those measured during the French flight tests "Operation Jericho Virage" (ref. 4) and those reported at this conference.[2] Figure 1 is a sketch of the ground pressures recorded under a Mirage IV aircraft in a 2.1g bank at the conditions specified (ref. 4). We see the "incident" N-wave clearly, the "reflected" wave with vestiges of the linear logarithmic infinity (e.g., trace i), and the "transmitted" and rapidly attenuated wave (trace a). We also see how the reflected and incident signal (trace c) have combined to produce the large overpressure shown in trace b. Although the pressure signatures that occur in practice are essentially N-waves, it is clear that if the behavior of a single shock wave near a caustic can be calculated, then the behavior of more complex signatures there can also be calculated.

FORMULATION AND DIFFERENCE EQUATIONS

We wish to solve the nonlinear equation

$$(\eta + \psi_\xi)\psi_{\xi\xi} - \psi_{\eta\eta} = 0 \tag{1}$$

[1] See p. 87.
[2] See p. 243

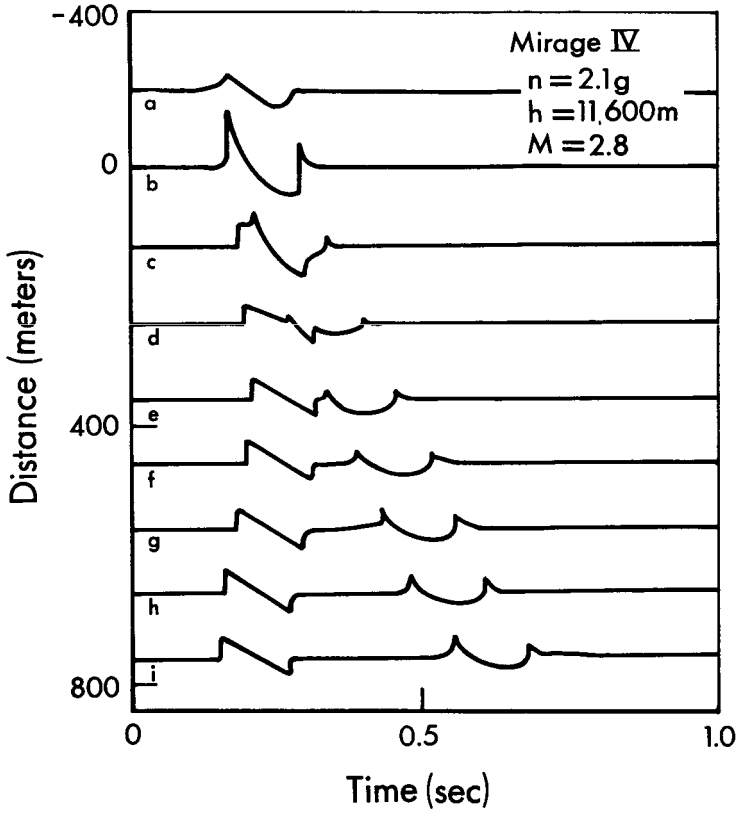

FIGURE 1.—Ground pressure measurements near a caustic for a 2.1g bank for the conditions indicated. (From ref. 4.)

with certain prescribed boundary conditions. The prescription of the boundary conditions for Tricomi's equation

$$\eta\psi_{\xi\xi} - \psi_{\eta\eta} = 0 \tag{2}$$

that insures the existence of a unique solution is well known (ref. 5). On physical grounds it is clear that an analogous prescription applies for equation (1). To calculate the solution to equation (1) by finite differences, it is necessary that we prescribe boundary conditions on a finite domain. We take the solution to equation (2) for a prescribed incoming signal at infinity as representing the asymptotic behavior of equation (1). In particular, we presume that the signal strength at $-\xi = \frac{2}{3}\eta^{3/2} = O(1)$ is small and characterized by a quantity μ, and that the linear solution is a valid approximation to the full solution on the boundary of a domain D,

consisting of the two characteristic arcs $\xi \pm 1 = \pm \frac{2}{3}\eta^{3/2}$ for $\eta > 0$, and the lines $|\xi| = 1$ and $\eta = -(3/2)^{2/3}$ for $\eta < 0$.

We pose, then, the following boundary-value problem: Solve equation (1) inside the domain D, depicted in figure 2, with boundary data determined by the solution to equation (2) in D. On that part of the characteristic arc $\xi + 1 = \frac{2}{3}\eta^{3/2}$ for which $\eta + \psi_\xi > 0$, we provide boundary data appropriate to a hyperbolic equation, namely ψ and ψ_ξ. On that part of the characteristic arc $\xi - 1 = -\frac{2}{3}\eta^{3/2}$ for which $\eta + \psi_\xi > 0$, no boundary data are provided because the solution is determined uniquely without them. On the remainder of the boundary $\eta + \psi_\xi < 0$ and boundary data appropriate to an elliptic equation, the values of ψ, are prescribed.

To effect a numerical solution, we divide the ξ axis of D into $2N$ equal intervals of length Δ and the η axis into the intervals determined by the family of linear characteristics emanating from the mesh points $\xi_i = i\Delta$, $i = 0, \pm 1, \ldots, \pm N$. Thus the mesh points are determined by

$$\xi_i = i\Delta$$
and (3)
$$\eta_j = (\tfrac{3}{2}\Delta\,|j|)^{2/3}\,\operatorname{sgn} j$$

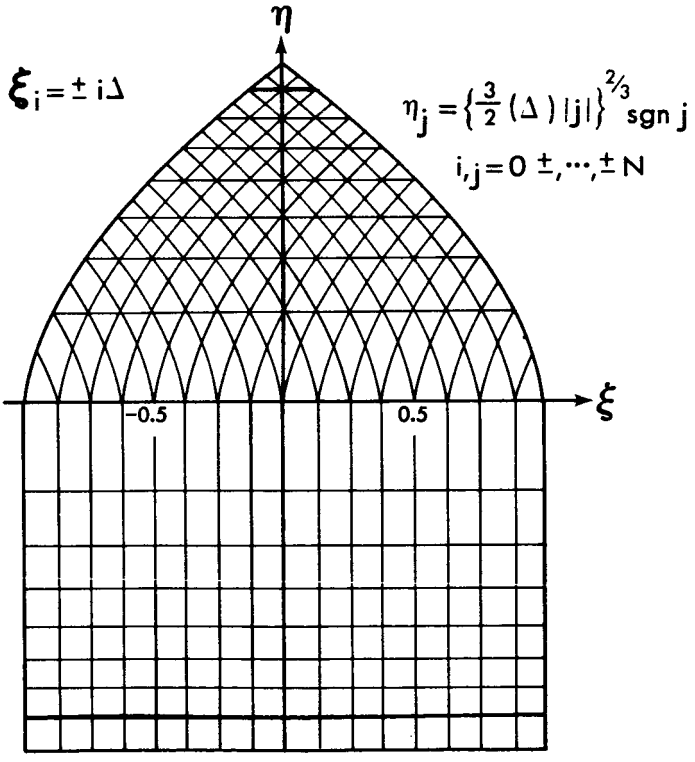

FIGURE 2.—Domain of solution and mesh spacing.

where $i, j=0, 1, \ldots, N$. We then solve the difference equation for equation (1) using a first-order implicit scheme when the equation is hyperbolic and a second-order centered scheme when it is elliptic. Reasons for choosing this scheme are discussed in references 2 and 3. Basically, we choose an implicit scheme in the hyperbolic domain to insure stability regardless of the mesh size in the timelike direction ξ. A first-order or third-order scheme in the hyperbolic domain insures that difference equations correspond to the underlying physical processes, which are dissipative. A second-order scheme in the hyperbolic region would be dispersive; in the related transonic calculations it was found to be inferior to the first-order scheme (ref. 3).

NUMERICAL SOLUTION

We wish to solve a set of difference equations of the form

$$f_j(\psi_{i,k}) = a_j\psi_{i,j+1} + b_j(\psi_{i+1,j}, \psi_{i-1,j}, \psi_{1,j})\psi_{i,j} + c_j\psi_{i,j-1} + d_j(\psi_{i+1,j}, \psi_{i-1,j}, \psi_{i-2,j}) = 0 \qquad (4)$$

with values of ψ or ψ_ξ prescribed on the appropriate boundaries of D. Here a_j and c_j are constants, and b_j and d_j depend on the ψ's indicated. The full equation is given in the appendix. Wherever ψ_ξ is required, we also give ψ at the corresponding η, one ξ mesh point outside the domain. To calculate the values of ψ along $\xi-1=-\frac{2}{3}\eta^{3/2}$, we resort to the method of characteristics. This insures that no signal is reflected from that boundary and that the reflected wave is unaffected by the boundary's presence. The set of nonlinear algebraic equations is solved by iteration for a fixed ξ, starting with an initial "guess" for the solution. With an initial guess for the solution $\psi_{i,j}^{(0)}$, we proceed to calculate $\psi_{-N,j}^{(1)}, \psi_{-N+1,j}^{(1)}, \ldots, \psi_{N,j}^{(1)}$ by solving the $2N-|i|$ equations (4) for $\psi_j^{(1)}$ at each successive ξ mesh point. Newton's method is employed to solve the nonlinear algebraic equations. For each i we compute the tridiagonal matrix

$$A_{jk} = \partial f_j/\partial\psi_{i,k}$$

and solve the matrix equation

$$A_{jk}(X_k^{\nu+1} - X_k^{\nu}) = f_j^{\nu}$$

where X_k is the transpose of the vector $(\psi_{i,-N}, \ldots, \psi_{i,j}, \ldots, \psi_{i,N-|i|})$ for the new estimate $X_k^{\nu+1}$. This procedure is continued until convergence is obtained or a prescribed number of revised estimates have been computed. The values of $\psi_{i,j}$ are then updated for that i, and equa-

tions (4) are solved for $\psi_{i+1,j}$. This procedure continues until new values have been computed for the whole domain. Then the procedure is repeated, starting as before at $i=-N$, until convergence is obtained.

Filippov (ref. 6) has shown that convergence is assured for the linear equation (2) and a similar numerical procedure (Gauss-Seidel). Here, of course, we assume convergence and rely on our numerical results to confirm our assumption. Whether or not convergence is obtained depends upon the accuracy of the initial guess. We compute the solution for small μ using the linear solution for our initial guess. For larger μ, we rely on the solution for a smaller μ, scaled as the linear solution would be with μ, for our initial guess. The linear solution is evaluated from the results given elsewhere in these proceedings; the incoming signal we have chosen is described there as well.[3] Various criteria could be used to determine whether convergence was obtained. Residuals at each mesh point corresponding to the equation (1) and to

$$\psi_{\xi\eta}-\psi_{\eta\xi}=0$$

were computed and were available to judge the accuracy of the results. But program termination was usually made on the intuitive judgment of the operator. If necessary, the program was restarted and further iterations computed.

RESULTS

We have computed results for incoming signal strengths μ ranging from 0.05 to 0.30. The signal is the discontinuity with strength

$$[\psi_\xi] \sim -\mu\eta^{-1/4}$$

and length $\delta=5.0$.[4] The computer output is both digital and graphical. The graphical output consists of computer-drawn characteristics and plots of $\psi_\xi \equiv u$ versus ξ for fixed η. Because of the finite mesh size, the signal originates with a finite thickness; "dissipation" proportional to the ξ mesh size further smears the signal. The computer-drawn characteristics are used to sketch the solution in the ξ, η-plane; computer-drawn ψ_ξ curves are used directly. Figure 3 depicts the characteristics, sonic line, and incoming and reflected wave for $\mu=0.10$, 0.20, 0.25, and 0.30. The finite width of the incoming signal is indicated by the shading. In the reflected wave the locus of the maximum of $\psi_{\xi\xi}$ is indicated by the dashed line. In figure 3(*b*) we see that the disturbance is so large for $\mu=0.20$ that it encroaches upon the boundary supplying the initial data. Consequently,

[3] See p. 87.

[4] See p. 87.

we shifted the location of the incoming signal for values of $\mu \geq 0.20$. The shifted results for $\mu = 0.20$ are shown in figure 3(*c*). There is no important difference between the two results. These shifted results were used in the graphs of $\psi_\xi (= u)$ versus ξ shown in figure 4. All results were computed for $N = 50$ (i.e., 100ξ mesh points).

The computations were carried out on an IBM 360/44. Initially the number N was taken to be 25. Each calculation of the solution with $N = 25$ takes 2 to 4 sec. The solution was iterated several hundred times until convergence was achieved. The number N was then doubled. With $N = 50$, each iterate takes 8 to 16 sec. Again, several hundred iterates are needed to achieve convergence. With $\mu = 0.30$, about 500 iterations were required. For this reason and because of the large distortion of the sonic line, larger values of μ were not attempted. For small values of μ, the first-order error in the difference scheme overrides any nonlinearities. For values of μ of practical interest, this error is not as important; however, to obtain a clear definition of the incident and reflected waves would require a much finer mesh near the wave. Such a calculation could be carried out in reasonable computer time on any of the large machines now available. Our course, however, will be to refine the difference scheme further until more satisfactory results are obtained before proceeding with more extensive numerical calculations.

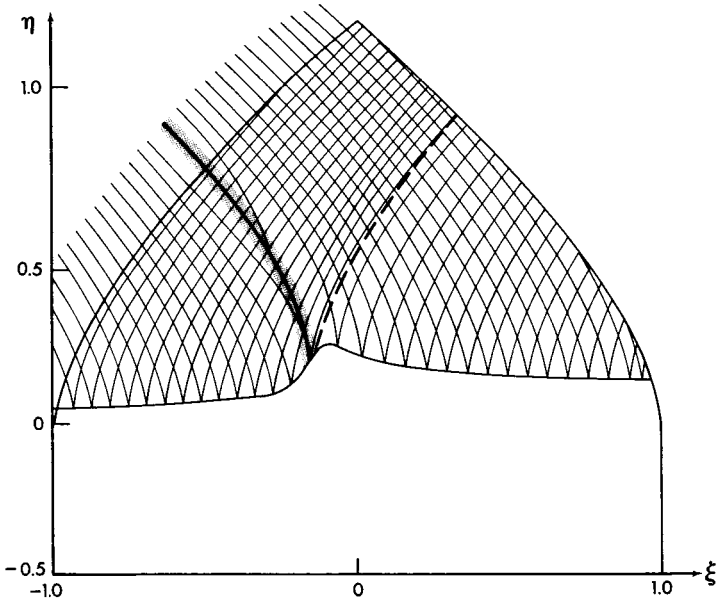

FIGURE 3.—Characteristics, sonic line, and incident and reflected waves for signal of strength μ. (*a*) $\mu = 0.10$.

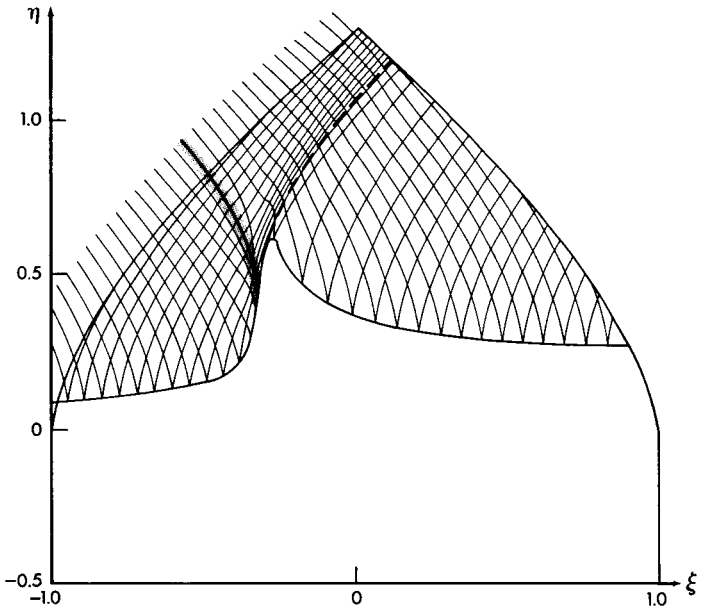

FIGURE 3 (continued). — (*b*) $\mu = 0.20$.

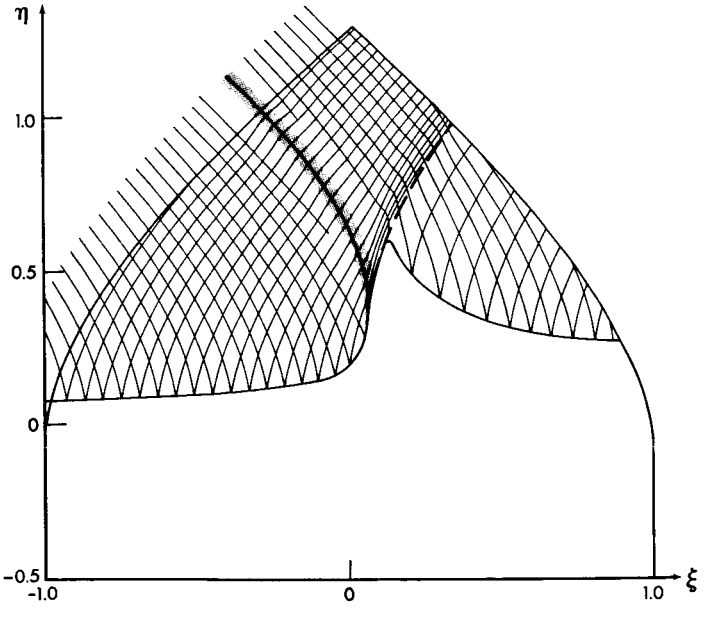

FIGURE 3 (continued). — (*c*) $\mu = 0.20$.

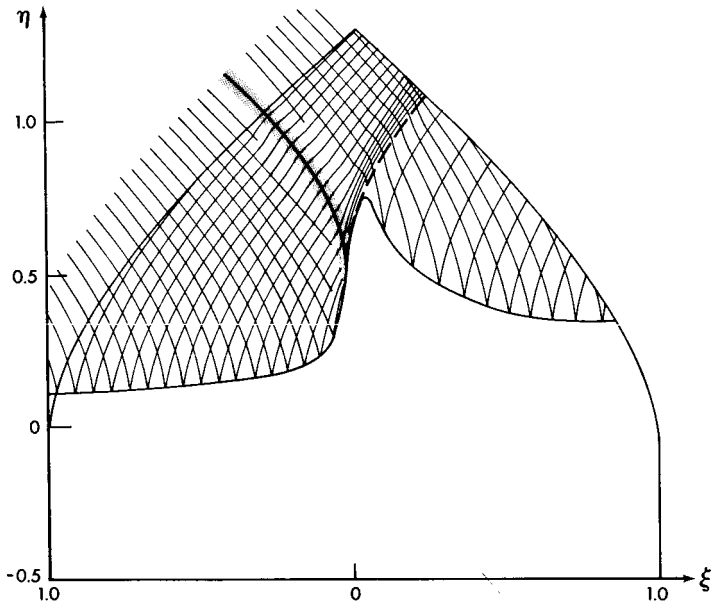

FIGURE 3 (continued). – (*d*) $\mu = 0.25$.

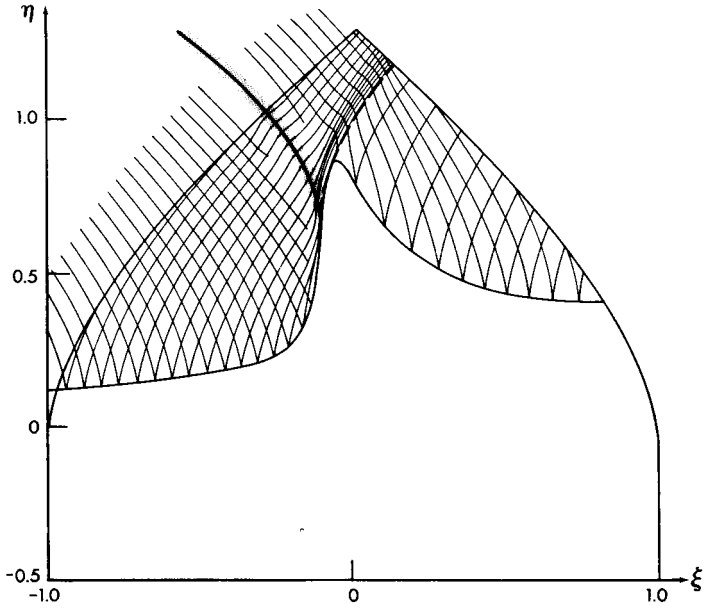

FIGURE 3 (concluded). – (*e*) $\mu = 0.30$.

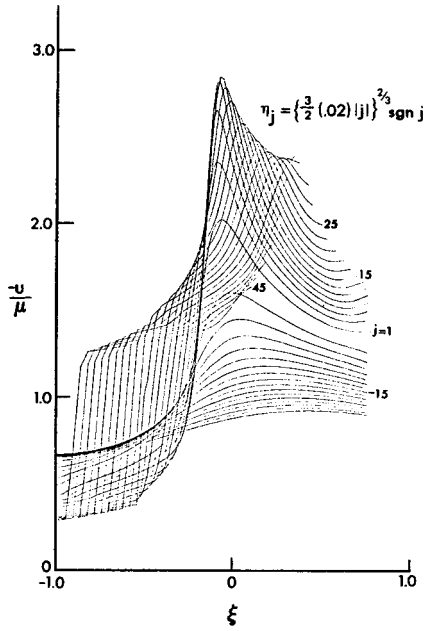

FIGURE 4.—Computer-drawn graphs of $\psi_\xi \equiv u$ as functions of ξ for fixed values of η. (*a*) $\mu = 0.10$.

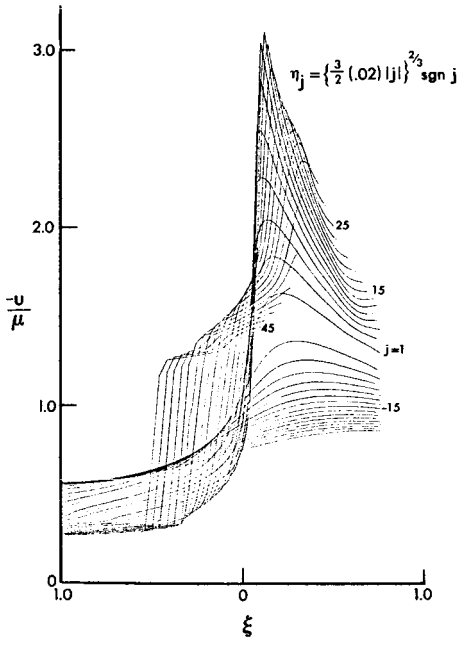

FIGURE 4 (continued).—(*b*) $\mu = 0.20$.

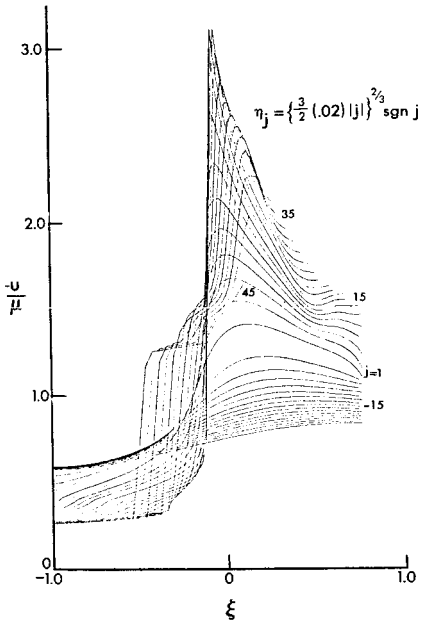

FIGURE 4 (concluded). – (c) $\mu = 0.30$.

APPENDIX

The basic difference equation for the nth iterate $\psi''_{i,j}$ is

$$\left[\frac{-2}{\delta_{j+1}(\delta_{j+1}+\delta_j)}\right]\psi''_{i,j+1} + \left[\begin{array}{l}\dfrac{2}{\delta_j\delta_{j+1}} - \dfrac{2\eta}{\Delta^2} - \dfrac{1}{\Delta^3}\left(\psi''^{-1}_{i+1,j} - \psi''_{i-1,j}\right) \\ \\ \dfrac{2}{\delta_j\delta_{j+1}} + \dfrac{\eta}{\Delta^2} + \dfrac{\psi''_{i,j}}{2\Delta^3} - \dfrac{\psi''_{i-1,j}}{\Delta^3}\end{array}\right]\psi''_{i,j}$$

$$+\left[\frac{-2}{\delta_j\ (\delta_{j+1}+\delta_j)}\right]\psi''_{i,j-1} + \left[\begin{array}{l}\dfrac{\eta_j}{\Delta^2}\left(\psi''^{-1}_{i+1,j} + \psi''_{i-1,j}\right) + \dfrac{1}{2\Delta^3}\left(\psi''^{-1^2}_{i+1,j} - \psi''^{-1^2}_{i-1,j}\right) \\ \\ \dfrac{\eta_j}{\Delta^2}\left(-2\psi''_{i-1,j} + \psi''_{i-2,j}\right) + \dfrac{1}{2\Delta^3}\left[\psi''^{2}_{i-1,j} - \left(\psi''_{i-1,j} - \psi''_{i-2,j}\right)^2\right]\end{array}\right] = 0$$

for

$$\eta_j + \frac{\psi''^{-1}_{i+1,j} - \psi''_{i-1,j}}{2\Delta} \leqq 0$$

where

$$\delta_j = \left(\tfrac{3}{2}\ \Delta\right)^{2/3}\ \left(|j|^{2/3} - |j-1|^{2/3}\right)$$

REFERENCES

1. HAYES, W. D.: Similarity Rules for Nonlinear Acoustic Propagation Through a Caustic. Second Conference on Sonic Boom Research, NASA SP-180, 1968, pp. 165-171.
2. MURMAN, E. M.; AND COLE, JULIAN D.: Calculation of Plane Steady Transonic Flows. AIAA Paper no. 70-188, 1970.
3. MURMAN, E. M.; AND KRUPP, J. A.: Solution of the Transonic Potential Equation Using a Mixed Finite Difference System. Paper presented at Second Int. Conf. Comp. Methods Fluid Dyn., Sept. 1970.
4. VALLEE, J.: Operation Jericho-Virage. Rapport d'Etude no. 277, Centre d'Essais en Vol Annexe d'Istres, 1969.
5. BITSADZE, S. A.: Equations of the Mixed Type. Pergamon Press, Inc., 1964, pp. 71-103.
6. FILIPPOV, A. F.: On the Application of Finite Differences to the Problem of Tricomi. Izv. Akad. Nauk. Ser. Mat., no. 21, 1957, pp. 73-88.

The Accuracy of the Landau-Whitham Shock Strength Rule in Some Near-Field Situations

A. R. GEORGE AND W. K. VAN MOORHEM
Cornell University

The unsteady reflection of weak waves from an arbitrary strength plane shock has been described in reference 1. This paper presents a simple extension of these results to nonplanar shocks. Of particular interest are cylindrical shocks, like those that occur in an equivalence plane model (ref. 2) for near-field sonic boom phenomena. It is necessary to make use of the equivalence plane because the investigation of reference 1 was carried out only for two-dimensional unsteady waves. The actual extension to three-dimensional steady problems appears to be relatively simple, but has not yet been carried out.

The interaction of a plane shock with two-dimensional weak waves of the progressing type (refs. 3 and 4) may be treated in full; however, for nonplanar shocks it is necessary to follow the wavefront using geometrical acoustics preceding and subsequent to the interaction. The use of geometrical acoustics in these cases then limits the results to the lowest order term in a progressing wave. The equivalence plane model does, however, yield an assessment of the accuracy of the one-dimensional Landau-Whitham theory for determining shock strength. The straightforward application of the Landau-Whitham result would just add the pressure change of the perturbation to the pressure jump across the shock. In these two-dimensional cases, significant errors are found when waves are incident on the shock rather obliquely.

The interaction of a conical flow field with a two-dimensional region is also considered. Of special interest here is the conical field produced at a wingtip. In this case the field produced is too strong to be considered in entirety; however, by limiting consideration to a region very near the Mach cone, the method of reference 1 may be applied.

The problem considered in reference 1 (see fig. 1) is that of a weak cylindrical wave incident from behind on a plane shock of initially constant strength. The shock is of arbitrary Mach number, and the wave may originate from a uniformly moving source (subsonic with respect to the flow behind the shock). Particular problems of this type have been inves-

420-093 O - 71 - 25

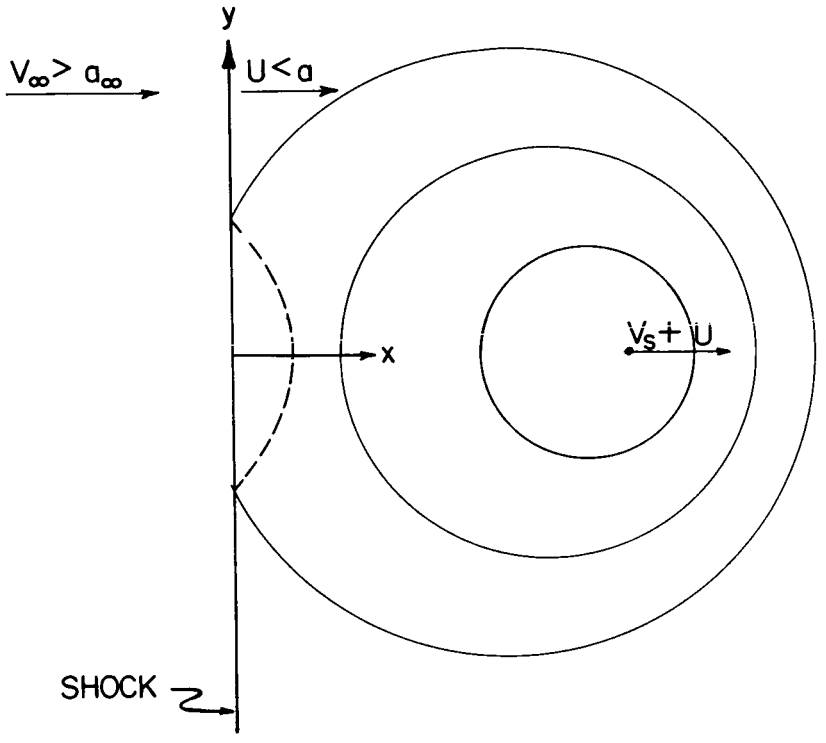

FIGURE 1.—Cylindrical waves from a moving source incident on a plane shock (ref. 1).

tigated by Freeman (refs. 5 and 6), Johnson and Laporte (ref. 7), Kovitz and Briscoe (ref. 8), and others, all of whom found that for their particular problems, the shock decayed as $t^{-3/2}$. Experimental studies have been made by Lapworth (ref. 9), Briscoe and Kovitz (ref. 10), and Bowman (ref. 11), all of whom verified the $t^{-3/2}$ decay, except for Bowman, who found a $t^{-1/2}$ decay. Reference 1 undertook to study the general problem of cylindrical waves incident on a planar shock to obtain a fundamental understanding of the problem and the varying experimental results.

The problem was formulated by considering small perturbations to the uniform flow behind the shock, with the flow equations reduced to the simple wave equation

$$P_{tt} = a^2 \nabla^2 P$$

for perturbation pressure in coordinates moving with the unperturbed flow behind the shock. By then using a Lorentz transformation of coordinates in a manner similar to that described by Sears (ref. 12), with

$$x_1 = \frac{X_1 + V_S T}{\beta_S}$$

$$y_1 = Y_1$$

$$t_1 = \frac{T_1 + \frac{V_S}{a^2} X_1}{\beta_S}$$

where V_S is the source velocity in the flow-fixed (x_1, y_1) coordinates and $\beta_S = \sqrt{1 - V_S^2/a^2}$, the source becomes stationary, while the wave equation is unchanged. In these Lorentz coordinates, a two-dimensional progressing wave is of the form

$$P = G(\Theta_1) \sum_{n=0} \frac{f_n(aT_1 - R_1)}{R^{1/2+n}}$$

where

$$G(\Theta_1) = \sin m\Theta_1 \quad \text{or} \quad \cos m\Theta_1 \qquad m = 0, 1, 2, \cdots$$

$$\Theta_1 = \tan^{-1} - \frac{Y_1}{X_1}$$

$$f'_{n+1}(aT_1 - R_1) = -\frac{(n+\tfrac{1}{2})^2 - m^2}{2(n+1)} f_n(aT_1 - R_1)$$

with $f_0(aT_1 - R_1)$ arbitrary and $R_1 = \sqrt{X_1^2 + Y_1^2}$. This is a valid solution for $(aT_1 - R_1)/R_1 \ll 1$, that is, close to the wavefront.

This incident wave may then be transformed back to physical coordinates, shock-fixed coordinates being most convenient, yielding

$$p = G(\theta_I) \sum_{n=0} \frac{f_n\left(at - \frac{V_S}{a}(x - Ut) - \sqrt{(x - (U+V_S)t)^2 + \beta_S^2 y^2}\right)}{[(x - (U+V_S)t)^2 + \beta_S^2 y^2]^{1/4 + n/2}}$$

where

$$\theta_I = \cos^{-1}\left(-\frac{x - (U+V_S)t}{\{[x - (U+V_S)t]^2 + \beta_S^2 y^2\}^{1/2}}\right)$$

and U is the flow velocity behind the fixed shock. Now, it is necessary that the pressure at the shock satisfy a boundary condition obtained in a manner similar to that of Ting and Ludloff (ref. 13). The incident wave alone fails to satisfy this boundary condition, and a reflected wave is necessary. The phase variable for the reflected wave is easily determined through use of a Lorentz-Galilean transformation,

$$x = \beta X$$

$$y = Y$$

$$t=\frac{T-\frac{U}{a^2}X}{\beta}$$

where $\beta=\sqrt{1-U^2/a^2}$. This transformation of coordinates results in a simple wave equation and a stationary shock in the (X, Y)-coordinates, with the incoming wave reflecting spectrally from the shock. Thus, with lines of constant phase for the incident wave given by

$$\frac{aT-\frac{U}{a}X}{\beta}-\frac{V_S}{a}\left(\frac{X-UT}{\beta}\right)-\sqrt{\left[\frac{\left(1+\frac{UV_S}{a^2}\right)X-(U+V_S)T}{\beta}\right]^2+\beta_S^2Y^2}=\text{const}$$

the lines of constant phase for the reflected wave are obtained by replacing X by $-X$ and are given as

$$\frac{aT+\frac{U}{a}X}{\beta}+\frac{V_S}{a}\left(\frac{X+UT}{\beta}\right)-\sqrt{\left[\frac{\left(1+\frac{UV_S}{a^2}\right)X+(U+V_S)T}{\beta}\right]^2+\beta_S^2Y^2}$$
$$=\text{const}$$

A progressing wave may then be found with this relation as the phase variable. The incident and reflected waves together are found to satisfy the shock boundary condition for particular choices of the amplitude and phase functions of the reflected waves. The reflected wave may then be written in shock-fixed coordinates as

$$P=F(\theta_R)G(\theta_R)\frac{f_0^R(\phi_R)}{\rho^{1/2}}$$
$$+\sum_{n=1}\frac{(-1)^{n+1}}{2^n}\frac{f_n^R(\phi_R)}{\rho^{1/2+n}}\prod_{i=0}^{n-1}\left[\frac{\left(n-i-\frac{1}{2}\right)^2+\frac{d^2}{d\theta_R^2}}{(n-i)}\right][G(\theta_R)F(\theta_R)]$$

where

$$\rho=\sqrt{\left(\frac{1+\frac{U^2}{a^2}}{\beta^2}X+2\frac{V_SU}{a^2}\frac{X}{\beta^2}+(U+V_S)t\right)^2+\beta_S^2y^2}$$

$$\phi_R=at+2\frac{U}{a}\frac{X}{\beta^2}+\frac{V_S}{a}\left(Ut+\frac{1+\frac{U^2}{a^2}}{\beta^2}X\right)-\rho$$

$$\theta_R=\cos^{-1}\left[\frac{\frac{1+\frac{U^2}{a^2}}{\beta^2}+2\frac{V_SU}{a^2}\frac{X}{\beta^2}+(U+V_S)t}{\rho}\right]$$

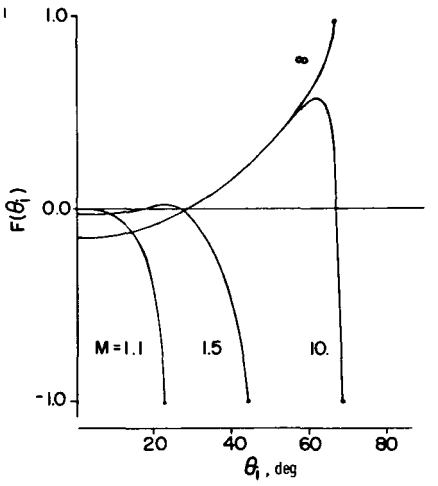

FIGURE 2.—The reflection coefficient for plane waves for shock Mach numbers of 1.1, 1.5, 10, and ∞ as a function of incidence angle.

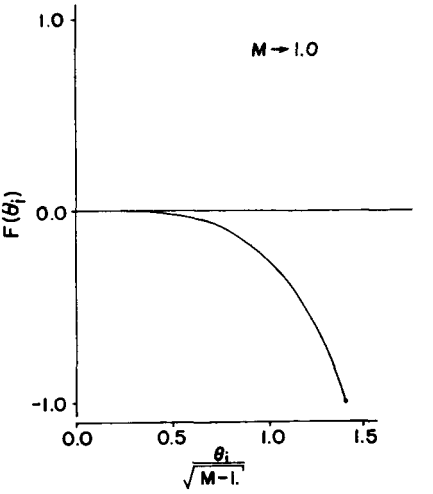

FIGURE 3.—The reflection coefficient for plane waves as $M \to 1$ as a function of incidence angle.

$$f^{R'}_{n+1}(\phi_R) = f^R_n(\phi_R) \qquad f^R_0(\phi_R) = f_0(\phi_R)$$

and

$$F(\theta_R) = -\frac{\left[A(M)\left(1+\frac{V_S U}{a^2}-\frac{U+V_S}{a}\cos\theta_R\right)^2-\beta^2\beta_S^2\sin^2\theta_R+2\frac{U}{a}\left(\frac{U+V_S}{a}-\left(1+\frac{V_S U}{a^2}\right)\cos\theta_R\right)\left(1+\frac{V_S U}{a^2}-\frac{U+V_S}{a}\cos\theta_R\right)\right]}{\left[A(M)\left(1+\frac{V_S U}{a^2}-\frac{U+V_S}{a}\cos\theta_R\right)^2-\beta^2\beta_S^2\sin^2\theta_R-2\frac{U}{a}\left(\frac{U+V_S}{a}-\left(1+\frac{V_S U}{a^2}\right)\cos\theta_R\right)\left(1+\frac{V_S U}{a^2}-\frac{U+V_S}{a}\cos\theta_R\right)\right]}$$

with $A(M) = (M^2+1)/M^2$ and $M = V_\infty/a_\infty$, the shock Mach number.

It must be noted at this point that both θ_I and θ_R are not physical angles, but rather anglelike variables describing a fixed point on a wavefront. The function $F(\theta_R)$ is the reflection coefficient, the ratio of reflected to incident wave amplitude, found by Moore (ref. 14) in his investigation of plane-wave reflection from a plane shock, but here is expressed in terms of θ_R rather than the incidence angle θ_i. See figures 2 and 3 for a plot of $F(\theta_i)$ as a function of incidence angle. Thus it can be seen that, to lowest order in $1/\rho$, a cylindrical wave reflects locally from the shock with the amplitude of a plane wave. The higher order terms, however, do not follow this simple result. The local angles of incidence

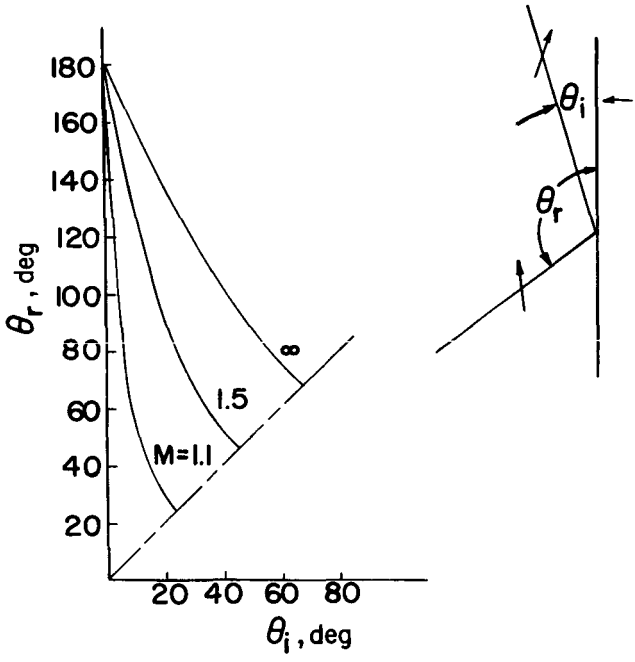

FIGURE 4.—The reflected wave angle as a function of incidence angle for Mach numbers of 1.1, 1.5, and ∞. At the critical value, both incident and reflected wave angles are equal.

and reflection for cylindrical waves are also found to be the same as for plane waves and are plotted in figure 4 for several Mach numbers.

Just as in the plane-wave case of Moore, a critical angle of incidence is found for which the wave can no longer catch the shock; i.e., the maximum angle for which energy is propagated toward the shock. In geometrical acoustics (ref. 15), energy is found to be propagated in the direction given by $\mathbf{U}+a\mathbf{n}$, where $\mathbf{n}$ is the normal to the wavefront, $\mathbf{U}$ is the flow velocity, and a is the speed of sound. Therefore, when the angle between the shock and wave is $\theta_{cr}=\cos^{-1} U/a$ (fig. 5), energy is no longer propagated toward the wave but parallel to it. This, then, is the limiting angle of incidence for which waves can be said to be incident upon the shock.

For plane waves incident at this critical angle, the reflection is found to be superimposed directly upon the incident wave (fig. 4) and completely cancels it for all finite Mach numbers. The reflection coefficient of -1 in figures 2 and 3 is indicative of this cancellation. The same phenomenon occurs for cylindrical waves, except that only the lowest order terms cancel, and pressure at the shock is then a result of the higher order terms. This cancellation is the source of the $t^{-3/2}$ decay discussed previously. For infinite Mach number shocks, the cancellation

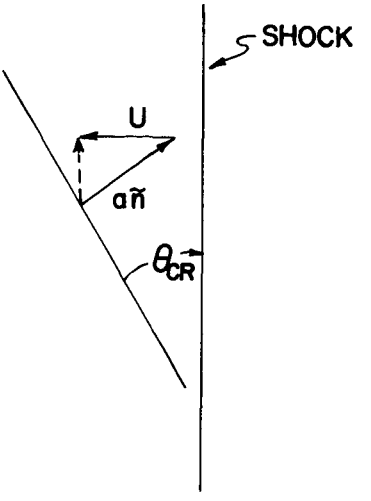

FIGURE 5.—At the critical angle, energy propagation velocity $\mathbf{U} + a\mathbf{n}$ is parallel to the shock.

does not occur, the reflection coefficient going to 1 as θ_i goes to θ_{cr}, and $t^{-1/2}$ decay is present. This had been noted by Freeman (ref. 5) and is also found in reference 16. It appears, therefore, that the previous investigations must have included only waves that always intersected the shock at the critical angle. It is easily shown that a cylindrical wave emitted when a planar shock passes over the wave source will always intersect the unperturbed shock at the critical angle. A wave emitted at a later time will intersect first at a zero incidence angle, then with an increasing angle, asymptotically going to the critical angle.

As has been previously mentioned, since thin weak waves will reflect from a nonplanar shock, to first order, in a locally plane manner and by following the propagation of the waves in the flow field behind a shock by geometrical acoustics, the interaction of the wave and shock may be computed. Using this technique, two cases have been computed graphically. Both cases are for diverging cylindrical shocks of Mach number 1.5 with a linear variation of flow velocity behind the shock.

In the first case (fig. 6), the wave is emitted at a point behind the shock. Here the incidence angle of the wave is always small, and the reflection coefficient given in the figure never varies significantly from the value of zero given by Landau-Whitham theory, even for this relatively strong shock. In the second case (fig. 7), however, the wave is emitted at the time of shock passage. Thus, the wave is initially at the critical angle but moves away from it because of the cylindrical geometry. In the regions of the shock where the wave intersected near the critical angle, the Landau-Whitham rule is found to be significantly in error.

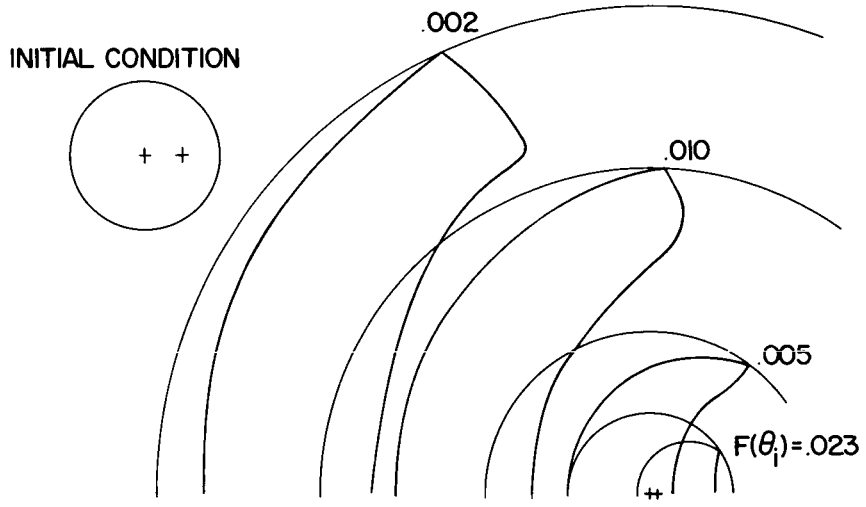

FIGURE 6.—Successive positions and reflection coefficients for a cylindrical wave emitted behind a Mach number 1.5 cylindrical shock.

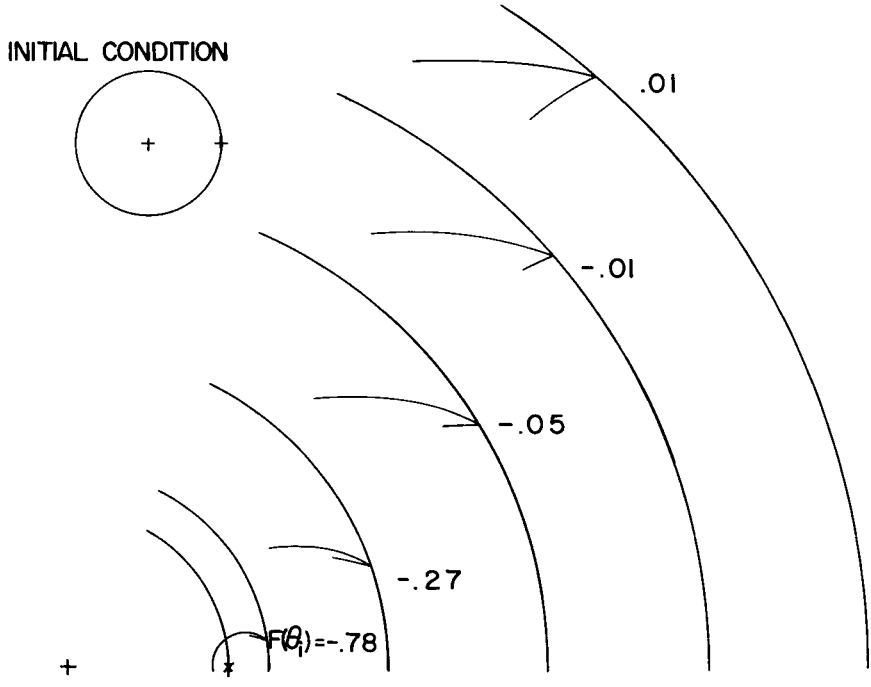

FIGURE 7.—Successive positions and reflection coefficients for a cylindrical wave emitted at a Mach number 1.5 shock.

This technique would allow investigation in the equivalence plane of an initially plane expansion wave moving in a diverging conical flow field, similar to the problem investigated by Oswatitsch and Sun (ref. 17). They are interested in the effects on the shock of the nominally plane expansion originating at the straight trailing edge of a delta wing with constant lift distribution. As the expansion propagates through the nonuniform conical flow field, the geometrical acoustics expression for ray velocity $\mathbf{U} + a\mathbf{n}$ shows that the initially plane fronts will become convex and weaker as the ray-tube areas increase. This is sketched in figure 8. This will occur even for the ray tube associated with the bicharacteristic propagating directly below the aircraft. Thus this effect will weaken the expansion below its "two-dimensional" value and will have to be taken into account in calculating the shock strength after its intersection with this expansion. Related effects will occur for the tip and "two-

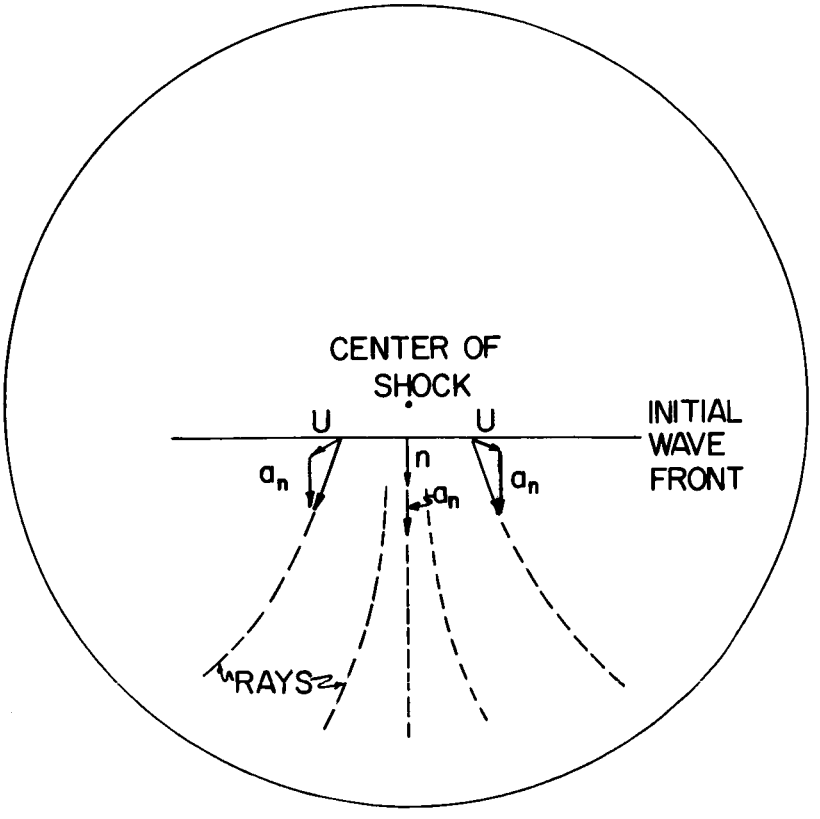

FIGURE 8.—Sketch of spreading of rays for an initially plane wave moving in a conical flow field.

dimensional" expansion in the flow field of the rectangular wing, as discussed by Davis.[1]

The interaction of conical fields and planar shocks can be investigated by the method of reference 1. The limitation to that portion of the field near the Mach cone where the disturbance is weak has been previously discussed. A second difficulty is the fact that conical flows in general cannot be expanded to all orders as outgoing progressing waves. However, considerable information can be obtained because the point of interest in these problems is the intersection of the Mach cone and shock where a singularity occurs. This singularity appears in the lowest order term of the progressing wave and, therefore, can be treated even if the entire field cannot.

In the equivalence plane, the conical field at a wingtip is generated at the same time as the shock, and the Mach cone will, therefore, always intersect the shock at the critical angle. As has been discussed, cylindrical waves intersecting a shock at the critical angle will generate a reflection that will cancel the lowest order term in the incident wave. This effect is shown by the reflection coefficients in figure 9. Thus for conical flows it is expected that the singularity will be canceled by its reflection. This cancellation has been observed previously for conical flows by Freeman (ref. 5).

A two-dimensional region bounded by a plane shock and conical wingtip waves moving into it, such as sketched in figure 9, can only

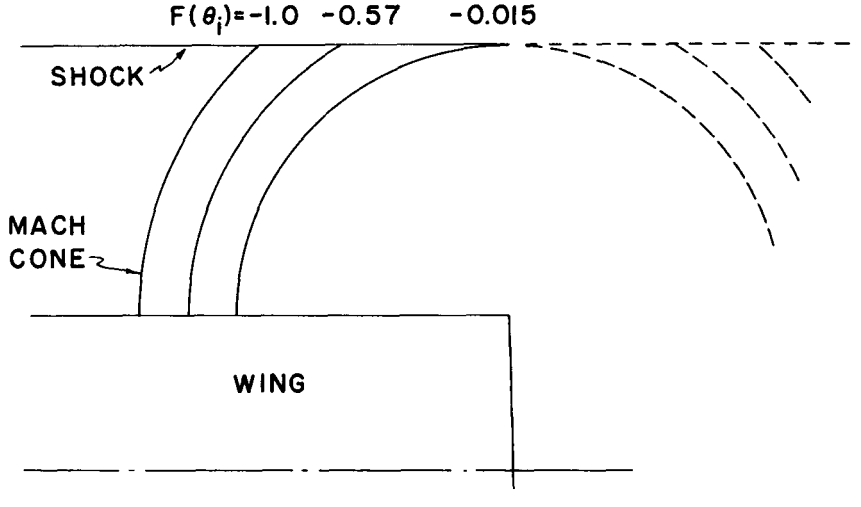

FIGURE 9.—Reflection coefficient for waves from a wingtip of a 10° half-angle wedge at Mach number 3 in the equivalence plane.

[1] See p. 219.

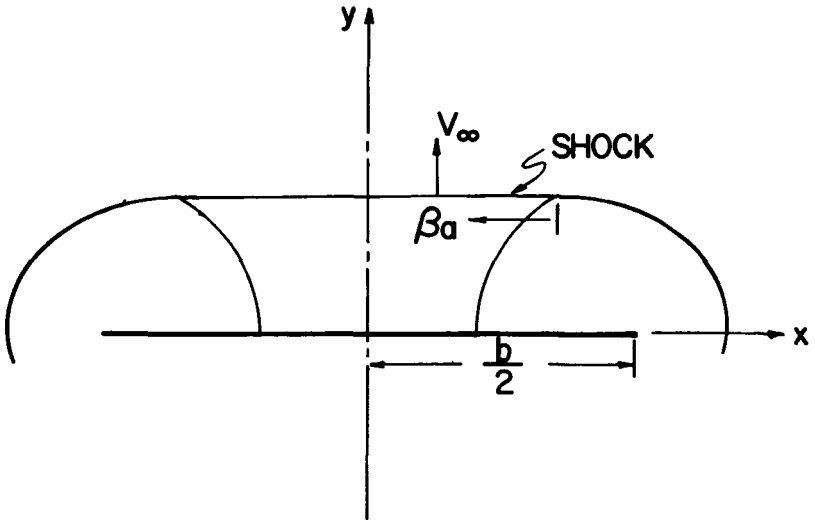

FIGURE 10. Equivalence plane view of a two-dimensional flow field bounded by a shock and the Mach cones of the tip flow.

exist for a finite length of time before the expanding waves fill the region. From figure 10 it can be seen that, with the shock moving out with velocity V_∞ and the shock wave front intersection moving along the shock at velocity βa, the trajectory of the intersection is given by

$$\frac{dy}{dx}=-\frac{\beta a}{V_\infty}$$

For a constant strength shock, and a wing semispan of $b/2$, the two-dimensional region extends a distance from the wing of

$$y=\frac{b}{2}\frac{V_\infty}{a}\frac{1}{\beta}$$

Thus for a rectangular wing, the two-dimensional region will not extend into the far field.

Several important effects in the near field for sonic boom problems have been discussed. The Landau-Whitham rule of simple pressure addition was seen to fail locally when waves reaching a shock are near the critical angle to it. The singularity occurring at the intersection of a conical flow field and a shock was shown to be canceled by reflected waves from the shock for finite Mach number shocks. However, the higher order terms necessary to determine the behavior at this point were not found by this technique. The propagation of waves through a non-uniform region before reaching a shock has been shown to affect the

strength of the waves and, therefore, the strength of the shock after its intersection with the wave. Regions of two-dimensional flow bounded by a shock and three-dimensional waves were shown to be eliminated as the three-dimensional waves propagate across the region. All of these effects can be expected to produce significant variations in near-field shock strengths.

REFERENCES

1. VAN MOORHEM, W. K.: Ph. D. thesis, Cornell University (in preparation).
2. HAYES, W. D.; AND PROBSTEIN, R. F.: Hypersonic Flow Theory. Vol. I. Academic Press, Inc., 1966, pp. 32–39.
3. COURANT, R.; AND HILBERT, D.: Methods of Mathematical Physics. Vol. II. Interscience Pubs., Inc., John Wiley & Sons, Inc., 1962, pp. 620–624.
4. FRIEDLANDER, F. G.: Sound Pulses. Cambridge Univ. Press, 1958, pp. 62–66.
5. FREEMAN, N. C.: A Theory of the Stability of Plane Shock Waves. Proc. Roy. Soc. Ser. A, vol. 228, 1955, pp. 341–362.
6. FREEMAN, N. C.: On the Stability of Plane Shock Waves. J. Fluid Mech., vol. 2, 1957, pp. 397–411.
7. JOHNSON, W. R.; AND LAPORTE, O.: Interaction of Cylindrical Sound Waves With a Stationary Shock. Phys. Fluids, vol. 1, 1958, pp. 82–94.
8. KOVITZ, A. A.; AND BRISCOE, M. G.: Stability of a Plane Wave in Free Space and in the Presence of Rigid or Interfacial Boundaries. J. Acoust. Soc. Amer., vol. 45, 1969, pp. 1157–1165.
9. LAPWORTH, K. C.: An Experimental Investigation of the Stability of Plane Shock Waves, J. Fluid Mech., vol. 2, 1957, pp. 341–362.
10. BRISCOE, M. G.; AND KOVITZ, A. A.: Experimental and Theoretical Study of the Stability of Plane Shock Waves Reflected Normally From Perturbed Flat Walls. J. Fluid Mech., vol. 31, 1968, pp. 529–546.
11. BOWMAN, R. M.: Investigation of Shock Front Topography in Shock Tubes. Ph. D. thesis, Calif. Inst. Tech., 1966.
12. SEARS, W. R.: Small Perturbation Theory. Princeton Univ. Press, 1960, pp. 58–59. Also W. R. SEARS, ED.: General Theory of High Speed Aerodynamics. Princeton Univ. Press, 1954.
13. TING, L.; AND LUDLOFF, H. F.: Aerodynamics of Blasts. J. Aeronaut. Sci., vol. 19, 1952, pp. 317–328.
14. MOORE, F. K.: Unsteady Oblique Interaction of a Shock Wave With a Plane Disturbance. NACA Rept. 1165.
15. HAYES, W. D.: Energy Invariant for Geometric Acoustics in a Moving Medium. Phys. Fluids, vol. 11, 1968, pp. 1654–1656.
16. GEORGE, A. R.: Nonuniform Hypersonic Flow Past a Wedge. Phys. Fluids, vol. 9, 1966, pp. 453–461.
17. OSWATITSCH, K.; AND SUN, Y. C.: The Influence of Near-Field Flow on the Sonic Boom. ICAS Paper no. 70–20, 1970.

On the Extrapolation of Measured Near-Field Pressure Signatures of Unconventional Configurations

JOEL P. MENDOZA AND RAYMOND M. HICKS
NASA Ames Research Center

The Whitham theory (ref. 1) accurately predicts the sonic boom characteristics of some configurations and fails to predict with the same degree of accuracy the sonic boom characteristics of other configurations. Nose bluntness, large values of lift, and large Mach number have been shown (refs. 2 to 6) to have adverse effects on the prediction of sonic boom characteristics. A technique (ref. 7) of extrapolating measured near-field overpressure data from one altitude to larger altitudes has been shown (ref. 8) to circumvent many of the weaknesses of the Whitham theory. A number of cases will be presented in this paper for which the Whitham theory either is not applicable or yields results that differ widely from the measured data. The extrapolation technique will be shown to be quite accurate in predicting the sonic boom characteristics of these cases.

DISCUSSION

A sketch of the different configurations studied in this paper are presented in figure 1. Overpressure data were measured at the Ames Research Center on the 6.48° cone-cylinder model and the two models of the straight-wing and delta-wing orbiters. Overpressure data on the wing-body and the two wing-alone models were obtained from references 6 and 9.

For each model, overpressure characteristics measured at some given altitude are extrapolated and compared to overpressure characteristics measured at a higher altitude. In cases for which the Whitham theory is considered applicable, a theoretical pressure signature is shown with the extrapolated and measured data.

The measured and predicted overpressure characteristics of the 6.48° cone cylinder at the Mach number of 1.68 are shown in figure 2. At the altitude of 20 cone lengths, the extrapolated pressure signature as well as the pressure signature computed by the Whitham theory are shown to agree quite well with the measured pressure signature. Because of the axisymmetric formulation of the theory, the excellent agreement shown is not too surprising.

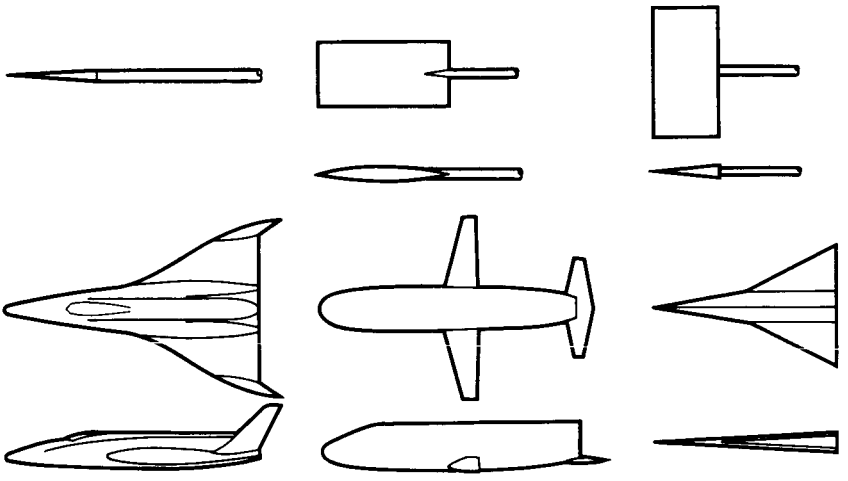

FIGURE 1.—Configurations used in wind-tunnel sonic boom tests.

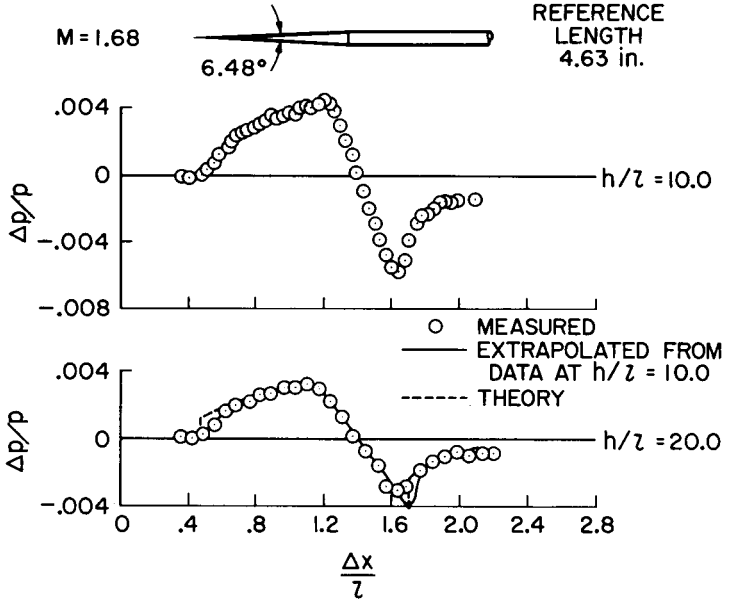

FIGURE 2.—Flow-field pressures of a cone cylinder.

Comparisons made between the measured and extrapolated pressure signatures at the Mach number of 2.01 are shown in figures 3 and 4 for wings with an aspect ratio of 1/2 and 2, respectively. The overpressure data were measured on a boundary layer bypass plate that was assumed to have a reflection factor of 2.0. For the wing with an aspect ratio of 1/2, it is noted that the measured and extrapolated data agree

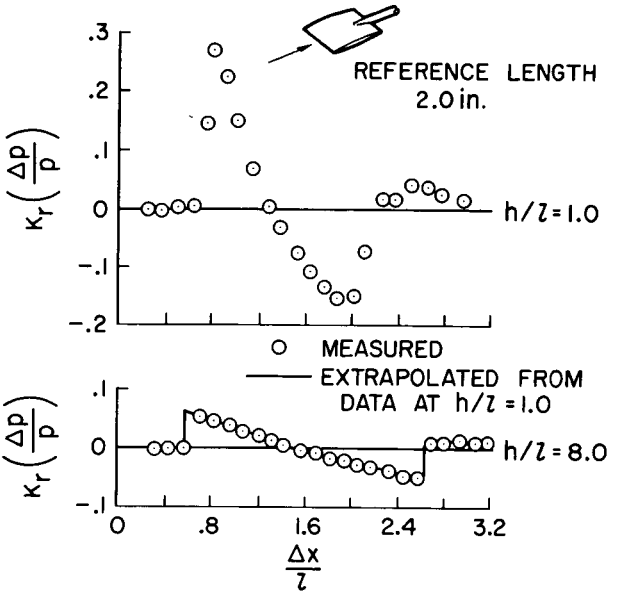

FIGURE 3.—Flow-field pressures of a wing with an aspect ratio of ½ measured on a boundary layer bypass plate, $M = 2.01$ and $K_r = 2.0$.

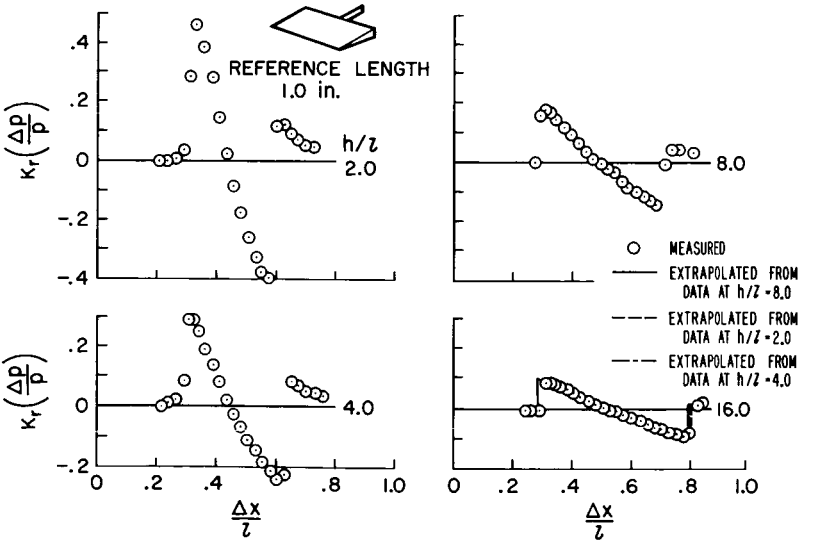

FIGURE 4.—Flow-field pressures of a wing with an aspect ratio of 2 measured on a boundary layer bypass plate, $M = 2.01$ and $K_r = 2.0$.

quite well at the altitude of eight chord lengths. Here the flow field was considered to become axisymmetric a short distance from the chord plane of the wing. In contrast, the wing with an aspect ratio of 2 was expected to retain its two-dimensional flow-field characteristics at a larger distance from the wing plane than the previous model. It is noted that pressure signatures extrapolated from signatures measured at successively increasing distances from the model exhibited successively improved correlations with the data measured at the altitude of 16 chord lengths.

Measured and predicted pressure signatures for a wing-body model at a Mach number of 4.63 are shown in figure 5 for two lift coefficients.

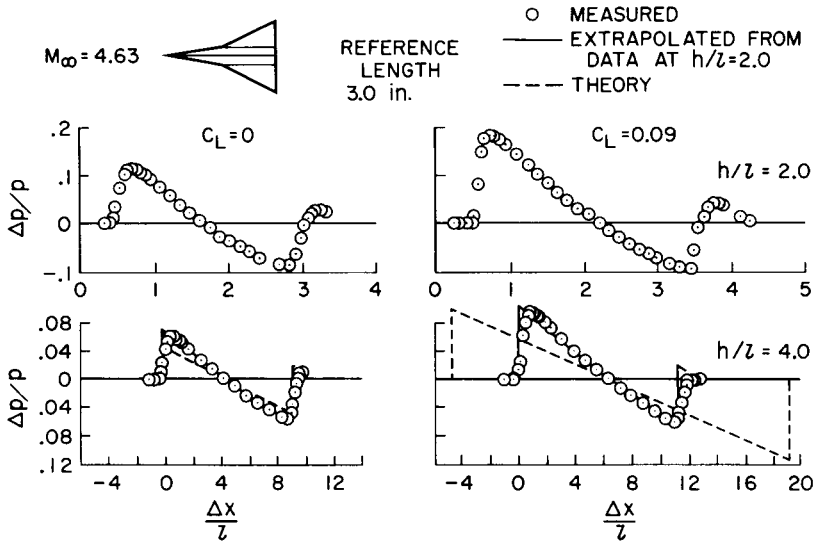

FIGURE 5.—Flow-field pressure of a wing-body model at a high supersonic Mach number.

At zero lift coefficient, both the extrapolated data and the theoretical pressure signature agree fairly well with the measured data at the altitude of four body lengths. At the lift coefficient of 0.09, however, theory predicts a longer pressure signature length. The extrapolated pressure signature agrees more closely with the measured data than theory does at the altitude of four body lengths.

The excellent correlations shown between the measured and extrapolated sonic boom characteristics of the models discussed up to this point might be attributed principally to the weak shocks they produce. However, it was discovered that the sonic boom characteristics of configurations producing strong shocks could be accurately predicted by the extrapolation technique. An example of such a configuration is shown in the shadowgraph (fig. 6) of a straight-wing orbiter at a Mach number of

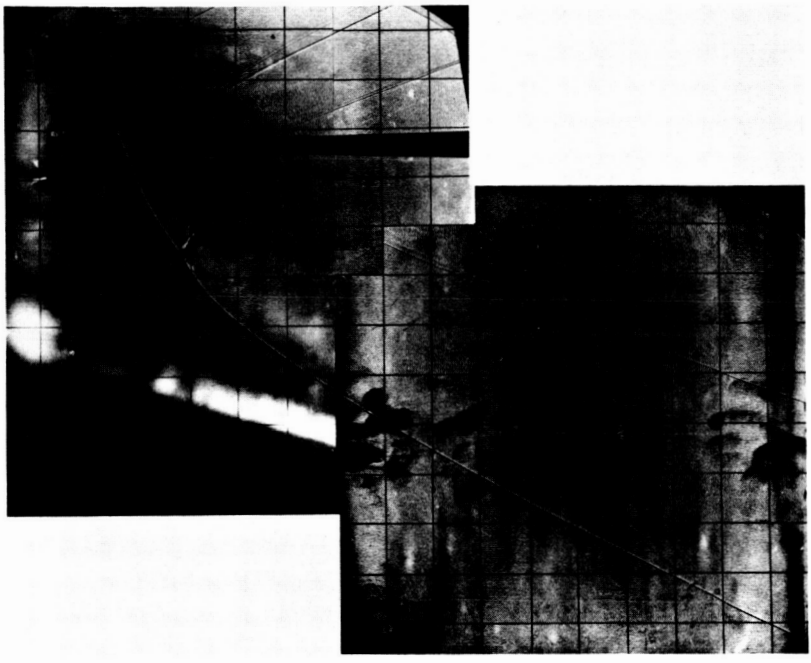

FIGURE 6.—Shadowgraph of the model of the straight-wing orbiter, $M = 2.7$ and $\alpha = 60°$.

2.7 and at an angle of attack of 60°. It is noted that a strong bow shock is produced by this model. An embedded rear shock is observed forming at a point some distance from the rear of the model. Quite clearly the flow-field characteristics of this model cannot be adequately described by small-disturbance theory.

The measured and extrapolated pressure signatures of the straight-wing and delta-wing orbiters at a Mach number of 2.7 and an angle of attack of 60° are shown in figures 7 and 8, respectively. At the higher altitudes, where only the positive portions of the pressure signatures were measured, excellent agreement is shown between the measured and extrapolated overpressure characteristics.

To determine the sonic boom levels on the ground produced by each of the two full-scale space shuttles flying their respective 60° angle-of-attack mission profiles, additional pressure signatures for the two models each at the angle of attack of 60° were measured at Mach numbers of 1.68 and 2.17. Presented in figure 9 are the predicted sonic boom levels on the ground produced by each of the two space shuttles. Included in the calculations of the sonic boom levels are the effects of some of the flight parameters such as flightpath angle, the time rate of change of the flightpath angle, and deceleration. The noted decrease in sonic boom levels with increasing Mach number is mainly an effect of altitude.

420-093 O - 71 - 26

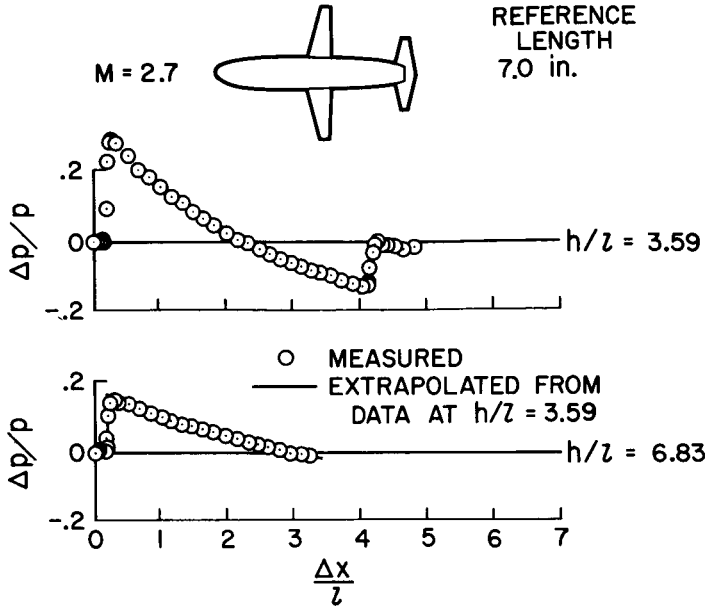

FIGURE 7.—Flow-field pressures of a straight-wing orbiter, $\alpha = 60°$.

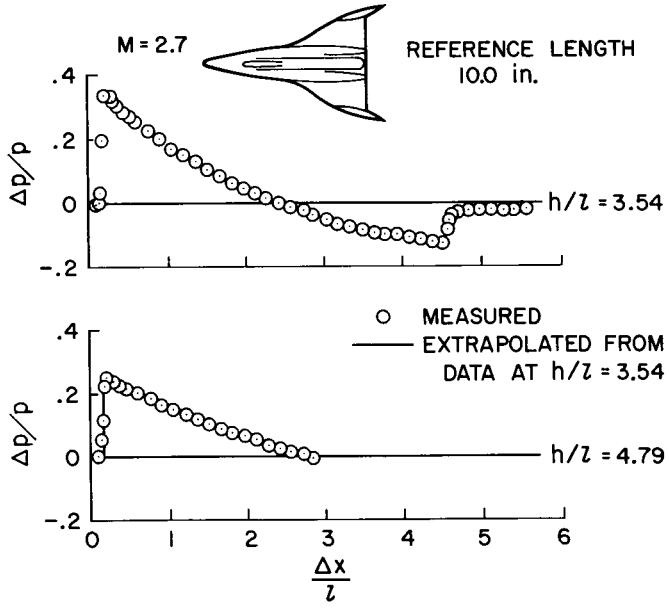

FIGURE 8.—Flow-field pressures of a delta-wing orbiter, $\alpha = 60°$.

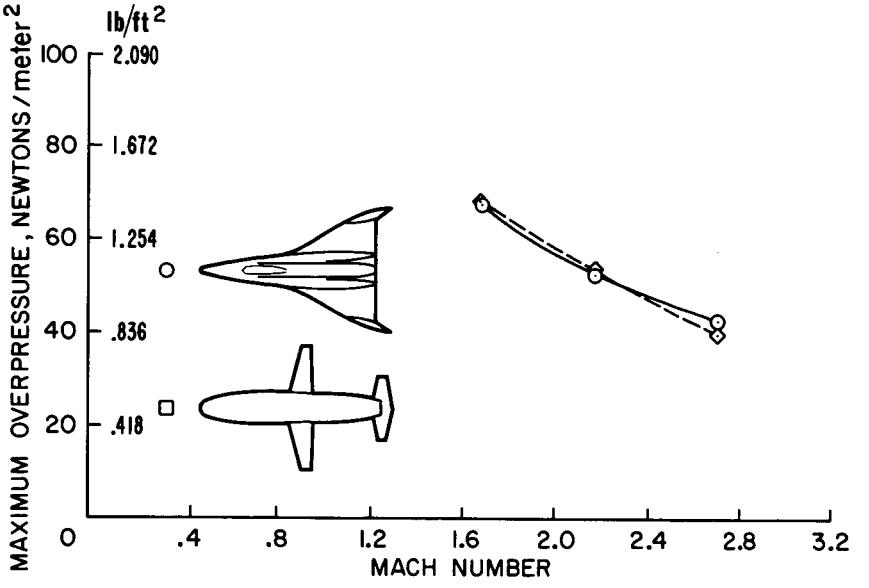

FIGURE 9.—Sonic boom levels for the delta-wing and straight-wing orbiters operating on their respective 60° mission profiles.

CONCLUSION

The extrapolation technique has been shown to accurately predict the sonic boom characteristics of the different configurations studied herein. Application of the extrapolation technique to overpressure data measured at Mach numbers as large as 4.63 may be made with some measure of confidence. Sonic boom levels of configurations producing strong shocks may be accurately estimated.

REFERENCES

1. WHITHAM, G. B.: The Flow Pattern of a Supersonic Projectile. Commun. Pure Appl. Math., vol. 5, 1952, pp. 301–348.
2. CARLSON, HARRY W.; MARK, ROBERT J.; AND MORRIS, ODELL A.: A Wind-Tunnel Investigation of the Effect of Body Shape on Sonic Boom Pressure Distributions. NASA TN D–3106, 1965.
3. MORRIS, ODELL A.; LAMB, MILTON; AND CARLSON, HARRY W.: Sonic Boom Characteristics in the Extreme Near Field of a Complex Airplane Model at Mach Numbers of 1.5, 1.8 and 2.5. NASA TN D–5755, 1970.
4. CARLSON, HARRY W.; MCLEAN, F. EDWARD; AND STROUT, BARRETT L.: A Wind Tunnel Study of Sonic Boom Characteristics for Basic and Modified Models of a Supersonic Transport. NASA TM X–1256, 1966.
5. STROUT, BARRETT L.; MACK, ROBERT J.; AND DOLLYHIGH, SAMUEL M.: A Wind Tunnel Investigation of Sonic Boom Pressure Distributions of Bodies of Revolution at Mach Numbers 2.96, 3.83 and 4.63. NASA TN D–6195, 1970.

6. MILLER, DAVID S.; MORRIS, ODELL A.; AND CARLSON, HARRY W.: Wind-Tunnel Investigation of Sonic-Boom Characteristics of Two Simple Wing-Body Models at Mach Numbers from 2.3 to 4.63. NASA TN D–6201, 1971.
7. HICKS, RAYMOND M.; AND MENDOZA, JOEL P.: Prediction of Aircraft Sonic Boom Characteristics From Experimental Near Field Results. NASA TM X–1477, 1967.
8. MENDOZA, JOEL P.; AND HICKS, RAYMOND M.: Further Studies of the Extrapolation of Near Field Overpressure Data. NASA TM X–2219, Mar. 1971.
9. CARLSON, HARRY W.: An Investigation of Some Aspects of the Sonic Boom by Means of Wind Tunnel Measurements of Pressures About Several Bodies at a Mach Number of 2.01. NASA TN D–161, 1959.

IV

PANEL AND OPEN CONFERENCE DISCUSSIONS

Chairman: E. H. LOMAX

Some Notes on the Present Status of Sonic Boom Prediction and Minimization Research

HARRY W. CARLSON
NASA Langley Research Center

GENERATION AND PROPAGATION

In the field of research dealing with the study of sonic boom generation and propagation, much has been accomplished since the first booms were generated by research and military aircraft shortly after World War II. There is now a general understanding of the way in which an airplane's shape, size, and operating conditions affect the generation of the boom and of the way in which flightpath variations and atmospheric conditions affect the propagation. Expected nominal overpressures may be predicted with reasonable accuracy through the use of current theoretical techniques, and the effects of atmospheric nonuniformities and turbulence may be estimated on the basis of statistical data from flight-test programs. Generally, there is far less uncertainty in the prediction of overpressure levels than there is in the prediction of the effect of these levels on people, animals, and structures.

Wind-tunnel and ballistic-range experimental programs have permitted detailed studies under controlled conditions of the generation and propagation of sonic boom pressure fields for a variety of basic shapes and typical airplane configurations. This work has been invaluable in the verification of the basic Hayes-Whitham theoretical treatment and in the development and refinement of computer-implemented prediction techniques. Other laboratory studies have provided a knowledge of the effects of atmospheric nonuniformities and turbulence and of the behavior of pressure signals at a focus.

In the assessment of the influence of airplane operational factors and atmospheric properties on sonic boom generation and propagation, the importance of flight-test programs cannot be overemphasized. These tests have provided an impressive amount of high-quality data, which has been of great value in the verification of theoretical methods for the prediction of nominal overpressures and in the estimation from a statistical standpoint of the modifying influence of unpredictable atmospheric nonuniformities.

The latest in the series of these flight tests, reported at this conference,[1] has yielded information directly applicable to the feasibility of overland operation of supersonic transports (SST's) at slightly greater than sound speed to prevent the boom from reaching the ground. Although such operation appears to be feasible and could be used to improve the utilization of the SST on the overland portion of worldwide route structures, there is little evidence from an engineering and economic feasibility viewpoint to justify transport design directed specfically toward sustained operation at transonic speeds.

Community overflight test programs such as those conducted at St. Louis and Oklahoma City have led to a much improved understanding of the impact of the boom on community life and resulting public reaction. Yet there is still no way of establishing tolerable levels of the boom nor of relating public reaction to boom levels in such a way as to permit meaningful extrapolation to routine long-term airline operation of SST's. It is hoped that experience with the Anglo-French Concorde will provide additional information relative to establishment of a rational basis for limitation of public exposure to sonic booms.

Looking ahead, there is clearly a need to resolve the difficulties associated with the analytic treatment of the caustic and atmospheric turbulence. Prediction of these effects may well continue to be treated statistically; however, a fundamental understanding of the relative importance of the factors involved is essential in the interpretation of data obtained in specific tests and extension of the results to aircraft operation under conditions far different from those encountered in the tests. Of even greater importance is the need for a broad-based exploration of sonic boom phenomena at hypersonic speeds. This work will entail wind-tunnel and laboratory experimentation and may require the development of new analytic techniques. Flight tests would become an important part of the research program as hypersonic research aircraft become available.

Many other present and proposed research efforts, however, are concerned with what must be regarded as details in the overall picture. Because of the relatively advanced state of knowledge of sonic boom generation and propagation, caution must be exercised in the selection of new research programs. Each of us who proposes new work or is called upon to review proposals should address himself to the following questions:

(1) Are the factors to be explored significant; is there a real need for the work?

[1] See p. 243.

(2) Will the proposed work be original and not simply a repetition of work already covered in the rapidly expanding volume of literature?
(3) Is the approach technically sound; can it withstand the scrutiny of recognized authorities?

MINIMIZATION

The search for airplane shaping concepts to minimize the sonic boom pressure field disturbance has been actively carried on for almost a decade. The earlier work, aimed at reduction of signature impulse and far-field shock strength, was found to be severely limited in practical application. At best, a sonic boom optimized design could be expected to have only a 10- to 15-percent reduction of shock strength relative to a comparable design that ignored boom considerations. Techniques for boom minimization based on the attainment of near-field signatures as pioneered by McLean and extended by Seebass permit a greater degree of minimization provided that shock strength or peak overpressure rather than signature impulse is the governing factor. These later techniques have been shown to offer practical benefits for the transonic speed range, but there remains some question of their effectiveness for SST cruise conditions, at least for the present status of aerodynamic, propulsion, and structural weight technology.

It has become very clear in NASA and industry studies that the problem of sonic boom minimization through airplane shaping is inseparable from the problems of optimization of aerodynamic efficiency, propulsion efficiency, and structural weight. Substantial improvement in any of these other factors would have a direct beneficial influence on sonic boom minimization. Airplane shaping based on sonic boom considerations alone, however, does not necessarily bring about improvement in the other factors. In fact, if great care is not taken in the application of sonic boom design principles, the whole purpose can be defeated by performance degradation, weight penalties, and a myriad of other practical considerations that arise in the airplane design process. These thoughts are intended not to discourage the application of sonic boom design principles but to point out the need for consideration of all aspects of the minimization problem in order to assess the true potential of any minimization scheme.

A case in point is offered by a review of the NASA–FAA Domestic SST Study. Following McLean's original discovery of extended near-field effects in 1964, an analysis of hypothetical airplane equivalent body area distributions indicated that there was some possibility of generating near-field signatures with maximum overpressures less than 1.0 lb/ft^2 for the entire mission of a Mach 2.7, 200-passenger SST with a range of

2500 n. mi. Subsequent studies by NASA indicated that the original overpressure estimate would have to be revised to about 1.2 to 1.3 lb/ft^2 because of consideration of a more realistic atmosphere model than the geometric mean previously used and because practical configuration arrangements that fully corresponded to the original hypothetical area distribution were not possible. Working under contract to FAA, North American Aviation, Inc., performed a feasibility study in which the NASA design concepts were retained and an attempt was made to develop an economically sound airplane for scheduled airline operation on domestic coast-to-coast routes. Some design compromises were found to be necessary, and the original weight estimates were found to be overly optimistic, the net result being that peak overpressures in the region of 1.4 to 1.5 lb/ft^2 were estimated at the conclusion of the study. Although these levels represented a considerable improvement compared to the booms to be expected from the larger intercontinental SST, there was no assurance that they would be acceptable for routine overland operations, and little further work was done. There is no evidence that within the constraints of present aerodynamic, propulsion, and structural weight technology, appreciably better sonic boom levels could be attained. A breakthrough in any one of these constraining technologies or an accumulation of benefits from several areas would, however, warrant a reexamination of the situation.

Extreme examples of near-field signatures that might offer sonic boom benefits are those that have finite rise times. It is generally conceded that the noise associated with sonic boom is considerably diminished by rise times that may be only a small fraction of the signature duration. At present, however, there is only a remote possibility for the planned achievement in practice of such signatures. The required airplane lengths in the application of airplane shaping techniques appear to be prohibitive, and the application of phantom-body or heat-field concepts, while worthy of further consideration, must be admitted to present severe, if not unsurmountable, problems of practical implementation.

There is some possibility that an ultimate solution to the sonic boom problem may be found in the development of a practical hypersonic transport, a possibility that should be vigorously explored. For instance, it is estimated that a hypersonic transport designed with no consideration of sonic boom minimization would produce overpressure levels of about 1 lb/ft^2 for operation at Mach numbers in the 6 to 8 range and corresponding cruise altitudes in excess of 100 000 ft. Overpressure levels decrease further with increasing speed, and, of course, at orbital speed there should be no perceptible boom. All such high-speed vehicles, however, must travel at transonic and moderate supersonic speeds for portions of the mission during which relatively intense booms would be generated. Thus the sonic boom problem cannot be completely avoided.

The multitude of problems associated with the development of aircraft for operation in this hostile environment cannot be discounted, but the potential benefit of efficient long-range transportation not appreciably restricted by boom considerations makes the solution of the problems a worthy goal. In this connection it is evident that there is a need for improved understanding of hypersonic boom phenomena and a need for the development of prediction and minimization techniques.

The attention of many talented researchers has been devoted to this most difficult endeavor of finding a completely acceptable solution to the sonic boom problem. As of now, there is no approach, even on the far horizon, to offer much hope for full achievement of that goal. The search must continue. In this search we must be aware of the danger of too great an assurance in our assumptions of what cannot be done (until tried) and must be alert to new possibilities, particularly those that may originate in presumably unrelated disciplines.

Comments on the Reduction of Sonic Boom

A. FERRI
New York University

The problem that we are trying to solve is that of decreasing the sonic boom signature to a level that can be considered acceptable for overland flights. Such a problem has two aspects; the first is the determination of acceptable levels of sonic boom signatures.

At present several phenomena, besides supersonic flight, both natural and man generated, produce sonic boom. Such sonic booms should be measured to evaluate the disturbance produced by such signatures because their signatures are already accepted by mankind. The results of such measurements would probably be more indicative than the results of experiments where sonic booms are produced by airplanes because in such experiments many other factors influence the conclusions.

The second problem is to investigate what possible lower limits of sonic boom signature can be obtained with practical airplanes. The work carried out in the last few years indicates that the sonic boom discontinuous overpressure can be reduced substantially by modifying the airplane configuration. Such conclusions obtained on the basis of analysis are presently accepted; however, they have not been confirmed by any experiments. The analysis involves several approximations, and it is worthwhile mentioning the consequences of such approximations.

First, the airplane is represented as an equivalent area distribution. In the definition of the equivalent area, three-dimensional effects are neglected; in addition, if standard analysis is used, linear theory is utilized in relating cross-sectional area volume and lift. This second approximation can be eliminated by taking into account second-order effects in determining the overpressure corresponding to lift. Therefore, when a given equivalent area distribution is defined and the end value of the equivalent area distribution corresponds to the weight of the airplane within the higher order theories, then such signatures will correspond to an airplane that has the correct lift and the correct length even when the other approximations are eliminated; however, the relation between the geometry and the area distribution will be different from that obtained with linear theory. The second approximation is in the propagation of the wave. If higher order terms are considered in the

analysis, the wave propagation in the vicinity of the airplane will change. Such changes will affect the position and origin of each wave carrying a given disturbance that produces the sonic boom signature. It therefore will change the airplane configuration corresponding to a given signature. At present the importance of such approximations is investigated by making experiments in wind tunnels and determining the sonic boom corresponding to a given geometry and given lift at some distance from the airplane. This type of investigation should permit changing the airplane configuration to take into account the higher order effects in order to have the predicted signature. While the basic approach is sound, experimental errors that are difficult to avoid can affect substantially the conclusions of these types of investigations. Nonuniformities that exist in all wind tunnels can introduce errors that are important for the sonic boom measurements when the intensity to be measured is small. In addition, model support and local flow separations due to the low Reynolds numbers of the tests can introduce substantial effects on the results. If experimental techniques are to be used, the importance of such errors should be recognized and evaluated carefully in each test.

I strongly recommend that a research program be organized and directed toward this purpose. Such a program cannot presently be carried on as a side effort of other research programs because it requires careful and detailed measurements of very small quantities.

The analysis presented indicates that a decrease in vehicle weight, flight altitude, and Mach number and an increase of dimensions can change substantially the sonic boom. Some work should be directed toward determining possible practical limitations or variations of such parameters.

Hypersonic flights are predicated on the possibility of longer range flights; therefore, the possibility of overland flights is important for hypersonic vehicle design. The effect of increasing the Mach number for supersonic airplanes should be investigated from the point of view of sonic boom generation. In this field many of the existing linear theories are not satisfactory. At the same time, careful investigations of hypersonic vehicles will probably indicate that the preliminary conclusions obtained indicating high sonic boom signature from oversimplified analyses are not necessarily correct. Because the weight of the airplane is an important parameter, some effort should be directed toward the investigation of the possible changes of engine fuel used and reduction of consumption of fuel, weight, and structural weight. When all of this information is available, it will be possible then to have a clear idea of what direction should be taken and what the real possibilities are for the next generation of supersonic airplanes.

Comments on Near-Field Effects

M. B. FRIEDMAN
Columbia University

It is not yet clear that major reductions in boom overpressures can be achieved by realizable modifications of aerodynamic configurations such as changes in planform, sweep, dihedral, redistribution of lift, etc. However, the theoretical and experimental research to date does indicate that some significant reductions can be obtained by varying these features. Even limited improvements may be of value in certain cases because of the amplification effect of focusing.

The difficulties encountered in determining the influence of changes in configuration are due to the limitations of both theoretical and experimental techniques presently available. Wind-tunnel experiments, by their nature, provide primarily near-field data which are then extrapolated into the far field through the F-function approach. But from the theoretical point of view, the near-field behavior for many configurations is not well modeled by F-functions. Consequently, although the overall decay character of the far field is approximated by their use, the influence of configuration asymmetries, etc., on the shocks and particularly on the signatures is not accounted for properly. Theoretical analysis might establish the extent of the near field and indicate where the F-function extrapolation can begin. In fact, the limited theoretical results available indicate that this is dependent upon the geometry of the configuration. But except for relatively simple geometries, it is not feasible at this time to determine the near field to predict the region beyond which F-functions may be properly employed. Thus it is difficult to assess the true influence of configuration changes.

A successful evaluation of the benefits of altering geometry would appear to require, at the least, more extensive analytical and/or numerical treatment of the near field. Such theoretical knowledge of the near field may also be important in attempting to develop configurations that maintain the near-field character for some large distance as, for example, by delaying coalescence of wing and body shocks. Certainly, in such cases, extrapolation procedures must be applied with great care. Another possible direction for utilizing near-field behavior is to take advantage of the redistribution of the field brought about by the strong three-dimen-

sional effects associated with diffraction phenomena induced by wing geometry. The study of simple geometries indicates that the experimentally noted favorable influence of such factors as dihedral may be attributed to exactly such diffraction phenomena. The study of focusing is also strongly dependent on the behavior of the near field. The customary far-field approximations associated with the F-function no longer remain valid beyond the caustic. Several investigators have reported work in these proceedings that appear to represent initial efforts in these directions.

Comments on the Caustic Problem

WALLACE D. HAYES
Princeton University

The problem of computing pressure signatures and shock intensities for a sonic boom in a caustic region remains an unresolved problem at this time. The primary difficulty is that for a shock wave entering a caustic, linear theory predicts infinite pressures. A theory that is essentially nonlinear is needed. A canonical equation for the phenomenon is known, together with corresponding similarity rules (ref. 1). Despite some partial success, adequate numerical solutions have not yet been found.

A particularly interesting development is the linearization of the canonical equation by R. Seebass.[1] By means of a transformation that incorporates a Legendre transformation, he has reduced the equation to the Tricomi equation. The result is that the caustic problem for all shock-free (bangless) signatures can be simply linearized, within, of course, the approximations leading to the canonical equation. The transformation may be interpreted as a two-dimensional (instead of one-dimensional) distortion of the Landau-Whitham type. The solution to the linear problem may be constructed as a superposition of known functions.

In the opinion of the writer, because of the shock conditions, Seebass' transformation will fail to linearize the problem if an entering shock is present. The shock is essentially a free boundary of the domain, with two boundary conditions or relations. These two conditions govern the orientation and intensity of the shock; i.e., where it goes and how strong it is. A number of other conditions may be derived, such as the useful condition of continuity of velocity potential across the shock, but *two* independent conditions always remain. If an arbitrary linear solution is given that, on transformation, requires a shock, a shock can generally be fitted using one condition. In general, the other independent condition is not met. Thus the linear solution must satisfy a compatibility condition to consistently support a shock. The conclusion must be made that the problem is inherently nonlinear because this particular boundary condition is nonlinear. In a particular case, as in the one reported here by

[1] See p. 87.

420-093 O - 71 - 27

Seebass, consistency in the shock conditions may be found to occur, at least to a high degree of accuracy.

In the case of the region near a conical singular ray, discussed in these proceedings by Hayes et al.,[2] the same situation holds. There are two independent shock conditions, and the shock must be located as part of the solution in the large.

In the standard Landau-Whitham theory for signal distortion and shock development, the solution is governed by an equation noted by Chandrasekhar and sometimes termed the inviscid Burgers' equation. Two shock conditions may be derived, one for shock speed and one for shock strength. A condition for continuity of velocity potential may be derived from these two. The situation is, however, different from that of the two problems discussed above. A first integral to the governing equation may be found, actually in the form considered as a governing equation by Poisson. The constant in this first integral may be shown to be zero and thereby continuous across a shock. This result links the two shock conditions so that they are not independent. In this problem, as is well known, shocks may be fitted, when needed, to an arbitrary signal.

It would seem, then, that a numerical solution to the caustic problem cannot be avoided. It would probably be worthwhile to increase the quite modest efforts now being made in this direction. The numerical problem is inherently a very difficult one, and more than one approach should be followed. If several approaches succeed, the ability to compare their results would be most valuable and would lend confidence in their accuracy.

REFERENCE

1. HAYES, WALLACE D.: Similarity Rules for Nonlinear Acoustic Propagation Through a Caustic. Second Conference on Sonic Boom Research, NASA SP–180, 1968, pp. 165–171.

[2] See p. 27.

Remarks on Nonlinear Effects

M. LANDAHL
Aeronautical Research Institute of Sweden

One of the main purposes of an analysis of nonlinear effects on the sonic boom is to assess the accuracy of first-order theory. From comparisons with the two-term expansion for large distances, one concludes that, for the very slender configurations of current interest, geometrical acoustics does indeed provide a very good approximation to the flow field that should hold to within a distance of very few body lengths, even at fairly high Mach numbers. The developed second-order solution allows one to get within a distance from the body of perhaps one body length. The usual method of determining the far field and the associated shocks by aid of the Whitham F-function would therefore be quite adequate, except that the F-function will differ from what is given by the linear theory by terms that are of second order in equivalent body thickness ratio. These may become important at Mach numbers of 3 and higher. For accurate sonic boom calculations, one would therefore need better information about the near field than that provided by linearized theory. Such could be obtained from theory, direct numerical calculations, or experiments, depending on whatever method is available with sufficient accuracy. Judging from its success in predicting surface pressures, second-order theory would be quite adequate for slender configurations, even at quite high Mach numbers. There is not much hope of finding a reasonably simple second-order analytical solution for a general three-dimensional flow field, but the simple structure of the axisymmetric solution gives helpful clues as to how one should construct good approximate ones. In the solution for axisymmetric flow, the main second-order effects are retained in the linear solution if the variables in this are transformed in such a manner that both families of characteristics are made straight. One would therefore conclude that any good approximate theory would need to account for the deformation of characteristic surfaces.

There are other possible applications of the nonlinear solution for large distances that readily suggest themselves. One is to the calculation of correction for near-field effects of experiments in a wind tunnel aimed at determining the Whitham F-function from measurements of the flow

field close to the body, as we reported.[1] Another use is for development of wind-tunnel correction formulas to account for nonuniformities in the flow that become very important for the kind of extremely slender low-boom configurations discussed by Dr. Ferri.[2] Correction for linear effects is simple, but for high Mach numbers the nonlinear effects of flow nonuniformity become important, and these can be worked out approximately from the second-order theory.

Finally, I would like to point out a somewhat subtle distinction between geometrical acoustics and Whitham's theory which is important in the understanding of higher order effects. The former says that the pressure decreases along the ray with distance as the inverse of the square root of the stream tube area; i.e., with r. The latter in addition states something more, namely that the pressure (or u-perturbation velocity) is the same function of the downstream characteristic coordinate as that given by linear theory. It is generally assumed that the characteristic variable value is obtained from the intercept of the curved characteristic line with the x-axis. However, Whitham's theory actually uses the specific form

$$x-\beta r=y-kr^{1/2}F(y)$$

which is a far-field approximation adjusted so that, formally, $x-\beta r=y$ for $r=0$. Actually the first-order far-field solution says that instead of y, any function of y would do; e.g., $g(y)$, so that in general

$$x-\beta r=g(y)-kr^{1/2}F(y)$$

with $g(y)$ arbitrary. There are several ways that one could choose g, the most reasonable way perhaps being to determine it from the true intercept (not the one predicted by the asymptotic expression) with the body surface. However, if one is to use the specific graphical technique usually employed in connection with Whitham's theory with lines of constant $x-\beta r$ being straight lines of slope $(kr)^{1/2}$ in the $F(y)$ diagram for each value of r, it is necessary that the labeling of each characteristic follow the Whitham formula. Thus, if one uses, for example, a graphical technique to determine the characteristic lines, it is important to select the labeling of each line characteristic so as to approach that given by the Whitham formula for large distances.

---

[1] See p. 285.

[2] See p. 255.

Comments on Sonic Boom in a Laminar Atmosphere

HARVARD LOMAX
NASA Ames Research Center

As Dr. Kurzweg mentioned in his opening remarks, we have made a significant increase in our understanding of the control of boom overpressures since the first Sonic Boom Conference held in 1967. At present our studies indicate that if the sonic boom were the only consideration, a 450 000-lb, 300-ft-long airplane could fly at a Mach number of 2.6 and create a noise hazard no more severe than the rumble of thunder. Assuming this noise level to be acceptable, there remains, however, the very difficult task of designing an airplane with this capability that is also aerodynamically efficient. This difficulty is certainly not lessened by our present environment of limited finances—finances, which must, for a rational development, support experiments made both in flight and in wind tunnels, as well as the advancement of theoretical prediction techniques for both laminar and turbulent atmospheres.

Speaking for the development and exploitation of the theoretical prediction of sonic booms in a laminar atmosphere, it is clear that the application of the Whitham theory to the cross-sectional area and lift of the airplane itself is inadequate at Mach numbers around 3.0 for many configurations. However, it appears to be generally accepted that signatures established some distance from the body (a few body lengths) can be extrapolated downward in a laminar atmosphere by theories based on the concept introduced by Whitham. It also appears that shapes of these "near-body" signatures can be formulated that will give acceptable near-field (around 150 body lengths) pressure distributions having a flattened N-wave appearance. One vital question at present is: What are the exact details of an airplane shape that will provide an appropriate near-body signature? It is this aspect of the overall problem for which theories that make solutions uniformly valid, that include the effects of higher order nonlinear terms, and that make use of finite differencing techniques have their highest value. To develop confidence in the reliability of such theories, they should be applied to identical airplane-like configurations, simple at first and then increasingly complex. Results of such applications should be compared, and discrepancies explained.

This will suggest the formulation of verifying wind-tunnel experiments. The successful accomplishment of such a combination of tasks would provide a powerful design tool for producing airplanes that would have acceptable sonic boom signatures.

Comments on Sonic Boom Research

R. SEEBASS
Cornell University

There is an advantage as well as a disadvantage in being the last to speak. The advantage accrues from previous speakers covering much of what needs to be said; the disadvantage is, of course, that they may have said everything that is worth hearing. Fortunately, they have done their work well and I can be brief; still, they left some important points to be made.

The current budget situation dictates that we adopt a pragmatic and tough-minded view of sonic boom research needs. We must determine today, as best we can, what the future direction and scope of sonic boom research will be, realizing that economic constraints limit this scope more than we would like. Also, we should adopt the view that the first few generations of supersonic transport (SST) aircraft, if they are built at all, will be limited to supersonic operation over oceanic and polar regions. With this in mind, let me discuss what I believe to be the major questions that further research must answer.

The superboom that occurs when SST's accelerate to supersonic speeds will usually occur in coastal waters; over a period of years, a significant number of vessels and their occupants will be subjected to them. Clearly, we must determine the nature of this superboom and be able to make reasonable predictions about its strength.

With SST aircraft restrained from operations that cause a sonic boom to reach the territorial surface of many countries, we must determine whether the increased utilization and speed of slightly supersonic operation is practical and feasible. Can we prescribe operational constraints that will insure that no unacceptable signals reach the ground? And if these conditions are violated, what are the consequences?

The pollutant aspect of the sonic boom has reduced the economic vindication of SST's from a resounding yes to a quiet question mark. But if we can design later generation SST's with truly acceptable sonic boom signatures, then there is no doubt that SST aircraft, as a class, will be economically successful. So we must know how well we can do, in principle and in fact, in alleviating the unacceptable feature of the overpressure signature. We cannot, however, wait for the "psychoacousti-

cians" to tell us how to weight signature parameters such as shock pressure rise, rise time, overpressure and impulse in determining sonic boom acceptability. Rather, we must tell them how well we can do in optimizing these parameters and ask the simpler question of whether or not any of the signatures we can achieve are likely to be acceptable.

Our progress in the area of sonic boom reduction has been dramatic since Mr. McLean noted the extent of the mid field in a homogeneous atmosphere and Professor Hayes showed us that signature distortions much beyond one scale height were negligible. The more we work on the minimization problem, the more difficult it becomes to rule out a domestic SST.

With the SST in financial trouble, we are beginning to hear more about a hypersonic transport (HST). For such a vehicle to make sense it must have a long range, and if it is to use that range effectively, it must have acceptable sonic boom characteristics. The sonic boom component of HST research seems to me to be sorely missing and in need of greater emphasis.

We must continue to test sound theoretical ideas in the wind tunnel, both to verify our theories and to test our wind-tunnel techniques so that we can be sure of them even when our theories fail. But we must avoid wind-tunnel tests that verify the obvious. Field tests are even more expensive and must be limited to projects with high scientific content.

Finally, let us not forget that one way to reduce the sonic boom is to increase the overall efficiency of the aircraft. Improvements in the lift-to-drag ratio, the engine thrust-to-weight ratio, structural efficiency, and specific fuel consumption reduce the aircraft's sonic boom. Any penalties in these parameters that result from modifications that reduce the sonic boom must indeed be modest to be acceptable. Sonic boom research must continue; perhaps it should be expanded. But certainly such expansion must not be at the expense of research that relates directly to the aircraft's performance.

GENERAL REMARKS

420-093 O - 71 - 28

Comments on Low Sonic Boom Configuration Research

LYNN W. HUNTON
NASA Ames Research Center

From results of numerous sonic boom tests of a wide range of wing-body configurations, it has been found that the available theoretical methods based on first-order theory for calculating lift and sonic boom (refs. 1 and 2, respectively) have limitations at moderately high Mach numbers (above 2) that are sufficiently restrictive to compromise to some extent the effectiveness of these methods for low-boom configuration research. As a result, basic design problems have been encountered in transforming an optimum area distribution for low boom to an equivalent lifting airplane configuration. An attempt is made here to comment on some of these design and testing problems as interpreted by Ames and to present a data sample in support of the discussion.

One problem in the assessment of sonic boom for a given airplane design is centered on the calculation of the vehicle lift distribution. Because the lift at cruise represents perhaps 50 to 70 percent of the equivalent cross-sectional area of the vehicle for sonic boom calculation purposes, small changes in the lift distribution due to either design changes or problems of accuracy in the theory can lead to significant effects in the final overpressure results. While it is generally recognized that the more sophisticated methods available for calculating loads on wing-body combinations at supersonic speed do provide quite accurate estimates of gross lift effects (e.g., lift curve slope), these same methods (refs. 1 and 3) do not yield accurate predictions of center of pressure at the higher Mach numbers. Deficiencies in the calculated loadings, usually a rearward shift of load for sweptback wings, are found to increase with increase in Mach number above 2, as illustrated in figure 6 of reference 4. Because the overpressure characteristics for low boom configuration concepts are generally rather sensitive to small deviations in the equivalent area distribution, any deficiency in loading theory can greatly compound the overall design problem.

Another factor influencing the design problem of wing-body shapes is the failure of the slender-body expansion method of Whitham to provide the accurate prediction of the F-function at the higher supersonic Mach

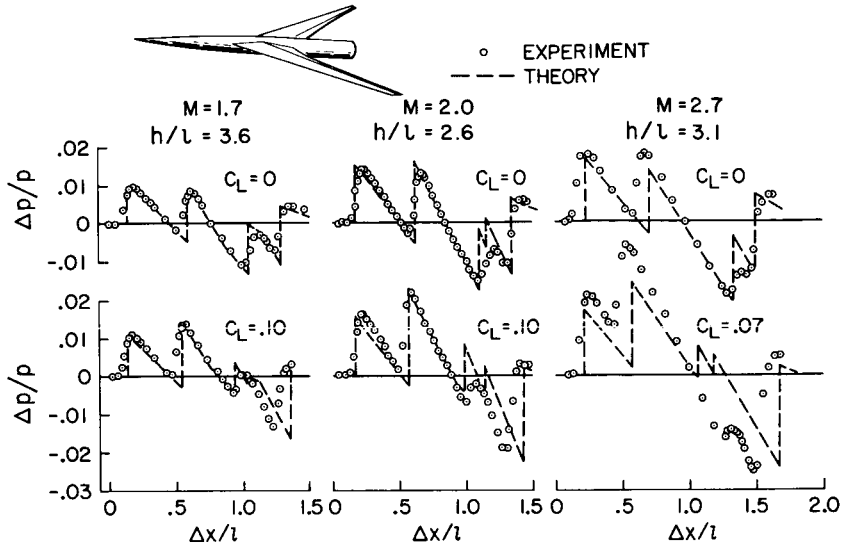

FIGURE 1.—Correlation of Mach number effect for sweptback wing model.

numbers that is required for the derivation and/or extrapolation of pressure signatures for midfield distances commensurate with flight altitudes. Studies conducted at Ames Research Center (also at Langley Research Center; see Morris' paper [1]) show this problem to be significant for Mach numbers above about 2. The limitations of the Whitham theory (that includes only first-order nonlinear effects) at the higher Mach numbers were reviewed by both Landahl [2] and Woodward [3] at this conference. An example of the discrepancy found between theory and experiment is shown in figure 1 for a swept-wing model tested at two values of lift coefficient at Mach numbers of 1.7, 2.0, and 2.7. The wing had a 69° sweptback leading edge and a symmetrical double-wedge section with a maximum thickness ratio of 0.05. In general, it is found that the theory tends to underestimate the maximum shock pressures, the pressure impulses, and the rates of pressure expansion behind each shock. The data also illustrate the deficiency of the theory in predicting the location of intermediate shocks as they progress toward either the bow or tail shocks with increase in lift coefficient. The comparisons at zero lift serve to isolate at least a portion of the deficiency in the boom theory. However, for the comparisons at lift, any division of the deficiency in theory between loading theory and boom theory will remain in question

[1] See p. 193.
[2] See pp. 3 and 285.
[3] See p. 437.

until pressure measurements on the model can be obtained. Attempts are continuing by several research teams (e.g., Landahl with his method of parametric differentiation as covered at this conference [4] and in ref. 5) to find improved analytical solutions for both the lift and the overpressure characteristics at high Mach numbers. In the meantime, on the basis of the information at hand, it is the consensus at Ames that the present first-order theories are limited in scope of application somewhat more than has been commonly accepted and, consequently, will provide only a preliminary guide to the overpressure characteristics for lifting configurations at Mach numbers greater than about 2.

The indicated lack of agreement between first-order theory and experiment can cause significant differences in the predicted boom characteristics at flight distance ratios. To illustrate for the case cited in figure 1, a comparison of the predicted overpressure ratio characteristics from theory and from experiment (extrapolated from wind-tunnel data for $h/l=3.1$) is shown in figure 2 for a distance ratio of 200 body lengths at a Mach number of 2.7 for two values of lift coefficient. These extrapolated signatures represent conditions on the ground with no reflection amplification for the subject configuration with a length of 300 ft cruising at a 60 000-ft altitude (weight of about 520 000 lb for the lifting condition indicated). The percentage discrepancy in figure 2 between theory and experiment can be seen to exceed 30 percent for either C_L tested. Unfortunately, this result is not unique because it has been found in a number of other similar analyses of theory and wind-tunnel results at Mach numbers above 2. The extrapolations here were made using the method of Thomas[5] that includes real atmosphere effects (use of an alternative method (ref. 6) would be expected to provide a similar extrapolation result). Under the indicated conditions, the reference pressure p is the atmospheric pressure at the ground. Use of a uniform-atmosphere solution in the extrapolation would increase the discrepancy between theory and experiment.

With regard to experimental problems in sonic boom research, it is essential that the techniques and assumptions used be continuously questioned as one requisite for assuring the maximum in reliability from experimental research. Professor Landahl[6] has suggested the role of second-order effects in the interpretation of experimental data obtained at high Mach numbers and, in addition, proposes an improved experimental technique utilizing measurements of flow inclination rather than the conventional direct measurement of pressures with a probe. Because of the critical problems encountered with high-Mach-number measure-

[4] See p. 3.
[5] See p. 205.
[6] See p. 285.

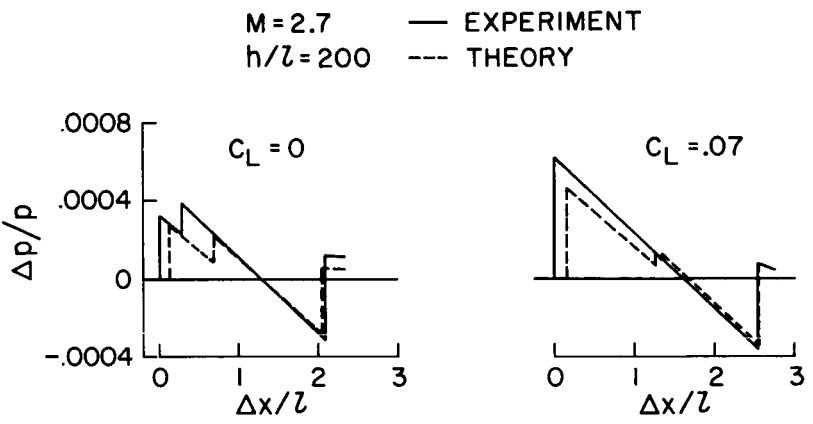

FIGURE 2.—Comparison of the predicted overpressure ratio characteristics from theory and experiment.

ments (e.g., probe design for large shock angle, sting interference, etc.), a comparison of these proposals with current testing procedures warrants a careful appraisal by the experimenter.

In summary, the available first-order analytical methods for predicting the sonic boom of lifting aircraft are found to be limited in accuracy for flight Mach numbers greater than 2. The underlying difficulty appears to stem from two sources; namely, deficiencies in the calculation methods for the lift distribution and for the boom. Until such time as ongoing studies produce improved analytical methods for the $M > 2$ case, it is believed that near-field measurements obtained in the wind tunnel will provide the most reliable basis for the prediction of the overpressure characteristics of general aircraft configurations. However, this observation is not to be interpreted to imply that a completely satisfactory level of competence has been reached in the status of wind-tunnel testing techniques that include the technology of scaled model design to accurately represent the flight airplane for near-field measurements. Principal design problems needing attention here include such details as the model shape adjustments required to represent the airplane scaling effects, to represent the engine nacelles, and to account for the body closure effects and the support sting hardware and attendant interference effects. Finally, real atmosphere effects cannot be neglected in studies of design concepts for low boom that depend on nonasymptotic effects for the improvements sought.

REFERENCES

1. WOODWARD, F. A.; TINOCO, E. N.; AND LARSEN, J. W.: Analysis and Design of Supersonic Wing-Body Combinations, Including Flow Properties in the Near Field, Part I: Theory and Application. NASA CR-73106, 1967.

2. WHITHAM, G. B.: The Flow Pattern of a Supersonic Projectile. Commun. Pure Appl. Math, vol. 5, 1952, pp. 301–348.
3. CARMICHAEL, R. L.; CASTELLANO, C. R.; AND CHEN, C. F.: The Use of Finite Element Methods for Predicting the Aerodynamics of Wing-Body Combinations. Analytic Methods in Aircraft Aerodynamics, NASA SP–228, 1970, pp. 37–51.
4. NELMS, W. P.; CARMICHAEL, R. L.; AND CASTELLANO, C. R.: An Experimental and Theoretical Investigation of a Symmetrical and a Cambered Delta Wing Configuration at Mach Numbers From 2.0 to 10.7. NASA TN D–5272, 1969.
5. LANDAHL, M. T.; RYHMING, I. L.; AND HILDING, L.: Nonlinear Effects on Sonic Boom Intensity. Second Conference on Sonic Boom Research, NASA SP–180, 1968, pp. 117–124.
6. HAYES, W. H.; HAEFELI, R. C.; AND KULSRUD, H. E.: Sonic Boom Propagation in a Stratified Atmosphere, With Computer Program. Rept. no. 116, Aeronautical Research Associates of Princeton, Inc., Dec. 1968.

On the Analytical Method of Characteristics

HELGE NØRSTRUD
Lockheed-Georgia Co.

In view of a paper (ref. 1) presented at the Second Conference on Sonic Boom Research, it seems appropriate to draw attention to some new, but seemingly unnoticed, developments on the subject of analytical prediction of nonlinear wave propagation. The paper expresses the need for analytical methods for the near-flow region about arbitrary aircraft configurations and labels the available theories either too cumbersome (e.g., method of characteristics) or too limited in their application. As also pointed out in reference 2, the theory of Whitham (ref. 3) exhibits limitations of the latter kind. It is my intention to describe briefly an analytical method of characteristics that has the potential of yielding improvements in both areas of concern.

There are several reported works that seek to predict more accurately the local disturbance field of a given origin (e.g., ref. 4) or the propagation pattern of these disturbances (ref. 5) in a more global frame. The major difficulties, however, lie in a simultaneous description of both these qualities. It is therefore of importance to realize that the theory, which subsequently will be discussed, is valid for the entire flow field and is exact within its order of approximation.

The first treatise on the analytical method of characteristics was published by Professor Oswatitsch in 1962 (ref. 6) and was concerned with isentropic wave propagation in two dimensions. Based on similar thoughts advanced by Lin (ref. 7), the independent variables chosen by Oswatitsch are the characteristic manifold. This insures the correct inclusion of the range of influence and the domain of dependence. The method was later extended to three independent variables (ref. 8) for which the role of the bicharacteristics became significant in its general formulation (e.g., ref. 9).

Lin's work has been referred to in reference 10 as a generalization of the method of strained coordinates (or the PLK method), which is also the technique adopted by Whitham (ref. 3). Hence, an analogy can be found between these methods and Oswatitsch's approach. However, the main difference is that the analytical method of characteristics always

uses a complete set of characteristic coordinates as the independent variables.

The conceptual steps in the method of Oswatitsch are first to express the physical coordinates x_i (including the time) in the characteristic space ξ, η, ζ in a series form of, in general, increasing order terms (identified with upper indices) of some small-perturbation parameter; i.e.,

$$x_i(\xi, \eta, \zeta) = x_i^{(0)}(\xi, \eta, \zeta) + x_i^{(1)}(\xi, \eta, \zeta) + \cdots \tag{1}$$

Likewise, the dependent variables v_j (kinematical and state quantities) are written as

$$v_j(\xi, \eta, \zeta) = v_j^{(0)}(\xi, \eta, \zeta) + v_j^{(1)}(\xi, \eta, \zeta) + \cdots \tag{2}$$

Series (1) and (2) are then substituted in the hyperbolic system under

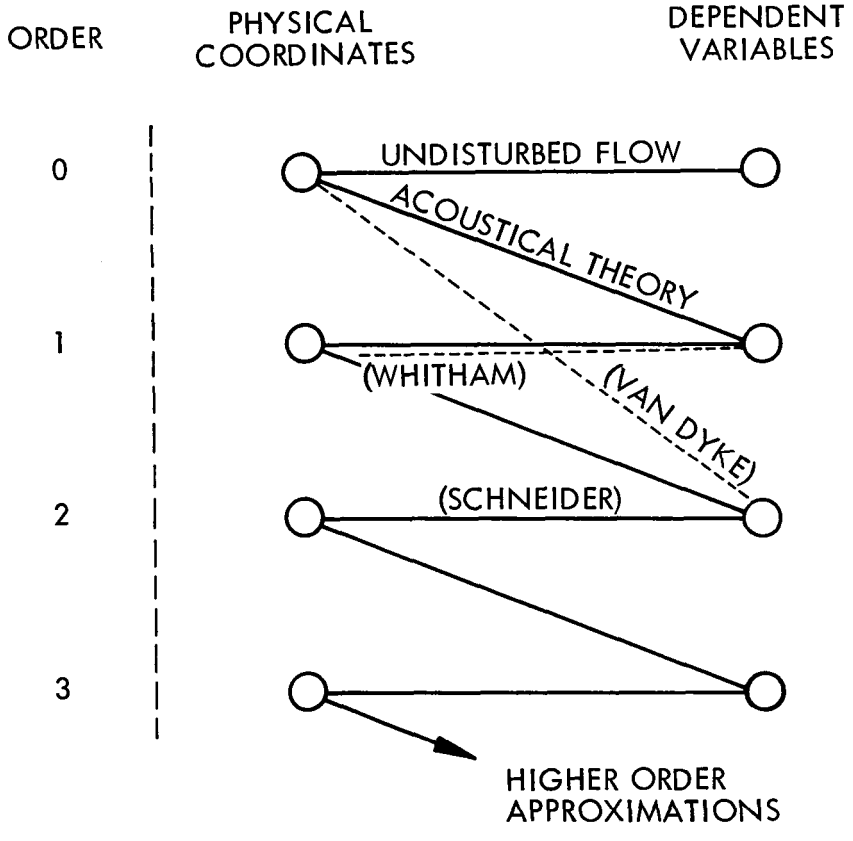

FIGURE 1.—Graphical representation of the analytical method of characteristics of Oswatitsch.

consideration, and the physical coordinates (now dependent variables) are obtained by integration along bicharacteristic lines. The dependent variables for given boundary and initial conditions (written in the characteristic space) are found from the compatibility relations. This procedure can now be repeated in an iterative manner until the desired degree of accuracy is reached (fig. 1).

Let the zeroth-order formulation of equations (1) and (2) correspond to some undisturbed supersonic flow. The solution given by the linearized acoustical (e.g., Ackeret) theory is then equivalent to a first-order approximation of the disturbances of the dependent variables (eq. (2)) in the undisturbed space. The cumulative effects of these disturbances at large distances away from their origin are well known and can be accounted for, in addition, by considering first-order terms in the coordinate relations (eq. (1)). Weak shocks and generalized Prandtl-Meyer expansions are included in this approximation (e.g., refs. 2, 11, 12), with the shocks being represented as overlapping of characteristic surfaces in the physical space. Complete agreement with results from Whitham's theory can be found by application of a first-order theory as reported by Schneider (ref. 13). Furthermore, his results for conical flow are compared in figure 2 with the various order approximations of Caughey (ref. 5). It is interesting to note the deviation between the two first-order solutions, which is due to the difference in the analytical space in which

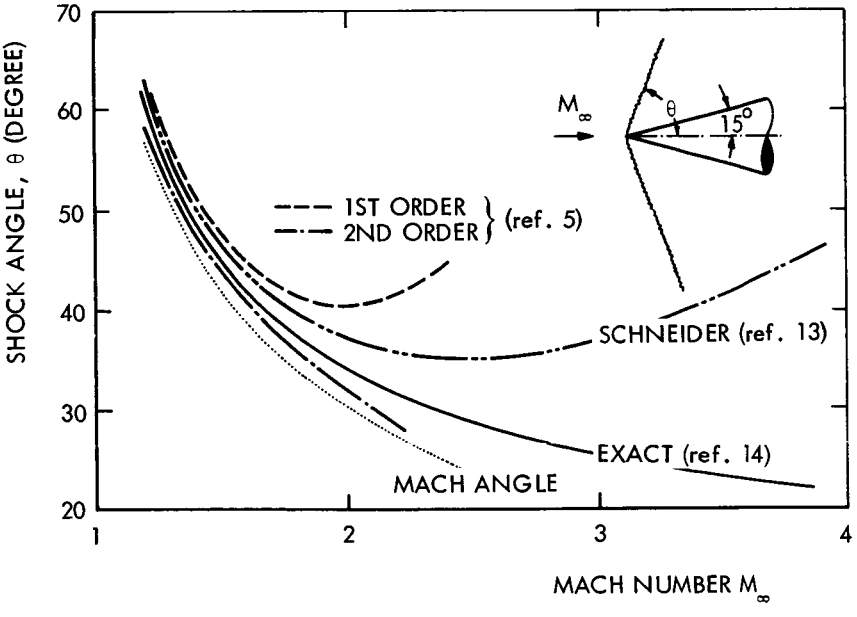

FIGURE 2.—Shock angle on a 15° cone in supersonic flow.

the order of approximation is being considered. Schneider also gives higher order solutions for this type of flow and shows these to be in excellent agreement with Van Dyke's second-order body solution (ref. 15).

Inhomogeneous effects on the wave propagation through an isothermal and polytropic stratified atmosphere, with partial inclusion of aircraft acceleration and deceleration, have been studied by Stuff (refs. 16 and 17, respectively) with a modified version of the method of Oswatitsch. He obtains, in particular, explicit relations for the decay properties of the shock strength under the assumed atmospheric conditions. (See also the written remarks by Stuff in this volume.) [1]

I have tried to summarize some of the pertinent points in connection with the analytical method of characteristics. It is felt that this method is fundamental to any study of supersonic flow and should not be overlooked in the theoretical aspect of the sonic boom problem. Indeed, the very fact that the method has apparently not been recognized by NASA has ruled out an analytical technique capable of treating three-dimensional aspects, which also might be useful for boom minimization.

REFERENCES

1. HUNTON, L. W.: Current Research in Sonic Boom. Second Conference on Sonic Boom Research, NASA SP–180, 1968, pp. 57–66.
2. OSWATITSCH, K.; AND SUN, Y. C.: The Influence of Near-Field Flow on the Sonic Boom. ICAS Paper no. 70–20, 1970.
3. WHITHAM, G. B.: The Flow Pattern of a Supersonic Projectile. Commun. Pure Appl. Math., vol. 5, 1952, pp. 301–348.
4. WOODWARD, F. A.; HUNTON, L. W.; AND GROSS, A. R.: A New Method for Calculating Near and Far Field Pressure About Arbitrary Configurations. Analytic Methods in Aircraft Aerodynamics, NASA SP–228, 1970, pp. 215–225.
5. CAUGHEY, D. A.: Second Order Wave Structure in Supersonic Flows. NASA CR–1438, 1969.
6. OSWATITSCH, K.: Das Ausbreiten von Wellen endlicher Amplitude. Z. Flugwiss., vol. 10, 1962, pp. 130–138.
7. LIN, C. C.: On a Perturbation Theory Based on the Method of Characteristics. J. Math. Phys., Cambridge, Mass., vol. 33, 1954, pp. 117–134.
8. OSWATITSCH, K.: Die Wellenausbreitung in der Ebene bei kleinen Störungen. Arch. Mech. Stosowanej, vol. 14, 1962, pp. 621–637.
9. LEITER, E.; AND OSWATITSCH, K.: Die Anwendung der Monge-Gleichung auf Ausbreitungsvorgänge in Gasen. Acta Mech., vol. 8, 1969, pp. 213–234.
10. VAN DYKE, M.: Perturbation Methods in Fluid Mechanics. Academic Press, Inc., 1964, p. 100.
11. OSWATITSCH, K.: Sonic Boom of Bodies of Revolution. AGARD Conf. Proc. no. 42, 1969, pp. 11–1 to 11–9.
12. LEITER, E.: Stationäre Expansionsströmungen an räumlichen Überschallkanten. Acta Mech., vol. 8, 1969, pp. 235–254.
13. SCHNEIDER, W.: Analytische Berechnung achsensymmetrischer Überschallströmungen mit Stössen. DVL-Bericht no. 275, 1963.
14. AMES RESEARCH STAFF: Equations, Tables, and Charts for Compressible Flow. NACA Rept. 1135, 1953.

[1] See p. 429.

15. VAN DYKE, M. D.: Second-Order Slender-Body Theory – Axisymmetric Flow. NASA TR R-47, 1959.
16. STUFF, R.: Die Theorie der Knallausbreitung in einer geschichteten Atmosphäre. Z. Flugwiss., vol. 17, 1969, pp. 156–164.
17. STUFF, R.: Die vertikale Ausbreitung von ebenen Stosswellen in einer schweregeschichteten Atmosphäre mit einem Temperaturgradienten. Z. Flugwiss., vol. 18, 1970, pp. 80–83.

Entropy and the Sonic Boom

BERTRAM PARISER
Columbia University

The motivation for the development of supersonic aircraft is to reduce the effective passenger and cargo transportation time over long distances. However, because of the sonic boom (a pressure disturbance of 1 to 4 lb/ft^2 on the ground), the future of the supersonic transport may be limited to flight over water. It is therefore necessary to remove this severe travel restriction by finding a way to reduce the sonic boom. Research, considering the entropy of the entire system, should be conducted in this area.

Entropy is a measure of the amount of disorder of a system. The second law of thermodynamics states that the entropy tends to be an increasing function, that a system tends toward more disorder. The system of energy associated with supersonic flight is shown below. Because the energy distribution is large, this system is in a state of high entropy or disorder. The second law of thermodynamics also states that work must be done to decrease the entropy. Therefore, to reduce the sonic boom and its energy contribution, work must be done on the system.

Energy System of the SST

Kinetic energy of the aircraft
Potential energy of the aircraft
Energy associated with shock dissipation:
- Bow shock
- Tail shock
- Other shock phenomena

Energy dissipation from the engines:
- Heat
- Light
- Sound

Energy associated with aerodynamic dissipation:
- Turbulence
- Drag

Atomic and molecular energy

The conventional approach to the sonic boom problem is to obtain a pressure signature by use of a Whitham F-function. Various valid and

well-documented proposals to minimize the pressure signature have been presented at this conference; e.g., a proposal to minimize the sonic boom through the introduction of a thermal fin, a proposal to introduce aerodynamic drag on a wing section of the aircraft, and a proposal to limit the cross-sectional area of the aircraft to several feet. These alternatives supply the work needed to decrease the entropy as the sonic boom is decreased. However, this work results in higher fuel consumption or slower airspeeds. In the design criteria of the supersonic transport, perhaps the entropy of the entire system should be considered before lengthy computer calculations are performed to minimize one part of that system, the sonic boom.

Finally, I strongly recommend using laser or microwave radiation to examine shock structure. Laser systems can be designed to measure changes in the index of refraction of air caused by the sonic boom. This diagnostic technique does not perturb the aerodynamic flow field. Consequently, laser systems offer a great advantage over static probes in the measurement of the sonic boom.

Some Recent Sonic Boom Research in Germany

ROLAND STUFF
Deutsche Forschungs- und Versuchsanstalt für Luft- und Raumfahrt (DFVLR)

In the Institute for Theoretical Gasdynamics of the DFVLR, several problems concerning sonic boom have been studied by means of an analytical characteristic method of Oswatitsch (refs. 1 to 8). Some recent work has been done with regard to sonic boom wind-tunnel measurements on an annular wing (ref. 9), to a delta wing with supersonic leading edges at an angle of attack (ref. 10), and to the influence of polytropic atmospheric stratification (ref. 11).

CLOSED-FORM SOLUTION FOR THE SONIC BOOM IN A POLYTROPIC ATMOSPHERE

Because the analytical solution describing the wave propagation in a polytropic atmosphere serves as the initial solution to the method of strained coordinates, it must be known previously. For a spherical source located at P (fig. 1), this solution is given by

$$\frac{U_{1N}}{c_0(z_0)} = \left(\frac{c_{0p}p_{0p}}{c_0(z_0)p_0(z_0)}\right)^{1/2} \frac{\partial F}{\partial t_0} \tag{1}$$

with

$$F = \frac{f\left(t_0 - \int_0^{s_0} \frac{ds_0}{c_0(s_0)}\right)}{\frac{c_0(z_0)}{c_{0p}} R_0} \tag{2}$$

where U_{1N} is the first-order perturbated velocity in the normal direction to the wavefront. $c_0(z_0)$ and $p_0(z_0)$ are the local sound velocity and the local static pressure, respectively, and c_{0p} and p_{0p} the corresponding quantities at flight altitude. F corresponds to the retarded potential of a homogeneous atmosphere, and R_0 is the instantaneous radius of the wavefront (fig. 1). The stretched coordinates are obtained by integrating along the bicharacteristics μ and ν.

420-093 O - 71 - 29

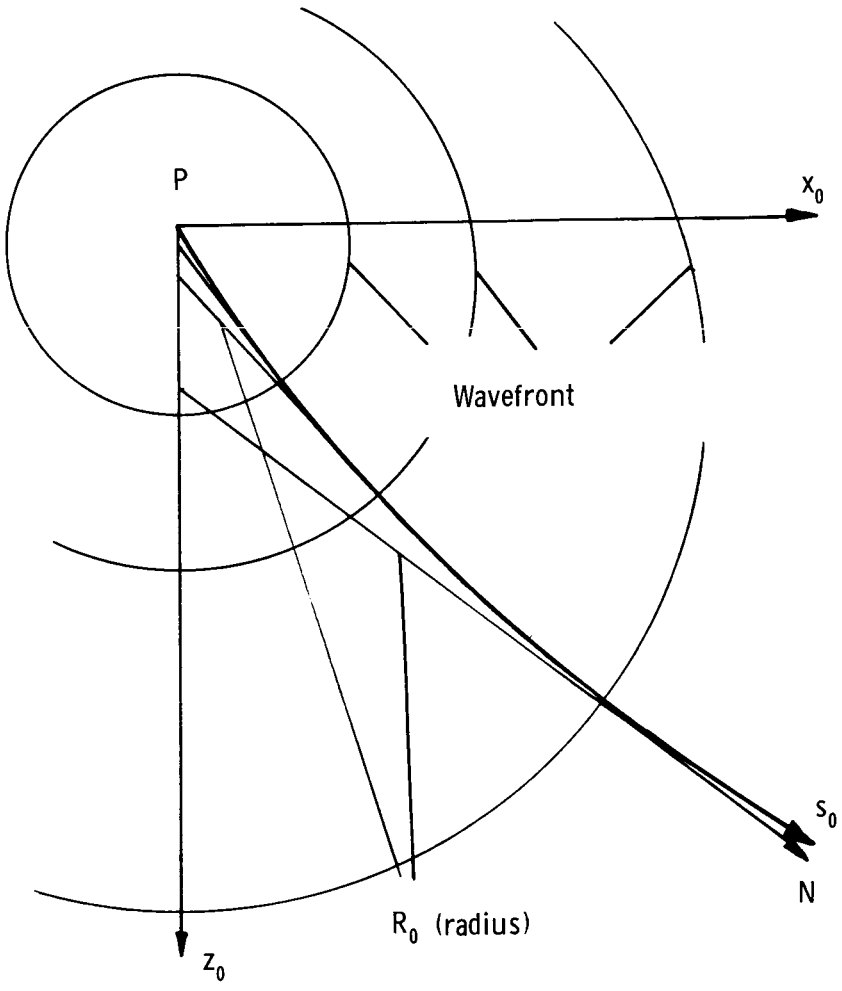

FIGURE 1.—Spherical source in a polytropic atmosphere.

$$\mu = \bar{t}_0 + \bar{s}_0 \tag{3}$$

$$\nu = \bar{t}_0 - \bar{s}_0 \tag{4}$$

with

$$\bar{s}_0 = \int_0^{s_0} \frac{c_{0p}}{c_0(\tilde{s}_0)}\, d\tilde{s}_0 \tag{5}$$

and

$$\bar{t}_0 = \frac{t_0 c_{0p}}{l} \tag{6}$$

where s_0 is the ray path, t_0 the real time, and l the body length.

The aircraft's flight is at supersonic velocities that are accelerated

or decelerated on a straight line as shown on figure 2. The flightpath lies in a vertical plane denoted by x_0 and z_0 and is inclined by the angle ζ to the horizontal x_0-axis. The perturbations propagating along ray s_0 will be observed. The vertical plane containing the ray makes a horizontal angle θ with the x_0-axes. The propagation below the aircraft is indicated by $\theta = 0°$. Now replacing the flight vehicle by a distribution of sources and sinks (eqs. (1) and (2)), the perturbated pressure p_1 is obtained by

$$\frac{p_1}{p_0} = \kappa M^2 \sqrt{\frac{M}{2}} F_1(2\nu M) \mathscr{G}'(\mu) \tag{7}$$

with κ as ratio of the specific heats, M as the Mach number related to c_{0p}, $F_1(2\nu M)$ as the Whitham function (eq. (8)), and $\mathscr{G}'(\mu)$ as the distance function defined by equation (9)

$$F_1(2\nu M) = \frac{1}{2\pi} \int_0^{2\nu M} \frac{s''(\xi)}{\sqrt{2\nu M - \xi'}} \, d\xi \tag{8}$$

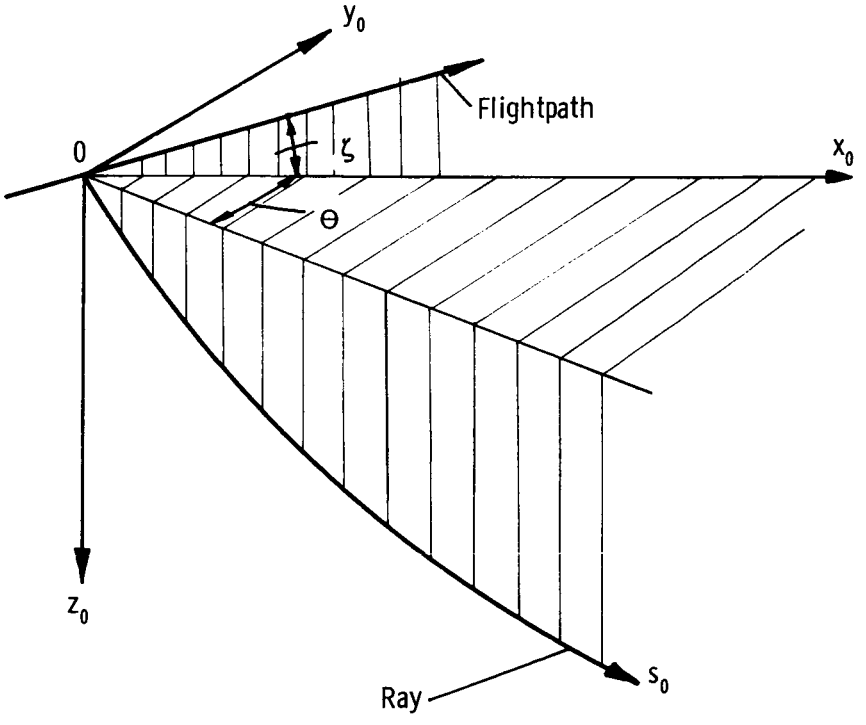

FIGURE 2.—Flightpath and ray.

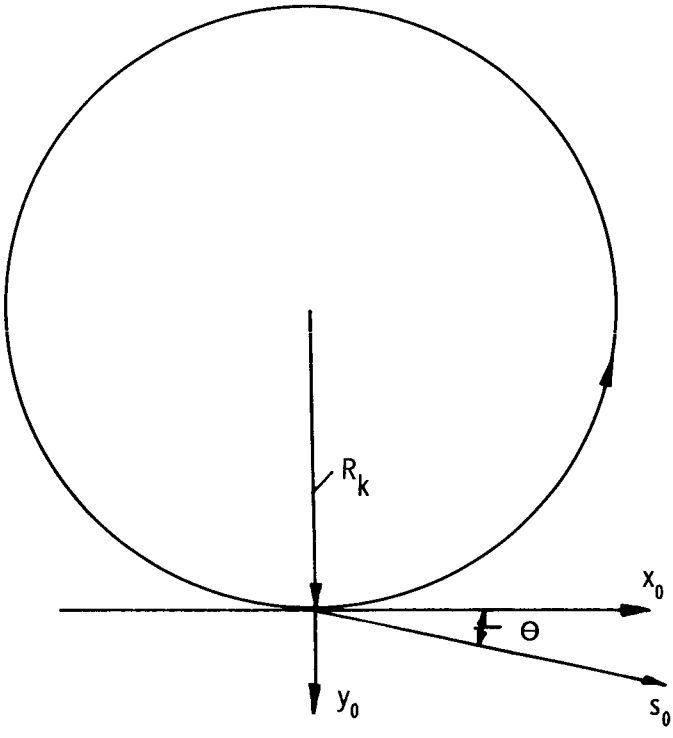

FIGURE 3.—Curved flight.

$$\mathcal{G}^1(\mu)=\left(\frac{c_{0p}p_{0p}}{c_0p_0}\right)^{1/2}\frac{c_{0p}}{c_0}\sqrt{\frac{M^2(\cos^2\zeta\cos^2\theta+\sin^2\zeta)-1}{(M^2-1)\dfrac{1}{A}\sinh|A\mu|\cosh|A\mu|}}$$

$$\times\left(M^2(\cos^2\zeta\cos^2\theta+\sin^2\zeta)-1\right.$$

$$\left.-\left([M\cos\theta\cos\zeta\sqrt{M^2(\cos^2\zeta\cos^2\theta+\sin^2\zeta)-1}+M\sin\zeta]A+\frac{B_t}{M}\right)\frac{1}{A}\tanh|A\mu|\right)^{-1/2} \tag{9}$$

$$A=\frac{\dfrac{dc_0}{dz_0}l}{c_{0p}}\qquad B_t=\frac{bl}{c_{0p}^2} \tag{10}$$

The constant A follows from the sound speed gradient dc_0/dz_0, and the constant B_t, from the real acceleration b. The denominator in equation (9) is zero when the waves form a cusp. However, this singularity is integrable, and the shocks behind the cusp can be calculated. For $\theta=0^0$ and $dc_0/dz_0=0$, the formulas for the isothermal atmosphere (ref. 12)

can be obtained. Because the flight vehicle is replaced by a distribution of sources and sinks, further flight maneuvers can be taken into account; e.g., for curved flight (fig. 3) we obtain

$$\mathcal{G}'(\mu)=\left(\frac{c_{0p}p_{0p}}{c_0p_0}\right)^{1/2}\frac{c_{0p}}{c_0}\sqrt{\frac{M^2\cos^2\theta-1}{(M^2-1)\frac{1}{A}\sinh|A\mu|\cosh|A\mu|}}$$
$$\times\left(M^2\cos^2\theta-1-\left(M\cos\theta\sqrt{M^2\cos^2\theta-1}\,A+\frac{1}{M}[B_t+\tan\theta B_r]\right)\right.$$
$$\left.\times\frac{1}{A}\tanh|A\mu|\right)^{-1/2} \tag{11}$$

with

$$B_r=\frac{M^2}{R_k}$$

Here B_r is the dimensionless angular acceleration. Defining

$$\mathcal{G}(\mu)=\int_0^{\mu}\mathcal{G}'(\bar{\mu})d\bar{\mu} \tag{12}$$

the μ, ν correspondence is given by the shock wave solution

$$\mathcal{G}(\mu)=\frac{\int_0^{\nu}F_1(2\bar{\nu}M)\,d\bar{\nu}}{\frac{\kappa+1}{8}M^2\sqrt{\frac{M}{2}}F_1^2(2\nu M)} \tag{13}$$

This formula is valid for the bow shock from the tip of the body up to infinity. The above equation can be calculated by a simple iteration using a small computer within 35 steps in general. Defining the characteristic ν^* running into the shock at a distance μ

$$F_1(2\nu^*M)=\sqrt{\frac{\int_0^{\nu_n}F_1(2\bar{\nu}M)\,d\bar{\nu}}{\frac{\kappa+1}{8}M^2\sqrt{\frac{M}{2}}\mathcal{G}(\mu)}} \tag{14}$$

and replacing the Whitham F_1-function in equation (7) by

$$F_1(2\nu M)=\sqrt{\frac{\int_0^{\nu^*}F_1(2\bar{\nu}M)\,d\nu}{\frac{\kappa+1}{8}M^2\sqrt{\frac{M}{2}}\mathcal{G}(\mu)}} \tag{15}$$

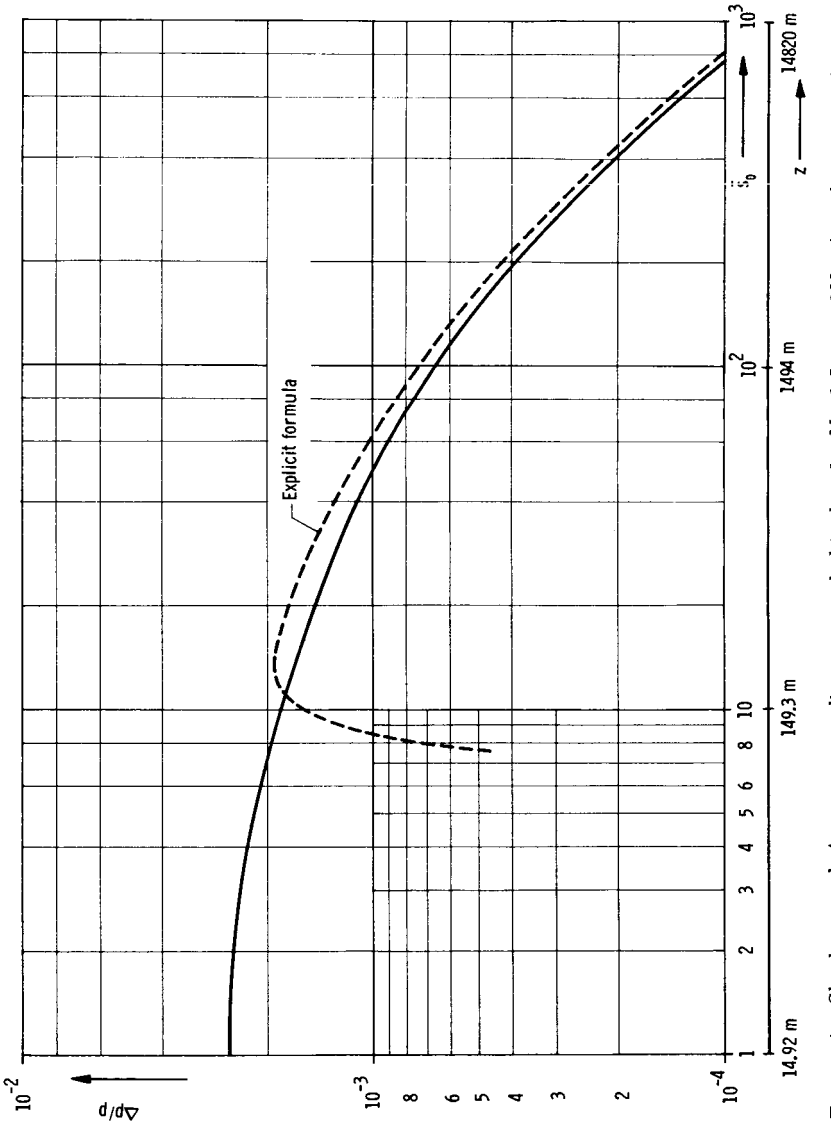

FIGURE 4.—Shock strength Δp versus ray distance s and altitude z for $M=1.5$, $c_{op}=300$ m/sec, $l=20$ m, and $\theta=0°$.

an explicit formula is obtained, ν_n being the neutral Mach line for which F_1 is zero. In figure 4 values are plotted for steady flight at $M=1.5$ below the aircraft at $\theta=0^0$ and $\zeta=0^0$. Δp is the pressure jump in the bow shock.

INFLUENCE OF NEAR-FIELD FLOW ON THE SONIC BOOM

Oswatitsch and Sun (ref. 10) calculated the sonic boom due to lift in the vertical plane of symmetry below a delta wing with supersonic leading edges and constant pressure distribution. They found that the bow shock is weakened at the distance y_a by a plane Prandtl-Meyer expansion centered in the trailing edge. For altitudes greater than y_a, the equivalent body of revolution cannot be applied. As is known, plane Prandtl-Meyer expansions do not change their intensity along the characteristics. This affects, for example, the differential equation for the bow shock in such a way that one term is weakened as $(\eta)^{-1}$ and not as $(\eta)^{-3/2}$, as one would obtain by applying the equivalent body of revolution. The shock terminates at a finite distance from the wing given by $\eta=2e^2y_a$.

APPROXIMATE METHOD TO CALCULATE THE SUPERSONIC FLOW AROUND AN ANNULAR WING

Wind-tunnel sonic boom signatures are always near-field signatures. The problem is to extrapolate the near-field signature to the far field. Rues calculated an annular wing in reference (9). He related the signature at the surface of an annular wing to a body at the axis by an integral equation of the Abel type. Then he calculated the inner and outer region of the surrounding supersonic flow. The author gives satisfying and accurate results if the radius of the wing is twice the length of the profile. Relating now the signature of the annular wing to a sonic boom wind-tunnel signature, the far field can be calculated.

REFERENCES

1. OSWATITSCH, K.: Die Wellenausbreitung in der Ebene bei kleinen Störungen. Arch. Mech. Stosowanej, vol. 14, 1962, pp. 621–637.
2. OSWATITSCH, K.: Das Ausbreiten von Wellen endlicher Amplitude. Z. Flugwiss., vol. 10, 1962, pp. 130–138.
3. SCHNEIDER, W.: Analytische Berechnung achsensymmetrischer Überschallströmungen mit Stössen. DVL-Bericht no. 275, 1963.
4. ROTHMANN, H.: Analytische Untersuchung der Ausbreitung von Kugel- und Zylinderwellen. DVL-Bericht no. 280, 1963.
5. SCHNEIDER, W.: Über die Ausbreitung des Mündungsknalles. DLR FB 67–50, 1967.
6. STUFF, R.: Analytische Berechnung von Verdichtungsstössen beschleunigter oder verzögerter Rotationskörper. DLR FB 68–62, 1968.
7. STUFF, R.: Knall und Widerstand eines spitzen Rotationskörpers. Z. Angew. Math. Phys., vol. 21, 1970, pp. 940–946.

8. OSWATITSCH, K.: Analytische Berechnung von Charakteristikenflächen bei Strömungsvorgängen. DLR FB 65–62, 1965.
9. RUES, D.: Eine Näherungsmethode für die Berechnung von Überschallströmungen um Ringflügel. Z. Flugwiss., vol. 18, 1970, pp. 70–73.
10. OSWATITSCH, K.; AND SUN, E. Y. C.: The Influence of Near-Field Flow on the Sonic Boom. ICAS Paper no. 70–20, 1970.
11. STUFF, R.: Closed Form Solution for the Sonic Boom in a Polytropic Atmosphere. To be published.
12. STUFF, R.: Die Theorie der Knallausbreitung in einer geschichteten Atmosphäre. Z. Flugwiss., vol. 17, 1969, pp. 156–164.

Pressure Signature Estimation at High Mach Numbers

FRANK A. WOODWARD
Aerophysics Research Corp.

Recent experimental data indicate that the Whitham theory fails to give acceptable estimates of near-field pressure signatures at high Mach numbers. This failure of the theory is particularly noticeable for non-slender configurations; for example, bodies that occupy a substantial fraction of the Mach cone from the nose and for supersonic leading edge wings at incidence. In these examples, the theory tends to underestimate the magnitude of the front shock wave and the rate of expansion of the pressure between the front and rear shocks. These effects are most pronounced in the extreme near field; that is, within five body lengths from the configuration and for Mach numbers greater than 2.

The principal reason for the failure of the Whitham theory to correctly predict the pressure signatures in the near field is the underlying assumption that the configuration is sufficiently slender that it can be represented by a line source distribution with strength proportional to the area of the equivalent body of revolution in each azimuthal plane. This slender-body theory assumption immediately implies a three-dimensional wave pattern in which the incremental pressure varies inversely as the square root of the distance from the body axis. On a given characteristic line originating at $x=x_0$ on the body axis,

$$\frac{\Delta p}{p}=-\gamma M^2 u=\gamma M^2 \frac{F(x_0)}{\sqrt{2\beta r}} \tag{1}$$

where $F(x_0)$ is Whitham's F-function, which depends only on the area distribution of the equivalent body. Using this approximate form for the pressure distribution in the field, the equations of the characteristic lines are given by

$$x=x_0+\beta r+\frac{\gamma+1}{2}\frac{M^4}{\beta}\int_0^r u(x_0, r)\, dr$$

$$=x_0+\beta r-\frac{\gamma+1}{\sqrt{2}}\frac{M^4}{\beta^{3/2}}F(x_0)\sqrt{r} \tag{2}$$

If the body is not slender but still lies within the Mach cone from the nose, linear theory may be applied to calculate the incremental pressure at any point in the field. In this case, the axial perturbation velocity u is a more complex function of x_0 and r than given by equation (1) and, in particular, cannot be expressed simply as a product of a function of x_0 and r except in the limit of very small values of the ratio x_0/r. In the linear theory approximation, the pressure distribution along a given characteristic line follows a smooth continuous variation from the surface pressure value to the Whitham value at large radial distance. Most importantly, the linear theory pressure increment is always less than that given by equation (1) for all values of r. Thus, the Mach line displacement is always less than that predicted by the Whitham theory, with the greatest differences occurring in the extreme near field in substantial agreement with the experimental evidence.

To compare linear theory pressure signatures with the Whitham theory, it is necessary to evaluate the integrals appearing in equation (2) for each of the singularity distributions used in the aerodynamic representation. In the present study, performed under contract for NASA Ames Research Center and reported in reference 1, the body is represented by a system of line sources and doublets located along the configuration axis, and the wing is represented by source and vortex distributions located on panels in the plane of the wing. Interference effects between the wing and body are accounted for by additional vortex panels on the body surface aft of the wing leading edge.

It is found that the body line source and doublet distributions rapidly approach the asymptotic form of the Whitham theory. The planar source and vortex distributions used to represent the wing converge less rapidly and show substantial differences with the Whitham theory in the near field. Considerable difficulty has been experienced in interpreting the new theoretical results, particularly for low-aspect-ratio wings with supersonic leading edges. The interaction of three-dimensional flow regions from the wingtips with the two-dimensional flow region behind the supersonic leading edge is not treated in a satisfactory manner by the present computer program and seriously limits the application of the method in general. In spite of this limitation, two examples are presented here to illustrate the effect of Mach number on the near-field pressure signatures of a cone-cylinder and delta-wing-body combination.

In the first example (fig. 1), the pressure signatures calculated for a 7.5° half-angle cone-cylinder model mounted on a tapered sting are compared with experimental data for Mach numbers between 2 and 5.5. The pressure signatures are calculated by linear theory and by the asymptotic or Whitham theory using the same source distribution to represent the body in each case for a given Mach number. Two distinct wave patterns are apparent in the theoretical signatures. The initial wave pattern

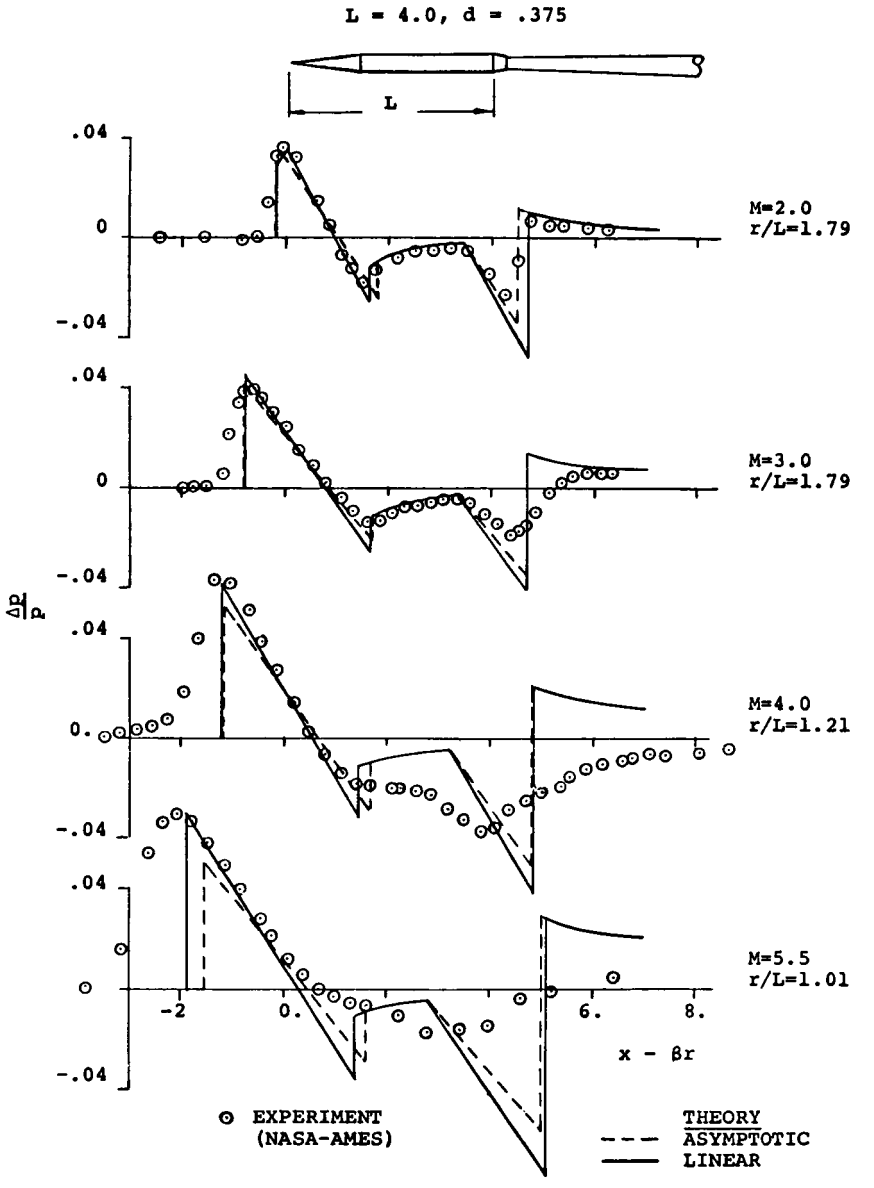

FIGURE 1.—Effect of Mach number on the near-field pressure signatures of a cone-cylinder combination.

is produced by the cone and the corner expansion fan and forms an incomplete N-wave followed by a gradual recompression associated with the cylindrical section ahead of the base. In this region, the linear theory provides a better estimate of the magnitude of the front shock wave and the rate of flow expansion immediately behind it than the

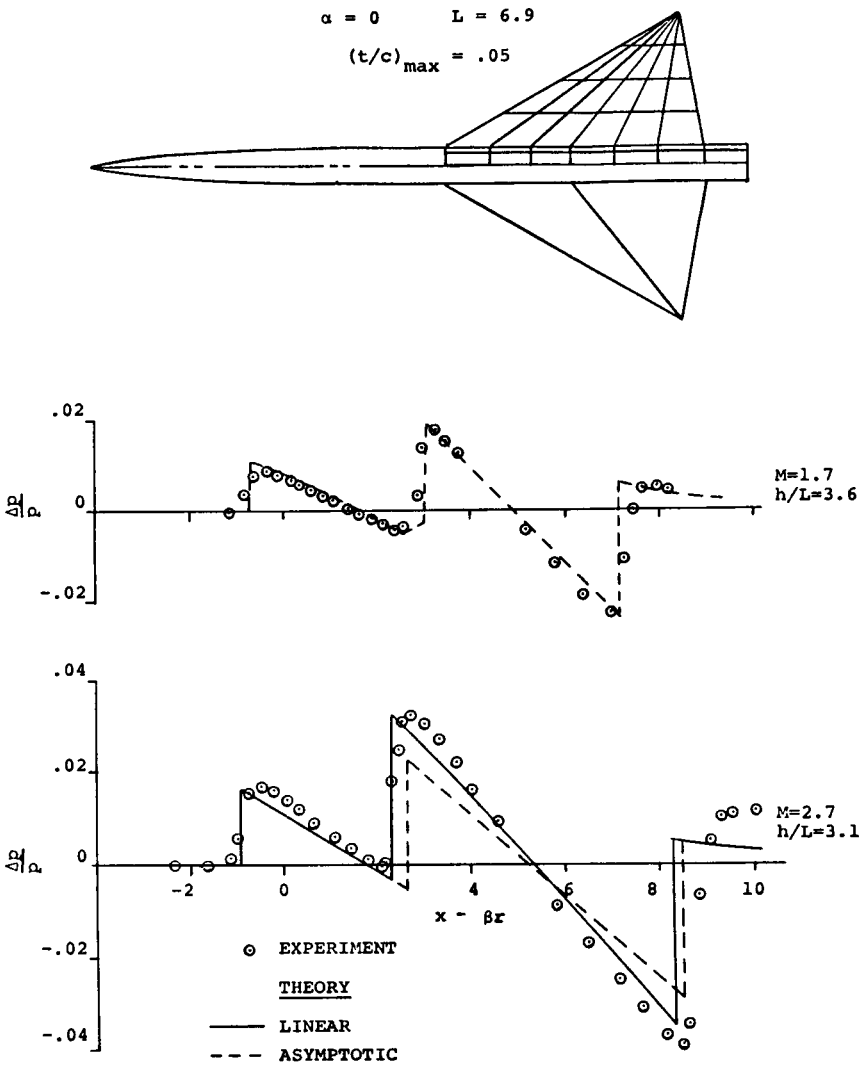

FIGURE 2.—Effect of Mach number on the near-field pressure signatures of a delta-wing-body combination.

asymptotic theory over the entire Mach number range. The rounding of the experimental pressure signature is believed to be due to model vibration. The higher the Mach number, the broader the rounded signature becomes because of the extremely oblique angle the front shock makes with the pressure probe. It is apparent from this comparison that either theoretical method would be acceptable for predicting the pressure signature up to $M = 3.0$ but that the linear theory gives a definite improvement at the higher Mach numbers.

The second wave pattern consists of an expansion fan from the base the cylinder followed by a shock wave produced by the tapered sting. e base of the body is represented by a 12° cone frustum ahead of the ig and generates a substantial linear pressure gradient followed by a ong shock wave in all the theoretical pressure signatures. This flow tern is not observed experimentally except at the lowest Mach num- s and suggests an alternate base representation having less severe ansion may be more appropriate at the higher Mach numbers.

The second example (fig. 2) compares the pressure signatures calcu- d at zero lift for a 59° sweep delta-wing-body combination with ex- imental data at two Mach numbers. The wing has a 5-percent-thick ible-wedge section and is centrally mounted on the body. The wave tern produced by the long slender parabolic nose is effectively sepa- ed from the wing wave pattern in these examples, which helps simplify interpretation of the results.

At $M = 1.7$, the wing has a subsonic leading edge. The pressure sig- ure is calculated only by the asymptotic form of the theory at this ch number and can be seen to agree well with the experimental nts. At $M = 2.7$, the wing has a supersonic leading edge, and the mptotic theory now falls well below the experimental data in that t of the signature generated by the wing. The linear theory calculation this configuration neglects body panel interference effects but shows reciable improvement in correlation with experiments in the wing ion. Further development of the computer program is required to ude all near-field effects in the pressure signatures of wing-body binations at high Mach numbers, but these examples illustrate the ential improvement of the linear theory approach.

REFERENCE

WOODWARD, F. A.: The Calculation of Pressure Signatures in the Near and Far Field Around Supersonic Wing-Body Combinations. To be published as NASA CR.

U.S. GOVERNMENT PRINTING OFFICE : 1971 OL—420-093